UNIVERSITY OF HAWAII
LIBRARY

APPLIED
SCIENTIFIC RESEARCH
B. ELECTROPHYSICS, ACOUSTICS, OPTICS, MATHEMATICAL METHODS

Governing Board:

Prof. ir. J. J. Broeze, Delft.
Prof. dr D. van Dantzig, Amsterdam.
Prof. dr H. B. Dorgelo, Eindhoven.
Ir Z. Th. Fetter, Den Haag.
Dr G. H. Reman, Amsterdam.
Prof. ir J. T. Thijsse, Delft.

Editorial Board:

Prof. dr R. Kronig, Delft (General Editor).
Prof. dr ir C. B. Biezeno, Delft.
Prof. dr L. J. F. Broer, Delft.
Dr W. de Groot, Eindhoven.
Prof. dr ir A. van Wijngaarden, Amsterdam.

National Editors:

Prof. dr G. Borelius, Stockholm, for Sweden.
Prof. dr D. R. Hartree, F. R. S., Cambridge, for England
Prof. dr A. van Itterbeek, Louvain, for Belgium.
Prof. J. Rybner, Copenhagen, for Denmark.
Prof. dr M. J. O. Strutt, Zürich, for Switzerland.
Prof. dr S. Westin, Trondheim, for Norway.

Articles should be sent to *the Secretary*, ir H. G. de Winter, Laboratorium voor Technische Physica, Mijnbouwplein 11, Delft.

N.V. VAN DE GARDE & CO'S DRUKKERIJ, ZALTBOMMEL

APPLIED SCIENTIFIC RESEARCH

ELECTROPHYSICS, ACOUSTICS, OPTICS, MATHEMATICAL METHODS

Reports published under the auspices of

The Central National Council for Applied Scientific
Research in the Nederlands (T.N.O.)
The Nederlands Physical Society,
Section for Applied Physics
The Royal Institute of Engineers of the Netherlands,
Section for Technical Scientific Research
The Mathematical Centre, Amsterdam

*

VOLUME B VII

THE HAGUE
MARTINUS NIJHOFF
1959

Copyright 1959 by Martinus Nijhoff, The Hague, Netherlands
All rights reserved, including the right to translate or to
reproduce this book or parts thereof in any form

PRINTED IN THE NETHERLANDS

65-27544

QC1
A75
v.7

INDEX OF AUTHORS AND PAPERS

page

Benthem, C. W., On the possible influence of electron interaction on the reflectivity of metals 275

Berkhout, C. W., see Jongenburger, P.

Blok, Joh., R. H. Dekker and C. J. H. Lock, Increased atmospheric radioactivity in the Netherlands after the Windscale accident — *Letter to the Editor* 150

Boerboom, A. J. H., Theory of the aberrations in the focusing properties of a magnetic field with one plane of symmetry. 52

Bosma, H., Two capacitive windows in a rectangular wave guide. 131

Broer, L. J. F., A. Deeleman and J. A. Rietdijk, A simple method for photographing transparent objects 184

Bruin, F. and D. van Ladensteyn, The influence of modulation on the recording of resonance phenomena 270

Burg, F. A. W. van den, Transmission in a rectangular waveguide loaded with an arbitrary number of capacitive screens 153

Collins, J. G., The theory of the anomalous skin effect in metals for obliquely incident radiation 1

Corbey, M. M. G., see Kok, J. A.

Cosslett, V. E., The comparative merits of different methods of microradiography 338

Croissette, D. H. le, Measurements on halogen quenched counters 409

Deeleman, A., see Broer L. J. F.

Dekker, R. H., see Blok, Joh.

Dirksen, H. J., A diagram for the description of photoconductivity 400

Duuren, K. van and G. J. Sizoo, The gasdischarge mechanism for the argon-alcohol proportional counter 379

Florescu, N. A., On the measurement of speed of a vacuum pump. 63

Frank, V., Hall coefficient of technically pure metals from 80°K to 800°K . . . 41
Frank, V. and H. Højgaard Jensen, Note on the reciprocity theorem for electrical systems . . . 145
Gelder, A. P. van, A. M. de Graaf and R. Kronig, New calculations on the Faraday effect in wave guides . . . 441
Gerven, L. van, A. van Itterbeek and L. de Laet, Magnetic absorption phenomena in germanium at low temperatures . . . 345
Graaf, A. M. de, see Gelder, A. P. van
Højgaard Jensen, H., see Frank, V.
Hoop, A. T. de, On the plane wave extinction cross-section of an obstacle . . . 463
Itterbeek, A. van, R. Pollentier and W. Peelaers, Measurements on the magnetic susceptibilities of Ag-Mn and Cu-Mn alloys . . . 329
Itterbeek, A. van, see Gerven, A. van
Jackson, H. L. W., see Power, G.
Jongenburger, P. and C. W. Berkhout, A null-coil magnetometer . . . 366
Kok, J. A. and M. M. G. Corbey, Aspects of electrical breakdown of liquid insulating material I . . . 257
Kronig, R., see Gelder, A. P. van
Laet, L. de, see Gerven, L. van
Ladensteyn, D. van, see Bruin, F.
Lock, C. J. H., see Blok, Joh.
Mientka, W. E., see Wait, J. R.
Ong Sing Poen and J. B. le Poole, A focusing aid for the X-ray projection microscope . . . 233
Ong Sing Poen and J. B. le Poole, A critical comparison of projection microradiography and the 2 X method . . . 265
Ong Sing Poen and J. B. le Poole, Comments on V. E. Cosslett: The comparative merits of different methods of microradiography . . . 343
Peelaers, W., see Itterbeek, A. van
Poole, J. B. le, see Ong Sing Poen
Power, G. and H. L. W. Jackson, Certain two-dimensional solutions to Poisson's equation . . . 249
Rietdijk, J. A., see Broer, L. J. F.

SÆRMARK, K., Scattering of a plane monochromatic wave by a system of strips 417
SIEGEL, K. M., Far field scattering from bodies of revolution. 293
SIZOO, G. J., see DUUREN, K. VAN
SNIEDER, J., Ferromagnetic resonance in polycrystalline ferrites 185
TAI, C. T., The electromagnetic theory of the spherical Luneberg lens 113
THIELENS, G., New scintillators for the detection of thermal neutrons — *Letter to the editor* 87
WAIT, J. R., Induction by an oscillating magnetic dipole over a two layer ground. 73
WAIT, J. R., On the calculations of transverse current loss in buried wire ground systems 81
WAIT, J. R., On the theory of reflection from a wire grid parallel to an interface between homogeneous media II 355
WAIT, J. R. and W. E. MIENTKA, Calculated patterns of slotted elliptic-cylinder antennas 449
WOLFF, P. M. DE, Particle statistics in X-ray diffractometry. I. General theory 102
WOODS, L. C., Some generalizations of the Schwarz-Christoffel mapping formula 89
YOUNG, F. J., Equivalent base resistance of point-contact transistors 361
YOUNG, F. J., *Erratum* — Equivalent base resistance of point-contact transistors 462

Appl. sci. Res.　　　Section B, Vol. 7

THE THEORY OF THE ANOMALOUS SKIN EFFECT IN METALS FOR OBLIQUELY INCIDENT RADIATION

by J. G. COLLINS *)

Department of Physics, University of Western Australia, Nedlands, Western Australia

Summary

The problem of the anomalous skin effect in metals is studied theoretically for the case of obliquely incident radiation. It is shown that at upper visible and ultra-violet frequencies, the effective surface impedance of a metal varies with the direction of polarization of the incident radiation. Differences are of the same order of magnitude as terms arising from the displacement current. As a result, formulae for refractive indices, reflectivities and the principal angles at oblique incidence must be rederived in terms of *two* surface impedances. By a generalization of Dingle's method [1]), expressions are obtained for the optical constants which are valid for all angles of incidence and for frequencies not lying within internal photoelectric absorption bands. Experimental results for the principal azimuth for silver are shown to be in closer agreement with the present theory than with either the Drude-Kronig theory or the theory of the anomalous skin effect assuming a single impedance. Suggestions are made to guide future experimental work in metal optics.

§ 1. *Introduction.*

1.1 The first satisfactory theory of the anomalous skin effect in metals for normally incident radiation was put forward by Reuter and Sondheimer [2]), using the general methods of the theory of metals together with the impedance concept of Schelkunoff [3]) [4]) and Kronig et al. [5]). In recent years their basic treatment has been subject to extensive addition and improvement (Dingle [1])[6])[7])[8])[9]); Holstein [10]); Wolfe [11]); Azbel and Kaganov [12]) [13]); Azbel [14]); Azbel and Kaner [15]); Ginzburg and Motulevich [16]) (review)), and has also been extended to the case of semi-conductors (Dingle [17]) [18])). The result has been a considerably greater concordance between theory and experiment in metal optics.

---

*) Present addres: St. John's College, Cambridge, England.

1.2 Anomalous skin effect for oblique incidence. In previous literature the theory of the anomalous skin effect in metals has not been investigated as thoroughly for oblique incidence as it has for normal incidence. Reuter and Sondheimer only examined the problem very briefly and (without detailing the proof) stated a value for the corresponding surface impedance in the form of an integral involving angular terms. After showing that these angular terms were comparable in magnitude with displacement terms and therefore negligible in the microwave and infra-red regions, they took over, unchanged, their *normal* incidence results for the surface impedance and applied them in *oblique* incidence formulae, e.g. those for the principal angles (§ 2). Although it is not made clear in their paper, it would appear that Reuter and Sondheimer only treated the particular case in which the electric vector **E** vibrates perpendicularly to the plane of incidence.

Since in general **E** has components both perpendicular and parallel to the plane of incidence, *two* possible polarizations of the wave must be considered for oblique incidence. Dingle [7]) noted that there would be a slightly different surface impedance for each polarization, but did not examine the matter in any detail. The present work has been undertaken to investigate these angular effects more thoroughly.

In taking account of the influence of the anomalous skin effect on optical constants, previous practice has been equivalent to translating known equations, expressed in terms of a refractive index, into surface impedance notation, and then using values of the surface impedance calculated for normal incidence. The resulting formulae make no distinction between refractive indices (or surface impedances) for the two different polarizations. It has therefore been found necessary to rederive expressions for the principal angle of incidence Θ, the principal azimuth Ψ, and the reflectivities $\mathscr{R}_s$ and $\mathscr{R}_p$, taking such distinctions explicitly into account.

1.3 The subsequent work is set out as follows: In § 2 general formulae in terms of two refractive indices are derived for reflection and absorption coefficients, and the principal angles. In § 3 the basic integro-differential equations for the electric field in the metal are set up, and in § 4 they are solved, using an extension of the method adopted by Dingle [1]). In §§ 5, 6 and 7, the solutions for the fields found in § 4 are applied to the formulae derived in

§ 2 to give final expressions for the surface impedances, refractive indices and reflectivities (§ 5), the principal angle of incidence (§ 6) and the principal azimuth (§ 7). Finally, in § 8, theoretical predictions are compared with some experimental results for silver, and suggestions are made to guide future experimental work.

§ 2. *General formulae for reflection and absorption coefficients, and the principal angles at oblique incidence.*

2.1 Electric vector perpendicular to the plane of incidence. Consider the electromagnetic wave $(E_x, 0, 0)$, $(0, H_y, H_z)$ incident at an angle θ on a metal, whose surface is in the x-y plane. The z-axis is directed normally into the metal and the x-axis normally into the page (see fig. 1). At the surface the wave is subject to the following boundary conditions:

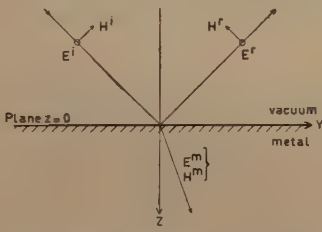

Fig. 1. Coordinate system and notation for incident and reflected field.

a) E_x continuous at $z = 0$ for all y,
b) H_y continuous at $z = 0$ for all y.
c) B_z continuous at $z = 0$ for all y.

It will be assumed throughout that the time-variation of all fields is of the form $e^{i\omega t}$, where ω is the circular frequency of the incident radiation. Further, since the boundary conditions must be satisfied for all values of y, all fields must have the same y-dependence on both sides of the boundary. In vacuo

$$\mathbf{E}, \mathbf{H} \propto \exp i\omega[t - (y \sin\theta + z\cos\theta)/c], \tag{2.1}$$

so that at $z = 0$

$$\mathbf{E}, \mathbf{H} \propto \exp i\omega[t - (y/c)\sin\theta] \tag{2.2}$$

on both sides of the bounding surface. For convenience the factor $\exp i\omega[t - (y/c)\sin\theta]$ in $\mathbf{E}$, $\mathbf{H}$, $\mathbf{J}$ etc. will be understood throughout the remainder of this investigation. From Maxwell's equations,

$$B_z = (c/i\omega)\partial E_x/\partial y = -E_x \sin\theta \tag{2.3}$$

in both vacuo and metal. Hence boundary condition *c*) reduces to boundary condition *a*).

The incident and reflected electric fields are of the form

$$\left.\begin{aligned} E_x^i(z) &= \exp[-\,i\omega(z/c)\cos\theta], \\ E_x^r(z) &= r_s \exp[i\omega(z/c)\cos\theta], \end{aligned}\right\} \tag{2.4}$$

where r_s is the amplitude reflection coefficient. The corresponding magnetic fields in the y-direction are

$$\left.\begin{aligned} H_y^i(z) &= \cos\theta.\exp[-\,i\omega(z/c)\cos\theta], \\ H_y^r(z) &= -\,r_s\cos\theta.\exp[i\omega(z/c)\cos\theta]. \end{aligned}\right\} \tag{2.5}$$

Boundary conditions *a*) and *b*) can now be written *)

$$1 + r_s = (E_x)^m_{z=0}, \quad (1 - r_s)\cos\theta = (H_y)^m_{z=0}, \tag{2.6}$$

so that

$$r_s = \frac{\cos\theta - (4\pi/c)Y_s}{\cos\theta + (4\pi/c)Y_s}, \tag{2.7}$$

where

$$(4\pi/c)Y_s = (H_y/E_x)^m_{z=0} = -\,(c/i\omega)\,(E_x'/E_x)^m_{z=0}, \tag{2.8}$$

primes denoting differentiation with respect to the depth z.

By analogy with the case of a dielectric medium, it is useful to express the reflection coefficient (2.7) in terms of a refractive index. In order to make a suitable choice consider first the form of (2.7) in the limit of the point relation $j(\mathbf{r}) \propto E(\mathbf{r})$, i.e. according to the Drude-Kronig theory. In this case the fields in the metal vary precisely exponentially with depth, and

$$E_x^m(z) \propto \exp[-\,i\omega\mathbf{n}(z/c)\cos\boldsymbol{\varphi}], \tag{2.9}$$

where $\mathbf{n}$, the single complex refractive index, $\boldsymbol{\varphi}$, the complex angle of refraction, and θ, the angle of incidence, are linked by Snell's Law **)

$$\sin\theta = \mathbf{n}\sin\boldsymbol{\varphi}. \tag{2.10}$$

---

*) The superscript m denotes fields within the metal (see fig. 1).

**) Snell's Law follows from the equality of the y-dependences of the incident and refracted waves, so that

$$\exp[-i\omega(y/c)\sin\theta] = \exp[-\,i\omega\mathbf{n}(y/c)\sin\boldsymbol{\varphi}],$$

i.e.

$$\sin\theta = \mathbf{n}\sin\boldsymbol{\varphi},$$

where $\mathbf{n}$ is independent of θ and the depth.

Eliminating $\boldsymbol{\varphi}$ from (2.9) by Snell's Law,

$$(4\pi/c)Y_s = -(c/i\omega)\,(E'_x/E_x)^m_{z=0} = (\mathbf{n}^2 - \sin^2\theta)^{\frac{1}{2}}. \qquad (2.11)$$

Thus an appropriate generalization is

$$\mathbf{n}_s(\theta) = \{[(4\pi/c)Y_s]^2 + \sin^2\theta\}^{\frac{1}{2}}. \qquad (2.12)$$

The reflection coefficient r_s can then be expressed in the form

$$r_s = \frac{\cos\theta - (\mathbf{n}_s^2 - \sin^2\theta)^{\frac{1}{2}}}{\cos\theta + (\mathbf{n}_s^2 - \sin^2\theta)^{\frac{1}{2}}}, \qquad (2.13)$$

which is a well known result apart from the subscript to $\mathbf{n}$.

2.2 Electric vector parallel to the plane of incidence. Consider now the electromagnetic wave $(0, E_y, E_z)$, $(H_x, 0, 0)$ incident on a metallic surface at an angle θ. The wave is subject to the following boundary conditions:

a) H_x continuous at $z = 0$ for all y,
b) E_y continuous at $z = 0$ for all y,
c) J_z continuous at $z = 0$ for all y,

where $\mathbf{J}$ is the *total* current density. From Maxwell's equations

$$c \operatorname{curl} \mathbf{E} = -i\omega\mathbf{H}, \quad c \operatorname{curl} \mathbf{H} = i\omega\mathbf{D} + 4\pi\mathbf{j} = 4\pi\mathbf{J}, \qquad (2.14)$$

where $\mathbf{D}$ is the electric displacement and $\mathbf{j}$ the free-electron current density; it follows by elimination of $\mathbf{H}$ that

$$\nabla^2\mathbf{E} = 4\pi i\omega\mathbf{J}/c^2, \qquad (2.15)$$

so that boundary condition *c*) can be replaced by the equivalent condition

c') $\nabla^2 E_z$ continuous at $z = 0$ for all y.

Again taking the factor $\exp i\omega[t - (y/c)\sin\theta]$ as understood, the incident and reflected electric and magnetic fields are of the form

$$\left.\begin{aligned}
E_y^i(z) &= \cos\theta\,.\exp[-i\omega(z/c)\cos\theta],\\
E_y^r(z) &= -r_p\cos\theta\,.\exp[i\omega(z/c)\cos\theta],\\
E_z^i(z) &= -\sin\theta\,.\exp[-i\omega(z/c)\cos\theta],\\
E_z^r(z) &= -r_p\sin\theta\,.\exp[i\omega(z/c)\cos\theta],\\
H_x^i(z) &= -\exp[-i\omega(z/c)\cos\theta],\\
H_x^r(z) &= -r_p\,.\exp[i\omega(z/c)\cos\theta],
\end{aligned}\right\} \qquad (2.16)$$

where r_p is the amplitude reflection coefficient for the fields. Substituting in the boundary conditions *a*), *b*) and *c'*),

$$\left.\begin{aligned} 1 + r_p &= -(H_x)^m_{z=0}, \\ (1 - r_p)\cos\theta &= (E_y)^m_{z=0}, \\ (1 + r_p)\omega^2 \sin\theta &= c^2(\nabla^2 E_z)^m_{z=0}. \end{aligned}\right\} \tag{2.17}$$

These three equations, together with Maxwell's equation

$$H_x = -(c/i\omega)\,(\partial E_z/\partial y - \partial E_y/\partial z) = (c/i\omega)E_y' + E_z \sin\theta, \tag{2.18}$$

can be solved to yield

$$r_p = \frac{(4\pi/c)Y_p\cos\theta - 1}{(4\pi/c)Y_p\cos\theta + 1}, \tag{2.19}$$

where

$$\begin{aligned}(4\pi/c)Y_p &= -(c/i\omega)\,(E_y'/E_y)^m_{z=0}[1 + (\omega^2/c^2)\sin^2\theta\,.\,(E_z/\nabla^2 E_z)^m_{z=0}]^{-1} \\ &= -(c/i\omega)\,(E_y'/E_y)^m_{z=0}[1 - (\omega^2/c^2)\sin^2\theta\,.\,(E_z/E_z'')^m_{z=0}]. \end{aligned} \tag{2.20}$$

As in § 2.1, in order to define a suitable refractive index $\mathbf{n}_p$ in terms of which to express the reflection coefficient r_p, it is instructive to evaluate Y_p in the point-relation limit $j(\mathbf{r}) \propto E(\mathbf{r})$. Under these conditions

$$E_y^m(z) \propto \exp[-i\omega\mathbf{n}(z/c)\cos\boldsymbol{\varphi}] = \exp[-i\omega(z/c)\,(\mathbf{n}^2 - \sin^2\theta)^{\frac{1}{2}}]. \tag{2.21}$$

Substituting for $(E_y'/E_y)^m_{z=0}$ and $(E_z/E_z'')^m_{z=0}$ in (2.20),

$$(4\pi/c)Y_p = \mathbf{n}^2(\mathbf{n}^2 - \sin^2\theta)^{-\frac{1}{2}}. \tag{2.22}$$

A generalized refractive index $\mathbf{n}_p(\theta)$ could be defined by replacing $\mathbf{n}$ by $\mathbf{n}_p$ in (2.22). However, as this leads to an awkward expression for $\mathbf{n}_p$ in terms of Y_p, it is more convenient to take the *product* of (2.22) and (2.11)

$$(4\pi/c)^2 Y_s Y_p = \mathbf{n}^2, \tag{2.23}$$

and replace $\mathbf{n}$ by the generalized index $\mathbf{n}_p(\theta)$. Thus

$$(4\pi/c)\,(Y_s Y_p)^{\frac{1}{2}} = \mathbf{n}_p(\theta), \tag{2.24}$$

so that

$$(4\pi/c)Y_p = \mathbf{n}_p^2(\mathbf{n}_s^2 - \sin^2\theta)^{-\frac{1}{2}}. \tag{2.25}$$

The reflection coefficient r_p can now be expressed in refractive index notation as

$$r_p = \frac{\mathbf{n}_p^2\cos\theta - (\mathbf{n}_s^2 - \sin^2\theta)^{\frac{1}{2}}}{\mathbf{n}_p^2\cos\theta + (\mathbf{n}_s^2 - \sin^2\theta)^{\frac{1}{2}}}, \tag{2.26}$$

which is once again a well known result apart from the subscripts to the $\mathbf{n}$'s.

2.3 The reflectivity and absorptivity of a metal. The reflectivity $\mathscr{R}$ of a metallic surface is defined as

$$\mathscr{R} = |r|^2, \tag{2.27}$$

and represents the fraction of the energy incident on the surface which is reflected. The corresponding absorptivity $\mathscr{A}$ is defined as

$$\mathscr{A} = 1 - \mathscr{R}. \tag{2.28}$$

By (2.13) and (2.26),

$$\mathscr{R}_s = \left| \frac{\cos\theta - (\mathbf{n}_s^2 - \sin^2\theta)^{\frac{1}{2}}}{\cos\theta + (\mathbf{n}_s^2 - \sin^2\theta)^{\frac{1}{2}}} \right|^2, \tag{2.29}$$

$$\mathscr{R}_p = \left| \frac{\mathbf{n}_p^2 \cos\theta - (\mathbf{n}_s^2 - \sin^2\theta)^{\frac{1}{2}}}{\mathbf{n}_p^2 \cos\theta + (\mathbf{n}_s^2 - \sin^2\theta)^{\frac{1}{2}}} \right|^2. \tag{2.30}$$

2.4 The principal angle of incidence Θ. Define

$$Pe^{i\Delta} = r_p/r_s, \tag{2.31}$$

so that Δ is the difference in phase shifts between the two polarizations after reflection from the metal. By combining (2.31) with (2.13) and (2.26), it follows that

$$\frac{1 + Pe^{i\Delta}}{1 - Pe^{i\Delta}} = \frac{r_s + r_p}{r_s - r_p} = \frac{\mathbf{n}_p^2 \cos^2\theta - (\mathbf{n}_s^2 - \sin^2\theta)}{\cos\theta\,.\,(1 - \mathbf{n}_p^2)\,(\mathbf{n}_s^2 - \sin^2\theta)^{\frac{1}{2}}}. \tag{2.32}$$

The principal angle of incidence Θ is defined as that value of the angle of incidence θ for which $\Delta = \frac{1}{2}\pi$, so that $e^{i\Delta} = i$. The reflected light is then elliptically polarized with the axes of the bounding ellipse at right angles. By setting $\Delta = \frac{1}{2}\pi$, and multiplying both sides of (2.32) by the conjugate complex quantities (denoted by an asterisk),

$$\begin{aligned} &\cos^2\Theta[(\mathbf{n}_s^2 - \sin^2\Theta)\,(\mathbf{n}_s^2 - \sin^2\Theta)^*]^{\frac{1}{2}} = \\ &= [\sin^2\Theta + (\mathbf{n}_p^2 - \mathbf{n}_s^2)/(1 - \mathbf{n}_p^2)]\,[\sin^2\Theta + (\mathbf{n}_p^2 - \mathbf{n}_s^2)/(1 - \mathbf{n}_p^2)]^*. \end{aligned} \tag{2.33}$$

In the limit of the point-relation, $\mathbf{n}_s = \mathbf{n}_p = \mathbf{n}$, and (2.33) reduces to

$$\cos^2\Theta\,.\,[(\mathbf{n}^2 - \sin^2\Theta)\,(\mathbf{n}^2 - \sin^2\Theta)^*]^{\frac{1}{2}} = \sin^4\Theta, \tag{2.34}$$

which is the generally accepted equation for the principal angle (c.f. Born [19]), p. 263).

2.5 The principal azimuth Ψ. The azimuth angle ψ is defined by the equation

$$\tan\psi = P = |r_p/r_s|. \tag{2.35}$$

Writing (2.32) as

$$\frac{1 - Pe^{i\Delta}}{1 + Pe^{i\Delta}} \cdot \frac{1 + Pe^{-i\Delta}}{1 + Pe^{-i\Delta}} = \frac{\cos\theta\,.\,(1 - \mathbf{n}_p^2)\,(\mathbf{n}_s^2 - \sin^2\theta)^{\frac{1}{2}}}{\mathbf{n}_p^2\cos^2\theta - (\mathbf{n}_s^2 - \sin^2\theta)}, \qquad (2.36)$$

multiplying out the left hand side of (2.36), and using (2.35), it is found that

$$\frac{\cos 2\psi - i\sin 2\psi\sin\Delta}{1 + \sin 2\psi\cos\Delta} = \frac{\cos\theta\,.\,(1 - \mathbf{n}_p^2)\,(\mathbf{n}_s^2 - \sin^2\theta)^{\frac{1}{2}}}{\mathbf{n}_p^2\cos^2\theta - (\mathbf{n}_s^2 - \sin^2\theta)}. \qquad (2.37)$$

The principal azimuth Ψ is defined as that value of the azimuth ψ for $\theta = \Theta$, $\Delta = \frac{1}{2}\pi$. For this value of Δ, (2.37) reduces to

$$\cos 2\Psi - i\sin 2\Psi = \frac{\cos\Theta\,.\,(\mathbf{n}_s^2 - \sin^2\Theta)^{\frac{1}{2}}}{\sin^2\Theta + (\mathbf{n}_p^2 - \mathbf{n}_s^2)/(1 - \mathbf{n}_p^2)}, \qquad (2.38)$$

i.e.

$$\tan 2\Psi = -\operatorname{Im}(\Xi)/\operatorname{Re}(\Xi), \qquad (2.39)$$

where Im denotes the imaginary part and Re the real part of Ξ, and

$$\Xi = \frac{\cos\Theta(\mathbf{n}_s^2 - \sin^2\Theta)^{\frac{1}{2}}}{\sin^2\Theta + (\mathbf{n}_p^2 - \mathbf{n}_s^2)\,/(1 - \mathbf{n}_p^2)}. \qquad (2.40)$$

In the limit of the point-relation, $\mathbf{n}_p = \mathbf{n}_s = \mathbf{n}$. Then

$$\Xi = \cos\Theta\,.\,\mathrm{cosec}^2\,\Theta\,.\,(\mathbf{n}^2 - \sin^2\Theta)^{\frac{1}{2}}, \qquad (2.41)$$

and (2.39) reduces to the standard formula for the principal azimuth (see, for example, Dingle 7), p. 343).

§ 3. *Derivation of the basic integro-differential equations.*

3.1 In this section, the basic integro-differential equations are derived for the electric field produced in the surface of a metal when the surface is irradiated with obliquely incident electromagnetic waves. In effect the problem reduces to that of finding a fundamental relation between the free-electron current density **j** and the electric field **E**. Substitution of this relation in (3.4) then gives the integro-differential equation to be solved for the electric field. There are two approaches to this problem:

a) Solution of the Boltzmann transport equation,

b) The pictorial kinetic method (e.g. Dingle 20)).

Here (*a*) alone is used; (*b*) yields identical results.

3.11 The following assumptions are made:

a) The thickness of the metal is very much greater than the penetration depth of the radiation.

b) The conduction electrons are regarded as quasi-free, i.e. their energy is taken as proportional to the square of their wave vector.

c) Contributions to the current density due to transitions between different energy bands in the metal, i.e. internal photoelectric effects, are not considered.

d) Following previous literature (Pippard [21]) [22]), Reuter and Sondheimer [2]), Dingle [1]) [7–9])), it is assumed that electron reflection at the inside surface of the metal can be expressed in terms of a parameter p, the fraction of electrons incident at the surface which undergoes specular reflection.

e) Collision phenomena in the metal can be described in terms of a mean free path l (or the equivalent time of relaxation τ). Strictly this assumption is only tenable in the limiting cases of very low and very high temperatures. At low temperatures electron scattering is due primarily to residual impurity atoms in the metal, and this can always be described in terms of a free path. Similarly a free path can always be defined for scattering by thermal lattice vibrations, if the temperature is above the Debye temperature. However for this investigation it may reasonably be assumed that a free path can be defined at all temperatures. It is interesting to note that in a recent paper Azbel and Kaner [15]) show that, for the case of normal incidence for $p = 0$ and $p = 1$, the use of an arbitrary collision integral to replace the relaxation time τ leads to the same values for the surface impedance of a metal as were obtained by Reuter and Sondheimer.

f) The magnetic permeability μ of ferro-magnetic materials is unity at optical frequencies (Rado et al. [23])).

3.2 Consider a semi-infinite metal with its surface in the x-y plane and the positive z-axis directed normally into the metal. The incident radiation (**E**, **H**) strikes the surface at an angle of incidence θ (see fig. 1).

In vacuo the propagation equation $\nabla^2\mathbf{E} + (\omega^2/c^2)\mathbf{E} = 0$ has solutions

$$\begin{aligned} \mathbf{E}^i &\propto \exp[-\,i\omega(y \sin\theta + z\cos\theta)/c], \\ \mathbf{E}^r &\propto \exp[-\,i\omega(y \sin\theta - z\cos\theta)/c], \end{aligned} \tag{3.1}$$

for the incident and reflected fields respectively. Within the metal the propagation equation is

$$\nabla^2\mathbf{E} + (\omega^2\varepsilon/c^2)\mathbf{E} = 4\pi i\omega\mathbf{j}/c^2, \tag{3.2}$$

where

$$\varepsilon = 1 + 4\pi \mathbf{P}_{ph}/\mathbf{E} + 4\pi \mathbf{P}_{core}/\mathbf{E}, \tag{3.3}$$

(see Dingle [7]), § 4). Here **P** is the electric polarization intensity and **j** is the free-electron contribution to the current density. Since the fields are independent of x, and the y-dependence is known (§ 2.1), the ∇^2-operator can be simplified, and (3.2) reduces to

$$(\partial^2/\partial z^2 - W^2\eta')\mathbf{E} = 4\pi i\omega \mathbf{j}/c^2, \tag{3.4}$$

where

$$W^2\eta' = -(\omega^2/c^2)\,(\varepsilon - \sin^2\theta). \tag{3.5}$$

3.21 The argument used here to obtain the **j** - **E** relation is identical with that employed by Reuter and Sondheimer for normal incidence, except for the addition of angular terms. The electron distribution function f in the presence of the electric field **E** can be written as

$$f(\mathbf{v}, \mathbf{r}, t) = f_0(\mathbf{v}) + f_1(\mathbf{v}, \mathbf{r})e^{i\omega t}, \tag{3.6}$$

where **v** is the electron velocity, **r** the electron position vector, $f_0(\mathbf{v})$ the equilibrium distribution function and $f_1(\mathbf{v}, \mathbf{r})$ an unknown function of **v** and **r** representing a small variation in f from the equilibrium value. Under the present conditions the Boltzmann equation (Wilson [24]), p. 196) reduces to

$$\frac{\partial f_1}{\partial z} + \frac{f_1}{\tau v_z}\left[1 + i\omega\tau\left(1 - \frac{v_y}{c}\sin\theta\right)\right] = \frac{e}{mv_z}\,\mathbf{E}.\nabla_{\mathbf{v}} f_0. \tag{3.7}$$

This equation differs in two respects from that of Reuter and Sondheimer (ref. [2]), eq. 5), in that

a) since all three components of the electric field must be considered, the term $(\partial f_0/\partial v_x)\,E_x(z)$ of Reuter and Sondheimer must be generalized to $\mathbf{E}.\nabla_{\mathbf{v}} f_0$,

b) there is an additional term $v_y(\partial f_1/\partial y) = -(f_1/\tau v_z)i\omega\tau(v_y/c)\sin\theta$ in (3.7) due to the y-variation of f_1.

The solution of (3.7) can be written down immediately by analogy with the case of normal incidence. Defining f_1^+ as the distribution function for electrons moving away from the surface, i.e. $v_z > 0$, and f_1^- as the distribution function for electrons moving towards the surface, i.e. $v_z < 0$, it follows from equations (11) and (12) of Reuter and Sondheimer that

$$f_1^+ = \frac{e}{mv_z}\int_0^z \mathrm{d}t\,.\exp\left[\frac{-\chi(z-t)}{\tau v_z}\right]\mathbf{E}\,.\nabla_{\mathbf{v}}\,f_0 + \frac{e}{mv_z}\,p\int_0^\infty \mathrm{d}t\,.\exp\left[\frac{-\chi(z+t)}{\tau v_z}\right]\mathbf{E}\,.\nabla_{\mathbf{v}}\,f_0, \tag{3.8}$$

$$f_1^- = \frac{-e}{mv_z}\int_z^\infty \mathrm{d}t\,.\exp\left[\frac{-\chi(z-t)}{\tau v_z}\right]\mathbf{E}\,.\nabla_{\mathbf{v}}f_0, \tag{3.9}$$

where

$$\chi = 1 + i\omega\tau[1 - (v_y/c)\sin\theta]. \tag{3.10}$$

3.22 The electron current density $\mathbf{j}$ can now be calculated from the usual formula

$$j_k = -2em^3h^{-3}\int v_k f\,\mathrm{d}^3v, \tag{3.11}$$

where $k = x, y$ or z, and e is taken with positive sign. This expression for $\mathbf{j}$ can be more easily handled in spherical polar coordinates (v, β, γ) in v-space. Therefore set

$$v_x = v\sin\beta\cos\gamma,\quad v_y = v\sin\beta\sin\gamma,\quad v_z = v\cos\beta, \tag{3.12}$$

so that

$$j_k = -2em^3h^{-3}\int_0^\infty \mathrm{d}v\int_0^{\frac{1}{2}\pi}\mathrm{d}\beta\int_0^{2\pi}\mathrm{d}\gamma\,.\,v^2\sin\beta\,.\,v_k f_1^+ - 2em^3h^{-3}\int_0^\infty \mathrm{d}v\int_{\frac{1}{2}\pi}^{\pi}\mathrm{d}\beta\int_0^{2\pi}\mathrm{d}\gamma\,.\,v^2\sin\beta\,.\,v_k f_1^-. \tag{3.13}$$

The evaluation of the dependence of each component of $\mathbf{j}$ on each of the field components E_x, E_y and E_z is quite straightforward but involves rather cumbersome expressions. Therefore the dependence of j_y on E_y only will be considered in detail (§ 3.221) to illustrate the method used; other results will be quoted.

3.221 If the relevant form $(k = y)$ of (3.13) is combined with the E_y-contributions to the distribution functions f_1^+ and f_1^- from (3.8) and (3.9), it is found that

$$j_y(z, E_y) = \frac{-2e^2m^2}{h^3}\int_0^\infty \mathrm{d}v\,.\,v^2(\partial f_0/\partial v)\int_0^{\frac{1}{2}\pi}\mathrm{d}\beta\,\frac{\sin^3\beta}{\cos\beta}\int_0^{2\pi}\mathrm{d}\gamma\,.\sin^2\gamma$$
$$\times\left\{\int_0^z \mathrm{d}t\,.\exp\left[\frac{-\chi(z-t)}{\tau v\cos\beta}\right].E_y(t) + p\int_0^\infty \mathrm{d}t\,.\exp\left[\frac{-\chi(z+t)}{\tau v\cos\beta}\right].E_y(t)\right\}$$

$$+\frac{2e^2m^2}{h^3}\int_0^\infty \mathrm{d}v\,.\,v^2(\partial f_0/\partial v)\int_{\frac{1}{2}\pi}^{\pi}\mathrm{d}\beta\,.\,\frac{\sin^3\beta}{\cos\beta}\int_0^{2\pi}\mathrm{d}\gamma\,.\sin^2\gamma$$

$$\times\int_z^\infty \mathrm{d}t\,.\exp\left[\frac{-\chi(z-t)}{\tau v\cos\beta}\right]E_y(t). \tag{3.14}$$

This can be immediately simplified by grouping all the integrations over β into the range 0 to $\frac{1}{2}\pi$, giving

$$j_y(z, E_y) = \frac{-2e^2m^2}{h^3}\int_0^\infty \mathrm{d}v\,.\,v^2(\partial f_0/\partial v)\int_0^{\frac{1}{2}\pi}\mathrm{d}\beta\,\frac{\sin^3\beta}{\cos\beta}\int_0^{2\pi}\mathrm{d}\gamma\,\sin^2\gamma$$

$$\times\int_0^\infty \mathrm{d}t\left\{p\exp\left[\frac{-\chi(z+t)}{\tau v\cos\beta}\right]+\exp\left[\frac{-\chi|z-t|}{\tau v\cos\beta}\right]\right\}E_y(t). \tag{3.15}$$

Assuming that the electrons form a highly degenerate system, the integration over v can be carried out by noting that

$$\int_0^\infty \mathrm{d}v\,.\,g(v)(\partial f_0/\partial v) \simeq -g(V), \tag{3.16}$$

where $g(v)$ is any relatively slowly varying function of v, and V is the velocity of electrons at the surface of the Fermi distribution. Therefore

$$j_y(z, E_y) = \frac{2e^2m^2V^2}{h^3}\int_0^{\frac{1}{2}\pi}\mathrm{d}\beta\,.\,\frac{\sin^3\beta}{\cos\beta}\int_0^{2\pi}\mathrm{d}\gamma\,.\sin^2\gamma\int_0^\infty \mathrm{d}t\,.\,E_y(t)$$

$$\times\left\{p\exp\left[\frac{-\chi(z+t)}{l\cos\beta}\right]+\exp\left[\frac{-\chi|z-t|}{l\cos\beta}\right]\right\}, \tag{3.17}$$

where $l = \tau V$ is the electronic mean free path at the surface of the Fermi distribution.

At this stage it proves convenient to alter the scale of depth from Gaussian units, i.e. cms., to units of the mean free path l. Therefore define

$$Z = z/l, \qquad T = t/l, \tag{3.18}$$

so that both Z and T are dimensionless measures of depth. The integration over γ in (3.17) can be taken as being over the range $-\frac{1}{2}\pi$ to $\frac{3}{2}\pi$ rather than from 0 to 2π. Since the function of γ to be integrated is symmetrical about $\gamma = \frac{1}{2}\pi$, (3.17) can be written

$$j_y(Z, E_y)/4e^2m^2V^2lh^{-3} = \int_0^{\frac{1}{2}\pi} \mathrm{d}\beta \,.\, \sin^3\beta \sec\beta \int_{-\frac{1}{2}\pi}^{\frac{1}{2}\pi} \mathrm{d}\gamma \,.\, \sin^2\gamma \int_0^{\infty} \mathrm{d}T \,.\, E_y(T)$$
$$\times \{p \exp[-\chi(Z+T)\sec\beta] + \exp[-\chi|Z-T|\sec\beta]\}. \quad (3.19)$$

At this juncture it is possible to integrate over γ by introducing Bessel functions, using the relation (Jahnke and Emde, p. 149)

$$J_n(\zeta) = (i^{-n}/2\pi) \int_0^{2\pi} \mathrm{d}\gamma \,.\, \exp(in\gamma) \,.\, \exp(i\zeta\cos\gamma).$$

However, as this makes later integration over T and β rather difficult, it is preferable instead to make the substitutions

$$r = \sin\gamma, \;\; s = \sec\beta, \;\; W = 1 + i\omega\tau, \quad (3.20)$$

which then give

$$j_y(Z, E_y)/4e^2m^2V^2lh^{-3} = \int_1^{\infty} \mathrm{d}s \,.\, (s^{-1} - s^{-3}) \int_{-1}^{1} \mathrm{d}r \,.\, r^2(1-r^2)^{-\frac{1}{2}} \int_0^{\infty} \mathrm{d}T \,.\, E_y(T)$$
$$\times \{p \exp[-\chi s(Z+T)] + \exp[-\chi s|Z-T|]\}, \quad (3.21)$$

where now

$$\chi = W[1 - \vartheta \sin\theta \,.\, rs^{-1}(s^2-1)^{\frac{1}{2}}], \;\; \vartheta = (i\omega\tau/W)\,(V/c). \quad (3.22)$$

Further simplification in writing can be effected by introducing the symbols

$$\hat{s} = s - \vartheta \sin\theta \,.\, r(s^2-1)^{\frac{1}{2}}, \quad (3.23)$$

$$K(Z, T) = p \exp[-W\hat{s}(Z+T)] + \exp[-W\hat{s}|Z-T|], \quad (3.24)$$

and the integral operators

$$S = \int_1^{\infty} \mathrm{d}s \,.\, (s^{-1} - s^{-3}) \ldots\ldots, \quad (3.25)$$

$$R = (2/\pi) \int_{-1}^{1} \mathrm{d}r \,.\, (1 - r^2)^{\frac{1}{2}} \ldots\ldots, \quad (3.26)$$

$$\tilde{R} = (2/\pi) \int_{-1}^{1} \mathrm{d}r \,.\, (1 - r^2)^{-\frac{1}{2}} \ldots\ldots \quad (3.27)$$

The current density contribution $j_y(Z, E_y)$ can now be expressed finally as

$$j_y(Z, E_y)/2\pi e^2m^2V^2lh^{-3} = S \,.\, (\tilde{R} - R) \int_0^{\infty} \mathrm{d}T \,.\, E_y(T) K(Z, T). \quad (3.28)$$

3.222 Similarly,

$$j_x(Z, \mathbf{E})/2\pi e^2m^2V^2lh^{-3} = S \,.\, R \int_0^{\infty} \mathrm{d}T \,.\, E_x(T) \,.\, K(Z, T), \quad (3.29)$$

$$j_y(Z, \mathbf{E})/2\pi e^2 m^2 V^2 l h^{-3} = S.(\tilde{R}-R).\int_0^\infty \mathrm{d}T.E_y(T).K(Z, T)$$
$$+\bar{S}.\bar{R}.\int_0^\infty \mathrm{d}T.E_z(T).\bar{K}(Z, T), \quad (3.30)$$

$$j_z(Z, \mathbf{E})/2\pi e^2 m^2 V^2 l h^{-3} = \tilde{S}.\tilde{R}.\int_0^\infty \mathrm{d}T.E_z(T)K(Z, T) +$$
$$+\bar{S}.\bar{R}.\int_0^\infty \mathrm{d}T.E_y(T).\bar{K}(Z, T), \quad (3.31)$$

where

$$\tilde{S} = \int_1^\infty \mathrm{d}s.s^{-3}\ldots\ldots, \quad (3.32)$$

$$\bar{S} = \int_1^\infty \mathrm{d}s.s^{-3}(s^2 - 1)^{\frac{1}{2}}\ldots\ldots, \quad (3.33)$$

$$\bar{R} = (2/\pi)\int_{-1}^1 \mathrm{d}r.r(1 - r^2)^{-\frac{1}{2}}\ldots\ldots \quad (3.34)$$

$$\bar{K}(Z, T) = p\, \exp[-W\hat{s}(Z + T)] \oplus \exp[-W\hat{s}|Z - T|], \quad (3.35)$$

and the symbol

$$\oplus = \frac{|Z - T|}{Z - T} = \begin{cases} +1, & Z > T \\ -1, & Z < T \end{cases}. \quad (3.36)$$

These expressions for the current density components show quite a significant departure from point-relation theory in that there is a 'cross' dependence of j_y and j_z on E_y and E_z. These 'cross' terms in (3.30) and (3.31) are identical in form and, as will be seen in § 4, are of order $0(V/c) \ll 1$ in comparison with the leading terms in each expression.

3.3 Integro-differential equations for the electric field components. It is now possible to combine the results of § 3.22 with the differential equation (3.4) to give the fundamental integro-differential equations for each of the field components E_x, E_y and E_z. They are:

a) E_x:

$$(\partial^2/\partial Z^2 - W^2\eta)E_x = i\alpha.S.R.\int_0^\infty \mathrm{d}T.E_x(T)K(Z, T), \quad (3.37)$$

b) E_y:

$$(\partial^2/\partial Z^2 - W^2\eta)E_y = i\alpha.S.(\tilde{R} - R)\int_0^\infty \mathrm{d}T.E_y(T)K(Z, T) +$$
$$+ i\alpha.\bar{S}.\bar{R}\int_0^\infty \mathrm{d}T.E_z(T)\bar{K}(Z, T), \quad (3.38)$$

c) E_z:

$$(\partial^2/\partial Z^2 - W^2\eta)E_z = i\alpha.\tilde{S}.\tilde{R}\int_0^\infty \mathrm{d}T.E_z(T).K(Z,T) +$$
$$+ i\alpha.\bar{S}.\bar{R}\int_0^\infty \mathrm{d}T.E_y(T).\bar{K}(Z,T), \quad (3.39)$$

where

$$\alpha = 8\pi^2 e^2 m^2 V^2 \omega l/c^2 h^3, \quad (3.40)$$

$$\eta = l\eta' = \vartheta^2(\varepsilon - \sin^2\theta). \quad (3.41)$$

§ 4. *Solution of the integro-differential equations.*

4.1 In this section the method of solution adopted by Dingle [1]) is extended to cover the more complicated case of oblique incidence. A detailed solution is obtained for E_y, but results only are given for E_x and E_z.

4.2 It is first necessary to expand the functions $K(Z, T)$ and $\bar{K}(Z, T)$ of § 3.3 as series in rising powers of

$$\vartheta \sin\theta = (i\omega\tau/W)\,(V/c)\sin\theta \ll 1. \quad (4.1)$$

From (3.24),

$$K(Z,T) = p\exp[-W\hat{s}(Z+T)] + \exp[-W\hat{s}|Z-T|], \quad (4.2)$$

where

$$\hat{s} = s - \lambda\vartheta\sin\theta, \quad \lambda = r(s^2-1)^{\frac{1}{2}}. \quad (4.3)$$

Expansion of the exponential terms in (4.2) gives

$$K(Z,T) = \sum_{n=0}^{\infty} \vartheta^n \sin^n\theta . K_n(Z,T), \quad (4.4)$$

where

$$n!K_n(Z,T) =$$
$$= (-\lambda W)^n[(Z+T)^n p\mathrm{e}^{-Ws(Z+T)} + |Z-T|^n \mathrm{e}^{-Ws|Z-T|}]. \quad (4.5)$$

Alternatively $K_n(Z, T)$ can be written in the form

$$n!K_n(Z,T) = (-\lambda\partial/\partial s)^n K_0(Z,T), \quad (4.6)$$

i.e. the complete function $K(Z, T)$ can be derived from the leading term $K_0(Z, T)$ by applying the operator $\exp(-\lambda\vartheta\sin\theta.\partial/\partial s)$. Thus

$$K(Z,T) = \exp(-\lambda\vartheta\sin\theta.\partial/\partial s).K_0(Z,T). \quad (4.7)$$

This is a most useful relation since $K_0(Z, T)$ is essentially the same function as the $k(x, y)$ of the normal incidence case (Dingle [1])). In fact $k(x, y) = S.K_0(Z, T)$. Similarly the function $\bar{K}(Z, T)$ can be expanded either as

$$\bar{K}(Z, T) = \sum_{n=0}^{\infty} \vartheta^n \sin^n \theta . \bar{K}_n(Z, T), \tag{4.8}$$

where

$$n!\bar{K}_n(Z, T) = \\ = (-\lambda W)^n [(Z + T)^n p e^{-Ws(Z+T)} \oplus |Z - T|^n e^{-Ws|Z-T|}], \tag{4.9}$$

or

$$\bar{K}(Z, T) = \exp(-\lambda\vartheta \sin \theta . \partial/\partial s) \bar{K}_0(Z, T). \tag{4.10}$$

4.3 Detailed solution for $E_y(Z)$. The basic integro-differential equation for $E_y(Z)$ is

$$(\partial^2/\partial Z^2 - W^2\eta) E_y(Z) = i\alpha . S . (\tilde{R} - R) . \int_0^\infty dT . E_y(T) . K(Z, T) \\ + i\alpha . \bar{S} . \bar{R} . \int_0^\infty dT . E_z(T) . \bar{K}(Z, T). \tag{4.11}$$

Substitution of the expansions for $K(Z, T)$ and $\bar{K}(Z, T)$ gives

$$(\partial^2/\partial Z^2 - W^2\eta) E_y(Z) = \\ = i\alpha . \sum_{n=0}^{\infty} \vartheta^n \sin^n \theta . S . (\tilde{R} - R) . \int_0^\infty dT . E_y(T) . K_n(Z, T) \\ + i\alpha . \sum_{n=0}^{\infty} \vartheta^n \sin^n \theta . \bar{S} . \bar{R} . \int_0^\infty dT . E_z(T) . \bar{K}_n(Z, T). \tag{4.12}$$

$$= i\alpha . S . (\tilde{R} - R) . [1 + \vartheta^2 \sin^2 \theta . (s^2 - 1) r^2 (\partial^2/\partial s^2)/2! + 0(\vartheta^4)] \\ \int_0^\infty dT . E_y(T) . K_0(Z, T) \\ + i\alpha . \bar{S} . \bar{R} . [\vartheta \sin \theta . (s^2 - 1)^{\frac{1}{2}} r (-\partial/\partial s) + 0(\vartheta^3)] \\ \int_0^\infty dT . E_z(T) . \bar{K}_0(Z, T). \tag{4.13}$$

Since $(\tilde{R} - R)$ is an even function of r, and $\bar{R}$ an odd function of r in the range $-1 \leq r \leq 1$, terms in $K(Z, T)$ which are *odd* functions of r, i.e. K_1, K_3, K_5 ..., and terms in $\bar{K}(Z, T)$ which are *even* functions of r, i.e. K_0, K_2, K_4 ..., are all zero after integration over r. Such terms have therefore been omitted in (4.13).

Since $K_0(Z, T)$ and $\bar{K}_0(Z, T)$ do not contain r, the integration over this variable in (4.13) can be carried out to give

$$(\partial^2/\partial Z^2 - W^2\eta) E_y(Z) = \\ i\alpha . S . [1 + 3\vartheta^2 \sin^2 \theta . (s^2 - 1) (\partial^2/\partial s^2)/8 + 0(\vartheta^4)] \\ \int_0^\infty dT . E_y(T) . K_0(Z, T) + i\alpha . \bar{S} . [\vartheta \sin \theta . (s^2 - 1)^{\frac{1}{2}} (-\partial/\partial s) + 0(\vartheta^3)] \\ \int_0^\infty dT . E_z(T) . \bar{K}_0(Z, T). \tag{4.14}$$

At this stage the value of E_z given by (4.32) must be inserted in (4.14). Since the E_z contribution to (4.14) is of order $0(\vartheta)$, it suffices here to take only the first approximation

$$E_z(Z) \propto \exp(-u_z W Z).$$

(If terms of order $0(\xi^2\vartheta)$ or higher are required in E_y, the leading anomalous term in E_z (4.33)

$$\xi \int_1^\infty \frac{\mathrm{d}s \,.\, \mathrm{e}^{-sWZ}}{s^2 - \eta} \,.\, I(s, u_z)$$

must be taken into account. However, since $\xi \sim 0(\vartheta^2)$ and $\vartheta^2 \sim 10^{-6}$, it is most unlikely that such a high order approximation would ever be required.) Therefore in (4.14) set

$$E_z(Z) = a\mathrm{e}^{-u_z WZ}, \tag{4.15}$$

where a is an amplitude factor independent of Z, and consider also the possible contribution

$$(E_y)_1 \propto \mathrm{e}^{-u_y WZ}. \tag{4.16}$$

Substituting (4.15) and (4.16) into (4.14),

$$\begin{aligned}(u_y^2 - \eta) W^2 \mathrm{e}^{-u_y WZ} \simeq{}& (i\alpha/W)[M(u_y)\mathrm{e}^{-u_y WZ} + \int_1^\infty \mathrm{d}s \,.\, G(s, u_y)\mathrm{e}^{-sWZ}] \\ &+ (i\alpha/W) a\vartheta \sin\theta [N(u_z)\mathrm{e}^{-u_z WZ} + \int_1^\infty \mathrm{d}s \,.\, H(s, u_z)\mathrm{e}^{-sWZ}],\end{aligned} \tag{4.17}$$

where

$$\begin{aligned}M(u_y) \simeq{}& \int_1^\infty \mathrm{d}s \,.\, (s^{-1} - s^{-3}) \\ &[1 + 3\vartheta^2 \sin^2\theta \,.\, (s^2 - 1)(\partial^2/\partial s^2)/8 + 0(\vartheta^4)][(s + u_y)^{-1} + (s - u_y)^{-1}],\end{aligned} \tag{4.18}$$

$$\begin{aligned}G(s, u_y) \simeq{}& (s^{-1} - s^{-3}) \\ &[1 + 3\vartheta^2 \sin^2\theta \,.\, (s^2 - 1)(\partial^2/\partial s^2)/8 + 0(\vartheta^4)][p(s + u_y)^{-1} - (s - u_y)^{-1}],\end{aligned} \tag{4.19}$$

$$N(u_z) \simeq \int_1^\infty \mathrm{d}s \,.\, (s^{-1} - s^{-3}) [1 + 0(\vartheta^2)] [(s - u_z)^{-2} - (s + u_z)^{-2}], \tag{4.20}$$

$$H(s, u_z) \simeq (s^{-1} - s^{-3}) [1 + 0(\vartheta^2)] [p(s + u_z)^{-2} - (s - u_z)^{-2}]. \tag{4.21}$$

The closest agreement between the left and right hand sides of (4.17) is obtained when u_y is chosen such that

$$u_y^2 - \eta = \xi[M(u_y) + a\vartheta \sin\theta \,.\, N(u_z)\mathrm{e}^{-(u_z - u_y)WZ}], \tag{4.22}$$

where

$$\xi = i\alpha/W^3, \tag{4.23}$$

thus leaving a remainder of order $(i\alpha/W)$ on the right hand side of (4.17). This can be cancelled by the addition of a further contribution

$$(E_y)_2 = \xi \int_1^\infty \mathrm{d}s\,.\,(s^2-\eta)^{-1}[G(s,u_y) + a\vartheta \sin\theta\,.\,H(s,u_z)]\mathrm{e}^{-sWZ}, \qquad (4.24)$$

which in turn leaves a remainder of order $(i\alpha)^2/W^4$ on the right hand side of (4.17). This can be cancelled by the addition of a suitable contribution $(E_y)_3$ of order ξ^2, leaving a further remainder of order $(i\alpha)^3/W^7$, and so on (c.f. Dingle [1])). Thus, provided

$$|\xi| = |i\alpha/W^3| \ll 1,$$

so that successive terms are of rapidly decreasing magnitude,

$$E_y(Z) \propto \mathrm{e}^{-u_yWZ} + \xi \int_1^\infty \mathrm{d}s\,.\,(s^2-\eta)^{-1}\,.$$
$$[G(s,u_y) + a\vartheta \sin\theta\,.\,H(s,u_z)]\mathrm{e}^{-sWZ} + 0(\xi^2). \qquad (4.25)$$

By repeated application of this procedure — ensuring that higher order terms in E_z are included in (4.14) when necessary — a solution for $E_y(Z)$ can be obtained to any desired power of ξ, while, by retaining higher powers of ϑ in (4.13) et seq., a solution can also be obtained to any desired power of ϑ.

The value of u_y can be found from (4.22). To a first approximation $u_z \simeq u_y$, so that

$$u_y^2 - \eta \simeq \xi[M(u_y) + a\vartheta \sin\theta\,.\,N(u_y)]$$
$$\simeq \xi[4/3 + 4u_y^2/15 + (8/15)a\vartheta \sin\theta\,.\,u_y]. \qquad (4.26)$$

To the present order of approximation (§ 5.2),

$$u_y \simeq (4\xi/3 + \eta)^{\frac{1}{2}}. \qquad (4.27)$$

4.4 Solutions for E_x and E_z. When the method outlined in § 4.3 is applied to (3.37) and (3.39), the following solutions are obtained:

a) E_x:

$$E_x(Z) \propto \mathrm{e}^{-u_xWZ} + \xi \int_1^\infty \mathrm{d}s\,.\,(s^2-\eta)^{-1}F(s,u_x)\mathrm{e}^{-sWZ} + 0(\xi^2), \qquad (4.28)$$

where

$$u_x^2 = \xi L(u_x) + \eta, \qquad (4.29)$$

$$L(u_x) \simeq \int_1^\infty \mathrm{d}s(s^{-1} - s^{-3})\;[1 + \vartheta^2 \sin^2\theta(s^2-1)\;(\partial^2/\partial s^2)/8 + 0(\vartheta^4)]$$
$$[(s+u_x)^{-1} + (s-u_x)^{-1}], \qquad (4.30)$$

$$F(s, u_x) \simeq (s^{-1} - s^{-3})$$
$$[1+\vartheta^2 \sin^2 \theta (s^2-1)\, (\partial^2/\partial s^2)/8 + 0(\vartheta^4)][p(s+u_x)^{-1} - (s-u_x)^{-1}], \quad (4.31)$$

b) E_z:

$$E_z(Z) \propto \mathrm{e}^{-u_z WZ} + \xi \int_1^\infty \mathrm{d}s (s^2 - \eta)^{-1}$$
$$[I(s, u_z) + b\vartheta \sin\theta . H(s, u_y)]\mathrm{e}^{-sWZ} + 0(\xi^2), \quad (4.32)$$

where b is an amplitude factor such that, to a first approximation, $E_y(Z) \simeq b \exp(-u_y WZ)$,

$$u_z^2 = \eta + \xi[P(u_z) + b\vartheta \sin\theta . N(u_y) . \mathrm{e}^{-(u_y - u_z)WZ}], \quad (4.33)$$

$$P(u_z) =$$
$$\int_1^\infty \mathrm{d}s . \frac{2}{s^3}\left[1 + \frac{\vartheta^2 \sin^2\theta}{4} . (s^2-1) \frac{\partial^2}{\partial s^2} + 0(\vartheta^4)\right]\left(\frac{1}{s+u_z} + \frac{1}{s-u_z}\right), \quad (4.34)$$

$$I(s, u_z) =$$
$$= \frac{2}{s^3}\left[1 + \frac{\vartheta^2 \sin^2\theta}{4} (s^2-1) \frac{\partial^2}{\partial s^2} + 0(\vartheta^4)\right]\left(\frac{p}{s+u_z} - \frac{1}{s-u_z}\right), \quad (4.35)$$

and $N(u_y)$ and $H(s, u_y)$ are defined by (4.20) and (4.21) respectively.

It is interesting to compare the depth dependences of the three field components E_x, E_y and E_z. Neglecting terms of order $0(\xi^2, \xi\vartheta^2, \vartheta^4)$, (4.28), (4.25) and (4.32) simplify to:

a) E_x:

$$E_x(Z) \propto \mathrm{e}^{-u_x WZ} - \xi(1-p)[\mathrm{Ei}_4(WZ) - \mathrm{Ei}_6(WZ)]$$
$$- u_x \xi (1+p)\, [\mathrm{Ei}_5(WZ) - \mathrm{Ei}_7(WZ)] + 0(\xi^2), \quad (4.36)$$

where

$$u_x \simeq [4\xi/3 + \vartheta^2(\varepsilon - \underline{\sin^2\theta)]^{\frac{1}{2}}}$$
$$\underline{\left\{1 + \frac{2\xi}{15}\left[\frac{4\xi/3 + \vartheta^2 \varepsilon}{4\xi/3 + \vartheta^2(\varepsilon - \sin^2\theta)}\right]\right\}} + 0(\xi^{5/2}). \quad (4.37)$$

b) E_y:

$$E_y(Z) \propto \mathrm{e}^{-u_y WZ} - \xi(1-p)\{\mathrm{Ei}_4(WZ) - \mathrm{Ei}_6(WZ)\}$$
$$-\xi[u_y(1+p) + \underline{a\vartheta \sin\theta . (1-p)}]\, [\mathrm{Ei}_5(WZ) - \mathrm{Ei}_7(WZ)] + 0(\xi^2), \quad (4.38)$$

where

$$u_y \simeq [4\xi/3 + \vartheta^2(\varepsilon - \underline{\sin^2\theta)]^{\frac{1}{2}}} .$$
$$. \left\{1 + \frac{2\xi}{15}\left[1 - \underline{\frac{2a\vartheta \sin\theta}{\{4\xi/3 + \vartheta^2(\varepsilon - \sin^2\theta)\}^{\frac{1}{2}}}}\right]\right\} + 0(\xi^{5/2}), \quad (4.39)$$

c) E_z:

$$E_z(Z) \propto \mathrm{e}^{-u_z WZ} - \underline{2\xi(1-p)\mathrm{Ei}_6(WZ)} - \underline{2\xi u_z(1+p)\mathrm{Ei}_7(WZ)}$$
$$\underline{-\,b(1-p)\xi\vartheta\sin\theta\,.\,[\mathrm{Ei}_5(WZ) - \mathrm{Ei}_7(WZ)]} + 0(\xi^2), \qquad (4.40)$$

where

$$u_z \simeq [4\xi/3 + \vartheta^2(\varepsilon \underline{-\sin^2\theta)}]^{\frac{1}{2}}\,.$$
$$.\left\{1 + \frac{2\xi}{5}\left[1 + \underline{\frac{2b\vartheta\sin\theta}{3\{4\xi/3 + \vartheta^2(\varepsilon - \sin^2\theta)\}^{\frac{1}{2}}}}\right]\right\} + 0(\xi^{5/2}). \qquad (4.41)$$

The exponential integral $\mathrm{Ei}_n(x)$ appearing in these expressions is defined by

$$\mathrm{Ei}_n(x) = \int_1^\infty s^{-n}\mathrm{e}^{-sx}\,\mathrm{d}s. \qquad (4.42)$$

The terms underlined are those which do not appear in the theory of the anomalous skin effect at normal incidence.

As will be seen in § 5.2, only terms up to $0(\xi)$ need be considered in the present investigation. To this order of approximation

$$u_x \simeq u_y \simeq u_z \simeq [4\xi/3 + \vartheta^2(\varepsilon - \sin^2\theta)]^{\frac{1}{2}}, \qquad (4.43)$$

and the only variation from normal incidence theory is in E_z, where the leading anomalous term differs from those in E_x and E_y.

§ 5. *Evaluation of optical constants I. Surface admittances, refractive indices and reflectivities.*

5.1 Notation. The final results for the optical constants are presented in the 'dimensionless coordinates introduced by Dingle[7]). These are defined as follows:

$$\boldsymbol{\nu} = \nu\left[\frac{2}{3}\frac{c}{v}\left(\frac{3\pi m}{Ne^2\mu}\right)^{\frac{1}{2}}\right] = \text{dimensionless frequency},$$

$$\boldsymbol{\sigma} = \sigma\left[\frac{v}{c}\left(\frac{3\pi m\mu}{Ne^2}\right)^{\frac{1}{2}}\right] = \text{dimensionless d.c. conductivity},$$

$$\mathbf{V} = V/c = \text{dimensionless Fermi velocity},$$

and are supplemented by the parameters

$$\Omega = 1 - (3/4)\boldsymbol{\nu}^2\mathbf{V}^2\varepsilon = 1 - \varepsilon\pi m\nu^2/Ne^2,$$
$$\Phi = 1 - (3/4)\boldsymbol{\nu}^2\mathbf{V}^2(\varepsilon - \sin^2\theta) = 1 - (\varepsilon - \sin^2\theta)\pi m\nu^2/Ne^2,$$

where

ν = frequency of the incident radiation,
σ = bulk d.c. conductivity of the metal,
V = electron velocity at the surface of the Fermi distribution,
m = effective electron mass,
N = number of conduction electrons per unit volume,
e = electronic charge, taken as positive,

$$\varepsilon = 1 + \frac{4\pi \mathbf{P}_{core}}{\mathbf{E}} + \frac{4}{\pi}\int_0^\infty \frac{(nk)_{ph}\cdot\nu' d\nu'}{(\nu')^2 - \nu^2} \text{ (Dingle }^{7}\text{), § 4).}$$

In this notation, the most commonly occurring quantities are

$\omega\tau = \boldsymbol{\sigma\nu}$,
$W = 1 + i\boldsymbol{\sigma\nu}$,
$\xi = i\boldsymbol{\sigma}^3\boldsymbol{\nu}(1 + i\boldsymbol{\sigma\nu})^{-3}$,
$\vartheta = i\boldsymbol{\sigma\nu}\mathbf{V}(1 + i\boldsymbol{\sigma\nu})^{-1}$,
$\eta = (i\boldsymbol{\sigma\nu})^2 (1 + i\boldsymbol{\sigma\nu})^{-2}\mathbf{V}^2(\varepsilon - \sin^2\theta)$.

5.2 Degree of approximation. It will be shown in §§ 5.3, 5.4 that displacement and angular effects are only appreciable in the upper visible and ultra-violet regions, when the parameter Ω differs appreciably from unity, i.e. when

$$\tfrac{3}{4}\boldsymbol{\nu}^2\mathbf{V}^2\varepsilon \sim 1.$$

For a typical monovalent metal, $\mathbf{V} \sim 5 \times 10^{-3}$, and $\varepsilon \sim 1$ to 5. This requires that $\boldsymbol{\nu} \sim 10^2$, i.e. the wavelength of the incident radiation $\leq 0.5\mu$. At optical frequencies,

$$\omega\tau = \boldsymbol{\sigma\nu} \gg 1,\ |\xi| \sim \boldsymbol{\nu}^{-2} \lll 1,\ u \sim \boldsymbol{\nu}^{-1} \ll 1,\ \boldsymbol{\nu}^{-1} \sim \mathbf{V},$$

so that the following approximations can be made:

a) Terms in $\boldsymbol{\nu}^2\mathbf{V}^2$ may be retained in comparison with unity,

b) Terms of order $0(\boldsymbol{\sigma}^{-2}\boldsymbol{\nu}^{-2}, \boldsymbol{\nu}^{-2}, \mathbf{V}^2, \boldsymbol{\nu}^{-1}\mathbf{V})$ with respect to the leading terms of the same phase may be neglected,

c) Ω may be considered to be in the range $0 < \Omega < 1$.

Particular emphasis must be placed on the qualification 'with respect to the leading terms of the same phase' in (*b*). Since real and imaginary terms play quite separate roles, *the leading real and imaginary terms of all expressions must be retained irrespective of their absolute orders of magnitude.*

5.3 Evaluation of $4\pi Y_s/c$ and $\mathbf{n}_s$. In view of the transformation in § 3 of the depth scale from cm to units of the mean free path l, (2.8) must now be written

$$4\pi Y_s/c = -(c/i\omega l)\,(E_x'/E_x)_{z=0} = \vartheta^{-1}(-\,E_x'/WE_x)_{z=0}. \tag{5.1}$$

From (4.28),

$$E_x(Z) \propto \mathrm{e}^{-uWZ} + \xi \int_1^\infty \mathrm{d}s\,.\,s^{-2}F(s,u)\mathrm{e}^{-sWZ} + 0(\xi^2), \tag{5.2}$$

so that

$$(-\,E_x'/WE_x)_{z=0} \simeq u + \xi \int_1^\infty \mathrm{d}s\,.\,s^{-1}F(s,u) + 0(\xi^{3/2}). \tag{5.3}$$

This is precisely the expression obtained in the normal incidence case (Dingle [1]), § 3), and the result can therefore be quoted as

$$(-\,E_x'/WE_x)_{z=0} \simeq (4\xi/3+\eta)^{\frac{1}{2}} - \tfrac{1}{4}\xi(1-p) + 0(\xi^{3/2}), \tag{5.4}$$

so that

$$4\pi Y_s/c \simeq \vartheta^{-1}[(4\xi/3+\eta)^{\frac{1}{2}} - \tfrac{1}{4}\xi(1-p)]. \tag{5.5}$$

The surface admittance can be expressed in terms of the dimensionless units $\boldsymbol{\sigma}$, $\boldsymbol{\nu}$, $\mathbf{V}$ and the parameter Φ by means of the substitutions given in § 5.1. Retaining the leading real *and* imaginary terms in (5.5),

$$(\boldsymbol{\nu}\mathbf{V})4\pi Y_s/c \simeq (1/\sqrt{3})\,(\boldsymbol{\sigma}\boldsymbol{\nu})^{-1}\Phi^{-\frac{1}{2}} + (\tfrac{1}{4})\boldsymbol{\nu}^{-1}(1-p) - i(2/\sqrt{3})\Phi^{\frac{1}{2}} \\ + 0(\boldsymbol{\nu}^{-2}, i\boldsymbol{\sigma}^{-1}\boldsymbol{\nu}^{-2}) \tag{5.6}$$

for $\Phi \neq 0$. This expression for the surface admittance $4\pi Y_s/c$ is identical with that obtained by Dingle [1]) for the case of normal incidence except that the parameter Ω is replaced here by the new parameter Φ. The transition from normal to oblique incidence thus involves changes in the surface impedance $4\pi Y_s/c$ of order $0(\boldsymbol{\nu}^2\mathbf{V}^2)$. These are only appreciable when $\boldsymbol{\nu}^2\mathbf{V}^2 \sim 1$, i.e. in the upper visible and ultra-violet (§ 5.2).

The complex refractive index $\mathbf{n}_s$ is given by

$$\mathbf{n}_s^2 = (4\pi Y_s/c)^2 + \sin^2\theta. \tag{5.7}$$

Separating this equation into its real and imaginary parts, and substituting from (5.6),

$$n^2 - k^2 - \sin^2\theta = (4\pi/c)^2\,(G_s^2 - B_s^2) \simeq -\,\tfrac{4}{3}(\boldsymbol{\nu}\mathbf{V})^{-2}\Phi,$$

$$nk = (4\pi/c)^2 G_s B_s \simeq \tfrac{2}{3}(\boldsymbol{\nu}\mathbf{V})^{-2}(\boldsymbol{\sigma}\boldsymbol{\nu})^{-1}[1+(\sqrt{3}/4)\,(1-p)\boldsymbol{\sigma}\Phi^{\frac{1}{2}}], \tag{5.8}$$

where

$$\mathbf{n}_s = n - ik, \quad Y_s = G_s - iB_s. \qquad (5.9)$$

5.4 Evaluation of $4\pi Y_p/c$ and $\mathbf{n}_p$. From (2.20),

$$4\pi Y_p/c = \vartheta^{-1}(-E_y'/WE_y)_{z=0}\{1 + \vartheta^2 \sin^2\theta (W^2E_z/E_z'')_{z=0}\}, \qquad (5.10)$$

where the depth Z is measured in units of the mean free path l. Further, from (4.25),

$$E_y(Z) \propto \mathrm{e}^{-uWZ} + \xi \int_1^\infty \mathrm{d}s\,.\,s^{-2}G(s, u)\mathrm{e}^{-sWZ} + 0(\xi^2), \qquad (5.11)$$

so that, to the present order of approximation

$$(-E_y'/WE_y)_{z=0} \simeq u + \xi \int_1^\infty \mathrm{d}s\,.\,s^{-1}F(s, u) \simeq (-E_x'/WE_x)_{z=0}. \qquad (5.12)$$

From (4.32),

$$E_z(Z) \propto \mathrm{e}^{-uWZ} + \xi \int_1^\infty \mathrm{d}s\,.\,s^{-2}I(s, u)\mathrm{e}^{-sWZ} + 0(\xi^2), \qquad (5.13)$$

so that

$$\begin{aligned}(W^2E_z/E_z'')_{z=0} &\simeq [u^2 + \xi \int_1^\infty \mathrm{d}s\,.\,I(s, u) + 0(\xi^2)]^{-1},\\ &\simeq [4\xi/3 + \vartheta^2(\varepsilon - \sin^2\theta) - 2\xi(1 - p)/3 + 0(\xi^2)]^{-1}. \qquad (5.14)\end{aligned}$$

It will be noted that the leading anomalous contribution to the second derivative E_z'' is of the *same order of magnitude* as that from the point relation. Thus

$$1 + \vartheta^2 \sin^2\theta\,.\,(W^2E_z/E_z'')_{z=0} \simeq \frac{\vartheta^2\varepsilon + \frac{2}{3}\xi(1 + p)}{\vartheta^2(\varepsilon - \sin^2\theta) + \frac{2}{3}\xi(1 + p)}, \qquad (5.15)$$

and, substituting in (5.10) from (5.5), (5.12) and (5.15),

$$(4\pi Y_p/c) \simeq (4\pi Y_s/c)\left[\frac{\vartheta^2\varepsilon + \frac{2}{3}\xi(1 + p)}{\vartheta^2(\varepsilon - \sin^2\theta) + \frac{2}{3}\xi(1 + p)}\right]. \qquad (5.16)$$

This can be written in dimensionless coordinates as

$$(4\pi Y_p/c) \simeq (4\pi Y_s/c)\left[\frac{\Omega - \frac{1}{2}(1 - p) + i(\boldsymbol{\sigma\nu})^{-1}(1 - \Omega)}{\Phi - \frac{1}{2}(1 - p) + i(\boldsymbol{\sigma\nu})^{-1}(1 - \Phi)}\right]. \qquad (5.17)$$

The complex ratio between the admittances is best expressed in terms of its separate real and imaginary parts as

$$(4\pi Y_p/c) \simeq (4\pi Y_s/c)\,(\alpha + i\beta), \qquad (5.18)$$

where

$$\left.\begin{aligned} \alpha &= \frac{[\Omega - \frac{1}{2}(1-p)]\,[\Phi - \frac{1}{2}(1-p)] + (\boldsymbol{\sigma\nu})^{-2}(1-\Omega)\,(1-\Phi)}{[\Phi - \frac{1}{2}(1-p)]^2 + (\boldsymbol{\sigma\nu})^{-2}(1-\Phi)^2}\,, \\ \beta &= \frac{\frac{1}{2}(\boldsymbol{\sigma\nu})^{-1}(1+p)\,(\Phi-\Omega)}{[\Phi - \frac{1}{2}(1-p)]^2 + (\boldsymbol{\sigma\nu})^{-2}(1-\Phi)^2}\,. \end{aligned}\right\} \qquad (5.19)$$

The refractive index $\mathbf{n}_p$ can be evaluated using (2.24), i.e.

$$\mathbf{n}_p^2 = (4\pi/c)^2 Y_s Y_p = (\mathbf{n}_s^2 - \sin^2\theta)\,(\alpha + i\beta). \qquad (5.20)$$

5.5 The Drude-Kronig formulae for $4\pi Y_s/c$ and $4\pi Y_p/c$. In the Drude-Kronig (or point-relation) limit, it is found that the quantities corresponding to the admittances $4\pi Y_s/c$ and $4\pi Y_p/c$ are*

$$\begin{aligned} (4\pi Y_s/c)_{DK} &\simeq \vartheta^{-1}(4\xi/3 + \eta)^{\frac{1}{2}}, \\ \frac{(4\pi Y_p/c)_{DK}}{(4\pi Y_s/c)_{DK}} &\simeq \left[\frac{\Omega + i(\boldsymbol{\sigma\nu})^{-1}(1-\Omega)}{\Phi + i(\boldsymbol{\sigma\nu})^{-1}(1-\Phi)}\right]. \end{aligned} \qquad (5.21)$$

Comparison of these two expressions with (5.5) and (5.17) respectively indicates that the differences in results obtained from the Drude-Kronig and 'angular anomalous' theories originate from:

a) the anomalous contribution $-\frac{1}{4}\xi(1-p)$ in $4\pi Y_s/c$,

b) the anomalous term $-\frac{1}{2}(1-p)$ in both the numerator and denominator of the admittance ratio $(\alpha + i\beta)$. [These terms are a result of the anomalous contribution to E_z'' in (5.14) being of the same order of magnitude as the Drude-Kronig contribution, and give rise to the marked differences in the behaviour of the Drude-Kronig and 'angular anomalous' values of the optical constants around $\Omega = \frac{1}{2}(1-p)$ and $\Phi = \frac{1}{2}(1-p)$ (see §§ 5.7, 6.2, 7.2).]

5.6 The reflectivity $\mathscr{R}_s$ for 'perpendicular' polarization. From (2.29),

$$\mathscr{R}_s = |(\cos\theta - 4\pi c^{-1} Y_s)/(\cos\theta + 4\pi c^{-1} Y_s)|^2, \qquad (5.22)$$

where $4\pi Y_s/c$ is given by (5.6). To the present order of approximation

$$\left(\frac{1-\mathscr{R}_s}{\boldsymbol{\nu}\mathbf{V}}\right)_\theta \simeq (\boldsymbol{\sigma\nu})^{-1}\cos\theta\,\frac{\sqrt{3}.\Phi^{-\frac{1}{2}} + \frac{3}{4}\sigma(1-p)}{\Phi + \frac{3}{4}\boldsymbol{\nu}^2\mathbf{V}^2\cos^2\theta}\,. \qquad (5.23)$$

---

*) It will be noted from (5.5) and (5.17) that in the present (optical frequency) approximation, 'point-relation' expressions can be obtained from the corresponding 'angular anomalous' expressions by setting $p = 1$.

At normal incidence $\Phi_{\theta=0} = \Omega$, and

$$\left(\frac{1-\mathscr{R}_s}{\boldsymbol{\nu}\mathbf{V}}\right)_{\theta=0} \simeq (\boldsymbol{\sigma\nu})^{-1}\,\frac{\sqrt{3}\,.\,\Omega^{-\frac{1}{2}} + \frac{3}{4}\boldsymbol{\sigma}(1-p)}{\Omega + \frac{3}{4}\boldsymbol{\nu}^2\mathbf{V}^2}\,, \tag{5.24}$$

(c.f. Dingle 7), eq. 10.5, 10.6; 1), § 5).

5.7 The reflectivity $\mathscr{R}_p$ for 'parallel' polarization. From (2.30)

$$\mathscr{R}_p = |(4\pi c^{-1}Y_p\cos\theta - 1)/(4\pi c^{-1}Y_p\cos\theta + 1)|^2, \tag{5.25}$$

where

$$4\pi Y_p/c = 4\pi(G_p - iB_p)/c = 4\pi(G_s - iB_s)\,(\alpha + i\beta)/c. \tag{5.26}$$

Owing to the singularities in α and β when $\Omega = \frac{1}{2}(1-p)$ and $\Phi = \frac{1}{2}(1-p)$ (see (5.19)), three separate approximations are required for $\mathscr{R}_p$.

a) $\Omega \neq \frac{1}{2}(1-p)$, $\Phi \neq \frac{1}{2}(1-p)$. In this case

$$\left.\begin{aligned} \alpha &\simeq [\Omega - \tfrac{1}{2}(1-p)]/[\Phi - \tfrac{1}{2}(1-p)], \\ \beta &\simeq (\boldsymbol{\sigma\nu})^{-1}\tfrac{1}{2}(1+p)\,(\Phi-\Omega)/[\Phi - \tfrac{1}{2}(1-p)]^2, \end{aligned}\right\} \tag{5.27}$$

so that, from (5.6), (5.25), (5.26) and (5.27),

$$\left(\frac{1-\mathscr{R}_p}{\boldsymbol{\nu}\mathbf{V}}\right)_{\theta} \simeq \cos\theta(\boldsymbol{\sigma\nu})^{-1}\,.$$

$$\cdot\,\frac{\left[\dfrac{\Omega-\frac{1}{2}(1-p)}{\Phi-\frac{1}{2}(1-p)}\right]\left[\sqrt{3}\,.\,\Phi^{-\frac{1}{2}}+\frac{3}{4}\boldsymbol{\sigma}(1-p)\right]+\sqrt{3}\,.\,\Phi^{\frac{1}{2}}\left\{\dfrac{(\Phi-\Omega)\,(1+p)}{[\Phi-\frac{1}{2}(1-p)]^2}\right\}}{\Phi\left[\dfrac{\Omega-\frac{1}{2}(1-p)}{\Phi-\frac{1}{2}(1-p)}\right]^2\cos^2\theta+\frac{3}{4}\boldsymbol{\nu}^2\mathbf{V}^2}\,. \tag{5.28}$$

At normal incidence, this expression reduces to the same value (5.24) as did $\mathscr{R}_s$.

b) $\Omega = \frac{1}{2}(1-p)$. At this particular frequency

$$\left.\begin{aligned} \alpha &\simeq (\boldsymbol{\sigma\nu})^{-2}\tfrac{1}{2}(1+p)\,(1-\Phi)/[\Phi - \tfrac{1}{2}(1-p)]^2, \\ \beta &\simeq (\boldsymbol{\sigma\nu})^{-1}\tfrac{1}{2}(1+p)/[\Phi - \tfrac{1}{2}(1-p)], \end{aligned}\right\} \tag{5.29}$$

so that, from (5.6) and (5.18)

$$\left.\begin{aligned} 4\pi G_p/c &\simeq (\boldsymbol{\nu}\mathbf{V})^{-1}(\boldsymbol{\sigma\nu})^{-1}(1+p)\Phi^{\frac{1}{2}}/\sqrt{3}[\Phi - \tfrac{1}{2}(1-p)], \\ 4\pi B_p/c &\simeq 0(\boldsymbol{\sigma\nu})^{-2}, \end{aligned}\right\} \tag{5.30}$$

and

$$\left(\frac{1-\mathscr{R}_p}{\boldsymbol{\nu}\mathbf{V}}\right)_{\Omega=\frac{1}{2}(1-p)} \simeq (\boldsymbol{\sigma\nu})^{-1}\cos\theta\,.\,(1+p)\,\frac{4}{\sqrt{3}}\,\frac{\Phi^{\frac{1}{2}}}{\Phi-\frac{1}{2}(1-p)}\,. \tag{5.31}$$

It should be noted that in the vicinity of the principal angle of incidence Θ the approximations used here are invalid. It will be shown in § 6.2 that when $\theta = \Theta$, $\sin^2 \theta \sim 0(\boldsymbol{\sigma\nu})^{-1}$, so that

$$\Phi - \tfrac{1}{2}(1 - p) \sim 0(\boldsymbol{\sigma\nu})^{-1},$$

and therefore in the expressions (5.19) for α and β the terms in $(\boldsymbol{\sigma\nu})^{-2}$ in the denominators *cannot* be neglected as has been done in obtaining (5.29)–(5.31). At this angle of incidence the *complete* expressions for α, β and $\mathscr{R}_p$ must therefore be used.

c) $\Phi = \tfrac{1}{2}(1 - p)$. In this particular case

$$\alpha = (1 - \Omega)/\tfrac{1}{2}(1 + p); \; \beta = (\boldsymbol{\sigma\nu})[\tfrac{1}{2}(1 - p) - \Omega]/\tfrac{1}{2}(1 + p), \quad (5.32)$$

so that

$$\begin{aligned} 4\pi G_p/c &\simeq (\boldsymbol{\nu}\mathbf{V})^{-1}(\boldsymbol{\sigma\nu})\,(4/\sqrt{6})\,(1 - p)^{\frac{1}{2}}[\tfrac{1}{2}(1 - p) - \Omega]/(1 + p), \\ 4\pi B_p/c &\simeq 0(1), \end{aligned} \quad (5.33)$$

and

$$\left(\frac{1-\mathscr{R}_p}{\boldsymbol{\nu}\mathbf{V}}\right)_{\Phi=\frac{1}{2}(1-p)} \simeq (\boldsymbol{\sigma\nu})^{-1} \sec\theta \left(\frac{6}{1 - p}\right)^{\frac{1}{2}} \frac{1 + p}{\tfrac{1}{2}(1 - p) - \Omega}. \quad (5.34)$$

As in case (*b*), if the value of θ should be such that

$$\Omega - \tfrac{1}{2}(1 - p) \sim 0(\boldsymbol{\sigma\nu})^{-1},$$

this approximation breaks down so that the complete expressions for G_p, B_p and $\mathscr{R}_p$ must be used.

§ 6. *Evaluation of optical constants II. The principal angle of incidence Θ.*

6.1 Combining (2.33) and (5.20), the general expression for the principal angle of incidence Θ can be written

$$\begin{aligned} &\cos^2\Theta.\{1-2\alpha(n^2-k^2-\sin^2\Theta)+(\alpha^2+\beta^2)[(n^2-k^2-\sin^2\Theta)^2+4n^2k^2]\}= \\ &= [(n^2-k^2-\sin^2\Theta)^2+4n^2k^2]^{\frac{1}{2}}\,[(\alpha\cos^2\Theta-1)^2+\beta^2\cos^4\Theta], \end{aligned} \quad (6.1)$$

where

$$\mathbf{n}_s = n - ik. \quad (6.2)$$

In order to solve (6.1) for Θ it is convenient to express Φ, n, k, α and β all in terms of the parameter Ω. Writing $\sin^2\Theta = x$:

$$\Phi = \Omega + (1 - \Omega)x/\varepsilon, \quad (6.3)$$

$$\left.\begin{aligned} \alpha &= \frac{[\Omega-\frac{1}{2}(1-p)][\Omega+(1-\Omega)x/\varepsilon-\frac{1}{2}(1-p)]+(\boldsymbol{\sigma\nu})^{-2}(1-\Omega)^2(1--x/\varepsilon)}{[\Omega+(1-\Omega)x/\varepsilon-\frac{1}{2}(1-p)]^2+(\boldsymbol{\sigma\nu})^{-2}(1-\Omega)^2(1-x/\varepsilon)^2}, \\ \beta &= \frac{\frac{1}{2}(\boldsymbol{\sigma\nu})^{-1}(1+p)\,(1-\Omega)x/\varepsilon}{[\Omega+(1-\Omega)x/\varepsilon-\frac{1}{2}(1-p)]^2+(\boldsymbol{\sigma\nu})^{-2}(1-\Omega)^2(1-x/\varepsilon)^2}, \end{aligned}\right\} \quad (6.4)$$

$$\left.\begin{aligned} -n^2+k^2+x &\simeq \varepsilon\Omega/(1-\Omega)+x, \\ 2nk &\simeq (\boldsymbol{\sigma\nu})^{-1}[\varepsilon/(1-\Omega)]\{1+(\sqrt{3}/4)(1-p)\boldsymbol{\sigma}[\Omega+(1-\Omega)x/\varepsilon]^{\frac{1}{2}}\}. \end{aligned}\right\} \quad (6.5)$$

Since at optical frequencies $\boldsymbol{\sigma\nu} \gg 1$, it is permissible to take $n^2 \ll k^2 + x$, $nk \ll k^2 + x$, thus simplifying (6.1) to

$$\begin{aligned} (1-x)\{[1+\alpha(k^2+x)]^2+\beta^2(k^2+x)^2\} &= \\ = (k^2+x)\{[\alpha(1-x)-1]^2+\beta^2(1-x)^2\}. &\quad (6.6) \end{aligned}$$

When substitutions are made for α, β^2 and k^2 from (6.4) and (6.5), the equation for x becomes

$$\begin{aligned} &(1-x)\big[([\Omega-\tfrac{1}{2}(1-p)+(1-\Omega)x/\varepsilon]\{[\Omega-\tfrac{1}{2}(1-p)]\,. \\ &\quad .\,[\varepsilon\Omega/(1-\Omega)+1+x]+(1-\Omega)x/\varepsilon\}+ \\ &\quad +(\boldsymbol{\sigma\nu})^{-2}(1-\Omega)^2[(\varepsilon-x)/\varepsilon][1+\varepsilon\Omega/(1-\Omega)+(\varepsilon-1)x/\varepsilon])^2+ \\ &\quad +(\boldsymbol{\sigma\nu})^{-2}(\tfrac{1}{4})(1+p)^2(1-\Omega)^2[\varepsilon\Omega/(1-\Omega)+x]^2x^2/\varepsilon^2\big] \simeq \\ &\simeq x^2[\varepsilon\Omega/(1-\Omega)+x](\{[\Omega-\tfrac{1}{2}(1-p)+(1-\Omega)x/\varepsilon]\,. \\ &\quad [\Omega-\tfrac{1}{2}(1-p)+(1-\Omega)/\varepsilon]+(\boldsymbol{\sigma\nu})^{-2}(1-\Omega)^2(\varepsilon-x)(\varepsilon-1)/\varepsilon^2\}^2+ \\ &\quad +(\boldsymbol{\sigma\nu})^{-2}(\tfrac{1}{4})(1+p)^2(1-\Omega)^2(1-x)^2/\varepsilon^2). \qquad (6.7) \end{aligned}$$

At frequencies such that $\Omega \neq \frac{1}{2}(1-p)$ and $\Phi \neq \frac{1}{2}(1-p)$, all terms in (6.7) of order $0(\boldsymbol{\sigma\nu})^{-2}$ and higher can be neglected. Then

$$\begin{aligned} &[\Omega-\tfrac{1}{2}(1-p)+(1-\Omega)x/\varepsilon]^2((1-x)\{[\Omega-\tfrac{1}{2}(1-p)]\,[\varepsilon\Omega/(1-\Omega)+1+x]+ \\ &+(1-\Omega)x/\varepsilon\}^2-x^2[\varepsilon\Omega/(1-\Omega)+x][\Omega-\tfrac{1}{2}(1-p)+(1-\Omega)/\varepsilon]^2)=0, \quad (6.8) \end{aligned}$$

and x is given by

$$[\Omega-\tfrac{1}{2}(1-p)+(1-\Omega)x/\varepsilon]^2=0, \qquad (6.9)$$

or by

$$\begin{aligned} &(1-x)\{[\Omega-\tfrac{1}{2}(1-p)]\,[\varepsilon\Omega/(1-\Omega)+1+x]+(1-\Omega)x/\varepsilon\}^2- \\ &\quad -x^2[\varepsilon\Omega/(1-\Omega)+x]\,[\Omega-\tfrac{1}{2}(1-p)+(1-\Omega)/\varepsilon]^2=0. \quad (6.10) \end{aligned}$$

Equation (6.9) gives the solution

$$x=[\varepsilon/(1-\Omega)]\,[\tfrac{1}{2}(1-p)-\Omega]. \qquad (6.11)$$

Due to the fact that x and Ω are restricted, i.e. $0 \leq x \leq 1, 0 \leq \Omega \leq 1,$

this particular solution only exists when

$$\tfrac{1}{2}(1-p) \geq \Omega \geq [\tfrac{1}{2}\varepsilon(1-p)-1]/(\varepsilon-1),\ \varepsilon \neq 1$$

or

$$\tfrac{1}{2}(1-p) \geq \Omega,\ \varepsilon = 1. \tag{6.12}$$

The alternative equation (6.10) can be expressed in a more condensed form by writing

$$k^2 = \Omega\varepsilon/(1-\Omega), \tag{6.5}$$

and defining

$$b^2 \doteq [\Omega - \tfrac{1}{2}(1-p)]\varepsilon/(1-\Omega). \tag{6.13}$$

Then, substituting in (6.10),

$$(1-x)\,[x(1+b^2)+b^2(1+k^2)]^2 - x^2(k^2+x)\,(1+b^2)^2 = 0. \tag{6.14}$$

Eq. (6.14) gives a solution for x for *all* values of Ω. However, owing to its complicated form, a *general* solution in terms of Ω and ε has not been found, since in practice it is simpler to solve for particular values of Ω and ε as required.

6.2 General considerations on the solutions for Θ. Before proceeding to a complete solution for a specific case, the general nature of the solutions for the principal angle Θ in various Ω (i.e. wavelength) ranges will be discussed.

a) $1 \geq \Omega > \tfrac{1}{2}(1-p)$. When $1 \geq \Omega > \tfrac{1}{2}(1-p)$, (6.14) alone yields a solution for x. At long wavelengths ($\Omega \to 1$, $\lambda \gg 1\mu$) an approximate solution is

$$x = \sin^2\Theta \simeq 1-(1-\Omega)/\varepsilon = 1-\tfrac{3}{4}\boldsymbol{\nu}^2\mathbf{V}^2 + 0(\boldsymbol{\nu}^4\mathbf{V}^4), \tag{6.15}$$

which agrees with the corresponding point-relation approximation (6.24). As $\Omega \to \tfrac{1}{2}(1-p)$, the values of x drop rapidly to almost zero, i.e. the principal angle decreases rapidly to near zero, corresponding to almost normal incidence.

b) $\Omega = \tfrac{1}{2}(1-p)$. At this frequency x reaches its minimum value of almost zero, and the approximation used in (6.8) becomes insufficient. This is due to the fact that the leading terms in α and β (see (6.4)) are either zero or so close to zero that the hitherto neglected terms in $(\boldsymbol{\sigma\nu})^{-2}$ become important. If a second approximation retaining terms in $(\boldsymbol{\sigma\nu})^{-2}$ is made in (6.7), it can be shown that the minimum value of x is not zero, but

$$x_{min} \simeq \varepsilon[(\varepsilon^2+\varepsilon+2)/(\varepsilon-1)]^{\frac{1}{2}}(\boldsymbol{\sigma\nu})^{-1},\ \varepsilon \neq 1,\ p = 0, \tag{6.16}$$

or

$$x_{min} \simeq \sqrt[3]{2}.(\boldsymbol{\sigma\nu})^{-2/3},\ \varepsilon = 1,\ p = 0.$$

Thus, at this particular wavelength, the principal angle of incidence is approximately given by

$$\Theta_{\Omega=\frac{1}{2}(1-p)} \simeq x_{min}^{\frac{1}{2}} \simeq [\varepsilon^2(\varepsilon^2+\varepsilon+2)/(\varepsilon-1)]^{\frac{1}{4}}(\boldsymbol{\sigma\nu})^{-\frac{1}{2}}, \qquad (6.17)$$

corresponding to almost normal incidence.

c) $\frac{1}{2}(1-p) > \Omega > [\frac{1}{2}\varepsilon(1-p)-1]/(\varepsilon-1)$. Within this region both equations (6.9) and (6.14) yield solutions for x. When $\varepsilon = 1$, which would correspond physically to the light wave striking the surface of a sea of completely free electrons, both solutions are identical, and there is only one principal angle of incidence at any one frequency. However for $\varepsilon > 1$ the two equations yield different solutions, the values of x obtained from (6.14) being in general greater than those obtained from (6.9) Both solutions are acceptable physically, and there are therefore *two* principal angles of incidence at any one frequency.

For solution (6.9) it is found that throughout this particular Ω-range Φ has the constant value $\frac{1}{2}(1-p)$, and therefore the values of the parameters α and β are determined by second order terms in $(\boldsymbol{\sigma\nu})^{-2}$. On the other hand, for solution (6.14) Φ is always greater than $\frac{1}{2}(1-p)$, except at the point $\Omega=[\frac{1}{2}\varepsilon(1-p)-1]/(\varepsilon-1)$, when it becomes equal to $\frac{1}{2}(1-p)$. Consequently, except at this latter point, α and β are determined by the factors of order unity in (6.4), with the result that α is negative throughout the greater part of the range. Although α can be negative, the surface conductance for 'parallel' polarization, $4\pi G_p/c = 4\pi(G_s\alpha + B_s\beta)/c$ is always positive since $|B_s\beta| > |G_s\alpha|$.

The general pattern of the behaviour of both solutions for x in this region consists of a sharp rise from near zero at $\Omega = \frac{1}{2}(1-p)$ to almost unity at $\Omega = [\frac{1}{2}\varepsilon(1-p)-1]/(\varepsilon-1)$. The principal angle thus varies very rapidly from near normal incidence to almost grazing incidence over quite a short wavelength range.

d) $\Omega = [\frac{1}{2}\varepsilon(1-p)-1]/(\varepsilon-1)$. At this point the approximate equations (6.9) and (6.14) are again insufficient, each giving a value $x = 1$. By returning to the complete equation (6.7) and retaining terms of order $0(\boldsymbol{\sigma\nu})^{-2}$, it is found that

$$x_{max} \simeq 1-(\varepsilon-1)\,(\boldsymbol{\sigma\nu})^{-2}, \qquad (6.18)$$

so that the principal angle corresponds to almost grazing incidence. For the case $\varepsilon = 1$ the question of a singularity at this point does not arise (see (6.12)).

e) $[\frac{1}{2}\varepsilon(1 - p) - 1]/(\varepsilon - 1) > \Omega \geq 0$. In this region there is again only one solution for x, namely that obtained from the cubic (6.14). The value of x drops from a maximum of almost unity to a final value dependent on the value of ε. When $\Omega = 0$ and $p = 0$ the equation for x is the cubic

$$2(2 - \varepsilon)^2 x^3 - (4 - \varepsilon^2)x^2 + \varepsilon(4 - \varepsilon)x - \varepsilon^2 = 0. \qquad (6.19)$$

Approximate solutions for a representative series of ε-values are

ε	1.0	1.25	1.5	2.0	3.0	4.0	5.0	6.0
$x_{\Omega=0}$	0.50	0.65	0.86	1.00	0.95	0.92	0.90	0.89

These solutions are in marked contrast to the Drude-Kronig solution (§ 6.3) of $x_{\Omega=0} = \frac{1}{2}$ for all ε. That is, whereas the Drude-Kronig theory gives a limit of $\Theta = \pi/4$ when $\Omega = 0$, the corresponding limit on angular anomalous theory varies between grazing incidence and $\pi/4$, depending on the value of ε. In general, the high frequency limit $\Omega = 0$ lies well into the ultra-violet region, e.g. for silver the value is $\lambda_{\Omega=0} \simeq 0.24\mu$.

6.3 The Drude-Kronig solution for Θ. The Drude-Kronig, or point-relation, equation for $\sin^2 \Theta = x$ can be obtained by setting $p = 1$ in (6.7) (see footnote to § 5.5). After some simplification this reduces to

$$(1 - x)(k^2 + x) - x^2 \simeq 0, \qquad (6.20)$$

i.e.

$$\sin^2 \Theta \tan^2 \Theta \simeq k^2 + \sin^2 \Theta, \qquad (6.21)$$

which is the well known 'classical' equation at high frequencies (see for example Dingle [7]), p. 343).

At long wavelengths ($\Omega \to 1$) an approximate solution is found to be

$$x_{\Omega\to 1} \simeq 1 - \tfrac{3}{4}\mathrm{v}^2\mathrm{V}^2, \qquad (6.22)$$

while at the short wavelength limit ($\Omega = 0$), the solution is $x_{\Omega=0} = \frac{1}{2}$ for all ε. The general solution for any Ω between 0 and 1 follows a smooth curve between the limits 1 and $\frac{1}{2}$.

6.4 Comparison between the angular anomalous and Drude-Kronig values for Θ for a typical metal. In order to illustrate more clearly the nature of the variation of $\sin^2 \Theta$ with frequency according to the 'angular anomalous' and Drude-Kronig theories, the solutions for $x = \sin^2 \Theta$ have been plotted as functions of Ω and λ for the typical values $\varepsilon = 3$, $p = 0$. In the case of the $\sin^2 \Theta$ vs. λ graph, λ has been calculated from Ω using the value $(V/c)_{Ag} \simeq 4.7 \times 10^{-3}$.

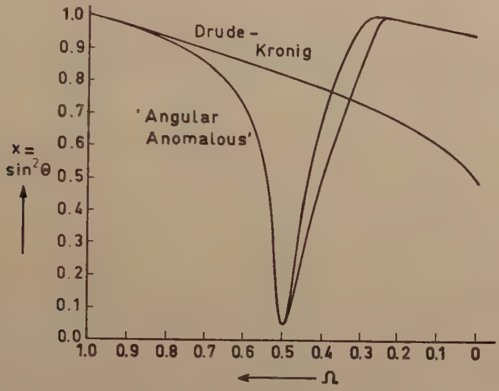

Fig. 2. $\text{Sin}^2 \Theta$ vs. Ω for Ag, with $\varepsilon = 3$, $p = 0$.

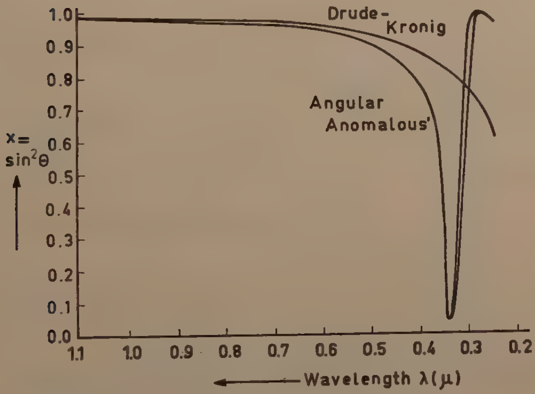

Fig. 3. $\text{Sin}^2 \Theta$ vs. $\lambda(\mu)$ for Ag, with $\varepsilon = 3$, $p = 0$.

A better idea of the relative importance and extent of the divergence between the two theories can be gained from the $\sin^2 \Theta$ vs. λ graph than from the $\sin^2 \Theta$ vs. Ω graph. For example, for silver the main region of divergence lies between wavelengths $\lambda \sim 0.40\mu$ and $\lambda \sim 0.25\mu$, i.e. in the near ultra-violet. Throughout the visible spectrum there is no great departure from point-relation theory, but the angular anomalous values for $\sin^2 \Theta$ are consistently slightly lower than the corresponding point-relation values.

§ 7. *Evaluation of optical constants III. The principal azimuth* Ψ.

7.1 From § 2.5,

$$\tan \Psi = |r_p/r_s| = -Im(\Xi)/Re(\Xi). \tag{7.1}$$

Using (5.20), and neglecting any *real factors* in Ξ — which is quite permissible since only the *ratio* of the real and imaginary parts of Ξ is required —

$$\Xi \propto [(\mathbf{n}_s^2 - \sin^2\Theta)^{\frac{1}{2}}]^* [(\alpha + i\beta)\cos^2\Theta - 1]^* [1 - (\alpha + i\beta)(\mathbf{n}_s^2 - \sin^2\Theta)]. \tag{7.2}$$

Writing $\sin^2\Theta = x$, and neglecting n^2 in comparison with $k^2 + x$ as in § 6, it follows that

$$\begin{aligned} Re(\Xi) \propto & -nk[\alpha(k^2 + x) - 1]\,[\alpha(1 - x) - 1] \\ & + \beta[(k^2 + x)\,(k^2 + 1) - \beta nk(k^2 + x)\,(1 - x) + 2n^2k^2], \end{aligned} \tag{7.3}$$

$$\begin{aligned} Im(\Xi) \propto & (k^2+x)\,[\alpha(k^2+x)+1]\,[\alpha(1-x)-1] + \beta^2(k^2+x)^2(1-x) \\ & + nk\{2nk\alpha[\alpha(1-x)-1] + \beta(k^2+2x-1) + 2\beta^2nk(1-x)\}. \end{aligned} \tag{7.4}$$

7.2 General considerations on the solutions for Ψ. Before proceeding to the evaluation of $\tan 2\Psi$, the relative magnitudes of α, β, k^2+x and nk must be examined with a view to simplifying (7.3) and (7.4). The question of magnitudes is bound up very closely with the values of Ω and the nature of the solutions for x in § 6, and therefore must be considered for the following separate cases:

a) $1 > \Omega > \frac{1}{2}(1 - p)$. In this range x is given by (6.14), and α, β and nk can be approximated by

$$\begin{aligned} \alpha & \simeq [\Omega - \tfrac{1}{2}(1 - p)]/[\Phi - \tfrac{1}{2}(1 - p)] = b^2/(b^2 + x), \\ \beta & \simeq \tfrac{1}{2}(\boldsymbol{\sigma\nu})^{-1}(1 + p)\,(\Phi - \Omega)/[\Phi - \tfrac{1}{2}(1 - p)]^2 = \\ & = \tfrac{1}{2}(\boldsymbol{\sigma\nu})^{-1}(1 + p)x(k^2 + \varepsilon)/(b^2 + x)^2, \end{aligned} \tag{7.5}$$

$$\begin{aligned} nk & = \tfrac{1}{2}(\boldsymbol{\sigma\nu})^{-1}\{1 + (\sqrt{3}/4)\boldsymbol{\sigma}(1-p)[\Omega + (1-\Omega)x/\varepsilon]^{\frac{1}{2}}\}\varepsilon/(1-\Omega) \\ & = \tfrac{1}{2}(\boldsymbol{\sigma\nu})^{-1}(k^2+\varepsilon)\{1 + (\sqrt{3}/4)\boldsymbol{\sigma}(1-p)[(k^2+x)/(k^2+\varepsilon)]^{\frac{1}{2}}\}. \end{aligned} \tag{7.6}$$

It is therefore possible to neglect β and nk, which are both of order $0(\boldsymbol{\sigma\nu})^{-1}$ in comparison with unity, in (7.3) and (7.4) so that the principal azimuth is given by

$$\tan 2\Psi = \\ = \frac{(k^2+x)\,[\alpha(k^2+x)+1]\,[\alpha(1-x)-1]}{nk[\alpha(k^2+x)-1]\,[\alpha(1-x)-1] - \beta(k^2+x)(k^2+1)} = \frac{k^2+x}{\Gamma nk}, \tag{7.7}$$

where

$$\Gamma = \frac{\alpha(k^2+x)-1}{\alpha(k^2+x)+1} + \frac{\beta(k^2+1)\,(k^2+x)}{nk[\alpha(k^2+x)+1]\,[1-\alpha(1-x)]} =$$

$$= \frac{b^2-(b^2+x)/(k^2+x)}{b^2+(b^2+x)/(k^2+x)} +$$

$$+ \frac{1+p}{1+(\sqrt{3}/4)\boldsymbol{\sigma}(1-p)[(k^2+x)/(k^2+\varepsilon)]^{\frac{1}{2}}} \cdot$$

$$\frac{1+k^2}{1+b^2} \cdot \frac{1}{b^2+(b^2+x)/(k^2+x)}. \qquad (7.8)$$

At long wavelengths ($\Omega \to 1$), $\Gamma \to 1$ and the values of $\tan 2\Psi$ approach very closely those obtained by Dingle [1]) [7]) using normal incidence theory. They differ considerably, however, from the corresponding point relation values, due to the presence of the anomalous term in $(1-p)$ occurring in nk (7.6). As $\Omega \to \frac{1}{2}(1-p)$, i.e. in the upper visible for most metals, the 'angular anomalous' values of $\tan 2\Psi$ drop rapidly towards zero in contrast to the gradual decrease of the Drude-Kronig and 'normal incidence' values.

b) $\Omega = \frac{1}{2}(1-p)$. When $\Omega = \frac{1}{2}(1-p)$ the parameters x, Φ, α, β, k^2 and nk have the following orders of magnitude:

$$x \sim 0(\boldsymbol{\sigma\nu})^{-1},\ \Phi - \tfrac{1}{2}(1-p) \sim 0(\boldsymbol{\sigma\nu})^{-1},\ \alpha \sim 0(1),$$

$$\beta \sim 0(1),\ k^2 \sim 0(1),\ nk \sim 0(\boldsymbol{\sigma\nu})^{-2},$$

and

$$(\tan 2\Psi)_{\Omega=\frac{1}{2}(1-p)} \simeq -\{[\alpha(k^2+x)+1][\alpha(1-x)-1]+$$

$$+\beta^2(k^2+x)\,(1-x)\}/\beta(k^2+1). \qquad (7.9)$$

Since α and β depend critically on the exact value of x, these quantities must be calculated from the complete expression (6.4) for each particular case under consideration.

At this point $\tan 2\Psi \sim 0(1)$ and Ψ is small.

c) $\frac{1}{2}(1-p) > \Omega > [\frac{1}{2}\varepsilon(1-p)-1]/(\varepsilon-1)$. In this region $\tan 2\Psi$ is given by (7.7) and (7.8) for *both* values of the principal angle (§ 6.2*c*). The values of Ψ are negative in this range. Physically Ψ can be interpreted as the angle between the diagonal of the bounding rectangle of the elliptical vibrations of the reflected light and the normal to the plane of incidence, so that a positive or negative value for $\tan 2\Psi$ refers purely to the direction in which this angle is measured.

d) $\Omega = [\frac{1}{2}\varepsilon(1-p)-1]/(\varepsilon-1)$. When $\Omega = [\frac{1}{2}\varepsilon(1-p)-1]/(\varepsilon-1)$, x, Φ, α, β, k^2 and nk have the following orders of magnitude:

$$1 - x \sim 0(\sigma\nu)^{-2},\ \Phi - \tfrac{1}{2}(1-p) \sim 0(\sigma\nu)^{-2},\ \alpha \sim 0(1),$$
$$\beta \sim 0(\sigma\nu),\ nk \sim 0(\sigma\nu)^{-1},\ k^2 \sim 0(1),$$

and (7.7) and (7.8) are still applicable. However care must be taken to ensure that in the calculation of Γ the second order variation of x from unity (6.18) is taken into account. At this point Γ is very large and consequently $\tan 2\Psi$ is nearly zero. The principal angle is close to $\frac{1}{2}\pi$; this corresponds to grazing incidence with the reflected light being almost completely plane polarised, i.e. E_p is almost completely absorbed.

e) $[\frac{1}{2}\varepsilon(1-p)-1]/(\varepsilon-1) > \Omega \geq 0$. Within this region there is again only one value for x at any given frequency and (7.7) and (7.8) apply. For $\varepsilon > 1$, $\tan 2\Psi$ is positive and rises steadily as $\Omega \to 0$. For $\varepsilon = 1$ the question of the singularity at the point does not arise (see (6.12)), and as $\Omega \to 0$, $\tan 2\Psi$ becomes increasingly negative.

7.3 The Drude-Kronig solution for Ψ. The Drude-Kronig solution for $\tan 2\Psi$ can be derived quite easily from (7.7) and (7.8) by setting the parameter p equal to unity (see footnote to § 5.5). Then

$$b^2_{p=1} = \varepsilon[\Omega - \tfrac{1}{2}(1-p)]/(1-\Omega) = k^2, \tag{7.10}$$

so that $\Gamma = 1$ and

$$\tan 2\Psi \simeq (k^2 + \sin^2 \Theta)/nk. \tag{7.11}$$

This is the well known optical frequency approximation of the Drude-Kronig formula for the principal azimuth (Dingle [7]), eq. 9.27).

7.4 Comparison between the 'angular anomalous' and Drude-Kronig values for $\tan 2\Psi$ for a typical metal. The general nature of the variation between the 'angular anomalous' and Drude-Kronig values for $\tan 2\Psi$ can best be understood by considering a particular case and plotting $\tan 2\Psi$ vs. Ω and λ for both theories. This has been done using the value of V/c for silver, and taking $\varepsilon = 3$, $p = 0$, and the values found for x in § 6. Further, the quantities n, k and $\sin^2 \Theta$ derived by Dingle [7]) when considering the anomalous skin effect at normal incidence have been substituted in (7.11), so that a comparison of this curve with the 'angular anomalous' curve provides an estimate of the effect of angular terms alone.

As noted earlier by Dingle 8), consideration of the anomalous nature of the skin effect gives values of $\lambda \tan 2\Psi$ which are about one half those of the Drude-Kronig theory. Furthermore it can be seen here that at wavelengths below $\lambda \sim 0.8\mu$, the 'angular anomalous' values of $\lambda \tan 2\Psi$ are appreciably lower than those of the normal incidence theory.

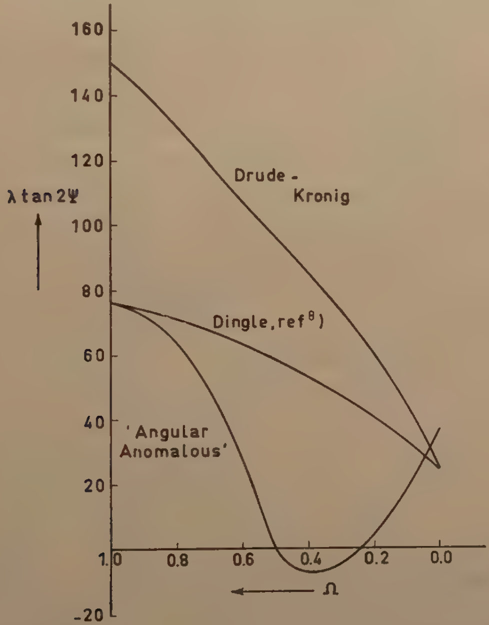

Fig. 4. Principal azimuth; λ tg 2Ψ vs. Ω for Ag, with $\varepsilon = 3$, $p = 0$.

§ 8. *Comparison between theory and experiment.*

8.1 The present theory is strictly applicable only to those metals which can be treated adequately on the one-band model — i.e. to the alkali and noble metals — and even then only to those frequency regions free from absorption bands.

The only extensive experimental work on the alkali metals appears to have been that of Ives and Briggs 25–27), who studied K, Na, Rb and Cs in the range $\lambda \sim 0.58\mu$ to 0.25μ. Unfortunately their results cannot be directly compared with the present theory, since their technique involved measurement of the azimuth ψ and the differential phase shift Δ for the two polarizations E_s and E_p *at a fixed angle of incidence* θ, followed by *calculations* of the optical constants $\mathscr{R}$, Θ, Ψ, n and k based on the Drude-Kronig equations. It has been shown above that these formulae are inadequate when the anomalous skin effect is taken into consideration, so that there is no point in comparing their calculated values with the present theory.

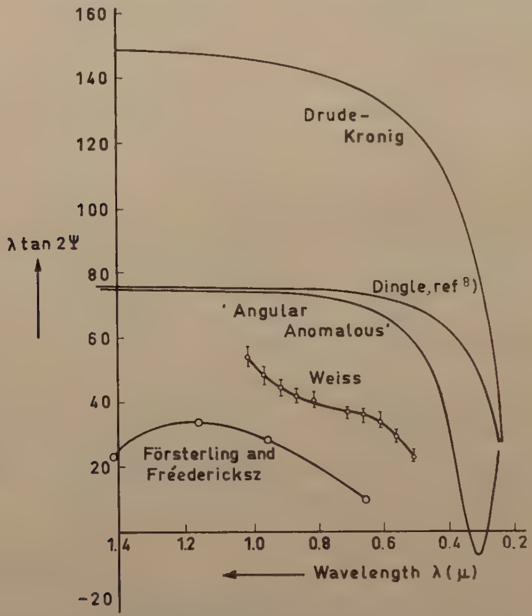

Fig. 5. λ tg 2Ψ vs. $\lambda(\mu)$ for Ag, with $\varepsilon = 3$, $p = 0$.

In the case of the noble metals, a study of the frequency regions in which internal photo-electric absorption bands occur (see, for example, Joos and Klopfer 28), Wilson 24), Friedel 29)) indicates that silver is relatively free from such effects at wavelengths greater than $\lambda \sim 0.33\mu$, and is therefore a suitable metal for comparing this theory with experiment. The only results for silver permitting a direct comparison with 'angular anomalous' theory are those of Försterling and Fréedericksz 30) and Weiss 31), who made direct measurements of the principal angles Θ and Ψ in the wavelength ranges 4.0 to 0.65μ and 1.0 to 0.5μ respectively. 'Angular anomalous' effects are negligible over a greater part of the former region, and are just becoming prominent in the latter. There are unfortunately no results available for the interesting range from 0.5μ to 0.3μ.

8.11 Principal angle of incidence. A comparison between the experimental (Weiss, Försterling and Fréedericksz) and theoretical curves of $\sin^2 \Theta$ against λ is inconclusive. At wavelengths above 0.5μ the 'angular anomalous' and Drude-Kronig curves, and the two experimental curves, lie very close together. In general, the experimental and 'angular anomalous' values of $\sin^2 \Theta$ are lower than the corresponding Drude-Kronig values. This measure of agreement between the 'angular anomalous' and point-relation theories is to be expected *at the longer wavelengths*, since $\sin^2 \Theta$ is predominantly a function of k^2 (6.14) which, to the present order of approximation, is unaffected by the anomalous skin effect.

8.12 The principal azimuth. It was shown by Dingle [8]) that at long wavelengths ($\nu^2 V^2 \ll 1$), consideration of the anomalous skin effect for normal incidence reduces the Drude-Kronig predictions for $\lambda \tan 2\Psi$ by a factor of about two for Ag at room temperatures.

From the accompanying graphs (figs. 4 and 5) it can be seen that, at shorter wavelengths ($\nu^2 V^2 \leq 1$), the 'angular anomalous' values of $\lambda \tan 2\Psi$ are initially slightly lower than those of Dingle, and then drop rapidly away to zero in the vicinity of $\lambda \sim 0.33\mu$. Between 0.33μ and 0.28μ, $\lambda(\tan 2\Psi)_{ang.\ anom.}$ is negative and a two valued function of the wavelength. As remarked in § 7.2(*c*), the change in sign is unimportant and merely refers to the direction in which the azimuth is measured, while the difference in magnitudes between the two values is so slight as to be negligible to the present order of approximation, and in any case unresolvable at present limits of experimental accuracy.

Although the general trend of Weiss' experimental values for $\lambda \tan 2\Psi$ agrees with the decrease predicted by 'angular anomalous' theory, they are consistently lower than the theoretical values by a factor of about two (c.f. a factor of 3 to 5 with point-relation theory). It is likely that this drop in the experimental values can be partially attributed to the influence of absorption bands below $\lambda \sim 0.33\mu$, but even so, it may still be concluded that consideration of 'angular anomalous' effects *does* improve agreement between theory and experiment above this region.

The results obtained by Försterling and Fréedericksz using mechanically polished specimens are lower than those of Weiss by a factor of about two, and are in poor agreement with all theories. Since mechanically polished surfaces have been shown to give lower values of k and higher values of n than do evaporated surfaces (Lowery et. al. [32]), and since $\tan 2\Psi \propto k/n$, this discrepancy between the two sets of experimental results is to be expected.

8.2 Suggestions for future experimental work. There exists at present a great need for experiments especially designed to facilitate comparison of results with the theory of the anomalous skin effect for oblique incidence. Suggestions for future investigations are:

a) Owing to the limitation of this theory to the simplest (i.e. the one-band) model, attention should be directed first to the alkali and noble metals, each group being studied systematically as a series. Later work should concentrate on the divalent alkaline earths, being the next most simple metals from a theoretical viewpoint, and then on other chemically related groups.

b) Experiments should be carried out on the same specimens over a wide frequency range, extending from the infra-red to the ultraviolet, rather than over small, isolated frequency regions, as has very often been the case in the past.

c) Experiments at normal incidence should concentrate on the reflectivity and absorptivity. Quite a wide variety of techniques can be employed in this type of measurement (see, for example, Hagen and Rubens [33]), Lameris [34]), Ramanathan [35]), Heinze [36]), Biondi [37]), and so on).

d) Experiments at oblique incidence should concentrate on measurements of the principal angles. Techniques used in the past include those of Minor [38]), Meier [39]), Försterling and Fréedericksz [30]), O'Bryan [40]), Ives and Briggs [25–27]), Hass [41]), Weiss [31]), while more recent suggestions as to the principles of measurement involved have been put forward by Bor [42]), Archard et al. [43]), Beattie and Conn [44]) and Beattie [45]). A study should also be made of the angular variations of the reflectivity and absorptivity.

e) Measurements of the optical constants should be made over a wide temperature range, extending from room to liquid He temperatures. This is most important since variations between the Drude-

Kronig and 'angular anomalous' theories are most marked when temperature dependences are considered.

f) Measurements of the resistivity of specimens should be made in conjunction with optical measurements, since the metallic mirrors used in optical experiments may not have the same electrical resistance as the bulk metal.

g) Optical experiments should be carried out on specimens prepared by electropolishing or vacuum deposition. Investigations have shown that these techniques give more consistent and more accurate results than do mechanical polishing, electrolysis or chemical deposition (see, for example, Lowery et al. [32]), Reynolds and Stilwell [46]).

h) Experiments should be designed so as to minimise the disturbing effects caused by abnormal surface layers.

Matthiessen's Rule states that the resistance of a metal is separable into two parts, one characteristic of the pure metal and the other due to impurities etc. Therefore it would be expected that

$$\sigma^{-1}_{surface}(T) = \sigma^{-1}_{pure}(T) + C_1,$$
$$\sigma^{-1}_{bulk}\ \ (T) = \sigma^{-1}_{pure}(T) + C_2,$$

where σ_{bulk} is the measured d.c. conductivity of the bulk metal at temperature T, and $\sigma_{surface}$ the conductivity calculated from optical experiments using 'angular anomalous' theory. Thus, subject to the condition that the relevant skin depth is the same for all frequencies considered, the correctness of the theory can be tested by checking the constancy of $\sigma^{-1}_{surface}(T) - \sigma^{-1}_{bulk}(T)$. Since at frequency ν the high frequency skin depth δ_{HF} is

$$\delta_{HF} = (c/2e)\ (m/\pi N)^{\frac{1}{2}}(1 - \varepsilon\pi m\nu^2/Ne^2)^{\frac{1}{2}},$$

the condition is fulfilled at optical frequencies ($\lambda < 1\mu$) for experimental runs in which $\nu^2\varepsilon(\nu)$ is kept constant.

Acknowledgements. The author would like to express his thanks to Dr. R. B. Dingle for first suggesting this problem, and for his constant assistance, guidance and criticism during the course of the investigation; to Professor C. J. B. Clews for his interest and for making available the facilities for carrying out this research; and to the Research Grants Committee of the University of Western Australia, and the C.S.I.R.O. for financial assistance.

Received 12th August, 1957.

REFERENCES

1) Dingle, R. B., Physica **19** (1953) 729.
2) Reuter, G. E. H. and E. H. Sondheimer, Proc. Roy. Soc. **A195** (1948) 336.
3) Schelkunoff, S. A., Bell Syst. Tech. J. **17** (1938) 17.
4) Schelkunoff, S. A., Electromagnetic Waves, van Nostrand, New York 1943.
5) Kronig, R. de L., B. S. Blaisse and J. J. van de Sande, Appl. Sci. Res. **B1** (1947) 63.
6) Dingle, R. B., Physica **18** (1952) 985.
7) Dingle, R. B., Physica **19** (1953) 311.
8) Dingle, R. B., Physica **19** (1953) 348.
9) Dingle, R. B., Physica **19** (1953) 1187.
10) Holstein, T., Phys. Rev. **88** (1952) 1425.
11) Wolfe, R., Proc. Phys. Soc. **A68** (1955) 121.
12) Azbel, M. Ya. and M. I. Kaganov, Dokl. Akad. Nauk S.S.S.R. **95** (1954) 41.
13) Azbel, M. Ya. and M. I. Kaganov, Dokl. Akad. Nauk S.S.S.R. **102** (1955) 49.
14) Azbel, M. Ya., Dokl. Akad. Nauk S.S.S.R. **100** (1955) 437.
15) Azbel, M. Ya. and A. A. Kaner, Zh. eksper. teor. Fiz. **29** (1955) 876. (In English: Soviet Physics J.E.T.P. **2**, 749.)
16) Ginzburg, V. L. and G. P. Motulevich, Uspekhi Fiz. Nauk **55** (1955) 469.
17) Dingle, R. B., Physica **22** (1956) 683.
18) Dingle, R. B., Physica **22** (1956) 1237.
19) Born, M., Optik, Julius Springer, Berlin 1933. (Photo-Lithoprint Reproduction: Edwards Bros, Michigan 1943.)
20) Dingle, R. B., Physica **22** (1956) 671.
21) Pippard, A. B., Proc. Roy. Soc. **A191** (1947) 385.
22) Pippard, A. B., Proc. Roy. Soc. **A191** (1947) 399.
23) Rado, G. T., R. W. Wright, W. H. Emerson and H. Terris, Phys. Rev. **88** (1952) 909.
24) Wilson, A. H., The Theory of Metals, Cambridge University Press, 2nd ed., 1953.
25) Ives, H. E. and H. B. Briggs, J. Opt. Soc. Amer. **26** (1936) 238.
26) Ives, H. E. and H. B. Briggs, J. Opt. Soc. Amer. **27** (1937)181.
27) Ives, H. E. and H. B. Briggs, J. Opt. Soc. Amer. **27** (1937) 395.
28) Joos, G. and A. Klopfer, Z. Phys. **138** (1954) 251.
29) Friedel, J., Proc. Phys. Soc. **B65** (1952) 769.
30) Försterling, K. and V. Fréedericksz, Ann. Phys. Lpz. **40** (1913) 201.
31) Weiss, K., Z. Naturforsch. **3A** (1948) 143.
32) Lowery, H., H. Wilkinson, and D. L. Smare, Phil. Mag. **22** (1936) 769.
33) Hagen, E. and H. Rubens, Ann. Phys. Lpz. **11** (1903) 873.
34) Lameris, P. F., Absorptiemetingen aan Eenige Metalen, Diss. Groningen 1936.
35) Ramanathan, K., Proc. Phys. Soc. **A65** (1952) 532.
36) Heinze, D., Z. Phys. **144** (1956) 455. (See also Diss. Heidelberg 1954.)
37) Biondi, M. A., Phys. Rev. **102** (1956) 964; Phys. Rev. **96** (1954) 534.
38) Minor, R. S., Ann. Phys. Lpz. **10** (1903) 581.
39) Meier, W., Ann. Phys. Lpz. **31** (1910) 1017.
40) O'Bryan, H. M., J. Opt. Soc. Amer. **26** (1936) 122.
41) Hass, G., Ann. Phys. Lpz. **31** (1938) 245.
42) Bor, J., Proc. Phys. Soc. **B65** (1952) 753.
43) Archard, J. F., P. L. Clegg, and A. M. Taylor, Proc. Phys. Soc. **B65** (1952) 758.
44) Beattie, J. R. and G. K. T. Conn, Phil. Mag. **46** (1955) 222.
45) Beattie, J. R., Phil. Mag. **46** (1955) 235.
46) Reynolds, F. W. and G. R. Stilwell, Phys. Rev. **88** (1952) 418.

Appl. sci. Res. Section B, Vol. 7

HALL COEFFICIENT OF TECHNICALLY PURE METALS FROM 80°K TO 800°K

II. RESULTS FOR Zr, W, Mo, Ta, Nb AND Al. SURVEY OF RESULTS FOR THE 4*d*- AND 5*d*-TRANSITION GROUP OF METALS

by V. FRANK

Physics Department, Technical University of Denmark, Copenhagen, Denmark

Summary

The Hall coefficients of W, Mo, Ta and Nb are all positive; they are practically independent of temperature for Mo, Ta and Nb, whereas R_H for W rises linearly with T for high T. R_H for Zr is positive and exhibits a maximum at 250°K with a strong decrease on the high temperature side. R_H for Al is negative, increasing (numerically) with T in the whole temperature range. Surveying existing data it becomes clear that there is no simple correspondence between the temperature variation of R_H and the behaviour of the specific resistance at high temperatures or the electronic structure of the metal. The variation of $r_H (= 1/n^*)$ with the number of conduction electrons is (neglecting all finer details) regular, exhibiting a positive peak ($r_H \simeq 2{,}5$) in the middle of the *d*-band for all three transition groups; interpretation in terms of a two-band model does not seem feasible.

§ 1. *Introduction.* In continuation of earlier work [1]) the results of further measurements on the temperature dependence of the Hall coefficient of metals are communicated. For a description of the measuring system, the heating and cooling arrangement etc. we refer to [1]) and [2]); the way of handling the data and the accuracy obtained are also described in [2]). Two minor modifications in the experimental procedure should be mentioned: *a*) the use of platinum instead of a silver alloy as a welding agent for connecting the copper strips to the sample often proved fruitful; *b*) in the case of Al the sample and connecting strips were cut from one big piece of foil and the copper strips were fastened to the aluminium strips *outside* the furnace; in this way it became possible to make measurements to 620°C without detoriation of the sample.

In § 2 the results obtained are given, compared when possible with existing data.

In § 3 a survey of existing data as regards the temperature variation of r_H is presented.

In § 4 a survey of existing data as regards the variation of r_H with electronic structure is given.

TABLE I

Sample	Impurity Content	$\rho(0°K)/\rho(273°K)$ z%	$\rho(0°C)$ $\mu\Omega$ cm	$10^3\alpha_{0-100}$ $(°K)^{-1}$
Zr I	0.3%	7	39.6	4.26
			(40.5)	(4.0)
Zr II	+ 2.4% Hf	9	40.2	4.24
W	< 0.1%	5.8	4.90 (4.89)	4.85 (4.83)
Ta I	< 0.15%	10–12	12.2	3.75
			(12.4)	(3.6)
Ta II	—	23	12.2	—
Nb	—	7–9	14.2 (13.1)	3.3 (3.9)
Mo	—	2.1	5.06 (5.03)	4.81 (4.7)
Al	< 0.5%	9	2.54 (2.50)	4.66 (4.67)

§ 2. *Results of measurements.* In table I some information about the samples is collected; the values of R_H are shown in fig. 1 and fig. 2. The impurity content will, when possible, be specified below. The column headed z gives the ratio between the specific resistance ρ at 0°K and at 273°K. $\rho(0°K)$ was obtained by comparing our $\rho(T)$-values with those of Holborn [3]), Meissner and Voigt [4]) and Potter [5]) and using Mathiessen's rule. Values of ρ (0°C) and α_{0-100} (the temperature coefficient of resistance between 0 and 100°C) corrected for the influence of the impurities are given in the last two columns of table I; the numbers in parentheses are the values of these quantities as compiled by Gerritsen [6]), except for Nb. For this metal Gerritsen quotes a value obtained by Bridgman ($\rho = 23.3 \mu\Omega$ cm), whereas van Arkel [7]) gives the values in table I (using data of Balke and of Bridgman; the resulting values must be considered as rather uncertain).

Zr. This metal was obtained in annealed form from The Foote Mineral Company, U.S.A.; impurities (according to the manufacturer): 0.1% Fe, 0.1% Ti, 2.40% Hf, other elements < 0.1% (total). From this foil two samples (Zr I and Zr II), differing 90° in orientation, were cut; fig. 2 shows no significant differences in R_H for

Zr I and Zr II, which may indicate that preferred crystal orientation is not present. The z-values in table I were obtained from the

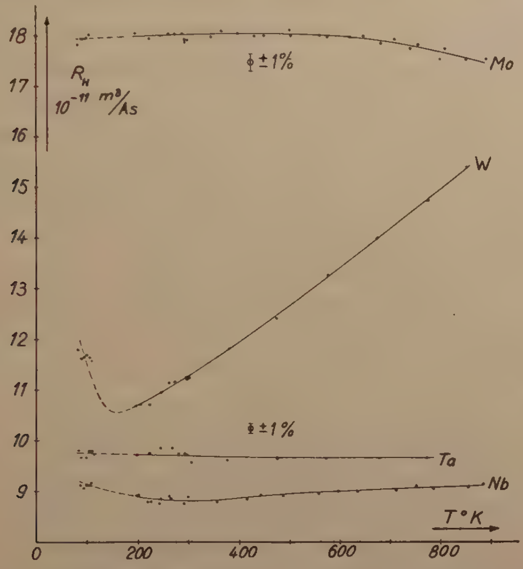

Fig. 1. R_H versus T for Mo, W, Ta and Nb; the sign of R_H is positive for all these metals. Note that the zero point on the ordinate has been suppressed.

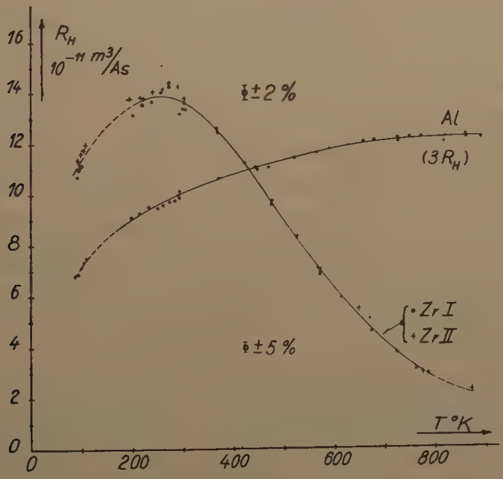

Fig. 2. R_H versus T for Zr (R_H positive) and Al (R_H negative); note that for Al the curve represents $3 \times R_H$.

resistance data at low temperatures only; the difference in z for the two samples may be due to experimental uncertainties and to the fact that Zr II was heated to 600°C against 500°C for Zr I. The high temperature data for Zr I and Zr II and the data of Potter [5]) were not in perfect agreement, but the discrepancies could be suppressed, using values of z only slightly different (2 to 3%) from those in table I. Thus it may be concluded that the high Hf-content does not influence the resistance seriously, which is not unreasonable in view of the similar electronic structure of Hf and Zr. At room temperature Foner [8]) gives $R_H = + 12{,}6 \times 10^{-11}$ m^3/As (purity of sample better than 99.8%).

The strong temperature dependence of R_H even at high temperatures seems to be a common feature for the hexagonal metals. For Zn it was observed by Frey [9]); preliminary measurements on Cd by the present author have revealed a strong effect (including thermal hysteresis for the coldworked sample). For Ti recent measurements by Scovil [10]) at high temperatures and by Berlincourt [11]) at low temperatures show pronounced temperature dependence: R_H shifts from negative to positive values as T is increased; unfortunately the room temperature values given by these authors and by Foner [12]) do not agree very well.

W. "as rolled tungsten blank" was obtained from Murex Ltd., England; impurities (according to the manufacturer): 0.02/0.05% Fe, other elements: traces only. The z-value in table I gave good agreement with the data of Holborn [3]) over the entire range of temperatures.

Ta. Annealed tantalum (TaI) was obtained from Murex Ltd.; impurities (according to the manufacturer): Nb $< 0.1\%$, C $< 0.01\%$, other elements: traces only. It was found that ρ (0°C) had increased somewhat after the high-temperature run, but R_H was not altered significantly; the agreement with the resistance data of Potter [5]) was not very good for a single value of z. Besides TaI another tantalum sample (Ta II) was also investigated (at high temperatures only) with the following results: $z = 23\%$; $R_H = + 9.22 \times 10^{-11}$m^3/As independent of T. Thus R_H for Ta II is only 5% lower than R_H for Ta I in spite of the great difference between the corresponding values of z. For this reason the data for Ta II have not been included in fig. 1.

Nb. The sample was of unknown origin. ρ(0°C) had increased somewhat after the high temperature run, but R_H was not altered; the agreement with the $\rho(T)$-values given by Potter [5]) was not very good.

Mo. The sample was of unknown origin; the agreement with the resistance data of Potter [5]) was good.

Values of R_H for W, Ta and Mo at 300°K are given by Smith [13]) (without statement of impurity content); they are $+ 11.8$, $+ 10.1$ and $+ 12.6 \times 10^{-11}$ m^3/As respectively; except for Mo the agreement with the present work is good.

R_H for Mo, Ta and Nb is practically independent of T (to a better approximation than is R_H for the "simple" metals Cu, Ag and Au). This is not readily explained because $\rho(T)$ for these metals does not behave as expected for an ideal metal (i.e. proportional to T, when $T > \theta$); furthermore W, the electronic structure of which is similar to that of Mo, does not show this unexpected constancy of R_H.

Al. This metal was included in the present work as an example of a polyvalent, cubic metal outside the transition groups. The sample was cut (see § 1 for details) from commercial foil with impurities mainly consisting of Fe (0.24%) and Si (0.19%); this rather high impurity content is reflected in the high value of z given in table I. The resistance data were in good agreement with those of Holborn [3]) for the value of z indicated. At room temperature Raethjen [14]) gives $R_H = - 3{,}44 \times 10^{-11}$ m^3/As, the same value was found by Jones [15]) working with single crystals of Al; the agreement with the present value is good. In the low temperature region our values compare reasonably with the data of Smith [16]) and of Alterthum [17]); at 20°K Alterthum gives a value which is numerically higher than the value at 80°K, thus leading to a minimum in $|R_H|$. The temperature variation of R_H for Al is of the same type as that observed for Pd and Pt [1]); as the three conduction electrons in Al are distributed in overlapping s–p bands, the influence of shifting and broadening of the Fermi distribution at high T could be responsible for the observed effect.

§ 3. *Temperature variation of r_H.* In fig. 3 the results from the present work and from ref. [1]) are collected. The ordinate gives the quantity r_H, where

$$r_H(T) = N(300°\mathrm{K})\ |e| R_H(T).$$

Here N is the number of *atoms* per unit volume and e is the charge of the electron. The value of N has been calculated using room-temperature values of the lattice constants; thus the *direct* effect of thermal dilatation is still included in $r_H(T)$; however the magnitude of this effect is only a few % at 800°K.

Included in fig. 3 are $r_H(T)$ for Y (purity 99.2%) and for La (purity 99.8%), calculated from the data given by Kevane et al. [18]); these authors state, that R_H for La is sensitive to thermal treatment. Included are also values of $r_H(T)$ for Au, Cu and Rh calculated from the data given by Teutsch and Love [19]), Berlincourt [11]) and Coles and Taylor [20]) respectively; as R_H was only measured at a few temperatures in these investigations, these results have been shown as dotted curves.

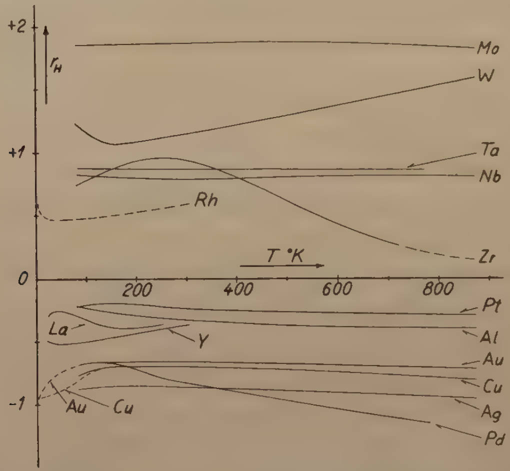

Fig. 3. r_H ($r_H = N|e|R_H$, where N is the number of atoms per unit volume) versus T. The values for Y and La are due to Kevane et al. [18]), for Rh to Coles and Taylor [20]) and for Au and Cu (at low temperatures) to Teutsch and Love [19]) and Berlincourt [11]) respectively.

From fig. 3 it is evident that for many of the metals (including Cu, Au and probably also Ag) R_H shows a significant variation at low temperatures. Sondheimer has obtained a rigorous solution of the Boltzmann equation for the case of a simple (one-band) metal in a magnetic field at low temperatures; the evidence is (unpublished, but quoted by Chambers [21]))that "R_H is inappreciably different from $-1/|e|n$" (n is the number of electrons per unit volume). When a two-band description is adopted, it is frequently found in the literature, that variation in R_H with temperature may be brought about by variation in the ratio of carrier mobilities for the two bands; this variation in turn is ascribed to the variation in lattice spacing. Especially in the hexagonal metals, where the Fermi surface may extend slightly across some Brillouin zone boundary, the properties of the metal are expected to be sensitive to the lattice expansion (see e.g. ^{10})). No detailed theory along these lines has, to our knowledges, been worked out.

At high T, $|R_H|$ is either practically constant or increases with increasing T; Zr (and some other hexagonal metals quoted in § 2, but not shown in fig. 3) are, however, exceptions to this "rule". A list of possible mechanisms leading to a temperature variation of R_H has been given in ref. ^{1}); of these the influence of thermal expansion on the scattering mechanism, as already discussed above, should still be operative at high T, leading to a variation of R_H in the same direction as at low T. This is certainly not the case for most of the metals depicted in fig. 3, so that other mechanisms must dominate at high T. One such possibility, namely the influence of shifting and broadening ("smearing") of the Fermi-distribution at high T, was discussed in some detail in ref. ^{1}) in connection with the data for Pd and Pt. This mechanism will be important for all metals where the following conditions are fulfilled: *a*) the carriers are distributed in two or more bands with different effective masses, *b*) inter-band transitions play a rôle in the scattering process and *c*) the width in energy of the filled or empty parts of one or more of the bands is of the order 0.1 to 0.2 eV (equivalent to 1000–2000°K). Such a situation as regards band structures is not unreasonable either for the hexagonal metals (which all, in so far as data exist, show strong temperature variation of R_H) or for the cubic transition metals. However, as remarked in § 2, there is no obvious correlation between the temperature dependence of R_H and the resistance anomalies (ρ rising faster or slower than T) observed for many of the metals in question. As these anomalies are also partially brought about by the shifting and "smearing" of the Fermi-distribution, it seems safe to conclude that the finer features of magnetoconductive phenomena in the transition metals depend in a complicated way on the details of the band structure of these metals.

Finally it should be noted that there is a partial correlation between the temperature variation of R_H for a metal and the position of this metal in the periodic system: R_H for Cu, Ag and Au behaves similarly, as does R_H for Pd and Pt and for Ta and Nb; R_H for Zr and Ti and for W and Mo behaves however dissimilarly.

§ 4. *Variation of r_H with electronic structure.* Until now only the temperature variation of R_H has been discussed; as regards the absolute values of r_H, the variation of this quantity with position in the periodic table is shown in fig. 4 and 5. Included in these graphs are (besides the data from fig. 3) the values of R_H for Cs and Rb from a survey by Krautz [22]), for Ru ($z = 6.8\%$) from the work of Justi [23]), for Ir ($z = 5.4\%$) from the work of Gehlhoff et al. [24]) and for Hf ($R_H = -0.16 \times 10^{-11}$ m^3/As) from work of Foner [8]). R_H for Re was determined by Aschermann and Justi [25]), the sintered sample ($z = 1.7\%$) gave $R_H = +31.5 \times 10^{-11}$ m^3/As; as the density of the sample was only 72% of the X-ray density, we have applied a correction formula on magneto-conductive phenomena in porous media from the note of Juretschke et al. [26]); their formula for the case of spherical cavities leads to R_H (corrected) $\simeq 24.4 \times 10^{-11}$ m^3/As (the applicability of this correction formula in the case of a hexagonal metal is uncertain, as is altogether the situation for polycrystalline material of a hexagonal metal). No values of R_H for Sr, Ba and Tc seem to be available; for Os preliminary measurements on pressed and sintered samples have given a very small value for R_H (private communication from prof. E. Justi; as the density of the samples was insufficient, this result is not considered definitive by prof. Justi). Finally the values of R_H for Ag-Pd alloys as obtained by Schindler [27]) at room temperature are also shown in fig. 4.

Quite a number of the metals included in fig. 4 and 5 are of hexagonal structure; as the values of r_H for these metals have been determined for polycrystalline samples and at low temperatures only, the picture is far from complete; however on a *coarse scale* the variation of r_H with the number of conduction electrons is to a certain degree regular and shows the same general behaviour for the two groups of metals in question. The same pattern is also found for the group of metals conducting by $4s/3d$-electrons, the high positive peak for r_H occurring at Cr (results of S. Foner [12]) [30])).

An interpretation of some of the results shown in fig. 4 and 5, using a two-band model, has been attempted by several authors; for the elements Ru, Rh, Pd and Ag and Re, Ir, Pt and Au a partially successful fit was obtained by Gehlhoff, Justi and Kohler [24]); one of the proposals of these authors is that in Ru and Re the s-band contributes a hole-like term to R_H. For Rh they propose $n_d \simeq 2$, $n_s \simeq 1$ and $\sigma_s/\sigma \simeq 0{,}1$ *); contrary to this interpretation the more extensive data for Rh obtained by Coles and Taylor [20]) could be very nicely fitted (including the strong field dependence of R_H observed at low temperatures) by the two-band formula with the following values of the parameters: $n_d \simeq 0.17$, $n_s \simeq 4.2$ and $\sigma_s/\sigma \simeq 0.68$. As the n-values are beyond the limits of physical

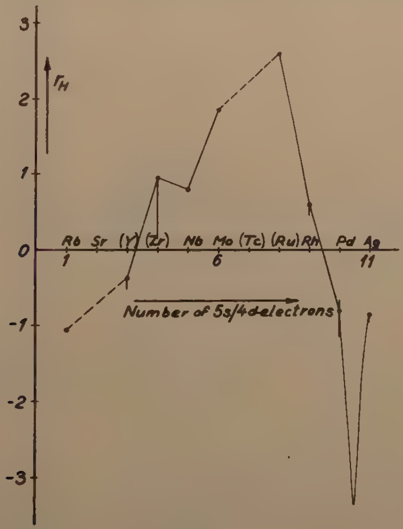

Fig. 4. r_H versus the number of $5s/4d$ electrons. The circles denote the room temperature value of r_H, while the vertical lines denote the range in which r_H has been observed at different temperatures. The symbols for the metals with hexagonal structure are given in parentheses. For sources of data see text.

significance, Coles and Taylor tentatively proposed a three-band description (overlapping of the $5s$-, $5p$- and $4d$-bands) in which case the two-band formula becomes a pure formal device. Schindler[27]), in his discussion of the data for the Pd-Ag alloys, concludes that these results cannot be understood on the basis of the two band model and lists several good reasons for the breakdown of this model when applied to real metals of the transition groups. Recent investigations, that of Overhauser and Schindler[28]) on the resistivity of Ni-Pd alloys and that of Hoare and Yates[29]) on the electronic specific heat of Ag-Pd alloys, give direct experimental evidence, as stated by the respective authors, that the electronic level density in the *d*-band of even these simpler transition metals is far from the parabolic form.

---

*) n denotes the number of electrons per atom and σ denotes conductivity.

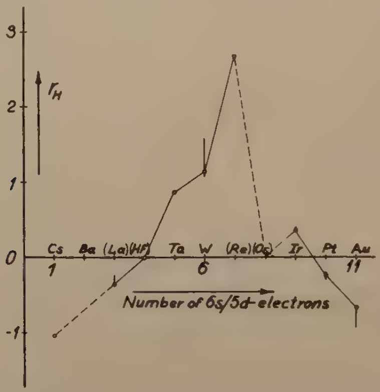

Fig. 5. r_H versus the number of $6s/5d$ electrons. Indications in the figure are the same as in fig. 4. The value of r_H for Os is not definite. For sources of data see text.

Thus it does not seem reasonable to fit the totality of data in fig. 4 and 5 to a two-band formula. Whatever interpretation is finally adopted, it seems that the high value of r_H for the metals in the middle of the periods is most difficult to explain; there may, however, be a connection between the well known low level density in the middle of the *d*-bands and the high values of r_H.

Acknowledgements. I am very grateful to The Foote Mineral Company, Inc., U.S.A. for donating a piece of zirconium foil. My best thanks are due to prof. E. Justi for information about the preliminary value of R_H for Os and to dr. S. Foner for information of his as yet unpublished values of R_H for Hf and Zr. Finally I want to thank "Den ingeniørvidenskabelige fond og G. A. Hagemann's mindefond" for a grant and prof. H. Højgaard Jensen and prof. A. Nielsen for commenting on the manuscript.

Received 29th June, 1957.

REFERENCES

1) Frank, V., Appl. Sci. Res. B **6** (1957) 379.
2) Frank, V., K. Danske Vidensk. Selsk. Mat.-fys. Medd. **30** (1955) nr. 4.
3) Holborn, L., Ann. Phys., Lpz. IV Folge **59** (1919) 145.
4) Meissner, W. and B. Voigt, ibid, V Folge, **7** (1930) 761 and 892.
5) Potter, H. H., Proc. Phys. Soc. Lond. **53** (1941) 695.
6) Gerritsen, A. N., Hdbch.d.Ph.XIX (Springer Verlag 1956) 156.
7) Arkel, A. E. van, Reine Metalle, Springer Verlag, Berlin 1939, p. 232.
8) Foner, S., unpublished.
9) Frey, W., Ann. Phys. Lpz. IV Folge **46** (1915) 1057.
10) Scovil, G. W., J. Appl. Phys. **27** (1956) 1197.
11) Berlincourt, T. G. Bull. Amer. Phys. Soc., series II, **2** (1957) no 3, 136.
12) Foner, S., Phys. Rev. **91** (1953) 447.
13) Smith, A. W., Phys. Rev. **8** (1916) 79.
14) Raethjen, P., Phys. Zeitschr. **25** (1924) 84.
15) Jones, P., Phil. Mag. **4** (1927) 1312.
16) Smith, A. W., Phys. Rev. **30** (1910) 1.
17) Alterthum, H., Ann. Phys., Lpz. IV Folge **39** (1912) 933.
18) Kevane, C. J., S. Legvold and F. H. Spedding, Phys. Rev. **91** (1953) 1372.
19) Teutsch, W. B. and W. F. Love, Phys. Rev. **105** (1957) 487.
20) Coles, B. R. and J. C. Taylor, J. Phys. Chem. Solids **1** (1957) 270.
21) Chambers, R. G., Proc. Phys. Soc. A **65** (1952) 909.
22) Krautz, E., Z. Naturforsch. **5a** (1950) 13.
23) Justi, E., ibid. **4a** (1949) 472.
24) Gehlhoff, P. O., E. Justi and M. Kohler, Z. Naturforsch. **5a** (1950) 16.
25) Aschermann, G. and E. Justi, Phys. Zeitschr. **43** (1942) 207.
26) Juretschke, H. J., R. Landauer and J. A. Swanson, J. Appl. Phys. **27** (1956) 838.
27) Schindler, A. I., J. Phys. Chem. Solids **1** (1956) 42.
28) Overhauser, A. W. and A. I. Schindler, J. Appl. Phys. **28** (1957) 544.
29) Hoare, F. E. and B. Yates, Proc. Roy. Soc. A **240** (1957) 42.
30) Foner, S., Phys. Rev., in press.

THEORY OF THE ABERRATIONS IN THE FOCUSING PROPERTIES OF A MAGNETIC FIELD WITH ONE PLANE OF SYMMETRY

by A. J. H. BOERBOOM

Laboratorium voor Massaspectrografie, Amsterdam, Netherlands

Summary

A general theory is given of the aberrations in focusing properties occurring in fields with one plane of symmetry. It appears that line to line imaging is possible and that ten geometrical aberrations of the second order exist, together with five chromatic aberrations. Names for these aberrations are proposed. The beam intensity distribution in the image is calculated.

§ 1. *Introduction.* Let us consider two planes perpendicular to the plane of symmetry of the magnetic field and perpendicular to the main ion trajectory. The first plane, having coordinates (x, y), is acting as an object plane. The second plane has coordinates (u, v). The y and v axes are perpendicular to the plane of symmetry, the x and u axes lie in this plane. The trajectory of an ion passing the x, y plane is projected on the symmetry plane and on a plane through the main orbit perpendicular to the symmetry plane. These projections make angles ξ and η with the main orbit. We confine ourselves to paraxial trajectories. The symmetry plane is supposed to be horizontal.

The trajectory of an ion with a certain momentum and charge will be completely defined by x, y, ξ and η; thus u and v are also determined by these four quantities. Hence in first approximation one may write

$$u = a_0 + a_1 x + a_2 y + a_3 \xi + a_4 \eta, \tag{1}$$

$$v = b_0 + b_1 x + b_2 y + b_3 \xi + b_4 \eta. \tag{2}$$

On replacing y by $-y$ and η by $-\eta$, x and ξ remaining unchanged,

v will change into $-v$, while u does not alter, so

$$u = a_0 + a_1x - a_2y + a_3\xi - a_4\eta, \tag{3}$$

$$-v = b_0 + b_1x - b_2y + b_3\xi - b_4\eta. \tag{4}$$

Subtraction of (3) from (1) and addition of (2) and (4) give

$$0 = 2a_2y + 2a_4\eta,\ 0 = 2b_0 + 2b_1x + 2b_3\xi.$$

These relations being valid for all values of x, y, ξ and η, it follows that

$$a_2 = a_4 = 0,\ b_0 = b_1 = b_3 = 0.$$

Hence in first approximation

$$u = a_0 + a_1x + a_3\xi, \tag{5}$$

$$v = \qquad b_2y + b_4\eta. \tag{6}$$

§ 2. Now all coefficients a and b are functions of the position of the u, v plane. Supposing the function a_3 becomes zero at some point, we transfer the plane to this point. In general the function b_4 will not be zero at this point. So in first approximation u depends only on x. This means that the ions originating from a point (x_0, y_0) will intersect the u, v plane in points (u_0, v) representing a line parallel to the v axis. This holds for all points (x_0, y) of a line in the object plane parallel to the y axis. So we may speak of a first order line to line mapping by the magnetic field. As follows from the formulae, a proportionality also exists between the distances of lines in the object plane and the corresponding distances in the image plane.

We could however, have transferred the u, v plane to the point where b_4 is zero. In that case lines in the object plane parallel to the symmetry plane are mapped in first approximation as lines. In general, there are two focusing planes which we may call the *sagittal* and the *meridional* image plane. A special case appears when both planes coincide. Then in first approximation a point to point mapping exists.

§ 3. It is interesting that the existence of the plane of symmetry is not necessary for the kind of imaging treated in the foregoing paragraph; every static electromagnetic field has the following focusing properties: through every point of the object space two lines pass which in first approximation are imaged as lines. There is one plane for which point to point imaging exists.

The proof goes as follows: Considering a main orbit and two planes perpendicular to this orbit, with respectively the coordinates (x, y) and (u, v), as a first approximation we may use (1) and (2). Now we perform a coordinate transformation in the u, v plane, such as to make the coefficient of η equal to zero in the new U coordinate and to make the coefficient of ξ equal to zero in the new V coordinate. Again we perform a coordinate transformation in the x, y plane, so as to make the coefficient of the new coordinate Y equal to zero in U, and the coefficient of X equal to zero in V.

We now get the equations

$$U = A_0 + A_1 X + A_3 \xi, \tag{7}$$

$$V = B_0 + B_2 Y + B_4 \eta, \tag{8}$$

and from here the same reasoning holds as used before to get two focusing planes.

This reasoning holding for every plane in the object space, we may remove the x, y plane such as to make $A_3 = B_4$, and this results in a point to point imaging.

§ 4. We return to the case of the field with the plane of symmetry. The aberrations of the first order focusing are given by the second order terms, which have been omitted in (5) and (6). From the symmetry condition again it follows that in u only those terms remain which are even in y and η together, i.e. the terms x^2, $x\xi$, ξ^2, y^2, $y\eta$ and η^2, whilst in v only the terms remain, that are odd in y and η together, i.e. the terms xy, ξy, $x\eta$ and $\xi\eta$. We call the respective proportionality coefficients D_1 to D_{10}.

In the case of the sagittal focusing ($a_3 = 0$) we are not interested in the second order terms in v, as they may be neglected with respect to the first order term $b_4\eta$. The error in u we will separate, as usual in optics, into the different terms.

In fig. 1 are shown the images produced from rectangular object slits if successively only one term enters. It is assumed that for every point of the object slit region the same ranges of values of ξ and η exist. In this figure we drew in the object slits a structure of lines and points with their respective images. The image of the object slit is their envelope.

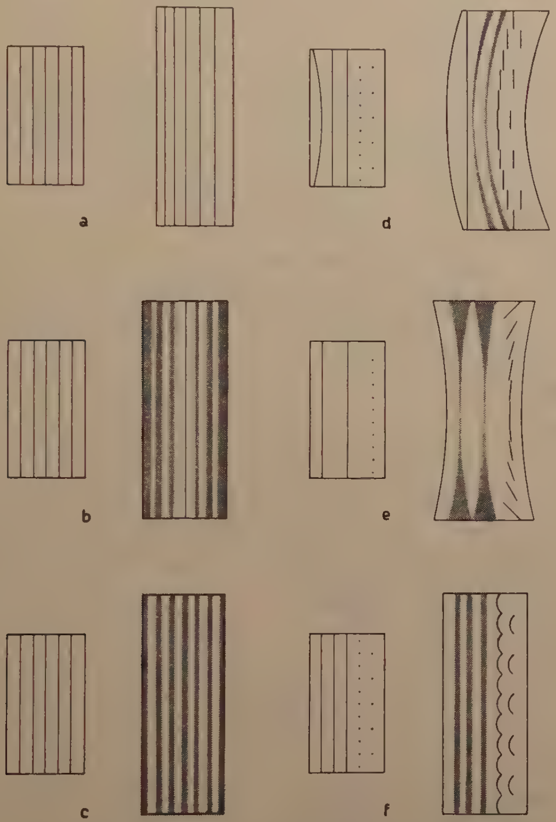

Fig. 1. The six sagittal aberrations.

a. distortion
b. image plane rotational aberration
c. meridional aperture aberration
d. curvature of the image
e. agammatism
f. sagittal aperture aberration

The first aberration (D_1x^2) causes a *distortion*: equidistant lines are no longer imaged at equal mutual distances. The image, however, is sharp.

The second aberration ($D_2x\xi$) causes a line broadening proportional to the distance from the central line. Ions, originating from an object line with positive x focus on one side of the u, v plane, those with negative x on the other side. The distances of the focusing lines to the u, v plane are proportional to x, so it is obvious that we get a sharp image by rotating the u, v plane around the central line over a certain angle. This aberration we designate *image plane rotational aberration.*

The third aberration ($D_3\xi^2$) causes a constant defocusing over the whole image plane, proportional to the square of the aperture in the median plane. This aberration we call the *meridional aperture aberration.* The paraxial image plane is also the plane of the least defocusing, contrary to the aperture error (spherical aberration) in rotationally symmetric systems.

The fourth aberration (D_4y^2) causes a straight line to be produced on the surface, described by a parabola, when this parabola moves along its top tangent. A defocusing and a *curvature of the image* result. There are, however, in the object plane parabolae $a_1x - D_4y^2 = C$ which are sharply imaged as straight lines.

The fifth aberration ($D_5y\eta$) causes a defocusing, proportional to the distance from the median plane. This defocusing is considerably less for distinct parabolae in the object plane. In analogy with the name astigmatism we could call this aberration *agammatism,* since a line is not imaged as a line.

The sixth aberration ($D_6\eta^2$) again causes a constant defocusing over the image plane. It is an aperture aberration which we will call *sagittal aperture aberration.* Here also the paraxial image plane is the plane of the least defocusing.

§ 5. The foregoing considerations are valid for ions of the same momentum and charge. If ions with a different momentum to charge ratio are considered, all expansion coefficients a and b will change. This causes an alteration of the image in three respects, so that there are three chromatic aberrations.

The change of a_0 results in a displacement of the image. It is an effect of the first order that is known under the name *dispersion.* If it is the intention to separate the ions according to mass or energy, the dispersion is not considered as an aberration.

The change of a_1 causes a change in the magnification; we could designate it as the *magnification error.*

The change of a_3 causes a displacement of the paraxial focusing plane. We call it the *sagittal focusing plane shift.*

§ 6. Now let us consider the meridional focusing. Here four aberrations of the second order appear, being the second order terms in v. In fig. 2 these aberrations are represented.

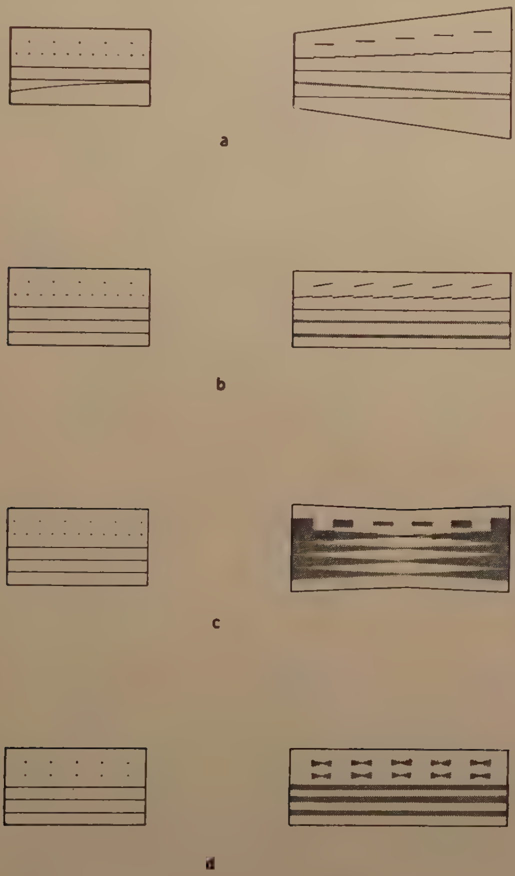

Fig. 2. The four meridional aberrations.

a. obliquity
b. inclination aberration
c. image plane rotational aberration
d. mixed aperture aberration

The first meridional aberration (D_7xy) causes an oblique, defocused image of lines parallel to the plane of symmetry. There are, however, hyperbolae which are sharply imaged, namely the hyperbolae $b_2y - D_7xy = C$. This aberration we designate *obliquity*.

The second meridional aberration $(D_8y\xi)$ again causes an unsharpness increasing with the distance from the central line. Certain hyperbolae exist that are imaged considerably sharper. We call this *inclination aberration.*

The third meridional aberration ($D_9 x\eta$) also causes an unsharpness, which can be removed, however, by a rotation of the image plane about the vertical central line. This aberration we again call the *image plane rotational aberration*, but now of the meridional image plane.

The last aberration ($D_{10}\xi\eta$) causes a constant defocusing over the whole image. It is an aperture defect which we will call the *mixed aperture aberration.*

Also in the meridional focusing, chromatic aberrations appear. A change of b_2 again causes a change in the magnification, while a change of b_4 displaces the focusing plane. These aberrations we call respectively the *meridional magnification error* and the *meridional focusing plane shift.* It is obvious that an analogue of the dispersion does not exist in meridional focusing.

In the case of § 3 (no plane of symmetry) in both focusing planes all fifteen aberrations appear.

§ 7. We shall now consider the influence of the sagittal aberrations on the brightness in the image. If the ion current density distribution in the object slit is known as a function of x, y, ξ and η, it is possible to compute the influence of the different aberrations on the current density in the image. This function in general has the form of a Gaussian probability curve, cut by diaphragms. The exact function will be found in the best way by experiment. We will perform the calculations on the simple assumption that a surface element $\mathrm{d}x\,\mathrm{d}y$ of the object slit radiates into a solid angle $\mathrm{d}\xi\,\mathrm{d}\eta$ an ion current equal to $I_0\,\mathrm{d}x\,\mathrm{d}y\,\mathrm{d}\xi\,\mathrm{d}\eta$ if x, y, ξ and η lie within certain small intervals

$$-a < x < +a, \quad -b < y < +b, \quad -\alpha < \xi < +\alpha, \quad -\beta < \eta < +\beta,$$

whereas the number of ions is zero if at least one of these variables is outside the considered interval.

In the image plane we take a line of constant v and we compute the number of ions passing through this plane in points with $v < c$. These ions originate from points in the fourdimensional interval defined above, lying at the side of the threedimensional subspace, corresponding to $v < c$.

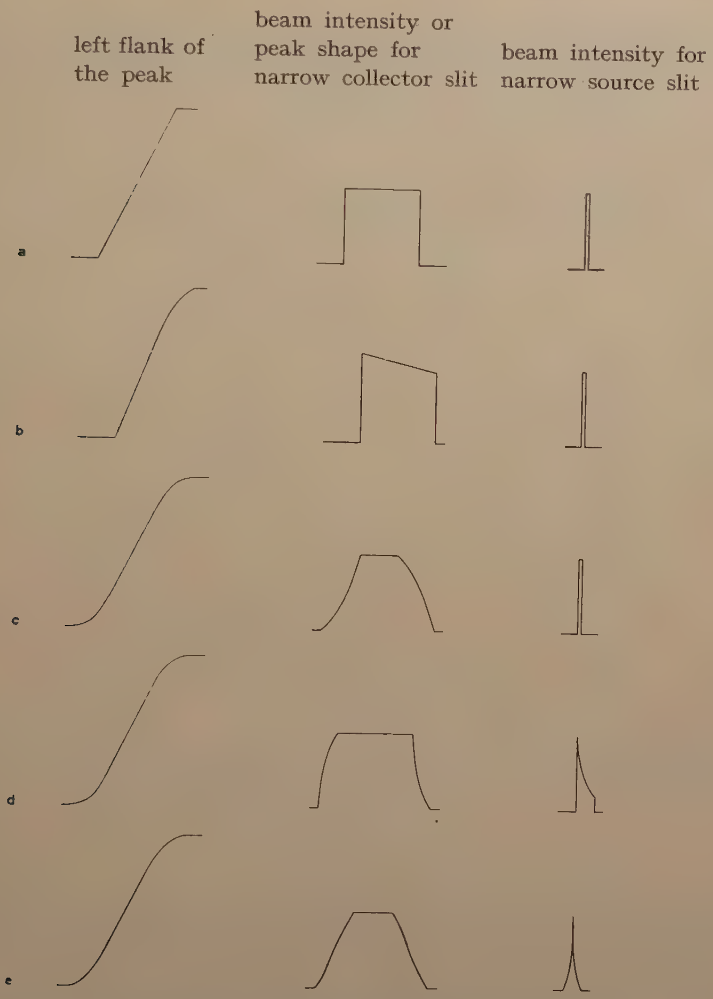
left flank of the peak
beam intensity or peak shape for narrow collector slit
beam intensity for narrow source slit
a
b
c
d
e

Fig. 3. Influence of the sagittal aberrations on the peak shape and the brightness of the image.

a. aberration free image
b. distortion
c. image plane rotational aberration
d. curvature of the image and both aperture aberrations
e. agammatism

The fourdimensional volume between two such subspaces c_1 and c_2 gives the number of ions, passing through a collector slit with edges $v = c_1$ and $v = c_2$. The threedimensional volume of the cross-section of $v = c$ with the interval gives the intensity of the ion beam for $v = c$. The cross-section of $v = c$ with $x = 0$ gives the ion beam intensity in the focusing plane in the case of a very narrow object slit.

§ 8. For an error free image $u = a_0 + a_1 x$, so the number of ions passing through the image plane in points with $u < c$ is given by

$$I(c) = I_0 \int_{-b}^{+b} \mathrm{d}y \int_{-\alpha}^{+\alpha} \mathrm{d}\xi \int_{-\beta}^{-\beta} \mathrm{d}\eta \int_{-a}^{x(c)} \mathrm{d}x, \tag{9}$$

where

$$\begin{aligned} x(c) &= -a && \text{for} && u < a_0 - a_1 a, \\ x(c) &= (u - a_0)/a_1 && && a_0 - a_1 a < u < a_0 + a_1 a, \\ x(c) &= +a && && a_0 + a_1 a < u. \end{aligned}$$

Hence for the three cases mentioned above, respectively,

$$\begin{aligned} I(c) &= 0, \\ &= 8\, b\alpha\beta\, I_0 \frac{c - a_0 + a_1 a}{a_1}, \\ &= 16\, ab\alpha\beta\, I_0. \end{aligned} \tag{10}$$

Differentiating with respect to c gives the beam intensity for $u = c$, i.e.

$$0, \quad \frac{8\, b\alpha\beta\, I_0}{a_1} \quad \text{and} \quad 0.$$

We perform the same integration for the successive aberrations. Complicated formulae result here, which can be simplified considerably by some change in notation. First we move the origin in the image plane such as to make $a_0 = 0$; then we change the unit of length to make $a_1 = 1$. For D_n we write D, whilst we take $I_0 = 1$.

If only the first aberration acts, we get $u = x + Dx^2$. Assuming $0 < D < 2/a$ the integral yields

$$\begin{aligned} \frac{I(u)}{8\, b\alpha\beta} &= 0 && \text{for} && u < -a + Da^2, \\ &= u - Du^2 + a && && -a + Da^2 < u < +a + Da^2, \\ &= 2a && && +a + Da^2 < u. \end{aligned} \tag{11}$$

If D is outside the assumed interval, we get similar results. Indeed the results depend on the relative magnitude of the occurring quantities. We do not consider here all possibilities.

In the same way the second error $u = x + Dx\xi$ yields, assuming that $0 < D < 1/\alpha$,

$$\begin{aligned}
\frac{I(u)}{4b\beta} &= 0 && \text{for } u < -a - Da\alpha, \\
&= a\alpha + \frac{u+a}{D} + \frac{u}{D}\ln(1 + D\alpha) - \frac{u}{D}\ln\frac{-u}{a} \\
& && \text{for } -a - Da\alpha < u < -a + Da\alpha, \\
&= 2a\alpha + \frac{u}{D}\ln\frac{1 + D\alpha}{1 - D\alpha} \\
& && \text{for } -a + Da\alpha < u < +a - Da\alpha, \\
&= 4a\alpha - \frac{I(-u)}{4b\beta} && \text{for } 0 < u.
\end{aligned} \tag{12}$$

This last formula can be proved by a simple geometric consideration.

For the third aberration we suppose $0 < D < 2a/\alpha^2$ and find

$$\begin{aligned}
\frac{I(u)}{4b\beta} &= 0 && \text{for } u < -a, \\
&= {}^4/_3 \frac{1}{\sqrt{D}}(u + a)^{3/2} && \text{for } -a < u < -a + D\alpha^2, \\
&= 2\alpha(u + a) - {}^2/_3 D\alpha^3 && \text{for } -a + D\alpha^2 < u < +a, \\
&= 2\alpha(u + a) - {}^2/_3 D\alpha^3 - {}^4/_3 \frac{(u + a)^{3/2}}{\sqrt{D}} \\
& && \text{for } +a < u < +a + D\alpha^2, \\
&= 4a\alpha && \text{for } +a + D\alpha^2 < u.
\end{aligned} \tag{13}$$

The fourth and sixth aberration give results, exactly similar to the third aberration, because the sections $u = c$ in these three cases are cylindrical paraboloids.

The fifth aberration gives, assuming $0 < D < a/b\beta$,

$$
\begin{aligned}
\frac{I(u)}{2\alpha} &= 0 && \text{for } u < -a - Db\beta, \\
&= {}^3/_2 Db^2\beta^2 + \frac{(u+a)^2}{2D} + 2b\beta(u+a) + \frac{(u+a)^2}{D}\ln\frac{-u-a}{Db\beta} \\
& && \text{for } -a - Db\beta < u < -a, \\
&= {}^3/_2 Db^2\beta^2 + \frac{3(u+a)^2}{2D} + 2b\beta(u+a) + \frac{(u+a)^2}{D}\ln\frac{Db\beta}{u+a} \qquad (14) \\
& && \text{for } -a < u < -a+Db\beta, \\
&= 5Db^2\beta^2 + 4b\beta(u + a - Db\beta) \\
& && \text{for } -a+Db\beta < u < +a-Db\beta,
\end{aligned}
$$

while $I(u)$ for $a - Db\beta < u$ is found from the general formula

$$I(u) = I(u - c) + 8\alpha b\beta c - I(u - 2b) \qquad (15)$$

where c has to be chosen in such a way that $-a + Db\beta < u - c < < + a - Db\beta$. This last formula again can be simply proved by geometric reasoning.

In fig. 3 the left flank of a peak is drawn for the successive aberrations, together with the beam intensity or the peak shape in the case of a very narrow collector slit and the beam intensity in the case of a very narrow source slit.

Acknowledgement. The author is indepted to Prof. Dr J. Kistemaker for his stimulating interest, to A. P. de Jongh for making the drawings and to Dr R. Rummel for reading the manuscript. This work is part of the research program of the Stichting voor Fundamenteel Onderzoek der Materie.

Received 20th July, 1957.

Appl. sci. Res. Section B, Vol. 7

ON THE MEASUREMENT OF SPEED OF A VACUUM PUMP

by N. A. FLORESCU

School of Applied Physics, N.S.W. University of Technology, Sydney, Australia

Summary

After pointing out the drawbacks of the conventional procedures of pumping speed measurement, an improved procedure is described in which the admitted gas is uniformly distributed over a cross section of a tube of the same size as the pump casing. The pressure is measured above this section, where the gas is in a static state. The actual as well as the intrinsic speed of the pump can accurately be determined. As the speed factor for indicating the pumping efficiency the ratio of these speeds is suggested. The intrinsic speed is a function of the intake pressure. The highest value of this speed was found to be 65 per cent of the conductance of a well designed pump. These results do not agree with the conclusions of the diffusion theory. Correction of the Langmuir formula suggested previously by the writer is confirmed.

§ 1. *Introduction.* Measurement of the pumping speed supplies both experimental data which are useful in indicating the practical performance of pumps, and information which can be used to check existing theories and to provide indications of the direction future improvements should take. Any attempt to check a theory of the vapour pump has been handicapped by the lack of adequate quantitative data. This was due to the difficulty of obtaining accurate value for the measured pumping speed.

Although several methods have been used to perform such measurements, all results so far obtained are inaccurate or just misleading. This fact was sufficient to warrant a careful investigation of the correct method of speed measurement. The main criticism which applies to almost the whole of the previous work on pumping speed measurement is that no attempt has been made to determine the true speed and to separate the effects of the error due to the measuring instruments and the method used.

The purpose of this paper is to show that the speed of a vacuum pump can be accurately measured, if the experimental procedure is properly carried out. The experiments reported here were mainly undertaken with a view of obtaining information regarding the theoretical value of the pumping speed.

§ 2. *Present position of speed measurement.* The simplest procedure for measuring the speed of a pump is as follows: the mouth of the pump is closed by a plate to which are attached two tubes, one serving to admit a measured rate of gas $\dot{Q}$, and the other being connected to a gauge that measures the pressure P. The pumping speed is then given by $S = \dot{Q}/P$.

Dayton [1]) first pointed out that such an arrangement leads to incorrect results. When the gas enters the mouth of the pump through a small hole, the gas molecules are beamed toward the pumping aperture. Few of them will be able to diffuse into the gauge, which therefore will give lower readings.

As a remedy for this drawback, Dayton emphasized the necessity of using a test dome larger than the pump casing to be attached to the pump mouth. The gas should be admitted at the top, the molecules being scattered by means of a baffle. The tube connecting the gauge should end at the bottom near the pump mouth, and having the opening pointing perpendicular to the pump axis. Kaye [2]) had already used a large bulb attached directly to the pump long before. However, the subsequent investigators did not appreciate the usefulness of such a suggestion.

Although this procedure is considered a standard method, it does not avoid the error in measuring the correct pressure at the pump mouth. Recently, Venema [3]) has experimentally shown that in the vicinity of the pump mouth the directional effect of the moving molecules upon the conventional instruments of pressure measurement is quite noticeable.

Any other methods so far used still require pressure measurements of a streaming gas. Therefore the difficulty discussed above is not eliminated. The suggestion by Oatley [4]) of measuring the pressure at the top of the test dome, did not improve the accuracy of the procedure, since this value is larger than that near the pump mouth, as proved by Venema. All these methods have also the disadvantage of using a small aperture at the pump mouth, therefore the pumping conditions are changed due to the beaming effect of molecules.

The above survey shows that all methods of pumping speed measurement are deficient. They give only approximate values which in many cases can be accepted, but they are of little use in vacuum investigations. Efforts are made by people associated with vacuum equipment manufacturing to standardize the methods of testing vapour pumps. So far Dayton's procedure [5]) in which the test dome has the same inside diameter as the pump casing has been recommended. It is obvious from the above discussion that this procedure is not perfect, although the method is correct.

All speed measurements so far reported have indicated only values of the speed at the pump mouth, i.e. the actual speed, but not the intrinsic *) speed which is obtained at the level of the pumping aperture. It is obvious that the conclusions drawn from such results may lead to discrepancies concerning the performance of various pumps. It is surprising that the measurement of the true speed was totally ignored, despite the fact that knowledge of this characteristic gives reliable information on the pumping efficiency.

We may conclude that any attempt to clear up the problem of pumping speed measurement should provide the answers to the following questions: 1) Where and how to admit gas into the system? 2) Where to measure the pressure? 3) How to obtain the true speed?

§ 3. *Procedure of speed measurement.* Amongst the methods for measuring pumping speeds which have been described, the metered leak method is the only one having its practical procedure susceptible of improvement in an easy manner. Our method for avoiding all the previously encountered objections is shown in fig. 1. A tube having the same inside diameter as the pump casing is closed at one end, and attached with the other end to the mouth M of a vapour pump. A measured quantity of gas can be introduced as uniformly as possible over the cross section of the tube at a level B. When the pump runs, a pressure gradient between B and the pumping aperture O arises. Between A and B, however, the pressure will be uniform in the steady state, and equal to the pressure at the level B. If the rate $\dot{Q}$ of gas admitted is known, and the pressure

---

*) This nomenclature may not agree with the definition already suggested.

P' at any point in the tube AB is measured, the speed at the level B can easily be calculated. In such an arrangement the beaming effect upon the pressure measurement, as well as upon the working of the pump is totally eliminated. The accuracy of the method depends on the uniform distribution of the leaking gas over the considered cross-section of the tube, provided that $\dot{Q}$ and P' are measured with proper instruments.

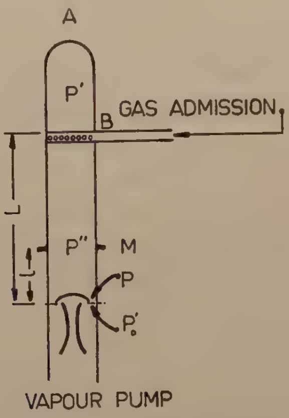

Fig. 1. Diagrammatic indication of the procedure for measurement of pumping speed.

If C is the conductance of the tube OB, then there is

$$\dot{Q} = C(P' - P) = S'P' = SP$$

where S' and S are the speeds at B and O, respectively, and P the pressure just above the pumping aperture. $\dot{Q}$ and P' are directly measured, whilst C is calculated from geometrical dimensions.

From the above relations it follows that

$$S' = \dot{Q}/P', \tag{1}$$

$$P = P' - \dot{Q}/C, \tag{2}$$

and

$$S = \dot{Q}C/(CP' - \dot{Q}). \tag{3}$$

The latter is the intrinsic speed. The speed at any other level, M for instance, can easily be deduced. From

$$\dot{Q} = C(P' - P) = c(P' - P'') = C'(P'' - P), \tag{4}$$

where

$$C = k/L,\ C' = k/l,\ c = k/(L - l),$$

it follows that

$$P'' = P - (P' - P)l/L, \tag{5}$$

and therefore

$$S'' = \frac{\dot{Q}}{P''} = \frac{\dot{Q}}{P - (P' - P)l/L}. \tag{6}$$

Suppose that at the level M the same rate of gas $\dot{Q}$ as in the previous experiment is introduced, then it follows from (1) and (4) that

$$S' = c(1 - P''/P'). \tag{7}$$

The speed, therefore, can be obtained by determining the conductance c of the tube MB, and the ratio of the pressures measured with the same gauge when the same rate of gas is introduced at M and B, respectively.

When the speed is measured using a test dome of diameter larger than that of the pump casing, the gas molecules flow into the pump from all directions, and therefore the pressure is not uniform across the pump mouth. The accuracy of speed measurement is thus illusory since the cross-section to which the speed is referred cannot be well defined.

With the arrangement described the measuring accuracy can be increased by using a long tube and admitting gas at a distance from the mouth as large as possible. A good procedure would be by means of hollow rings of different radii which are kept concentrically in the same plane, each having small holes pointing perpendicularly to the pump axis.

The experimental equipment used in this investigation is shown diagrammatically in fig. 2*a*. It consisted of a two-stage oil vapour pump, having attached to its mouth a tube of the same inside diameter as the casing, 4.7 cm. Air was admitted at the level B through two semi-circular tubes (fig. 2*b*) provided with numerous holes. This section was 14 cm above the annular aperture at the level of the nozzle outlet. The distance was chosen larger than that to the pump mouth in order to reduce the distortion of the conductance by the cowl of the chimney. This conductance was calculated taking as length of the tube just 14 cm. The gauge was attached to a tube T. The distance of its opening to the section B could be varied. Two such tubes were used, having the openings parallel and perpendicular to the pump axis, respectively.

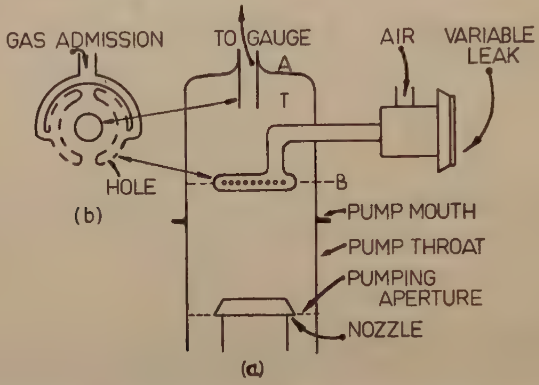

Fig. 2. Experimental arrangement for the measurement of pumping speed.

§ 4. *Results.* Preliminary measurements were carried out with the purpose of checking the distribution of the pressure along the portion AB of the tube. Fig. 3 shows that above the level B the pressure has the same value in various cross-sections, provided that the rate of admitted gas is maintained constant. The gauge readings remain constant, whether the opening of the tube T faces the pump

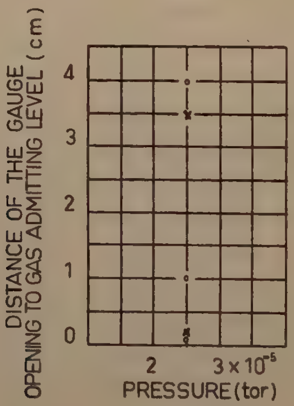

Fig. 3. The constancy of the gauge reading at various levels above the gas leaking level. *o*-gauge opening perpendicular to the pump axis; *x*-gauge opening parallel to the pump axis.

or the perpendicular direction. This result has ascertained that in the arrangement described the directional effect of flowing molecules upon the pressure measurement is avoided. If the gas is injected uniformly in the section B, then the pressure in this section is rigorously equal to that measured at any point in the tube AB. The pressure gauge may therefore be placed within this portion of the tube, provided that the electrodes are protected by a baffle.

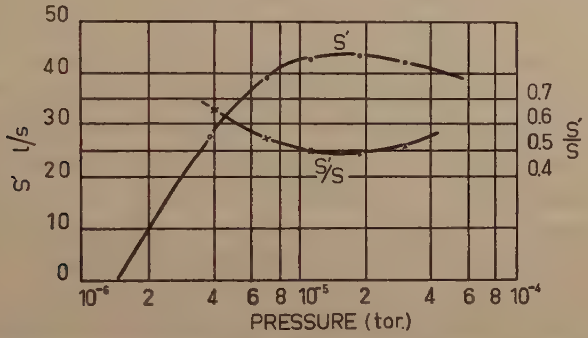

Fig. 4. Variation of the speed S' and the speed factor S'/S as functions of pressure.

Pumping speed measurements were carried out using air in the range of pressures below 3×10^{-3} tor. Fig. 4 shows the variation of the speed S' in the section B as a function of pressure. The actual speed can be calculated from (6). However, this calculation was not performed. In table I are indicated the pressure P just above the pumping aperture and the corresponding intrinsic speed S, both calculated by means of (2) and (3), respectively.

TABLE I

$C = 85\ l/\text{s}$ $C_0 = 135.6\ l/\text{s}$
(Calculated for air at 22°C)
$A = 17.34\ \text{cm}^2$ $a = 5.72\ \text{cm}^2$

Measured			Calculated				
P_0 tor	P' tor	$\dot{Q} \times 10^3$ l.tor/s	S l/s	P tor	S_L l/s	P_0' tor	S/C_0
1.4×10^{-6}	3.9×10^{-6}	0.107	41.4	2.6×10^{-6}	52	2.34×10^{-6}	0.30
	7×10^{-6}	0.274	72.1	3.8×10^{-6}	85.7	3.13×10^{-6}	0.53
	1.1×10^{-5}	0.469	82.5	5.48×10^{-6}	101	4.34×10^{-6}	0.62
	1.9×10^{-5}	0.825	88.7	9.3×10^{-6}	122	7.34×10^{-6}	0.65
	3×10^{-5}	1.263	81	1.5×10^{-5}	123	1.20×10^{-5}	0.60

It is obvious that the measured value P' is the total pressure, while the required value represents the partial pressure of the admitted gas. We might assume that this latter value would be equal to $P' - P_0$, where P_0, the measured ultimate pressure, is supposed to be the residual pressure of the gas evolved within the pump. If now we calculate S using $P' - P_0$, the values obtained exceed the conductance C_0 of the pump. This, of course, cannot be accepted. Therefore, the partial pressure of the components other than the gas used is below the measured ultimate pressure P_0. This result gives an acceptable justification of using P' as the pressure of the incoming gas. Any small error introduced by this assumption will not change our conclusions.

In calculating the conductance C of the tube, the coefficient of conductance given by Knudsen [6]) was used, not that tabulated by Clausing [7]). This observation has already been pointed out [8]).

The intrinsic speed should also be obtained from the Langmuir relation

$$S_L = C_0(1 - P_0/P). \tag{8}$$

However, table I shows that S_L is larger than S, the difference $S_L - S$ being outside any acceptable error. This result agrees with the writer's previous finding [9]) that for an actual vapour pump the correct relation should be

$$S = C_0'(1 - P_0'/P), \tag{9}$$

where $P_0' > P_0$ and C_0' is the actual conductance of the annular aperture. This latter value is given by

$$C_0' = \frac{C_0}{1 - (A - a)/A} = \frac{C_0 A}{a}$$

where A and a are the areas of the cross section of the pump casing and the nozzle, respectively. From (9) P_0' can be calculated, which is the actual ultimate pressure while gas is removed by the pump. When the throughput is zero, on both sides of the pumping aperature the pressures are equal to the ultimate vacuum P_0. For any value of the throughput different from zero the pressures on both sides of the annular aperture will be P and P_0', respectively.

§ 5. *Conclusions.* The procedure of performing the pumping speed measurement emphasized in this work is characterized by the uniform distribution of the admitted gas over a cross-section of the tube attached to the pump mouth, and by the measurement of the pressure with a gauge whose opening may be placed at any point in the tube between this section and the closed end. The location of the gauge opening is different from that advocated by other workers.

The measuring accuracy may be increased by taking the distance OB three to five times the diameter of the pump casing. The length of the portion AB should not have any influence on the pressure measurements. However, a reasonable length is necessary in order to reduce the fluctuations of the readings.

The intrinsic speed can be obtained by simple calculation. The previous investigators had failed to realize the great importance of measuring the intrinsic speed. This value is the only one which expresses the specific performance of a pump, depending on the pump design and working conditions.

The highest intrinsic speed measured was 88.7 l/s, which is 65 per cent of the conductance $C_0 = 135.6\ l$/s of the pumping aperture. This result obtained with an improved design of the vapour pump indicates that such a vacuum device has a higher efficiency than suggested by some writers. From theoretical considerations [10] [11]) the following relation has been derived:

$$\frac{S}{C_0} = \frac{1}{1 + \bar{c}/4v}, \tag{10}$$

where $\bar{c}$ is the mean velocity of the gas molecules and v the velocity of the vapour blast. In accordance with the above relation S should remain constant for the same heater input irrespective of the gas throughput. On the contrary the results in table I indicate considerable variation of S. Further, relation (10) cannot be satisfied by the largest experimental value obtained $S/C_0 = 0.65$ unless v, in our case the velocity of a stream of Apiezon-B oil vapour, can become larger than 21×10^3 cm/s, a value which experimentally was not obtained. It seems therefore that the validity of (10), which sets an upper limit to S/C_0 of less than 0.6 for the present experimental conditions, could not be established.

On many occasions the efficiency of a pump has been expressed by a speed factor defined by the ratio between the actual speed and the pump conductance. This coefficient, however, does not give a reliable comparison of pump performances. Firstly, the upper limit of this ratio is unknown. It was taken equal to 0.5 because a larger value could not be obtained experimentally. Secondly, it expresses the ratio of two quantities having different meanings.

A better suggestion would be taking the ratio

$$\frac{\text{Actual speed}}{\text{Intrinsic speed}}$$

as speed factor, whose upper limit is unity. Both these speeds are obtained from the same experiment (see fig. 4).

Received 23rd July, 1957.

REFERENCES

1) Dayton, B. B., Industr. Engng Chem. **40** (1948) 795.
2) Kaye, G. W. C., High Vacua p. 162; Longmans, Green & Co., London, 1927.
3) Venema, A., Vacuum **4** (1954, published in 1957) 272.
4) Oatley, C. W., Brit. J. Appl. Phys. **5** (1954) 358.
5) Dayton, B. B., Trans. Vac. Symposium 1955, 91–98.
6) Knudsen, M., Ann. Phys. (4) **28** (1909) 75.
7) Clausing, P., Ann. Phys. (5) **12** (1932) 961.
8) Florescu, N. A., Investig. Phys. Nr. **1** (1954), 4 pp.
9) Florescu, N. A., Investig. Phys. Nr. **2** (1955), 7 pp.
10) Jaeckel, R., Z. Naturforsch. **2a** (1947) 666.
11) Nöller, H. G., Z. angew. Phys. **7** (1955) 225.

INDUCTION BY AN OSCILLATING MAGNETIC DIPOLE OVER A TWO LAYER GROUND

by JAMES R. WAIT *)

Department of Electrical Engineering, University of Toronto, Toronto, Canada

Summary

An expression for the mutual electromagnetic coupling between two small loops over a two-layer ground is derived. The result is expressed in a form which is suitable for calculation by a digital computer. When the heights or separation of the loops are large compared to the skin depth in the ground, simple asymptotic formulas for the fields can de developed. The results are employed to obtain a convenient formula for the self-impedance of a loop over a two-layer ground.

§ 1. *Introduction.* It is the purpose of this note to extend some of the available formulae for the fields of an oscillating magnetic dipole over a two-layer ground [1]). Both the vertical and horizontal dipoles are considered. The distance between the source dipole and the observer is much less than a free space wavelength.

It is shown that the magnetic field components can be expressed conveniently in terms of three basic integrals T_0, T_1, and T_2 in analogy to the case for the homogeneous ground [2]). These are in suitable form for numerical integration. Asymptotic expansions for these integrals are developed. The results are used to calculate the self impedance of an arbitrarily oriented loop over a two-layer ground.

§ 2. *Formulation.* Choosing a rectangular coordinate system (x, y, z), the source loop can be represented as a magnetic dipole of strength C at $(0, 0, h)$ with respect to the ground defined for all negative values of z. The ground is homogeneous between $z = 0$ and $z = -d$ with conductivity σ_1 and dielectric constant ε_1. The region below $z = -d$ is also homogeneous with constants σ_2 and ε_2. The permeability of the whole space is taken μ_0 $(= 4\pi \times 10^{-7})$.

---

*) Present address: National Bureau of Standards, Boulder, Colorado, U.S.A.

Subject to the limination that all significant distances in the upper half-space are to be much less than a free space wavelength, the fields for $z > 0$ are a solution of Laplace's equation and hence derivable from a scalar potential. On the other hand, the fields in the lower regions are solutions of the appropriate wave equation. The validity of this quasi-static approach was previously investigated [1]).

For a vertical or z directed dipole at $(0, 0, h)$ the magnetic fields for $z > 0$ can be written

$$\mathbf{H} = -\operatorname{grad} \Phi^v, \tag{1}$$

where

$$\Phi^v = -\frac{\partial}{\partial z}\left[\frac{1}{r} + \int_0^\infty R(\lambda) \mathrm{e}^{-\lambda(z+h)} J_0(\lambda\rho)\,\mathrm{d}\lambda\right] C, \tag{2}$$

with $r = [\rho^2 + (z - h)]^{\frac{1}{2}}$, $\rho = (x^2 + y^2)^{\frac{1}{2}}$,

$$R(\lambda) = \frac{(u_1 + \lambda)\,(u_1 - u_2)\mathrm{e}^{-2u_1 d} - (u_1 - \lambda)\,(u_1 + u_2)}{(u_1 + \lambda)\,(u_1 + u_2) - (u_1 - \lambda)\,(u_1 - u_2)\mathrm{e}^{-2u_1 d}}, \tag{3}$$

$$u_1 = (\lambda^2 + \gamma_1^2)^{\frac{1}{2}},\ u_2 = (\lambda^2 + \gamma_2^2)^{\frac{1}{2}}$$

and

$$\gamma_1^2 = i\sigma_1\mu_0\omega - \varepsilon_1\mu_0\omega^2,\ \gamma_2^2 = i\sigma_2\mu_0\omega - \varepsilon_2\mu_0\omega^2.$$

For the case of a horizontal or a y directed dipole, the fields are obtained from

$$\mathbf{H} = -\operatorname{grad} \Phi^h, \tag{4}$$

where

$$\Phi^h = -\frac{\partial}{\partial y}\left[\frac{1}{r} - \int_0^\infty R(\lambda) \mathrm{e}^{-\lambda(z+h)} J_0(\lambda\rho)\,\mathrm{d}\lambda\right] C, \tag{5}$$

with r and $R(\lambda)$ as defined above.

The three cartesian components of the magnetic field in the upper half-space for both vertical and horizontal components can be expressed in terms of three basic integrals T_0, T_1 and T_2 which are functions of the dimensionless quantities A, B and k which are defined by

$$A = (z + h)/\delta, \quad B = \rho/\delta$$

where

$$\delta = \left[\frac{2}{(\sigma_1 + i\omega\varepsilon_1)\mu_0\omega}\right]^{\frac{1}{2}}, \quad k = \frac{\sigma_2 + i\omega\varepsilon_2}{\sigma_1 + i\omega\varepsilon_1}.$$

For frequencies in the audio range, the displacement currents in the ground are usually negligible in which case the skin depth $\delta \simeq (2/\sigma_1\mu_0\omega)^{\frac{1}{2}}$ is real and $k \simeq \sigma_2/\sigma_1$ is also real. In what follows, δ and k may retain their more general meaning unless explicitly stated otherwise.

Using the above results, the formulae for the magnetic field components are summarized as follows:

The vertical dipole.

Primary fields:

$$\left.\begin{aligned} H_x^p &= \frac{3Cx(z-h)}{r^5}, \\ H_y^p &= \frac{3Cy(z-h)}{r^5}, \\ H_z^p &= \frac{3Cz(z-h)}{r^5} - \frac{C}{r^3}, \end{aligned}\right\} \tag{6}$$

where $r = [(z-h)^2 + x^2 + y^2]^{\frac{1}{2}}$.

Secondary fields:

$$\left.\begin{aligned} H_x^s &= -\frac{C}{\delta^3}\, T_1(A, B)\left(\frac{x}{\rho}\right), \\ H_y^s &= -\frac{C}{\delta^3}\, T_1(A, B)\left(\frac{y}{\rho}\right), \\ H_z^s &= -\frac{C}{\delta^3}\, T_0(A, B). \end{aligned}\right\} \tag{7}$$

The horizontal dipole.

Primary fields:

$$\left.\begin{aligned} H_x^p &= \frac{3Cxy}{r^5}, \\ H_y^p &= \frac{3Cy^2}{r^5} - \frac{C}{r^3}, \\ H_z^p &= \frac{3Cy(z-h)}{r^5}. \end{aligned}\right\} \tag{8}$$

Secondary fields:

$$\left.\begin{aligned} H_x^s &= \frac{C}{\delta^3}\left(\frac{xy}{\rho^2}\right)\left[\frac{2}{B}\, T_2(A, B) - T_0(A, B)\right], \\ H_y^s &= \frac{C}{\delta^3}\left(\frac{y^2}{\rho^2}\right)\left[\left(1 - \frac{x^2}{y^2}\right)\frac{1}{B}\, T_2(A, B) - T_0(A, B)\right], \\ H_z^s &= \frac{C}{\delta^3}\left(\frac{y}{\rho}\right) T_1(A, B). \end{aligned}\right\} \tag{9}$$

The basic integrals are given as follows:

$$T_0 = \int_0^\infty R(g) g^2 e^{-gA} J_0(gB) dg, \tag{10}$$

$$T_1 = \int_0^\infty R(g) g^2 e^{-gA} J_1(gB) dg, \tag{11}$$

$$T_2 = \int_0^\infty R(g) g e^{-gA} J_1(gB) dg, \tag{12}$$

where

$$R(g) = 1 - 2g \frac{I(g)}{J(g)}, \tag{13}$$

$$I(g) = (U + V) + (U - V) e^{-UD},$$

$$J(g) = (U + g)(U + V) - (U - g)(U - V) e^{-UD},$$

$$U = (g^2 + 2i)^{\frac{1}{2}},\quad V = (g^2 + 2ik)^{\frac{1}{2}},\ \text{and}\ D = 2d/\delta.$$

§ 3. *Mutual impedance formulation.* In most applications the source can be represented by a circular loop of area S_1 with N_1 turns. The field of the source loop can then be observed by a receiving loop with area S_2 and N_2 turns. Under the approximation that the separation ρ between these loops is small compared with the wavelength, but large compared with the respective diameters of the loops, the mutual impedance between the loops assumes a simple form. When the loops are co-planar and situated in free space, it follows that $Z_0 = K$, where $K = i\omega N_1 N_2 S_1 S_2 \times 10^{-7}/\rho^3$ in MKS units. When the loops are co-axial it follows that $Z_0 = 2K$.

The mutual impedance Z between the loops above the two-layer ground can then be expressed conveniently as a ratio to Z_0 in terms of the integrals T_0, T_1 and T_2. The four cases of special interest are listed as follows. In each case the loops are at a height h above the ground and separated by a distance ρ between loop centers.

I. Co-planar loops with axes vertical:

$$Z = K(1 + B^3 T_0). \tag{14}$$

II. The first loop has its axis vertical and the second loop has its axis parallel to the ground along a radius from the first loop:

$$Z = K B^3 T_1. \tag{15}$$

III. Co-axial loops with axes horizontal:

$$Z = 2K\left[1 + \frac{B^2}{2}(T_2 - BT_0)\right]. \tag{16}$$

IV. Co-planar loops with axes horizontal:

$$Z = K(1 + B^2T_2). \tag{17}$$

In the above $A = 2h/\delta$ and $B = \rho/\delta$.

§ 4. *Asymptotic evaluation of the integrals.* Subject to A or B being large, it is possible to develop asymptotic expansions for the integrals T_0, T_1 and T_2. For example, $R(g)$ may be developed into a Taylor expansion about $g = 0$ in the manner

$$R(g) = \sum_{m=0}^{\infty} A_m g^m, \tag{18}$$

where

$$A_m = \frac{1}{m!}\left[\frac{\partial^m}{\partial g^m} R(g)\right]_{g=0}. \tag{19}$$

The integrals to contend with are then of the form

$$\int_0^\infty g^n e^{-gA} J_0(gB) dg = P_n \tag{20}$$

and

$$\int_0^\infty g^n e^{-gA} J_1(gB) dg = Q_n, \tag{21}$$

where n is an integer. Noting that

$$\int_0^\infty e^{-gA} J_0(gB) dg = (A^2 + B^2)^{-\frac{1}{2}}, \tag{22}$$

it is seen that

$$P_n = (-1)^n \left(\frac{\partial}{\partial A}\right)^n (A^2 + B^2)^{-\frac{1}{2}} \tag{23}$$

and

$$Q_n = (-1)^n \left(\frac{\partial}{\partial A}\right)^{n-1} \frac{\partial}{\partial B} (A^2 + B^2)^{-\frac{1}{2}}. \tag{24}$$

Consequently

$$T_0 = \sum_{m=0}^{\infty} A_m (-1)^{m+2} \left(\frac{\partial}{\partial A}\right)^{m+2} (A^2 + B^2)^{-\frac{1}{2}}, \tag{25}$$

$$T_1 = \sum_{m=0}^{\infty} A_m(-1)^{m+2}\left(\frac{\partial}{\partial A}\right)^{m+1} \frac{\partial}{\partial B}(A^2+B^2)^{-\frac{1}{2}}, \tag{26}$$

and

$$T_2 = \sum_{m=0}^{\infty} A_m(-1)^{m+1}\left(\frac{\partial}{\partial A}\right)^{m} \frac{\partial}{\partial B}(A^2+B^2)^{-\frac{1}{2}}. \tag{27}$$

The first three coefficients are $A_0 = 1$, $A_1 = -(2/i)^{\frac{1}{2}}Q$, $A_2 = -iQ^2$, where

$$Q = \frac{(1+k^{\frac{1}{2}}) + (1-k^{\frac{1}{2}})\exp[-(2i)^{\frac{1}{2}}D]}{(1+k^{\frac{1}{2}}) - (1-k^{\frac{1}{2}})\exp[-(2i)^{\frac{1}{2}}D]}. \tag{28}$$

Retaining only the first three leading terms, asymptotic expansions for the integrals are

$$T_0 \cong \frac{2A^2-B^2}{(A^2+B^2)^{5/2}} - \left(\frac{2}{i}\right)^{1/2} Q \frac{6A^3-9AB^2}{(A^2+B^2)^{7/2}} - \\ - iQ^2 \frac{24A^4-72A^2B^2+9B^4}{(A^2+B^2)^{9/2}}, \tag{29}$$

$$T_1 \cong \frac{3AB}{(A^2+B^2)^{5/2}} - \left(\frac{2}{i}\right)^{1/2} Q \frac{12A^2B-3B^3}{(A^2+B^2)^{7/2}} - \\ - iQ^2 \frac{60A^3B-45AB^3}{(A^2+B^2)^{9/2}}. \tag{30}$$

$$T_2 \cong \frac{B}{(A^2+B^2)^{3/2}} - \left(\frac{2}{i}\right)^{1/2} Q \frac{3AB}{(A^2+B^2)^{5/2}} - \\ - iQ^2 \frac{12A^2B-3B^3}{(A^2+B^2)^{7/2}}. \tag{31}$$

Inserting these expressions into (14) to (17) yields asymptotic representations for the mutual impedance between loops over a two-layer ground. They are valid for A or B large compared to unity.

§ 5. *Extension to the self impedance of a loop.* The formulae quoted above for the mutual impedance are restricted to the case where the separation ρ is much greater than the loop diameters. The mutual impedance can then be written

$$Z = Z_0 + Z_s$$

where Z_0 is the mutual impedance of the loops in free space and Z_s is the secondary influence. Now, as ρ tends to zero, Z_0 is the self impedance and can be determined from the geometry of the loop. Z_s can then be computed from a knowledge of the secondary field $\mathbf{H}^s$ due to the magnetic dipole at $(0, 0, h)$. The dipole is contained in the (y, z) plane and makes an angle θ with the vertical (i.e., the z axis). The loop then has a magnetic dipole moment C_h in the y direction and C_v in the z direction where $C_h = C \sin\theta$ and $C_v = C\cos\theta$ in terms of the resultant dipole moment defined by $C = i\mu\omega ISN/4\pi$ for a loop of area S containing N turns. The secondary magnetic fields at the source dipole due to the component dipoles C_h and C_v have only a y and z component, respectively.

These secondary fields are given by

$$H_y^s = C_h \frac{1}{\delta^3}\left[\frac{T_2(A,B)}{B} - T_0(A,B)\right]_{B\to 0} = \\ = -C_h \frac{1}{\delta^3}\left[\frac{T_0(A,0)}{2}\right], \tag{32}$$

where $A = 2h/\delta$ and

$$H_z^s = -C_v \frac{1}{\delta^3}[T_0(A,B)]_{B\to 0} = -C_v \frac{1}{\delta^3} T_0(A,0). \tag{33}$$

The secondary voltage induced in the loop is then

$$v = i\mu\omega SN(H_z^s \cos\theta + H_y^s \sin\theta)_{z=h}.$$

Writing $Z_s = \Delta R + i\Delta X$, it is seen that

$$\Delta R = \frac{\mu\omega S^2N^2}{4\pi\delta^3}\left(\cos^2\theta + \frac{\sin^2\theta}{2}\right)|\mathrm{Im}\, T_0(A,0)|, \tag{34}$$

$$\Delta X = -\frac{\mu\omega S^2N^2}{4\pi\delta^3}\left(\cos^2\theta - \frac{\sin^2\theta}{2}\right)\mathrm{Re}\, T_0(A,0), \tag{35}$$

where

$$T_0(A,0) \cong \frac{2}{A^3} - \left(\frac{2}{i}\right)^{\frac{1}{2}} Q\frac{6}{A^4} - iQ^2\frac{24}{A^5} - \frac{Q^3}{(2i)^{3/2}}\frac{60}{A^6}. \tag{36}$$

In the case of the homogeneous earth ($D \to \infty$) it follows for negligible displacement currents that

$$\Delta R_1 \cong \frac{3\mu\omega S^2N^2}{16\pi h^3}\left(\cos^2\theta + \frac{\sin^2\theta}{2}\right)\left(\frac{1}{A} - \frac{4}{A^2} + \frac{5}{A^3}\cdots\right), \tag{37}$$

$$\Delta X_1 \cong -\frac{\mu\omega S^2N^2}{16\pi h^3}\left(\cos^2\theta - \frac{\sin^2\theta}{2}\right)\left(1 - \frac{3}{A} + \frac{15}{A^2}\cdots\right), \tag{38}$$

since A is real and $Q = 1$.

The above equation for ΔR_1 in the case of a vertical loop ($\theta = 0°$) is in agreement with a result previously derived by a different method [3].

The computation of ΔR or ΔX for the stratified ground requires an evaluation of the series for $T_0(A, 0)$. When A is sufficiently large so that only the leading two terms are sufficient, it follows that ratio of the incremental resistance for a stratified and homogeneous ground is

$$\Delta R/\Delta R_1 \simeq \sqrt{2}\,|Q| \sin(\tfrac{1}{4}\pi - q), \tag{39}$$

where $Q = |Q|e^{iq}$. Numerical values [4] for the complex factor Q have been given previously where it was indicated that, if d is greater than about 3δ, Q is within 1% of unity.

I would like to thank Alyce M. Conda for checking the equations.

Received 17th September, 1957.

REFERENCES

1) Wait, J. R., Canad. J. Phys. **29** (1951) 577 and **30** (1952) 450.
2) Wait, J. R., Geophysics **20** (1955) 630, also **21** (1956) 479; many references are given here.
3) Wait, J. R., J. Appl. Phys. **24** (1953) 646.
4) Wait, J. R., Appl. Sci. Res. **B3** (1953) 279.

Appl. sci. Res. Section B, Vol. 7

ON THE CALCULATIONS OF TRANSVERSE CURRENT LOSS IN BURIED WIRE GROUND SYSTEMS

by JAMES R. WAIT

National Bureau of Standards, Boulder, Colorado, U.S.A.

Summary

A formula is developed for the impedance between a wire grid buried in a homogeneous ground and an overhead conducting plane. The result can be employed to calculate the power lost due to transverse currents in buried wire ground systems for antennae.

§ 1. *Introduction.* The efficiency of low frequency antennae is limited mainly by the excessive power loss in the ground. To reduce this somewhat, a buried wire grating is usually installed in the immediate neighbourhood of the antenna.

A systematic procedure for the design of buried wire ground systems was first given by Abbott [1]). A method for calculating the input impedance of monopole antennae with such ground systems was presented by Wait and Pope [2]). In this work an approximate boundary condition was introduced to facilitate the computation of the energy flow into the ground. The use of such boundary conditions is valid when the earth currents flow essentially in the radial direction. Such is usually the case in most transmitting installations. At very low radio frequencies, however, this condition becomes violated particularly for high power installations where the top loading may extend over a large area. In this case, there is an appreciable loss due to the current flowing transversely to the buried wires or normal to the ground surface.

It is the purpose of this note to present an analysis of the transverse current loss based on an idealized model. Attention will be confined to the case where the current flow is normal to the ground. It is also assumed that the potential of the wires is the same as that of the immediately adjacent soil. This latter restriction can be relaxed by separately computing the loss at the interface of the wire and soil from the knowledge of the interfacial impedance and the total current.

§ 2. *Statement of the problem.* The immediate problem is to compute the impedance between a parallel-wire grid buried to a depth h in a homogeneous ground and a plane conductor at height s above the ground. The situation is illustrated in fig. 1. The ground surface is at $x = 0$ and the wires are parallel to the z axis and $x = h$ and $y = nd$ where $n = 0, \pm 1, \pm 2 \ldots$ and d is the grid spacing. The radius of the wires a is assumed to be small compared to d. The conductivity and dielectric constant of the ground are denoted as σ and ε, respectively. The space between the ground and the upper conducting plane is air with a dielectric constant ε_0.

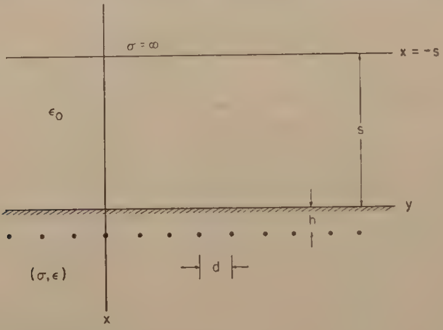

Fig. 1. Illustrating buried wire grid and the elevated conducting plane.

It is now assumed that the fields which vary as $\exp(i\omega t)$ in all the regions are solutions of Laplace's equation since the angular frequency ω is sufficiently low so that all significant dimensions are small compared to the wavelength. Each wire is now considered to be a source of current I ampere per metre of length. Letting the potential of the elevated conducting plane be zero, the problem is now to evaluate the potential V at the wires. The impedance between the wire grid and the conducting plane is then equal to the ratio V/I.

§ 3. *The solution.* The method of solution is similar to one employed by the author [3]) in calculating the reflection coefficient of a plane wave at oblique incidence on a wire grid parallel to an interface between two dissimilar dielectrics. The primary potential ψ^p in the ground of the array of a line current source is expressed as

$$2\pi\psi^p = \frac{I}{2(\sigma + i\omega\varepsilon)d} \sum_{m=-\infty}^{+\infty} \exp(i2\pi my/d)\exp(-2\pi|x-h|M/d)M^{-1}, \quad (1)$$

where

$$M = [m^2 - (kd/2\pi)^2]^{\frac{1}{2}}, \quad k^2 = (\varepsilon - i\sigma/\omega)\mu\omega^2.$$

In view of the limitations already specified, k could be set equal to zero so that $M = |m|$ for $m \neq 0$ and $M = ikd/2\pi$ for $m = 0$. To retain the correspondence with the earlier analysis, however, the general form of M will be retained. Equation (1) for ψ^p is directly analogous to equation (4) in reference [3]) for the Hertz potential of a wire grid carrying a constant longitudinal current. It can be verified by seeing that: 1. it is a solution of the wave equation $(\nabla^2+k^2)\psi^p=0$, which is Laplace's equation when k is zero. 2. it has a periodicity d in the y direction. 3. it gives rise to an outgoing current density, $J_x = (I/2d)\exp(-ik|x-h|)$ for $|x-h| \gg d$, 4. an application of the Poisson summation formula leads to

$$\psi^p = \frac{I}{2\pi(\sigma + i\omega\varepsilon)} \sum_{n=-\infty}^{+\infty} \ln[(x-h)^2 + (nd-y)^2]^{\frac{1}{2}} + \text{constant} \qquad (2)$$

for $k = 0$. Each term of the latter series can be identified as the potential of an individual current line source located at $x = h$ and $y = nd$.

The secondary potential ψ^s within the ground is that quantity which, when added to ψ^p, satisfies the boundary conditions at the air-ground interface $x = 0$. An appropriate form for it is

$$2\pi\psi^s = \\ = \frac{I}{2(\sigma+i\omega\varepsilon)d} \sum_{m=-\infty}^{+\infty} A_m \exp(i2\pi my/d) \exp[-2\pi(x+h)M/d]M^{-1}, \quad (3)$$

which is also a solution of $(\nabla^2 + k^2)\psi^s = 0$, is periodic in y and vanishes exponentially as x becomes large. The coefficient A_m is to be determined from the boundary conditions.

The potential function ψ_0 appropriate for the air space between $x = 0$ and $x = -s$ is appropriately written

$$2\pi\psi_0 = \\ = \frac{I}{2(\sigma+i\omega\varepsilon)d} \sum_{m=-\infty}^{+\infty} B_m \exp(i2\pi my/d) \sinh[2\pi(x+s)M_0/d]M_0^{-1}, \quad (4)$$

where $M_0 = [m^2 - (k_0 d/2\pi)^2]^{\frac{1}{2}}$, $k_0^2 = \varepsilon_0\mu\omega^2$ and B_m is a coefficient as yet unspecified. It can be seen that ψ_0 is a solution of $(\nabla^2 + k_0^2)\psi_0 = 0$, is periodic in y and vanishes at $x = -s$ as it must.

The determination of the coefficients A_m and B_m are now obtaining from the boundary conditions

$$\psi = \psi_0 \text{ and } (\sigma + i\omega\varepsilon) \frac{\partial\psi}{\partial x} = i\omega\varepsilon_0 \frac{\partial\psi_0}{\partial x}$$

at $x = 0$. These yield

$$A_m = \frac{M(\sigma + i\omega\varepsilon) \tanh(2\pi s M_0/d) - M_0\sigma_0}{M(\sigma + i\omega\varepsilon) \tanh(2\pi s M_0/d) + M_0\sigma_0} \tag{5}$$

and

$$B_m = \frac{\sigma}{\sigma_0} \frac{1 - A_m}{\sinh(2\pi s M_0/d)} \exp(-2\pi h M/d). \tag{6}$$

Inserting these expressions for the coefficients into (3) and (4) provide complete and explicit expressions for the respective potential functions. The potential at the wires is obtained by letting $x = h + a$. Furthermore, without loss of generality, y can be set equal to zero since the wires are all at the same potential. Then defining $V = \psi$ for $x = h + a$, $y = 0$, $k = 0$, it follows that

$$V = \frac{I}{d}\left(\frac{h}{\sigma + i\omega\varepsilon} + \frac{s}{i\omega\varepsilon_0}\right) + \frac{I}{2\pi(\sigma + i\omega\varepsilon)} \sum_{m=1}^{+\infty} \frac{e^{-2\pi a m/d}}{m}$$
$$+ \frac{I}{2\pi(\sigma + i\omega\varepsilon)} \sum_{1}^{\infty} \left[\frac{(\sigma + i\omega\varepsilon)\tanh(2\pi s m/d) - \sigma_0}{(\sigma + i\omega\varepsilon)\tanh(2\pi s m/d) + \sigma_0}\right] \frac{e^{-2\pi(2h+a)m/d}}{m} \tag{7}$$

The factor in square brackets in the latter summation can be written

$$[\quad] = \frac{R_0 - \exp(4\pi s m/d)}{1 - R_0 \exp(4\pi s m/d)}$$
$$= R_0 + (R_0^2 - 1) \sum_{n=0}^{\infty} R^n \exp[-(n+1)4\pi s m/d], \tag{8}$$

where

$$R_0 = \frac{\sigma + i\omega(\varepsilon - \varepsilon_0)}{\sigma + i\omega(\varepsilon + \varepsilon_0)}.$$

Utilizing the identity 4)

$$\sum_{m=1}^{\infty} \frac{e^{-\alpha m}}{m} = -\ln(1 - e^{-\alpha}) \tag{9}$$

it follows that

$$V = \frac{I}{d}\left(\frac{h}{\sigma + i\omega\varepsilon} + \frac{s}{i\omega\varepsilon_0}\right) +$$
$$\frac{I}{2\pi(\sigma + i\omega\varepsilon)}\left\{\ln\frac{d}{2\pi a} + R_0 \ln \frac{1}{[1 - \exp(-2\pi(2h+a)/d)]} + \Delta\right\}, \tag{10}$$

where

$$\Delta = (R_0^2 - 1) \sum_{n=0}^{\infty} R_0^n \ln \frac{1}{[1-\exp(-2\pi(2h+a)/d-(n+1)4\pi s/d)]}.$$

The average complex admittance Y per unit area between the elevated conducting plane and the buried wire grid is then given by $Y = 1/Z$, where

$$Z = \frac{h}{\sigma + i\omega\varepsilon} + \frac{s}{i\omega\varepsilon_0} + \frac{d}{2\pi(\sigma + i\omega\varepsilon)} \cdot \left\{ \ln \frac{d}{2\pi a} + R_0 \ln \frac{1}{[1 - \exp(-2\pi(2h + a)/d)]} + \Delta \right\}. \tag{11}$$

In this expression, the first term can be identified as the impedance of a parallel plate condenser of separation h containing a "lossy" material with complex dielectric constant $\varepsilon - i\sigma/\omega$. The second term is the impedance of a corresponding parallel plate condenser of thickness h containing a material of dielectric constant ε_0. The next three terms are corrections to account for the finite value of the grid spacing d. Since s is usually large compared to d, the quantity Δ is negligible compared to the other terms.

§ 4. *The effective depth.* In some instances it may be convenient to define an equivalent depth $\bar{h}$ of the buried grid such that

$$Z = \frac{\bar{h}}{\sigma + i\omega\varepsilon} + \frac{s}{i\omega\varepsilon_0}. \tag{12}$$

It is immediately seen that

$$\bar{h} \simeq h + \frac{d}{2\pi} \left\{ \ln \frac{d}{2\pi a} + R_0 \ln \frac{1}{[1 - \exp(-2\pi(2h + a)/d)]} \right\} \tag{13}$$

if $s \gg d$. When $d \gg 2h + a$, this is further simplified to

$$\bar{h} \simeq h + \frac{d}{2\pi} \left[\ln \frac{d}{2\pi a} + R_0 \ln \frac{d}{2\pi(2h + a)} \right]. \tag{14}$$

In the limiting case when the wire grid is symmetrically located in the interface ($h = 0$) it follows that

$$\bar{h} \simeq (1 + R_0) \frac{d}{2\pi} \ln \frac{d}{2\pi a} \tag{15}$$

or
$$\frac{\bar{h}}{\sigma + i\omega\varepsilon} = \frac{d}{\pi(\sigma + i\omega\varepsilon + i\omega\varepsilon_0)} \ln \frac{d}{2\pi a}.$$

In general, it can be seen that $\bar{h}$ is complex.

Complete formulae are thus available for calculating the impedance between a buried wire grid and an overhead conducting plane.

§ 5. *The power calculation.* The power loss ΔP per unit area of ground surface is then given by
$$\Delta P = \tfrac{1}{2}\mathrm{R}|I/d|^2 \tag{16}$$
where R = real part of Z. It may be of interest to express ΔP in terms of the average vertical electric field E_0 in the air just above the ground. Since
$$i\varepsilon_0\omega\, E_0 = I/d \tag{17}$$
and $\sigma \gg \varepsilon\omega$ or $\varepsilon_0\omega$, it follows that
$$\Delta P \cong \tfrac{1}{2}\frac{\bar{h}}{\sigma}(\varepsilon_0\omega)^2|E_0|^2, \tag{18}$$
where
$$\bar{h} \cong h + \frac{d}{2\pi}\left[\ln\frac{d}{2\pi a} + \ln\frac{1}{(1 - \mathrm{e}^{-4\pi h/d})}\right]. \tag{19}$$
for $h \gg a$ and $s \gg d$.

The foregoing results *), although derived for a wire grid of constant spacing, can be applied to the computation of power loss for a buried radial wire system by an appropriate integration of ΔP if d and E_0 were slowly varying. An approach such as this has been recently suggested by C. E. Smith and H. A. Wheeler ⁵). It was the purpose of the present note to provide the theoretical basis for such a computation.

I would like to thank H. Cotlony and A. D. Watt for their helpful comments.

Received 17th September, 1957.

REFERENCES

1) Abbott, F. R., Proc. Inst. Radio Engrs **40** (1952) 846.
2) Wait, J. R. and W. A. Pope, Wireless Engr **32** (1955) 131; also J. Appl. Phys. **25** (1954) 553.
3) Wait, J. R., Appl. Sci. Res. **B6** (1957) 259.
4) Wheelon, A. D., J. Appl. Phys. **25** (1954) 113.
5) Private communication.

---

*) The factor $\frac{1}{2}$ in (16) and (18) is to be omitted if I and E_0 are r.m.s. values.

LETTER TO THE EDITOR

New scintillators for the detection of thermal neutrons

The detection of slow neutrons is no longer limited to the use of a BF_3 gas-filled countertube, due to the fact that since a few years liquid and solid scintillators are largely used for this purpose. Both procedures are based on the (n, α) reaction of a slow neutron with the B^{10} nucleus. The low efficiency and the great dimensions of the BF_3 counter have largely determined the search for scintillators with high boron density, good luminosity, low gamma sensitivity and short lightflash.

An attempt for the use of a luminescent organoboron compound (tri-α-naphtylborine) in a solid form has already been reported [1]). The results gave little hope for its usefulness, at least in the form and under the conditions mentioned by the authors. There are, however, still other luminescent organoboron compounds which were not used until now. The first three substances mentioned below were prepared according to a procedure described in the literature, while a fourth one, 9-phenantrylboric acid, was prepared for the first time. The very intense luminescence of this phenanthrene derivative was remarkable.

TABLE I

Product	wavelength region of fluorescence spectrum	Maximum
tri-α-naphtylborine	from 480 mμ to 600 mμ	525 mμ
α-naphtylboric acid	400 mμ to 480 mμ	430 mμ
α-naphtylboron oxide		
9-phenanthrylboric acid	430 mμ to 560 mμ	490 mμ

Investigation of the fluorescence spectra of these compounds in the solid state, gave the results shown in table I. Each of the four products was melted on a circular quartz plate and cooled rapidly so that it solidified to slightly yellowish transparent layers of glassy structure. The layers had a thickness of about 2 mm with a diameter of 30 mm. In all the substances the boronisotope ratio was the natural one.

Each sample on its quartz support was fixed on a Dumont 6292 photomultiplier, connected to a classical counting unit which consisted of amplifier, one-channel pulse analyser, scaler and monitor. In its form described above only α-naphtylboric acid produced the expected results as a usable neutron scintillator.

The differential pulse-height diagram is given in fig. 1. The counting results were obtained using the scintillators described above, which were irradiated by a neutron and gamma-, or by a gamma-flux only. As neutron source the thermal column of the BR I reactor of the C.A.E.N. at Mol was used.

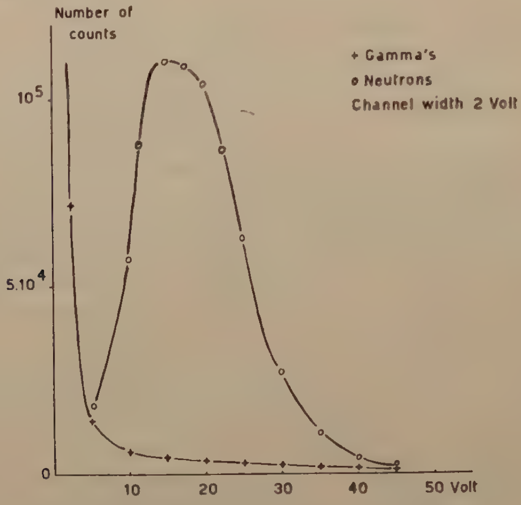

Fig. 1. Differential pulse-height diagram.

The efficiency of the α-naphtylboric acid scintillator for the detection of thermal neutrons was about 80%. The poor results obtained with the other compounds seem only to be due to their loose adherence to the quartz plate and their sintered structure. At the present time we develop different methods in order to obtain single crystals, of which we expect that their properties will be more suitable for neutron scintillators.

This work is part of a research programme sponsered by the Institut Interuniversitaire des Sciences Nucléaires. The author wishes to thank Prof. Dr. J. L. Verhaeghe, who initiated and conducted this investigation, and Prof. Dr. R. Goubau for their interest and advice. He is also indebted to the Centre d'Études pour les Applications de l'Énergie Nucléaire, where part of the experiments were made with helpful assistance of Lic. H. Ceulemans.

G. Thielens
Natuurkundig Laboratorium
Rijksuniversiteit Gent, Belgium

Received 14th November, 1957.

REFERENCE

1) Zolingen, J. J. van, and J. J. Went, Physica **18** (1952) 976.

Appl. sci. Res. Section B, Vol. 7

SOME GENERALIZATIONS OF THE SCHWARZ-CHRISTOFFEL MAPPING FORMULA *)

by L. C. WOODS

Department of Mechanical Engineering, N.S.W. University of Technology,
Sydney, Australia

Summary

The Schwarz-Christoffel formula for the mapping of a polygon in the z-plane on an upper half-plane (the w-plane) is extended to deal with singly-connected domains of quite general shape. The mapping problem in the general case is shown to depend on the solution of an awkward integro-differential equation and an iterative method of finding this solution is indicated. Two further generalizations are made to the formula; these are (i) the boundary of the singly-connected domain in the z-plane is mapped on to a *finite* interval of the real axis of the w-plane instead of the whole of it, and (ii) the formula is extended to deal with doubly-connected domains.

§ 1. *Introduction.* The well-known formula for the mapping of a polygon in the z-plane ($z = x + iy$) on to the upper half of the w-plane ($w = \varphi + i\psi$) can be written in the form

$$\frac{dz}{dw} = K \prod_{n=1}^{N} (w - \varphi_n)^{-\alpha_n/\pi}, \tag{1}$$

where α_n, $n = 1, 2, 3, \ldots . N$, are the external angles of the polygon (see fig. 1) at the vertices z_n, and φ_n are the points on the real axis in the w-plane on to which these vertices z_n are mapped by (1). In order to deal with *curved* rather than polygonal shapes it is natural to seek a generalization of (1) in which the angles α_n tend to zero with the intervals $z_{n+1} - z_n$, and $\varphi_{n+1} - \varphi_n$. It is quite easy to derive this generalization by a formal calculation based on (1).

---

*) Paper, read at the first annual general meeting of the Australian Mathematical Society at Sydney, August, 1957.

Let θ_n denote the slope of the side $z_{n+1} - z_n$, then $\alpha_n = \theta_n - \theta_{n-1}$, and the logarithm of (1) can be written

$$\ln \frac{dz}{dw} = \ln K - \frac{1}{\pi} \sum_{n=1}^{N} \ln (w - \varphi_n)(\theta_n - \theta_{n-1}).$$

In the limit $\alpha_n \to 0$ this becomes

$$\tau(w) \equiv \ln \frac{dz}{dw} = \ln K - \frac{1}{\pi} \int_{-\infty}^{\infty} \ln (w - \varphi)\, d\theta_0(\varphi), \tag{2}$$

where the integral is a Riemann-Stieltjes integral.

To make this derivation of (2) rigorous we would first have to recast the usual proof of (1) into a form which permits the limiting process just used, and this would be difficult if not impossible. We shall therefore give a proof of (2) not depending on (1), but in fact containing an alternative proof of (1) as a special case.

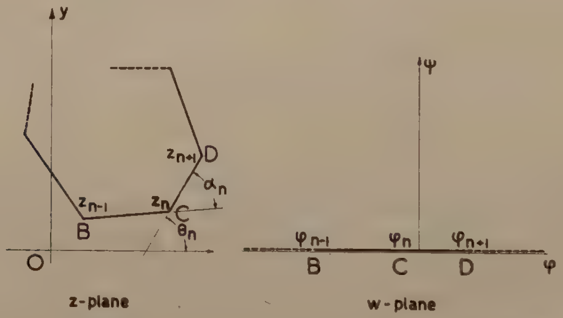

Fig. 1. Mapping a polygon onto an upper-half plane.

The point P, say, in the z-plane, which is mapped on to $w = \infty$ by (2), must clearly lie on the contour Γ. An obvious further generalization of (2) is to take P to be some point lying *within* Γ, and this necessarily means that Γ must map on to a *finite* interval of $\psi = 0$, instead of the whole of $\psi = 0$. This generalization, which is more useful than (2) in some practical applications, is given in § 4.

The next step in generalizing the mapping formula is to deal with the doubly-connected region lying between two non-intersecting contours Γ and Γ'; this theory is given in § 5.

In this last generalization let Γ' lie within Γ. Then to return to the Schwarz-Christoffel (S—C) mapping formula, we must first let Γ' shrink to a single point P — this gives our second generalization — then let P tend to a point on Γ, giving our first generalization, and finally we obtain (1) by letting $\theta_0(\varphi)$ be a step-function.

Although the generalizations of the S—C formula given in this paper are obvious, they do not seem to have appeared in the literature (cf. Beckenbach [1])) of the subject. However, there is such a volume of published papers on conformal mapping, that one cannot be sure on this point. There is some Russian work by Goluzin (see p. 272 of Beckenbach [1])) on the doubly-connected region between polygons, of which the work in § 5 below is a generalization, and there is also the well-known work of Leathem [3]) which introduces "curve-factors" into the S—C formula.

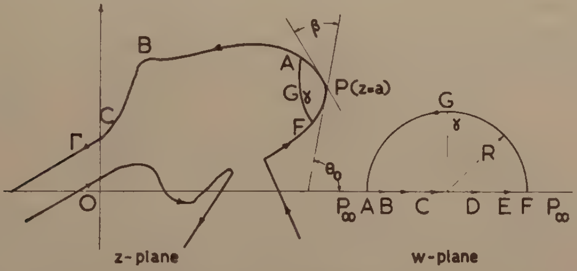

Fig. 2. Mapping a curved figure onto an upper half-plane.

§ 2. *Proof of the first generalization.* We shall map the singly-connected region bounded by the contour $\Gamma = \text{PABCD}_\infty\text{E}_\infty\text{FP}$ shown in fig. 2 on to the upper half of the w-plane in such a way that the point P maps on to the point at infinity in the w-plane. The contour Γ is assumed to have a continuously turning tangent save for a finite number of exceptional points, where simple discontinuities in the slope θ_0 of Γ may exist (e.g. points B and C in fig. 2). Also a finite number of points of Γ are assumed to be at infinity (e.g. points D_∞ and E_∞). The point P which will be moved to infinity by the transformation may be an ordinary point of Γ or one of the exceptional points (e.g. B, C, D_∞ or E_∞) just described. In the figure P is shown to be at a point where the tangent jumps through an angle β; an ordinary point is obtained if $\beta = 0$, while P is a point at infinity if $\beta = \pi$ (e.g. as at D_∞) or if $\pi < \beta \leq 2\pi$

(as at E_∞). The particular cases $\beta = 0$, π and 2π are especially important in practical applications of the theory.

The contour is indented about P by a curve $\gamma =$ FGA of such a shape that it maps into the large semi-circle $w = Re^{ix}$ in the w-plane. We shall need the relation between w and z on this indentation. There are three distinct cases to consider.

First let P be in the finite part of the plane, at $z = a$, say. Then the corner at P will be straightened by a transformation of the type $z_1 \sim (z-a)^n$, where $n = 1/(1-\beta/\pi)$, $(-\pi \leq \beta < \pi)$, and then transformed to infinity by the inversion $w \sim 1/z_1$. Apart from these singularities the relation between w and z will be regular near $z = a$. Thus in this neighbourhood we can write

$$w = \frac{A}{(z-a)^n} + a_0 + a_1(z-a) + a_2(z-a)^2 + \ldots, \quad (-\pi \leq \beta < \pi), \qquad (3)$$

where A, a_0, a_1, ... are constants. Inverting this series and differentiating the result we find that

$$\frac{dz}{dw} = B\, w^{-(1-1/n)} \left\{1 + 0\left(\frac{1}{w}\right)\right\},$$

$$\text{i.e. } \tau \equiv \ln\left(\frac{dz}{dw}\right) = -\left(2 - \frac{\beta}{\pi}\right) \ln w + C + 0\left(\frac{1}{w}\right), \quad (-\pi \leq \beta < \pi), \qquad (4)$$

where B and C are new constants, and n has been eliminated in favour of β.

Secondly suppose P is at infinity, and that the angle β does not equal π (i.e. we exclude the case $n = \infty$, which applies at points like D_∞ in fig. 2). In this case the "corner" at infinity is removed by the transformation $w \sim z^{-n}$, and instead of (3) we have

$$w = Az^{-n} + a_0 + \frac{a_1}{z} + \frac{a_2}{z^2} + \ldots \quad (\pi < \beta \leq 2\pi). \qquad (5)$$

It is easily verified from (5) that (4) also holds for $\pi < \beta \leq 2\pi$.

Finally let $\beta = \pi$. If (4) is still valid for this value of β, then $dz/dw = A/w \ldots$, i.e.

$$w = Ae^{-bz} + a_0 + \ldots, \quad (\beta = \pi), \qquad (6)$$

where A, b and a_0 are constants. That this is the correct form for w is most easily verified by letting $|a|$ tend to zero in (3). The acute angle $\pi - \beta$ tends to zero with $|a|^{-1}$, i.e. $n = \pi/(\pi - \beta)$ tends to infinity with $|a|$, so we can write $a = n/b$, where b remains finite in the limit $n \to \infty$. Modifying the constants in (3) and using the result $\lim\limits_{n\to\infty} (1 - zb/n)^{-n} = e^{-bz}$, we then arrive at (6) as the limiting form of (3).

We have now established that (4) is valid for all values of β in the range $(-\pi, 2\pi)$, i.e. for all choices of the point P that is to be mapped on to $w = \infty$. From (4) it follows that

$$\lim_{w\to\infty} \frac{d\tau}{dw} = 0. \tag{7}$$

Now let $|dz/dw| = 1/q$, and $\arg(dz/dw) = \theta$, then θ is the angle between the x-axis and the curves $\psi =$ constant, for if $d\psi = 0$,

$$\theta = \arg\left(\frac{dx}{d\varphi} + i\frac{dy}{d\varphi}\right) = \tan^{-1}\left(\frac{dy}{dz}\right),$$

which is clearly the slope of the curves $d\psi = 0$, or $\psi =$ constant. The contour Γ is the curve $\psi = 0$, and we shall denote the slope of this curve by θ_0.

Let
$$\tau \equiv \ln\frac{dz}{dw} = \ln\left(\frac{1}{q}e^{i\theta}\right) = \Omega + i\theta, \tag{8}$$

where

$$\Omega = \ln\frac{1}{q}, \tag{9}$$

then

$$\frac{d\tau}{dw} = \frac{\partial\Omega}{\partial\varphi} + i\frac{\partial\theta}{\partial\varphi}, \tag{10}$$

is an analytic function in the w-plane whose imaginary part takes the value

$$\frac{d\theta_0}{d\varphi} = \theta_0'(\varphi), \tag{11}$$

on $\psi = 0$, and which vanishes at infinity (see (7)).

By Cauchy's integral applied to the semi-circular contour shown in fig. 2

$$\frac{d\tau}{dw} = \frac{1}{2\pi i}\int_{-R}^{R}\frac{(d\tau/d\varphi)\,d\varphi}{\varphi - w} + \frac{1}{2\pi}\int_{0}^{\pi}\frac{d\tau}{d(Re^{i\chi})}\,\frac{Re^{i\chi}\,d\chi}{Re^{i\chi} - w},$$

where w is a point within the contour.

Equation (7) and the limit $R \to \infty$ yields

$$\frac{\mathrm{d}\tau}{\mathrm{d}w} = \frac{1}{2\pi i}\int_{-\infty}^{\infty} \frac{\mathrm{d}\tau(\varphi)}{\varphi - w}\,. \tag{12}$$

Similarly

$$0 = \frac{1}{2\pi i}\int_{-\infty}^{\infty} \frac{\mathrm{d}\tau(\varphi)}{\varphi - \bar{w}}\,,$$

as $\bar{w}$ lies *outside* the semi-circular contour. Subtracting the conjugate of this equation from (12), and using (10) we find

$$\frac{\mathrm{d}\tau}{\mathrm{d}w} = \frac{1}{\pi}\int_{-\infty}^{\infty} \frac{\mathrm{d}\theta_0(\varphi)}{\varphi - w}\,. \tag{13}$$

Finally integration with respect to w gives

$$\tau = \ln \frac{\mathrm{d}z}{\mathrm{d}w} = \ln K - \frac{1}{\pi}\int_{-\infty}^{\infty} \ln\,(w - \varphi)\,\mathrm{d}\theta_0(\varphi), \tag{14}$$

where $\ln K$ is the constant of integration. The proof of (2) is now almost complete.

The only gap in this proof is that we have not justified writing the integral in (14) as a *Stieltjes* integral, i.e. permitting $\theta_0'(\varphi)$ to be a delta function at a finite number of points in the range of integration. The validity of this is readily established by the usual method of indenting the contour in the w-plane by small semi-circles about the singular points on the real axis, and then letting the radii of these indentations tend to zero. Alternatively we can take the contour in (4) to be $\psi = \varepsilon$ instead of $\psi = 0$, then let $\varepsilon \to 0$ after evaluating the integral. We find in this approach that at a discontinuity of amount α in θ_0 at the point $\varphi = a$ the correct meaning to give $\theta_0'(\varphi)\,\mathrm{d}\varphi$ is

$$\mathrm{d}\theta_0(\varphi) = \theta_0'(\varphi)\,\mathrm{d}\varphi = \frac{\alpha}{\pi}\lim_{\epsilon\to 0} \mathrm{d}\left\{\tan^{-1}\left(\frac{\varphi - a}{\varepsilon}\right)\right\} = \frac{\alpha}{\pi}\,\mathrm{d}U(\varphi - a)$$

$$= \frac{\alpha}{\pi}\,\delta(\varphi - a)\,\mathrm{d}\varphi \tag{15}$$

where $U(\varphi - a)$ is the unit function and $\delta(\varphi - a)$ is its derivative, the delta function.

If $\theta_0(\varphi)$ is a step-function with discontinuities in magnitude of α_n at φ_n, $n = 1, 2, \ldots N$, then the Stieltjes integral in (14) degenerates to the sum $-1/\pi \sum \alpha_n \ln (w - \varphi_n)$, and we obtain (1) as a special case. Our proof of (2) is now complete.

From fig. 2 it is apparent that $\theta(\varphi)$ cannot be chosen arbitrarily, but must satisfy

$$\int\limits_{-\infty}^{\infty} \mathrm{d}\theta_0(\varphi) = 2\pi - \beta. \tag{16}$$

Where θ_0 is continuous we write $\mathrm{d}\theta_0 = \theta_0'(\varphi)\, \mathrm{d}\varphi$ in (14) and the required mapping function follows from a knowledge of $\theta_0 = \theta_0(\varphi)$ and two integrations. In practical problems however it will be the *shape* of Γ that is known, and not the relation $\theta_0(\varphi)$. This case is somewhat more difficult and is considered in § 3.

From (14) it follows that

$$z = z_p + K \int\limits_{\infty}^{w} \exp\left\{ -\frac{1}{\pi} \int\limits_{-\infty}^{\infty} \ln (w - \varphi)\, \mathrm{d}\theta_0(\varphi) \right\} \mathrm{d}w, \tag{17}$$

where z_p is the value of z at the point P. The value of the factor K depends on the scale of the mapping and the orientation of the contour Γ in the z-plane. Its value will be fixed if two other corresponding points, say z_0 and w_0 are assigned. Thus for the unique definition of the mapping we have to assign the two correspondences $z_p \to \infty$, and $z_0 \to w_0$.

An alternative method of determining the modulus of K is frequently useful. For simplicity consider the case in which no points of Γ are at infinity — the general case can be treated by a similar method. If s is the distance measured around Γ in an anti-clockwise direction from P, i.e. from $\varphi = -\infty$, we find from (17) and (18) that

$$s(\varphi) = |K| \int\limits_{-\infty}^{\varphi} \exp\left\{ -\frac{1}{\pi} \int\limits_{-\infty}^{\infty} \ln |\varphi^* - \varphi|\, \mathrm{d}\theta_0(\varphi^*) \right\} \mathrm{d}\varphi, \tag{18}$$

and

$$l = |K| \int\limits_{-\infty}^{\infty} \exp\left\{ -\frac{1}{\pi} \int\limits_{-\infty}^{\infty} \ln |\varphi^* - \varphi|\, \mathrm{d}\theta_0(\varphi^*) \right\} \mathrm{d}\varphi, \tag{19}$$

where l is the length of Γ. Thus, for a given distribution $\theta_0(\varphi)$, $|K|$ is directly proportional to l.

§ 3. *The basic integral equation of mapping theory.* Knowledge of the shape of Γ enables us to compute its intrinsic equation $s = s(\theta)$, and hence its radius of curvature $R = s'(\theta)$. On $\psi =$ constant

$$\frac{1}{q} = \left|\frac{dz}{dw}\right| = \left|\frac{dx}{d\varphi} + i\frac{dy}{d\varphi}\right| = \sqrt{\left\{\left(\frac{dx}{d\varphi}\right)^2 + \left(\frac{dy}{d\varphi}\right)^2\right\}};$$

so on $\psi = 0$

$$\frac{1}{q} = \frac{ds}{d\varphi} = \frac{ds}{d\theta_0}\frac{d\theta_0}{d\varphi} = R\theta_0'(\varphi). \tag{20}$$

On Γ at $w = \varphi$ the real part of (14) yields

$$\ln\frac{1}{q} = \ln|K| - \frac{1}{\pi}\int_{-\infty}^{\infty}\ln|\varphi^* - \varphi|\,d\theta_0(\varphi^*),$$

and combining this with (20) we arrive at the basic integro-differential equation for $\theta_0(\varphi)$, namely

$$\ln\theta_0'(\varphi) = \ln|K| - \ln R\{\theta_0(\varphi)\} - \frac{1}{\pi}\int_{-\infty}^{\infty}\theta_0'(\varphi)\ln|\varphi^* - \varphi|\,d\varphi^*, \tag{21}$$

where $|K|$ itself is a function of $\theta_0(\varphi)$ determined by (19) when Γ is finite, and an equation similar to (19) in the general case. The function $\theta_0'(\varphi)$ can be a delta function at a finite number of points in the range.

When Γ is finite, we have

$$\ln\theta_0'(\varphi) = \ln\left[\int_{-\infty}^{\infty}\exp\left\{-\frac{1}{\pi}\int_{-\infty}^{\infty}\theta_0'(\varphi^*)\ln|\varphi^* - \varphi|\,d\varphi^*\right\}\right] - \ln\frac{R}{l}\{\theta_0(\varphi)\}$$
$$- \frac{1}{\pi}\int_{-\infty}^{\infty}\theta_0'(\varphi^*)\ln|\varphi^* - \varphi|\,d\varphi^*, \tag{22}$$

an equation quite beyond the standard methods of solution. Numerical or iterative methods must be employed. When $\theta_0(\varphi)$ is found from (22) it is substituted in (14) to give the required mapping relation.

Probably the best method of solving (22) is as follows. First Γ is approximated to by a figure comprised of sections over each of which $\theta_0'(\varphi)$ has a constant value, i.e. $\theta_0'(\varphi)$ is a step function. When the constant value is zero the section will be a straight line, otherwise it will be curved having a slowly varying curvature. Convergence of the integral in (22) requires that we choose $\theta_0'(\varphi)$ to vanish in the intervals bounded by $\varphi = -\infty$ and $\varphi = \infty$. In practice we can start with an approximating polygon, then round off those corners not corresponding to corners on Γ by giving $\theta_0'(\varphi)$ a non-zero value over intervals containing these corners. If $\theta_0'(\varphi) = k$ in the interval $\varphi_0 - \frac{1}{2}a \leq \varphi \leq \varphi_0 + \frac{1}{2}a$ containing a corner of the polygon corresponding to a discontinuity in θ_0 of τ in this interval, then a and k must be chosen to satisfy $\tau = ak$. Other choices of $\theta_0'(\varphi)$ are of course possible (see § 4), and with experience it is not difficult to select $\theta_0'(\varphi)$ so as to obtain a fair approximation to Γ.

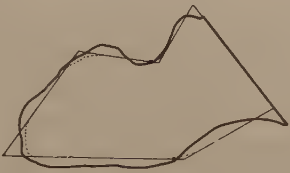

Fig. 3. Approximation to a curved contour.

———— Γ,

———— approximate polygon,

············ rounding off.

Denote the approximating curve by Γ_1, and let $\theta_1(\varphi)$ be the known distribution of θ on Γ_1. Also let the length of Γ_1 be equal to l, the length of the given curve Γ. Then the substitution of the function $\theta_1'(\varphi)$ in (18) and (19) gives the corresponding function $s_1(\varphi)$. The next step is to make the approximation $s(\varphi) = s_1(\varphi)$ (we have already set $s(\infty) = l = s_1(\infty)$). Then from the known relations $R(s)$, $\theta(s)$ on Γ we find the approximate functions $R_2(\varphi)$, $\theta_2(\varphi)$ and $\theta_2'(\varphi)$, using our approximate $s(\varphi)$ relation. With $R_2(\varphi)$ and $\theta_2'(\varphi)$ in the left hand side of (22) we obtain a new approximation for $\theta_0'(\varphi)$, say $\theta_3'(\varphi)$, from the left hand side of (22). This is now inserted in (18) and (19) to yield the corresponding function $s_3(\varphi)$; we then set $s(\varphi) = s_3(\varphi)$, and so on, until the process has converged.

From the author's experience it seems that convergence is always quite rapid, and if Γ_1 is reasonably close to Γ, the contour resulting from the distribution $\theta_3'(\varphi)$ will be undistinguishable from Γ for practical purposes.

A similar method can be applied to the case when Γ has some points at infinity. In this case a separate $s_1(\varphi)$ function has to be derived for each section of Γ, and of course s has to be measured from some point on Γ close to, but not at infinity.

In all but the simplest cases the integrals in (18), (19) and (21) have to be evaluated numerically, but once a numerical scheme has been worked out for one example subsequent problems can be handled quite quickly.

§ 4. *Mapping points within Γ on to infinity.* If a point P within Γ is to be mapped on to the point at infinity in the w-plane then Γ must map on to a finite section of the real axis of the w-plane. Let this be $-a \leq \varphi \leq a$, then the lines $\varphi = \pm a$ correspond to opposite sides of some curve AP, where A lies on Γ (see fig. 4).

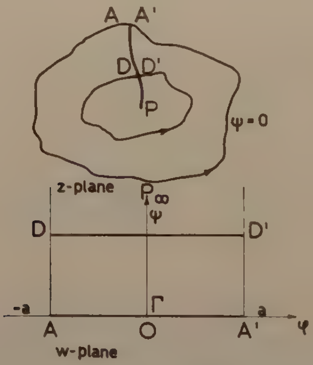

Fig. 4. Mapping a singly-connected domain onto a semi-infinite strip.

Curves $\psi =$ constant must enclose P, which is the "curve" $\psi = \infty$. Thus the domain within Γ maps on to the semi-infinite strip $0 \leq \psi \leq \infty$, $-a \leq \varphi \leq a$.

Each complete cycle about contours $\psi =$ constant increases φ by $2a$, so that the domain within Γ can be regarded as being mapped on to each of the strips $0 \leq \psi \leq \infty$, $(2n-1)a \leq \varphi \leq$ $\leq (2n+1)a$, $a = 0, \pm 1, \pm 2, \ldots \pm \infty$. Therefore the boundary value $\theta_0(\varphi)$ is periodic over $-\infty \leq \varphi \leq \infty$, i.e. satisfies $\theta_0(\varphi) = \theta_0(\varphi + 2a)$. Using this condition in (13) we get *)

$$\frac{\mathrm{d}\tau}{\mathrm{d}w} = \frac{1}{\pi} \lim_{N\to\infty} \sum_{n=N}^{N} \int_{-a}^{a} \frac{\mathrm{d}\theta_0(\varphi)}{\varphi + 2na - w}\,.$$

Using a well-known result for the limit of the sum in this equation we arrive at

$$\frac{\mathrm{d}\tau}{\mathrm{d}w} = \frac{1}{2a} \int_{-a}^{a} \cot \frac{\pi}{2a} (\varphi - w)\, \mathrm{d}\theta_0(\varphi). \tag{23}$$

Integration now gives

$$\tau = \ln K - \frac{1}{\pi} \int_{-a}^{a} \ln \sin \frac{\pi}{2a} (w - \varphi)\, \mathrm{d}\theta_0(\varphi), \tag{24}$$

which is the required generalization of equation (2). The special form taken by this equation when Γ is a polygon, and the integral degenerates to a sum is due to Bickley [2]).

This equation is particularly useful for the mapping of nearly circular domains, which occur frequently in practical problems. First consider a circle of radius R, centre $z = z_0$. If z_0 is mapped on to $w = \infty$, then by symmetry $\theta'(\varphi)$ will be constant, and clearly equal to $2\pi/2a = \pi/a$. Substituting this value in (24) and evaluating the constants we arrive at $\tau = \ln (i\pi R/a) + i\pi w/a$, so

$$z = z_0 + R\mathrm{e}^{i\pi w/a}. \tag{25}$$

With nearly circular domains we can set $s/l = \varphi/2a$ in order to commence the iterative process described in § 3, and furthermore we can take advantage of the fact that $\theta'(\varphi) - \pi/a$ will be small over most of the range $-a \leq \varphi \leq a$.

It is sometimes useful to map these domains on to unit circle in the ζ-plane by $\zeta = \mathrm{e}^{i\pi w/a}$, (cf. (25)), but in most applications the semi-infinite strip in the w-plane is more convenient.

The value of z_p, i.e. the position of the point P which is mapped on to $w = \infty$, can be found from

---

*) Note from the equation preceding (12) that the meaning to be given to $\int_{-\infty}^{\infty}$ is $\lim_{R\to\infty} \int_{-R}^{R}$, i.e. the Cauchy Principal Value at infinity.

$$z_p = \frac{1}{2a}\int_{-\infty}^{a} z(\varphi)\,d\varphi, \qquad (26)$$

after the integro-differential equation implicit in (24) (derived as in § 3) is solved. Equation (26) follows by taking the limit $w \to \infty$ in

$$z(w) = \frac{1}{2ai}\int_{-a}^{a} z(\varphi)\cot\frac{\pi}{2a}(\varphi - w)\,d\varphi$$

which follows from Cauchy's integral for $z(w)$ in the upper half plane, and the periodic nature of $z(\varphi)$ (cf. (23)).

§ 5. *Doubly-connected regions.* In order to map the region between two curves Γ and Γ', such as shown in fig. 5, into a suitable canonical domain, we first make it singly-connected by inserting a barrier AB,

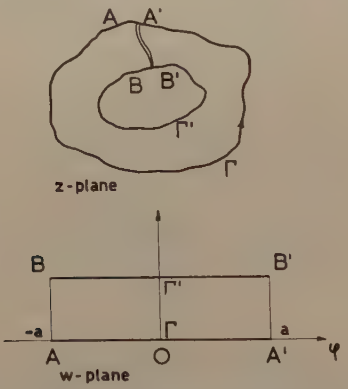

Fig. 5. Mapping a doubly-connected region onto a rectangle.

then map the resulting region onto the rectangle $-a \leq \varphi \leq a$, $0 \leq \psi \leq h$. In this rectangle τ is an analytic function of given imaginary parts θ_0 on $\psi = 0$ and θ_h on $\psi = h$ and periodic in the φ-direction, having a period of $2a$.

The solution to this problem can be derived by the same technique as employed in § 3 and § 4, but we shall omit the details, and refer the reader to a recent paper (Woods [5])), which contains the required solution in a slightly different form. Converting equation (65) of the author's earlier paper to the present problem we have

$$\tau = \ln K - \frac{1}{\pi}\int\limits_{-a}^{a} \ln \vartheta_1 \left\{ \frac{\pi}{2a}(\varphi - w) \,\middle|\, \frac{ih}{a} \right\} \mathrm{d}\theta_0(\varphi) +$$

$$+ \frac{1}{\pi}\int\limits_{-a}^{a} \ln \vartheta_4 \left\{ \frac{\pi}{2a}(\varphi - w) \,\middle|\, \frac{ih}{a} \right\} \mathrm{d}\theta_h(\varphi), \qquad (27)$$

where the notation employed for the theta functions is the same as in Whittaker and Watson's text [4]). Equation (27) contains the S—C mapping formula, and our earlier generalizations of this formula, as special cases.

When the exponential of (27) is integrated to give a formula for $z(w)$ there will be four unknown constants appearing in the equation, namely k, a, h and one additional constant of integration. In general this will require that four corresponding points in the z- and w-planes must be specified for a unique mapping.

By a calculation similar to that given in § 3 we can derive a pair of simultaneous integro-differential equations from (27) for $\theta_0'(\varphi)$ and $\theta_n'(\varphi)$, and these can be solved by the same type of iterative process as that outlined for the simpler case.

Received 18th September, 1957.

REFERENCES

1) Beckenbach, E. F., Construction and Applications of Conformal Maps, National Bureau of Standards. Applied Maths Series 18 U.S. Gov. Printing Office, Washington 25, D.C., 1952.
2) Bickley, W. G., Phil. Trans. **A 228** (1929) 235.
3) Leathem, I. G., Phil. Trans. **A 215** (1915) 439.
4) Whittaker, E. T. and G. N. Watson, Modern Analysis, Cambridge University Press, 1952.
5) Woods, L. C., Proc. Roy. Soc. **A 229** (1955) 63.

Appl. sci. Res. Section B, Vol. 7

PARTICLE STATISTICS IN X-RAY DIFFRACTOMETRY

I. GENERAL THEORY *)

by P. M. DE WOLFF **)

Philips Laboratories, Irvington-on-Hudson, N.Y., U.S.A.

Summary

Expressions are derived for the relative r.m.s. error σ of diffractometer intensity measurements. The result for stationary specimens:

$$\sigma = 4R[\sin\theta/m\ w\ h\ N_{eff}]^{\frac{1}{2}},$$

with $h = \frac{1}{2}(h_F + h_S)$ and $N_{eff} = cA\bar{v}/\mu v^2$, is identical with the result of Alexander c.s. 1), except for a slight difference in the numerical constant and in the definition of w. The value of this parameter is found to lie between $\varepsilon R + (w_F, w_S)_{min}$ (the last term indicating the smallest of the widths w_F and w_S) and $\varepsilon R + \frac{1}{2}(w_F + w_S)$; it reaches the latter limit in the case of integrated intensities being measured by totalizing counts while scanning through a line. For rotating specimens the particle statistics error turns out to be almost independent of w. The following approximative formula is established: $\sigma = 6.5R \sin\Theta/h(mN_{eff})^{\frac{1}{2}}$, showing that the factor of improvement resulting from specimen rotation is of the order of $(h/w)^{\frac{1}{2}}$.

List of symbols

A	area of cross-section of primary beam at the goniometer axis.
c	volume concentration in the specimen of the reflecting phase.
ε	rocking angle of the reflecting phase, in radians.
h_F	length of focal line.
h_S	length of receiving slit.
μ	average absorption coefficient of the specimen.
m	multiplicity factor of reflection under investigation.
I	measured intensity minus background.
J	intensity contribution from a single particle.
N_{eff}	effective number of irradiated particles of reflecting phase.

---

*) Part. II: Experiments, by P. M. de Wolff, Jeanne M. Taylor and W. Parrish, is in the course of preparation.

**) Work done when on leave of absence (Nov. 1954–May 1955) from Technisch Physische Dienst T.N.O. and T.H., Delft, Netherlands.

R	distance source-goniometer axis, distance goniometer axis-receiving slit.
v	volume of particle of reflecting phase.
w_F	apparent width of focal line.
w_S	width of receiving slit.

§ 1. *Introduction.* The use of direct intensity-recording diffractometers in many cases where formerly only photographic methods have been applied calls for a detailed study of random errors on account of two reasons. First, statistical fluctuations which are obvious at the first glance on a photographically recorded pattern may be very difficult or impossible to detect in a record obtained by direct scanning. Second, the high precision attainable by the latter method as compared with the photographic one sets a very low limit to the statistical error which can be tolerated if this accuracy is to be of any use.

A paper by Alexander, Klug and Kummer[1]) contains the results of an investigation, both theoretical and experimental, of the statistical factors involved in the diffractometer. More recently, however, the rotating specimen device has come into use as a means of reducing random errors. The resulting reduction in random fluctuations is generally stated to be large, but no attempt at an exact calculation or measurement seems so far to have been published. This, then, will be the main purpose of the present paper.

§ 2. *General considerations.* The following propositions will be used later on and may prove helpful to solve the powder statistics problem for any situation not included here. If the diffraction intensity J from a single power particle can be written as a product:

$$J = f_1(x_1) f_2(x_2) f_3(x_3) \ldots, \tag{1}$$

the f_i's being given functions of mutually independent variables x_i (such as the orientation and position coordinates and the volume of the particle), then obviously

$$\overline{J^2} = (\bar{J})^2 r_1 r_2 r_3 \ldots, \tag{2}$$

where

$$r_i = \overline{f_i^2}/(\bar{f_i})^2 = \int p_i(x) f_i^2(x) \mathrm{d}x / [\int p_i(x) f_i(x) \mathrm{d}x]^2, \tag{3}$$

the bars indicating unweighted mean values over all particles and $p_i(x)\mathrm{d}x$ being the probability for x_i to lie between x_i and $x_i + \mathrm{d}x_i$.

If the measured intensity I is obtained from a specimen containing N' irradiated particles, the relative mean-square deviation σ^2 of I is $1/N'$ times that of J:

$$\sigma^2 = [\overline{J^2}/(\bar{J})^2 - 1]/N' = (r_1 r_2 r_3 \ldots - 1)/N'.$$

Since the number N' of irradiated particles in the specimen is never known, it is better to introduce N'' as the total number of particles in an imaginary batch from which a small fraction is taken to form the specimen. Introducing also an extra f_0-function in (1) equal to 1 for those particles from the batch which happen to get into the irradiated volume and zero otherwise, we find $\bar{f}_0 = \overline{f_0^2} = N/N''$, hence $r_0 = N''/N$, N being the mathematical expectation of the (not accurately known) number of irradiated particles in the specimen. The number N'' being arbitrary, we may take it infinitely large and obtain

$$\sigma^2 = \lim_{N'' \to \infty} \left(\frac{N''}{N} r_1 r_2 r_3, \ldots - 1 \right) \Big/ N'' = \frac{1}{N} r_1 r_2 r_3 \ldots \tag{4}$$

Actually, the contribution from a single particle cannot be adequately described by the above smooth function (1) since it may well average less than one quantum. There is, however, no interaction between counter statistics and particle statistics. The former merely contributes to σ^2 a term inversely proportional to I, which will be disregarded in the following.

The dependence of σ on the irradiated specimen area and on the absorption coefficient of the specimen can easily be found by applying (4). Since it has already been calculated by Alexander c.s. [1]), we shall merely mention the result:

$$\sigma^2 = (1/N_{eff}) r_3 r_4 r_5 \ldots, \tag{5}$$

where r_3 etc. refer to orientation parameters and

$$N_{eff} = (\bar{v}/\overline{v^2})\,(cA/\mu) \tag{6}$$

is an effective number of irradiated particles depending on the average particle volume v and the volume concentration c of the reflecting component, as well as the average absorption coefficient μ of the specimen and the cross-section A of the primary beam. The latter is supposed to be intercepted entirely by the specimen.

Equations (5) and (6) are valid for stationary specimens. That they can also be applied in the case of rotating specimens, will be demonstrated in § 5.

§ 3. *Stationary specimen*. The geometry of the usual parafocussing diffractometer is drawn in fig. 1 and will be described with reference to the "vertical" direction (parallel to the linear focal spot) and, at right angles to this direction, the horizontal plane.

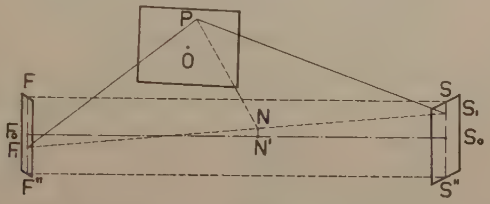

Fig. 1. Diffractometer geometry, illustrating the vertical spread of lattice plane normals of reflecting crystals in a stationary specimen.

a) Whether a lattice plane in a particle at P contributes to the measured intensity depends on the direction of its normal PN. The vertical component of such normals is most easily studied in a vertical plane FF″SS″ through the focal spot FF″ and the centre line SS″ of the slit. If N is the intersection of the lattice plane normal PN with this plane, a ray coming from point F_1 in the focal spot and reflected at P will intersect the same plane in a point S_1 such that F_1, N and S_1 lie on a straight line (namely, the intersection of the plane FF″SS″ with the plane containing F_1P, NP and S_1P, the existence of which follows from elementary optics). Therefore no reflected ray can enter the receiving slit unless N is situated within the rectangle FF″SS″. We assume that focal spot and receiving slit have the same height $h = FF'' = SS''$. The length of PN being $R \sin \theta$, we obtain for the vertical spread $\delta\beta$ of normals of contributing lattice planes

$$\delta\beta = h/R \sin \theta.$$

The fraction q_0 of particles at P which contributes to the measured intensity is

$$q_0 = m\, \delta\alpha\, \delta\beta/4\pi,$$

m being the multiplicity factor of the reflection and $\delta\alpha$ the horizontal spread, i.e. the range of azimuth angles of PN (P being fixed and PN horizontal) for which reflection occurs. We shall characterize this range by a new variable $w = \delta\alpha R$ and discuss it separately in § 4.

If all reflecting particles contributed equally, a function f_3 could be constructed so that $f_3 = 1$ for contributing particles and $f_3 = 0$ for non-contributing particles. Application of § 2 yields $r_3 = 1/q_0$ and, from (5),

$$\sigma^2 = 1/q_0 N_{eff} = 4\pi R^2 \sin\theta / mwhN_{eff}. \tag{7}$$

This formula is almost identical with the one derived by Alexander c.s. ^{1}) (If FF″ $= h_F$ does not equal SS″ $= h_S$, h should obviously be replaced by $(h_F + h_S)/2$). It might be criticized for two reasons, which we shall now consider in detail.

b) The contribution of a particle, if not zero, obviously depends very much on the position of P and on the exact orientation of PN within the cone defined by $\delta\alpha$ and $\delta\beta$. Even if PN is horizontal, the contribution will not be constant; it will be a maximum when N is situated in the central line F_0S_0. Thus we may assume, as a first approximation, that it is proportional to $(\frac{1}{2}h - \mathrm{NN}')$, N′ being the vertical projection of N on this central line. This distribution causes a factor $f_3'(t) = t$ to enter into J, with (cf. (1)) $p_3'(t) = q_0$ for $0 < t < 1$; $p_3'(t) = 0$ for $t < 0$ and $t > 1$; $p_3'(0) = \infty$ with $\int_{0-}^{0+} p_3'(t)\mathrm{d}t = 1 - q_0$. The corresponding r-factor is found from (3) to be

$$r_3' = \tfrac{1}{3}/q_0(\tfrac{1}{2})^2 = 4/3q_0$$

and

$$\sigma^2 = 4/3q_0 N_{eff}. \tag{8}$$

It thus appears that a very radical change in the distribution of intensities may affect the statistical error only slightly (in this case by an increase of 15%).

c) The picture drawn in *b*) is still far from exact since it does not take into account various complications originating from normals PN inclined to the horizontal plane. For such normals the horizontal spread is larger than $\delta\alpha$ as defined above. Also the intensity distribution is not as simple as in *b*). On close inspection, again the latter effect (which tends to increase σ) is found to have much less influence than the increase in horizontal spread and, consequently, in the number of contributing particles (decreasing σ). We arrive at σ^2-values between 1.33 and roughly 1.1. times $1/q_0 N_{eff}$. It can therefore be said that, for all practical purposes, the following modification of formula (7) is sufficiently accurate:

$$\sigma = 4R(\sin\theta/mwhN_{eff})^{\frac{1}{2}}. \tag{9}$$

§ 4. *The horizontal spread.* Alexander c.s. [1]) put the angular range $\delta\alpha$ of the azimuth of PN equal to $\varepsilon + w_F/R$, ε being the rocking angle of the crystals. In doing so, they neglect the spectral line width as well as the receiving slit width w_S. As a matter of fact, $\delta\alpha$ is a function symmetrical in w_F and w_S because the diffraction phenomenon is reversible.

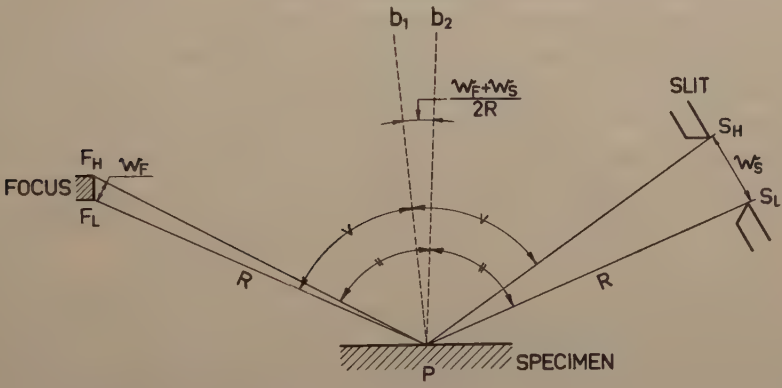

Fig. 2. Diagram illustrating the horizontal spread of lattice plane normals of reflecting crystallites at P.

Taking into account the effects of spectral profile and of w_S will, in general, result in hopelessly complicated formulae. There is one case, however, for which at least one of these effects, the spectral line width, has no effect, viz. the case of integrated intensities being measured by scanning through a line. Moreover, the geometric contribution to $\delta\alpha$ then takes a very simple form: At any moment, the horizontal range of normals PN (P being fixed) is limited by the bissectrices b_1 and b_2 of the angles F_LPS_H and F_HPS_L between the ultimate rays just touching the edges of focus and slit (see fig. 2). The resulting range $\frac{1}{2}(w_F + w_S)/R$ is fully effective because for each normal within it, and for each wave length in the spectral line, the corresponding Bragg angle is realized some time during the scan, whereas the bissectrices b_1 and b_2 retain their direction relative to the specimen all the time.

Hence the only complication is the rocking angle, and the final result for integrated intensities being measured by scanning is

$$\delta\alpha = \varepsilon + \tfrac{1}{2}(w_F + w_S)/R$$

or

$$w = \delta\alpha R = \varepsilon R + \tfrac{1}{2}(w_F + w_S). \tag{10}$$

For peak intensity measurements, the range determined by b_1 and b_2 (fig. 2) need not be effective in full, since part of the normals within this range may correspond to wave lengths outside the spectral line. However, at the peak position it is certain that the central ray of the mean wave length through the smallest of the apertures w_F and w_S (to be indicated by $(w_F, w_S)_{min}$) will be reflected. It follows that *all* rays of the mean wave length through this smallest aperture are reflected, so that even for an infinitely narrow spectral line the geometrical range is at least $(w_F, w_S)_{min}/R$. Hence for peak intensity measurements

$$\varepsilon R + \tfrac{1}{2}(w_F + w_S) > w > \varepsilon R + (w_F, w_S)_{min}. \tag{11}$$

§ 5. *Rotating specimen: rough estimate of* σ. Consider now a specimen rotating about an axis through the centre O and normal to its surface (fig. 2). Such a device (a) allows many more crystallites to take part in diffraction, (b) profoundly influences the distribution of contributed intensity per particle. Just as for the stationary case we shall examine the numerical effect first.

In order to reflect the primary beam, the normal PN of a particle should make an angle $\frac{1}{2}\pi - \theta$ with it. Since the angle between primary beam and rotation axis is $\frac{1}{2}\pi - \theta$, it follows that $< \mathrm{F_0PN}$ upon rotation oscillates between limits on either side of this value and therefore must some time equal it: *all* particles pass through positions in which they reflect the primary beam, though the reflection does reach the detector only for a certain fraction of the total number of particles (or for the present purpose (cf. § 2): a fraction of the effective number N_{eff} defined by (6)). In order to calculate this fraction, we shall first assume that it is equal to the fraction of favourable orientations of PN for a particle situated at O on the axis of rotation. For this particle it follows from § 3 that it contributes when (cf. fig. 3) MN $< \frac{1}{2}h$, because in the reflecting position MN is obviously vertical and therefore equal to its vertical component NN′ which should obey $NN' < \frac{1}{2}h$. Hence the favourable orientations of PN fill a cone with height $R \sin\theta$ and base diameter h, the spherical top angle being approximately $\pi h^2/4R^2 \sin^2\theta$. Thus the desired fraction is $h^2/16R^2 \sin^2\theta$, and $\sigma^2 = 16R^2 \sin^2\theta/h^2 m N_{eff}$ or

$$\sigma = 4R \sin\theta/h\sqrt{mN_{eff}}. \tag{12}$$

In this equation N_{eff} is defined by (6). This may seem strange since the effective number of particles irradiated during rotation of the specimen is larger than the number (6) corresponding to a stationary specimen, except when the irradiated area is a circle. The paradox is solved by considering the focussing cylinder, that is, the vertical cylinder containing the focussing circle (fig. 3). All particles for which the lattice plane normals pass through a point Q on this cylinder reach their reflecting position simultaneously when Q, upon rotation of the specimen, arrives at Q′ in a narrow "reflection band" *) which runs vertically through the intersection T of the specimen rotation axis with the sphere. The density of reflecting normals at Q, or any other point on the focussing cylinder

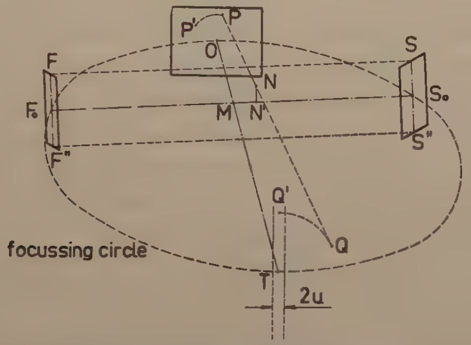

Fig. 3. Diagram illustrating the conditions for reflection by a particle P in a rotating specimen.

---

*) This band is nothing but the horizontal spread of normals of reflecting particles, projected on the focussing cylinder. The advantage of using it rather than the horizontal spread is that, owing to the focussing geometry, the band (though fixed in space) determines the limits of reflection regardless of the particle position.

The width $2u$ of the reflection band depends on source and slit width and on the rocking angle. The fact that it does not appear in (12) gives rise to the supposition that it will have very little influence on the actual statistical error. This will be proved in a more quantitative way later on. The quastion which value of u should be used will be discussed at the end of § 6.

in the neighbourhood of T, is therefore determined by the irradiated area of a virtually stationary specimen. The point T is an exception for which the circular area irradiated during rotation is valid; the influence of this small singularity is, however, negligible.

The reasoning just mentioned also shows the way to a more correct estimate of the contributing fraction of particles. All we have to do is to calculate which part of the normals through Q′ obeys NN′ $< \frac{1}{2}h$ and therefore passes between the horizontal lines FS and F″S″, as a function of the distance TQ′. Integration of this expression leads to a relative r.m.s. error

$$\sigma = 4R \sin \theta / h \sqrt{m N_{eff} (1 + \tfrac{1}{3} \cos^4 \theta)}. \qquad (13)$$

The difference of at most 15% with (12) does not justify this refinement of a numerical theory which disregards enormous variations in the contribution per particle. We shall therefore stick to (12) as a first rough estimate based on the numerical theory.

§ 6. *Rotating specimen: influence of J-distribution.* The concept of a "reflection band" through T is a very convenient one also for the purpose of computing the *J*-distribution.

1) The total contribution of a particle is proportional to the time during which Q remains in a "reflection band" of the constant width $2u$. Putting TQ $= x$, this time is found to be proportional to

$$f(x) = \arc\sin u/x \quad \text{for } x > u, \qquad (14)$$

$$f(x) = \tfrac{1}{2}\pi \quad \text{for } x < u. \qquad (15)$$

2) Superposed upon this variation is the one discussed in § 3*b*, *c*: the contribution depends on the length of NN′ and on the slope of PN when the particle is in a reflecting position.

3) Finally, of course, this position has to be such that the particle is irradiated during the time it is able to reflect.

The effects 1)–3) are interlinked by the condition that Q, N and P lie on a straight line (namely, the normal of the reflecting lattice plane). None of them is therefore strictly independent of the two others, so that the procedure of § 2 cannot be applied rigorously. However, the function $f(x)$ defining the first effect has such a very sharp peak for $x = 0$ that we cannot be far off the truth in combining the smooth and wide ranges of 2) and 3) merely into the definition of an effective upper boundary s for x. For a particle situated on the axis of rotation the limit is $s = \frac{1}{2}h\mathrm{PQ}/\mathrm{PN} = \frac{1}{2}h/\sin^2\theta$.

We shall adopt this as the effective boundary since for $\theta = 90°$ it is also equal to the real sharp boundary $\frac{1}{2}h$; for small angles the approximation will be less good, but this case is not very easy to cover exactly anyhow. Therefore we apply (3) with the function $f(x)$ defined by (14) and (15) and

$$\begin{aligned} p(x)\mathrm{d}x &= 2\pi x\mathrm{d}x/\pi s^2 = 2x\mathrm{d}x/s^2 \text{ for } 0 < x < s, \\ p(x) &= 0 \qquad\qquad\qquad\qquad \text{for } x > s \text{ and } x < 0. \end{aligned}$$

Bearing in mind that $s \gg u$, we find easily for the integral occurring in the denominator of r (cf. (3))

$$\int_0^s p(x)f(x)\mathrm{d}x = 2u/s.$$

The numerator

$$\int_0^s p(x)f^2(x)\mathrm{d}x = \frac{1}{s^2}\left[\int_0^u \tfrac{1}{4}\,\pi^2.2x\mathrm{d}x + \int_n^s \left(\arcsin\frac{u}{x}\right)^2 2x\mathrm{d}x\right] =$$

$$= \frac{u^2}{s^2}\left[\tfrac{1}{4}\pi^2 + 2\int_1^{s/u}\left(\operatorname{arc\,sin}\frac{1}{t}\right)^2 t\mathrm{d}t\right]$$

has been evaluated by putting arc $\sin(1/t)$ equal to $1/t$ for $t > 3$ and computing the integral from $t = 1$ to $t = 3$ numerically. The result is

$$\int_0^s p(x)f^2(x)\mathrm{d}x = [3.00 + 2\ln(s/u)]\ (u^2/s^2)$$

and (cf (3))

$$r = 0.75 + \tfrac{1}{2}\ln(s/u).$$

This brings us to the question which value of u shall be used for a given experiment. Strictly speaking the "horizontal spread" is now not merely the sum of a geometrical range (such as given by b_2 and b_2 in fig. 2) and the rocking angle. The correct procedure would be to let the "reflection band" in fig. 3 correspond to the geometrical range and to smear out the point Q into a circular area corresponding to the rocking angle. We expect, however, that the first-mentioned additive procedure is sufficiently accurate, so that we may put $2u = \delta\alpha R/\sin\theta$, $\delta\alpha$ being defined as in §§ 3 and 4 or, since $w = \delta\alpha R$, $2u = w/\sin\theta$. Inserting also $s = \frac{1}{2}h\sin^2\theta$, the last r-factor applied to (12) yields

$$\sigma = 4R\sin\theta[0.75 + \tfrac{1}{2}\ln(h/w\sin\theta)]^{\frac{1}{2}}/h\sqrt{mN_{eff}}. \qquad (16)$$

Now a value of w below 0.1 mm or exceeding 1.0 mm will be very rare. For $h = 10$ mm and $\sin\theta$ between 0.25 and 1 this means that $h/w\sin\theta$ lies between 400 and 10. The corresponding values of $\sqrt{r}$ are 1.94 and 1.38. Hence a mean value $\sqrt{r} = 1.6$, or

$$\sigma = 6.5R\sin\theta/h\sqrt{mN_{eff}} \qquad (17)$$

is seen to cover almost every possible situation to within 20%.

§ 7. *Discussion.* Comparing the formula (17) for the rotating specimen with (9) for the stationary specimen, we find that the major difference is the replacement of $(hw)^{\frac{1}{2}}$ in the denominator of the latter by h in (17). The "factor of improvement" resulting from rotation will therefore be of the order of $(h/w)^{\frac{1}{2}}$. Its actual value will in general be somewhat smaller because of the difference between the numerical coefficients. However, the difference in dependence on θ is to the advantage of the rotating specimen, so that for small values of θ a gain in accuracy of even more than a factor $(h/w)^{\frac{1}{2}}$ may occur.

In practical applications there will nearly always be a large uncertainty in N_{eff} because the effective particle volume is difficult to measure. Also the value of w is very uncertain, since it is the sum of one term (εR) which can hardly be measured independently and another which is a symmetrical but not always a well-defined function of source and slit-width. However, the value of w has very little influence on the particle statistics error for a rotating sample, so that at least for this case a quantitative test of the present theory can be envisaged.

Finally, the author wishes to express his gratitude to Mrs Jeanne Taylor for much valuable criticism of the manuscript and to Dr W. Parrish for suggesting and helpfully discussing the problem.

Received 18th September, 1957.

REFERENCE

1) Alexander, L., H. P. Klug and E. Kummer, J. Appl. Phys. **19** (1948) 742.

THE ELECTROMAGNETIC THEORY OF THE SPHERICAL LUNEBERG LENS *)

by C. T. TAI

Antenna Laboratory, Department of Electrical Engineering, The Ohio State University, Columbus 10, Ohio, U.S.A. **)

Summary

A solution has been obtained for the spherical or the three-dimensional Luneberg lens. The paper starts with a general discussion of the vector wave functions which can be used to represent the electromagnetic field in a radially stratified medium. It is then applied specifically to the Luneberg lens. Four essential vector wave functions are defined in terms of two scalar wave functions. One of them contains the confluent hypergeometric function, and the other involves a "generalized" confluent hypergeometric function. The latter satisfies a differential equation which can be obtained by a proper confluence of three regular singularities of an equation with five regular singularities. The confluence differs from the confluences employed to obtain the differential equations commonly encountered in certain branches of mathematical physics. It is, therefore, concluded that the "generalized" confluent hypergeometric function is an entirely new function which is not simply related to other well-known functions. The paper finally presents a number of important formulae pertinent to the problem. The solution to another class of stratified lenses is briefly discussed.

§ 1. *Introduction.* The Luneberg lens [1]) is characterized by a refractive index which varies according to the relation

$$n = \left(2 - \frac{r^2}{a^2}\right)^{\frac{1}{2}},$$

where n is the refractive index, a is the radius of the outer rim of the spherical lens, and r is the radial distance measured from the centre of the lens. According to Luneberg's original theory, which is based upon the method of geometrical optics, the lens has the property of converting the radiation of a point source placed at the rim of the lens into a collimated beam on the opposite side of the lens. The original theory, of course, was not formulated as a boundary-value problem.

---

*) The research reported here was sponsored in part by the Air Research and Development Command, Wright Air Development Center under Contract AF 33(616)–3353.

**) Presently at Instituto Technologico de Aeronautica, São José dos Campos, São Paulo, Brazil.

An exact theory of the cylindrical or the two-dimensional Luneberg lens has recently been obtained by Jasik [2]). A brief discussion of the problem of the spherical lens is also reported in his paper.

The present work starts with a general discussion of the electromagnetic field involved in a radially stratified medium. It is then applied specifically to the spherical Luneberg lens. The general expression for the electromagnetic field due to a dipole placed in the neighbourhood of the lens is derived. When the dipole is moved to the rim of the sphere, the condition corresponding to the excitation of the Luneberg lens is obtained. The scattered field produced by the lens due to a plane-wave incidence is obtained by removing the dipole to infinity. Both expressions are derived in this paper.

In the course of this study a new function is encountered. The analytic nature of this function is examined in detail. Because of its close relationship to the ordinary confluent hypergeometric function it is designated as the "generalized" confluent hypergeometric function. The name is merely for proper identification.

§ 2. *Vector wave functions for a radially stratified medium.* The electromagnetic field associated with a radially stratified medium has recently been discussed by a number of writers. A rather systematic treatment is given by Marcuvitz [3]). Special topics involving rotationally symmetrical excitations have been discussed by Friedman [4]), Nomura and Takaku [5]). In the present work the vector wave-function method of Hansen and Stratton [6]) will first be extended to represent the fields in a radially stratified medium without any restriction upon the exact nature of the index of refraction and the symmetry of the field. The method is rather compact in form and offers certain simplicity in the algebraic manipulation of the various field components, particularly in dealing with the matching of the tangential fields in satisfying the boundary conditions when applied to specific problems.

In a *radially stratified medium* where the dielectric constant is a function only of the radial distance r measured from the origin of a coordinate system, the Maxwell equations in a source-free region can be written in the form:

$$\nabla \times \mathbf{E} = i\omega\mu\mathbf{H}, \tag{1}$$

$$\nabla \times \mathbf{H} = -\, i\omega\varepsilon_0\kappa(r)\mathbf{E}, \tag{2}$$

$$\nabla \cdot [\kappa(r)\mathbf{E}] = 0, \tag{3}$$

$$\nabla \cdot \mathbf{H} = 0, \tag{4}$$

where $\kappa(r)$ denotes the relative dielectric constant with respect to ε_0. The index of refraction $n(r)$ is related to $\kappa(r)$ by the equation

$$n^2(r) = \kappa(r). \tag{5}$$

It is assumed in the present work that the time dependence is of the form $e^{-i\omega t}$, which has been omitted for all the electromagnetic quantities. By eliminating either **H** or **E** from (1) and (2) one obtains the following two vector wave equations:

$$\nabla \times \nabla \times \mathbf{E} - k^2\kappa\mathbf{E} = 0, \tag{6}$$

$$\nabla \times \nabla \times \mathbf{H} - \frac{\nabla\kappa}{\kappa} \times \nabla \times \mathbf{H} - k^2\kappa\mathbf{H} = 0, \tag{7}$$

where $k^2 = \omega^2\mu\varepsilon_0$, and it is implied henceforth that κ is an abbreviation for $\kappa(r)$. The fact that $\kappa\mathbf{E}$ and **H** are both solenoidal vectors as specified by (3) and (4) is implied in (6) and (7). This can be shown by taking the divergence of the last two equations, and by applying the vector identities.

Analogous to the problems of homogeneous spheres, two sets of wave functions will be defined which are general solutions for (6) and (7).

A. The magnetic or the transverse electric modes. The magnetic or the transverse electric modes are derived by assuming the *electric field* to be proportional to a vector wave function defined by

$$\mathbf{M}^{(m)} = \nabla \times (\psi^{(m)}\hat{r}), \tag{8}$$

where the superscript (m) denotes the magnetic type and $\hat{r}$ denotes the unit vector in the radial direction. By substituting (8) into (6) for **E** and evaluating the operator $\nabla \times \nabla \times (\ )$ in a spherical coordinate system one finds that $\mathbf{M}^{(m)}$ is a solution for that equation if $\psi^{(m)}$ satisfies

$$\frac{\partial^2\psi^{(m)}}{\partial r^2} + \frac{1}{r^2 \sin\theta}\frac{\partial}{\partial\theta}\left(\sin\theta\,\frac{\partial\psi^{(m)}}{\partial\theta}\right) + \frac{1}{r^2\sin^2\theta}\,\frac{\partial^2\psi^{(m)}}{\partial^2\phi^2} + {} + k^2\kappa\psi^{(m)} = 0. \tag{9}$$

By applying the method of separating variables to (9), one finds that the general solutions are given by

$$\psi^{(m)}_{\substack{e\\o}mn} = S_n(r)P_n^m(\cos\theta)\,{\cos \atop \sin}\, m\phi \tag{10}$$

where $P_n^m(\cos\theta)$ denotes the associated Legendre function. The radial function $S_n(r)$ satisfies the differential equation

$$\frac{d^2S_n}{dr^2} + \left[k^2\kappa - \frac{n(n+1)}{r^2}\right]S_n = 0. \tag{11}$$

The general solution for (11) will be discussed later with κ having the radial variation corresponding to the Luneberg lens. On account of (1) and (4) the vector wave functions which are appropriate to represent the corresponding magnetic field would be given by

$$\mathbf{N}^{(m)}_{\substack{e\\o}mn} = \frac{1}{k}\nabla\times\mathbf{M}^{(m)}_{\substack{e\\o}mn}, \tag{12}$$

where by definition

$$\mathbf{M}^{(m)}_{\substack{e\\o}mn} = \nabla\times(\psi^{(m)}_{\substack{e\\o}mn}\,\hat{r}). \tag{13}$$

The constant k^{-1} is introduced for the convenience of proper normalization. It can further be shown that the functions $\mathbf{N}^{(m)}_{\substack{e\\o}mn}$ do satisfy (7) and an identity similar to (12) exists, namely,

$$\mathbf{M}^{(m)}_{\substack{e\\o}mn} = \frac{1}{k\kappa}\nabla\times\mathbf{N}^{(m)}_{\substack{e\\o}mn}. \tag{14}$$

The long expressions for the two vector wave functions involved in the magnetic case are given by

$$\mathbf{M}^{(m)}_{\substack{e\\o}mn} = \frac{S_n}{r}\left(\mp\frac{mP_n^m}{\sin\theta}\,{\sin \atop \cos}\,m\phi\,\hat{\theta} - \frac{\partial P_n^m}{\partial\theta}\,{\cos \atop \sin}\,m\phi\,\hat{\phi}\right) = \frac{S_n}{r}\,\mathbf{m}_{\substack{e\\o}mn} \tag{15}$$

and

$$\mathbf{N}^{(m)}_{\substack{e\\o}mn} = \frac{1}{k}\left[\frac{n(n+1)}{r^2} S_n P_n^m \begin{matrix}\cos\\ \sin\end{matrix}\, m\phi\, \hat{r} + \right.$$

$$\left. + \frac{1}{r}\frac{\partial S_n}{\partial r}\left(\frac{\partial P_n^m}{\partial \theta} \begin{matrix}\cos\\ \sin\end{matrix}\, m\phi\, \hat{\theta} \mp \frac{m P_n^m}{\sin\theta} \begin{matrix}\sin\\ \cos\end{matrix}\, m\phi\, \hat{\phi}\right)\right]$$

$$= \frac{1}{k}\left[\frac{S_n}{r^2}\mathbf{l}_{\substack{e\\o}mn} + \frac{1}{r}\frac{\partial S_n}{\partial r}(\hat{r}\times \mathbf{m}_{\substack{e\\o}mn})\right]. \qquad (16)$$

The angular vector functions $\mathbf{m}_{\substack{e\\o}mn}$ and $\mathbf{l}_{\substack{e\\o}mn}$ are defined by

$$\mathbf{m}_{\substack{e\\o}mn} = \mp \frac{m P_n^m}{\sin\theta} \begin{matrix}\sin\\ \cos\end{matrix}\, m\phi\, \hat{\theta} - \frac{\partial P_n^m}{\partial\theta} \begin{matrix}\cos\\ \sin\end{matrix}\, m\phi\, \hat{\phi} \qquad (17)$$

and

$$\mathbf{l}_{\substack{e\\o}mn} = n(n+1) P_n^m \begin{matrix}\cos\\ \sin\end{matrix}\, m\phi\, \hat{r}. \qquad (18)$$

These angular functions, with different normalization factors have previously been used by Morse and Feshbach 7) for spherical problems. *) The orthogonal properties of these functions are contained in the following equations:

$$\mathbf{l}_{\substack{e\\o}mn} \cdot \mathbf{m}_{\substack{e\\o}mn} = 0,\ \mathbf{l}_{\substack{e\\o}mn} \cdot (\hat{r}\times\mathbf{m}_{\substack{e\\o}mn}) = 0,\ \mathbf{m}_{\substack{e\\o}mn} \cdot (\hat{r}\times\mathbf{m}_{\substack{e\\o}mn}) = 0. \qquad (19)$$

$$\int_0^{\pi}\int_0^{2\pi} (\mathbf{l}_{\substack{e\\o}mn} \cdot \mathbf{l}_{\substack{e\\o}mn}) \sin\theta\, d\theta d\phi = \begin{cases} 0;\ m \neq m',\ \text{or}\ n \neq n' \\ \dfrac{2n^2(n+1)^2}{2n+1}\dfrac{(n+m)!}{(n-m)!}(1+\delta_0)\pi; \\ \qquad m = m',\ n = n', \end{cases}$$

$$\int_0^{\pi}\int_0^{2\pi} (\mathbf{m}_{\substack{e\\o}un} \cdot \mathbf{m}_{\substack{e\\o}m'n'}) \sin\theta\, d\theta d\phi$$

$$= \int_0^{\pi}\int_0^{2\pi} [(\hat{r}\times\mathbf{m}_{\substack{e\\o}mn}) \cdot (\hat{r}\times\mathbf{m}_{\substack{e\\o}m'n'})] \sin\theta\, d\theta d\phi$$

$$= \begin{cases} 0;\ m \neq m',\ \text{or}\ n \neq n' \\ \dfrac{2n(n+1)}{2n+1}\dfrac{(n+m)!}{(n-m)!}(1+\delta_0)\pi;\ m = m',\ n = n', \end{cases}$$

where $\delta_0 = \begin{cases} 1,\ m = 0 \\ 0,\ m > 0. \end{cases}$

---

*) The $\mathbf{l}_{\substack{e\\o}mn}$ and $\mathbf{m}_{\substack{e\\o}mn}$ functions defined here are different from the functions defined by Stratton 6), where the same notations are used.

B. The electric or the transverse magnetic modes. The electric or the transverse magnetic modes are derived by assuming the magnetic field to be proportional to a vector wave function defined by

$$\mathbf{M}^{(e)} = \nabla \times (\psi^{(e)}\hat{r}), \tag{20}$$

where the superscript (e) denotes the electric type. By substituting (20) into (7) for $\mathbf{H}$ one finds that $\mathbf{M}^{(e)}$ is a solution for that equation if $\psi^{(e)}$ satisfies

$$\frac{\partial^2\psi^{(e)}}{\partial r^2} - \frac{1}{\kappa}\frac{d\kappa}{dr}\frac{\partial\psi^{(e)}}{\partial r} + \frac{1}{r^2 \sin\theta}\frac{\partial}{\partial\theta}\left(\sin\theta\frac{\partial\psi^{(e)}}{\partial\theta}\right) + \\ + \frac{1}{r^2\sin^2\theta}\frac{\partial^2\psi^{(e)}}{\partial\phi^2} + k^2\kappa\psi^{(e)} = 0. \tag{21}$$

The general solutions for (21) are given by

$$\psi^{(e)}_{\substack{e\\o}mn} = T_n(r)P_n^m(\cos\theta)\begin{matrix}\cos\\ \sin\end{matrix}\, m\phi, \tag{22}$$

where $T_n(r)$ satisfies the differential equation

$$\frac{d^2T_n}{dr^2} - \frac{1}{\kappa}\frac{d\kappa}{dr}\frac{dT_n}{dr} + \left[k^2\kappa - \frac{n(n+1)}{r^2}\right]T_n = 0. \tag{23}$$

Eq. (23) differs considerably from (11) when κ is a function of r. They become the same equation if κ is a constant. The vector wave functions which are appropriate to represent the electric field in this case are defined by

$$\mathbf{N}^{(e)}_{\substack{e\\o}mn} = \frac{1}{k\kappa}\nabla \times \mathbf{M}^{(e)}_{\substack{e\\o}mn}, \tag{24}$$

where

$$\mathbf{M}^{(e)}_{\substack{e\\o}mn} = \nabla \times (\psi^{(e)}_{\substack{e\\o}mn}\hat{r}). \tag{25}$$

It can be verified that the functions $\mathbf{N}^{(e)}_{\substack{e\\o}mn}$ indeed satisfy (6) and an identity similar to (24) exists, namely,

$$\mathbf{M}^{(e)}_{\substack{e\\o}mn} = \frac{1}{k}\nabla \times \mathbf{N}^{(e)}_{\substack{e\\o}mn}. \tag{26}$$

The long expressions for the two vector wave functions involved in the electric case are given by

$$\mathbf{M}^{(e)}_{\substack{e\\o}mn} = \frac{T_n}{r}\mathbf{m}_{\substack{e\\o}mn}, \tag{27}$$

$$\mathbf{N}^{(e)}_{\substack{e\\o}mn} = \frac{1}{k\kappa}\left[\frac{T_n}{r^2}\mathbf{l}_{\substack{e\\o}mn} + \frac{1}{r}\frac{\partial T_n}{\partial r}(\hat{r} \times \mathbf{m}_{\substack{e\\o}mn})\right], \tag{28}$$

where the angular functions are the same as previously defined by (17) and (18). In summarizing the above discussion one observes that the electromagnetic field associated with a radially stratified medium in a source-free region can in general be represented by the following pair of equations:

$$\mathbf{E} = \sum_n (A_n\mathbf{M}^{(m)}_n + B_n\mathbf{N}^{(e)}_n), \tag{29}$$

$$\mathbf{H} = \frac{k}{i\omega\mu}\sum_n (A_n\mathbf{N}^{(m)}_n + B_n\mathbf{M}^{(e)}_n), \tag{30}$$

where the four essential vector wave functions are defined by (15), (16), (27), and (28). Here the subscript n represents the two indices of summation. The functions may be even or odd. The formulation is onviously an extension of the Hansen-Stratton method to a radially stratified medium. The main difference is that instead of two types of vector wave functions, we need four in the present case. As mentioned previously, when κ is constant the S_n and T_n functions become the same; hence there is no difference between the magnetic and the electric type of vector wave functions. If we take the cross product of (29) and (30) with $\hat{r}$, the resultant equations become schematically the same as the two vector transmission-line equations discussed by Marcuvitz 8).

§ 3. *On the nature of S_n and T_n functions for the spherical Luneberg lens.* The spherical Luneberg lens is characterized by a dielectric constant which varies according to the relation

$$\kappa = 2 - \left(\frac{r}{a}\right)^2, \quad 0 \leq r \leq a, \tag{31}$$

where a is the radius of the outer rim of the lens, the centre of which coincides with the origin of the spherical coordinate system. When (31) is substituted into (11) for κ, the resultant equation is transformable into the confluent hypergeometric equation. It has been shown by Jasik 9) that one solution for that equation, which is finite at $r = 0$, is given by

$$S_n = \rho^{n+1}\mathrm{e}^{-\varrho^2/2\varrho_a}{}_1F_1(\alpha, \gamma, \rho^2/\rho_a), \tag{32}$$

where $\rho = kr$, $\rho_a = ka$, $\alpha = \frac{1}{2}(n + \frac{3}{2} - \rho_a)$, $\gamma = n + \frac{3}{2}$. ${}_1F_1(\alpha, \gamma, z)$ denotes the confluent hypergeometric function or Kummer's function [10]) which satisfies the differential equation

$$\frac{d^2w}{dz^2} + \left(\frac{\gamma}{z} - 1\right)\frac{dw}{dz} - \frac{\alpha}{z} w = 0. \tag{33}$$

For the analysis of the Luneberg lens with the exciting source placed outside or at the rim of the sphere, the other independent solution

$$z^{1-\gamma}{}_1F_1(\alpha - \gamma + 1, 2 - \gamma, z)$$

is not needed. It will be implied henceforth that the S_n function of the spherical Luneberg lens is the one defined by (32). The vector wave functions $\mathbf{M}^{(m)}_{\substack{e\\o}mn}$ and $\mathbf{N}^{(m)}_{\substack{e\\o}mn}$ are thus defined into terms of this function.

When (31) is substituted into (23), the resultant equation becomes

$$\frac{d^2T_n}{d\rho^2} + \frac{2\rho}{2\rho_a^2 - \rho^2}\frac{dT_n}{d\rho} + \left[2 - \frac{\rho^2}{\rho_a^2} - \frac{n(n+1)}{\rho^2}\right] T_n = 0 \tag{34}$$

where ρ and ρ_a denote, respectively, kr and ka. Let

$$T_n = (2\rho_a^2 - \rho^2)^{\frac{1}{2}}\rho^{n+1} e^{-\varrho^2/2\varrho_a} U_n. \tag{35}$$

Then U_n satisfies the equation

$$\frac{d^2U_n}{d\rho^2} + 2\left(\frac{n+1}{\rho} - \frac{\rho}{\rho_a}\right)\frac{dU_n}{d\rho} + \left[2 - \frac{2n+3}{\rho_a} - \right.$$
$$\left. - \frac{1}{2\rho_a^2 - \rho^2} - \frac{3\rho^2}{(2\rho_a^2 - \rho^2)^2}\right] U_n = 0. \tag{36}$$

A further transformation of the independent variable $z = \rho^2/\rho_a$ converts (36) into

$$\frac{d^2U_n}{dz^2} + \left(\frac{\gamma}{z} - 1\right)\frac{dU_n}{dz} - \left[\frac{\alpha_1}{z} + \frac{2\alpha_2}{z - a_2} - \frac{2a_2\alpha_3}{(z - a_2)^2}\right] U_n = 0, \tag{37}$$

where the various constants are defined by

$$\gamma = n + \tfrac{3}{2},$$

$$\alpha_1 = \tfrac{1}{2}\left(n + \tfrac{3}{2} - \rho_a + \frac{1}{4\rho_a}\right),$$

$$\alpha_2 = -\frac{1}{16\rho_a}, \quad \alpha_3 = -\frac{3}{16\rho_a}, \quad a_2 = 2\rho_a.$$

Eq. (37) is similar to the confluent hypergeometric equation defined by (33), except that it has another regular singularity at $z = a_2$. The constants in the equation have purposely been so arranged in order to simplify the series solution discussed later. In order to appreciate more fully the nature of the solution to eq. (37) it is profitable to digress to a discussion of the general characteristics of this equation. Like the hypergeometric equation it has a regular singularity at $z = 0$ with exponents 0 and $1 - \gamma$ 11) and an irregular singularity at ∞. The exponents of the regular singularity at $z = a_2$ are equal to $\frac{3}{2}$ and $-\frac{1}{2}$. In the theory of differential equations it is known that the confluent hypergeometric equation can be obtained by the confluence of two regular singularities of the hypergeometric equation. The confluence is more easily seen by starting with the Papperitz equation or the Riemann *P*-equation 12). It is, therefore, anticipated that the new equation defined by (37) perhaps can be obtained by the suitable confluence of a number of regular singularities of a second-order differential equation with at least four or more regular singularities. It can be shown that unless the constants α_1, α_2, and α_3 are related in a certain special way, in general, we need a second-order differential equation with five regular singularities to start with. The equation which fulfills this requirement is given by Whittaker and Watson 13), and can be written in the form

$$\frac{d^2u}{dz^2} + \sum_{r=1}^{4} \frac{1 - \lambda_r - \lambda_r'}{z - a_r} \frac{du}{dz} + \frac{1}{\prod\limits_{r=1}^{4} (z - a_r)} \left[Az^2 + Bz + C + \sum_{r=1}^{4} \frac{C_r}{z - a_r} \right] u = 0, \qquad (38)\ ^{*)}$$

where a_1, a_2, a_3, and a_4 denote the four regular singularities. Their exponents are λ_r and λ_r'. The point $z = \infty$ is another regular point with exponents designated by μ and μ'. The constants A and the C_r's are given by

$$\alpha^2 - [3 - \sum_{r=1}^{4} (\lambda_r + \lambda_r')]\, \alpha + A = 0, \quad \alpha = \mu \text{ or } \mu',$$

$$C_r = \frac{\lambda_r \lambda_r'}{\prod\limits_{s} (a_r - a_s)}, \quad s = 1, 2, \ldots, s \neq r.$$

---

*) The constants A, B, C in the present equation are not the same as those in Whittaker and Watson's equation.

The constants B and C are so far arbitrary. It is observed that because we have put (38) in a different form, the indicial equation for μ and μ' is also changed in its appearance. Equation (38) is most conveniently presented by using the Riemann scheme

$$P\left\{\begin{array}{cccccc} a_1 & a_2 & a_3 & a_4 & \infty & \\ \lambda_1 & \lambda_2 & \lambda_3 & \lambda_4 & \mu & z \\ \lambda_1' & \lambda_2' & \lambda_3' & \lambda_4' & \mu' & \end{array}\right\}$$

In order to reduce (38) into (37) we first let

$$a_1 = 0,\ \lambda_1 = 0,\ \lambda_1' = 1 - \gamma$$
$$a_2 = a_2,\ \lambda_2 = \tfrac{3}{2},\ \lambda_2' = -\tfrac{1}{2},$$

which correspond to the two regular points and their exponents of (37). Without restricting ourselves to the exact procedure of the limiting process, if we assume then when a_3 and a_4 approach infinity

$$\left.\begin{array}{l} \dfrac{1-\lambda_3-\lambda_3'}{a_3} + \dfrac{1-\lambda_4-\lambda_4'}{a_4} \to -1, \\[2ex] \dfrac{A}{a_3 a_4} \to 0, \\[2ex] \dfrac{B}{a_3 a_4},\ \dfrac{C}{a_3 a_4},\ \dfrac{\lambda_3\lambda_3'(a_3-a_4)}{a_4},\ \dfrac{\lambda_4\lambda_4'(a_3-a_4)}{a_3} \to \text{finite}, \end{array}\right\} \quad (39)$$

then (38) immediately reduces to the form

$$\frac{d^2u}{dz^2} + \left(\frac{\gamma}{z} - 1\right)\frac{du}{dz} + \left[\frac{\beta}{z-a_2} + \frac{\delta}{z(z-a_2)} + \frac{\lambda_2\lambda_2' a_2}{z(z-a_2)^2}\right] u = 0 \quad (40)$$

where β and δ are two arbitrary constants. By rearranging the terms in the last brackets and introducing two new arbitrary constants α_1 and α_2, we can write (40) in the form

$$\frac{d^2u}{dz^2} + \left(\frac{\gamma}{z} - 1\right)\frac{du}{dz} - \left[\frac{\alpha_1}{z} + \frac{2\alpha_2}{z-a_2} - \frac{\lambda_2\lambda_2'}{(z-a_2)^2}\right] u = 0, \quad (41)$$

which is identical in form to (37), observing that

$$\lambda_2\lambda_2' = 2a_2\alpha_3 = -\tfrac{3}{4}.$$

The foregoing discussion on the analytical nature of the function U_n is simply to show that while the confluent hypergeometric equation is obtained by the confluence of two regular singularities of the Papperitz equation, the "generalized" *) confluent hypergeometric equation as defined by (37) can be obtained by the confluence of three regular singularities of (38). It may be remarked that the above procedure is not the only way to deduce (37) from a more general second-order linear differential equation. An alternative procedure is to start with an equation of five regular singularities and with the point at infinity considered to be an ordinary point. The same result can thus be achieved *). It is, therefore, concluded that at least five regular singularities are needed to execute the proper confluence in obtaining (37). The foregoing discussion demonstrates the fact that analytically the differential equation for T_n is basically different from the differential equation for S_n and no simple connection exists between them. It also shows that the "generalized" confluent hypergeometric function is an entirely new function which is not related to other well-known functions.

---

*) This designation may not be the best one.

For the Luneberg lens problem it is necessary to obtain a series expansion for U_n, hence T_n, which is finite at $z = 0$. Recall that the two exponents at $z = 0$ are 0 and $1 - \gamma$, where γ is greater than one for this problem. The series solution which remains finite at the origin is therefore associated with the exponent equal to zero. On the other hand, the exponent $1 - \gamma$ leads to a solution which is singular at the origin. The desirable solution plays the same role as the Kummer function in (11). The series solution of interest is of the form

$$U_n = \sum_{m=0}^{\infty} A_m z^m. \tag{42}$$

By substituting (42) into (37), one finds that

$$\left.\begin{aligned}
&\frac{A_1}{A_0} = \frac{\alpha_1}{\gamma}, \\
&\frac{A_2}{A_0} = \tfrac{1}{2}\,\frac{\alpha_1(\alpha_1+1)}{\gamma(\gamma+1)} - \frac{\alpha_2+\alpha_3}{(\gamma+1)a_2}, \\
&\frac{A_3}{A_0} = \frac{1}{3!}\,\frac{\alpha_1(\alpha_1+1)\,(\alpha_1+2)}{\gamma(\gamma+1)\,(\gamma+2)} \\
&-\frac{1}{3(\gamma+2)}\left[\frac{(\alpha_1+2)\,(\alpha_2+\alpha_3)}{(\gamma+1)a_2} + \frac{2\alpha_1(\alpha_2+\alpha_3)}{\gamma a_2} + \frac{2(\alpha_2+2\alpha_3)}{a_2^2}\right].
\end{aligned}\right\} \tag{43}$$

---

*) If one uses the nation of Ince (Ordinary Diff. Equations, pp. 497–504, Dover Publications, New York, 1944), (37) can be classified as of the type $(0, 2, 1_2)$ which can be derived, by confluence of singularities, from the equations $(8, 0, 0)$.

For $m \geq 3$, the coefficient can be obtained from the following four-term recurrence relationship:

$$a_2^2(m+1)(m+\gamma)A_{m+1} - a_2[a_2(m+\alpha_1) + 2n(\gamma - m+1)]A_m$$
$$+ [2a_2(\alpha_1 + \alpha_2 + \alpha_3 + m - 1) + (n-1)(\gamma + m - 2)]A_{m-1}$$
$$- (\alpha_1 + 2\alpha_2 + m - 2)A_{m-2} = 0. \tag{44}$$

The series solution for U_n converges uniformly and absolutely for $|z| < a_2$ or $\rho < 2\rho_a$. Actually, in the Luneberg lens problem the values of ρ never exceed ρ_a. It is observed that for large values of ρ_a the leading term of A_m/A_0 is practically the same as the corresponding coefficient of the series expansion of the Kummer function, which is given by

$${}_1F_1(\alpha, \gamma, z) = 1 + \frac{\alpha}{\gamma} z + \frac{\alpha(\alpha+1)}{\gamma(\gamma+1)} \frac{z^2}{2!} + $$
$$+ \frac{\alpha(\alpha+1)(\alpha+2)}{\gamma(\gamma+1)(\gamma+2)} \frac{z^3}{3!} + \cdots .$$

For example, when ρ_a is large,

$$\alpha_1 \simeq \alpha = \tfrac{1}{2}(n + \tfrac{3}{2} - \rho_a)$$

and

$$-\frac{\alpha_2 + \alpha_3}{a_2} = \frac{5}{32\rho_a^2}.$$

The second term of A_2/A_0 is, therefore, much smaller than the first term. It is very likely that for numerical work it may not be necessary at all to compute the U_n function separately. The T_n function, in view of (35), is then practically equal to the S_n function

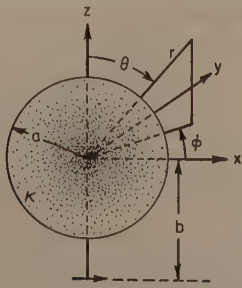

Fig. 1. Horizontal dipole placed in front of a spherical Luneberg lens, $\varkappa = 2 - (r/a)^2$.

at $\rho = \rho_a$. The same is true for the derivative of T_n with respect to r when ρ_a is sufficiently large.

§ 4. *Radiation from electric dipoles in the presence of a spherical Luneberg lens.* The remaining part of this paper concerns the derivation of the formal expressions of the electromagnetic field associated with the spherical Luneberg lens when the exciting sources are assumed to be made of electric dipoles. The treatment for magnetic dipoles is practically the same.

Assume that a horizontal electric dipole of moment p_x is pointed in the x-direction and located at $r = b$, $\theta = \pi$, $\phi = 0$ as shown in fig. 1. The electromagnetic field due to the dipole in the *absence* of the sphere is given by [14])

$$\mathbf{E}^i = \frac{ik^3 p_x}{4\pi\varepsilon} \sum_{n=1}^{\infty} \frac{2n+1}{n(n+1)} (-1)^n . \\ \cdot \left\{ \begin{array}{ll} h_n^{(1)}(\rho_b)\mathbf{M}^{(1)}_{o1n} - \dfrac{[\rho_b h_n^{(1)}(\rho_b)]'}{\rho_b} \mathbf{N}^{(1)}_{e1n}, & r \leq b \\ j_n(\rho)\mathbf{M}^{(3)}_{o1n} - \dfrac{[\rho_b j_n(\rho_b)]'}{\rho_b} \mathbf{N}^{(3)}_{e1n}, & r \geq b \end{array} \right. \tag{45}$$

$$\mathbf{H}^i = \frac{\omega k^2 p_x}{4\pi} \sum_{n=1}^{\infty} \frac{2n+1}{n(n+1)} (-1)^n . \\ \cdot \left\{ \begin{array}{ll} h_n^{(1)}(\rho_b)\mathbf{N}^{(1)}_{o1n} - \dfrac{[\rho_b h_n^{(1)}(\rho_b)]'}{\rho_b} \mathbf{M}^{(1)}_{e1n}, & r \leq b \\ j_n(\rho_b)\mathbf{N}^{(3)}_{o1n} - \dfrac{[\rho_b j_n(\rho_b)]'}{\rho_b} \mathbf{M}^{(3)}_{e1n}, & r \geq b \end{array} \right. \tag{46}$$

where

$$\rho_b = kb,$$

$$\mathbf{M}^{(1)}_{\substack{e\\o}1n} = \nabla \times \left[r j_n(kr) P_n^1(\cos\theta) \begin{matrix}\cos\\ \sin\end{matrix}\,\phi\hat{r} \right],$$

$$\mathbf{N}^{(1)}_{\substack{e\\o}1n} = \frac{1}{k} \nabla \times \mathbf{M}^{(1)}_{\substack{e\\o}1n}.$$

The vector wave functions of the third kind are obtained by replacing $j_n(kr)$ by $h_n^{(1)}(kr)$. The primes in (45) denote the derivative with respect to the argument ρ_b. Referring to (29) and (30), we see that the scattered field in the presence of the lens, and the transmitted field inside the lens, must be of the form

$$\left.\begin{aligned}
\mathbf{E}^s &= \frac{ik^3 p_x}{4\pi\varepsilon} \sum_{n=1}^{\infty} \frac{2n+1}{n(n+1)} (-1)^n \Bigg\{ \alpha_n^{(m)} h_n^{(1)}(\rho_b) \mathbf{M}_{o1n}^{(3)} - \\
&\qquad - \alpha_n^{(e)} \frac{[\rho_b h_n^{(1)}(\rho_b)]'}{\rho_b} \mathbf{N}_{e1n}^{(3)} \Bigg\}, \\
\mathbf{H}^s &= \frac{k^2 p_x \omega}{4\pi} \sum_{n=1}^{\infty} \frac{2n+1}{n(n+1)} (-1)^n \Bigg\{ \alpha_n^{(m)} h_n^{(1)}(\rho_b) \mathbf{N}_{o1n}^{(3)} - \\
&\qquad - \alpha_n^{(e)} \frac{[\rho_b h_n^{(1)}(\rho_b)]'}{\rho_b} \mathbf{M}_{e1n}^{(3)} \Bigg\}, \quad r \geq a,
\end{aligned}\right\} \qquad (47)$$

$$\left.\begin{aligned}
\mathbf{E}^t &= \frac{ik^3 p_x}{4\pi\varepsilon} \sum_{n=1}^{\infty} \frac{2n+1}{n(n+1)} (-1)^n \Bigg\{ \beta_n^{(m)} h_n^{(1)}(\rho_b) \mathbf{M}_{o1n}^{(m)} \\
&\qquad - \beta_n^{(e)} \frac{[\rho_b h_n^{(1)}(\rho_b)]'}{\rho_b} \mathbf{N}_{e1n}^{(e)} \Bigg\}, \\
\mathbf{H}^t &= \frac{k^2 p_x \omega}{4\pi} \sum_{n=1}^{\infty} \frac{2n+1}{n(n+1)} (-1)^n \Bigg\{ \beta_n^{(m)} h(^{(1)}_{n} \rho_b) \mathbf{N}_{o1n}^{(m)} - \\
&\qquad - \beta_n^{(e)} \frac{[\rho_b h_n^{(1)}(\rho_b)]'}{\rho_b} \mathbf{M}_{e1n}^{(e)} \Bigg\}, \quad r \leq a,
\end{aligned}\right\} \qquad (48)$$

where the vector wave functions for the lens have previously been defined in terms of the S_n and T_n functions of (32), (35) and (42). The unknown coefficients $\alpha_n^{(m)}$, $\alpha_n^{(e)}$, $\beta_n^{(m)}$, and $\beta_n^{(e)}$ can be determined by applying the boundary conditions that $\hat{r} \times \mathbf{E}$ and $\hat{r} \times \mathbf{H}$ are continuous at $r = a$. Introducing the notations:

$$R_1 = \rho_a j_n(\rho_a), \qquad R_1' = \frac{\mathrm{d}}{\mathrm{d}\rho_a} [\rho_a j_n(\rho_a)],$$

$$R_3 = \rho_a h_n^{(1)}(\rho_a), \qquad R_3' = \frac{\mathrm{d}}{\mathrm{d}\rho_a} [\rho_a h_n^{(1)} (\rho_a)],$$

$$S_a = S_n(\rho_a), \qquad S_a' = \frac{\mathrm{d}}{\mathrm{d}\rho_a} S_n(\rho_a),$$

$$T_a = T_n(\rho_a), \qquad T_a' = \frac{\mathrm{d}}{\mathrm{d}\rho_a} T_n(\rho_a),$$

one finds that the boundary conditions are satisfied when for the magnetic type

$$\left.\begin{aligned} R_1 + \alpha_n^{(m)} R_3 &= \beta_n^{(m)} S_a, \\ R_1' + \alpha_n^{(m)} R_3' &= \beta_n^{(m)} S_a', \end{aligned}\right\} \tag{49}$$

and for the electric type

$$\begin{aligned} R_1 + \alpha_n^{(e)} R_3 &= \beta_n^{(e)} T_a, \\ R_1' + \alpha_n^{(e)} R_1' &= \beta_n^{(e)} T_a'. \end{aligned} \tag{50}$$

This gives

$$\left.\begin{aligned} \alpha_n^{(m)} &= \frac{R_1}{R_3}\left(\frac{R_1'}{R_1} - \frac{S_a'}{S_a}\right)\Bigg/\left(\frac{S_a'}{S_a} - \frac{R_3'}{R_3}\right), \\ \beta_n^{(m)} &= \frac{R_1}{S_a}\left(\frac{R_1'}{R_1} - \frac{R_3'}{R_3}\right)\Bigg/\left(\frac{S_a'}{S_a} - \frac{R_3'}{R_3}\right), \end{aligned}\right\} \tag{51}$$

$$\left.\begin{aligned} \alpha_n^{(e)} &= \frac{R_1}{R_3}\left(\frac{R_1'}{R_1} - \frac{T_a'}{T_a}\right)\Bigg/\left(\frac{T_a'}{T_a} - \frac{R_3'}{R_3}\right), \\ \beta_n^{(e)} &= \frac{R_1}{T_a}\left(\frac{R_1'}{R_1} - \frac{R_3'}{R_3}\right)\Bigg/\left(\frac{T_a'}{T_a} - \frac{R_3'}{R_3}\right). \end{aligned}\right\} \tag{52}$$

According to the original requirement of the excitation of a Luneberg lens the source should be situated at the rim of the sphere corresponding to $b = a$. By combining $\mathbf{E}^i$ and $\mathbf{E}^s$ and letting $b = a$, we obtain a rather compact expression for the total electric field due to the dipole in the presence of the lens, namely

$$\begin{aligned} \mathbf{E}_{total} &= \frac{k^2 p_x}{4\pi\varepsilon a} \sum_{n=1}^{\infty} (-1)^{n+1} \frac{2n+1}{n(n+1)} \cdot \\ &\quad \cdot \frac{1}{R_3}\left[\frac{\mathbf{M}_{o1n}^{(3)}}{\left(\frac{R_3'}{R_3} - \frac{S_a'}{S_a}\right)} - \frac{\mathbf{N}_{e1n}^{(3)}}{\left(\frac{T_a}{T_a'}\frac{R_3'}{R_3} - 1\right)}\right]. \end{aligned} \tag{53}$$

The far-zone expression for $\mathbf{E}_{total}$, valid for large values of ρ, is obtained by using the asymptotic expressions for $\mathbf{M}_{o1n}^{(3)}$ and $\mathbf{N}_{e1n}^{(3)}$, namely

$$\mathbf{M}_{o1n}^{(3)} \simeq (-i)^{n+1} \frac{e^{i\rho}}{\rho} \mathbf{m}_{o1n},$$

and

$$\mathbf{N}_{e1n}^{(3)} \simeq (-i)^{n} \frac{e^{i\rho}}{\rho} (\hat{r} \times \mathbf{m}_{e1n});$$

where $\rho = kr$, this gives

$$E_{far\ zone} = \frac{k^2 p_x}{4\pi\varepsilon a}\left(\frac{e^{i\rho}}{\rho}\right)\sum_{n=1}^{\infty}(i)^n \frac{2n+1}{n(n+1)}$$

$$\cdot \frac{1}{R_3}\left[\frac{i\mathbf{m}_{o1n}}{\left(\frac{R_3'}{R_3} - \frac{S_a'}{S_a}\right)} + \frac{\hat{r} \times \mathbf{m}_{e1n}}{\left(\frac{T_a}{T_a'}\frac{R_3'}{R_3} - 1\right)}\right]. \tag{54}$$

The terms within the summation sign can be used to compute the radiation pattern of the spherical Luneberg lens. The numerical work, however, has not yet been done and will be reported later.

If we let b approach infinity, then the problem reduces to the incidence of a plane wave upon the lens. The relation between the amplitude of the plane wave and the various parameters is

$$E_0 = \frac{k^2 p_x e^{ikb}}{4\pi\varepsilon b}.$$

The total electric field for $r > a$ is then given by

$$\mathbf{E} = E_0 \sum_{n=1}^{\infty}(i)^n \frac{2n+1}{n(n+1)}\left[(\mathbf{M}_{o1n}^{(1)} + \alpha_n^{(m)}\mathbf{M}_{o1n}^{(3)}) - i(\mathbf{N}_{e1n}^{(1)} + \alpha_n^{(e)}\mathbf{N}_{e1n}^{(3)})\right], \tag{55}$$

where the α's are the same as defined by (51) and (52). The part without the α's is simply the series expansion of the plane wave $\mathbf{E}^i = \hat{x}E_0 e^{ikz}$ [15]. The terms containing the α's represent the scattered field.

Although from the practical point of view a Luneberg lens probably will never be operated with a radial dipole as an exciting source, for completeness the expression for $\mathbf{E}^s$ corresponding to a radial dipole placed at $r = b$, $\theta = \pi$ has also been derived:

$$\mathbf{E}^s = \left\{\begin{matrix} \dfrac{ik^2 p_r}{4\pi\varepsilon b}\displaystyle\sum_{n=1}^{\infty}(-1)^n(2n+1)\alpha_n^{(e)} h_n^{(1)}(\rho_b)\mathbf{N}_{eon}^{(1)}, & r < b \\ \dfrac{ik^2 p_r}{4\pi\varepsilon b}\displaystyle\sum_{n=1}^{\infty}(-1)^n(2n+1)\alpha_n^{(e)} j_n(\rho_b)\mathbf{N}_{eon}^{(3)}, & r > b \end{matrix}\right\} \tag{56}$$

where p_r denotes the moment of the radial dipole, and

$$\mathbf{N}_{eon}^{(1)} = \frac{1}{k}\nabla \times \nabla \times [r j_n(kr) P_n(\cos\theta)\hat{r}].$$

The coefficient $\alpha_n^{(e)}$ is the same as the one previously defined by (52). This completes the derivation of the fundamental formulae involved in the electromagnetic theory of the spherical Luneberg lens. *)

§ 5. *Other stratified lenses.* The method which we discussed in § 2 can be used to investigate a large number of radial stratified lenses. Among them we may mention the Maxwell fish eye, and the $(A + B/r)$ lens of Luneberg [16]. In general, we arrive at two scalar differential equations for S_n and T_n, which form the central core of such an investigation. As an example, we will conclude this paper with a brief discussion of one type of lens, the dielectric constant of which varies according to

$$\kappa = \left(\frac{r}{a}\right)^{2m}. \tag{57}$$

Such a variation has previously been investigated by Nomura and Takaku [17] in their study of wave propagation in an inhomogeneous atmosphere. The differential equations for S_n and T_n become the special cases of Malmstén's equation [18]. When (57) is substituted into (11) and (23) one finds that the solutions are

$$S_n = \rho^{\frac{1}{2}} J_\gamma \left[\frac{\rho^{m+1}}{(m+1)\rho_a^m}\right], \quad \gamma = \frac{n+\frac{1}{2}}{m+1} \tag{58}$$

and

$$T_n = \rho^{m+\frac{1}{2}} J_{\gamma'} \left[\frac{\rho^{m+1}}{(m+1)\rho_a^m}\right], \quad \gamma' = \frac{\sqrt{(n+\frac{1}{2})^2 + m^2 + m}}{m+1}, \tag{59}$$

provided that $m \neq -1$. The case corresponding to $m = 1$ gives a distribution which would produce a cylindrical phase front according to Eaton's investigation based again upon the method of geometrical optics [19]. It would be interesting to obtain some numerical results based upon the present formulation so that the exact characteristics of such a lens can be revealed. For the case $m = -1$, (11) and (23) reduce to homogeneous differential equations. The appropriate solutions for S_n and T_n are simply

---

*) A report by C. H. Wilcox (Tech. Report MSD 1802, Lockheed Aircraft Corp. June 1956) has recently come to the attention of the author. In this report the problem of the diffraction of a plane wave by a spherical Luneberg lens is solved. The result of course compares with the one obtained here. Wilcox obtained an expansion for $T_n(x)/x$ directly, and he remarked that the series is useful when the argument is sufficiently small. In obtaining numerical results it would seem more profitable to determine $T_n(x)$ from the expansion of $U_n(x)$ introduced here.

$$S_n = \rho^{\frac{1}{2}} \sin\{[4(\rho_a^2 - n^2 - n) - 1]^{\frac{1}{2}} \ln \rho\}, \tag{60}$$

$$T_n = \rho^{-\frac{1}{2}} \sin\{[4(\rho_a^2 - n^2 - n) - 1]^{\frac{1}{2}} \ln \rho\}. \tag{61}$$

Numerical calculation based upon the inverse-square-power lens is relatively simple and may show some interesting characteristics which, after all, may not be too much different from the Luneberg lens. This is, however, merely a conjecture.

Acknowledgement. The author is most grateful to Dr. Robert G. Kouyoumjian for his careful and critical reading of the manuscript and for many valuable suggestions.

Received 26th September, 1957.

REFERENCES

1) Luneberg, R. K., The Mathematical Theory of Optics, Brown University Press 1944, pp. 212–213.
2) Jasik, H., The Electromagnetic Theory of the Luneberg Lens, Dissertation, Department of Electrical Engineering, Polytechnical Institute of Brooklyn, New York, 1954; also available as a technical report published by the Electronics Research Directorate, Air Force Cambridge Research Center, Air Research and Development Command; Report No. AFCRC-TR-54-121, November 1954.
3) Marcuvitz, N., Comm. Pure Appl. Math. **4** (1951) 263.
4) Friedman, B., Comm. Pure Appl. Math. **4** (1951) 317.
5) Nomura, Yukichi and Takaku, Kôshun, On the Propagation of the Electromagnetic Waves in an Inhomogeneous Atmosphere, I. Science Report, Research Institute of Tôhoku University, Sendai, Japan, **7** (1955) 107.
6) Stratton, J. A., Electromagnetic Theory, McGraw-Hill Book Company, New York, 1941, pp. 414–418.
7) Morse, P. M. and H. Feshbach, Methods of Theoretical Physics, McGraw-Hill Book Company, New York, 1953, pp. 1898–1899.
8) Marcuvitz, N., loc. cit.
9) Jasik, H., loc. cit.
10) Copson, E. T., Theory of Functions of a Complex Variable, Oxford University Press, London, 1948, p. 260.
11) Copson, E. T., loc. cit., Chap. X.
12) Morse, P. H. and H. Feshbach, loc. cit., p. 551.
13) Whittaker, E. T. and G. N. Watson, Modern Analysis, Cambridge University Press, Cambridge, 1943, p. 203.
14) Tai, C. T., Some Electromagnetic Problems Involving a Sphere, Tech. Report No. 41, Aircraft Radiation Systems Laboratory, Stanford Research Institute, Stanford, California, 1953.
15) Stratton, J. A., loc. cit., p. 419.
16) Luneberg, R. K., loc. cit., pp. 197–208.
17) Nomura and Takaku, loc. cit.
18) Watson, G. N., Bessel Functions, Cambridge University Press, Cambridge, 1945, p. 99.
19) Eaton, J. E., Trans. Instn. Radio Engrs, Prof. Group of Antennas and Propagation, **4** (1952) 66.

Appl. sci. Res. Section B, Vol. 7

TWO CAPACITIVE WINDOWS IN A RECTANGULAR WAVE GUIDE

by H. BOSMA

Laboratorium voor Theoretische Elektriciteitsleer der Technische Hogeschool, Delft, Netherlands

Summary

The behaviour of two capacitive windows in a rectangular wave guide, located at small distances apart in comparison with the wave length, is investigated. The three-dimensional problem is reduced to a two-dimensional one. Two simultaneous integral equations for the electric field intensities in the apertures are derived. A solution for these unknown quantities can be obtained, representing them by a Fourier series and approximating the kernel functions. Expressions for the reflection and transmission coefficients are given. Absolute values of the transmission coefficient are obtained, both theoretically and experimentally.

§ 1. *Introduction*. The investigation of the behaviour of obstacles in wave guides gives rise to complicated problems. During the last decades much work has been done in this field. Most of these studies have been done at frequencies in the usual bands of commercial wave guides. For instance, the influence of a capacitive window on the field in a rectangular wave guide is at the moment rather well-known [1]) [2]) [3]).

All these cases deal with only one propagating mode, viz. the TE_{01}-mode; all other modes are assumed to be evanescent. At some distance from the discontinuity only the principal mode is dominating; the influence of all others may be neglected.

If obstacles are located at arbitrary but not too small distances apart (compared with the wave length), their behaviour can be described by using the well-known transmission line equivalence theory. In calculating the interaction of a number of these obstacles one only has to take into account the reflection and transmission coefficients of the propagating mode.

The present paper is concerned with the properties of two capacitive windows located at small distances apart. In this case the calculation of the interaction is complicated, since all the evanescent modes, excited by the obstacles, have to be taken into account. In fact, there is a mutual influence of the two obstacles, a kind of coupling between them.

We restrict ourselves to the commercial wave guide with rectangular cross-section and its normal frequencies. The incident wave is the TE_{01}-mode; all other modes are assumed to be evanescent. The field quantities are harmonic in time via $\exp(-i\omega t)$. Furthermore, we suppose the medium in the wave guide to be homogeneous, isotropic and without dielectric losses, whereas the wave guide walls are assumed to be perfect conductors. The edges of the apertures are parallel to the long side (a) of the wave guide.

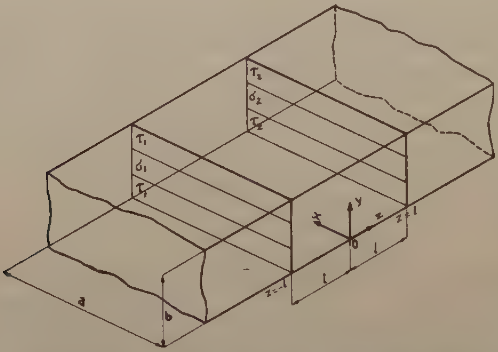

Fig. 1. The investigated constellation and the coordinate system used.

The electric field intensity of the incident wave is parallel to the short side (b) and hence perpendicular to the edges. $\tau_{1,2}$ denotes the screens and $\sigma_{1,2}$ the apertures of the windows. The windows are located at $z = -l$ and $z = +l$ respectively, their distance thus being $2l$. The short walls of the wave guide lie in the yz-plane at $x = 0$ and $x = a$ and the long walls in the xz-plane at $y = 0$ and $y = b$ (fig. 1).

§ 2. *Basic equations.* At each point in the rectangular wave guide the electromagnetic field quantities satisfy Maxwell's equations

$$\operatorname{curl} \mathbf{H} = -i\omega\varepsilon\mathbf{E}, \tag{1}$$

$$\operatorname{curl} \mathbf{E} = i\omega\mu\mathbf{H} \tag{2}$$

and the equations

$$\operatorname{div} \mathbf{E} = 0, \tag{3}$$

$$\operatorname{div} \mathbf{H} = 0. \tag{4}$$

Introducing [4]) the Hertzian vector $\mathbf{\Pi}^* = \mathbf{\Pi}^*\ (x, y, z)$ via

$$\mathbf{H} = \operatorname{curl} \operatorname{curl} \mathbf{\Pi}^* \tag{5}$$

and

$$\mathbf{E} = i\omega\mu \operatorname{curl} \mathbf{\Pi}^* \tag{6}$$

and a scalar $\Phi^* = \Phi^*(x, y, z)$ such that

$$\Phi^* = - \operatorname{div} \mathbf{\Pi}^*, \tag{7}$$

$\mathbf{\Pi}^*$ satisfies the homogeneous wave equation

$$(\nabla^2 + k^2)\mathbf{\Pi}^* = \mathbf{0}, \tag{8}$$

with

$$k^2 = \omega^2\mu\varepsilon = (2\pi/\lambda)^2. \tag{9}$$

Since the obstacles are cylindrical in the x-direction and the magnetic field intensity of the incident wave has only an x-component, the total field can be expressed in terms of a one-component Hertzian vector

$$\mathbf{\Pi}^* = \Pi \mathbf{i}_x. \tag{10}$$

Furthermore, the x-dependence is the same as that of the incident wave. Hence

$$\Pi = \varphi(y, z) \sin(\pi x/a), \tag{11}$$

where $\varphi(y, z)$ satisfies the two-dimensional wave equation

$$(\partial^2/\partial y^2 + \partial^2/\partial z^2 + h_0^2)\varphi(y, z) = 0, \tag{12}$$

with

$$h_0^2 = k^2 - (\pi/a)^2. \tag{13}$$

The boundary conditions to be imposed on φ are

$$\partial\varphi/\partial y = 0, \text{ at } y = 0, b, \ -\infty < z < \infty, \tag{14}$$

$$\partial\varphi/\partial z = 0, \text{ at } z = -l, \ y \in \tau_1, \tag{15}$$

$$\partial\varphi/\partial z = 0, \text{ at } z = l, \quad y \in \tau_2. \tag{16}$$

At $x = a/2$ the field intensities as obtained from (5), (6) and (11) are

$$E_x(\tfrac{1}{2}a, y, z) = 0, \tag{17}$$

$$E_y(\tfrac{1}{2}a, y, z) = i\omega\mu(\partial\varphi/\partial z), \tag{18}$$

$$E_z(\tfrac{1}{2}a, y, z) = -i\omega\mu(\partial\varphi/\partial z), \tag{19}$$

$$H_x(\tfrac{1}{2}a, y, z) = h_0^2\varphi, \tag{20}$$

$$H_y(\tfrac{1}{2}a, y, z) = 0, \tag{21}$$

$$H_z(\tfrac{1}{2}a, y, z) = 0. \tag{22}$$

The three-dimensional problem has now been reduced to the two-dimensional one of two capacitive screens between two infinite parallel planes, located at $y = 0$ and $y = b$.

§ 3. *Derivation of the integral equations.* In order to derive integral equations for the aperture distributions we apply Green's theorem

$$\int_{S_{1,2,3}} [G^{(1,2,3)}\nabla^2\varphi^{(1,2,3)} - \varphi^{(1,2,3)}\nabla^2 G^{(1,2,3)}]\mathrm{d}S_{1,2,3} = \\ = \int_{C_{1,2,3}} [G^{(1,2,3)}(\partial\varphi^{(1,2,3)}/\partial n) - \varphi^{(1,2,3)}(\partial G^{(1,2,3)}/\partial n)]\mathrm{d}C_{1,2,3} \tag{23}$$

to the regions to the left of the obstacles (1), in between (2) and to the right of them (3) respectively (fig. 2). In (23) $S_{1,2,3}$ is the domain

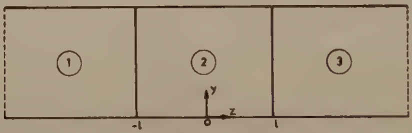

Fig. 2. The three regions to which Green's theorem is applied.

bounded by $C_{1,2,3}$ and $\varphi^{(1,2,3)}(y, z)$ is the unknown function. The Green's functions, $G^{(1,2,3)}(y, z; y', z')$, must satisfy the inhomogeneous wave equation

$$[\partial^2/\partial y^2 + \partial^2/\partial z^2 + h_0^2]G^{(1,2,3)}(y, z; y', z') = -\delta(y - y', z - z'), \tag{24}$$

where $\delta(y - y', z - z')$ denotes the two-dimensional Dirac delta function. The boundary conditions are

$$\partial G^{(1,2,3)}(y, z; y', z')/\partial y = 0 \text{ at } y = 0, b, \quad -\infty < z < \infty, \tag{25}$$

$$\partial G^{(1,2)}(y, z; y', z')/\partial z = 0 \text{ at } z = -l, \quad 0 < y < b, \tag{26}$$

$$\partial G^{(2,3)}(y, z; y', z')/\partial z = 0 \text{ at } z = l, \quad 0 < y < b. \tag{27}$$

Moreover, $G^{(1,3)}$ have to satisfy the radiation condition in the appropriate region. A procedure analogous to the one used by Lewin [5]) gives

$$G^{(1)}(y, z; y', z') = i \sum_{n=0}^{\infty} \frac{\varepsilon_n}{2bh_n} \cos(n\pi y/b) \cos(n\pi y'/b) \times$$
$$\times \{\exp[ih_n|z - z'|] + \exp[-ih_n(z + z' + 2l)]\}, \tag{28}$$

$$G^{(2)}(y, z; y', z') = i \sum_{n=0}^{\infty} \frac{\varepsilon_n}{2bh_n} \cos(n\pi y/b) \cos(n\pi y'/b) \times$$
$$\times \{\exp[ih_n|z - z'|] + i \frac{\exp(i2h_n l)}{\sin 2h_n l} [\cos(h_n(z + z')) +$$
$$+ \cos(h_n|z - z'|)]\}, \tag{29}$$

$$G^{(3)}(y, z; y', z') = i \sum_{n=0}^{\infty} \frac{\varepsilon_n}{2bh_n} \cos(n\pi y/b) \cos(n\pi y'/b) \times$$
$$\times \{\exp[ih_n|z - z'|] + \exp[ih_n(z + z' - 2l)]\}, \tag{30}$$

where

$$h_n^2 = h_0^2 - (\pi n/b)^2 \tag{31}$$

and ε_n is Neumann's number: $\varepsilon_0 = 1$, $\varepsilon_n = 2$ $(n \geq 1)$. Corresponding to (14) we assume

$$\varphi^{(1,2,3)}(y, z) = \sum_{n=0}^{\infty} f_n^{(1,2,3)}(z) \cos(n\pi y/b) \tag{32}$$

and

$$f_n^{(1,2,3)}(z) = C_n^{(1,2,3)} \exp(ih_n z) + D_n^{(1,2,3)} \exp(-ih_n z). \tag{33}$$

From the fact that the incident wave comes from the left and consists only of the TE_{01}-mode there results $C_n^{(1)} = 0$, $n = 1, 2, 3, \ldots$ and, as the wave guide is supposed to be matched to the right, $D_n^{(3)} = 0$, $n = 0, 1, 2, \ldots$. Furthermore, we put $C_0^{(1)} = 1$. Since E_y is continuous at the apertures and vanishes at the screens, (18) gives

$$M_1(y) = [\partial\varphi^{(1)}(y, z)/\partial z]_{z=-l} = [\partial\varphi^{(2)}(y, z)/\partial z]_{z=-l} \tag{34}$$

and

$$M_2(y) = [\partial\varphi^{(2)}(y, z)/\partial z]_{z=l} = [\partial\varphi^{(3)}(y, z)/\partial z]_{z=l}, \tag{35}$$

where

$$M_1(y) \begin{cases} = 0, & \text{if } y \in \tau_1, \\ \neq 0, & \text{if } y \in \sigma_1, \end{cases} \tag{36}$$

and

$$M_2(y) \begin{cases} = 0, & \text{if } y \in \tau_2, \\ \neq 0, & \text{if } y \in \sigma_2. \end{cases} \tag{37}$$

Substitution of these results into (23) gives

$$\varphi^{(1)}(y, z) = \exp(ih_0 z) + \exp[-ih_0(z + 2l)] + \\ + \int_{\sigma_1} G^{(1)}(y, z; y', -l)\, M_1(y')\mathrm{d}y', \tag{38}$$

$$\varphi^{(2)}(y, z) = -\int_{\sigma_1} G^{(2)}(y, z; y', -l) M_1(y')\mathrm{d}y' + \\ + \int_{\sigma_2} G^{(2)}(y, z; y', l) M_2(y')\mathrm{d}y', \tag{39}$$

$$\varphi^{(3)}(y, z) = -\int_{\sigma_2} G^{(3)}(y, z; y', l) M_2(y')\mathrm{d}y'. \tag{40}$$

In these equations $M_1(y)$ and $M_2(y)$ are the two unknown functions to be determined. The continuity of H_x in the apertures leads, with (20), to the following simultaneous integral equations in $M_1(y)$ and $M_2(y)$:

$$2\exp(-ih_0 l) - \frac{\exp(-i2h_0 l)}{bh_0 \sin 2h_0 l} \int_{\sigma_1} M_1(y')\mathrm{d}y' - \int_{\sigma_1} K_1(y; y') M_1(y')\mathrm{d}y' = \\ = -\frac{1}{bh_0 \sin 2h_0 l} \int_{\sigma_2} M_2(y')\mathrm{d}y' - \int_{\sigma_2} K_2(y; y') M_2(y')\mathrm{d}y', \tag{41}$$

$$\frac{1}{bh_0 \sin 2h_0 l} \int_{\sigma_1} M_1(y')\mathrm{d}y' + \int_{\sigma_1} K_2(y; y') M_1(y')\mathrm{d}y' = \\ = \frac{\exp(-i2h_0 l)}{bh_0 \sin 2h_0 l} \int_{\sigma_2} M_2(y')\mathrm{d}y' + \int_{\sigma_2} K_1(y; y') M_2(y')\mathrm{d}y', \tag{42}$$

where $K_1(y; y')$ and $K_2(y; y')$ are given by

$$K_1(y; y') = \sum_{n=1}^{\infty} \frac{2\exp(-i2h_n l)}{bh_n \sin 2h_n l} \cos(n\pi y/b) \cos(n\pi y'/b), \tag{43}$$

$$K_2(y; y') = \sum_{n=1}^{\infty} \frac{2}{bh_n \sin 2h_n l} \cos(n\pi y/b) \cos(n\pi y'/b), \tag{44}$$

if $y,\ y' \in \sigma_{1,2}$.

§ 4. *Solution of the integral equations.* The present section is closely connected to the work done by Miles [3]). We withdraw from the kernel functions the part for the stationary field, following a method given by Schwinger [5]). After a little work and substituting

$$h_n = i\gamma_n, \tag{45}$$

where γ_n is real if $n \geq 1$, we can write for (43) and (44)

$$K_1(y; y') = (2/\pi) \ln |2[\cos(\pi y/b) - \cos(\pi y'/b)]| - \sum_{n=1}^{\infty} (4/\pi) \Delta_n \cos(n\pi y/b) \cos(n\pi y'/b) \tag{46}$$

and

$$K_2(y; y') = - \sum_{n=1}^{\infty} (4/\pi) E_n \cos(n\pi y/b) \cos(n\pi y'/b). \tag{47}$$

In these expressions

$$\Delta_n = n^{-1}\{[1 - (h_0 b/n\pi)^2]^{-\frac{1}{2}} . [1 - \exp(- 4\gamma_n l)]^{-1} - 1\} \tag{48}$$

and

$$E_n = n^{-1}[1 - (h_0 b/n\pi)^2]^{-\frac{1}{2}} . [1 - \exp(- 4\gamma_n l)]^{-1} \exp(-2\gamma_n l). \tag{49}$$

Investigation of these expressions teaches that $\Delta_n = 0(n^{-3})$ and $E_n = 0[n^{-1} \exp(- 2n\pi l/b)]$ as $n \to \infty$. Therefore, the series in (46) and (47) are rapidly convergent.

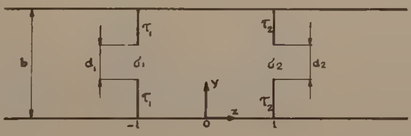

Fig. 3. The two symmetrical windows with aperture widths d_1 and d_2 for which a solution is calculated.

We now limit this study to the case of two symmetrical windows (fig. 3). When $y \in \sigma_v$ $(v = 1, 2)$, the relation

$$\tfrac{1}{2}(b - d_v) < y < \tfrac{1}{2}(b + d_v) \quad (v = 1, 2) \tag{50}$$

holds. A new variable u is now defined by the equation

$$\cos(\pi y/b) = \alpha_v \cos u \quad (v = 1, 2), \tag{51}$$

where

$$\alpha_v = \sin(\pi d_v/2b) \quad (v = 1, 2). \tag{52}$$

In these expressions $v = 1$ or 2 denotes the first and second window respectively. Furthermore, we define a new unknown function $U_v(u)$, related to $M_v(y)$ by

$$M_v(y)(dy/du) = (b/\pi) U_v(u). \tag{53}$$

Further, let

$$I_{v,r}^{(m)} = (2/\pi)\int_0^\pi \cos[r \arccos(\alpha_v \cos u')] \cos(mu')\,\mathrm{d}u'. \tag{54}$$

Some values of $I_{v,r}^{(m)}$ are given in table I.

TABLE I

$r \backslash n$	$I_{v,r}^{(n)}$ 0	 2
0	2	0
2	$2(\alpha_v^2 - 1)$	α_v^2

We now assume $U_v(u)$ to be a Fourier series of the form

$$U_v(u) = \sum_{n=0}^{\infty} a_{v,n} \cos nu. \tag{55}$$

Substituting all these expressions into the integral equations we obtain two identities in u in the interval $0 < u < \pi$, which lead to two infinite systems of simultaneous linear algebraic equations in the coefficients $a_{1,n}$ and $a_{2,n}$, viz.

$$\begin{aligned} 2\exp(-\,ih_0l) - \left[\frac{\exp(-\,i2h_0l)}{h_0 \sin 2h_0l} + 2b\ln(\alpha_1/\pi)\right] a_{1,0} + \\ + (b/\pi)\sum_{r=1}^{\infty} \Delta_r I_{1,r}^{(0)} \sum_{m=0}^{\infty} I_{1,r}^{(m)} a_{1,m} = \\ = -\frac{1}{h_0 \sin 2h_0l} a_{2,0} + (b/\pi)\sum_{r=1}^{\infty} E_r I_{2,r}^{(0)} \sum_{m=0}^{\infty} I_{2,r}^{(m)} a_{2,m}, \end{aligned} \tag{56}$$

$$\frac{1}{n} a_{1,n} + \sum_{r=1}^{\infty} \Delta_r I_{1,r}^{(n)} \sum_{m=0}^{\infty} I_{1,r}^{(m)} a_{1,m} = \sum_{r=1}^{\infty} E_r I_{2,r}^{(n)} \sum_{m=0}^{\infty} I_{2,r}^{(m)} a_{2,m}, \tag{57}$$

$$\begin{aligned} -\frac{1}{h_0 \sin 2h_0l} a_{1,0} + (b/\pi)\sum_{r=1}^{\infty} E_r I_{1,r}^{(0)} \sum_{m=0}^{\infty} I_{1,r}^{(m)} a_{1,m} = \\ = -\left[\frac{\exp(-\,i2h_0l)}{h_0 \sin 2h_0l} + 2b\ln(\alpha_2/\pi)\right] a_{2,0} + \\ + (b/\pi)\sum_{r=1}^{\infty} \Delta_r I_{2,r}^{(0)} \sum_{m=0}^{\infty} I_{2,r}^{(m)} a_{2,m} \end{aligned} \tag{58}$$

and

$$\frac{1}{n} a_{2,n} + \sum_{r=1}^{\infty} \Delta_r I_{2,r}^{(n)} \sum_{m=0}^{\infty} I_{2,r}^{(m)} a_{2,m} = \sum_{r=1}^{\infty} E_r I_{1,r}^{(n)} \sum_{m=0}^{\infty} I_{1,r}^{(m)} a_{1,m}. \tag{59}$$

The method followed can also be applied in the case of unsymmetrical and non-identical screens, but the work involved is tiresome.

§ 5. *Reflection and transmission coefficient.* Substitution of (55) into (38) and (40) leads to $\varphi^{(1)}(y, z)$ and $\varphi^{(3)}(y, z)$ expressed in terms of $a_{1,n}$ and $a_{2,n}$. With these expressions, together with (18), also the y-component of the electric field intensity can be expressed in terms of $a_{1,n}$ and $a_{2,n}$. Since we are only interested in the behaviour of the field at some distance from the windows, we obtain for the reflection and transmission coefficients

$$R = -[\exp(-\, i2h_0 l) + i(a_{1,0}/h_0) \exp(-\, ih_0 l)] \tag{60}$$

and

$$T = -\, i(a_{2,0}/h_0) \exp(-\, ih_0 l). \tag{61}$$

Consequently, in order to find the values for R and T, only $a_{1,0}$ and $a_{2,0}$ need be solved from (56) to (59).

§ 6. *First order approximation.* So far, this study has been restricted to symmetrical windows in order to reduce the work involved. As a further simplification (for the same reason) we now restrict the problem to two symmetrical and identical windows. In this case

$$\alpha_1 = \alpha_2 = \alpha \tag{62}$$

and, hence,

$$I^{(n)}_{1,r} = I^{(n)}_{2,r} = I^{(n)}_{r}. \tag{63}$$

Since the windows are symmetrical, the coefficients of $U_v(u)$, $v = 1, 2$, with odd values of n vanish. Introducing the expressions

$$A = \frac{\exp(-\, i2h_0 l)}{h_0 \sin 2h_0 l} + (2b/\pi) \ln \alpha \tag{64}$$

and

$$B = [h_0 \sin 2h_0 l]^{-1} \tag{65}$$

and taking $\Delta_4 = \Delta_6 = \ldots = 0$, $E_4 = E_6 = \ldots = 0$, the equations (56) to (59) can be written as

$$a_{1,0}\Delta_2 I_2^{(2)} I_2^{(0)} - a_{2,0}E_2 I_2^{(2)} I_2^{(0)} + \\ + a_{1,2}[\tfrac{1}{2} + \Delta_2 (I_2^{(2)})^2] - a_{2,2}E_2(I_2^{(2)})^2 = 0, \tag{66}$$

$$\begin{aligned} a_{1,0}E_2I_2^{(2)}I_2^{(0)} - a_{2,0}\Delta_2I_2^{(2)}I_2^{(0)} &+ \\ + a_{1,2}E_2(I_2^{(2)})^2 - a_{2,2}[\tfrac{1}{2} + \Delta_2(I_2^{(2)})^2] &= 0, \end{aligned} \tag{67}$$

$$\begin{aligned} a_{1,0}[A - (b/\pi)\Delta_2(I_2^{(0)})^2] - a_{2,0}[B - (b/\pi)E_2(I_2^{(0)})^2] &+ \\ - a_{1,2}(b/\pi)\Delta_2I_2^{(0)}I_2^{(2)} + a_{2,2}(b/\pi)E_2I_2^{(0)}I_2^{(2)} &= 2\exp(-ih_0l), \end{aligned} \tag{68}$$

$$\begin{aligned} a_{1,0}[B - (b/\pi)E_2(I_2^{(0)})^2] - a_{2,0}[A - (b/\pi)\Delta_2(I_2^{(0)})^2] &+ \\ - a_{1,2}(b/\pi)E_2I_2^{(0)}I_2^{(2)} + a_{2,2}(b/\pi)\Delta_2I_2^{(0)}I_2^{(2)} &= 0. \end{aligned} \tag{69}$$

From these equations $a_{1,0}$ and $a_{2,0}$ can be determined.

Since Δ_2 and E_2 are small compared with unity, we only retain the first power of these expressions. Substituting the values of $a_{1,0}$ and $a_{2,0}$ into (60) and (61) we obtain the approximate reflection and transmission coefficients

$$R = -\exp(-i2h_0l)\left\{1 + i2\,\frac{A - \dfrac{(b/\pi)\Delta_2(I_2^{(0)})^2}{1 + 4\Delta_2(I_2^{(2)})^2}}{h_0\left[(A^2 - B^2) - \dfrac{(2b/\pi)(A\Delta_2 - BE_2)(I_2^{(0)})^2}{1 + 4\Delta_2(I_2^{(2)})^2}\right]}\right\} \tag{70}$$

and

$$T = -i2\exp(-i2h_0l)\cdot\frac{B - \dfrac{(b/\pi)E_2(I_2^{(0)})^2}{1 + 4\Delta_2(I_2^{(2)})^2}}{h_0\left[(A^2 - B^2) - \dfrac{(2b/\pi)(A\Delta_2 - BE_2)(I_2^{(0)})^2}{1 + 4\Delta_2(I_2^{(2)})^2}\right]}. \tag{71}$$

§ 7. *Numerical and experimental results.* For one particular frequency the absolute values of the transmission coefficients are calculated with the aid of expression (71) as a function of the window parameters l and d. These values are a measure for the transmitted power in virtue of

$$\frac{P_0}{P_i} = |T|^2, \tag{72}$$

where P_i is the power of the incident wave and P_0 of the outgoing one. The calculations are done for the following values: $\lambda_0 = 10.00$ cm, $\lambda_g = 13.74$ cm, $a = 7.21$ cm and $b = 3.41$ cm (a and b are the width and the height of the commercial 10 cm-band wave guide respectively). The numerical values for the different distances between the windows $2l$ and the various widths of the apertures d are tabulated in table II.

TABLE II

Calculated transmission coefficients

d	$2l$					
mm	$\lambda_g/32$	$\lambda_g/16$	$\lambda_g/8$	$\lambda_g/4$	$\lambda_g/2$	λ_g
1	0.32	0.74	0.70	0.23	0.32	0.32
2	0.37	0.69	0.97	0.37	0.40	0.40
4	0.45	0.75	0.98	0.60	0.52	0.52
6	0.58	0.81	0.95	0.86	0.62	0.62
10	0.66	0.87	0.94	0.93	0.75	0.75
15	0.83	0.93	0.94	0.98	0.88	0.88
20	0.92	0.97	0.98	0.99	0.99	0.99
25	0.99	0.99	1.00	1.00	0.99	0.99

In these calculations it appears that in the most unfavorable case $E_2 = 0.3$ and $\Delta_2 = 0.15$, whereas in most cases these quantities are of the order of magnitude 10^{-2} or smaller. Therefore, we may conclude that the approximations made are justifiable.

TABLE III

Measured transmission coefficients

d	$2l$					
mm	$\lambda_g/32$	$\lambda_g/16$	$\lambda_g/8$	$\lambda_g/4$	$\lambda_g/2$	λ_g
1	0.29	0.85	0.45	0.28	0.35	0.29
2	0.34	0.72	0.80	0.38	0.47	0.39
4	0.43	0.73	1.00	0.57	0.52	0.47
6	0.53	0.78	0.97	0.76	0.58	0.57
10	0.71	0.87	0.95	0.93	0.75	0.75
15	0.85	0.94	0.97	0.99	0.89	0.89
20	0.93	0.97	0.98	0.99	0.96	0.96
25	0.99	0.99	1.00	1.00	0.99	0.99

In all these cases the transmission coefficients have been measured too. These results are shown in table III. The results of tables II and III are represented in figs. 4, 5 and 6. There happens to be a rather close agreement between the theoretical and experimental results. The differences observed between them may be caused by e.g., the approximations in the theoretically obtained values, the finite conductivity of the screens and the wave guide walls and the finite thickness of the obstacles.

On account of the remarkable behaviour for small distances between the windows the transmission coefficients are also calculated for $2l = \lambda_g/16$ and still smaller apertures. These values are to be found in table IV and fig. 7.

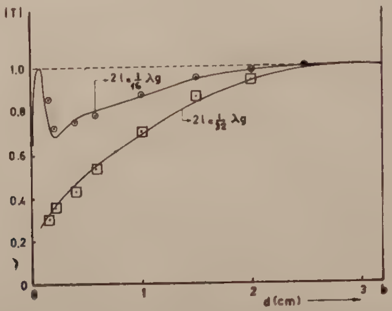

Fig. 4. The absolute value of the transmission coefficient as a function of the aperture width taking the distance between the windows as parameter: $2l = \lambda_g/32$ and $2l = \lambda_g/16$. The solid lines are the theoretically obtained results and the dots the measured values.

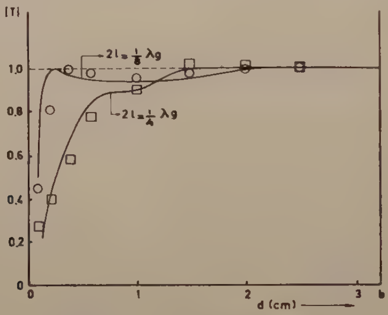

Fig. 5. Ditto. $2l = \lambda_g/8$ and $2l = \lambda_g/4$.

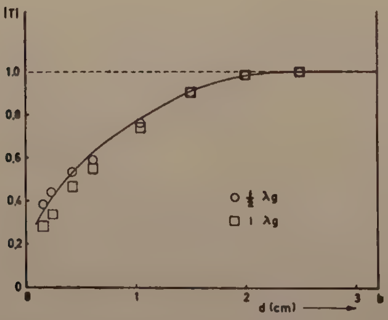

Fig. 6. Ditto. $2l = \lambda_g/2$ and $2l = \lambda_g$.

§ 8. *Concluding remarks.* We may formulate the following remarks:

a) There is a close agreement between the theoretically obtained results and the values found experimentally.

b) The expressions for the transmission and reflection coefficients obtained in this way are sufficiently accurate for practical purposes.

c) On account of the particular behaviour for small apertures in the windows it may be useful to analyse the investigated constellation further in order to consider its possible features as a wave guide filter.

d) The method used in the present paper may also be useful in picturing the field intensities and may be extended for different and a larger number of windows.

TABLE IV

Calculated transmission coefficients $2l = \lambda_g/16$

d mm	$\|T\|$	d mm	$\|T\|$
0.8	0.79	0.2	0.98
0.6	0.84	0.1	0.78
0.5	0.88	0.05	0.46
0.3	1.00		

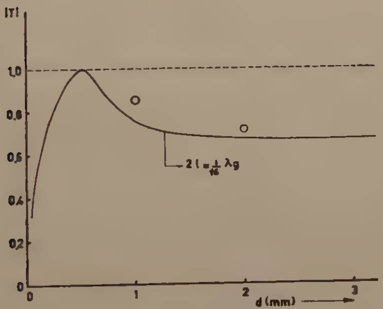

Fig. 7. The absolute value of the transmission coefficient as a function of very small aperture widths; $2l = \lambda_g/16$.

The author likes to mention here the work of Mr. B. J. Beukelman, now at N.V. Philips, Nijmegen, Netherlands, who obtained an equivalent circuit for two identical capacitive windows using stationary expressions of the Schwinger type [5]). The network elements of this circuit are calculated by the author of the present paper with the aid of the method described above. This calculation resulted in slightly more correct expressions than the ones obtained by Beukelman.

Acknowledgement. The author wishes to express his gratitude to Professor J. P. Schouten and Mr. A. T. de Hoop, of the Laboratorium voor Theoretische Elektriciteitsleer, Technische Hogeschool, Delft, Netherlands, for their stimulating interest and their helpful suggestions.

Received 4th October, 1957.

REFERENCES

1) Marcuvitz, N., Waveguide Handbook, M. I. T. Rad. Lab. Series, Vol. 10, McGraw-Hill, New York, 1951, p. 218.
2) Borgnis, F. E. and C. H. Papas, Randwertprobleme der Mikrowellenphysik, Springer, Berlin, 1955, p. 101.
3) Miles, J. W., Quart. Appl. Math. **7** (1949) 45.
4) Stratton, J. A., Electromagnetic theory, McGraw-Hill, New York, 1941, p. 29.
5) Saxon, D. S., Discontinuities in Waveguides, Notes on lectures by J. Schwinger, unpublished.

Appl. sci. Res. Section B, Vol. 7

NOTE ON THE RECIPROCITY THEOREM FOR ELECTRICAL SYSTEMS

by V. FRANK and H. HØJGAARD JENSEN

Physics Department, Technical University of Denmark, Copenhagen, Denmark

Summary

It is shown by means of Maxwell's equations that the admittance matrix of a passive linear multipole placed in a constant magnetic field $\boldsymbol{B}_0$ satisfies the extended reciprocity relation $G_{ik}(\boldsymbol{B}_0) = G_{ki}(-\boldsymbol{B}_0)$ if the conductivity, permittivity and permeability tensors of the materials forming the multipole all satisfy the spatial symmetry relation $T_{\alpha\beta}(\boldsymbol{B}_0) = T_{\beta\alpha}(-\boldsymbol{B}_0)$.

From the theory of electrical networks it is known that the admittance matrix G_{ik} of a passive linear multipole containing resistances, capacitances, inductances and mutual inductances is symmetrical. This is called the reciprocity theorem for networks. G_{ik} is defined in the following way:

Consider a passive network with $M + 1$ terminals numbered 0, 1, $\ldots i$, $\ldots k$, $\ldots M$. The potentials on the terminals and the currents entering into them are denoted by V_k and I_k (in complex notation). We choose $V_0 = 0$. In the stationary case $\sum_{k=0}^{M} J_k = 0$. The M independent currents I_1 to I_M will then be linearly connected with the M independent potentials V_1 to V_M by the relation

$$I_i = G_{ik} V_k \tag{1}$$

(summation from 1 to M is to be carried out for indices occurring twice in a product or a quotient).

The reciprocity theorem states that

$$G_{ik} = G_{ki}. \tag{2}$$

For reversible networks (i.e. networks containing only reactive elements) (2) can be proved thermodynamically. By means of

Kirchhoff's equations the validity of (2) is readily extended to networks containing simple lumped Ohmic resistances. For this case, and also for systems with distributed resistances, (2) may be taken as a special case of Onsager's reciprocity relation. From this theorem it also follows that when the system is placed in a constant magnetic field $\boldsymbol{B}_0$, (2) has to be modified into

$$G_{ik}(\boldsymbol{B}_0) = G_{ki}(-\boldsymbol{B}_0). \tag{3}$$

This means that the symmetrical part of G_{ik} is an even function of $\boldsymbol{B}_0$, while the antisymmetrical part is uneven. The relation (3) is of special importance for the Hall-gyrator.

Casimir [1]) has shown that (3) leads to an analogous *spatial* symmetry relation for the conductivity tensor of a medium in a magnetic field:

$$\sigma_{\alpha\beta}(\boldsymbol{B}_0) = \sigma_{\beta\alpha}(-\boldsymbol{B}_0) \tag{4}$$

(Greek indices refer to cartesian components).

Instead of using thermodynamics of irreversible processes as described above, it is possible to start from kinetic theory, i.e. Boltzmann's transport equation. Meixner [2]) and Kohler [3]) have shown that (4) follows from this equation when certain, not very restrictive, assumptions are made and when terms that are non-linear in the electric field strength are disregarded.

The aim of this note is to show that when (4) is established kinetically, the experimentally controllable relation (3) follows from (4) and Maxwell's equations. The d.c. case is treated in detail, and afterwards we give the main steps in an extension to harmonically varying fields, showing that when relations analogous to (4) also are known to hold for the permittivity and permeability tensors, (3) is valid quite generally.

We consider (see fig. 1) an anisotropic and inhomogeneous medium bounded partly by ideal conductors (terminals), partly by non-conducting surroundings. The medium is placed in a homogeneous *) constant magnetic field $\boldsymbol{B}_0$. In the stationary case the electric field strength $\boldsymbol{E}(\boldsymbol{r})$ will satisfy rot $\boldsymbol{E} = 0$ and consequently can be derived from a potential $\varphi(\boldsymbol{r})$. This and the current density $\boldsymbol{i}(\boldsymbol{r})$ are solutions to the equations

---

*) The proof still holds even if the external magnetic field is *inhomogeneous*; however the notation for G_{ik} must be changed, so that e.g. (3) reads: $G_{ik}(+) = G_{ki}(-)$, where + refers to an arbitrary external field $\boldsymbol{B}_0^+(\boldsymbol{r})$, while — refers to a field $\boldsymbol{B}_0^-(\boldsymbol{r})$ given by $\boldsymbol{B}_0^-(\boldsymbol{r}) = -\boldsymbol{B}_0^+(\boldsymbol{r})$ (at every point $\boldsymbol{r}$).

$$\operatorname{div} \boldsymbol{i} \overset{\text{def}}{=} \frac{\partial i_\alpha}{\partial x_\alpha} = 0, \tag{5}$$

$$i_\alpha(\boldsymbol{r}) = \sigma_{\alpha\beta}(\boldsymbol{r}) E_\beta(\boldsymbol{r}) = -\sigma_{\alpha\beta}(\boldsymbol{r}) \frac{\partial \varphi(\boldsymbol{r})}{\partial x_\beta}, \tag{6}$$

together with the boundary conditions

$$\varphi = V_k \text{ on } C_k, \tag{7}$$

$$i_n = -\sigma_{\alpha\beta} \frac{\partial \varphi}{\partial x_\beta} n_\alpha = 0 \text{ on N}, \tag{8}$$

where C_k is the boundary of the k'th terminal and the n_α are the components of the outer normal to the non-conducting boundary N.

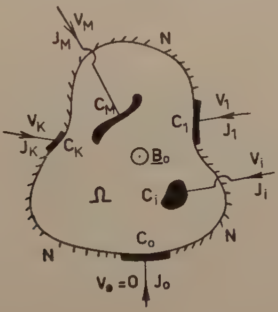

Fig. 1. Ω: space occupied by the medium.
C: conducting boundaries (terminals).
N: non-conducting boundary
$\boldsymbol{B}_0$: external magnetic field.

We now consider two situations denoted by unprimed and primed quantities respectively. In the first situation terminal l is kept at the potential V while all other V_k are zero. The currents then are $I_k = G_{kl}V$. In the second situation $V_m' = V$ while the rest are zero. At the same time $\boldsymbol{B}_0$ is changed into $\boldsymbol{B}_0'$ and consequently $G_{kl}(\boldsymbol{B}_0)$ is altered to $G'_{kl} = G_{kl}(\boldsymbol{B}_0')$, so that the currents now are $I_k' = G'_{km}V$. The potentials $\varphi(\boldsymbol{r})$ and $\varphi'(\boldsymbol{r})$ are proportional to V and are written as $V\psi_l(\boldsymbol{r})$ and $V\psi'_m(\boldsymbol{r})$ respectively. We next calculate the sum $V_s' I_s = V^2 G_{ml}$:

$$V^2 G_{ml} = V_s' I_s = -\int_C \varphi' i_n \mathrm{d}S = -\int_{C+N} \varphi' i_n \mathrm{d}S,$$

where we have extended the surface integration to the complete boundary by means of (8). By transformation to a volume integral by means of Gauss' theorem and by application of (5) we get

$$V^2G_{ml} = -\int_{\Omega} \frac{\partial}{\partial x_\alpha} (\varphi' i_\alpha) \mathrm{d}\Omega = -\int_{\Omega} i_\alpha \frac{\partial \varphi'}{\partial x_\alpha} \mathrm{d}\Omega$$

or by means of (6)

$$G_{ml} = \int_{\Omega} \sigma_{\alpha\beta}(\boldsymbol{r}) \frac{\partial \psi_l}{\partial x_\beta} \frac{\partial \psi_m'}{\partial x_\alpha} \mathrm{d}\Omega. \tag{9}$$

In the same way G'_{lm} is found from the sum $V_s I_s'$ or from (9) by interchanging l and m together with the priming:

$$G'_{lm} = \int_{\Omega} \sigma'_{\alpha\beta}(\boldsymbol{r}) \frac{\partial \psi_m'}{\partial x_\beta} \frac{\partial \psi_l}{\partial x_\alpha} \mathrm{d}\Omega = \int_{\Omega} \sigma'_{\beta\alpha}(\boldsymbol{r}) \frac{\partial \psi_l}{\partial x_\beta} \frac{\partial \psi_m'}{\partial x_\alpha} \mathrm{d}\Omega, \tag{10}$$

where we finally have interchanged the summation indices α and β.

From (9) and (10) it is seen that $G_{lm}(\boldsymbol{B}_0')$ is related to the tensor $\sigma_{\beta\alpha}(\boldsymbol{r}, \boldsymbol{B}_0')$ in exactly the same way as is $G_{ml}(\boldsymbol{B}_0)$ to $\sigma_{\alpha\beta}(\boldsymbol{r}, \boldsymbol{B}_0)$. If, therefore, there exists an algebraic relation of the form

$$C_1(\boldsymbol{B}_0)\sigma_{\alpha\beta}(\boldsymbol{r}, \boldsymbol{B}_0) + C_2(\boldsymbol{B}_0')\sigma_{\beta\alpha}(\boldsymbol{r}, \boldsymbol{B}_0') = 0 \tag{11}$$

$$(C_1 \text{ and } C_2 \textit{ independent} \text{ of } \boldsymbol{r})$$

between the (3×3) conductivity matrix and its transposed in some other magnetic field (or external parameter of another kind), then the $(N \times N)$ admittance matrix satisfies the same algebraic relation.

As a special case (3) follows immediately from (4). It should be noted that the proof is valid even if the medium is inhomogeneous provided only (4) holds everywhere in the medium.

We now turn to the case of the linear passive multipole, subject to harmonically varying fields. In this case the permittivity and permeability tensors are also of importance. We shall not go into much detail but only indicate the steps in a proof leading to an equation like (9).

It is of course necessary that the frequency is such that it is possible to speak in a well-defined way about potentials on and currents to the terminals. The multipole may be a shielded box with a number of terminals with shielded, e.g. coaxial, outer connections.

As above we consider two situations, primed and unprimed. From Maxwells equations we derive the following equations:

$$-\int_{N} (\boldsymbol{E}' \times \boldsymbol{H})_n \mathrm{d}S = \int_{\Omega} \left(\boldsymbol{E}' \cdot \boldsymbol{i} + \boldsymbol{E}' \cdot \frac{\partial \boldsymbol{D}}{\partial t} + \boldsymbol{H} \cdot \frac{\partial \boldsymbol{B}'}{\partial t} \right) \mathrm{d}\Omega. \quad (12)$$

This equation is very much like the usual energy equation, only all products contain both a primed and an unprimed quantity.

For the multipole described above the left-hand side of (12) can be shown to be equal to the sum $V_s{}'I_s$. When the fields are varying sinusoidally, perhaps apart from a constant external magnetic field, (12) leads to an equation for the complex admittance matrix, analogous to (9), only with dielectric and magnetic contributions from the last two terms in (12) included:

$$G_{ml} = \int_{\Omega} [(\sigma_{\alpha\beta} + j\omega\varepsilon_{\alpha\beta}) e'_{m,\alpha} e_{l,\beta} + j\omega\mu'_{\alpha\beta} h_{l,\alpha} h'_{m,\beta}] \mathrm{d}\Omega. \quad (13)$$

Here $\varepsilon_{\alpha\beta}$ and $\mu_{\alpha\beta}$ are the spatially varying complex permittivity and permeability tensors of the medium for the frequency ω. The complex vector $\boldsymbol{e}_l(\boldsymbol{r})$ corresponds to gradψ_l in (9); $\boldsymbol{e}_l(\boldsymbol{r})$ and $\boldsymbol{h}_l(\boldsymbol{r})$ are defined so, that when a potential V $\mathrm{e}^{j\omega t}$ is applied to the l'th terminal, all other terminals being grounded, this creates an electric field strength $V\mathrm{e}^{j\omega t}\,\boldsymbol{e}_l(\boldsymbol{r})$ and a magnetic field strength $V\mathrm{e}^{j\omega t}\boldsymbol{h}_l(\boldsymbol{r})$ at the point $\boldsymbol{r}$.

From (13) if follows that when the conductivity tensor $\sigma_{\alpha\beta}$, the permittivity tensor $\varepsilon_{\alpha\beta}$ and the tensor $(\mu^{-1})_{\alpha\beta}$ *(inverse to the permeability tensor* $\mu_{\alpha\beta}$) all obey the *same* algebraic relation of the form (11), then the admittance matrix satisfies the same algebraic relation. In case of relations like (4) the distinction between the permeability tensor and its inverse is of course unnecessary.

Received 25th January, 1958.

REFERENCES

1) Casimir, H. B. G., Rev. Mod. Phys. **17** (1945) 343.
2) Meixner, J., Ann. Phys. V Folge, **40** (1941) 165.
3) Kohler, M., ibid. **40** (1941) 601.

LETTER TO THE EDITOR

Increased atmospheric radioactivity in the Netherlands after the Windscale accident

Measurement of airborne radioactivity after an accidental release of radioactive substances can be of value in providing information on the air currents which carry small particles over great distances. In the Netherlands an increase of the radioactivity in the air was observed on October 11th lasting until October 16th 1957; its origin could be traced to the accident at the Windscale no. 1 pile on October 10th. The present paper reports the levels of radioactivity found during this period and the way in which its properties differed from those of the background of fission products from nuclear weapons.

Airborne radioactivity is sampled on a routine basis at four stations in the Netherlands, viz. Den Helder (52°58′ N, 4°45′ E), De Bilt (52°6′ N, 5°11′ E), Rijswijk (52°1′ N, 4°28′ E) and Eindhoven (51°26′ N, 5°30′ E), by drawing air through membrane filters (manufactured by Membranfiltergesellschaft, Göttingen, Germany) during 24 hours. Daily at 9 a.m. filters are changed. After use the filters are treated with a solution of formvar in 1,2-dichloroethane (20 g per liter) to fix the collected dust on the filter paper. The radioactivity of the filters is measured at the Medical Biological Laboratory of the National Defence Research Council, at least three days after sampling to allow for the decay of natural radioactive substances. The total volume of processed air is measured by means of a gasmeter and amounts to 30 to 50 m^3 in 24 hours.

The beta radioactivity of the filters is assayed using an end-window Geiger-Müller tube (Philips 18506) with a diameter of 3 cm and a window thickness of 3 mg/cm^2. The efficiency of the counting set-up, including a correction for absorption of soft beta's in the window, is estimated at 30% on an average for a mixture of fission products between 10 and 360 days after the explosion of an atom bomb.

Occasionally alpha activity was assessed using a proportional gas flow counter (Nuclear Chicago Model D 47) with a plastic window of less than 0.15 mg/cm^2. The geometrical efficiency in this case is about 40%. The total efficiency has rather arbitrarily been put at 25% including self-absorption of alpha particles. The latter is bound to vary with the size of the samples of dust and their distribution on the paper after the treatment of the filters with formvar.

Analysis of the decay of the beta activity collected during the period

October 11th–16th and measured up to 13th December 1957, showed a longlived component with an effective half-life between 39 and 49 days. Only in three instances a longer half-life (53, 55 and 62 days resp.) was demonstrated. Qualitatively this longlived component is undistinguishable from fall-out originating from atom bomb explosions. The dust, collected at Rijswijk on October 8th and 9th, in which only such a fall-out is to be expected, contained longlived components with half-lives of 57 and 52 days respectively. On October 17th and 18th longlived components of 39 and 35 days were found.

Subtraction of the activity due to the longlived component from the total activity showed the presence of a shortlived component with an average half-life of 3 to 5 days occurring during the period October 11th–16th and one with a half-life of 6 to 10 days in the samples before and after this period. In the latter samples this shortlived component represented about 30% of the total activity at the time of sampling, whereas from October 11th–16th the percentage shortlived activity was much higher. Most of this shortlived activity apparently originated from the Windscale accident.

In the first half of November the filters which had been exposed between October 11th and 16th were measured with a gammaspectrometer at AERE, Health Physics Division, Harwell. A ^{131}I peak at 365 keV was still detectable in most of the filters. Part of the shortlived activity can therefore be ascribed to this iodine isotope (half-life 8 days). From the fact that the measured half-life (3–5 days) is so much shorter than 8 days, the conclusion may be drawn that other fission products with half-lives of the order of 1 or 2 days, probably other iodine isotopes and ^{132}Te, were also present.

In the air filters from October 11th–16th an amount of alpha-activity was found, which could not be attributed to either atom bomb explosions or to the naturally occurring concentration of ^{210}Po in air. By radiochemical analysis of filters exposed in Harwell during the period mentioned, it could be shown that the alpha-activity was due to the presence of ^{210}Po, which evaporated apparently from the pile during the fire. At Rijswijk the alpha-activity of the filters was measured between October 22th and 31st and again between November 19th and December 12th. In all these measurements a uraniumoxide sample was used as a standard. The weighted mean of the decay constants, estimated from these measurements, is 0.0044 days^{-1} with a standard error of 0.0006 days^{-1}. This value is in agreement with the universally accepted value of 0.0050 days^{-1} for ^{210}Po.

The activity levels are summarized in the table. The figures given for the air activity at the time of exposure of the filters are calculated by extrapolation of the decay curves. To facilitate meteorological interpretation the activity values at a common date have been included. A date after October 16th had to be chosen to reduce the influence of errors in the determination of the half-life.

From the table it follows that no quantitative relation exists between the various kinds of radioactivity. It is clear however that only a fraction of the shortlived activity originated from the ^{131}I.

Evidently a radioactive cloud first reached the southern parts of the

TABLE I

	Station	Air activity in pc/m^3									
		date of sampling					value on Oct. 19th				
		11/12	12/13	13/14	14/15	15/16	11/12	12/13	13/14	14/15	15/16
half-life ~ 45 d	H	1.4	1.4	10	11	4.7	1.3	1.3	9.5	9.9	4.5
	B	1.9	1.5	3.2	6.1	2.9	1.7	1.3	3.0	5.8	2.8
	R[3]	5.7	4.2		13	3.1	5.2	3.9		12	3.0
	E	9.1	5.5	6.6	6.4	1.6	8.0	4.9	6.1	6.0	1.5
half-life ~ 3.5 d	H	2.0	1.5	33	24	7.3	0.90	0.43	13	13	4.9
	B	8.7	2.1	15	17	5.6	2.9	0.55	7.0	9.1	2.8
	R[3]	22	12		32	6.3	9.0	3.7		14	3.7
	E	35	17	22	16	1.8	12	5.8	7.7	7.2	0.96
^{131}I [1]	H	nil [2]	nil	5.1	7.2	2.8	nil	nil	3.1	4.9	2.1
	B	3.3	nil	3.4	4.6	nil	1.7	nil	2.1	3.1	nil
	R[3]	9.2	4.6		8.4	0.7	4.8	2·9		5.7	0.5
	E	19	6.8	4.7	3.8	nil	9.8	3.9	2.9	2.6	nil
^{210}Po	H	0.026	<0.010	0.42	0.44	0.16	0.025	<0.010	0.41	0.43	0.16
	B	0.061	<0.010	0.19	0.29	0.10	0.059	<0.010	0.19	0.29	0.099
	R[3]	0.17	0.088		0.48	0.098	0.17	0.086		0.47	0.097
	E	0.30	0.22	0.25	0.25	0.040	0.29	0.21	0.24	0.24	0.040

1) Measured by gamma spectrometry at Harwell.
2) Not dectable at time of measurement.
3) At Rijswijk filters were not changed on October 13th.
H = Den Helder; B = De Bilt; R = Rijswijk; E = Eindhoven.

Netherlands; somewhat later higher activities were observed in the north.

On the days, when little or no ^{131}I or ^{210}Po activity was present in the fall-out at Den Helder and De Bilt, still a component with a half-life of about 3 days could be demonstrated. Therefore it is concluded that even then some activity from the Windscale reactor was present.

We are indebted to the Health Physics Division at Harwell, notably to Mr. N. G. Stewart and Mr. R. N. Crooks, for valuable discussions and for their willingness to measure the ^{131}I content of our filters. We gratefully acknowledge the cooperation of the Royal Netherlands Meteorological Institute which performed the sampling of dust at the stations De Bilt, Den Helder and Eindhoven.

Joh. Blok
R. H. Dekker
C. J. H. Lock
Medical Biological Laboratory of the
National Defence Research Council T.N.O.,
Rijswijk, Netherlands

Received 14th February, 1958.

Appl. sci. Res. Section B, Vol. 7

TRANSMISSION IN A RECTANGULAR WAVEGUIDE LOADED WITH AN ARBITRARY NUMBER OF CAPACITIVE SCREENS

by F. A. W. VAN DEN BURG

Laboratorium voor theoretische electrotechniek en electromagnetische straling,
Technische Hogeschool, Delft, Netherlands

Summary

Green's theorem is applied to individual domains consisting of the walls of a rectangular waveguide and two neighbouring slotted capacitive screens. In addition this theorem is applied to the two end domains, that is, the one containing the incident field and the other containing the transmitted field only. Using the continuity of the electromagnetic field intensities in the slits, a system of simultaneous integral equations is obtained in terms of field intensity functions within the slits. By a change of variables a system of ∞^2 linear algebraic equations is derived, and formulae for the principal mode transmission and reflection coefficients are given to any approximation desired. Conditions for a full transmission are derived, especially to a first order approximation. Some applications with regard to the filter properties of the waveguide system are discussed and the theory developed is compared with measurements.

§ 1. *Introduction and statement of the problem.* In a recent paper, Bosma [1]) showed that the data available on the equivalent circuit of a capacitive screen cannot be used for an accurate description of the transmission of an electromagnetic wave through a waveguide loaded with two screens, as soon as the distance between the screens becomes small compared with the wavelength. Moreover his method, based upon work of Schwinger and since used e.g. by Miles [2]), Borgnis and Papas [3]), contains all the information necessary for describing the electromagnetic field in the apertures. Bosma pointed out too that the configuration shows bandfilter properties.

Besides the work of Bosma, the investigation of Frank [4]) should be mentioned. Frank considered the case of two symmetrical inductive windows where the interaction of the slits is not negligible.

Finally Szepesi 5) mentioned an unexpected increase of the transmission coefficient for an H_{11}-type wave in a circular guide when the distance between two ring-shaped filter elements becomes small compared with the wavelength. His remark indicates the possibility of constructing compact microwave filters.

Especially with regard to the filter properties, the case of the transmission in a rectangular waveguide loaded with an arbitrary number of capacitive windows, spaced at arbitrary distances and with different apertures, though all situated symmetrically with respect to the half height of the waveguide, will be treated here as a natural extension of Bosma's investigation. Thus, criteria for full transmission will be derived.

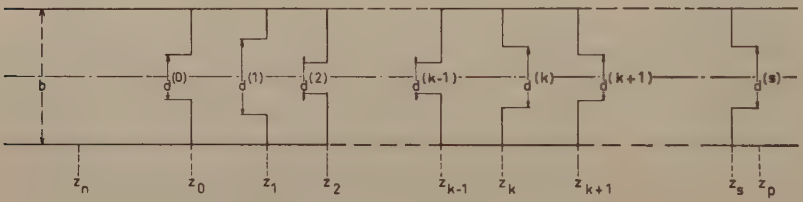

Fig. 1. Configuration of the system.

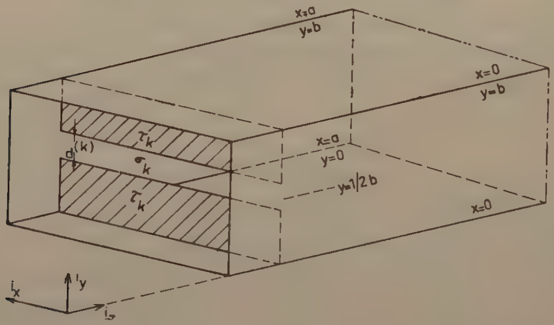

Fig. 2. Coordinate system; configuration of a screen.

The configuration of the screens and the waveguide, as well as some obvious notations are given in figs. 1, 2, 3. An incident wave of the TE_{01}-mode comes from $z = -\infty$; so with $k^2 = \omega^2\varepsilon\mu$, $\varepsilon = \varepsilon_r\varepsilon_0$, $\mu = \mu_r\mu_0$:

$$(\pi/a)^2 < k^2,\ (n\pi/a)^2 > k^2,\ (m\pi/b)^2 > k^2, \quad (n > 1, m > 0). \tag{1}$$

Using the time dependence $e^{-j\omega t}$ and setting $h_0^2 = k^2 - (\pi/a)^2$, the incident electric fieldstrength $\mathbf{E}^i$ can be written as

$$\mathbf{E}^i = \mathbf{i}_y \sin(\pi x/a)\, e^{jh_0 z}.$$

Introduction of the Fitzgerald vector $\mathbf{\Pi}$ according to

$$\mathbf{E} = -\mu \operatorname{curl}(\partial/\partial t)\, \mathbf{\Pi}, \quad \mathbf{H} = \operatorname{curl} \operatorname{curl} \mathbf{\Pi}$$

and substitution in Maxwell's equations leads to the wave equation

$$[(\partial^2/\partial x^2) + (\partial^2/\partial y^2) + (\partial^2/\partial z^2) + k^2]\mathbf{\Pi} = \mathbf{0}.$$

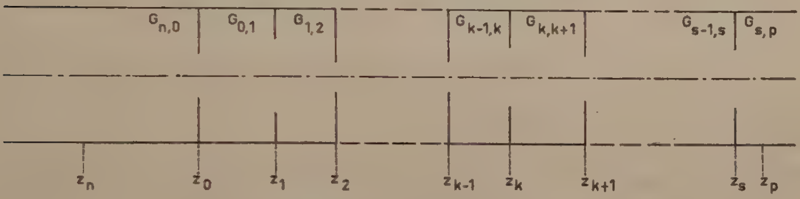

Fig. 3. Notation of the domains.

Since $E_x = 0$, $\mathbf{\Pi} = \Pi \mathbf{i}_x$. Assuming $\Pi = \varphi(y, z) \sin(\pi x/b)$, the following relations hold:

$$\begin{aligned} &E_x(\tfrac{1}{2}a, y, z) = 0, && H_x(\tfrac{1}{2}a, y, z) = h_0{}^2\varphi, \\ &E_y(\tfrac{1}{2}a, y, z) = j\omega\mu\, \partial\varphi/\partial z, && H_y(\tfrac{1}{2}a, y, z) = 0, \\ &E_z(\tfrac{1}{2}a, y, z) = -j\omega\mu\, \partial\varphi/\partial y, && H_z(\tfrac{1}{2}a, y, z) = 0, \end{aligned} \tag{2}$$

$$[(\partial^2/\partial y^2) + (\partial^2/\partial z^2) + h_0{}^2]\varphi = 0. \tag{3}$$

The boundary conditions $E_z = 0$ at $y = 0, b$ and $E_y = 0$ at $z = z_k$, $y \epsilon \tau_k$, can be expressed as

$$\partial\varphi/\partial y = 0,\ y = 0, b;\ \partial\varphi/\partial z = 0,\ z = z_k,\ y \epsilon \tau_k. \tag{4}$$

The two-dimensional problem is to find a function $\varphi(y, z)$ satisfying (3) and (4). In solving that problem, Green's theorem will be applied to the domains $G_{n,0}$, $G_{k,k+1} (k = 0, 1, \ldots, s-1)$, $G_{s,p}$, indicated in fig. 3.

§ 2. *Derivation of the Green's functions.* The Green's functions $G^{(k,k+1)}(y, z; y', z')$, proper to the domains $G_{k,k+1}$, have to satisfy

$$[(\partial^2/\partial y^2) + (\partial^2/\partial z^2) + h_0{}^2]\, G^{(k,k+1)} = -\delta(y - y')\, \delta(z - z'); \tag{5}$$

$$\partial G^{(k,k+1)}/\partial y = 0,\ y = 0, b;\ \partial G^{(k,k+1)}/\partial z = 0,\ z = z_k (k = 0, \ldots, s). \tag{6}$$

The Green's functions $G^{(n,0)}(y, z; y', z')$ and $G^{(s,p)}(y, z; y', z')$ have to satisfy, in addition to the conditions (5) and (6), the "radiation conditions". Let

$$G^{(k,k+1)} = \sum_{n=0}^{\infty} g_n^{(k,k+1)}\,(z; y', z')\cos(n\pi y/b)$$

be substituted in (5). Multiplying the result by $\cos(m\pi y/b)$, then summing over $m = 0,1, \ldots\ldots, \infty$, the integration of the outcome with respect to y from $y = 0$ to $y = b$ will give a contribution for $m = n$ only. The equation for $g_n^{(k,k+1)}$ now appears as

$$\sum_{n=0}^{\infty} (b/\varepsilon_n)[(\partial^2/\partial z^2) + h_n^2]\, g_n^{(k,k+1)} = -\,\delta(z - z') \sum_{n=0}^{\infty} \cos(n\pi y'/b),$$

with Neumann's number $\varepsilon_n = 1$, $n = 0$ and $\varepsilon_n = 2$, $n \neq 0$; moreover $h_n^2 = h_0^2 - (n\pi/b)^2$. The supposition

$$g_n^{(k,k+1)}(z; y', z') = (\varepsilon_n/b)\cos(n\pi y'/b)\, f_n^{(k,k+1)}(z; z')$$

will give the following expression for $G^{(k,k+1)}$:

$$G^{(k,k+1)} = \sum_{n=0}^{\infty} (\varepsilon_n/b)\cos(n\pi y'/b)\, f_n^{(k,k+1)}, \tag{7}$$

with $f_n^{(k,k+1)}$, also in connection with (6), satisfying

$$[(\partial^2/\partial z^2) + h_n^2] f_n^{(k,k+1)} = -\,\delta(z - z'), \quad (k = 0,1, \ldots, s - 1), \tag{8}$$

$$\partial f_n^{(k,k+1)}/\partial z = 0, \quad z = z_k, \qquad (k = 0,1, \ldots\ldots, s). \tag{9}$$

The analogous functions $f_n^{(n,0)}$, $f_n^{(s,p)}$ must obey the relations (8), (9) and the "radiation conditions". To this purpose, let

$$f_n^{(n,0)} = [C_n^{(n,0)} + D_n^{(n,0)}]\, e^{jh_n(z'-z_0)}, \quad z \leq z' \leq z_0, \tag{10}$$

$$f_n^{(n,0)} = C_n^{(n,0)}\, e^{jh_n(z-z')} + D_n^{(n,0)}\, e^{jh_n(z'-z_0)}, \; z' \leq z \leq z_0. \tag{11}$$

Clearly $f_n^{(n,0)}$ meets the "radiation" requirements; moreover $f_n^{(n,0)}(z; z')$ is continuous at $z = z'$. On the one side, integration of (8) between $z = z' - \varepsilon$ and $z = z' + \varepsilon$ yields on taking the limit $\varepsilon \to 0$:

$$\lim_{\varepsilon \to 0} \left. \frac{\partial f_n^{(n,0)}}{\partial z} \right|_{z'-\varepsilon}^{z'+\varepsilon} = -\,1.$$

On the other side evaluation of this limit, using (10) and (11), will give $2jh_nC_n^{(n,0)}$; thus $C_n^{(n,0)} = j/2h_n$.

Using (11), evaluation of $\partial f_n^{(n,0)}/\partial z$ taken at $z = z_0$ will give in connection with (9)

$$[\partial f_n^{(n,0)}/\partial z]_{z_0} = C_n^{(n,0)}\, jh_n\, \mathrm{e}^{jh_n(z_0-z')} - D_n^{(n,0)}\, jh_n\, \mathrm{e}^{jh_n(z'-z_0)} = 0.$$

As $C_n^{(n,0)} = j/2h_n$, $D_n^{(n,0)}$ can be determined. Then $f_n^{(n,0)}$ is determined from (10), (11); in conclusion, substitution in (7) yields

$$G^{(n,0)} =$$

$$= j\sum_{n=0}^{\infty} (\varepsilon_n/2bh_n) \cos(n\pi y/b) \cos(n\pi y'/b) [\mathrm{e}^{jh_n|z'-z|} + \mathrm{e}^{jh_n(2z_0-z'-z)}]. \quad (12)$$

Symmetry considerations immediately give

$$G^{(s,p)} = j\sum_{n=0}^{\infty} (\varepsilon_n/2bh_n) \cos(n\pi y/b) \cos(n\pi y'/b)\ .$$

$$. \ [\mathrm{e}^{jh_n|z'-z|} + \mathrm{e}^{jh_n(z+z'-2z_0)}]. \quad (13)$$

For the determination of $G^{(k,k+1)}$ $(k = 0, 1, \ldots, s-1)$, let

$$f_n^{(k,k+1)} = [C_n^{(k,k+1)} + E_n^{(k,k+1)}]\, \mathrm{e}^{jh_n(z'-z)} +$$

$$+ D_n^{(k,k+1)}\, \mathrm{e}^{jh_n(z-z')}, \quad z_k \leq z \leq z' \leq z_{k+1}, \quad (14)$$

$$f_n^{(k,k+1)} = [C_n^{(k,k+1)} + D_n^{(k,k+1)}]\, \mathrm{e}^{jh_n(z-z')} +$$

$$+ E_n^{(k,k+1)}\, \mathrm{e}^{jh_n(z'-z)}, \quad z_k \leq z' \leq z \leq z_{k+1}. \quad (15)$$

The method for the evaluation of $C_n^{(k,k+1)}$ is identical with the one used for $C_n^{(n,0)}$; the result is $C_n^{(k,k+1)} = j/2h_n$. The determination of $\partial f_n^{(k,k+1)}/\partial z$, once at $z = z_k$ and once at $z = z_{k+1}$, using (14) and (15) respectively, will give in connection with (9) two linear equations in $C_n^{(k,k+1)}$, $D_n^{(k,k+1)}$, $E_n^{(k,k+1)}$. With $C_n^{(k,k+1)} = j/2h_n$, the other constants can be determined. Then $f_n^{(k,k+1)}$ is determined from (14) and (15). In conclusion, the Green's functions $G^{(k,k+1)}$ can be written as

$$G^{(k,k+1)} = j\sum_{n=0}^{\infty} (\varepsilon_n/2bh_n) \cos(n\pi y/b) \cos(n\pi y'/b)\ .$$

$$. \left\{\mathrm{e}^{jh_n|z'-z|} + j\,\frac{\cos[h_n(z+z'-z_{k+1}-z_k)] + \cos[h_n(z-z')]\mathrm{e}^{jh_n(z_{k+1}-z_k)}}{\sin[h_n(z_{k+1}-z_k)]}\right\} \quad (16)$$

Formulae (12), (13), (16) give the Green's functions needed.

§ 3. *The integral equations.* In applying Green's theorem

$$\int_V (G\nabla^2\varphi - \varphi\nabla^2 G)\, \mathrm{d}v' = \int_S (G\partial\varphi/\partial n - \varphi\partial G/\partial n)\, \mathrm{d}s' \quad (17)$$

to the domains $G_{n,0}$, $G_{k,k+1}$ $(k = 0,1, \ldots, s-1)$ and $G_{s,p}$, the assumption (temporarily omitting the indices n, 0 and k, $k+1$ and s, p)

$$\varphi = \sum_{m=0}^{\infty} [C_m \, \mathrm{e}^{jh_m z} + D_m \, \mathrm{e}^{-jh_m z}] \cos(m\pi y/b) \tag{18}$$

meets all the requirements (4). These functions φ and the Green's functions (12), (13) and (16) are independent of x and x'. Thus the contributions to the surface integral, where $\partial/\partial n$ equals $\pm\, \partial/\partial x'$, are zero. Then (17) can be integrated with respect to x' over the interval $(0, a)$ and the result divided by a. On substitution of (3) and (5) the result is

$$\varphi(y, z) = \int_C (G \, \partial\varphi/\partial n - \varphi \, \partial G/\partial n) \, \mathrm{d}c' \tag{19}$$

for every y, z of the chosen domain; elsewhere $\varphi(y, z) = 0$; C is the perimeter of the intersection of the plane $x = \frac{1}{2}a$ with the chosen domain. According to (4), (6) and the symmetry-property of G with relation to y and y' for every element on C with $y = 0$, b, we have $\partial\varphi/\partial n = \pm\, \partial\varphi/\partial y' = 0$ and $\partial G/\partial n = \pm \partial G/\partial y' = 0$. Taking care of the sign in $\partial/\partial n = \pm\, \partial/\partial z'$, (19) now can be written as

$$\varphi(y, z) = \int_{C_l} (-\, G \, \partial\varphi/\partial z' + \varphi \, \partial G/\partial z') \, \mathrm{d}y' + \\ + \int_{C_r} (G \, \partial\varphi/\partial z' - \varphi \, \partial G/\partial z') \, \mathrm{d}y'. \tag{20}$$

C_l is the "left" part of the boundary of the correct domain at $x = \frac{1}{2}a$ and C_r the "right" part of it. Bearing in mind the boundary-conditions (4) and (6) at $z = z_k$ $(k = 0,1, \ldots\ldots, s)$, the relation (20) suited for the domains $G_{n,0}$, $G_{k,k+1}$ $(k = 0,1, \ldots, s-1)$ and $G_{s,p}$ yields

$$\varphi^{(n,0)} = \int_0^b \Bigl\{ -\, G^{(n,0)}(y, z; y', z_n) \left[\frac{\partial\varphi^{(n,0)}}{\partial z'}\right]_{z'=z_n} + \\ + \varphi^{(n,0)}(y', z_n) \left[\frac{\partial G^{(n,0)}(y, z; y', z')}{\partial z'}\right]_{z'=z_n} \Bigr\} \mathrm{d}y' + \\ + \int_{\sigma_0} G^{(n,0)}(y, z; y', z_0) \, [\partial\varphi^{(n,0)}/\partial z']_{z'=z_0} \, \mathrm{d}y', \tag{21}$$

$$\varphi^{(k,k+1)} = \int_{\sigma_k} -\, G^{(k,k+1)}(y, z; y', z_k) \left[\frac{\partial\varphi^{(k,k+1)}}{\partial z'}\right]_{z'=z_k} \mathrm{d}y' + \\ + \int_{\sigma_{k+1}} G^{(k,k+1)}(y, z; y', z_{k+1}) \left[\frac{\partial\varphi^{(k,k+1)}}{\partial z'}\right]_{z'=z_{k+1}} \mathrm{d}y', \tag{22}$$

$$\begin{aligned}\varphi^{(s,p)} = \int_{\sigma_s} &- G^{(s,p)}(y, z; y', z_s)\,[\partial\varphi^{(s,p)}/\partial z']_{z'=z_s}\,\mathrm{d}y' + \\ &+ \int_0^b \Big\{ G^{(s,p)}(y, z; y', z_p) \left[\frac{\partial\varphi^{(s,p)}}{\partial z'}\right]_{z'=z_p} - \\ &- \varphi^{(s,p)}(y', z_p) \left[\frac{\partial G^{(s,p)}(y, z; y', z')}{\partial z'}\right]_{z'=z_p} \Big\}\,\mathrm{d}y'. \qquad (23)\end{aligned}$$

In (21), (22) and (23) the formulae (12), (16) and (13) and the formulae (18) must be substituted. Before, assigning to the incident TE_{01}-wave an amplitude 1 and assuming the waveguide to be matched at $z > z_p$, the constants $C_m^{(n,0)}$ and $D_m^{(s,p)}$ appearing in (18) are fixed as $C_0^{(n,0)} = 1$, $C_m^{(n,0)} = 0$ $(m \neq 0)$, $D_m^{(s,p)} = 0$. Now it is easy to show that the first integral in (21) will give the contribution $\mathrm{e}^{jh_0 z} + \mathrm{e}^{jh_0(2z_0 - z)}$, and that the last integral in (23) will vanish.

E must be continuous in the apertures; according to (2) this means that $\partial\varphi/\partial z'$ is continuous at $z = z_k (k = 0, 1, \ldots, s)$. Thus the following functions $M_k(y')$ can be defined:

$$\begin{aligned}M_k(y') &= [\partial\varphi^{(k-1,k)}/\partial z']_{z'=z_k} = \\ &= [\partial\varphi^{(k,k+1)}/\partial z']_{z'=z_k}, \ (k = 0, 1, \ldots, s;\ -1 = n,\ s+1 = p), \qquad (24)\end{aligned}$$

and (21), (22) and (23) can be rewritten as

$$\varphi^{(n,0)} = \mathrm{e}^{jh_0 z} + \mathrm{e}^{jh_0(2z_0 - z)} + \int_{\sigma_0} G^{(n,0)}(y, z; y', z_0)\, M_0(y')\,\mathrm{d}y', \qquad (25)$$

$$\begin{aligned}\varphi^{(k,k+1)} = &- \int_{\sigma_k} G^{(k,k+1)}(y, z; y', z_k)\, M_k(y')\,\mathrm{d}y' + \\ &+ \int_{\sigma_{k+1}} G^{(k,k+1)}(y, z; y', z_{k+1})\, M_{k+1}(y')\,\mathrm{d}y', \qquad (26)\end{aligned}$$

$$\varphi^{(s,p)} = - \int_{\sigma_s} G^{(s,p)}(y, z; y', z_s)\, M_s(y')\,\mathrm{d}y'. \qquad (27)$$

But **H**, too, must be continuous in the aperture, so that according to (2) the φ-functions yield the $(s + 1)$ relations

$$\begin{aligned}2\,\mathrm{e}^{jh_0 z_0} + \int_{\sigma_0} G^{(n,0)}(y, z_0; y', z_0)\, M_0(y')\,\mathrm{d}y' &= \\ = - \int_{\sigma_0} G^{(0,1)}(y, z_0; y', z_0)\, M_0(y')\,\mathrm{d}y' &+ \\ + \int_{\sigma_1} G^{(0,1)}(y, z_0; y', z_1) M_1(y')\,\mathrm{d}y', & \qquad (28)\end{aligned}$$

$$\begin{aligned}
&-\int_{\sigma_{k-1}} G^{(k-1,k)}(y, z_k; y', z_{k-1})\, M_{k-1}(y')\, dy' + \\
&\qquad + \int_{\sigma_k} G^{(k-1,k)}(y, z_k; y', z_k)\, M_k(y')\, dy' = \\
&\qquad = -\int_{\sigma_k} G^{(k,k+1)}(y, z_k; y', z_k)\, M_k(y')\, dy' + \\
&+\int_{\sigma_{k+1}} G^{(k,k+1)}(y, z_k; y', z_{k+1})\, M_{k+1}(y')\, dy', \quad (k = 1,2, \ldots, s-1),
\end{aligned} \tag{29}$$

$$\begin{aligned}
&-\int_{\sigma_{s-1}} G^{(s-1,s)}(y, z_s; y', z_{s-1})\, M_{s-1}(y')\, dy' + \\
&\qquad + \int_{\sigma_s} G^{(s-1,s)}(y, z_s; y', z_s) M_s(y')\, dy' = \\
&\qquad = -\int_{\sigma_s} G^{(s,p)}(y, z_s; y', z_s)\, M_s(y')\, dy'.
\end{aligned} \tag{30}$$

Lastly on substitution of (12), (16) and (13), there follow, after some elementary calculations, the $(s+1)$ integral equations

$$\begin{aligned}
&+\int_{\sigma_0} \sum_{n=0}^{\infty} (\varepsilon_n/bh_n) \cos(n\pi y/b) \cos(n\pi y'/b)\,. \\
&\qquad .\, [\mathrm{ctg} h_n(z_1 - z_0) - j]\, M_0(y')\, dy' - \\
&\qquad - \int_{\sigma_1} \sum_{n=0}^{\infty} (\varepsilon_n/bh_n) \cos(n\pi y/b) \cos(n\pi y'/b)\,. \\
&\qquad .\, [1/\sinh_n(z_1 - z_0)]\, M_1(y')\, dy' = 2\, e^{jh_0 z_0},
\end{aligned} \tag{31}$$

$$\begin{aligned}
&-\int_{\sigma_{k-1}} \sum_{n=0}^{\infty} (\varepsilon_n/bh_n) \cos(n\pi y/b) \cos(n\pi y'/b)\,. \\
&\quad .\, [1/\sinh_n(z_k - z_{k-1})]\, M_{k-1}(y')\, dy' + \\
&\quad + \int_{\sigma_k} \sum_{n=0}^{\infty} (\varepsilon_n/bh_n) \cos(n\pi y/b) \cos(n\pi y'/b)\,. \\
&\quad .\, [\mathrm{ctg} h_n(z_k - z_{k-1}) + \mathrm{ctg} h_n(z_{k+1} - z_k)]\, M_k(y')\, dy' - \\
&\quad - \int_{\sigma_{k+1}} \sum_{n=0}^{\infty} (\varepsilon_n/bh_n) \cos(n\pi y/b) \cos(n\pi y'/b)\,. \\
&\quad .\, [1/\sinh_n(z_{k+1} - z_k)]\, M_{k+1}(y')\, dy' = 0, \quad (k = 1,2, \ldots, s-1),
\end{aligned} \tag{32}$$

$$\begin{aligned}
&-\int_{\sigma_{s-1}} \sum_{n=0}^{\infty} (\varepsilon_n/bh_n) \cos(n\pi y/b) \cos(n\pi y'/b)\,. \\
&.\, [1/\sinh_n(z_s - z_{s-1})]\, M_{s-1}(y')\, dy' + \\
&+\int_{\sigma_s} \sum_{n=0}^{\infty} (\varepsilon_n/bh_n) \cos(n\pi y/b) \cos(n\pi y'/b)\,. \\
&.\, [\mathrm{ctg} h_n(z_s - z_{s-1}) - j]\, M_s(y')\, dy' = 0.
\end{aligned} \tag{33}$$

Anticipating the method of Schwinger 1,2,3,) in solving these equations and observing that in $h_0 = [\omega^2\varepsilon\mu - (\pi/a)^2]^{\frac{1}{2}}$ and $h_n = j\gamma_n = j[(n\pi/b)^2 - h_0{}^2]^{\frac{1}{2}}$, $(n > 0)$, the factors h_0 and γ_n are real, it is advantageous to split the summations over n into a term for $n = 0$ and the rest, from which is separated the "static" part 6). Moreover all the equations (31), (32) and (33) are divided by 2; for $n > 0$

$$(\varepsilon_n/2bh_n)\,[1/\sin h_n(z_p - z_q)] = -\,(1/b\gamma_n)\,[1/\mathrm{sh}\,\gamma_n(z_p - z_q)],$$

$$(\varepsilon_n/2bh_n)\,\mathrm{ctg}\,h_n(z_p - z_q) = -\,(1/b\gamma_n)\,\mathrm{ctgh}\,\gamma_n(z_p - z_q).$$

Hence, the integral equations to be solved are

$$\begin{aligned}
&+\int_{\sigma_0}(1/2bh_0)[\mathrm{ctg}\,h_0(z_1 - z_0) - j]\,M_0(y')\,dy' +\\
&\qquad+\int_{\sigma_0}\sum_{n=1}^{\infty}\{(2/n\pi) - (1/b\gamma_n)\,[\mathrm{ctgh}\,\gamma_n(z_1 - z_0) + 1]\}\,.\\
&\qquad.\,\cos(n\pi y/b)\cos(n\pi y'/b)\,M_0(y')\,dy' -\\
&\qquad-\int_{\sigma_0}\sum_{n=1}^{\infty}(2/n\pi)\cos(n\pi y/b)\cos(n\pi y'/b)\,M_0(y')\,dy' -\\
&\qquad-\int_{\sigma_1}(1/2bh_0)[1/\sin h_0(z_1 - z_0)]\,M_1(y')\,dy' +\\
&\qquad+\int_{\sigma_1}\sum_{n=1}^{\infty}(1/b\gamma_n)\,[1/\mathrm{sh}\,\gamma_n(z_1 - z_0)]\,.\\
&\qquad.\,\cos(n\pi y/b)\cos(n\pi y'/b)\,M_1(y')\,dy' = e^{jh_0z_0},
\end{aligned}\tag{34}$$

$$\begin{aligned}
&-\int_{\sigma_{k-1}}(1/2bh_0)[1/\sin h_0(z_k - z_{k-1})]M_{k-1}(y')\,dy' +\\
&\qquad+\int_{\sigma_{k-1}}\sum_{n=1}^{\infty}(1/b\gamma_n)[1/\mathrm{sh}\,\gamma_n(z_k - z_{k-1})]\,.\\
&\qquad.\,\cos(n\pi y/b)\cos(n\pi y'/b)\,M_{k-1}(y')\,dy' +\\
&\quad+\int_{\sigma_k}(1/2bh_0)[\mathrm{ctg}\,h_0(z_k - z_{k-1}) + \mathrm{ctg}\,h_0(z_{k+1} - z_k)]\,M_k(y')\,dy' +\\
&\quad+\int_{\sigma_k}\sum_{n=1}^{\infty}\{(2/n\pi) - (1/b\gamma_n)\,[\mathrm{ctgh}\,\gamma_n(z_k - z_{k-1}) +\\
&\quad+\mathrm{ctgh}\,\gamma_n(z_{k+1} - z_k)]\}\cos(n\pi y/b)\cos(n\pi y'/b)\,M_k(y')\,dy' -\\
&\quad-\int_{\sigma_k}\sum_{n=1}^{\infty}(2/n\pi)\cos(n\pi y/b)\cos(n\pi y'/b)\,M_k(y')\,dy' -\\
&\quad-\int_{\sigma_{k+1}}(1/2bh_0)[1/\sin h_0(z_{k+1} - z_k)]M_{k+1}(y')\,dy' +\\
&\quad+\int_{\sigma_{k+1}}\sum_{n=1}^{\infty}(1/b\gamma_n)[1/\mathrm{sh}\,\gamma_n(z_{k+1} - z_k)]\,.\\
&\quad.\,\cos(n\pi y/b)\cos(n\pi y'/b)\,M_{k+1}(y')\,dy' = 0,\\
&\qquad\qquad\qquad\qquad(k = 1,2,\ldots\ldots, s-1),
\end{aligned}\tag{35}$$

$$
\begin{aligned}
-\int_{\sigma_{s-1}} & (1/2bh_0)\,[1/\sinh_0(z_s - z_{s-1})]\, M_{s-1}(y')\, \mathrm{d}y' + \\
& + \int_{\sigma_{s-1}} \sum_{n=1}^{\infty} (1/b\gamma_n)\,[1/\mathrm{sh}\gamma_n(z_s - z_{s-1})]\,. \\
& .\cos(n\pi y/b)\cos(n\pi y'/b)\, M_{s-1}(y')\, \mathrm{d}y' + \\
& + \int_{\sigma_s} (1/2bh_0)[\mathrm{ctg}h_0(z_s - z_{s-1}) - j]\, M_s(y')\, \mathrm{d}y' + \\
& + \int_{\sigma_s} \sum_{n=1}^{\infty} \{(2/n\pi) - (1/b\gamma_n)[\mathrm{ctgh}\gamma_n(z_s - z_{s-1}) + 1]\}\,. \\
& .\cos(n\pi y/b)\cos(n\pi y'/b)\, M_s(y')\, \mathrm{d}y' - \\
& - \int_{\sigma_s} \sum_{n=1}^{\infty} (2/n\pi)\cos(n\pi y/b)\cos(n\pi y'/b)\, M_s(y')\, \mathrm{d}y' = 0. \qquad (36)
\end{aligned}
$$

§ 4. *Change of variables* 6); *transposition of integral equations into algebraic equations.* Defining u and u' by

$$\cos(\pi y/b) = \alpha_k \cos u,\ \cos(\pi y'/b) = \alpha_k \cos u',\ \alpha_k = \sin(\pi\alpha_k/2b), \qquad (37)$$

y (analogously by y') and $\mathrm{d}y/\mathrm{d}u$ will be

$$y = (b/\pi)\arccos(\alpha_k \cos u),\ \mathrm{d}y/\mathrm{d}u = (b/\pi)[1 - (\alpha_k \cos u)^2]^{\frac{1}{2}}\,\alpha_k \sin u. \qquad (38)$$

The y domain $\frac{1}{2}(b - d^{(k)})$ to $\frac{1}{2}(b + d^{(k)})$ is transformed into the u domain 0 to π, independent of z_k. Moreover, let

$$U_k(u') = (\pi/bh_0)\, M_k(y')\, \mathrm{d}y'/\mathrm{d}u',$$

then on substitution of (37) and

$$M_k(y')\, \mathrm{d}y' = (bh_0/\pi)\, U_k(u')\, \mathrm{d}u' \qquad (39)$$

into the integral equations (34), (35) and (36) two types of integrals will enter the calculations. By virtue of the identity

$$\sum_{n=1}^{\infty} (1/n)\cos(n\pi y/b)\cos(n\pi y'/b) = -\tfrac{1}{2}\ln|2[\cos(\pi y/b) - \cos(\pi y'/b)]| \qquad (40)$$

one of the types can be transformed by

$$
\begin{aligned}
-\int_{\sigma_k} \sum_{n=1}^{\infty} & (2/n\pi)\cos(n\pi y/b)\cos(n\pi y'/b)\, M_k(y')\, \mathrm{d}y' = \\
& = (bh_0/\pi)[(1/\pi)\,(\ln\alpha_k)\int_0^{\pi} U_k(u')\, \mathrm{d}u' - \\
& - \int_0^{\pi} \sum_{n=1}^{\infty} (2/n\pi)\cos(nu)\cos(nu')\, U_k(u')\, \mathrm{d}u'. \qquad (41)
\end{aligned}
$$

Now, if $U_k(u)$ is represented by the series

$$U_k(u) = \sum_{r=0}^{\infty} \varepsilon_r a_r^{(k)} \cos(ru), \tag{42}$$

ε_r being the Neumann-number, (41) can be written as

$$-\int_{\sigma_k} \sum_{n=1}^{\infty} (2/n\pi) \cos(n\pi y/b) \cos(n\pi y'/b)\, M_k(y')\, \mathrm{d}y' =$$

$$= a_0^{(k)}(bh_0/\pi) \ln\alpha_k - (bh_0/\pi) \sum_{m=1}^{\infty} (1/m) a_m^{(k)} \varepsilon_m \cos(mu). \tag{43}$$

The second type of integrals can be transposed by

$$\int_{\sigma_k} \cos(n\pi y/b) \cos(n\pi y'/b)\, M_k(y')\, \mathrm{d}y' =$$

$$= bh_0 \cos[n \arccos(\alpha_k \cos u)]\,.$$

$$.\sum_{r=0}^{\infty} (\varepsilon_r/\pi) \int_0^{\pi} \cos[n \arccos(\alpha_k \cos u')]\, a_r^{(k)} \cos(ru')\, \mathrm{d}u'. \tag{44}$$

Now the integral

$$I_n^r(\alpha_k) = (\varepsilon_r/\pi) \int_0^{\pi} \cos[n \arccos(\alpha_k \cos u')] \cos(ru')\, \mathrm{d}u' \tag{45}$$

is known [2]) (note that here all I_m^m differ by the factor 2 from the definition of Miles; here $I_m^m(\alpha) = \alpha^m$). Hence the $I_n^r(\alpha_k)$ are the Fourier-coefficients of the expansion of $\cos[n \arccos(\alpha_k \cos u)]$ in the even Fourier-series in $\cos(ru)$, so

$$\cos[n \arccos(\alpha_k \cos u)] = \sum_{m=0}^{\infty} I_n^m(\alpha_k) \cos mu. \tag{46}$$

The second type of integrals now can be written as

$$\int_{\sigma_k} \cos(n\pi y/b) \cos(n\pi y'/b)\, M_k(y')\, \mathrm{d}y' =$$

$$= bh_0 \sum_{m=0}^{\infty} I_n^m(\alpha_k) \cos(mu) \sum_{r=0}^{\infty} a_r^{(k)} I_n^r(\alpha_k). \tag{47}$$

Derived from Miles' calculations, some of the polynomials $I_n^m(\alpha)$ with m, n even numbers are given in table I.

TABLE I

m n	0	2	4
0	1	0	0
2	$(\alpha^2 - 1)$	α^2	0
4	$(3\alpha^2 - 1)(\alpha^2 - 1)$	$4\alpha^2(\alpha^2 - 1)$	α^4

In particular

$$I_q^{\,p} = 0, \qquad p > q. \tag{48}$$

Bearing in mind (43), (47) and (48), the above-mentioned substitution of (37) and (39) into the integral equations (34), (35) and (36) can be carried out and will give the algebraic equations:

$$\begin{aligned}
&+ \tfrac{1}{2}[\mathrm{ctg}\,h_0(z_1 - z_0) - j]\, I_0^{\,0}(\alpha_0)\, I_0^{\,0}(\alpha_0)\, a_0^{(0)} + \\
&\quad + \sum_{n=1}^{\infty} \{(2bh_0/n\pi) - (h_0/\gamma_n)\,[\mathrm{ctgh}\,\gamma_n(z_1 - z_0) + 1]\}\,. \\
&\quad . \sum_{m=0}^{\infty} I_n^{\,m}(\alpha_0) \cos mu \sum_{r=0}^{\infty} a_r^{(0)} I_n^{\,r}(\alpha_0) + \\
&\quad + a_0^{(0)}(bh_0/\pi)\, \ln\alpha_0 - (bh_0/\pi) \sum_{m=1}^{\infty} (1/m)\, a_m^{(0)}\, \varepsilon_m \cos mu - \\
&\quad - [1/2\sin h_0(z_1 - z_0)]\, I_0^{\,0}(\alpha_1)\, I_0^{\,0}(\alpha_1)\, a_0^{(1)} + \\
&\quad + \sum_{n=1}^{\infty} (h_0/\gamma_n)[1/\mathrm{sh}\,\gamma_n(z_1 - z_0)]\,. \\
&\quad . \sum_{m=0}^{\infty} I_n^{\,m}(\alpha_1) \cos mu \sum_{r=0}^{\infty} a_r^{(1)}\, I_n^{\,r}(\alpha_1) = e^{jh_0z_0},
\end{aligned} \tag{49}$$

$$\begin{aligned}
&- [1/\sin h_0(z_k - z_{k-1})]\, I_0^{\,0}(\alpha_{k-1})\, I_0^{\,0}(\alpha_{k-1})\, a_0^{(k-1)} + \\
&\quad + \sum_{n=1}^{\infty} (h_0/\gamma_n)[1/\mathrm{sh}\,\gamma_n(z_k - z_{k-1})]\,. \\
&\quad . \sum_{m=0}^{\infty} I_n^{\,m}(\alpha_{k-1}) \cos mu \sum_{r=0}^{\infty} a_r^{(k-1)}\, I_n^{\,r}(\alpha_{k-1}) + \\
&\quad + \tfrac{1}{2}[\mathrm{ctg}\,h_0(z_k - z_{k-1}) + \mathrm{ctg}\,h_0(z_{k+1} - z_k)]\, I_0^{\,0}(\alpha_k)\, I_0^{\,0}(\alpha_k) + \\
&\quad + \sum_{n=1}^{\infty} \{(2bh_0/n\pi) - (h_0/\gamma_n)[\mathrm{ctgh}\,\gamma_n(z_k - z_{k-1}) + \\
&\quad + \mathrm{ctgh}\,\gamma_n(z_{k+1} - z_k)]\}\,. \sum_{m=0}^{\infty} I_n^{\,m}(\alpha_k) \cos mu \sum_{r=0}^{\infty} a_r^{(k)} I_n^{\,r}(\alpha_k) + \\
&\quad + a_0^{(k)}(bh_0/\pi)\ln\alpha_k - (bh_0/\pi) \sum_{m=1}^{\infty} (1/m) a_m^{(k)}\, \varepsilon_m \cos mu - \\
&\quad - [1/2\, \sin h_0(z_{k+1} - z_k)]\, I_0^{\,0}(\alpha_{k+1}) I_0^{\,0}(\alpha_{k+1}) a_0^{(k+1)} + \\
&\quad + \sum_{n=1}^{\infty} (h_0/\gamma_n)\, [1/\mathrm{sh}\,\gamma_n(z_{k+1} - z_k)]\,. \\
&\quad . \sum_{m=0}^{\infty} I_n^{\,m}(\alpha_{k+1}) \cos mu \sum_{r=0}^{\infty} a_r^{(k+1)}\, I_n^{\,r}(\alpha_{k+1}) = 0, \\
&\qquad\qquad\qquad\qquad\qquad (k = 1, 2, \ldots\ldots, s-1),
\end{aligned} \tag{50}$$

$$
\begin{aligned}
&- [1/2 \sin h_0(z_s - z_{s-1})]\, I_0{}^0(\alpha_{s-1})\, I_0{}^0(\alpha_{s-1}) + \\
&\qquad + \sum_{n=1}^{\infty} (h_0/\gamma_n)[1/\mathrm{sh}\gamma_n(z_s - z_{s-1})] \,. \\
&\qquad . \sum_{m=0}^{\infty} I_n{}^m(\alpha_{s-1}) \cos mu \sum_{r=0}^{\infty} a_r{}^{(s-1)} I_n{}^r(\alpha_{s-1}) + \\
&\qquad + \tfrac{1}{2}[\mathrm{ctg} h_0(z_s - z_{s-1}) - j] I_0{}^0(\alpha_s)\, I_0{}^0(\alpha_s) a_0{}^{(s)} + \\
&\qquad + \sum_{n=1}^{\infty} \{(2bh_0/\pi) - (h_0/\gamma_n)[\mathrm{ctgh}\gamma_n(z_s - z_{s-1}) + 1]\} \,. \\
&\qquad . \sum_{m=0}^{\infty} I_n{}^m(\alpha_s) \cos mu \sum_{r=0}^{\infty} a_r{}^{(s)}\, I_n{}^r(\alpha_s) + \\
&\qquad + a_0{}^{(s)}\, (bh_0/\pi) \ln \alpha_s - (bh_0/\pi) \sum_{m=1}^{\infty} (1/m)\, \varepsilon_m \cos mu = 0 \,. \qquad (51)
\end{aligned}
$$

Before equating the coefficients of cosmu of the left and the right members of the identities in u (49), (50) and (51) for all admitted values of m, use can be made of the symmetry properties of the electromagnetic field in the apertures about $y = \frac{1}{2}b$, i.e. about $u = \frac{1}{2}\pi$, Hence in (46), m and n may assume only even integral values; according to these properties, in (42) all $a_r{}^{(k)}$ with odd indices r are zero; thus for m, n and r only even integers are allowed. Moreover, with regard to $I_q{}^p = 0$ if $p > q$, the symbol $[m, r]$ is introduced, $[m, r]$ meaning the greatest of the values of m and r. Noting $I_0{}^0(\alpha) = +1$, the above mentioned identifications yield:

a) if $m = 0$:

$$
\begin{aligned}
&+ a_0{}^{(0)} \{(bh_0/\pi) \ln \alpha_0 + \tfrac{1}{2}[\mathrm{ctg} h_0(z_1 - z_0) - j]\} + \\
&+ \sum_{r=0}^{\infty} a_r{}^{(0)} \sum_{n=[2,r]}^{\infty} I_n{}^0(\alpha_0)\, I_n{}^r(\alpha_0)\, \{(2bh_0/\pi) - \\
&- (h_0/\gamma_n)\, [\mathrm{ctgh}\gamma_n(z_1 - z_0) + 1]\} - \\
&- a_0{}^{(1)}[1/\sin h_0(z_1 - z_0)] + \sum_{r=0}^{\infty} a_r{}^{(1)} \sum_{n=[2,r]}^{\infty} I_n{}^0(\alpha_1) \,. \\
&. \, I_n{}^r(\alpha_1)(h_0/\gamma_n)[1/\mathrm{sh}\gamma_n(z_1 - z_0)] = e^{jh_0 z_0} \,, \qquad (52)
\end{aligned}
$$

$$
\begin{aligned}
&- a_0{}^{(k-1)}[1/2 \sin h_0(z_k - z_{k-1})] + \\
&\quad + \sum_{r=0}^{\infty} a_r{}^{(k-1)} \sum_{n=[2,r]}^{\infty} I_n{}^0(\alpha_{k-1}) I_n{}^r(\alpha_{k-1})(h_0/\gamma_n)[1/\mathrm{sh}\gamma_n(z_k - z_{k-1})] + \\
&\quad + a_0{}^{(k)}\{(bh_0/\pi) \ln \alpha_k + \tfrac{1}{2}[\mathrm{ctg} h_0(z_k - z_{k-1}) + \mathrm{ctg} h_0(z_{k+1} - z_k)]\} +
\end{aligned}
$$

$$\begin{aligned}
&+ \sum_{r=0}^{\infty} a_r^{(k)} \sum_{n=[2,r]}^{\infty} I_n^0(\alpha_k)\, I_n^r(\alpha_k)\{(2bh_0/n\pi) - \\
&- (h_0/\gamma_n)[\mathrm{ctgh}\gamma_n(z_k - z_{k-1}) + \mathrm{ctgh}\gamma_n(z_{k+1} - z_k)]\} - \\
&- a_0^{(k+1)}[1/2 \sin h_0(z_{k+1} - z_k)] + \sum_{r=0}^{\infty} a_r^{(k+1)} \sum_{n=[2,r]}^{\infty} I_n(\alpha_{k+1})\, I_n^r(\alpha_{k+1}) \,. \\
&.\, (h_0/\gamma_n)[1/\mathrm{sh}\gamma_n(z_{k+1} - z_k)] = 0, \quad (k = 1,2 \ldots, s-1), \qquad (53)
\end{aligned}$$

$$\begin{aligned}
&- a_0^{(s-1)}[1/2 \sin h_0(z_s - z_{s-1})] + \\
&+ \sum_{r=0}^{\infty} a_r^{(s-1)} \sum_{n=[2,r]}^{\infty} I_n^0(\alpha_{s-1})\, I_n^r(\alpha_{s-1})\, (h_0/\gamma_n)[1/\mathrm{sh}\gamma_n(z_s - z_{s-1})] + \\
&+ a_0^{(s)}\{(bh_0/\pi) \ln\alpha_s + \tfrac{1}{2}[\mathrm{ctg}h_0(z_s - z_{s-1}) - j]\} + \\
&+ \sum_{r=0}^{\infty} a_r^{(s)} \sum_{n=[2,r]}^{\infty} I_n^0(\alpha_s) \,. \\
&.\, I_n^r(\alpha^s)\{(2bh_0/n\pi) - (h_0/\gamma_n)[\mathrm{ctgh}\gamma_n\,(z_s - z_{s-1}) + 1]\} = 0, \qquad (54)
\end{aligned}$$

b) if $m \neq 0$, i.e. $m = 2,4 \ldots\ldots, \infty$:

$$\begin{aligned}
&- (2bh_0/m\pi) a_m^{(0)} + \sum_{r=0}^{\infty} a_r^{(0)} \sum_{n=[m,r]}^{\infty} I_n^m(\alpha_0)\, I_n^r(\alpha_0) \,. \\
&.\, \{(2bh_0/n\pi) - (h_0/\gamma_n)[\mathrm{ctgh}\gamma_n(z_1 - z_0) + 1]\} + \\
&+ \sum_{r=0}^{\infty} a_r^{(1)} \sum_{n=[m,r]}^{\infty} I_n^m(\alpha_1)\, I_n^r(\alpha_1)(h_0/\gamma_n)[1/\mathrm{sh}\gamma_n(z_1 - z_0)] = 0, \qquad (55)
\end{aligned}$$

$$\begin{aligned}
&\sum_{r=0}^{\infty} a_r^{(k-1)} \sum_{n=[m,r]}^{\infty} I_n^m(\alpha_{k-1})\, I_n^r(\alpha_{k-1})(h_0/\gamma_n)\, [1/\mathrm{sh}\gamma_n(z_k - z_{k-1})] - \\
&- (2bh_0/m\pi)\, a_m^{(k)} + \sum_{r=0}^{\infty} a_r^{(k)} \sum_{n=[m,r]}^{\infty} I_n^m(\alpha_k)\, I_n^r(\alpha_k) \,. \\
&.\, \{(2bh_0/n\pi) - (h_0/\gamma_n)[\mathrm{ctgh}\gamma_n(z_k - z_{k-1}) + \\
&+ \mathrm{ctgh}\gamma_n(z_{k+1} - z_k)]\} + \sum_{r=0}^{\infty} a_r^{(k+1)} \sum_{n=[m,r]}^{\infty} I_n^m(\alpha_{k+1}) \,. \\
&.\, I_n^r(\alpha_{k+1})(h_0/\gamma_n)[1/\mathrm{sh}\gamma_n(z_{k+1} - z_k)] = 0, \\
&\qquad\qquad (k = 1,2, \ldots\ldots, s-1), \qquad (56)
\end{aligned}$$

$$\begin{aligned}
&\sum_{r=0}^{\infty} a_r^{(s-1)} \sum_{n=[m,r]}^{\infty} I_n^m(\alpha_{s-1})\, I_n^r(\alpha_{s-1})(h_0/\gamma_n)\, [1/\mathrm{sh}\gamma_n(z_s - z_{s-1})] - \\
&- (2bh_0/m\pi) a_m^{(s)} + \sum_{r=0}^{\infty} a_r^{(s)} \sum_{n=[m,r]}^{\infty} I_n^m(\alpha_s)\, I_n^r(\alpha_s) \,. \\
&.\, \{(2bh_0/n\pi) - (h_0/\gamma_n)[\mathrm{ctgh}\gamma_n\,(z_s - z_{s-1}) + 1]\} = 0. \qquad (57)
\end{aligned}$$

The equations (52) up to (57) inclusive can be put in a surveyable form by introducing the constants $A_{m,r}^{(3k)}$, $(k = 0,1, \ldots, s)$, and $A_{m,r}^{(3k\pm1)}$, $(3k \pm 1 = 1,2,4,5,7, \ldots, 3s - 1)$. Introducing apart from the symbol $[m,r]$ the symbol $[2, m, r]$ meaning the greatest integer out of 2, m and r and using the Kronecker symbol $\delta_q^p (\delta_q^p = 0$ if $p \neq q$, $\delta_q^p = +1$ if $p = q)$, the constants A are defined by

$$A_{m,r}^{(0)} = \delta_0^m \delta_0^r \{(bh_0/\pi) \ln \alpha_0 + \tfrac{1}{2}[\mathrm{ctg} h_0(z_1 - z_0) - j]\} -$$

$$- \delta_{r\neq0}^{m\neq0}(2bh_0/m\pi) + \sum_{n=[2,m,r]}^{\infty} I_n^m(\alpha_0) I_n^r(\alpha_0) \;.$$

$$. \{(2bh_0/n\pi) - (h_0/\gamma_n)[\mathrm{ctgh} \gamma_n(z_1 - z_0) + 1]\}, \tag{58}$$

$$A_{m,r}^{(3k)} = \delta_0^m \delta_0^r \{(bh_0/\pi) \ln \alpha_k + \tfrac{1}{2}[\mathrm{ctg} h_0(z_k - z_{k-1}) +$$

$$+ \mathrm{ctg} h_0(z_{k+1} - z_k)]\} - \delta_{r\neq0}^{m\neq0}(2bh_0/m\pi) +$$

$$+ \sum_{n=[2,m,r,]}^{\infty} I_n^m(\alpha_k)\, I_n^r(\alpha_k)\, \{(2bh_0/n\pi) -$$

$$- (h_0/\gamma_n)[\mathrm{ctgh} \gamma_n(z_k - z_{k-1}) + \mathrm{ctgh} \gamma_n(z_{k+1} - z_k)]\}, \tag{59}$$

$$A_{m,r}^{(3s)} = \delta_0^m \delta_0^r \{(bh_0/\pi) \ln \alpha_s + \tfrac{1}{2}[\mathrm{ctg} h_0(z_s - z_{s-1}) - j]\} -$$

$$- \delta_{r\neq0}^{m\neq0}(2bh_0/m\pi) + \sum_{n=[2,m,r]}^{\infty} I_n^m(\alpha_s) I_n^r(\alpha_s) \;.$$

$$. \{(2bh_0/n\pi) - (h_0/\gamma_n)[\mathrm{ctgh} \gamma_n (z_s - z_{s-1}) + 1]\}, \tag{60}$$

$$A_{m,r}^{(3k-1)} = - \delta_0^m \delta_0^r [1/2 \sin h_0(z_k - z_{k-1})] +$$

$$+ \sum_{n=[2,m,r]}^{\infty} I_n^m(\alpha_{k-1})\, I_n^r(\alpha_{k-1})(h_0/\gamma_n)\, [1/\mathrm{sh} \gamma_n(z_k - z_{k-1})], \tag{61}$$

$$A_{m,r}^{(3k+1)} = - \delta_0^m \delta_0^r\, [1/2 \sin h_0(z_{k+1} - z_k)] +$$

$$+ \sum_{n=[2,m,r]}^{\infty} I_n^m(\alpha_{k+1})\, I_n^r(\alpha_{k+1})(h_0/\gamma_n)\, [1/\mathrm{sh} \gamma_n(z_{k+1} - z_k)]. \tag{62}$$

Remark: note that always $A_{m,r}^{(p)} = A_{r,m}^{(p)}$.

By inspection of (52) up to (62) inclusive, the equations (52) up to (57) inclusive can be written as

$$\sum_{r=0}^{\infty} a_r^{(0)}\, A_{m,r}^{(0)} + \sum_{r=0}^{\infty} a_r^{(1)} A_{m,r}^{(1)} = \delta_m^0\, e^{jh_0 z_0}, \tag{63}$$

$$\sum_{r=0}^{\infty} a_r^{(k-1)} A_{m,r}^{(3k-1)} + \sum_{r=0}^{\infty} a_r^{(k)} A_{m,r}^{(3k)} + \\ + \sum_{r=0}^{\infty} a_r^{(k+1)} A_{m,r}^{(3k+1)} = 0, \quad (64)$$

$$\sum_{r=0}^{\infty} a_r^{(s-1)} A_{m,r}^{(3s-1)} + \sum_{r=0}^{\infty} a_r^{(s)} A_{m,r}^{(3s)} = 0. \quad (65)$$

The equations (63), (64) and (65) represent $\frac{1}{2}m(s+1)$ linear algebraic equations; there are $\frac{1}{2}r(s+1)$ unknown amplitudes $a_r^{(k)}$ to be determined; but m and r may grow beyond all limit, so with $m = r \to \infty$ all amplitudes $a_r^{(k)}$ can, at least in principle, be calculated.

Now it is of prime importance to derive, which of the amplitudes $a_r^{(k)}$ $(k = 0, 1, \ldots\ldots, s;\ r = 0, 2, 4, \ldots\ldots, \infty)$ will enter in the formulae for the transmission coefficient T and for the reflection coefficient R.

§ 5. *Reflection coefficient and transmission coefficient.* Using $z' = z_0$ in (12), and substituting this result in (25), furthermore splitting the summation over n from 0 to ∞ into a term for $n = 0$ and a sum over n from 2 to ∞, the following expression for $\varphi^{(n,0)}(y, z)$ is found:

$$\varphi^{(n,0)} = e^{jh_0 z} + e^{jh_0(2z_0 - z)} + ja_0^{(0)} e^{jh_0(z_0 - z)} + \\ + 2 \int_{\sigma_0} \sum_{n=2}^{\infty} (1/b\gamma_n)\, e^{-\gamma_n(z_0 - z)} \cos(n\pi y/b) \cos(n\pi y'/b)\, M_0(y')\, dy'. \quad (66)$$

For sufficiently large positive values of $z_0 - z$ the integral in (66) will vanish. This means that in the undisturbed field, the potential $\varphi^{(n,0)} = \varphi_{un}^{(n,0)}$ satisfies

$$\varphi_{un}^{(n,0)} = e^{jh_0 z} + e^{jh_0(2z_0 - z)} + ja_0^{(0)} e^{jh_0(z_0 - z)}. \quad (67)$$

In a similar way by substituting (13) with $z' = z_s$ in (27) and by splitting up the summation over n, the potential $\varphi^{(s,p)}$ in the region of the undisturbed field becomes

$$\varphi_{un}^{(s,p)} = -\, ja_0^{(s)} e^{jh_0(z - z_0)}. \quad (68)$$

According to (2) the y-component of $\mathbf{E}$ in the undisturbed field regions of the end domains can be calculated with aid of (67) and (68). The results are

$$E_{y,un}{}^{(n,0)} = -\,\omega\mu h_0\, \mathrm{e}^{jh_0 z} + \omega\mu h_0\, \mathrm{e}^{-jh_0 z}\,[\mathrm{e}^{2jh_0 z} + ja_0{}^{(0)}\, \mathrm{e}^{jh_0 z_0}], \quad (69)$$

$$E_{y,un}{}^{(s,p)} = +\, j\omega\mu h_0\, a_0{}^{(s)}\, \mathrm{e}^{jh_0(z-z_s)}. \quad (70)$$

The first term in (69) represents the incident wave, the second term the reflected wave. In (70) the right member represents the transmitted wave only. Hence the principal-mode transmission coefficient T and the principal-mode reflection coefficient R are

$$T(z) = \dot{-}\, ja_0{}^{(s)}\, \mathrm{e}^{jh_0(z-z_s)}, \quad (71)$$

$$R(z) = -\, \mathrm{e}^{2jh_0(z_0-z)}\,[1 + ja_0{}^{(0)}\, \mathrm{e}^{-jh_0 z_0}]. \quad (72)$$

Because the structure studied is nondissipative, the relation $|R|^2 = 1 - |T|^2$ must hold. So the conditions for full transmission can be expressed either as $R = 0$ or as $|T| = 1$. It will be shown explicitly that these formulations are equivalent.

§ 6. *Conditions for full transmission.* The determinant D of the equations (63), (64) and (65) in the unknown amplitudes $a_r{}^{(k)}$ can be written in $(m \times r)$ blocks of $(s+1)^2$ elements each. Such a block is the subdeterminant $D_{m,r}{}^{(sub)}$ of D, containing zeros and the constants $A_{m,r}{}^{(p)}$, m and r fixed, $p = 0,1, \ldots, 3s$, i.e.

$$D_{m,r}{}^{(sub)} = \begin{vmatrix} A_{m,r}{}^{(0)} & A_{m,r}{}^{(1)} & \cdot & \cdot & & & \cdot \\ A_{m,r}{}^{(2)} & A_{m,r}{}^{(3)} & A_{m,r}{}^{(4)} & \cdot & & & \cdot \\ \cdot & A_{m,r}{}^{(5)} & \times & \times & & & \cdot \\ & & & & & & \\ \cdot & & & \times & \times & \times & \cdot \\ \cdot & & & \cdot & \times & \times & A_{m,r}{}^{(3s-2)} \\ \cdot & & & \cdot & \cdot & A_{m,r}{}^{(3s-1)} & A_{m,r}{}^{(3s)} \end{vmatrix} . \quad (73)$$

The dots represent zeros, the crosses constants $A_{m,r}{}^{(p)}$. The elements $A_{0,0}{}^{(0)}$ and $A_{0,0}{}^{(3s)}$ of D are complex, all other elements are real, as can be verified by inspection of (58) to (62) inclusive. In particular

$$A_{0,0}{}^{(0)} = -\,\tfrac{1}{2}j + \mathrm{Re}(A_{0,0}{}^{(0)}),\; A_{0,0}{}^{(3s)} = -\,\tfrac{1}{2}j + \mathrm{Re}(A_{0,0}{}^{(3s)}). \quad (74)$$

Let the rows and columns of D be numbered $0,1, \ldots, s, 0', 1', \ldots, s', 0'', 1'', \ldots, s''$, etc. Moreover let $D_{pqr,stu}$ denote the determinant obtained from D by the suppression of the rows p, q, r and the columns s, t, u. Finally let $D^{(r)}$ mean the determinant obtained from D by suppressing the term $-\frac{1}{2}j$ in the elements $A_{0,0}{}^{(0)}$ and $A_{0,0}{}^{(3s)}$. Then

$$a_0{}^{(0)} = \mathrm{e}^{jh_0 z_0}\, D_{0,0}/D,\ a_0{}^{(s)} = (-1)^s\, \mathrm{e}^{jh_0 z_0}\, \mathrm{D}_{0,s}/D. \tag{74}$$

Substitution in (71) and (72) yields

$$T = (-1)^{s+1}\, \mathrm{e}^{jh_0[z-(z_s-z_0)]}\, jD_{0,s}/D, \tag{75}$$

$$R = -\, \mathrm{e}^{2jh_0(z_0-z)}\, (1 + jD_{0,0}/D). \tag{76}$$

The condition for full transmission can be formulated either as $|T| = 1$ or as $|R| = 0$. In connection with (75), $|T| = 1$ means $|D_{0,s}| = |D|$ or

$$D_{0,s}.D_{0,s} = \tfrac{1}{4}(\mathrm{Re}\, D_{0,0} + \mathrm{Re}\, D_{s,s})^2 + (D^{(r)} - \tfrac{1}{4}D_{0s,0s})^2. \tag{77}$$

In connection with (76), $|R| = 0$ means $D_{0,0} = jD$ or, splitting up the equation in real and imaginary parts,

$$0 = \tfrac{1}{2}(\mathrm{Re}\, D_{0,0} - \mathrm{Re}\, D_{s,s}),\ 0 = D^{(r)} + \tfrac{1}{4}D_{0s,0s}. \tag{78a, b}$$

Summing up the right member of (77) and the quadratures of the right members of (78a) and (78b), equating this result to the analogous sum of the left members of those equations, the following result is obtained:

$$D_{0,s}D_{0,s} = \mathrm{Re}\, D_{0,0}\, \mathrm{Re}\, D_{s,s} - D^{(r)}D_{0s,0s}. \tag{79}$$

Because the structure studied has reciprocity properties, (75) gives $D_{0,s} = D_{s,0}$. Then (79) is an identity 7), so the condition $|T| = 1$ is equivalent to $|R| = 0$. It is to be noted that subtraction of (79) from (77) would give the condition

$$\tfrac{1}{4}(\mathrm{Re}\, D_{0,0} - \mathrm{Re}\, D_{s,s})^2 + (D^{(r)} - \tfrac{1}{4}D_{0s,0s})^2 = 0,$$

which is realizable, only if (78a) as well as (78b) holds.

§ 7. *Approximations.* The constants $A_{m,r}{}^{(p)}$ defined by (58) up to (62) inclusive contain series over n from $n \geqq 2$ to $n \to \infty$, either of the type

$$S_1 = \sum_{n=[2,m,r]}^{\infty} I_n{}^m(\alpha^k)\, I_n{}^r(\alpha_k)\, \{(2bh_0/\pi) - (h_0/\gamma_n)\, .$$
$$.\, [\mathrm{ctgh}\gamma_n(z_k - z_{k-1}) + \mathrm{ctgh}\gamma_n(z_{k+1} - z_k)]\}, \tag{80}$$

where, to obtain the series of (58) and (60) respectively, the distances $z_{k+1} - z_k$ and $z_k - z_{k-1}$ respectively may grow beyond all limit, resulting in $\text{ctgh}\gamma_n(z_{k+1} - z_k) = 1$ and $\text{ctgh}\gamma_n(z_k - z_{k-1}) = 1$, or of the type

$$S_2 = \sum_{n=[2,m,r]}^{\infty} I_n{}^m(\alpha_{k\pm1})\, I_n{}^r(\alpha_{k\pm1})(h_0/\gamma_n)\, [1/\text{sh}\gamma_n|z_{k\pm1} - z_k|]. \quad (81)$$

The series $\sum_{n=2}^{\infty} \{(bh_0/\pi) - (h_0/\gamma_n)\,\text{ctgh}\gamma_n|z_{k\pm1} - z_k|\}$ as well as the series $\sum_{n=2}^{\infty} (h_0/\gamma_n)\, [1/\text{sh}\gamma_n|z_{k\pm1} - z_k|]$ are strongly convergent. Moreover, the products $I_n{}^m(\alpha_p)\, I_n{}^r(\alpha_p)$ will have, as can be shown, absolute values ≤ 1. Hence the series (80) and (81) still have strongly convergent properties.

Thus it is plausible to define the zero, the first, ..., the q^{th} order approximation, the approximation obtained by omitting in (58) up to (60) inclusive the terms with $n \geq 2$, resp. $n \geq 4$, ..., resp. $n \geq 2(q + 1)$. In the q^{th} order approximation (55), (56) and (57) give for every $m \geq 2\,(q + 1)$

$$-(2bh_0/m\pi)a_m{}^{(0)} = 0; \quad -(2bh_0/m\pi)\, a_m{}^{(k)} = 0; \quad -(2bh_0/m\pi)a_m{}^s = 0.$$

So $a_m{}^{(p)} = 0$ $(p = 0,1, ..., s)$ if $m \geq 2\,(q + 1)$, meaning that in the q^{th} order approximation only the amplitudes $a_m{}^{(p)}$ with $m \leq 2q$ may be non-zero.

The system determinant $D^{(q)}$ of the equations (63), (64) and (65) in the q^{th} order approximation will then be obtained by retaining only the subdeterminants $D_{m,r}{}^{(sub)}$ with $m,r \leq 2q$ of the infinite system determinant D and moreover extending the series over n in the elements of every $D_{m,r}{}^{(sub)}$ only up to $n = 2q$ inclusive.

Hence, the nondiagonal elements of $D^{(q)}$ appearing in the subdeterminants $D_{m,r}{}^{(sub)}$ with $m = 2q$ or $r = 2q$ $(q \neq 0)$ consist only of terms of the series (80) or (81) for $n = 2q$. On account of the strongly convergent properties of the series, the just mentioned nondiagonal elements are small compared to all other elements. Then it can be shown by elementary calculations on determinants that the order of approximation of $D^{(q)}$ is not altered by omitting these nondiagonal elements.

Thus, representing the mentioned nondiagonal element by dots, the remaining non-zero elements by crosses and the zero elements by empty spaces, the following relation holds in the first order approximation:

$$D^{(1)} = \left|\begin{array}{cccccc|cccccc}
\times & \times & & & & & \cdot & \cdot & & & & \\
\times & \times & \times & & & & \cdot & \cdot & \cdot & & & \\
& \times & \times & \times & & & & \cdot & \cdot & \cdot & & \\[1em]
& & & \times & \times & \times & & & & \cdot & \cdot & \cdot \\
& & & & \times & \times & & & & & \cdot & \cdot \\
\hline
\cdot & \cdot & & & & & \times & \cdot & & & & \\
\cdot & \cdot & \cdot & & & & \cdot & \times & \cdot & & & \\
& \cdot & \cdot & \cdot & & & & \cdot & \times & \cdot & & \\[1em]
& & & \cdot & \cdot & \cdot & & & & \cdot & \times & \cdot \\
& & & & \cdot & \cdot & & & & & \cdot & \times
\end{array}\right| = \left|\begin{array}{cccccc|cccccc}
\times & \times & & & & & & & & & & \\
\times & \times & \times & & & & & & & & & \\
& \times & \times & \times & & & & & & & & \\[1em]
& & & \times & \times & \times & & & & & & \\
& & & & \times & \times & & & & & & \\
\hline
& & & & & & \times & & & & & \\
& & & & & & & \times & & & & \\
& & & & & & & & \times & & & \\[1em]
& & & & & & & & & & \times & \\
& & & & & & & & & & & \times
\end{array}\right| .$$

Now the determination of the amplitudes $a_0^{(k)}$ in the first approximation depends only on the ratio of minors of elements of the subdeterminant $D_{0,0}^{(sub)}$ to $D^{(1)}$. As the subdeterminant $D_{2,2}^{(sub)}$ contains only main-diagonal elements, the mentioned ratio can as well be calculated as the ratio of the analogous minors of the determinant $D_{0,0}^{(sub)}$ alone (written in first order approximation) to $D_{0,0}^{(sub)}$ to the same approximation. In this respect the relations (78a,b) for full transmission will be reviewed for the first order approximation.

§ 8. *Conditions for full transmission in the first order approximation.* The general conditions for full transmission (78a,b) can be written as

$$D_{0,0}^{(r)}/D_{0s,0s}^{(r)} = D_{s,s}^{(r)}/D_{0s,0s}^{(r)}, \tag{82a}$$

$$D^{(r)}/D_{0s,0s}^{(r)} + \tfrac{1}{4} = 0, \tag{82b}$$

because $\operatorname{Re} D_{0,0} = D_{0,0}^{(r)}$, $\operatorname{Re} D_{s,s} = D_{s,s}^{(r)}$ and $D_{0s,0s} = D_{0s,0s}^{(r)}$. According to § 7 the determinant ratios of (82a, b) can as well be calculated to the first order approximation as analogous determinant ratios starting with

$$D = \left|\begin{array}{ccccccc}
a_0 & a_1 & & & & & \\
a_2 & a_3 & a_4 & & & & \\
& a_5 & \times & \times & & & \\
& & \times & \times & \times & & \\
& & & \times & \times & \times & \\
& & & & \times & a_{3s-3} & a_{3s-2} \\
& & & & & a_{3s-1} & a_{3s}
\end{array}\right| ,$$

where a_p ($p = 1, 2, \ldots\ldots, 3s - 1$) stands for $A_{0,0}{}^{(p)}$ in the first order approximation, a_0 and a_{3s} stand for Re $A_{0,0}{}^{(0)}$ and Re $A_{s,s}{}^{(0)}$, respectively to the same approximations. With these notations (82a, b) will give

$$D_{0,0}/D_{0s,0s} = D_{s,s}/D_{0s,0s}, \tag{84a}$$

$$D/D_{0s,0s} + \tfrac{1}{4} = 0. \tag{84b}$$

As is well-known [8]), the determinant ratios of the equation (84a) can be expressed as continued fractions. Indeed

$$D = a_0 D_{0,0} - a_1 D_{0,1}; \quad D_{0,1} = a_2 D_{01,01} - a_4 D_{01,12};$$
$$D_{01,12} = a_7 D_{012,123}.$$

Repeated substitution of the recurrence formulae yields

$$\frac{D}{D_{0,0}} = a_0 - \frac{a_1 a_2 \rvert}{\lvert a_3} - \frac{a_4 a_5 \rvert}{\lvert a_6} - \ldots\ldots - \frac{a_{3s-2} a_{3s-1} \rvert}{\lvert a_{3s}}.$$

Defining

$$K_{\kappa,\lambda} = a_{3\kappa} - \frac{a_{3\kappa+1} a_{3\kappa+2} \rvert}{\lvert a_{3\kappa+3}} - \ldots\ldots - \frac{a_{3\lambda-2} a_{3\lambda-1} \rvert}{\lvert a^{3\lambda}}, \tag{85}$$

(84a) can be written as

$$K_{s,1} = K_{0,s-1}. \tag{86}$$

The calculation of a similar expression for the equation (84b) is a bit more involved. Starting with

$$D = a_0 D_{0,0} - a_1 a_2 D_{01,01},$$

$$D_{0,0} = a_{3s} D_{0s,0s} - a_{3s-1} a_{3s-2} D_{0(s-1)s,0(s-1)s},$$

$$D_{01,01} = a_{3s} D_{01s,01s} - a_{3s-1} a_{3s-2} D_{01(s-1)s,01(s-1)s},$$

the substitution of the last two equations in the preceding equation will give, upon dividing the result by $D_{0s,0s}$,

$$D/D_{0s,0s} = a_0 a_{3s} - a_0 a_{3s-1} a_{3s-2}/K_{s-1,1} - a_{3s} a_1 a_2/K_{1,s-1} +$$
$$+ a_1 a_2 a_{3s-1} a_{3s-2} D_{01(s-1)s,01(s-1)s}/D_{0s,0s}. \tag{87}$$

The last term of equation (87) can be transformed into

$$(a_1 a_2/K_{1,s-1})(a_{3s-1} a_{3s-2}/K_{s-1,1}) \cdot$$
$$\cdot\ (D_{0s,0s} D_{01(s-1)s,01(s-1)s}/D_{01s,01s} D_{0(s-1)s,0(s-1)s}).$$

Using the identity 7)

$$D_{0s,0s}D_{01(s-1)s,01(s-1)s} =$$
$$= D_{01s,01s}D_{0(s-1)s,0(s-1)s} - D_{01s,0(s-1)s}D_{0(s-1)s,01s},$$

this last term can be written as

$$(a_1a_2/K_{1,s-1})(a_{3s-1}a_{3s-2}/K_{s-1,1}) \cdot$$
$$\cdot [1 - (D_{01s,0(s-1)s}D_{0(s-1)s,01s}D_{01s,01s}D_{0(s-1)s,0(s-1)s})].$$

Now

$$D_{01s,0(s-1)s} = a_5a_8 \ldots a_{3s-7}a_{3s-4}, \quad D_{0(s-1)s,01s} = a_4a_7 \ldots a_{3s-8}a_{3s-5},$$

and with the help of these expressions the last term of (87) can be made equal to

$$(a_1a_2/K_{1,s-1})(a_{3s-2}a_{3s-1}/K_{s-1,1}) -$$
$$- [a_1a_2a_4a_5 \ldots a_{3s-4}a_{3s-2}a_{3s-1}/)D_{0s,0s})^2].$$

Finally, (87) becomes

$$D/D_{0s,0s} = K_{0,s-1}K_{s,1} - [a_1a_2a_4 \ldots a_{3s-1}/(D_{0s,0s})^2],$$

and by virtue of (84b) the second condition for full transmission becomes

$$K_{0,s-1}K_{s,1} = [a_1a_2a_4 \ldots a_{3s-1}/(D_{0s,0s})^2] - \tfrac{1}{4}. \qquad (88)$$

The equations (86) and (88) are also valid if $s = 1$, provided the value of the determinant $D_{0s,0s}$ is taken as unity.

§ 9. *Applications.*

a) Full transmission through two screens; $s = 1$. In this case (86) and (88) will give

$$a_0 = a_3, \quad a_0a_3 = a_1a_2 - \tfrac{1}{4}. \qquad (89a,b)$$

Equation (89a) can be written as

$$(bh_0/\pi) \ln\alpha_0 + \tfrac{1}{2} \operatorname{ctg}h_0(z_1 - z_0) +$$
$$+ (\alpha_0^2 - 1)^2\{(bh_0/\pi) - (h_0/\gamma_2) [\operatorname{ctgh}\gamma_2(z_1 - z_0) + 1]\} =$$
$$= (bh_0/\pi) \ln\alpha_1 + \tfrac{1}{2} \operatorname{ctg}h_0(z_1 - z_0) +$$
$$+ (\alpha_1^2 - 1)^2\{(bh_0/\pi) - (h_0/\gamma_2)[\operatorname{ctgh}\gamma_2(z_1 - z_0) + 1]\}.$$

If $\alpha_0 = \alpha_1$, i.e. if the configuration is symmetrical about $z = \frac{1}{2}(z_1 - z_0)$, (89a) holds for every frequency. In this case of *two identical screens*, the case considered by Bosma [1]), $\alpha_0 = \alpha_1 = \alpha$, $a_0 = a_3$ and $a_1 = a_2$. Then condition (89b) requires that $a_0^2 - a_1^2 + \frac{1}{4} = 0$. Let $z_1 - z_0 = \zeta$ and

$$B^{(0)} = (bh_0/\pi) \ln\alpha + \tfrac{1}{2} \operatorname{ctg} h_0\zeta, \tag{90a}$$

$$b^{(0)} = (\alpha^2 - 1)^2[(bh_0/\pi) - (h_0/\gamma_2)(\operatorname{ctgh}\gamma_2 \zeta + 1)], \tag{90b}$$

$$B^{(1)} = -(1/2 \sin h_0\zeta), \tag{90c}$$

$$b^{(1)} = (\alpha^2 - 1)^2(h_0/\gamma_2)(1/\operatorname{sh}\gamma_2\zeta), \tag{90d}$$

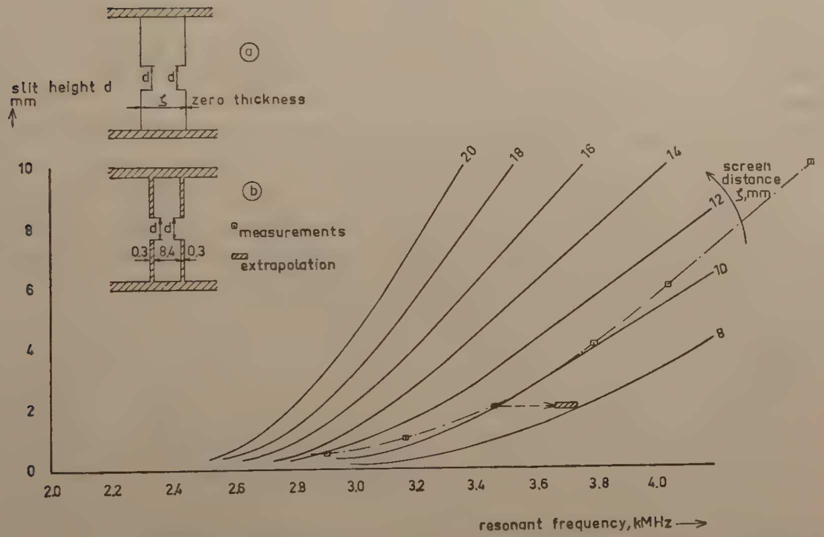

Fig. 4. The resonant frequency for two identical screens; *d* large; a: configuration in accordance with theory; b: configuration in accordance with measurements.

so that $|b^{(0)}|$, $|b^{(1)}|$ are small compared with $|B^{(0)}|$, $|B^{(1)}|$, then (89b) requires to the first approximation that

$$(B^{(0)})^2 - (B^{(1)})^2 + \tfrac{1}{4} + 2(B^{(0)}b^{(0)} - B^{(1)}b^{(1)}) = 0.$$

Upon substitution of (90), the following results:

$$\operatorname{ctg} h_0\zeta = (bh_0/\pi) \ln (1/\alpha) + (2B^{(0)}b^{(0)} - 2B^{(1)}b^{(1)})/(bh_0/\pi) \ln (1/\alpha). \tag{91}$$

The zero order approximation would give

$$\operatorname{ctg} h_0\zeta = (bh_0/\pi) \ln(1/\alpha). \tag{92}$$

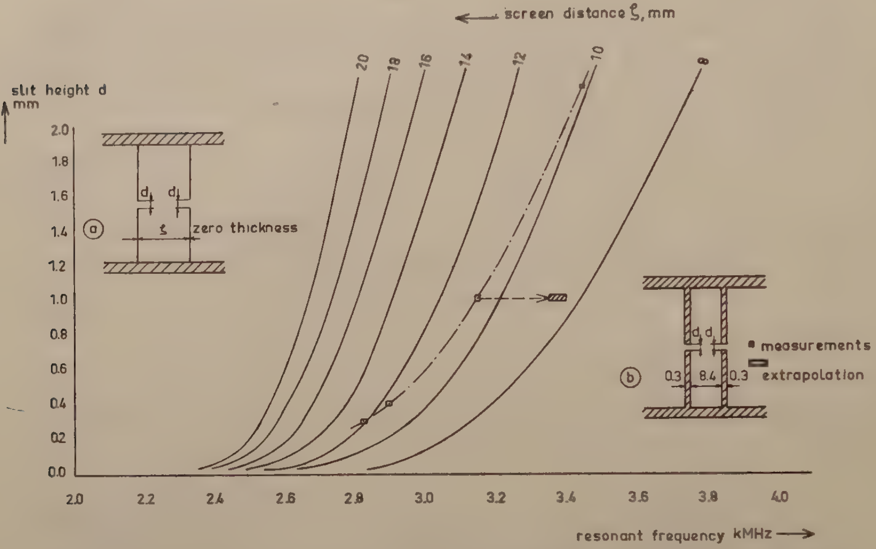

Fig. 5. The resonant frequency for two identical screens; *d* small; a: configuration in accordance with theory; b: configuration in accordance with measurements.

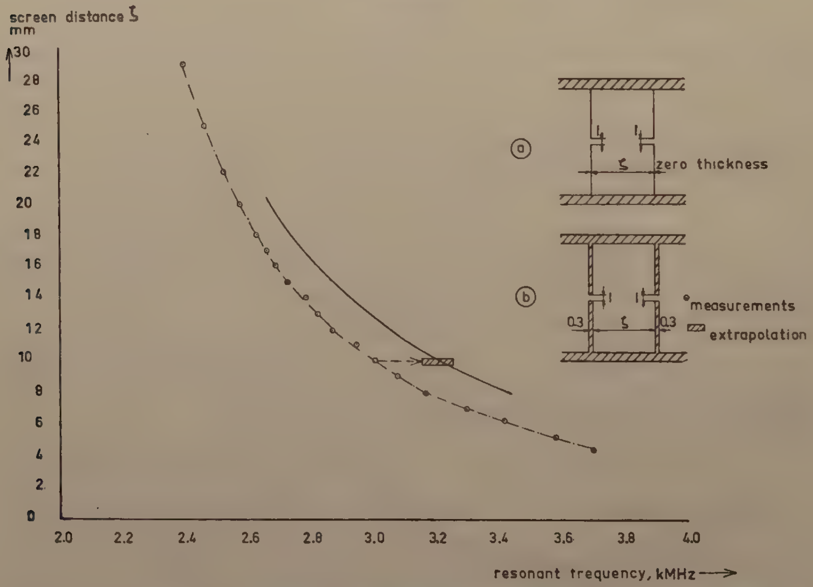

Fig. 6. The resonant frequency for two screens; $d^{(0)} = d^{(1)} = 1$ mm; a: configuration in accordance with theory; b: configuration in accordance with to measurements.

Using (92) for the determination of the second (the smallest) term of the right member of (91), the condition (91) can be expressed as

$$(\pi/bh_0)\ \mathrm{ctg}\,h_0\zeta = \ln(1/\alpha) + C, \tag{93}$$

$$C = (1-\alpha)^2\{1-(\pi/b\gamma_2)[1+(\mathrm{ch}\,\gamma_2\zeta-\cos h_0\zeta)/\mathrm{sh}\,\gamma_2\zeta]\}. \tag{94}$$

Figs. 4 and 5 give plots of the theoretical dependence of the "resonant frequency" on the height of the slits and the distance of the

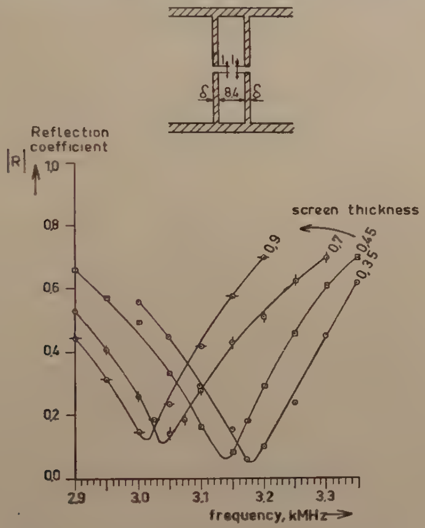

Fig. 7. Influence of screen thickness.

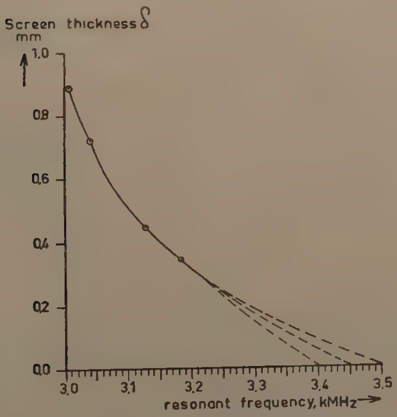

Fig. 8. Extrapolation curve.

screens of zero thickness, calculated for a conventional S-band waveguide, with $a = 7.21$ cm, $b = 3.41$ cm. The dashed lines indicate experimental results for screens of 0.3 mm thickness.

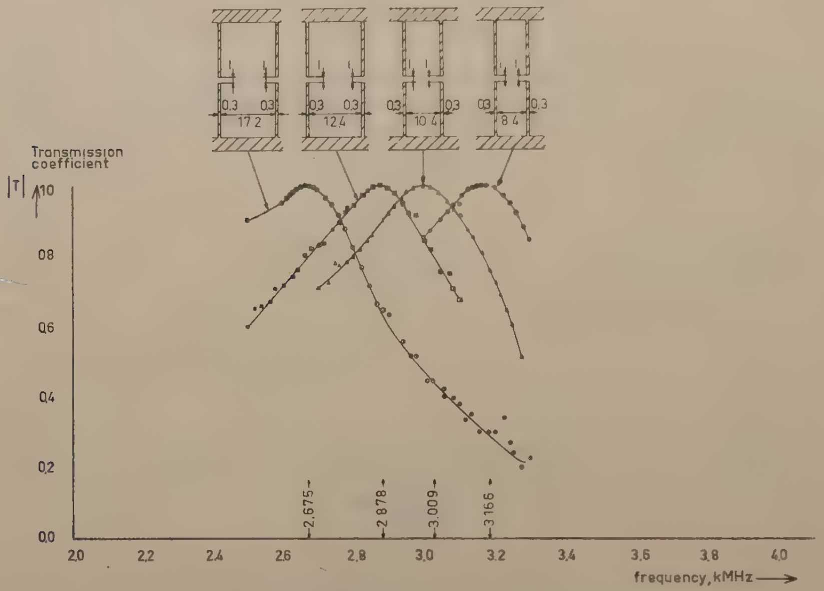

Fig. 9. Filter characteristics for $d^{(0)} = d^{(1)} = 1$ mm.

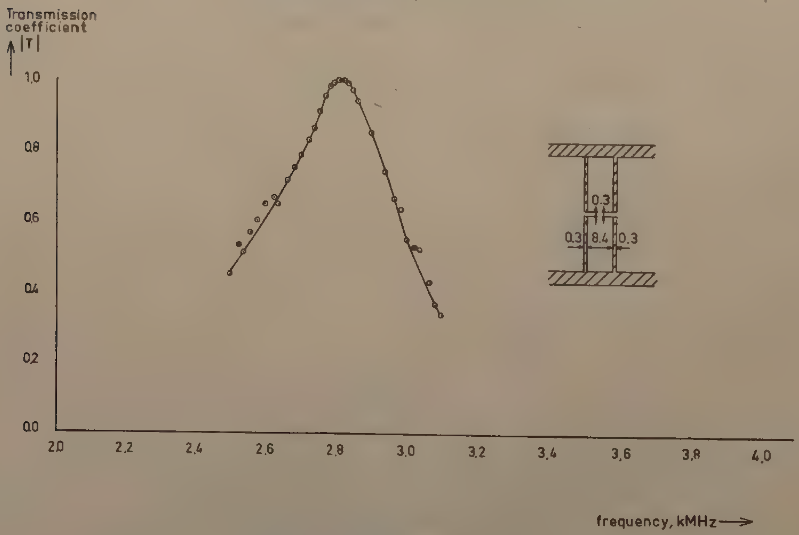

Fig. 10. Filter characteristic for $d^{(0)} = d^{(1)} = 0.3$ mm.

Fig. 6 gives a plot of the theoretical dependence of the "resonant frequency" on the screen distance ζ for $d^{(0)} = d^{(1)} = 1$ mm. The dashed line is found by experiment, for screens of 0.3 mm thickness.

The arrows in figs 4, 5 and 6 point to a region, where in agreement with the measurements in fig. 7, the extrapolation for measurements with screens of zero thickness must lie. This extrapolation is accomplished by measuring $|R|$ as a function of the frequency for screens with different thicknesses; figs. 7 and 8 show the results. It can be concluded that the measurements confirm the theory fairly well.

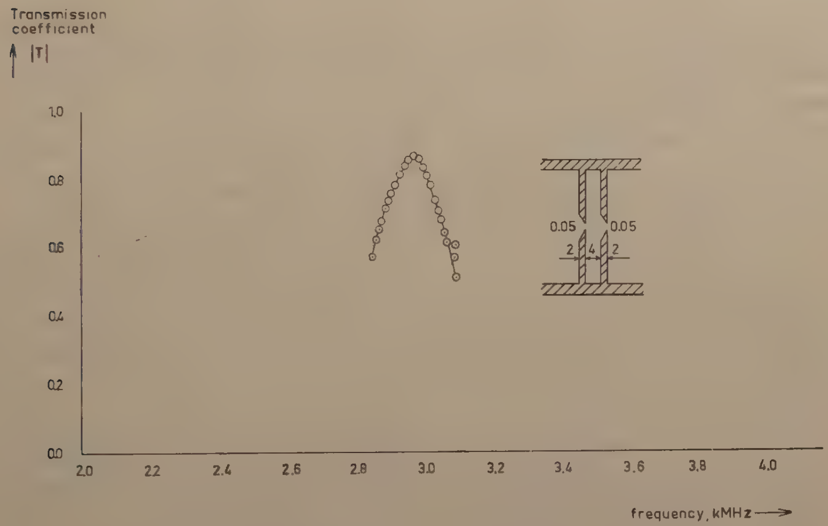

Fig. 11. Filter characteristic for $d^{(0)} = d^{(1)} = 0.05$ mm.

Finally the fig. 9, 10 and 11 give filter characteristics obtained for the configuration with two identical screens.

b) Full transmission through three screens; $s = 2$. In this case (86) and (88) will give

$$a_0 - a_1 a_2/a_3 = a_6 - a_4 a_5/a_3, \tag{95a}$$

$$(a_0 - a_1 a_2/a_3)(a_6 - a_4 a_5/a_3) = [a_1 a_2 a_4 a_5/(a_3)^2] - \tfrac{1}{4}. \tag{95b}$$

Considering the case with symmetry about $z = \frac{1}{2}(z_2 - z_0)$, we have $\alpha_0 = \alpha_3$, so $a_0 = a_6$ and according to (95a) $a_1 a_2 = a_4 a_5$; then

(95b) requires

$$a_0^2 - (2a_0a_1a_2/a_3) + \tfrac{1}{4} = 0. \tag{96}$$

Let $z_1 - z_0 = z_2 - z_1 = \zeta$, then in a zero order approximation (96) gives rise to

$$\begin{aligned}(\mathrm{ctg}^2 h_0\zeta)\,[\tfrac{1}{2}(bh_0/\pi)\ln\alpha_0 + \tfrac{1}{4}(bh_0/\pi)\ln\alpha_1] &+ \\ + (\mathrm{ctg}h_0\zeta)[(bh_0/\pi)\ln\alpha_0 + (bh_0/\pi)\ln\alpha_1] &+ \\ + [(bh_0/\pi)\ln\alpha_0]^2[(bh_0/\pi)\ln\alpha_1] &- \\ - \tfrac{1}{2}(bh_0/\pi)\ln\alpha_0 + \tfrac{1}{4}(bh_0/\pi)\ln\alpha_1 &= 0.\end{aligned} \tag{97}$$

In the zero order approximation one resonant frequency is obtained this being the case when the discriminant of the equation (97) in $\mathrm{ctg}h_0\zeta$ vanishes or when

$$\ln(1/\alpha_1) = 2\ln(1/\alpha_0)\sqrt{[(bh_0/\pi)\ln(1/\alpha_0)]^2 + 1}. \tag{98}$$

Under condition (98) the common root of (97) will be

$$\mathrm{ctg}h_0\zeta = \ln(1/\alpha_0)\{1 + 1/[1 + 2\ln(1/\alpha_0)/\ln(1/\alpha_1)]\}. \tag{99}$$

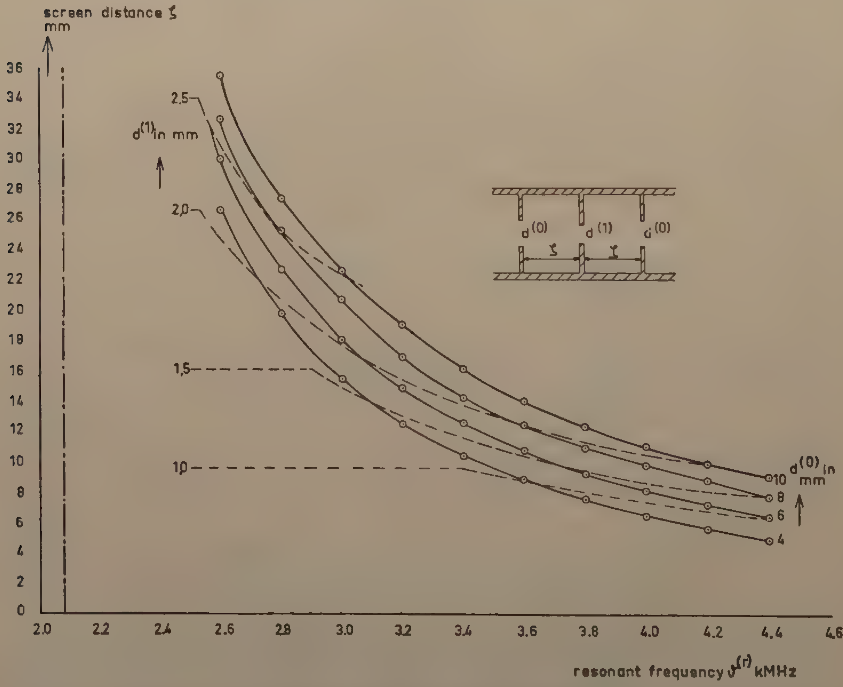

Fig. 12. Resonant frequency in zero order approximation for three screens.

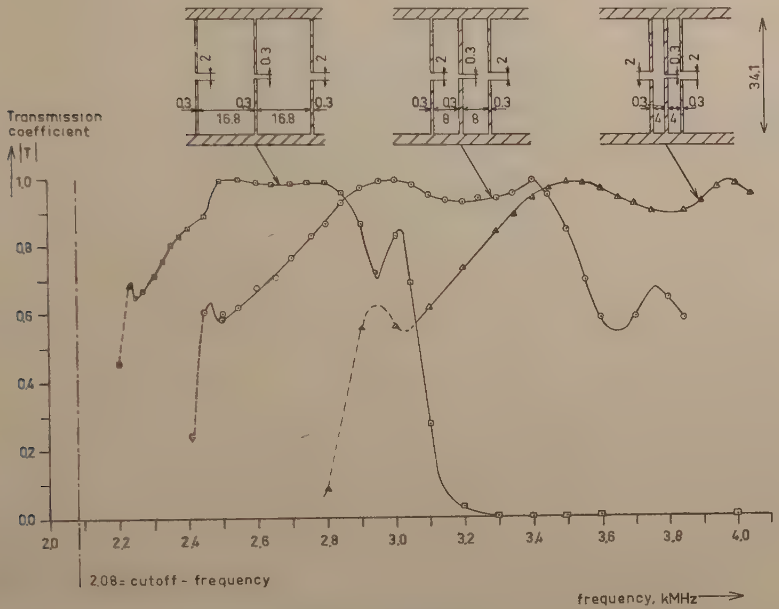

Fig. 13. Filter charcteristics for three screens; $d^{(0)}=d^{(2)}=2$ mm; $d^{(1)}=0.3$ mm

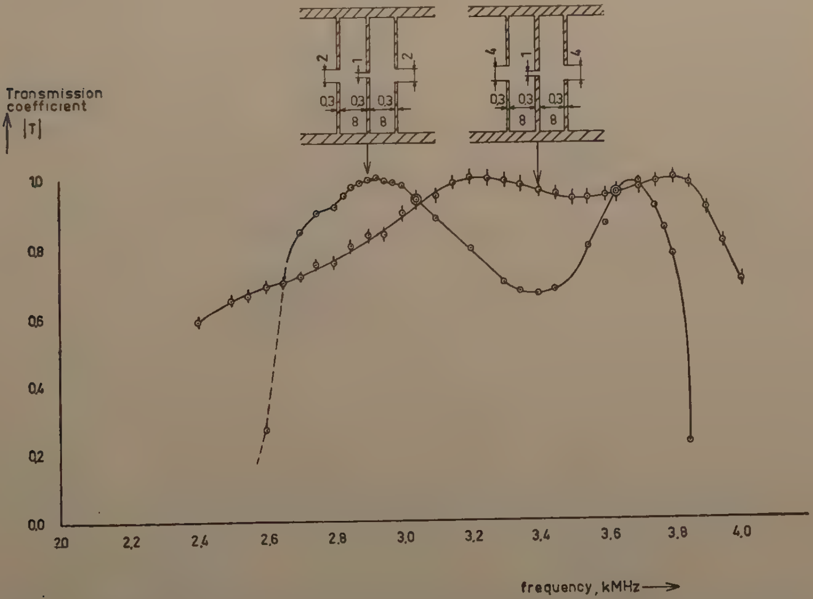

Fig. 14. Filter characteristics for three screens; $d^{(0)}=d^{(2)}=4$ mm; $d^{(1)}=1$ mm.

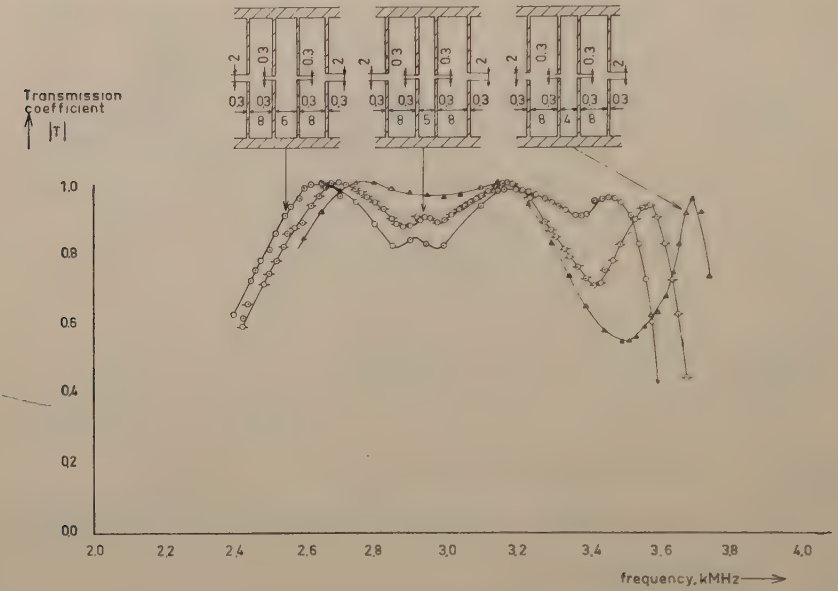

Fig. 15. Filter characteristics for four screens; $d^{(0)} = d^{(3)} = 2$ mm; $d^{(1)} = d^{(2)} = 0.3$ mm.

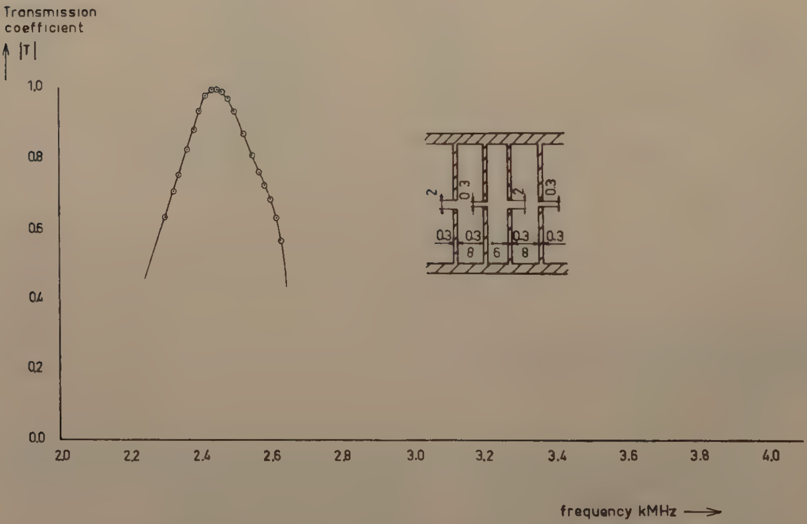

Fig. 16. Filter characteristic for four screens; $d^{(0)} = d^{(2)} = 2$ mm; $d^{(1)} = d^{(3)} = 0.3$ mm.

The theoretical interdependence of the single resonant frequency, ζ, $d^{(0)}$ and $d^{(1)}$ in the zero order approximation according to (99) is given in fig. 12 for screens with zero thicknesses, again calculated for an S-band waveguide. These calculations were used as a rough guide for the construction of filters. Figs. 13 and 14 show the results of some measurements with screens of 0.3 mm thickness. It can be seen that the zero order approximation gives only a rough design procedure.

c) Full transmission through four screens; $s = 3$. For this case some measurements only are given in the figs. 15 and 16.

§ 10. *Final remarks.* The theory developed in this article and the measurements given indicate that the construction of compact bandfilters for microwaves using capacitive screens with relative small interspaces is possible. Accurate results can be obtained by using a first order approximation.

Received 21st November, 1957

REFERENCES

1) Bosma, H., Appl. Sci. Res. B**7** (1958) 131.
2) Miles, John W. Quart. Appl. Math. **7** (1950) 45.
3) Borgnis und Papas, Randwertprobleme der Mikrowellenphysik, Springer-Verlag, Berlin, 1955.
4) Frank, N. H., RL Report No. 197, February 1943.
5) Szepesi, Zoltan, Onde elect. **30** (1950) 296.
6) Marcuvitz, N., Waveguide Handbook, McGraw-Hill, N.Y. 1951, p. 146, 147.
7) Scott, R. F. and G. B. Mathews, The Theory of determinants and their applications 2d. ed., Cambridge 1904, p. 64.
8) Perron, Oscar, Die Lehre von den Kettenbrüchen, Leipzig 1913.

A SIMPLE METHOD FOR PHOTOGRAPHING TRANSPARENT OBJECTS

ADDENDUM

by L. J. F. BROER, A. DEELEMAN and J. A. RIETDIJK

Laboratorium voor Aero- en Hydrodynamica van de Technische Hogeschool the Delft, Netherlands

Recently, some time after the publication of our note ¹), we have found that the method given there has been described already by Schardin ²), who apparently did not realise its advantages over the ordinary schlieren technique for many applications.

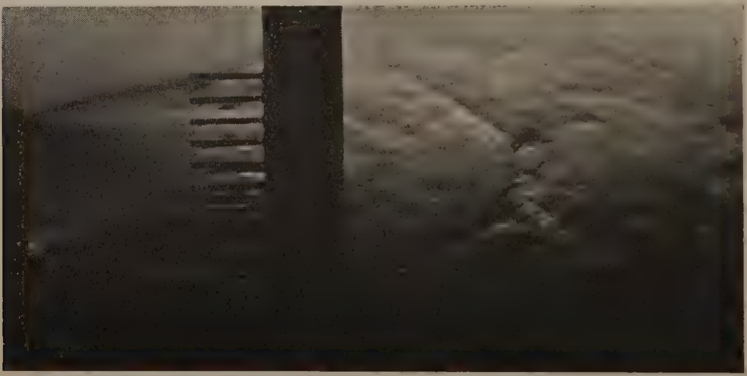

Fig. 1. Rake of small total head tubes in a supersonic flow.

We use this opportunity to point out that the pictures shown in our note ¹) are somewhat blurred due to vibrations of the waves connected with the noise of the jet. Since then we have obtained a powerful flash lamp (Microflash 1530-A from General Radio). With this light source we can make sharp pictures with an exposure of a few microseconds. An example is given here, showing a rake of small total head tubes in a supersonic flow. Turbulent density fluctuations show up clearly at this exposure.

Received 21st October, 1957.

REFERENCES

1) Broer, L. J. F., A. Deeleman and J. A. Rietdijk, Appl. Sci. Res. **B6** (1957) 253.
2) Schardin, H., Erg. Ex. Naturwissensch. **20** (1942) 303.

Appl. sci. Res. Section B, Vol. 7

FERROMAGNETIC RESONANCE IN POLYCRYSTALLINE FERRITES

by J. SNIEDER

Physical Laboratory of the National Defence Research Council T.N.O., Waalsdorp,
The Hague, Netherlands

Summary

An experimental and theoretical study is made of the propagation of TE_{11}-waves of wavelength 3.2 cm in a round wave guide containing a concentric round rod of Ferroxcube IV magnetized by a static magnetic field in a longitudinal direction. The Faraday rotation and the ellipticity when the wave has passed a given length of rod is determined as a function of the static field strength through resonance and of the temperature over a range from -30 to 100°C. On the basis of the theory of ferromagnetic resonance with damping the elements of the gyromagnetic permeability tensor are computed. With them the rotation angle and ellipticity can be expressed in terms of the angular frequency of the wave, the radius of the wave guide, the radius and length of the rod, the static field strength, the static magnetization, the gyromagnetic ratio and the damping constant. The gyromagnetic ratio is determined from resonance measurements on spheres of Ferroxcube while the damping constant is chosen so as to give the best agreement between theory and experiment. An interpretation of the values of the gyromagnetic ratio and of the resonance width in terms of the porosity of the ferrites is given. The behaviour of the damping constant as a function of porosity is briefly discussed.

CHAPTER I. INTRODUCTION

The purpose of the present investigation is on the one hand the experimental determination of a number of quantities which are characteristic for the behaviour of various ferromagnetic ferrites under the influence of high frequency electromagnetic fields, and on the other hand the interpretation of the data thus obtained in terms of the theory of ferromagnetic resonance.

In Chapter II the phenomenological description of ferromagnetic materials in the simultaneous presence of a static and a high frequency magnetic field with the aid of a gyromagnetic permeability tensor is briefly summarized. The possibility of losses is explicitly taken into account. With a view to the experiments to be described in Chapter III the theory governing the propagation of electromagnetic waves in a round wave guide, containing a concentric round rod of ferromagnetic material under the influence of a static longitudinal magnetic field, is gone into in greater detail. By generalizing earlier work of van Trier[1]) a relation expressing the rotation of the plane of polarization and ellipticity of a TE_{11}-wave, after traversing a given length of the guide, in terms of the permeability tensor of the ferromagnetic material is given.

In Chapter III two kinds of experimental arrangements are described. In the first of these the rotation of the plane of polarization and the ellipticity referred to above can actually be measured at a wavelength of 3.2 cm, for a static longitudinal magnetic field ranging from 0 to 5×10^5 A/m and at a temperature between -40 and 120°C. The second arrangement serves to study the absorption of high frequency electromagnetic energy in small spheres of the materials investigated, contained in a cavity, for three frequencies, corresponding to wavelengths of 3.2, 1.6 and 1.25 cm, as a function of a static magnetic field ranging up to 8×10^5 A/m and of the temperature in the interval already mentioned. By varying the magnetic field the value can be found for which the absorption is a maximum, corresponding to resonance. The ratio of the angular frequency and the field strength at resonance is the so-called gyromagnetic ratio of the material.

In Chapter IV the experimental results are collected both for the rotation and the resonance experiments. Several sources of error which may affect the measurements are discussed, together with the precautions necessary to avoid them. The degree of accuracy of the measured values is also estimated here.

In Chapter V the theory of ferromagnetic resonance with a damping term in the fundamental equation is reviewed. The elements of the gyromagnetic permeability tensor introduced in Chapter II are computed from this theory for a ferromagnetic medium in the presence of a static magnetic field and in the case that magnetic saturation is completely or almost completely attained. They can be expressed in terms of the gyromagnetic ratio, the damping constant, the angular frequency, the static field strength and the static magnetization. After a survey of ferromagnetic resonance in spheres, the theoretical values of the elements of the permeability tensor are substituted into the expressions derived in Chapter II for the rotation angle and ellipticity of a TE_{11}-wave traversing a longitudinally magnetized ferrite rod in a round wave guide. By choosing a suitable value of the unknown damping constant, the theoretical curves can be made to conform to the experimental curves. In this way the damping constant can be determined for the various ferrites as a function of the temperature. The temperature dependence is found to be relatively slight, but there appears a strong influence of the porosity, in the sense that the greater the porosity the larger the damping constant. Using the damping constant giving the best fit, the computed values of the resonance field strength are compared with the observed ones, extrapolated to vanishing radius of the rods. A reasonable agreement is found.

In Chapter VI it is investigated why the gyromagnetic ratio as determined from resonance measurements on small spheres of the same ferrites used in the rotation experiments has values depending on the temperature and on the wavelength. It is shown that the inhomogeneity of the material arising from its porous structure accounts essentially for this dependence.

The porosity of the ferrites is accompanied by an inhomogeneity of the static field inside the material. As a consequence a broadening of the resonance frequency takes place in addition to broadening due to other causes. In Chapter VII an estimate of the width due to porosity is made under some simplifying assumptions and compared with experiment. We also give a brief discussion of the mechanism operative in ferromagnetic damping as manifested in the ferromagnetic damping constant and its dependence on porosity.

Chapter II. THE PHENOMENOLOGICAL DESCRIPTION OF THE HIGH FREQUENCY MAGNETIC BEHAVIOUR OF FERRITES

§ 1. *The permeability tensor.* If in an isotropic ferromagnetic material, or one which by reason of its polycrystalline structure may be considered as isotropic, a static magnetic field H_0 is applied, then, as discussed e.g. in the thesis of van Trier[1]), the reaction of this material to a high frequency magnetic field can suitably be described by a gyromagnetic permeability tensor of the form

$$\|\mu\| = \left\| \begin{matrix} \mu_1 & -j\mu_2 & 0 \\ j\mu_2 & \mu_1 & 0 \\ 0 & 0 & \mu_3 \end{matrix} \right\|, \tag{2.1}$$

relating the components of the high frequency part of the magnetic induction ***B*** to the components of the high frequency part of the magnetic field strength ***H***. In the thesis of van Trier, who was concerned with the behaviour far below resonance, μ_1, μ_2 and μ_3 were considered as real quantities, signifying the absence of magnetic losses. Here we shall take into account from the beginning the possibility of such losses, and we shall hence assume μ_1, μ_2 and μ_3 to be complex:

$$\mu_1 = \mu_1' - j\mu_1'',\ \mu_2 = \mu_2' - j\mu_2'',\ \mu_3 = \mu_3' - j\mu_3'', \tag{2.2}$$

where μ_1', μ_1'', μ_2', μ_2'', μ_3', μ_3'' are real. These quantities will depend on the kind of material, the value of H_0, the temperature T and the angular frequency ω of the alternating field. Following van Trier we assume the dielectric behaviour of the ferrites to be describable by one dielectric constant

$$\varepsilon = \varepsilon' - j\varepsilon'', \tag{2.3}$$

independent of direction, which, however, in contrast to him we also allow to be complex.

§ 2. *Propagation of electromagnetic waves in round wave guides containing a concentric round ferromagnetic rod.* We consider now a round wave guide with a wall that may be regarded as perfectly conducting, containing a concentric round rod of a ferromagnetic ferrite which can be characterized by a gyromagnetic permeability tensor (2,1), (2.2) and a dielectic constant (2.3) as discussed in § 1. In particular we give our attention to a TE_{11}-mode in the empty wave guide and the changes in its propagation arising from the presence of a ferrite rod with radius ρ_1 very much smaller than the radius ρ_0 of the wave guide. The TE_{11}-mode in the empty guide may be resolved into two circularly polarized modes, depending on the azimuth ϑ around the axis of the guide through the factor exp $(\pm j\vartheta)$.

As shown by van Trier the propagation constant $\gamma_0 = j\beta_0$ of the TE_{11}-mode (which is purely imaginary since in the empty guide no losses occur) is altered in a different way for the two circularly polarized modes by the introduction of the rod, becoming (see his equation (2.118))

$$\gamma_\pm = \gamma_0 - c_1\gamma_0\left(\frac{\mu_1 \pm \mu_2 - \mu_0}{\mu_1 \pm \mu_2 + \mu_0} + c_2\frac{\varepsilon - \varepsilon_0}{\varepsilon + \varepsilon_0}\right)\rho_1{}^2. \tag{2.4}$$

Here the constants c_1 and c_2 are given by

$$c_1 = \frac{\pi\sigma_0 N_1{}'(\sigma_0\rho_0)}{4\rho_0 J_1{}''(\sigma_0\rho_0)}, \; c_2 = -\frac{\omega^2\varepsilon_0\mu_0}{\gamma_0{}^2}, \tag{2.5}$$

with ε_0, μ_0 the dielectric constant and permeability of vacuum, σ_0 follows form $J_1{}'(\sigma_0\rho_0) = 0$ as first root, γ_0 from

$$\gamma_0{}^2 = \sigma_0{}^2 - \omega^2\varepsilon_0\mu_0, \tag{2.6}$$

and N_1 and J_1 are the Neumann- and Besselfunctions of order 1, the primes denoting differentiation with respect to the argument. By an approximation method in which they started from an empty wave guide and computed the first order perturbation produced by the presence of the thin rod Suhl and Walker[2]) could confirm the result of van Trier.

As was mentioned before, van Trier was primarily interested in the practically lossless case at frequencies far below resonance. It appears, however, that his derivation applies unchanged in case μ_1, μ_2, μ_3 and ε are complex as supposed in (2.2) and (2.3). As a consequence of (2.4) $\gamma_\pm$ will then also be complex. Writing

$$\gamma_\pm = \alpha_\pm + j\beta_\pm \tag{2.7}$$

and equating real and imaginary parts in (2.7) and (2.4) we find

$$\alpha_\pm = 2c_1\beta_0\left[\frac{\mu_0(\mu_1'' \pm \mu_2'')}{(\mu_1' \pm \mu_2' + \mu_0)^2 + (\mu_1'' \pm \mu_2'')^2} + \right.$$
$$\left. + c_2\frac{\varepsilon_0\varepsilon''}{(\varepsilon' + \varepsilon_0)^2 + \varepsilon''^2}\right]\rho_1{}^2, \tag{2.8}$$

$$\beta_\pm = \beta_0 - c_1\beta_0\left[\frac{(\mu_1' \pm \mu_2')^2 - \mu_0{}^2 + (\mu_1'' \pm \mu_2'')^2}{(\mu_1' \pm \mu_2' + \mu_0)^2 + (\mu_1'' \pm \mu_2'')^2} + \right.$$
$$\left. + c_2\frac{\varepsilon'^2 - \varepsilon_0{}^2 + \varepsilon''^2}{(\varepsilon' + \varepsilon_0)^2 + \varepsilon''^2}\right]\rho_1{}^2. \tag{2.9}$$

§ 3. *Faraday rotation and ellipticity.* The electric fields of the two circularly polarized components orginally constituting the TE$_{11}$-wave in their dependence on the time t, the coordinate z measured along the guide in the direction of propagation and the azimuth ϑ around the axis of the guide, can be written as

$$\begin{aligned} \boldsymbol{E}_+ &= \hat{\boldsymbol{E}}_+ \exp(-\alpha_+ z) \exp j(\omega t + \vartheta - \beta_+ z), \\ \boldsymbol{E}_- &= \hat{\boldsymbol{E}}_- \exp(-\alpha_- z) \exp j(\omega t - \vartheta - \beta_- z), \end{aligned} \tag{2.10}$$

$\boldsymbol{E}_+$, $\boldsymbol{E}_-$, $\hat{\boldsymbol{E}}_+$, $\hat{\boldsymbol{E}}_-$ being perpendicular to the axis of the guide. Let us assume that for $z = 0$ we have equal amplitudes so that $\hat{\boldsymbol{E}}_+ = \hat{\boldsymbol{E}}_- = \hat{\boldsymbol{E}}$. The result of the superposition of the two expressions (2.10) can then be written as

$$\begin{aligned} \boldsymbol{E} = \boldsymbol{E}_+ + \boldsymbol{E}_- = 2\hat{\boldsymbol{E}} \exp[-\tfrac{1}{2}(\alpha_+ + \alpha_-)z] \exp j[\omega t - \tfrac{1}{2}(\beta_+ + \beta_-)z]. \\ .\{\cosh[-\tfrac{1}{2}(\alpha_+ - \alpha_-)z] \cos[\vartheta - \tfrac{1}{2}(\beta_+ - \beta_-)z] + \\ + j \sinh[-\tfrac{1}{2}(\alpha_+ - \alpha_-)z] \sin[\vartheta - \tfrac{1}{2}(\beta_+ - \beta_-)z]\}. \end{aligned} \tag{2.11}$$

From the factor in brackets { } in (2.11) it appears that for a given z the vector $\boldsymbol{E}$ consists of two components, 90° out of phase in time, the first of which has its maximum value for $\vartheta = \frac{1}{2}(\beta_+ - \beta_-)z$, the second for $\vartheta = \frac{1}{2}(\beta_+ - \beta_-)z + \frac{1}{2}\pi$. We see thus that on passing through a distance z the direction of maximum $\boldsymbol{E}$ for both components turns through an angle

$$\vartheta = \tfrac{1}{2}(\beta_+ - \beta_-)z. \tag{2.12}$$

The rotation over unit distance

$$\Theta = \tfrac{1}{2}(\beta_+ - \beta_-) \tag{2.13}$$

is called the Faraday rotation. The ratio of the maximum values of the two components is suitably called the ellipticity and is according to (2.11) given by

$$\eta = \coth \tfrac{1}{2}(\alpha_+ - \alpha_-)z. \tag{2.14}$$

By means of (2.8), (2.9, (2.5) and (2.6) ϑ and η as given by (2.12) and (2.14) can be expressed in terms of the elements of the gyromagnetic permeability tensor and the dielectric constant of the ferromagnetic material, together with the angular frequency ω, the propagation constant γ_0 of the empty guide and the radii ρ_0 and ρ_1 of guide and rod.

From substitution of (2.8) and (2.9) in (2.12) and (2.14) it appears that due to cancellation of terms the dielectric behaviour does not enter into the quantities ϑ and η.

CHAPTER III. EXPERIMENTAL ARRANGEMENTS

§ 4. *The materials used and their preparation.* The materials studied were the same as those used by van Trier[1]), viz. Ferroxcube IV, A, B, C, D, E, prepared at the Philips Laboratories in Eindhoven. They are nickel zinc ferrites with nickel and zinc in different proportions, produced by a sintering process which gives rise to a certain porosity. We repeat in table I the data on the chemical composition, specific gravity and porosity which have already been given by van Trier.

TABLE I

Ferroxcube	Chemical composition in mol %		Specific gravity	Porosity %
	NiO	ZnO		
IV A	17.5	33.2	4.45	16.6
IV B	24.9	24.9	4.80	11.0
IV C	31.7	16.5	4.52	16.2
IV D	39.0	9.4	3.98	26.2
IV E	48.2	0.7	3.80	29.5

In the Faraday rotation experiments the rods of ferrite were the ones investigated by van Trier. The method of their preparation has been described by him in detail.

The ferrite spheres for the resonance absorption experiments were obtained as follows. Samples of roughly equal dimensions in all three directions were cut from the material. These samples were placed into a vertical cylinder, the side wall of which was covered on the inside with emery paper. The bottom of the cylinder was closed, the top contained an orifice covered with gauze, permitting the passage of air. The samples were introduced into the cylinder and by means of a strong air jet, blown tangentially into the cylinder through the side wall, were violently thrown about, finally obtaining a spherical shape. On continuing the process the spheres could be ground down to smaller diameters. By observing the rolling of the spheres on a slightly inclined plane glass plate their roundness could be checked, imperfections manifesting themselves by deviations from rectilinear motion.

§ 5. *Electronic equipment for the study of the Faraday effect in rods of ferrite.* Fig. 1 represents the apparatus employed in the form of a block diagram. The klystron was of the type 723 A/B, working in the 3 cm-band. The electromagnetic wave emitted passed a wavemeter, furnishing the frequency, a calibrated variable attenuator and a uniline which provided the decoupling of the klystron. The wave then entered a rectangular wave guide of such dimensions that only the TE_{01}-mode can be propagated. This wave guide gradually changed over into a round wave guide, called the rotator, in which the TE_{01}-mode becomes a TE_{11}-mode. The round wave guide was composed of two identical parts which could be rotated with respect to each other around their common axis. The second part changed continuously into a rectangular guide of the same dimensions as the one preceding the first part, bearing a crystal detector at its end. The detector is connected to a galvanometer. The angle through which the second part of the rotator was turned with respect to the first part could be read on a scale.

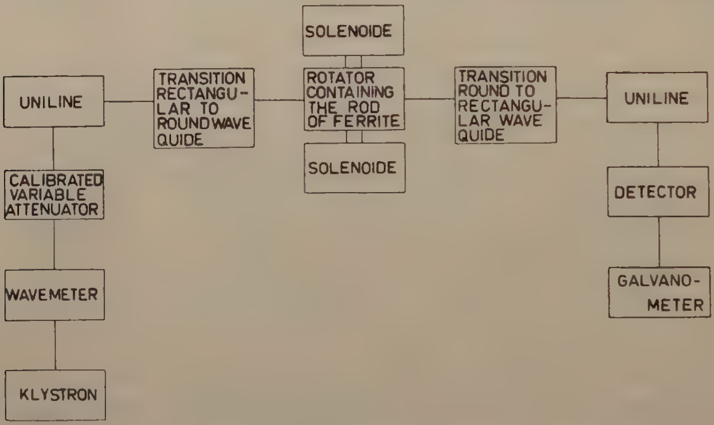
SOLENOIDE
UNILINE
TRANSITION RECTANGULAR TO ROUND WAVE GUIDE
ROTATOR CONTAINING THE ROD OF FERRITE
TRANSITION ROUND TO RECTANGULAR WAVE GUIDE
UNILINE
SOLENOIDE
CALIBRATED VARIABLE ATTENUATOR
DETECTOR
WAVEMETER
GALVANOMETER
KLYSTRON

Fig. 1. Block diagram of the Faraday rotation equipment.

In each part of the rotator near its outward end a plate of conducting material (paper covered with carbon black) through the axis and parallel to the long side of the attached rectangular wave guide was present. This plate absorbed any component wave of which the plane of polarization coincided with it, the component wave polarized perpendicular to the plate not suffering any damping.

In the middle of the rotator along its axis the rods of ferrite to be investigated were situated. They were supported by a wedge of (rigid) foam plastic attached to the inside of a hollow cylinder of the same material which was then introduced into the guide as shown in fig. 2. In mounting the rod on the wedge care was taken by means of a special metal fitting to place the rod precisely in a concentric position. The electromagnetic behaviour of the foam plastic is identical with that of air (or of free space) within the accuracy of our measurements. The method of supporting the rod was so chosen as to have a free channel along it through which air could be passed. By pre-cooling or pre-heating the air current the temperature of the rod could be varied. A solenoid around the rotator could furnish a longitudinal magnetic field. The construction and the field of this solenoid will be considered in § 6.

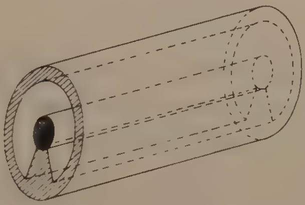

Fig. 2. Attachment of the ferrite rod to the foam plastic cylinder.

Before the rod was introduced into the rotator, the zero reading of the rotator scale could be determined by turning the second half into such a position that a maximum signal was read on the galvanometer. The position 90° further on where the signal is a minimum could be fixed still more accurately because for it the power entering the rotator could be chosen larger, giving a big deflection of the galvanometer already for small deviations from the minimum position. After the rod had been introduced, it was first demagnetized by an alternating current through the solenoid. Then the rotation angle to which the rod gave rise when a static magnetic field was generated parallel to it by means of a direct current through the solenoid could be measured by finding the new position of minimum reading.

With the aid of the variable calibrated attenuator we could determine the intensity ratio for the positions of maximum and minimum reading and thus the square of the ellipticity, conveniently expressed in decibels. Similarly by measuring the intensity ratio for the empty guide and the guide containing the magnetized ferrite rod for the position of maximum reading we could obtain the insertion loss in decibels.

§ 6. *The solenoid and its magnetic field.* The static magnetic field to be applied to the ferrite rod in the rotator was produced by a solenoid consisting of two separate parts which were placed end to end as shown in fig. 3, where also the dimensions are indicated. The end plates of each part, made of brass, were joined by a brass cylinder. They were water-cooled, no further cooling being used. The windings of insulated copper wire, 3 mm in diameter, were placed around the cylinder without additional insulation. A thermocouple, introduced in the region of the coils which became warmest, allowed to measure the temperature there.

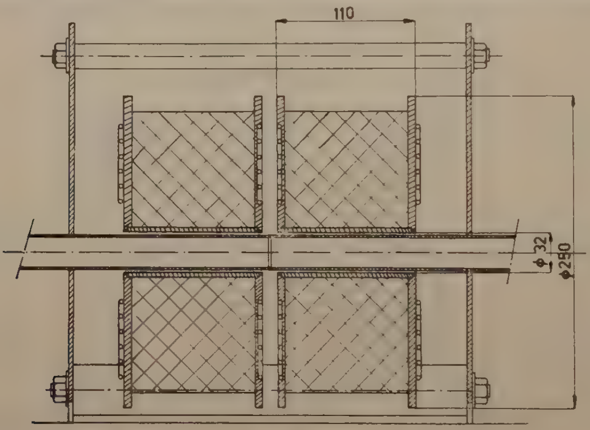

Fig. 3. Watercooled solenoids for the Faraday rotation experiments. Distances in mm.

The magnetic field strength along the axis of the solenoid was measured by turning a small test coil quickly through 180° from a parallel into an antiparallel position and by taking the reading of a ballistic galvanometer connected to it. The scale of the galvanometer had been calibrated with magnetic fields of known strength, very accurately determined by means of proton-resonance. Fig. 4 represents the axial field strength for a current of 12 A through the windings along the central 12 cm of the pair of solenoids when in an adjacent position.

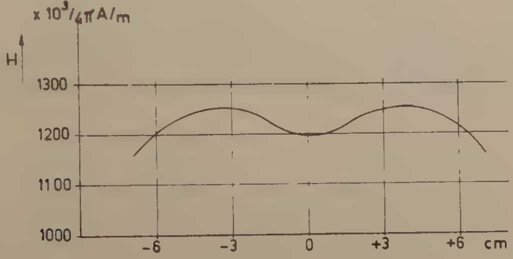

Fig. 4. Axial field strength in the solenoid of fig. 3 at a current of 12A.

The field strength could be varied continuously from 0 to 5 × 10^5 A/m. At the higher values the time available for measurements was limited by the heating of the coils. With a view to the insulation a maximum temperature of 120°C was permissible.

By separating the solenoids and introducing iron cores inside, fairly homogeneous magnetic fields of considerably greater strength could be produced in a limited region between the end surfaces of these cores.

§ 7. *Arrangement for measuring the magnetization of the rods.* In connection with the theoretical interpretation of the Faraday rotation and ellipticity observed in our experiments on ferrite rods a knowledge of the magnetization produced by the static magnetic field is required. The arrangement for determining this consisted of two short coils in series with a galvanometer. The two coils were identical, except in being wound in opposite direction. In each of the two parts of the solenoid described in § 6 one coil was placed coaxially at the centre, the two parts being sufficiently separated from each other so that no magnetic coupling between the coils occurred. If the same current was passed through the two parts of the solenoid, then on varying this current or on reversing its direction the galvanometer did not show a deflection by reason of the opposite sense of winding of the coils.

On introducing a ferrite rod into one of the coils an additional flux proportional to the magnetization of the rod passed through this coil, and when the current through the parts of the solenoid was reversed, a deflection of the galvanometer was caused. Repeating the procedure with a nickel rod of the same dimensions as the ferrite rod, the ratio of the galvanometer deflections gave the ratio of the magnetizations in the two cases. From the known magnetic properties of nickel [3]) the magnetization of the ferrite rod could then be computed.

§ 8. *Equipment for regulating and measuring the temperature.* For measurements above room temperature the air that passes the ferrite rod through the channel in the foam plastic mounting mentioned in § 5 was pumped through the interspace between two concentric tubes, on the inner one of which an electrically heated spiral was wound. By adjusting the heating current of the spiral and the speed of the air, the temperature could be varied from room temperature to about 150°C, the softening point of the solder connecting the sections of the wave guide. For measurements below room temperature the air was pumped through a helical tube in a heat exchanger connected to a frigidaire cooling-machine. The temperature of the cold air could either be varied by changing its speed or by admixing air of room temperature, the temperature range being from —40°C to room temperature.

The temperature of the ferrite rods in the rotator was measured with two calibrated constantan-copper thermocouples, one placed at the entrance, the other at the exit of the rotator. The average of the two temperatures was taken as the temperature of the rod. This procedure was justified by some test-runs in which a third thermocouple was placed next to the rod near its centre.

§ 9. *Electronic equipment for the study of resonance in spherical probes of ferrite.* The electronic set-up for the measurements in question is shown diagrammatically in fig. 5. The klystron was sawtooth-modulated in its repeller tension. The modulated signal passed a wavemeter, a variable attenuator and a uniline, arriving in the magic tee. One of the other guides of this magic tee was closed by a shortcircuit piston, the other two were respectively connected to a crystal detector and a half-wavelength cavity. The coupling of this cavity to the guide was achieved by means of a coupling hole. The small sphere to be studied was supported in the cavity on a slab of foam plastic in such a position that the high frequency magnetic and electric field there had a maximum value and the value zero respectively. The static magnetic field could be applied to the cavity by means of the solenoid already described in § 6. Without this field the mode of the klystron appeared on the oscilloscope when its base was modulated in the same way as the klystron.

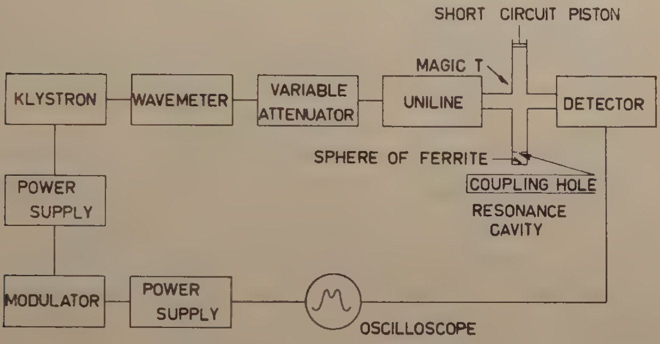

Fig. 5. Block diagram of the resonance equipment for measurements on spheres.

When in the absence of a static magnetic field the frequency was adjusted so as to make half the wavelength equal to the length of the cavity, a dip could be seen in the mode of the klystron which is due to the absorption of the cavity. Care was taken to have this dip at the centre of the mode on the oscilloscope. On gradually applying the static magnetic field in a direction perpendicular to that of the high frequency magnetic field at first a decrease of the dip and a shift to one side were observed as ferromagnetic resonance in the sphere was approached. Indeed, under these conditions the presence of the sphere will noticeably alter the resonance frequency of the cavity as well as its quality factor. On increasing the static field the dip attained a minimum value, at the same time returning to its original position. On still further increasing the static field the dip passed to the other side and gradually increased again. The minimum of the dip corresponds to the maximum of ferromagnetic resonance absorption.

The value of the static magnetic field at which this occurs will be denoted by H_r. By the relation

$$\omega = \Gamma H_r, \tag{3.1}$$

where ω is the angular frequency of the wave used, as determined by the wavemeter, we can introduce the gyromagnetic ratio Γ which thus can be found experimentally.

Measurements similar to the ones described could be performed with a transmission cavity having a coupling hole at either end and replacing the magic tee in fig. 5. The length of the cavity must be an integral number of half wavelengths. Actually it was equal to one wavelength. The procedure was otherwise the same as in the previous case.

It should be noted that the dielectric behaviour of the sphere was immaterial for the resonance phenomenon discussed. In the first place this behaviour is not influenced by a static magnetic field, but besides, as already stated, the position of the sphere in our measurements was so chosen as to make the high frequency electric field near it practically zero.

CHAPTER IV. THE EXPERIMENTAL RESULTS

§ 10. *Faraday rotation and ellipticity measurements on ferrite rods.* With the electric equipment described in §§ 5 and 6 the Faraday rotation and ellipticity produced in the TE_{11}-wave of a round wave guide by concentric ferrite rods of length $l = 3.45$ cm as mentioned in § 4 were investigated at a wavelength $\lambda = 3.2$ cm and as a function of the static longitudinal magnetic field H_0, for various radii ρ_1 of the rods and at three temperatures $T = -32$°C, room temperature (20–22°C), 120°C.

In figs 6–11 the results for the dependence on H_0 at room temperature are represented for rods of the various kinds of ferrite, having respectively radii of 0.5 (in case of rod IV C this was 0.6), 1.0 and 1.5 mm. Figs 6, 8 and 10 show the rotation angle ϑ as defined in § 3 in degrees, figs 7, 9 and 11 the ellipticity η, or more precisely $20_{10} \log \eta$ in decibels. In the last three figures the insertion loss as discussed in § 5, i.e. the intensity ratio at the position of maximum reading for the empty guide and the guide containing the magnetized rod, is also given, expressed in decibels. Actually this intensity ratio was found by first measuring once and for all the ratio for the empty guide and the guide containing the demagnetized rod, and thereupon the ratio for the guide containing the demagnetized rod and the guide containing the magnetized rod.

From these figures we see at once that the value of H_0 at which the curve for the Faraday rotation crosses the axis ($\vartheta = 0$) in all cases is the same (within the accuracy of the curves) as the value

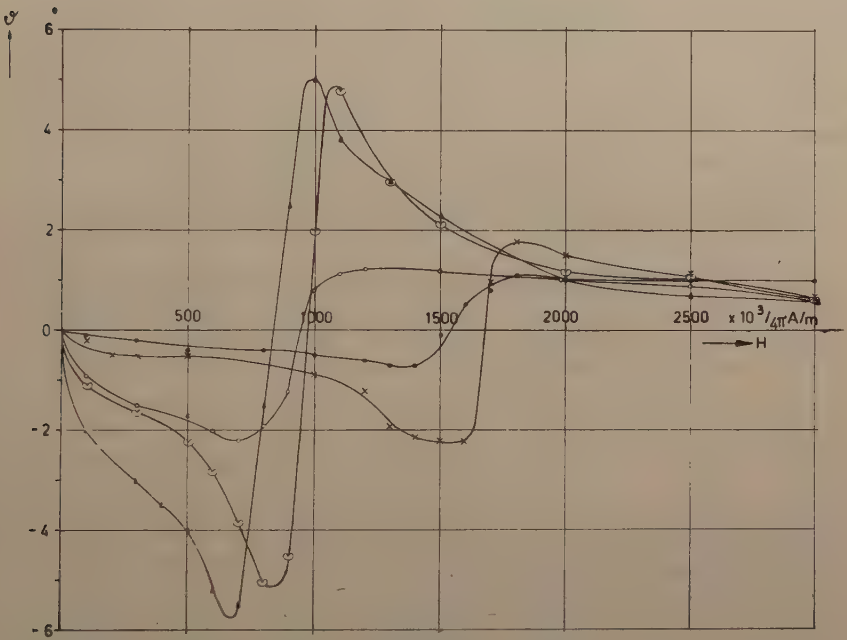

Fig. 6. The rotation angle ϑ vs. the static magnetic field strength H_0 for rods of the ferrites A(×), B(∞), C(△), D(⊙), E(.) at a wavelength $\lambda =$ $= 3.2$ cm and a temperature $T = 22$°C. Length of the rods $1 = 3.5$ cm, radius $\rho_1 = 0.05$ cm for A, B, D and E and 0.06 cm for C.

at which the ellipticity curve for the same rod has a minimum. This is also true for the other temperatures, —32°C and 120°C, for which the curves have not been included here since they are of the same type as those of figs 6–11. We may hence call this value H_r of H_0 the effective resonance value.

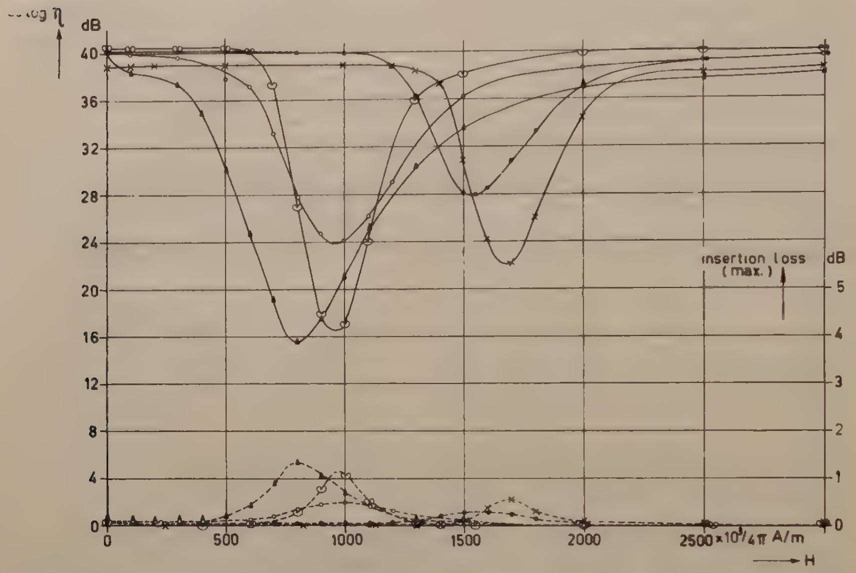

Fig. 7. The measured ellipticity vs. the static magnetic field strength H_0 for rods of the ferrites A(×), B(∞), C(△), D(⊙) and E(. .) at a wavelength $\lambda = 3.2$ cm and a temperature $T = 22$°C. Length of the rods $l = 3.5$ cm, radius $\rho_1 = 0.05$ cm for A, B, D and E and 0.06 cm for C.

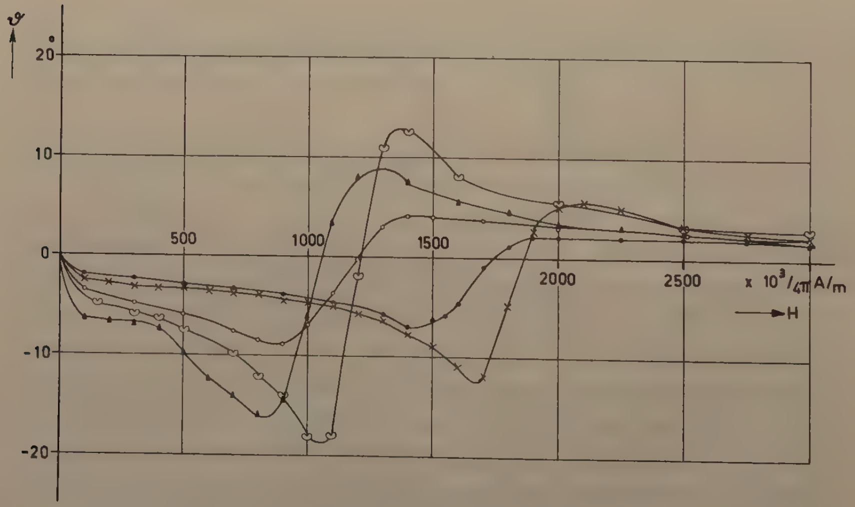

Fig. 8. Same as fig. 6, but for $\rho_1 = 0.1$ cm.

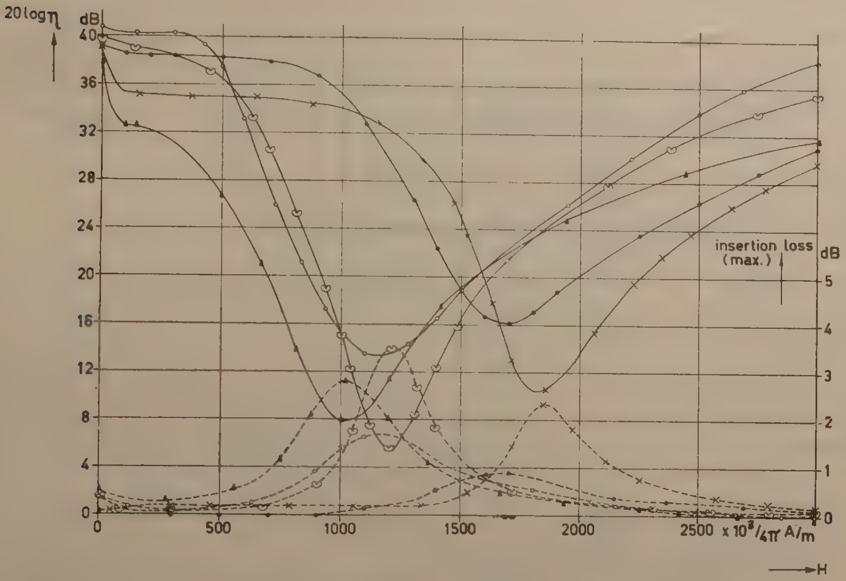

Fig. 9. Same as fig. 7, but for $\rho_1 = 0.1$ cm.

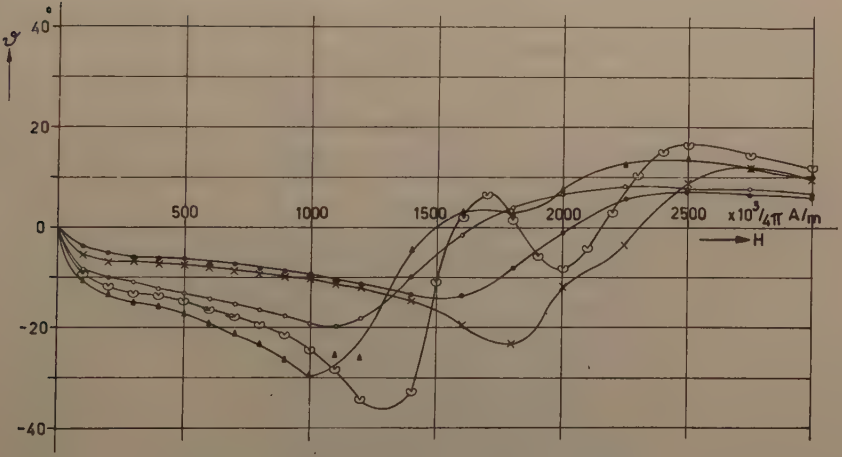

Fig. 10. Same as fig. 6, but for $\rho_1 = 0.15$ cm.

It appears from our measurements that H_r is a function of the radius ρ_1 of the rods. In figs 12, 13 and 14 H_r is shown for the different kinds of ferrite as a function of ρ_1 for $T = -32°\text{C}$, room

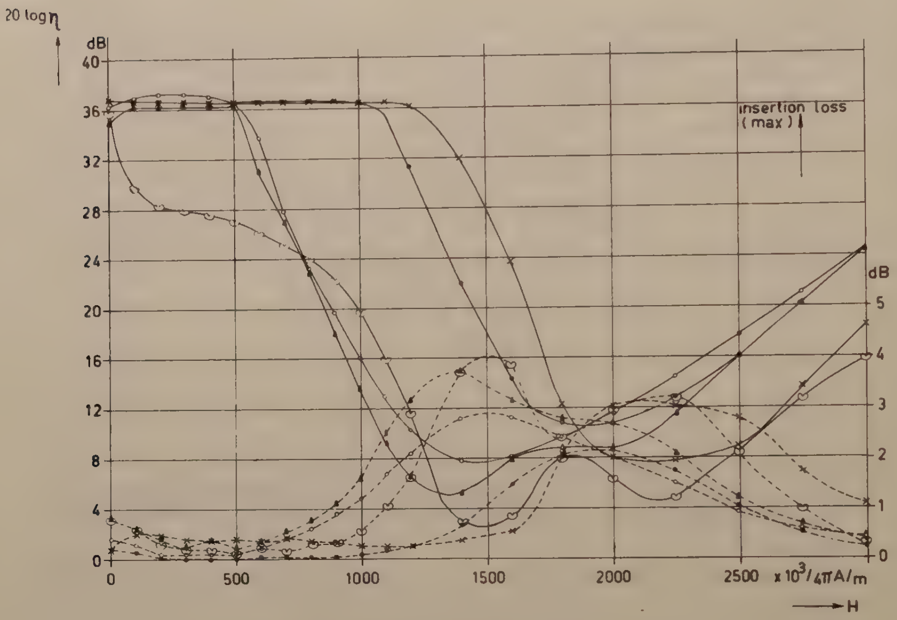

Fig. 11. Same as fig. 7, but for $\rho_1 = 0.15$ cm.

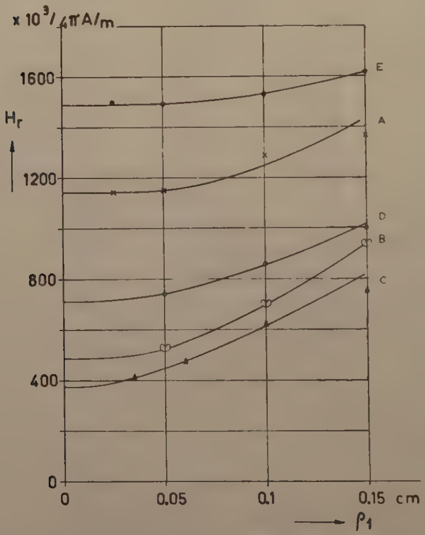

Fig. 12. The magnetic field strength at resonance H_r vs. the radius ρ_1 for rods of the ferrities A, B, C, D and E. $\lambda = 3.2$ cm, $T = -32$°C.

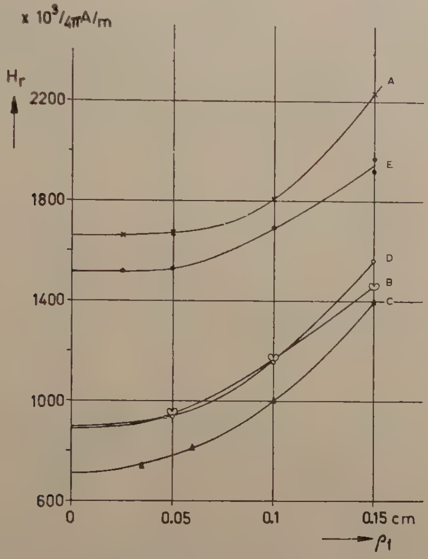

Fig. 13. Same as fig. 12, but for $T = 22°C$.

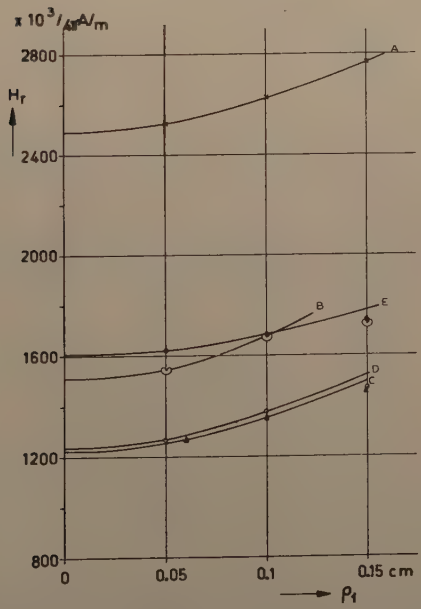

Fig. 14. Same as fig. 12, but for $T = 120°C$.

temperature and 120°C. For some rods with a radius smaller than 0.5 mm no complete resonance curves have been obtained, but only the immediate neighbourhood of the resonance value H_r has been investigated in order to find H_r. These values of H_r have been included in figs 12, 13 and 14.

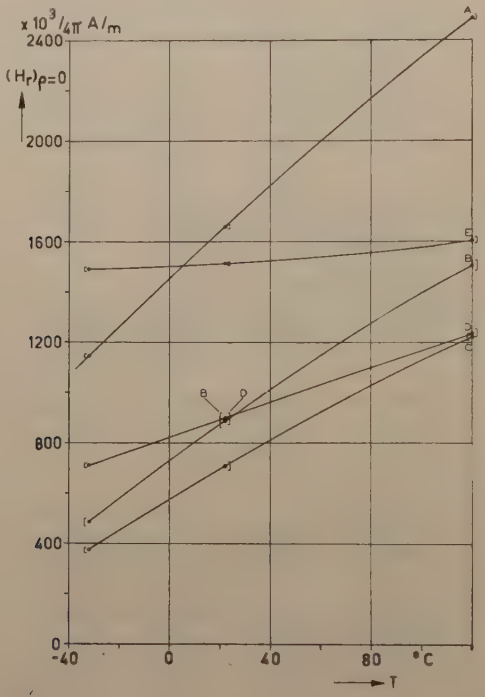

Fig. 15. The magnetic field strength at resonance H_r, extrapolated to vanishing radius ρ_1 of the ferrite rods, vs. the temperature. The brackets indicate the uncertainty of the extrapolation.

The phenomenological treatment of Chapter II is an approximation, valid only in the case of small radii ρ_1. In order to be able in Chapter V et seq. to relate the atomistic theory of ferromagnetic resonance to our measurements we have extrapolated H_r in figs 12, 13 and 14 to $\rho_1 = 0$ and represented these extrapolated values of H_r as a function of the temperature in fig. 15.

§ 11. *Sources of error in the rotation and ellipticity measurements.* The phenomenological theory of Chapter II for the Faraday rotation and ellipticity is based on the assumption that both the wave guide and the concentric rod are infinitely extended. The rods used by us were of finite length, and it is hence conceivable that end effects would introduce an error. It is to be expected that the relative size of this error will increase with increasing radius of the rods. Measurements of the Faraday rotation were therefore carried out for rods of the same radius and different lengths to see in how far the rotation angle was proportional to the length. For the rods ultimately used by us strict proportionality was found within the accuracy of the angular readings of about 0.1° if the radius did not exceed 1.5 mm. End corrections may then be neglected.

The error in the readings of the attenuator used to determine the ellipticity and insertion loss is about 0.1 db.

As can be seen from fig. 4, the static longitudinal magnetic field produced by the solenoid is not quite constant over the length $l = 3.45$ cm of the rods used. Since the rods were placed at the centre of the solenoid, the deviation from the average is about 1%.

The accuracy with which the temperature was defined was about 1°C. For this reason the data collected under the heading "room temperature" have been considered together, although actually this temperature lay between 20 and 22°C.

§ 12. *Measurements of the magnetization.* The magnetization for the various ferrite rods has been measured as a function of the magnetic field strength in the way described in § 7, for temperatures of —27°, 20° and 100°C. The results are given in fig. 16. The magnetization at saturation following from this figure is represented as a function of the temperature in fig. 17.

Some measurements of the initial permeability have also been made, the results being collected in table II.

TABLE II

$T = 20°C$						
Ferrite	A'	A	B	C	D	E
Initial permeability . . .	736	342	286	138	54.1	16.6

§ 13. *Resonance measurements on ferrite spheres.* Spheres of the ferrites mentioned in § 4, prepared in the way described there, were studied for their behaviour in the presence of a static and a high frequency magnetic field by means of the apparatus discussed in § 9. At the wavelength $\lambda = 3.2$ cm a sphere of radius 0.2 mm, at $\lambda = 1.6$ cm and 1.25 cm a sphere of radius 0.125 mm was used.

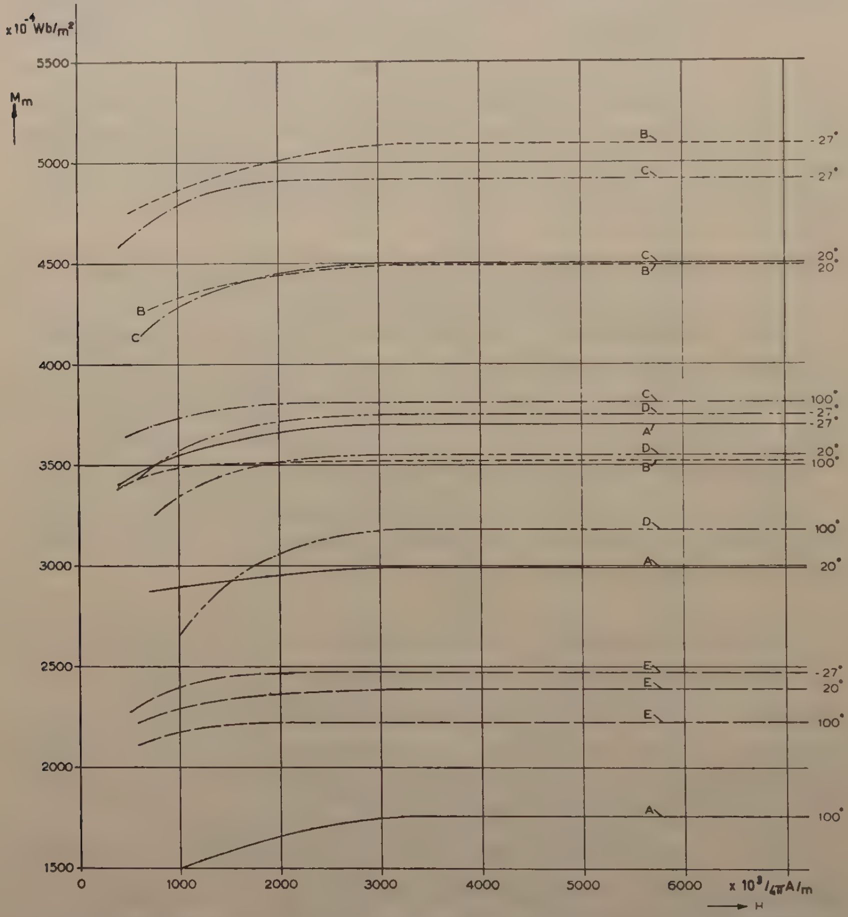

Fig. 16. The measured magnetization M_0 for the rods of ferrite A, B, C, D, E vs. the static magnetic field strength H_0 at temperatures $T = -27°C$, $+20°C$ and $100°C$.

From the known angular frequency ω and the value H_r of the static magnetic field at which resonance occurred the gyromagnetic ratio Γ as defined by (3.1) could be determined.

In view of the theoretical discussion in the following chapters we have expressed the Γ thus found in terms of the quantity $\mu_0\, e/2m$ as unit, where e is the electronic charge and m the electronic mass:

$$\Gamma = g\,\frac{\mu_0 e}{2m}\,. \tag{4.1}$$

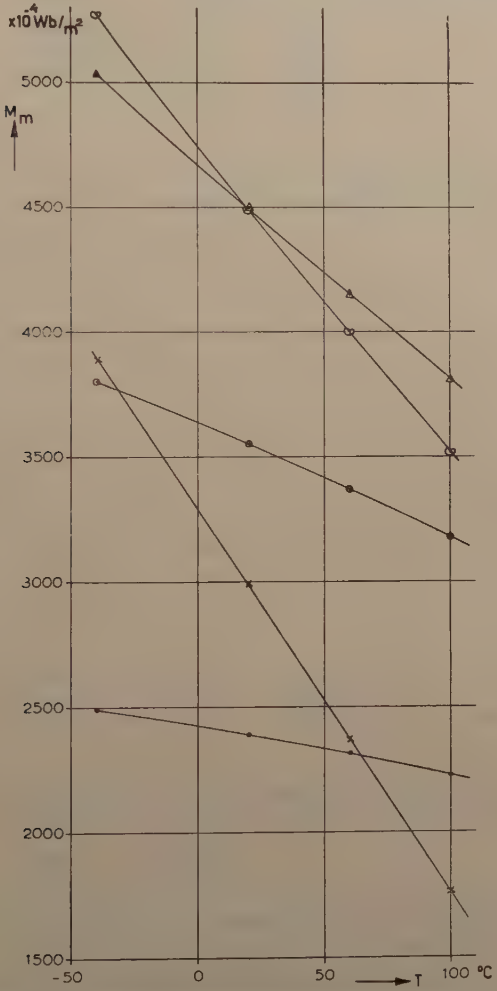

Fig. 17. The saturation magnetization for the ferrites A, B, C, D and E vs. the temperature.

For reasons that will become apparent later the quantity g, commonly called the spectroscopic splitting-factor, thus obtained is an effective one; we have denoted it by g_{eff}.

In figs 18–22 some of the results of our measurements with reference to g_{eff} have been represented graphically. Figs 18 and 19 show g_{eff} for the various ferrites as a function of the temperature T, the wavelength used being $\lambda = 3.2$ and 1.6 cm respectively. Figs 20, 21 and 22 show the dependence of g_{eff} on λ for the three temperatures $T = -30°$, 20° and 100°C. This dependence has also been observed by Okamura and his collaborators [4]).

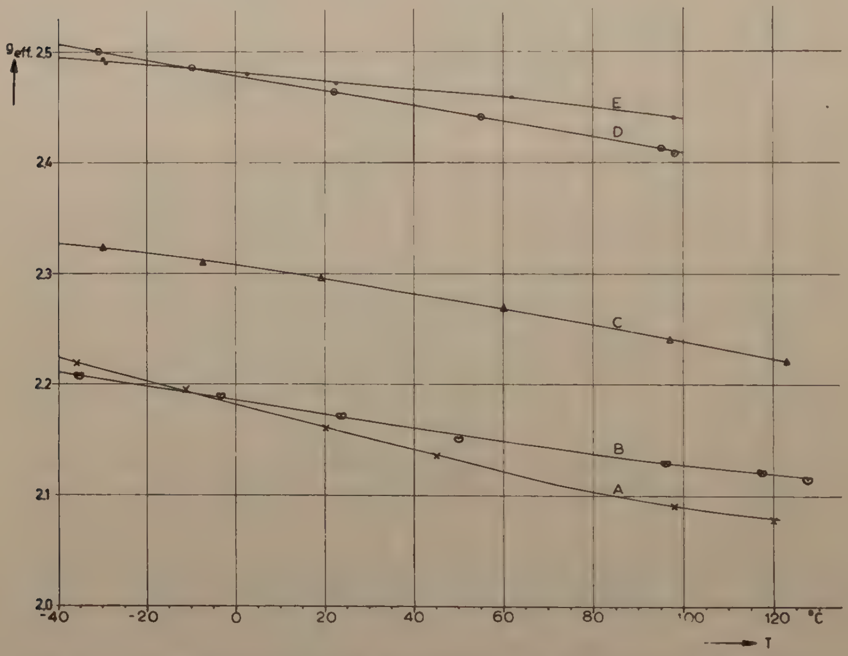

Fig. 18. The effective g-value for the ferrites A, B, C, D and E vs. the temperature at a wavelength $\lambda = 3.2$ cm, determined for spheres of radius 0.02 cm.

§ 14. *Sources of error in the resonance measurements.* In the resonance measurements on spheres reasonable care has to be taken to mount the spheres in the proper position on the axis inside the cavity. We have investigated how the value of g_{eff}, as defined in the preceding paragraph, is affected when the sphere is placed very close to the bottom of the cavity. Fig. 23 illustrates what happens for the case of a sphere of radius 0.125 mm. The explanation must be sought in the formation of images [5]) [6]). Reference [6]) reports similar effects for a case of dielectric measurements.

Experimentally we also found that the value of g_{eff} depended somewhat on the diameter of the coupling holes both for reflection and transmission cavities. Fig. 24 illustrates this. The g-values obtained for different diameters of the coupling holes should

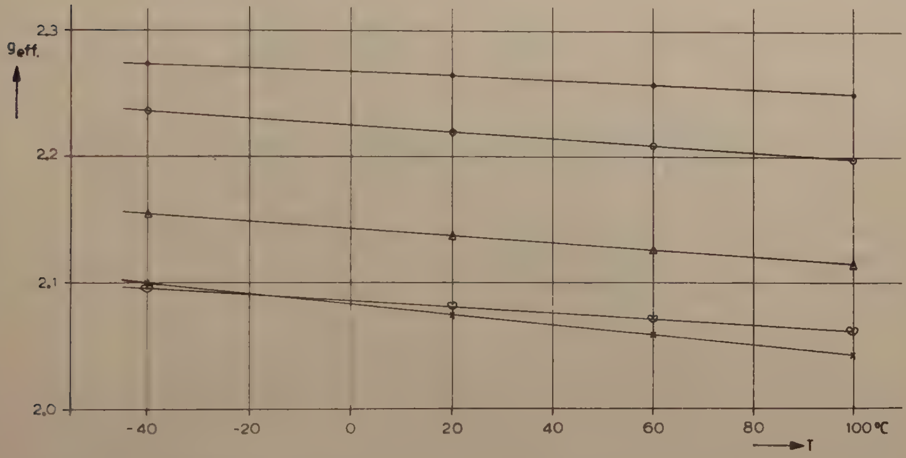

Fig. 19. The effective g-value for the ferrites A, B, C, D and E vs. the temperature at a wavelength $\lambda = 1.6$ cm for spheres of radius 0.0125 cm.

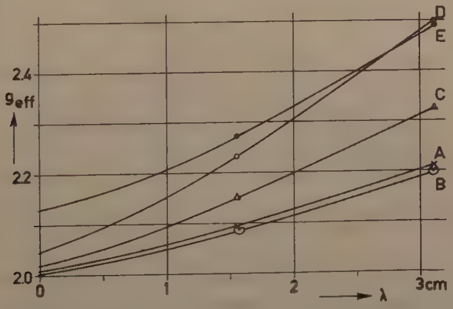

Fig. 20. The effective g-value for the ferrites A, B, C, D and E vs. the wavelength at a temperature $T = -30°\text{C}$.

therefore be extrapolated to zero diameter for very accurate determinations.

On account of the small dimensions of the spheres the skin effect played no rôle in our measurements and the inaccuracy in the values of the static magnetic field was less than in the rotation experiments, say 0.5%. The inaccuracy of the temperature T was the same in both cases, that is to say of the order of 1%. The values of g_{eff} are subject to an error of the same size.

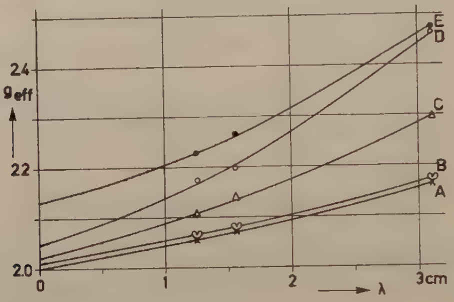

Fig. 21. Same as fig. 20, but for T = 20°C.

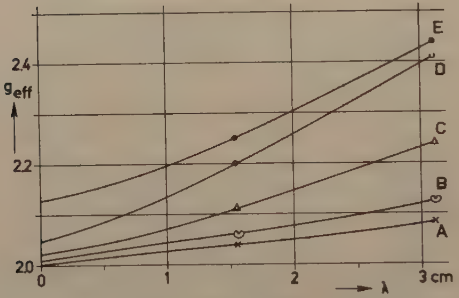

Fig. 22. Same as fig. 20, but for T = 100°C.

It may be mentioned here that we checked our results for H_r with a Pound stabilized measuring equipment. Within an error of 0.5% agreement was found. With this apparatus the half-width ΔH_{oe} of the resonance curve (width at half the height of the maximum) could also be determined. The results are shown in table III. The measurements at $\lambda = 3.2$ cm were made on a sphere of 0.2 mm radius, those at $\lambda = 1.25$ cm on a sphere of 0.125 mm radius.

TABLE III

λ cm	3.2		1.25
T °C	− 40	20	20
Ferrite	ΔH_{oe} Ø	ΔH_{oe} Ø	ΔH_{oe} Ø
IV A	376	415	690
IV B	294	259	570
IV C	521	458	845
IV D	694	669	1265
IV E	910	856	

CHAPTER V. INTERPRETATION OF THE ROTATION AND ELLIPTICITY MEASUREMENTS IN TERMS OF FERROMAGNETIC RESONANCE

§ 15. *The permeability tensor.* The theory of ferromagnetic resonance starts from the fundamental equation, first given by Landau and Lifschitz [7]), for the time dependence of the magnetization $\boldsymbol{M}$

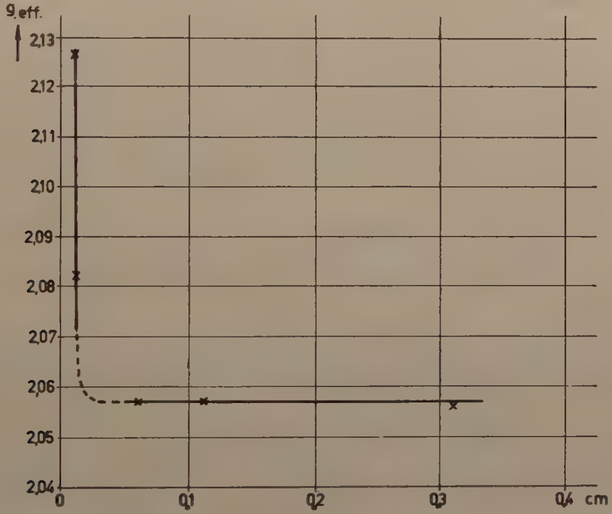

Fig. 23. The effective g-value for a sphere of ferrite A of radius 0.0125 cm at a temperature $T = 20°\text{C}$ and a wavelength $\lambda = 1.25$ cm as a function of the distance between the centre of the sphere and the wall: "Wall effect".

$$\frac{\mathrm{d}\boldsymbol{M}}{\mathrm{d}t} = \Gamma \boldsymbol{M} \times \boldsymbol{H} - \frac{\kappa \Gamma}{M} \boldsymbol{M} \times (\boldsymbol{M} \times \boldsymbol{H}), \tag{5.1}$$

where Γ is the gyromagnetic ratio, already referred to in § 13, $\boldsymbol{H}$

the local magnetic field strength acting on the magnetization and κ a damping constant. Without the damping term (5.1) formed the basis of the original considerations of Kittel [8]).

In the thesis of van Trier [1]) previously mentioned expressions for the elements of the gyromagnetic permeability tensor (2.1) have

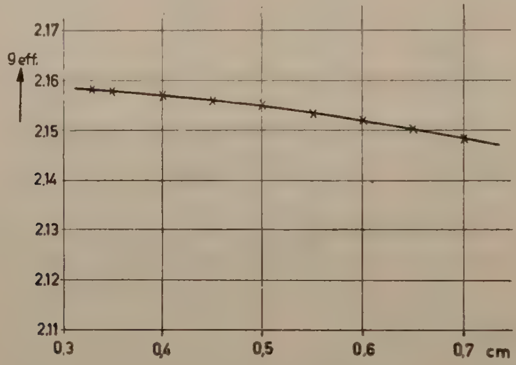

Fig. 24. The effective g-value for a sphere of ferrite A of radius 0.02 cm at a temperature $T = 20°\text{C}$ and a wavelength $\lambda = 3.2$ cm as a function of the radius of the coupling hole in the resonance cavity.

been derived from (5.1) for the case of no losses $\kappa = 0$. The procedure followed by him can be generalized to the case $\kappa \neq 0$.

If in a given region of the ferromagnetic medium we choose a local coordinate system such that its z-axis, carrying the unit vector $\boldsymbol{k}$, coincides with the static part of the magnetic field $H_0\boldsymbol{k}$ there, then the magnetic field may be written as

$$\boldsymbol{H} = H_0\boldsymbol{k} + \boldsymbol{H}_1 \exp j\omega t, \tag{5.2}$$

the second term on the right-hand side being the high frequency part of the magnetic field. Similarly we may split the magnetization into its static and high frequency parts:

$$\boldsymbol{M} = M_0\boldsymbol{k} + \boldsymbol{M}_1 \exp j\omega t. \tag{5.3}$$

On the assumption, always realized in our experiments, that $H_1 \ll H_0$, $M_1 \ll M_0$ we may on substitution of (5.2) and (5.3) in (5.1) neglect terms of second and third degree in quantities bearing the index 1 and get thus

$$j\omega\boldsymbol{M}_1 = \Gamma(H_0\boldsymbol{M}_1 - M_0\boldsymbol{H}_1)\times\boldsymbol{k} + \kappa\,\Gamma[(H_0\boldsymbol{M}_1 - M_0\boldsymbol{H}_1)\times\boldsymbol{k}]\times\boldsymbol{k}. \tag{5.4}$$

Writing the high frequency part of the magnetic induction with the aid of the gyromagnetic permeability tensor (2.1), (2.2) as

$$\boldsymbol{B}_1 = \mu_0 \boldsymbol{H}_1 + \boldsymbol{M}_1 = ||\mu||\,\boldsymbol{H}_1$$

or in components

$$\left.\begin{aligned}
B_{1x} &= \mu_0 H_{1x} + M_{1x} = (\mu_1' - j\mu_1'')\,H_{1x} - j(\mu_2' - j\mu_2'')\,H_{1y},\\
B_{1y} &= \mu_0 H_{1y} + M_{1y} = j(\mu_2' - j\mu_2'')\,H_{1x} + (\mu_1' - j\mu_1'')\,H_{1y},\\
B_{1z} &= \mu_0 H_{1z} + M_{1z} = (\mu_3' - j\mu_3'')\,H_{1z},
\end{aligned}\right\} \quad (5.5)$$

we find by solving (5.4) for the components of $\boldsymbol{M}_1$, substituting into (5.5) and equating the coefficients of H_{1x} and H_{1y} on the right and left

$$\mu_1' = \mu_0 + \frac{\Gamma^2 M_0 H_0 \{(1+\kappa^2)\,[(1+\kappa^2)\,\Gamma^2 H_0^2 - \omega^2] + 2\kappa^2\omega^2\}}{[(1+\kappa^2)\,\Gamma^2 H_0^2 - \omega^2]^2 + 4\kappa^2\omega^2\Gamma^2 H_0^2}, \quad (5.6)$$

$$\mu_1'' = \frac{\kappa\omega\Gamma M_0[(1+\kappa^2)\,\Gamma^2 H_0^2 + \omega^2]}{[(1+\kappa^2)\,\Gamma^2 H_0^2 - \omega^2]^2 + 4\kappa^2\omega^2\Gamma^2 H_0^2}, \quad (5.7)$$

$$\mu_2' = \frac{\omega\Gamma M_0[(1+\kappa^2)\,\Gamma^2 H_0^2 - \omega^2]}{[(1+\kappa^2)\,\Gamma^2 H_0^2 - \omega^2]^2 + 4\kappa^2\omega^2\Gamma^2 H_0^2}, \quad (5.8)$$

$$\mu_2'' = \frac{2\kappa\omega^2\Gamma^2 M_0 H_0}{[(1+\kappa^2)\,\Gamma^2 H_0^2 - \omega^2]^2 + 4\kappa^2\omega^2\Gamma^2 H_0^2}. \quad (5.9)$$

The quantities (5.6)–(5.9) may be termed the local values of the elements of the permeability tensor since they refer to the local coordinate system introduced. Let us now suppose

a) that the ferromagnetic medium is subjected to a homogeneous external static field $\boldsymbol{H}_{0e}$ of such magnitude as to give rise to magnetic saturation,

b) that the specimen used is of ellipsoidal shape and that in consequence the demagnetizing static field is also homogeneous,

c) that the fields due to crystal anisotropy and magnetostriction are negligible,

then both $\boldsymbol{H}_0$ and $\boldsymbol{M}_0$ will have the same magnitude and direction everywhere in the specimen and the expressions (5.6)–(5.9) may be regarded as the elements of the permeability tensor with respect to one and the same coordinate system with the z-axis in the direction of $\boldsymbol{H}_0$ at all points of the medium.

Both in our experiments on the Faraday rotation in rods and on ferromagnetic resonance in spheres the fields in the resonance region, of the order 1000–8000 oerstedt, were such that magnetic saturation was at least approximately realized, as can be seen by inspection of fig. 16. Also the rods used were so thin compared with their length that they may be identified with the limiting case of a very elongated ellipsoid for which the internal static field H_0 is practically equal to the external static field H_{0e} applied in a longitudinal direction, the demagnetizing field practically vanishing. Finally the anisotropy fields may indeed, at the field strengths of interest, be considered as small corrections.

A feature which we shall forget at present is the fact that the materials investigated, due to their porosity, actually are not homogeneous. The influence of the porosity will form the subject of the following chapters.

§ 16. *Ferromagnetic resonance in spheres.* Inside a sphere placed in a homogeneous external magnetic field the resultant magnetic field is equal to the external field diminished by one third of the magnetization divided by μ_0. Thus if the sphere is small compared with the wavelength of the high frequency field we have both

$$H_0 = H_{0e} - M_0/3\mu_0., \quad H_1 = H_{1e} - M_1/3\mu_0.$$

Let us take $\boldsymbol{H}_{0e}$ in the z-direction, $\boldsymbol{H}_{1e}$ in the x-direction. Then we find from (5.4)

$$\begin{aligned} j\omega M_{1x} &= \Gamma H_{0e} M_{1y} - \kappa\Gamma H_{0e} M_{1x} + \kappa\Gamma M_0 H_{1e}, \\ j\omega M_{1y} &= -\Gamma H_{0e} M_{1x} + \Gamma M_0 H_{1e} - \kappa\Gamma H_{0e} M_{1y}. \end{aligned}$$

Solving for M_{1x} and M_{1y} from these two equations, expressions are obtained with the denominator

$$[(1 + \kappa^2)\, \Gamma^2 H_{0e}{}^2 - \omega^2]^2 + 4\kappa^2\omega^2\Gamma^2 H_{0e}{}^2,$$

showing that resonance occurs for a value H_r of H_{0e} given by

$$\omega = \Gamma H_r \sqrt{1 + \kappa^2}. \tag{5.10}$$

Since we shall find later that κ in the ferrites studied averages about 0.05 and is never more than 0.1, we see that the damping correction influences (5.10) at most by $\frac{1}{2}\%$ and may hence be neglected in view of the accuracy of our measurements. The experimental definition of Γ as given in (3.1) is thereby justified.

§ 17. *Determination of the damping constant κ from the rotation and ellipticity measurements.* We proceed now to compute numerically from (5.6)–(5.9) the quantities μ_1', μ_1'', μ_2', μ_2'' for the frequency 9375 MHz, corresponding to the wavelength $\lambda = 3.2$ cm used in the Faraday rotation experiments, for various temperatures and for various values of the external field, which, as previously mentioned, may here be identified with the quantity H_0 in the above equations.

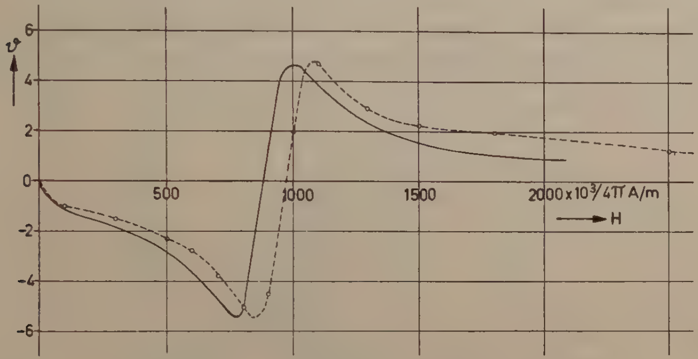

Fig. 25. Measured (---) and calculated (—) rotation angle ϑ as a function of the static magnetic field strength for a rod of ferrite B of length $l = 3.5$ cm and radius $\rho_1 = 0.05$ cm at a wavelength $\lambda = 3.2$ cm and a temperature $T = 20$°C. In the calculation the following values were used $\kappa = 0.032$, $g_{\text{eff}} = 2.12$, $M_0 = 0.456$ Wb/m².

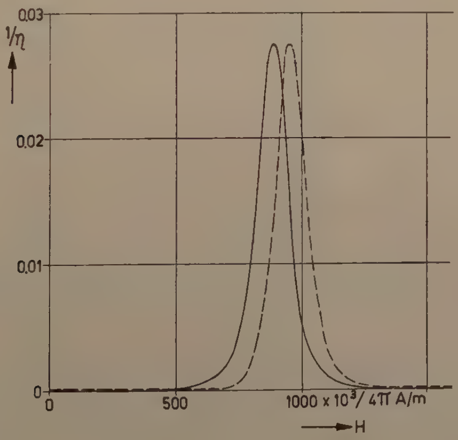

Fig. 26. Measured (---) and calculated (—) reciprocal ellipticity $1/\eta$ for the case of fig. 25.

For Γ we employ the value of the gyromagnetic ratio found from measurements of the resonance field H_r in a sphere of the same material and at the same frequency and temperature, as described in § 13. For M_0 we introduce the value of the magnetization at the temperature and magnetic field strength under consideration. Finally we assume a tentative value for κ.

The values of μ_1', μ_1'', μ_2', μ_2'' thus obtained are then substituted in the expressions (2.8) en (2.9) for the quantities $\alpha_\pm$ and $\beta_\pm$, which in their turn determine the value of the rotation angle ϑ and the ellipticity η according to (2.12) and (2.14).

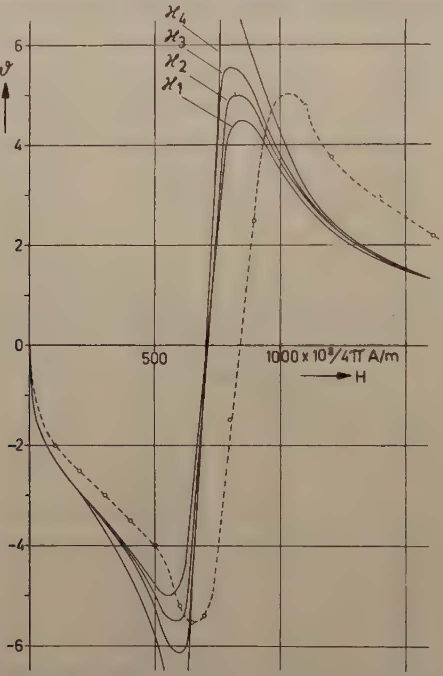

Fig. 27. Influence of the choice of κ on the calculated rotation angle ϑ for a rod of ferrite C of length $l = 3.5$ cm and radius $\rho_1 = 0.06$ cm at a wavelength $\lambda = 3.2$ cm and a temperature $T = 20$°C. In the calculation the following values were used $\kappa_1 = 0.05$, $\kappa_2 = 0.045$, $\kappa_3 = 0.04$, $\kappa_4 = 0.03$, $g_{\mathrm{eff}} = 2.244$, $M_0 = 0.456$ Wb/m^2.

Figs 25 and 26 show for a rod of ferroxcube IV B both the measured curves for ϑ and $1/\eta$ and the curves calculated in the way just described, using the value $\kappa = 0.032$ which gave the best fit.

It is seen that the theoretical and experimental curves agree very well except that the theoretical curves at resonance are shifted over a distance of about 70 oerstedt to the left with respect to the experimental curves. This can be understood if it is remembered that (2.8) and (2.9) hold strictly only in the limit of vanishing radius of the rod. Indeed, experiments with rods of different radii show that the shift decreases toward zero with diminishing radius. Also it is found that κ is practically unaffected by variations in ρ_1.

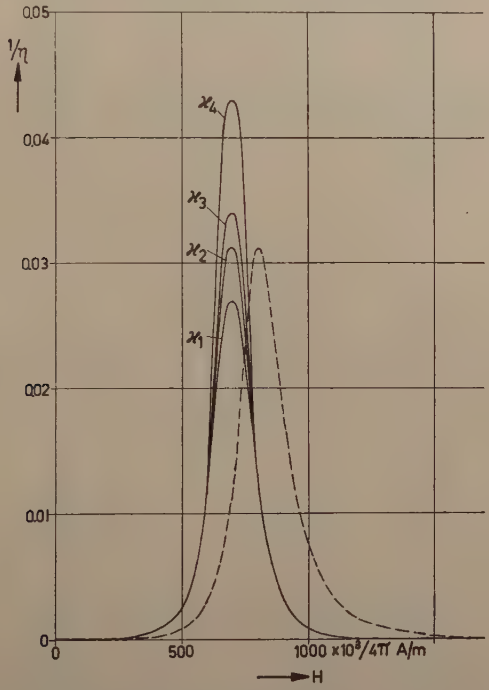

Fig. 28. Influence of the choice of κ on the calculated ellipticity, same case as fig. 27.

An impression of the sensitivity of the computed curves for the choice of κ is given by figs 27 and 28 which refer to rotation and ellipticity measurements in ferroxcube IV C. Here too the shift already mentioned manifests itself. It is clear that the value $\kappa_2 = 0.045$ gives the best fit and that the adjustment is rather critical.

Figs 29 and 30 represent the values of κ thus obtained for the different ferrites as a function of the temperature and the porosity respectively. Fig. 31 shows that there is no very simple connection between κ and the percentage NiO contained in the ferrites. To the interpretation of these results we shall return in Chapter VII.

It is interesting to compute the resonance value H_r of the field at which the rotation angle ϑ vanishes. According to (2.12) this requires $\beta_+ - \beta_- = 0$. Using (2.9) we thus find the condition

$$[(\mu_1'+\mu_0)^2-\mu_2'^2-\mu_1''^2-\mu_2''^2]\,\mu_2'+2(\mu_1'+\mu_0)\,\mu_1''\mu_2''=0. \qquad (5.11)$$

With the expressions (5.6) to (5.9) for μ_1', μ_1'', μ_2', μ_2'' it is verified by substitution that (5.11) is satisfied if we put for H_0 the value

$$H_r = \frac{\omega}{\Gamma\sqrt{1+\kappa^2}} - \frac{M_0}{2\mu_0}. \qquad (5.12)$$

TABLE IV

T °C	ferrite	$(H_r)_{exp}$ Ø	$(H_r)_{calc}$ M_0 at H_r Ø	$(H_r)_{calc}$ M_0 at saturation Ø
— 27	A	1190 ± 9	1228 ± 24	1166 ± 24
	B	525 ± 17	652 ± 28	484 ± 28
	C	405 ± 13	539 ± 27	371 ± 27
	D	728 ± 13	910 ± 22	880 ± 22
	E	1490 ± 14	1438 ± 20	1428 ± 20
20	A	1639 ± 10	1617 ± 22	1589 ± 22
	B	874 ± 33	916 ± 26	824 ± 26
	C	695 ± 17	913 ± 26	648 ± 26
	D	890 ± 24	1021 ± 23	899 ± 23
	E	1510 ± 10	1503 ± 20	1478 ± 20
100	A	2331 ± 16	2344 ± 20	2317 ± 20
	B	1391 ± 27	1384 ± 25	1377 ± 25
	C	1123 ± 18	1202 ± 25	1072 ± 25
	D	1168 ± 19	1366 ± 22	1161 ± 22
	E	1580 ± 17	1608 ± 20	1603 ± 20

The third column in table IV gives the experimental values of H_r in oerstedt, extrapolated to zero value of the radius ρ_1 of the ferrite rods as shown in figs 12, 13, 14 and 15, the fourth column the values calculated from (5.12). In the majority of cases the experimental values are equal, within the experimental error, to the theoretical ones or somewhat lower, the difference increasing with decreasing H_r. This can be understood if we remember that at the

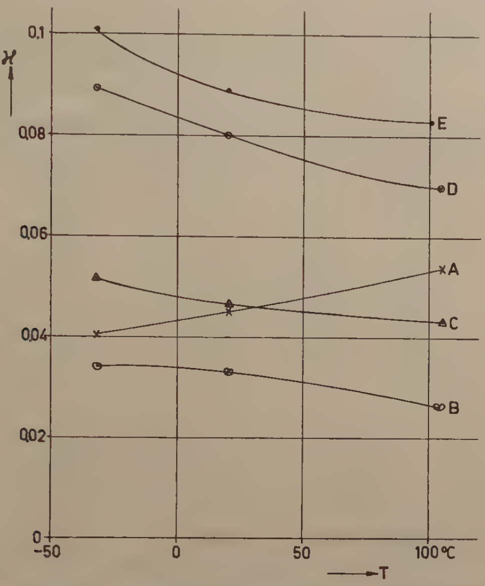

Fig. 29. The damping constant κ for the ferrites A, B, C, D, E as a function of the temperature.

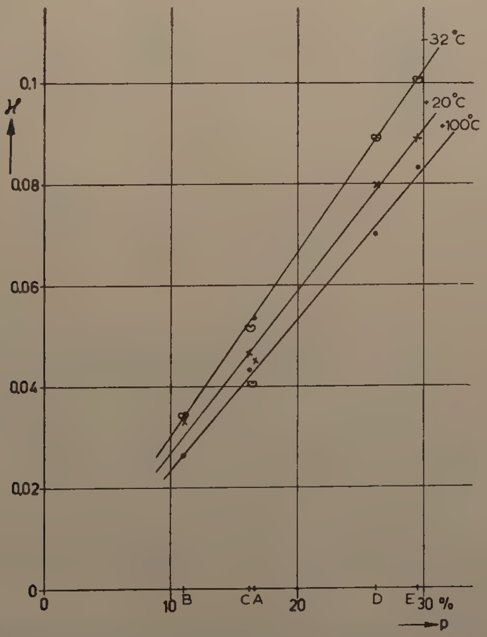

Fig. 30. The damping constant κ for the ferrites A, B, C, D, E as a function of the porosity for the temperatures $T = -32°C$, 20°C and 100°C.

lower field strengths we have not yet attained full magnetic saturation (see fig. 16). As we have mentioned before, our theoretical expressions in the first place hold strictly only when saturation is attained. But besides, as we shall see in the following chapter, the porosity actually makes the magnetic field inhomogeneous in the material and lets the field strength take on local values greater than the average. The values of M_0 which ought to be substituted in our equations are hence larger than those corresponding to the external static field H_0. By using for M_0 the magnetization at saturation, we should get a lower bound for H_r as computed from theory. In the fifth column of table IV these values have also been given.

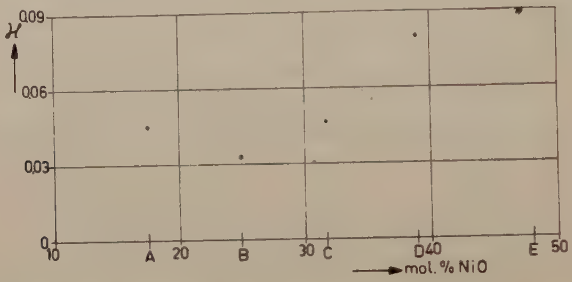

Fig. 31. The damping constant κ for the ferrites A, B, C, D, E as a function of the percentage NiO at a temperature $T = 20°C$.

CHAPTER VI. THE INFLUENCE OF POROSITY ON THE RESONANCE CONDITIONS

§ 18. *Outline of the problem.* In view of the available measuring equipment and because of its simplicity we have studied the resonance phenomenon in spheres of ferrite over a wider range of conditions than the Faraday rotation in rods. For a sphere we found in § 15 the resonance relation (5.10), which on account of the small value of κ (< 0.1) practically reduces to the relation (3.1). As mentioned already in § 13 it is customary for purposes of theory to express Γ in the unit $\mu_0 e/2m$ by means of (4.1), leading us to the spectroscopic splitting factor g.

If the magnetization of a substance is entirely due to electron spins, one expects the value $g = 2$. As discussed e.g. by Van Vleck 9),

g may become larger, say $2 + \delta$, if the electronic orbital motion also contributes to the magnetization. In most ferromagnetics δ lies below 0.1. Besides g another quantity g', the magneto-mechanical factor plays a rôle in magnetized media. It represents the ratio of the magnetic moment to the mechanical moment of momentum manifesting itself in the Einstein-de Haas effect, again expressing this ratio in the unit $\mu_0 e/2m$. For small values of δ theory 10) 11) shows that $g' = 2 - \delta$, so that we have the relation $g - 2 = 2 - g'$. In conformity with this relation also g' in general is found to differ from 2 by less than 0.1. By reason of its fundamental physical significance g should be essentially a constant characteristic of the material and hence independent of the wavelength used in the resonance experiments and of the temperature.

In contrast to other ferromagnetics our figs 18 to 22 show effective g-values ranging up to 2.5. In addition the values g_{eff} are seen to depend noticeably on the temperature and strongly on the wavelength employed. It is the purpose of this chapter to investigate the causes of these discrepancies.

The dependence of g_{eff} on wavelength had already been noted by Okamura and his collaborators 4) 12). This author introduced into the resonance equation an internal field H_i, which he assumed to be temperature-dependent, by writting instead of (3.1)

$$\omega = \Gamma(H_r + H_i).$$

By measuring H_r at two different frequencies, Γ and H_i could then be computed. Suggestions were made about the physical origin of the field H_i without leading to definite conclusions.

§ 19. *The influence of porosity on the g-values.* Polycrystalline ferrites are sintered materials always showing pores. It is impossible to prepare them with the same bulk behaviour, but without porosity. Having arisen in a partially melted material of a ceramic nature, the pores may reasonably be assumed to have in general a spherical shape due to the effects of surface tension, a hypothesis confirmed by microphotographs of polished sections. A polycrystalline ferrite may hence be considered as pure ferrite with inclusions of air.

In this section we shall proceed as if the ferrites used in our experiments were homogeneous substances for which the magnetization due to a given static external field H_{0e}, and hence also the demagnetizing field, has a value differing from that in an ideal ferrite without air inclusions. We shall then calculate the external field H_{0e}' that would have to be applied to the ideal ferrite in order to make the internal field the same as in the real ferrite.

For a homogeneous sphere of the real ferrite the external field H_{0e}, the internal field H_0 and the magnetization M_0 are related by

$$H_{0e} = H_0 + \frac{M_0}{3\mu_0}. \tag{6.1}$$

For the ideal ferrite at the same internal field H_0 we have similarly

$$H_{0e}' = H_0 + \frac{M_0'}{3\mu_0}. \tag{6.2}$$

Hence from (6.1) and (6.2)

$$H_{0e}' = H_{0e} + H_p, \tag{6.3}$$

the corrective field H_p due to porosity being

$$H_p = \frac{M_0' - M_0}{3\mu_0}. \tag{6.4}$$

Since the magnetization M_0 in the real ferrite, on account of the presence of air, will be less at the same internal field strength H_0 than the magnetization M_0' of the ideal ferrite, H_p is positive. If we could have performed our resonance experiments on a sphere of the ideal ferrite, we would have found a larger resonance field strength H_r' for a given frequency ω and accordingly from (3.1) and (4.1) a smaller g-value provided the effect of the pores on the high frequency field can be neglected.

There are two cases for which the difference $M_0' - M_0$ in (6.4) can be calculated exactly. The simplest is the one where the magnetization may be assumed to have everywhere the same fixed value M_0 in the direction of the external field, irrespective of whether the sphere be solid or porous, so that on removing the ferromagnetic material from the solid sphere in the regions occupied by the pores, the magnetization remains "frozen in" in the rest of the material both as regards magnitude and direction. Then evidently the magnetization M_0 of the real ferrite is $(1 - q)$ times the magnetization M_0' of the ideal ferrite, q being the fraction of the volume occupied by the pores. Hence

$$M_0' = \frac{1}{1-q} M_0, \quad M_0' - M_0 = \frac{q}{1-q} M_0 \tag{6.5}$$

and from (6.4)

$$H_p = \frac{p}{100 - p} \frac{M_0}{3\mu_0} \tag{6.6}$$

if we express the porosity $p = 100\,q$ in per cent. Clearly this expression is a lower bound, for even at saturation the introduction of the pores will disorientate the magnetization and thereby increase $M_0' - M_0$ above the value (6.5).

The second case amenable to exact treatment is that of a linear medium in which the magnetization is everywhere proportional to the local magnetic field strength and parallel to it. Then the law of mixtures due to Maxwell [13]) can be applied, leading to

$$\frac{M_0' - M_0}{3\mu_0 H_0 + M_0 + 2M_0'} = q\,\frac{M_0'}{3\mu_0 H_0 + 2M_0'}, \tag{6.7}$$

M_0 and M_0' being the values of the magnetization at the same internal field strength H_0 for the real and the ideal ferrite. Now the external field strength H_{0e} for a sphere of the real ferrite is related to H_0 by (6.1). Introducing H_{0e} instead of H_0 in (6.7) this becomes

$$\frac{M_0' - M_0}{3\mu_0 H_{0e} + 2M_0'} = q\,\frac{M_0'}{3\mu_0 H_{0e} - M_0 + 2M_0'}. \tag{6.8}$$

For the quantity $\Delta M_0 = M_0' - M_0$ we get from (6.8) the quadratic equation

$$2(1 - q)(\Delta M_0)^2 +$$
$$+ [(1 - q)3\mu_0 H_{0e} + (1 - 4q)M_0]\,\Delta M_0 - q(3\mu_0 H_{0e} + 2M_0)M_0 = 0.$$

Its positive solution, expanded in powers of q up to the second power is

$$M_0' - M_0 =$$
$$= \frac{q}{1 - q}\,\frac{(3\mu_0 H_{0e} + 2M_0)M_0}{3\mu_0 H_{0e} + M_0}\left[1 + q\,\frac{(3\mu_0 H_{0e} - M_0)M_0}{(3\mu_0 H_{0e} + M_0)^2} + \ldots\right]. \tag{6.9}$$

Using again $p = 100\,q$ to describe the porosity in per cent, we have from (6.4) and (6.9)

$$H_p = \frac{p}{100 - p}\,\frac{(3\mu_0 H_{0e} + 2M_0)M_0}{3\mu_0(3\mu_0 H_{0e} + M_0)}\,\cdot$$
$$\cdot\left[1 + \frac{p}{100}\,\frac{(3\mu_0 H_{0e} - M_0)M_0}{(3\mu_0 H_{0e} + M_0)^2} + \ldots\ldots\right]. \tag{6.10}$$

For the high field strengths $H_{0e} = H_r$ of more than 2500 Ø at which in our experiments resonance occurs the real ferrite may be expected to behave in good approximation according to (6.10). The magnetization, it is true, does not vary linearly with H_0, being near saturation, but the effective susceptibility M_0/H_0 changes only slightly in the small range of values taken by the local field in the neighbourhood of the pores. The direction of the magnetization on the other hand, will everywhere be parallel to that of the local field, as assumed in the derivation.

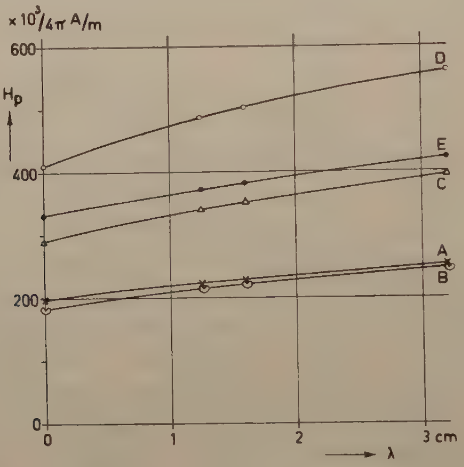

Fig. 32. The corrective field H_p according to (6.10) vs. the wavelength at a temperature $T = 20°\text{C}$.

In fig. 32 we have represented the field H_p as given by (6.10) for the various ferrites at resonance as a function of the wavelength λ, the temperature being $T = 20°\text{C}$. As λ goes to zero, the value of the external field H_{0e} at which resonance occurs increases indefinitely. Since M_0 does not exceed its saturation value, it then follows from (6.10) that H_p for $\lambda \to 0$ approaches the value (6.6) as a limit. In fig. 32 this value is hence represented by the intercept of the curves with the ordinate axis. The figure shows that the amount by which H_p exceeds this lower bound in general is less than 30 per cent at the wavelengths considered. In figs 33 and 34 the field H_p following from (6.10) is shown for the various ferrites as a function of the temperature T, fig. 33 referring to resonance at $\lambda = 3.2$ cm, fig. 34

to resonance at $\lambda = 1.6$ cm. The order of magnitude of H_p runs from about 100 to 600 oerstedt.

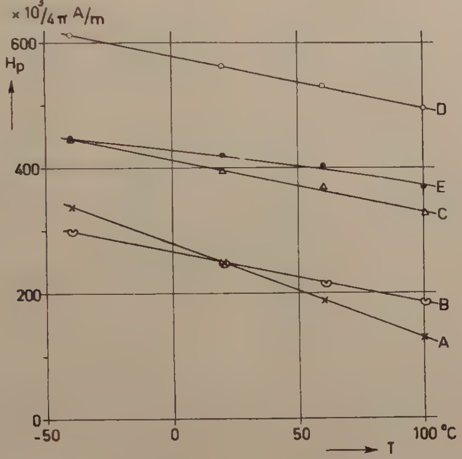

Fig. 33. The corrective field H_p according to (6.10) vs the temperature for a wavelength λ — 3.2 cm.

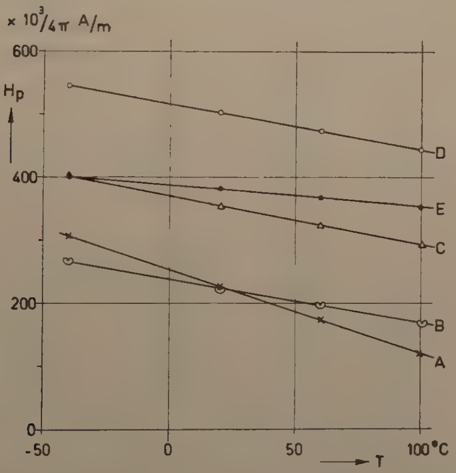

Fig. 34. Same as fig. 33, but for $\lambda = 1.6$ cm.

With the values of H_p given by (6.10) new g-values g_p have been computed by writing

$$\omega = \Gamma(H_r + H_p). \tag{6.11}$$

These g_p values are shown in tables V and VI. It is seen that the

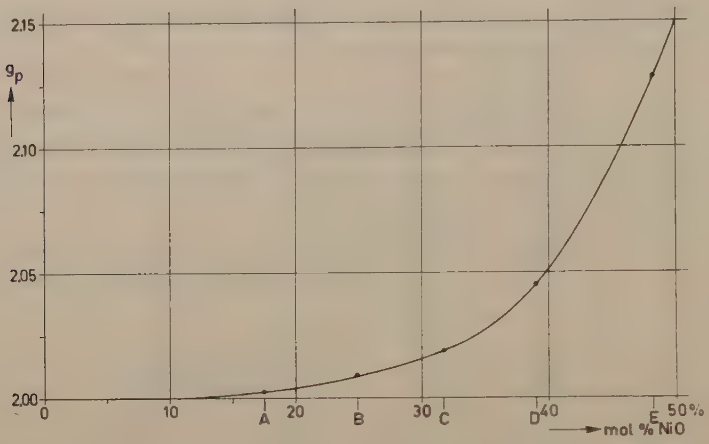

Fig. 35. The g-value corrrected for porosity vs. the percentage NiO.

TABLE V

		λ = 3.2 cm				λ = 1.6 cm			
Ferrite	T °C	H_r O	$M_0\mu_0$ O	H_p O	g_p	H_r O	$M_0\mu_0$ O	H_p O	g_p
IV A	— 40	2993	3890	340	2.00	6320	3890	308	2.00
	20	3078	2990	252	2.00	6397	2990	229	2.00
	60	3138	2370	193	2.00	6447	2370	177	2.00
	100	3190	1660	129	2.01	6497	1660	120	2.01
IV B	— 40	3012	5270	300	2.01	6330	5270	268	2.01
	20	3064	4490	248	2.01	6378	4490	222	2.01
	60	3099	4000	217	2.01	6407	4000	195	2.01
	100	3130	3520	187	2.01	6437	3520	167	2.01
IV C	— 40	2861	5030	449	2.01	6156	5030	401	2.02
	20	2900	4500	396	2.02	6208	4500	353	2.02
	60	2935	4150	371	2.01	6241	4150	322	2.02
	100	2974	3810	325	2.02	6277	3810	292	2.02
IV D	— 40	2652	3800	613	2.04	5933	3800	544	2.05
	20	2700	3550	564	2.04	5977	3550	503	2.05
	60	2733	3370	532	2.04	6007	3370	474	2.05
	100	2766	3185	496	2.04	6038	3185	445	2.05
IV E	— 40	2668	2490	445	2.14	5837	2490	401	2.13
	20	2691	2390	425	2.14	5860	2390	382	2.13
	60	2709	2310	407	2.14	5877	2310	369	2.12
	100	2729	2225	390	2.13	5895	2225	354	2.12

TABLE VI

Ferrite	T °C	$\lambda = 1.25$ cm			
		H_r Ø	$M_0 \mu_0$ Ø	H_p Ø	g_p
IV A	20	8331	2990	224	2.00
IV B		8316	4490	216	2.01
IV C		8144	4500	340	2.02
IV D		7887	3550	486	2.05
IV E		7704	2390	372	2.12

values of g_p lie much closer to 2 than the values g_{eff} shown in figs 18 — 22 and moreover are independent of T and λ. In fig. 35 g_p is shown as a function of the percentage NiO.

CHAPTER VII. THE INFLUENCE OF POROSITY ON THE LINE WIDTH

§ 20. *Outline of the problem.* Consider a sphere of ideal non-porous ferrite placed in a homogeneous external static magnetic field of sufficient strength to produce approximately saturation. The field inside the sphere will then be homogeneous. A cavity, introduced into the ferrite, will give rise in its neighbourhood to a distortion of the internal field, both as regards magnitude and direction. On applying an alternating magnetic field of given angular frequency, the different volume elements of the ferrite around the cavity will hence be in resonance at different values of the external field. The resonance absorption, when represented as a function of the external field will consequently show a broadening, suitably termed porosity broadening.

In the next paragraph we shall try to arrive at a rough estimate of this broadening under the following simplifying assumptions.

a) The ferrite is supposed to behave as a linear medium in the sense discussed in § 19, meaning that the magnetization is everywhere parallel and proportional to the local field. In § 19 we saw that at the high field strengths necessary for resonance in our experiments on ferrites this assumption is reasonably close to reality.

b) The cavities in the ferrite are supposed to be spherical in shape. In § 19 we also discussed the justification of this assumption in our case.

c) The porosity p is supposed to be so small that the distortion of the field by a given cavity is practically zero at the distance where on the average the neighbouring cavities are located. The effects of the different cavities on the field are then essentially independent. This condition is also inherent in Maxwell's law of mixtures which we used in § 19 and which led to satisfactory results for the g-values there. It is best realized for ferrite IV B ($p = 11.0$ per cent), least for ferrite IV E ($p = 29.5$ per cent).

§ 21. *Estimate of the line width.* If in a piece of ferrite without cavities a homogeneous magnetic field H_0 acts in the z-direction, then the modification of this field produced by a spherical cavity of radius a can be described outside the cavity as the field $\boldsymbol{h}$ of a dipole, located at the centre of the cavity and having a magnetic moment opposite to the direction of H_0 equal to

$$m = -\, 4\pi\mu_0\, a^3 \frac{H_0 M_0'}{3\mu_0 H_0 + 2M_0'}, \tag{7.1}$$

where M_0' is the magnetization at the field strength H_0 in the ideal ferrite. If we employ polar coordinates r, ϑ with the centre of the sphere as origin and the z-axis as polar axis, then the components of the field due to the dipole (7.1) in the xz-plane are

$$h_x = -\frac{3m \sin\vartheta \cos\vartheta}{4\pi\mu_0 r^3},\ h_z = -\frac{m(1 - 3\cos^2\vartheta)}{4\pi\mu_0 r^3},\ r \geq a. \tag{7.2}$$

In view of the roughness of our estimate we shall henceforth restrict ourselves to terms linear in m and we thus find that the total field strength at a point outside the cavity is simply $H_0 + h_z$.

We next inquire in what fraction of the volume occupied by the ferrite the field h_z has a value between h_z and $h_z + \mathrm{d}h_z$. To make this problem definite we imagine the cavities to have equal radii and to be arranged in a cubical array. Then we may take each cavity as surrounded by a concentric cube of such size that the ratio of the volume of the cavity to that of the cube just corresponds to the porosity of the ferrite. It is in this cube that the volume fraction in question must be determined. Since the orientation of the cube with respect to the field H_0 may be chosen at random, it seems reasonable to average over all orientations of the cube.

The actual calculations were made by drawing in the xz-plane a set of curves on which the quantity

$$u = -\frac{4\pi\mu_0 a^3}{m} h_z = \frac{3\mu_0 H_0 + 2M_0'}{H_0 M_0'} h_z = \left(\frac{a}{r}\right)^3 (1 - 3\cos^2\vartheta) \tag{7.3}$$

has a constant value (see fig. 36) and by computing the volume of the solid obtained by revolving a zone between two adjacent curves

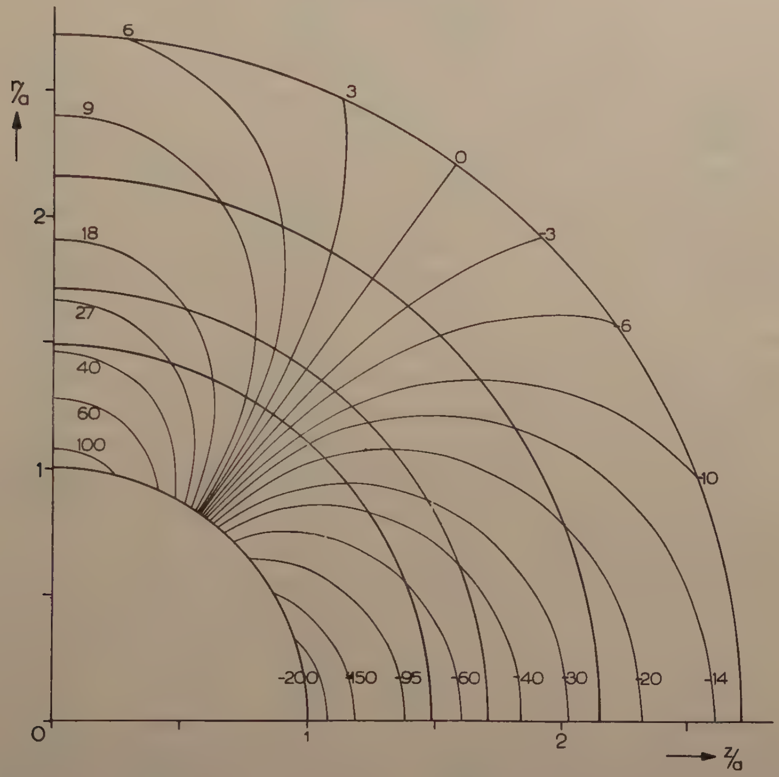

Fig. 36. Curves of constant u around a spherical cavity. The values of u are found by dividing the numbers at the curves by 125.

around the z-axis. Proper weights must be given to those parts of the zones (between the inscribed and the circumscribed sphere of the cube) which do not fall inside the cube for every orientation of the latter. The probability $P(u)\,\mathrm{d}u$ of u lying between u and $u + \mathrm{d}u$ is then a function of the porosity p only.

In fig. 37 the function $P(u)$ is shown for $p = 16$ per cent. The curve is asymmetrical and has a halfwidth (width at half the height of the maximum) $\Delta u = 0.26$. We compare this theoretical curve with experimental data for the ferrite IV C for which p has the same value. According to (7.3)

$$\Delta h_z = \frac{H_0 M_0'}{3\mu_0 H_0 + 2M_0'} \Delta u. \tag{7.4}$$

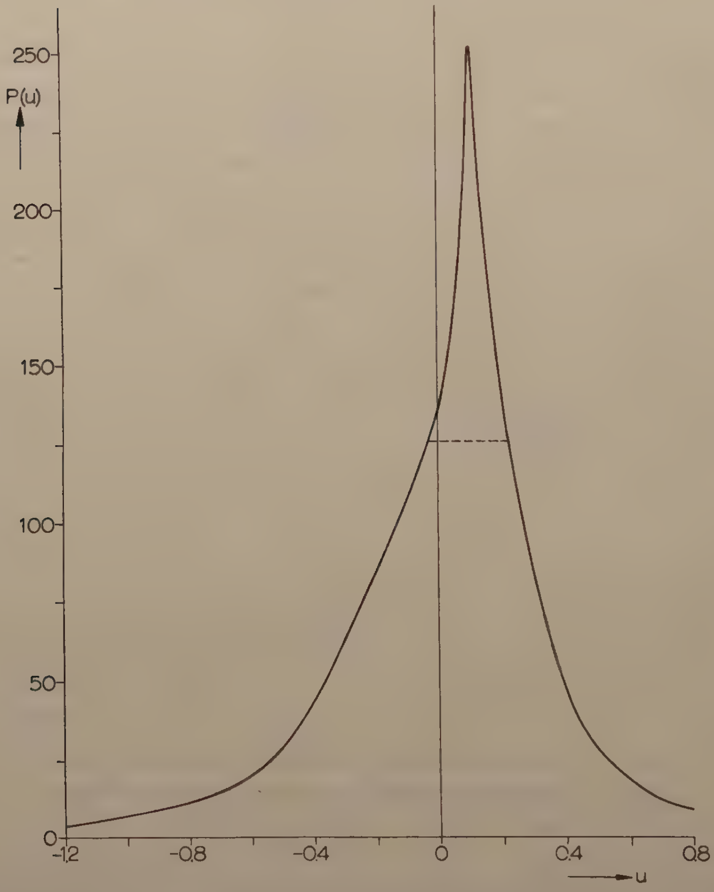

Fig. 37. The function $P(u)$. The ordinate is in arbitrary units.

For a linear medium where all the field strengths are proportional we then would have for the external field from (7.4)

$$\Delta H_{0e} = \frac{H_{0e} M_0'}{3\mu_0 H_0 + 2M_0'} \Delta u.$$

If we now make use of (6.4) to express M_0' in terms of the magnetization M_0 of the porous ferrite and of (6.1) to express H_0 in terms of H_{0e}, we finally get

$$\varDelta H_{0e} = \frac{H_{0e}(3\mu_0 H_p + M_0)}{3\mu_0(H_{0e} + 2H_p) + M_0} \varDelta u. \tag{7.5}$$

With the values of $H_{0e} = H_r$, H_p and M_0 at resonance for $\lambda = 3.2$ cm and $T = -40$ and 20°C (see table V) and with the value of $\varDelta u$ given above we find from (7.5) values of $\varDelta H_{0e}$ of 292 and 275 oerstedt respectively. The experimental values which we obtained with the Pound equipment [14]) referred to in table III at the end of § 14 are 521 and 458 oerstedt respectively. For $\lambda = 1.25$ cm and $T = 20$°C the theoretical and experimental values are 378 and 845 oerstedt.

Similar calculations can be made for other values of the porosity. They show that the line width for a material of given composition and for a given wavelength and temperature is approximately proportional to the porosity, in qualitative conformity with the empirical results shown in table III of § 14.

We may hence conclude that certainly a large part of the line width is accounted for by the porosity broadening. The many approximations in our estimate make it impossible at this stage to decide whether additional mechanisms of broadening are operative besides the one considered.

§ 22. *The damping constant* κ. In the discussion of the Faraday rotation experiments in Chapter V we introduced a damping constant κ to account formally for our results. It is clear that just as the resonance in spheres of ferrite the phenomena considered there will be affected by porosity broadening. We found in particular (see fig. 30) that κ increased markedly with porosity, and this is quite in line with our expectations. Here too, however, a more quantitative interpretation would require a very careful analysis of the influence of the cavities in the ferrites as dependent on their size, shape and spatial distribution.

Acknowledgement. The author wishes to express his sincere thanks to Prof. Dr. R. Kronig for numerous suggestions regarding the preparation of this thesis. He is also greatly indebted to the board of the Netherlands Defence Research Council, the director and his chief engineer of the Physical Laboratory of this organisation for being given the opportunity to perform these measurements as well as for permission to publish the results. He wishes to acknowledge the instructive discussions he had with other members of the staff, and the helpful assistance of the workshop and the drawing office of the laboratory. The Philips Laboratories at Eindhoven kindly put at his disposal the instruments necessary for measuring line widths and initial permeabilities.

Received 3rd February, 1958.

REFERENCES

1) Van Trier, A. A. T. M., Thesis Delft, 1953; Appl. Sci. Res. **B3** (1953) 142, 305.
2) Suhl, H. and L. R. Walker., Bell. Syst. Techn. J. **33** (1954) 1133.
3) Bozorth, R. M., Ferromagnetism, Van Nostrand Comp. Inc., N.Y., 1951, p. 270.
4) Okamura, T., Sci. Rep. Inst. Tôhôku Univ. **6A** (1954) 89.
5) Spencer, E. G. and R. L. Le Craw., J. Appl. Phys. **26** (1955) 250.
6) Saunders, W. K., I.R.E. Conv. Rec. **3** (1955) 8, 81.
7) Landau, L. and E. Lifshitz, Phys. Z. USSR **8** (1935) 153.
8) Kittel, C., Phys. Rev. **73** (1948) 155.
9) Van Vleck, H. J., Phys. Rev. **78** (1950) 266.
10) Polder, D., Phys. Rev. **73** (1948) 1116.
11) Kittel, C., Phys. Rev. **76** (1949) 743.
12) Kojima, Y., Sci. Rep. Inst. Tôhôku Univ. **6A** (1954) 614.
13) Maxwell, C., Treatise on electricity and magnetism, Vol. 1, Oxford, 1873, p. 365.
14) Beljers, H. G., Philips Res. Rep. **13** (1958) 10.

Appl. sci. Res. Section B, Vol. 7

A FOCUSING AID FOR THE X-RAY PROJECTION MICROSCOPE

by ONG SING POEN and J. B. LE POOLE

Technical Physics Laboratory, Technological University, Delft, the Netherlands

Summary

Part of the electrons reflected by the target of an X-ray microscope pass the demagnifying lens in opposite direction and form a magnified image of the focus in the electron source. This secondary image can be caught on a fluorescent screen and observed. The position, shape and size of the image give information on alignment, focusing conditions and image errors. The brightness is a factor 10^3 to 10^4 higher than that of the X-ray fluorescent image under normal focusing conditions. If a magnetic objective is used, centering can be done very accurately (angle of tilt $< 1/600$ radians). In practice this method proves to be very satisfactory, even for voltages as low as 6 kV and less. At these voltages the depth of penetration of the electrons in gold is less than 500 Å, so that for a 0.1 μ resolution there is no need for a thin target.

§ 1. *Introduction.* An X-ray projection microscope ¹) ⁴) mainly consists of an electron source, a demagnifying electron lens and a vacuum sealing target. A highly demagnified image of the electron source is formed on the target in which X-rays are produced. The specimen is mounted near the target and an enlarged X-ray image will be projected on a photographic plate. The resolution depends on the size of the X-ray source and consequently on the accuracy of focusing.

To obtain focusing conditions the specimen is replaced by a fine metal grid and the film by a fluorescent screen. The image on this screen is observed through an eyepiece and the lens current adjusted until the sharpest image has been obtained. Besides being inconvenient this method of focusing has some shortcomings:

1) focusing and exposure are two separate operations,

2) the image cannot be viewed during exposure,

3) changes, either electrical or mechanical, cannot be detected nor corrected.

Due to the poor contrast of the fluorescent image, small lens errors cannot be seen. For low voltages critical focusing becomes impossible since the X-ray energy is proportional to the third power of the voltage used.

§ 2. *A new focusing aid.* The focusing aid which will be described here makes use of the fact that part of the electrons striking the target are elastically reflected. The energy distribution of the total secondary emission for a primary energy of about 155 V is given in the literature ³) ⁵) ¹⁰) ¹¹), see fig. 1. It has a sharp peak for an energy equal to that of the primary electrons. The secondary electrons enter the lens in opposite direction. Part of them pass the aperture, and those which are elastically reflected form a magnified and sharp secondary image at the electron source.

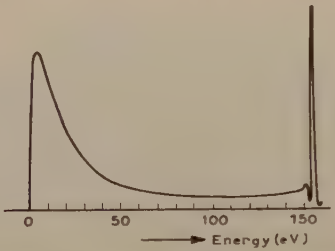

Fig. 1. Energy distribution of secondary electrons for a primary energy of 155 eV according to Rudberg ¹⁰) ¹¹).

If the instrument is perfectly aligned, this image will be exactly at the electron source. By introducing a transverse magnetic field (fig. 2*a*) the returning beam can be separated from the primary beam, thus allowing observation of the secondary image on a fluorescent screen. If a magnetic lens is used, the transverse field can be obtained conveniently by slightly tilting the objective lens (fig. 2*b*). If the lens has no errors and the target is in focus, the secondary image will be equal in size and shape to the electron source. As its diameter is about 40μ, an optical magnification of some 10 times is required to obtain the necessary information from this image.

§ 3. *Separation of the beams.* The separation of the primary and the returning beam by tilting the lens can be considered as caused by the rotation of the lens and will now be examined more closely.

In fig. 3 the magnetic lens is represented by a cylinder. The direction of the magnetic field is indicated by the arrow B. The image rotations for electrons coming from C and T are in the directions indicated by D_C and D_T respectively. As can be derived from fig. 3, D_C and D_T have the same sense of rotation.

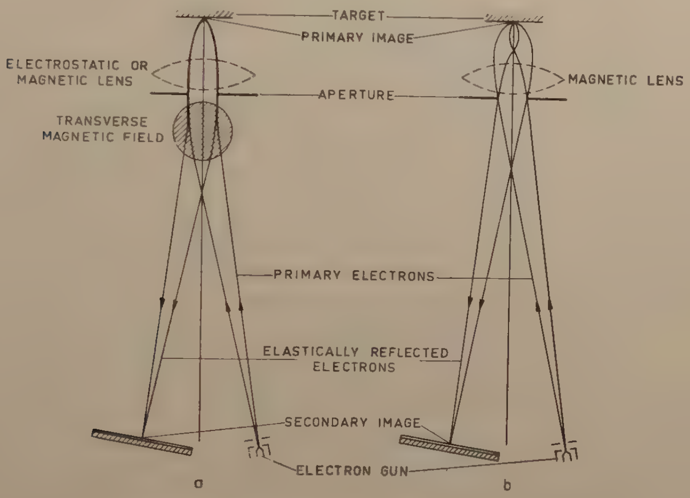
TARGET
PRIMARY IMAGE
ELECTROSTATIC OR MAGNETIC LENS
MAGNETIC LENS
APERTURE
TRANSVERSE MAGNETIC FIELD
PRIMARY ELECTRONS
ELASTICALLY REFLECTED ELECTRONS
SECONDARY IMAGE
ELECTRON GUN
a
b

Fig. 2. Separation of the primary and returning beams.
a. in case of a transverse magnetic field.
b. in case of electrons directed obliquely to the magnetic lens.

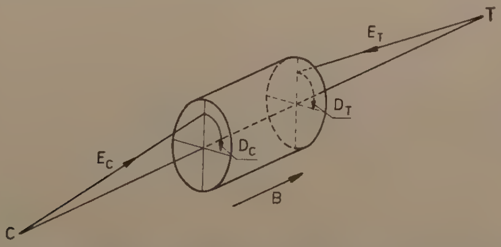

Fig. 3. Elucidation of the beam separation caused by image rotation. The lens is represented by a cylinder with magnetic field B. The image rotations for electrons coming from C and T are indicated by D_C and D_T. Projected on a plane perpendicular to the optical axis D_C and D_T will have the same direction.

To elucidate the separation of the rays caused by this rotation we examine the projection on a plane perpendicular to the optical axis (fig. 4*b*). The lens is now represented by a circle and the optical axis by the centre A. Instead of tilting the lens the electrons are directed obliquely to the lens. On doing so, the electron source is represented by C, not coinciding with the optical axis. If there were no rotation, the primary image on the target would be represented by P, CA/AP being the demagnification. Due to the rotation over the angle θ the projection of the primary image comes in C′.

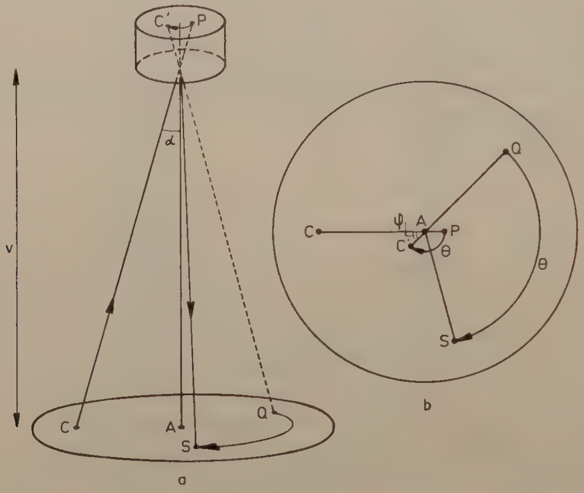

Fig. 4. Construction of the projection diagram (fig. 4*b*).

Without rotation the elastically reflected electrons coming from C′ would give a secondary image in Q. With rotation in the same direction and over the same angle θ the secondary image now comes in S, SA/AC′ = CA/AP being the magnification.

In our projection diagram the angle CAS $= 2\varphi = 2(180° - \theta)$. Further we can derive that

$$\mathrm{CS} = 2\mathrm{CA}\sin\varphi = 2\,\mathrm{CA}\sin(180° - \theta). \tag{1}$$

CS will be zero, that is, the secondary image S coincides with the electron source if CA = 0 or if $\theta = n \times 180°$, $n = 0, 1, 2, \ldots$.

CA = 0 means that the electron source is situated on the optical axis and consequently that the lens is exactly aligned. Since it can be proved that $0 < \theta < 180°$, the beams are always separated when the lens is not exactly aligned. If in this case the lens power is varied, the secondary image S besides getting blurred will describe an arc. If S coincides with C, that is, if the lens is centered, the displacement according to (1) is zero and the image is only blurred.

§ 4. *Accuracy of alignment.* In order to avoid inadmissible image errors the angle of tilt α between the optical axis of the lens and that of the electron source must be kept small. From fig. 4*a* it can be derived that

$$\alpha = \mathrm{CA}/v = \mathrm{CS}/2v \sin \varphi. \tag{2}$$

At a given rotation angle θ and distance v between source and lens the distance CS between electron source and secondary image must therefore be small. To realize this the focusing screen must be placed in the primary beam and provided with a hole to allow the primary electrons to pass. The smallest distance CS is then determined by the radius of this hole. At a given value of CS the tilting angle is a minimum if $\sin \varphi = 1$ or $\varphi = 90°$ and thus $\theta = 90°$. Furthermore (2) shows that the alignment improves with increasing v. Note that the projection diagram as shown in fig. 4*b* can in fact represent the focusing screen if we assume C to be fixed at the hole in the screen. In this case the centre A is displaced by tilting the lens.

In our microscope CS = 1 mm, $v = 400$ mm, $\varphi \approx 60°$ [2], $\sin \varphi = \frac{1}{2}\sqrt{3}$. So $\alpha < 1/600$ radius. Note that this angle is much smaller than can be obtained by centering by means of the X-ray image in the conventional way. In our apparatus this critical centering characteristic is used also for alignment of the condensor lens. See also § 10.

§ 5. *Focusing accuracy.* As in this device the errors are repeated on the return, the focusing accuracy can be high. Let us investigate what happens if the target is not in focus. In fig. 5 C represents the electron source, T the target, B the paraxial focal plane and L the objective. If the focal distance of the lens is f, we may write (see fig. 5) according to the paraxial lens equation

$$v = fb/(b - f). \tag{3}$$

The radius of the blur on the target equals

$$\varepsilon = (t - b)\frac{h}{b} = \left(\frac{t}{b} - 1\right)h. \tag{4}$$

The secondary image of the blur is sharp in M at a distance v' from the lens, in which

$$v' = ft/(t - f). \tag{5}$$

Apart from the effect of changes in the intensity distribution, the blur at the electron source will have a radius

$$\rho = 2(v - v')\,\frac{h}{v'} = 2h\left(\frac{v}{v'} - 1\right).$$

Substitution of (5) gives

$$\rho = 2h\left(\frac{v}{f} - \frac{v}{t} - 1\right). \tag{6}$$

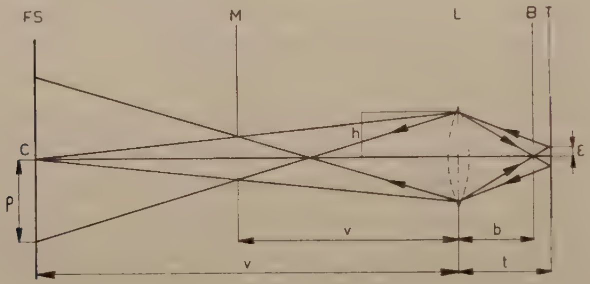

Fig. 5. The unsharpness of the secondary image due to incorrect focusing. FS = focusing screen, C = electron source, M = image plane of the secondary image, L = objective lens, B = image plane of the primary image, T = target, ρ = radius of the unsharpness on the focusing screen, ε = radius of the unsharpness of the primary image.

Putting the expression in parentheses equal to zero gives the well-known lens equation

$$\frac{1}{v} + \frac{1}{t} = \frac{1}{f}. \tag{7}$$

Assuming a Gaussian intensity distribution, a more accurate calculation shows that instead of (6) we should write

$$\rho = \sqrt{2}\,h\left(\frac{v}{f} - \frac{v}{t} - 1\right). \tag{8}$$

In the neighbourhood of the focusing point $\rho = 0$ we may write

$$\rho = \rho_0 + \left(\frac{\partial \rho}{\partial f}\right)_0 \Delta f + \left(\frac{\partial^2 \rho}{\partial f^2}\right)_0 (\Delta f)^2 + \ldots. \tag{9}$$

For small values of Δf we may neglect the terms of second and higher power in Δf and taking into account that $\rho_0 = 0$ we get

$$\rho = \left(\frac{\partial \rho}{\partial f}\right)_0 \Delta f. \tag{10}$$

According to (8)
$$\frac{\partial \rho}{\partial f} = -\frac{\sqrt{2}\,hv}{f^2}. \tag{11}$$

With (7) this becomes
$$\left(\frac{\partial \rho}{\partial f}\right)_0 = -\frac{\sqrt{2}\,h(t^2 + 2tv + v^2)}{vt^2}.$$

In general $v \gg t$; so we may write
$$\left(\frac{\partial \rho}{\partial f}\right)_0 = \frac{-\sqrt{2}\,hv}{t^2} = \frac{-\sqrt{2}\,hM}{t}, \tag{12}$$

in which
$$M = v/t \tag{13}$$

is the demagnification for the primary image and magnification for the secondary image. Further $M \gg 1$ and $t \approx f$, which gives for (12)
$$\left(\frac{\partial \rho}{\partial f}\right)_0 = -\sqrt{2}\,hM/f \tag{14}$$

and for (10)
$$\rho = -\sqrt{2}\,hM\,\Delta f/f. \tag{15}$$

Putting the resolution δ equal to the diameter of the primary image d we get according to (13)
$$M = c/d = c/\delta, \tag{16}$$

in which c is the diameter of the electron source. Equation (15) can then be transformed to
$$\frac{\rho}{c} = -\sqrt{2}\frac{h}{\delta}\frac{\Delta f}{f}. \tag{17}$$

Inserting $\delta = 0.1\ \mu$, $h = 80\ \mu$, $\rho/c = 1$ we get $|\Delta f/f| = 10^{-3}$.

The radius of the blur in the primary image amounts to (fig. 5)
$$\varepsilon = h\Delta f/f. \tag{18}$$

Inserting this in (17) gives
$$\rho/c = -\sqrt{2}\,\varepsilon/\delta, \tag{19}$$

in which ρ/c is the relative error in the secondary image and ε/δ the relative error in the primary image. For focusing we have to satisfy the condition $|\varepsilon/\delta| < 1$ and so the condition for good focusing becomes
$$|\rho/c| < \sqrt{2}. \tag{20}$$

As shown, this is independent of the resolution δ. The minimum value of $|\rho/c|$ is determined by the lens errors only.

§ 6. *Position of the focusing screen.* It was shown that the secondary image is in the plane of the source. As this place is inaccessible, we shall investigate the admissible distance Δv between source and screen. In fig. 6 FS represents the focusing screen. With the target in focus the radius of the blurring at FS equals

$$\rho_S = \frac{\Delta v}{v} h. \tag{21}$$

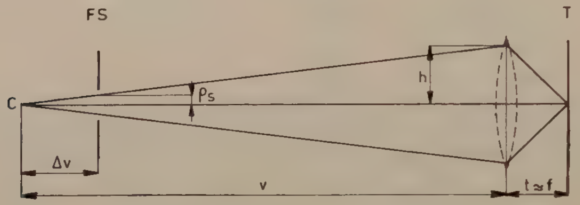

Fig. 6. Position of the focusing screen. Due to the great depth of focus it is not necessary to place the focusing screen at the electron source level. T = target, C = electron source.

The half-angle aperture of the objective is $\gamma = h/f$. Further $v/f \approx M$ and $M = c/\delta$. So

$$\rho_s = \frac{\Delta v}{c} \delta\gamma. \tag{22}$$

We have to ensure that $\rho_s/c < 1$ and thus

$$\Delta v < c^2/\delta\gamma. \tag{23}$$

In our microscope we use $\gamma \approx 0.08$ for $\delta = 0.1\ \mu$ and $c \approx 40\ \mu$. So the condition (23) becomes $\Delta V < 200$ mm. With increasing δ a more correct position of the screen is required.

§ 7. *Brightness of secondary image.* In practice the secondary image has proved to be sufficiently bright, even when the X-ray intensity is so low that focusing by the conventional method is impossible. This however is only partly due to the fact that the reflection coefficient for the electrons is greater than the X-ray efficiency. The main reason is that the electrons are focused to a small spot while the X-rays diverge to illuminate a large plane.

In fig. 7 T represents the target, RS the X-ray fluorescent screen, G the test grid, P the primary electron image and FS the focusing screen. The current density in P amounts to

$$j_p = \pi\gamma^2 B, \tag{24}$$

in which B is the brightness of the electron source. If the reflected electrons follow Lambert's law, the brightness for the secondary radiation is

$$B_s = \eta_e\gamma^2 B, \tag{25}$$

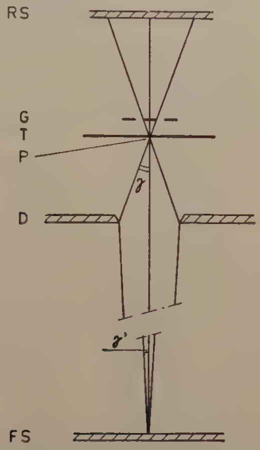

Fig. 7. Comparison of the intensities on the X-ray screen and focusing screen. RS = X-ray screen, G = test grid, T = target, P = primary image, D = diaphragm, FS = focusing screen.

in which η_e is the reflection coefficient. The current density of the secondary image on the focusing screen FS therefore amounts to

$$j_s = \pi\eta_e\gamma^2\gamma'^2 B, \tag{26}$$

and with $\gamma' = \gamma/M$ and $M = \delta/c$ this becomes

$$j_s = \pi\eta_e\gamma^4(\delta/c)^2 B. \tag{27}$$

The half-angle γ is determined by spherical aberration to be

$$\gamma = (2\delta/C_s)^{\frac{1}{3}}, \tag{28}$$

C_s being the spherical aberration constant.

Equation (27) then becomes

$$j_s = \frac{\pi\eta_e\delta^{10/3}B}{(^1/_2\, C_s)^{4/3}\, c^2}\,. \tag{29}$$

Hence the current density is inversely proportional to the 4/3 rd power of the spherical aberration constant C_s. As far as we know this is the only example in electron optics where the spherical aberration constant plays such an important rôle. Assuming a current density in the primary image of $j_p = \pi\gamma^2 B = 0.5$ A/mm^2 we get by inserting into (27): $\eta_e = 2.3 \times 10^{-3}$ *), $\gamma = 0.08$, $\delta = 0.1\ \mu$, $c = 40\ \mu$, $j_s = 4 \times 10^{-11}$ A/mm^2. Assuming an efficiency of the fluorescent screen of $\eta_l = 30$ lm/w, the brightness of the visual secondary image becomes $B_l = 7.2$ nt. A rough calculation shows that this is some 10^3 to 10^4 times higher than that of the X-ray image.

It is true that the intensity of a plane and that of a spot are not strictly comparable and that we have neglected the effect of the background. On the other hand the X-ray image is lacking contrast too, especially when using the thin test grid, while the reflection method yields a more critical indication.

§ 8. *Influence of lens errors.* At this stage of the investigation we cannot yet judge the influence of lens errors on the focusing accuracy. The results and optical analogon experiments, however, have proved that correct focusing can be obtained if the lens aperture is adapted to the demagnification M and spherical aberration constant C_s. It is even more difficult to estimate the effect of astigmatism as the error need not be the same for the primary and the returning beam as a result of the image rotation. Investigations are in progress and will be published in the near future. Curiously no trace of astigmatism has been detected in our best X-ray pictures (see fig. 15), although a comparatively large aperture was used ($\gamma = 0.08$). Although the pole pieces have been manufactured with great care, there is no reason to believe that the astigmatism is smaller than 1 μ.

§ 9. *Magnetic stray field.* In § 4 it was shown that correct alignment can be obtained by having the secondary image coincide approximately with the electron source. This, however, is only true if there is no transverse magnetic field between electron source and objective lens.

We shall now calculate the maximum field intensity which gives a negligible effect. Assuming there is a weak magnetic field B perpendicular to the plane of the diagram (fig. 8) and acting from the source C over a distance l we may write (see fig. 8) $CS = \xi l$ and $\xi = l/R$ with $R = 3.38 \times 10^{-6} V^{1/2}/B$, where CS, l and R are in m, V in V, B in Wb/m^2. So $CS = l^2 B/3.38 \times 10^{-6} V^{1/2}$. We require $CS < 10^{-3}$ m and get the condition

---

*) The value of η_e depends on the electron energy and target material. According to Rudberg [10] [11]) we get for gold at 150 V, $\eta_e = 2.5$ to 5% [2]). We here take the value of η_e a factor 10 lower for 6 kV.

$$B < 3.38 \times 10^{-9} V^{1/2}/l^2. \tag{30}$$

In our case $l = 0.4$ m, $V = 6.10^3$ V, we have to fulfill $B < 1.6 \times \times 10^{-6}$ Wb/m^2.

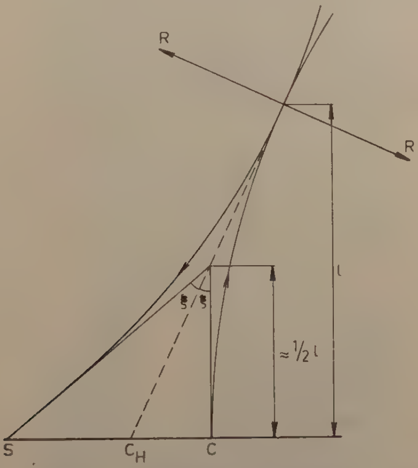

Fig. 8. Computation of the admissible transverse magnetic stray-field. C = electron source, C_H = the apparent electron source, S = secondary image, R = radius of the electron beam curvature.

In the presence of a stray field it is still possible by correctly tilting the objective to have the secondary image coincide with the source. This means that no conclusion as regards the alignment can be drawn from this coincidence.

§ 10. *Practical performance.* An improvised arrangement proved the intensity of the secondary image to be amply sufficient for focusing. One of our first photographs, using this focusing aid, was taken with such a low X-ray intensity that for correct exposure it takes 1 to 2 hours at 4 kV and 6 mm film distance.

From this provisional apparatus valuable information has been obtained for an experimental microscope in which this focusing aid is incorporated. Fig. 9 shows a simplified cross-section of this microscope (a more final design is under construction now).

Immediately under the focusing screen there is an aperture allowing only a narrow beam to enter into the microscope. This is necessary to suppress the background caused by reflection at the diaphragm.

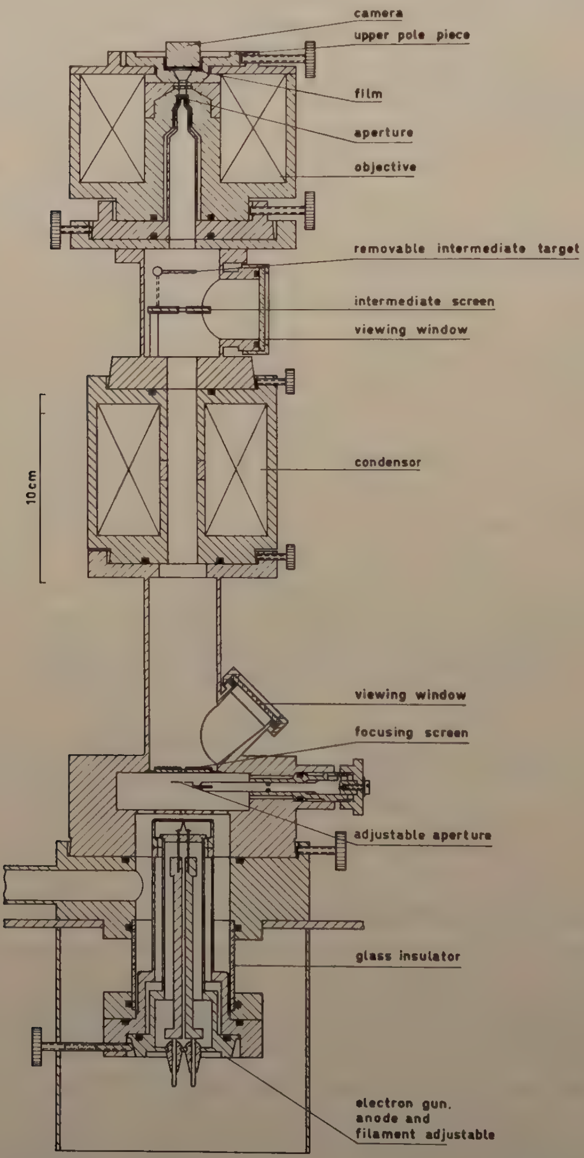

Fig. 9. Simplified cross-section of the experimental X-ray microscope.

An intermediate screen and a removable intermediate target are provided between objective and condensor. The screen enables us to catch the secondary image even when the lens is tilted too much. The intermediate target is used to centre the condensor. Electrical insulation makes it possible to measure the electron current if necessary. So these two parts are only used for preliminary alignment. The objective aperture can be centered during operation as a high accuracy is required. Previously the objective could also be

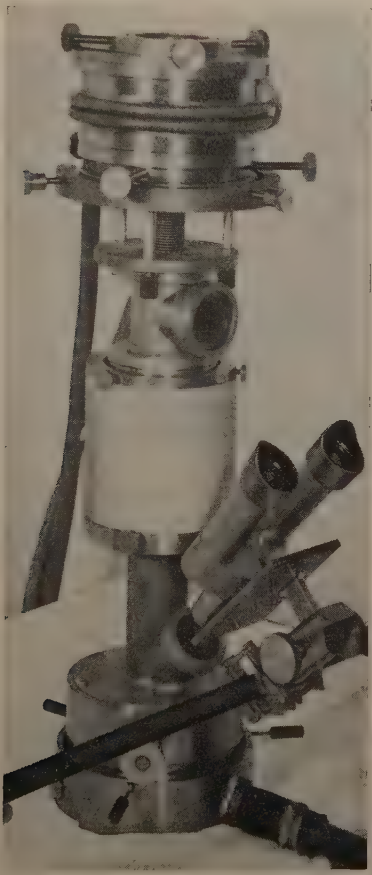

Fig. 10. The Delft X-ray projection microscope, constructed early in 1957. Binocular observation of the focusing screen. In its present form the tilting is omitted and a 30 × monocular microscope is used for focusing (cf. fig. 9).

tilted (see fig. 10), but this proved impractical since tilting and shifting in fact have the same effect. In our present apparatus the tilting therefore is omitted, as shown in fig. 9. It was found that positioning of the pole pieces during operation is more convenient than tilting the objective (see fig. 11).

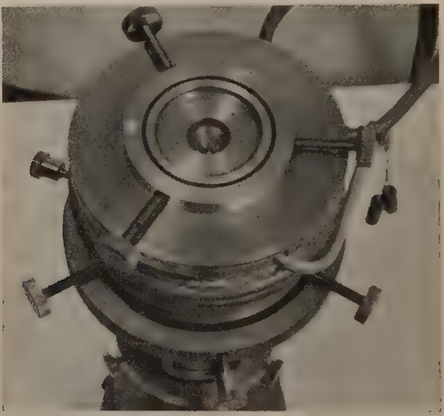

Fig. 11. Close-up of the upper pole piece.

Great care was taken to minimize the spherical aberration of the objective lens ($C_s \approx 0.5$ mm) [6] [7]).

At first the secondary image was observed through a 10 × binocular. Later on it was found that a 30 × magnification gives much better results.

§ 11. *Experimental results.* Centering the condensor according to (2) can be done very simply. Due to the small distance of this lens to the electron source and the small rotation angle θ, however, the accuracy is not high. It is advisable to choose the position of the intermediate target so that $\theta \approx 90°$. In our present apparatus this was not taken into consideration.

To align the objective and center the aperture stop the projection diagram as described before has proved very valuable. When the microscope is correctly aligned, focusing is achieved very easily since the focusing point is very critical. In fig. 12*a* a through-focal series of the secondary image is shown, taken directly from the screen. From left to right the lens power increases in regular steps. The asymmetry of the focusing curve is obvious. The hole in the screen is faintly distinguishable. The border of this hole is contaminated by fluorescent material which lights up strongly under irradiation by electrons, scattered at the diaphragm below. Fig. 14*b* shows a through-focal series of the secondary image with the lens aperture not correctly centered. Focusing is impossible in this case.

It proved that carbon contamination is not directly serious. A target which was previously covered with a discharge carbon film of about 500 Å at first gives a vague reflection image. When the microscope is nearly in focus, the brightness and sharpness increase until after 1 or 2 minutes the final brightness is attained. After electron bombardment during a long period the target roughened. Prolonged high-loading of the same area leads to crater formation. The roughness is visible in the secondary image if the lens is slightly under focus. In this case the apparatus acts as a reflection microscope and vague spots appear. When the microscope is focused, the brightness of the secondary image highly depends on the irradiated part of the target. Neither this nor the distinct increase in intensity of the X-ray output with the brightness of the secondary image is understood. These effects should be borne in mind in those cases where the X-ray intensity must be constant during long periods. Fig. 13 shows electron micrographs of a pre-shadowed carbon replica of an irradiated target. The craters caused by intense electron bombardment during long periods are clearly distinguishable. The maximum distance between the craters amounts to some $10\,\mu$. Since the focal distance was ≈ 1 mm, the maximum tilt used was some 1/200 radians. At larger tilt angles the effect shown in fig. 12*b* appears. Around the craters an area of some 50 μ in diameter is very rough. Fig. 14 shows an electron-micrograph of a part of such an area.

It thus appears that the maximum admissible tilt angle for correct focusing amounts to $\approx 1/200$ radians. If the target is fixed with respect to the objective, this implies that only an area with radius

$$r = f/200 \tag{31}$$

can be utilized, f being the focal distance of the objective. In view of the roughening and crater formation it is advisable to make the target movable with respect to the pole-pieces of the lens. If necessary a suitable part of the target could be selected for each exposure. Refocusing, of course, offers no difficulties at all. Finally we show some microradiographs, demonstrating the resolution that has been obtained. The anode voltage used was always 6 kV, except for the picture shown in fig. 16. At this tension the depth of penetration of the electrons in gold according to the Thomson-Whiddington law [12]) amounts to approximately 500 Å. So for a 0.1 μ resolution we do not need an unsupported target of 0.1 μ thickness as Nixon [8]) [9]) does. The target we use is an evaporated 5 μ Al-foil, coated with a gold layer of 0.1 μ. The exposure time is some 20 minutes at a film distance of 1 cm. The resolution seems to be limited by insufficient stability (electrical, mechanical and thermal) during long exposure. To demonstrate the focusing accuracy, we show two pictures of the well-known 1500 mesh (17 μ) silver test grid in fig. 15*a* and 15*b*. Fig. 15*b* is taken after defocusing and refocusing again. Both pictures show the first Fresnel fringe. Fig. 16 shows the 1500 mesh silver testgrid mounted on a 200 mesh coppergrid, taken with a Cu target at 12 kV, at which voltage the depth of penetration is some 0.5 μ. It proves that at higher tensions the focusing aid also works satisfactorily. Figs 17*a* and 17*b* show two microradiographs of gold-shadowed bull sperms. The heads are approximately 10 μ long. The tails show details reminding of electron micrographs. Fig. 17*c* shows untreated bull sperms. Although the contrast is very poor, particularly in the flat head, the first Fresnel fringe is still visible. Finally fig. 18 shows a transverse section of wood.

Acknowledgement. The authors wish to express their thanks to the electron microscope division of the Technical Physics Department, T.N.O. and T.H. for its cooperation in these experiments.

Received 10th February, 1958.

REFERENCES

1) Ardenne, M. v., Naturwissenschaften **27**, (1939) 485.
2) Ardenne, M. v., Tabellen der Elektronenphysik Band I, Deutscher Verlag der Wissenschaften, Berlin, 1956, p. 109.
3) Bruining, H., Physics and applications of secondary electron emission. Pergamon Press Ltd, London 1954.
4) Cosslett, V. E. and W. C. Nixon, Proc. Roy. Soc. **B140**, (1952) 422.
5) Jonker, J. L. H., Phil. Res. Rep. **6**, (1951) 372.
6) Liebmann, G. and E. M. Grad, Proc. Phys. Soc. **64B** (1951) 956.
7) Ments, M. v. and J. B. Le Poole, Appl. Sci. Res. **B1** (1947) 1.
8) Nixon, W. C., Proc. Roy. Soc. **A 232**, (1955) 475.
9) Nixon, W. C., Nature **175**, (1955) 1078.
10) Rudberg, E., Proc. Roy. Soc. **127 A** (1930) 111.
11) Rudberg, E., Phys. Rev. **50**, (1936) 138.
12) Whiddington, R., Proc. Roy. Soc. **89 A** (1914) 554.

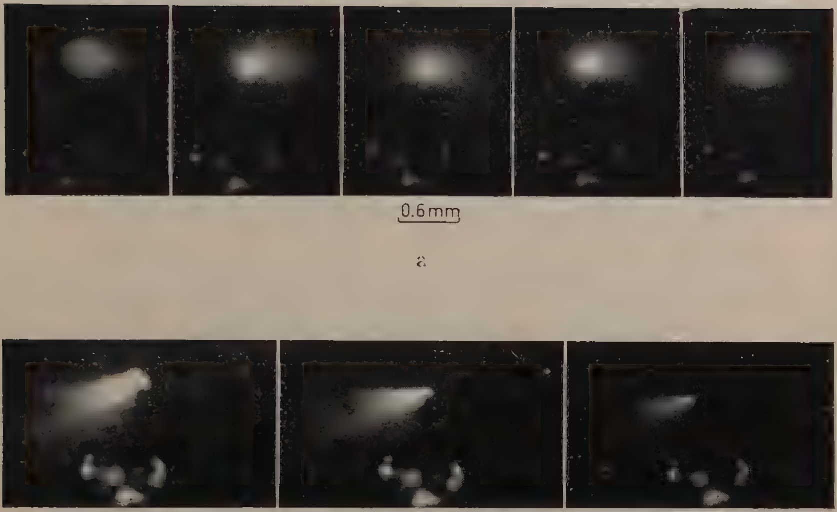

FIG. 12. Through-focal series of the secondary image directly photographed from the focusing screen. From left to right increasing lens power.
a. instrument aligned, b. aperture not well centred.

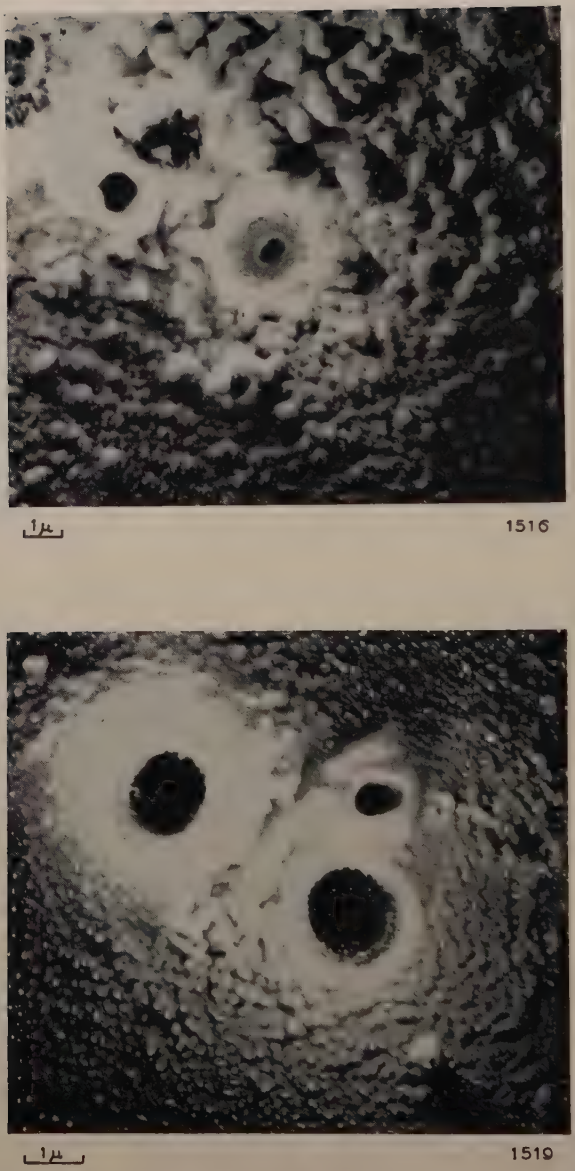

FIG. 13. Electron micrographs of irradiated targets. Craters are formed in places which have been used as X-ray source. Pre-shadowed carbon replicas. (Courtesy electron microscope division of the Technical Physics Department T.N.O. and T.H.)

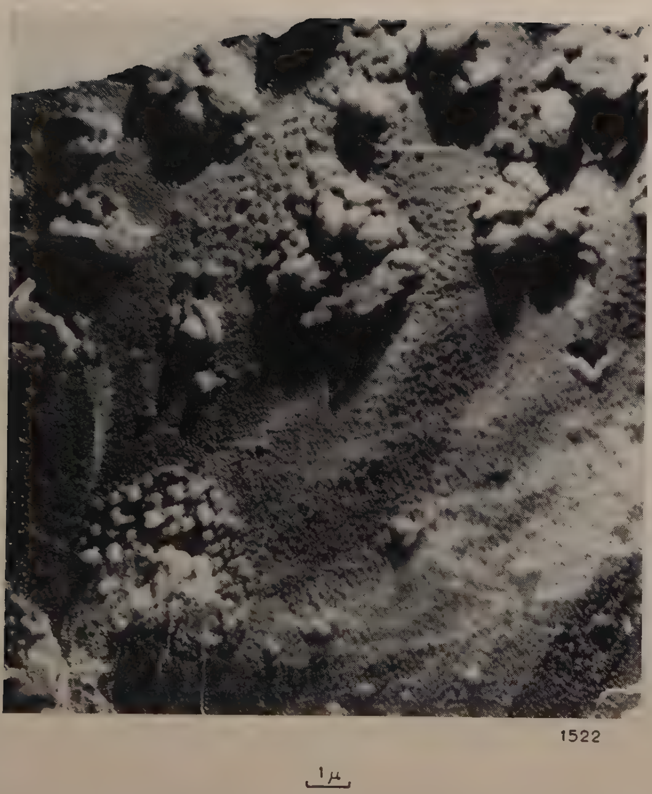

FIG. 14. Electron micrograph of the rough area around the craters. Pre-shadowed carbon replica. (Courtesy electron microscope division of the Technical Physics Department T.N.O. and T.H.)

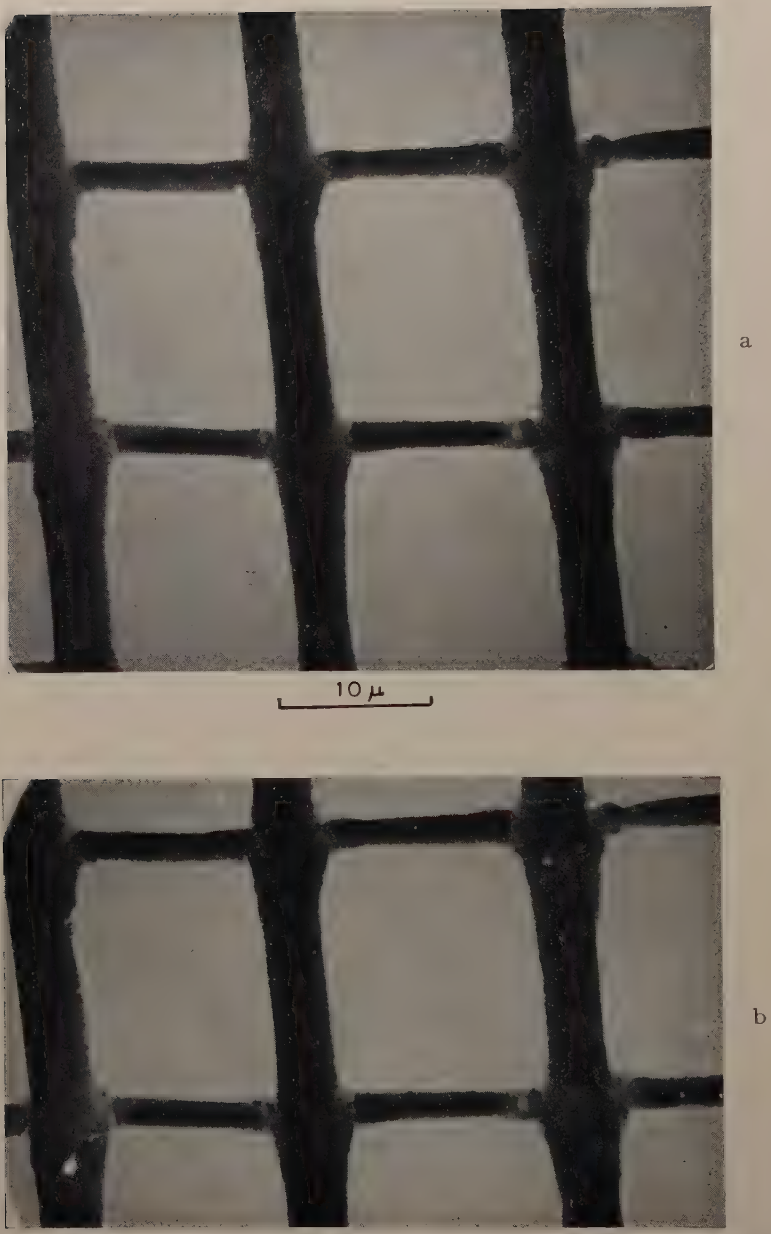

FIG. 15. X-ray micrographs of 1500 mesh (17 μ) silver grid demonstrating the focusing accuracy. b. is taken after defocusing and refocusing again. Both pictures show Fresnel fringe. Anode voltage: 6 kV, exposure time: 20 min., film distance: 10 mm. Target: evaporated 5 μ Al- foil, coated with a gold layer of 0.1 μ. Magnification on film: 200 x, total magnification appr. 2000 x.

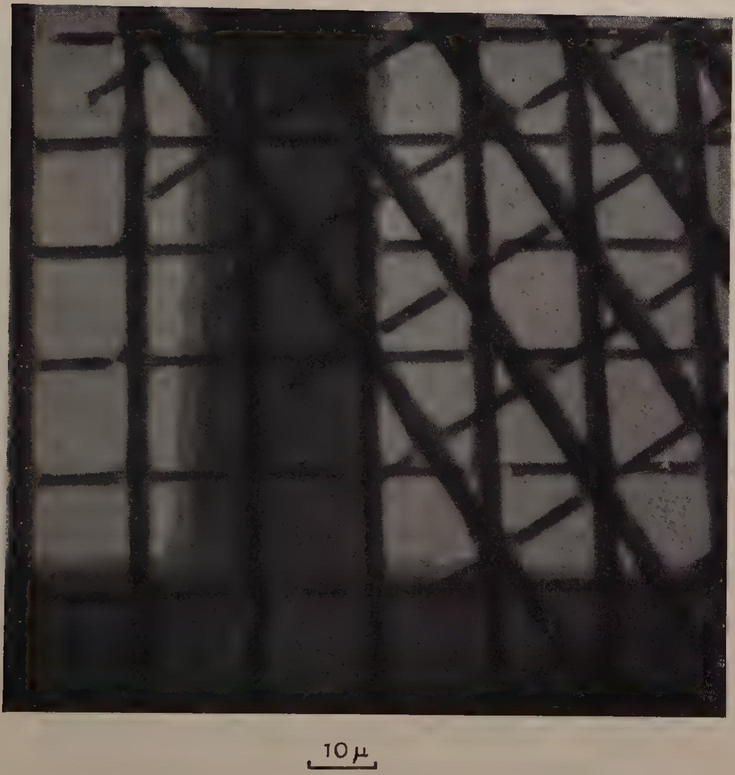

FIG. 16. X-ray micrograph of 1500 mesh silvergrid mounted on 200 mesh copper grid. Cu target 12 kV, total magnification appr. 900 x.

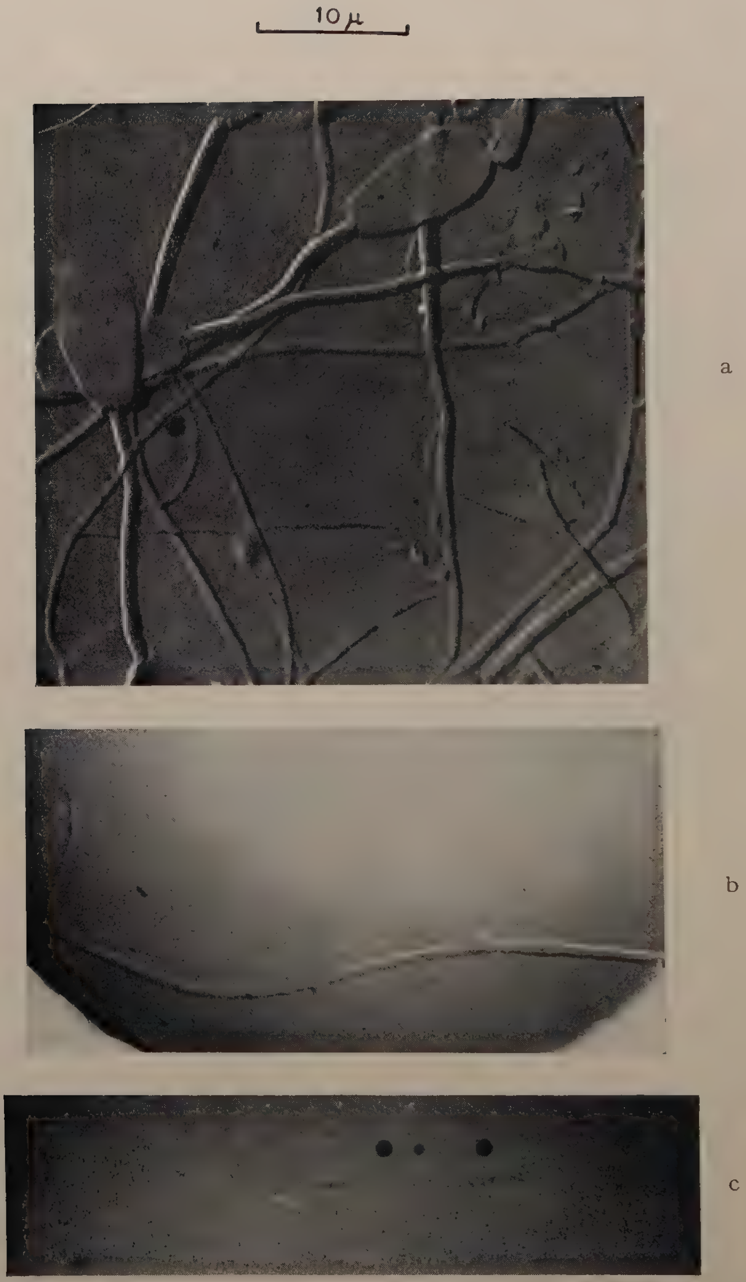

FIG. 17. X ray micrograph of gold shadowed bull sperms. Total magnification appr. 2000 x. Exposure conditions as fig. 14. a. heavily shadowed, b. slightly shadowed, c. X-ray micrograph of untreated bull sperms. Total magnification appr. 2000 x.

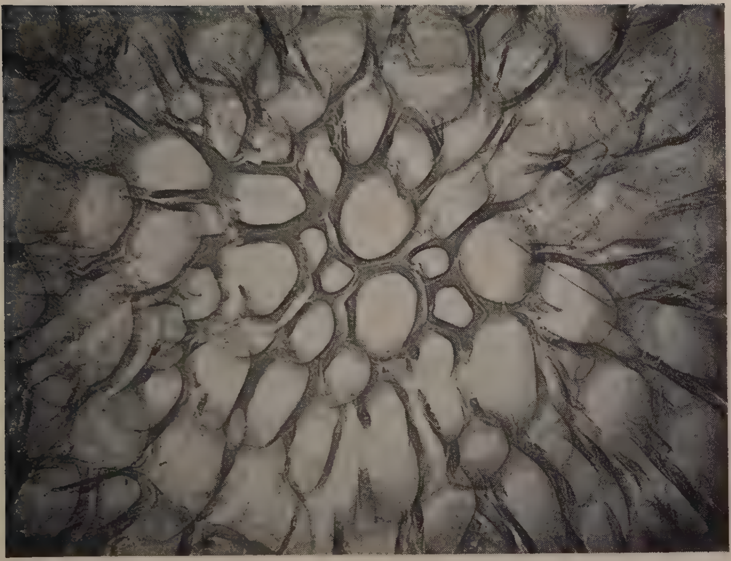

FIG. 18. X-ray micrograph of a transverse section of ashwood, 50 μ thick. Au target 6 kV, total magnification appr. 400 x.

Appl. sci. Res. Section B, Vol. 7

CERTAIN TWO-DIMENSIONAL SOLUTIONS TO POISSON'S EQUATION

by G. POWER

Nottingham University

and H. L. W. JACKSON

Nottingham Technical College, England

Summary

A method is presented which derives the solution to Poisson's equation in two dimensions, subject to boundary conditions of sufficient generality to be applicable to many branches of mathematical physics. In the first instance, a circular boundary is considered, and by means of conformal transformation an indication is given showing how the solution can be adapted to other boundary shapes.

§ 1. *Introduction.* A large number of problems in mathematical physics involve the solution of Poisson's equation, subject to certain boundary conditions. Where the boundaries that appear have intricate shape, any accurate solution is impossible, but in many cases with less complicated boundary form a general type of solution can be found.

We shall here consider two-dimensional problems with only one finite boundary which, in the first instance, will be taken as a circle of unit radius, and results will be obtained by employing complex variable technique.

The use of conformal transformations can extend these results to cases where non-circular boundary shapes are involved. If these are not whole-plane transformations, a certain amount of care has to be taken, and often problems involving only one region, either exterior or interior to the boundary, may be solved by this method.

§ 2. *Circular boundary.* Consider functions $\phi_1(x, y)$, $\phi_2(x, y)$, defined respectively in the regions $|z| \leqslant 1$, $|z| \geqslant 1$, $z = x + iy$, satisfying the differential equations

$$\nabla^2\phi_1 = f_1(x, y),\ \nabla^2\phi_2 = f_2(x, y), \tag{1}$$

where $f_1(x, y)$, $f_2(x, y)$ are known functions.

Let us assume that the following conditions have to be satisfied,

$$\left.\begin{aligned} \phi_1(x, y) &= \phi_2(x, y) \\ k_1 \frac{\partial\phi_1(x, y)}{\partial r} &= k_2 \frac{\partial\phi_2(x, y)}{\partial r} \end{aligned}\right\} \text{ when } |z| = 1, \tag{2}$$

where $r = |z|$, and k_1, k_2 are constants. These are the boundary conditions that obviously apply to the theories of hydrodynamics, magnetism and electricity.

By making the substitutions

$$\Phi_1(x, y) = \phi_1(x, y) - g_1(x, y),$$
$$\Phi_2(x, y) = \phi_2(x, y) - g_2(x, y),$$

where $g_1(x, y)$, $g_2(x, y)$ are particular solutions of the differential equations $\nabla^2 g_1(x, y) = f_1(x, y)$, $\nabla^2 g_2(x, y) = f_2(x, y)$ respectively, (1) becomes $\nabla^2\Phi_1(x, y) = 0$, $\nabla^2\Phi_2(x, y) = 0$. We thus see that

$$\phi_1(x, y) = g_1(x, y) + h_1(x, y),\ \phi_2(x, y) = g_2(x, y) + h_2(x, y),$$

where $h_1(x, y)$, $h_2(x, y)$ are harmonic functions yet to be determined.

Since $z = x + iy$, $\bar{z} = x - iy$,

$$\phi_1(x, y) = G_1(z, \bar{z}) + \operatorname{Re} H_1\left(z, \frac{1}{z}\right),\ \phi_2(x, y) = G_2(z, \bar{z}) + \operatorname{Re} H_2\left(z, \frac{1}{z}\right),$$

where

$$G_1(z, \bar{z}) \equiv g_1(x, y),\ G_2(z, \bar{z}) \equiv g_2(x, y),$$

$$\operatorname{Re} H_1\left(z, \frac{1}{z}\right) = h_1(x, y),\ \operatorname{Re} H_2\left(z, \frac{1}{z}\right) = h_2(x, y).$$

The first of the boundary conditions (2) shows that

$$G_1(z, \bar{z}) + \bar{G}_1(\bar{z}, z) + H_1\left(z, \frac{1}{z}\right) + \bar{H}_1\left(\bar{z}, \frac{1}{\bar{z}}\right) =$$
$$= G_2(z, \bar{z}) + \bar{G}_2(\bar{z}, z) + H_2\left(z, \frac{1}{z}\right) + \bar{H}_2\left(\bar{z}, \frac{1}{\bar{z}}\right), \tag{3}$$

on the boundary $z\bar{z} = 1$. Now substitute $\bar{z} = 1/z$ and assume

$$G_1\left(z, \frac{1}{z}\right) = G_3(z) + G_4\left(\frac{1}{z}\right), \quad G_2\left(z, \frac{1}{z}\right) = G_5(z) + G_6\left(\frac{1}{z}\right),$$

$$H_1\left(z, \frac{1}{z}\right) = H_3(z) + H_4\left(\frac{1}{z}\right), \quad H_2\left(z, \frac{1}{z}\right) = H_5(z) + H_6\left(\frac{1}{z}\right),$$

any term independent of z or $1/z$ being ignored. Equation (3) shows immediately that on the boundary

$$G_3(z) + \bar{G}_4(z) + H_3(z) + \bar{H}_4(z) = G_5(z) + \bar{G}_6(z) + H_5(z) + \bar{H}_6(z). \quad (4)$$

The second of the boundary conditions (2) can be written

$$k_1\left(\frac{\partial g_1}{\partial r} + \frac{\partial h_1}{\partial r}\right) = k_2\left(\frac{\partial g_2}{\partial r} + \frac{\partial h_2}{\partial r}\right) \quad \text{when } |z| = 1,$$

and since

$$h_1(x, y) + i\beta_1(x, y) = H_1(z, 1/z), \quad h_2(x, y) + i\beta_2(x, y) = H_2(z, 1/z),$$

this is

$$k_1\left(\frac{\partial g_1}{\partial r} + \frac{\partial \beta_1}{\partial s}\right) = k_2\left(\frac{\partial g_2}{\partial r} + \frac{\partial \beta_2}{\partial s}\right) \quad \text{when } |z| = 1,$$

where $s = \theta$ represents arc length of the unit circular boundary. On integrating, this becomes

$$k_1(g_3 + \beta_1) = k_2(g_4 + \beta_2) \qquad \text{when } |z| = 1,$$

where $\partial g_3/\partial\theta = \partial g_1/\partial r$, $\partial g_4/\partial\theta = \partial g_2/\partial r$, that is to say

$$k_1 \mathrm{Im}\left[P_1(z, \bar{z}) + H_1\left(z, \frac{1}{z}\right)\right] = k_2 \mathrm{Im}\left[P_2(z, \bar{z}) + H_2\left(z, \frac{1}{z}\right)\right] \quad (5)$$

on the boundary $z\bar{z} = 1$, where

$$P_1(z, \bar{z}) \equiv ig_3(x, y) \text{ and } P_2(z, \bar{z}) \equiv ig_4(x, y).$$

On substituting $\bar{z} = 1/z$, and assuming

$$P_1\left(z, \frac{1}{z}\right) = P_3(z) + P_4\left(\frac{1}{z}\right), P_2\left(z, \frac{1}{z}\right) = P_5(z) + P_6\left(\frac{1}{z}\right),$$

(5) yields

$$k_1\left[P_3(z)+P_4\left(\frac{1}{z}\right)-\bar{P}_3\left(\frac{1}{z}\right)-\bar{P}_4(z)+H_3(z)+\right.$$
$$\left.+H_4\left(\frac{1}{z}\right)-\bar{H}_3\left(\frac{1}{z}\right)-\bar{H}_4(z)\right]=$$
$$=k_2\left[P_5(z)+P_6\left(\frac{1}{z}\right)-\bar{P}_5\left(\frac{1}{z}\right)-\bar{P}_4(z)+H_5(z)+\right.$$
$$\left.+H_6\left(\frac{1}{z}\right)-\bar{H}_5\left(\frac{1}{z}\right)-\bar{H}_6(z)\right].$$

From this we obtain immediately, on the boundary,

$$k_1\,[P_3(z)-\bar{P}_4(z)+H_3(z)-\bar{H}_4(z)]=$$
$$=k_2\,[P_5(z)-\bar{P}_6(z)+H_5(z)-\bar{H}_6(z)]. \quad (6)$$

We have so far considered the boundary conditions which lead to the two equations (4) and (6), involving the four unknowns $H_3(z)$, $H_4(1/z)$, $H_5(z)$, $H_6(1/z)$. Two more equations are needed, and these are obtained from the form of $\phi_1(x, y)$ near the origin and of $\phi_2(x, y)$ at infinity. Assume that near the origin $\phi_1(x, y) \to \chi_1(x, y)$, and at large distance from the origin $\phi_2(x, y) \to \chi_2(x, y)$, the functions $\chi_1(x, y)$, $\chi_2(x, y)$ being known. We thus see that

$$\left.\begin{aligned}\mathrm{Re}H_4\left(\frac{1}{z}\right)+g_{10}\,(x, y)&=\chi_1(x, y),\\ \mathrm{Re}H_5\,(z)+g_{2\infty}(x, y)&=\chi_2(x, y)\end{aligned}\right\} \quad (7)$$

where $g_{10}(x, y)$ is the form taken by $g_1(x, y)$ near the origin, and $g_{2\infty}(x, y)$ that taken by $g_2(x, y)$ at large distance from the origin. The condition (7) will usually determine the choice of the particular solutions $g_1(x, y)$, $g_2(x, y)$.

Equations (4), (6), (7) constitute the solution to the problem, with

$$\phi_1=g_1(x, y)+\mathrm{Re}\left[H_3(z)+H_4\left(\frac{1}{z}\right)\right],$$
$$\phi_2=g_2(x, y)+\mathrm{Re}\left[H_5(z)+\mathrm{H}_6\left(\frac{1}{z}\right)\right].$$

Logarithmic terms can easily be incorporated.

Examples. (*a*) Let $g_1(x, y) = g_2(x, y) = 0$. Equations (4) and (6) yield

$$\left.\begin{aligned} H_3(z) + \bar{H}_4(z) &= H_5(z) + \bar{H}_6(z), \\ k_1[H_3(z) - \bar{H}_4(z)] &= k_2[H_5(z) - \bar{H}_6(z)]. \end{aligned}\right\} \tag{8}$$

Let the condition at the origin give $H_4(z) = 0$; the condition at infinity shows that $H_5(z)$ represents an unperturbed complex potential. Solving (8)

$$\bar{H}_6(z) = \left(\frac{k_2 - k_1}{k_1 + k_2}\right) H_5(z), \quad H_3(z) = \left(\frac{2k_2}{k_1 + k_2}\right) H_5(z).$$

From this result one obtains immediately the external circle theorem in electricity and magnetism [1]). The internal circle theorem can be obtained similarly.

(*b*) The problem of a circular cylinder in an incompressible flow of constant vorticity can be deduced by letting $f_2(x, y) = \omega$, a known constant, and by ignoring the internal field. From (4) the boundary condition is simply

$$G_5(z) + \bar{G}_6(\bar{z}) + H_5(z) + \bar{H}_6(z) = 0. \tag{9}$$

We now have to state the form of $\phi(x, y)$ at large distances from the boundary. Let us assume that it is one of constant shear parallel to the x-axis, so that from (7) $\mathrm{Re} H_5(z) + g_{2\infty}(x, y) = Uy + \frac{1}{2}\omega y^2$, where U is known. It is easy to see that the general form of $g_2(x, y)$ is given by

$$g_2(x, y) = \frac{\omega}{2(a + b)} (ax^2 + by^2 + 2hxy + 2gx + 2fy),$$

where a, b, h, g, f, are constants yet to be determined.

The above condition shows that we may take $f = g = h = 0$, together with

$$H_5(z) = -iUz - \frac{a\omega z^2}{2(a + b)}.$$

Then, since

$$g_2(x, y) = \frac{\omega}{8(a + b)} [z^2(a - b) + \bar{z}^2(a - b) + 2z\bar{z}(a + b)],$$

we obtain, on setting $\bar{z} = 1/z$,

$$G_5(z) = \frac{\omega(a - b)z^2}{8(a + b)}, \quad G_6(1/z) = \frac{\omega(a - b)}{8(a + b)} \frac{1}{z^2}.$$

Equation (9) now gives

$$-\bar{H}_6(z) = \frac{\omega(a-b)\,z^2}{8(a+b)} + \frac{\omega(a-b)\,z^2}{8(a+b)} - iUz - \frac{a\omega z^2}{2(a+b)},$$

so that $H_6(1/z) = -iU/z + \frac{1}{4}\omega/z^2$. Thus $\phi(x, y)$, the stream function, is given by

$$\phi(x, y) = Uy\left(1 - \frac{1}{x^2+y^2}\right) + \frac{wy^2}{2} + \frac{\omega(x^2-y^2)}{4(x^2+y^2)^2}.$$

Note that this result is independent of the value of the constants a, b; moreover, it is easily seen that we could obtain the same result for values of f, g, h other that zero. This indicates the uniqueness of the solution.

§ 3. *Non-circular boundaries.* The method indicated in § 2 can be adapted for other boundary shapes by the use of conformal transformations. Suppose the function ϕ satisfies the differential equation

$$\frac{\partial^2\phi}{\partial\xi^2} + \frac{\partial^2\phi}{\partial\eta^2} = F(\xi, \eta) \tag{10}$$

and let C, the given boundary in the ζ-plane, where $\zeta = \xi + i\eta$, be suitable transformed into the unit circle in the z-plane by $z = z(\zeta)$. It is easy to see that

$$\frac{\partial^2\phi}{\partial\xi^2} + \frac{\partial^2\phi}{\partial\eta^2} = \left(\frac{\mathrm{d}z}{\mathrm{d}\zeta}\right)\left(\frac{\mathrm{d}\bar{z}}{\mathrm{d}\bar{\xi}}\right)\left(\frac{\partial^2\phi}{\partial x^2} + \frac{\partial^2\phi}{\partial y^2}\right),$$

so that (10) can be written in the form

$$\frac{\partial^2\phi}{\partial x^2} + \frac{\partial^2\phi}{\partial y^2} = f(x, y),$$

and this is precisely the problem that has previously been discussed.

Care must be exercised with the mapping $z = z(\zeta)$ which normally is not a whole-plane transformation, in which case only the region either inside or outside the boundary C can be considered.

Example. For an elliptic cylinder in an incompressible flow of constant vorticity, we consider the transformation

$$\zeta = \gamma z + \frac{\delta}{z} \text{ where } \gamma = \frac{A+B}{2}, \ \delta = \frac{A-B}{2},$$

in which the exterior regions of the ellipse

$$\frac{\xi^2}{A^2}+\frac{\eta^2}{B^2}=1,\ \ \zeta=\xi+i\eta$$

and the unit circle in the z-plane correspond. Now

$$\left(\frac{d\zeta}{dz}\right)\left(\frac{d\bar{\zeta}}{d\bar{z}}\right)=\left(\gamma-\frac{\delta}{z^2}\right)\left(\gamma-\frac{\delta}{\bar{z}^2}\right),$$

so that we seek a solution to

$$\frac{4\partial^2\phi}{\partial z\partial\bar{z}}=\frac{\partial^2\phi}{\partial x^2}+\frac{\partial^2\phi}{\partial y^2}=\omega\left[\gamma^2-\gamma\delta\left(\frac{1}{z^2}+\frac{1}{\bar{z}^2}\right)+\frac{\delta^2}{z^2\bar{z}^2}\right]$$

where ω is constant, such that ϕ, the stream function in this context, is constant on the unit circle. We may therefore take

$$g(x,y)=\frac{\omega\gamma^2}{2(a+b)}(ax^2+by^2+2hxy+2gx+2fy)+$$
$$+\frac{\omega}{4}\left[\gamma\delta\left(\frac{\bar{z}}{z}+\frac{z}{\bar{z}}\right)+\frac{\delta^2}{z\bar{z}}\right].$$

If the flow is one of constant shear parallel to the ξ-axis, at a great distance from the elliptic cylinder ϕ behaves like $U\eta+\frac{1}{2}\omega\eta^2$, which in the z-plane becomes $U\gamma y+\frac{1}{2}\omega\gamma^2y^2$. In this case

$$\mathrm{Re}H_5(z)+g_{2\infty}(x,y)=U\gamma y+\frac{\omega}{2}\gamma^2y^2.$$

As in example (b) of § 2, we may take the constants f, g, h to be zero together with

$$H_5(z)=-iU\gamma z-\frac{a\omega\gamma^2z^2}{2(a+b)}.$$

This leads to

$$H_6(1/z)=-iU\gamma/z+\tfrac{1}{4}\omega(\gamma^2-2\gamma\delta)/z^2,$$

and finally

$$\phi=U\gamma y\left(1-\frac{1}{x^2+y^2}\right)+$$
$$+\frac{\omega}{2}\gamma^2y^2+\frac{\omega}{4}(\gamma^2-2\gamma\delta)\frac{(x^2-y^2)}{(x^2+y^2)^2}+\frac{\omega}{4}\left\{\frac{\delta^2+2\gamma\delta(x^2-y^2)}{(x^2+y^2)}\right\}.$$

Since

$$\xi = x\left[\gamma + \frac{\delta}{x^2 + y^2}\right], \quad \eta = y\left[\gamma - \frac{\delta}{x^2 + y^2}\right],$$

the result if required may be obtained in terms of (ξ, η). We again note the uniqueness of the solution.

Received 21st March, 1958.

REFERENCE

1) Power, G. and H. L. W. Jackson, Appl. Sci. Res. B6 (1957) 456.

ERRATUM

Appl. sci. Res. **B6** (1957) 456

A GENERAL CIRCLE THEOREM

by G. POWER and H. L. W. JACKSON

For $\dfrac{\partial w_e}{\partial z}$ read $\dfrac{\partial w_e}{\partial |z|}$ and for $\dfrac{\partial w_i}{\partial z}$ read $\dfrac{\partial w_i}{\partial |z|}$ throughout.

Received 2nd Febr. 1958.

Appl. sci. Res. Section B, Vol. 7

ASPECTS OF ELECTRICAL BREAKDOWN OF LIQUID INSULATING MATERIAL I

by J. A. KOK and M. M. G. CORBEY

Philips Research Laboratories, N.V. Philips' Gloeilampenfabrieken, Eindhoven, Netherlands

Summary

The electrical breakdown strength of insulating oil depends on the size of foreign particles which may form bridges in a place of maximum electric stress. This theoretical relation was verified with colloid suspensions of particles of known radius. Mineral oils may deteriorate if the particles unite by the process of flocculation, the occurrence of which depends on the relative magnitudes of the attractive London-Van der Waals forces acting between the particles and the repulsive forces between their ion atmospheres. The possibility of using a mineral oil as an insulator depends on the existence of an upper limit of the size of particle complexes due to the rapid fall-off of the L.-v.d.W. forces at diameters exceeding 500 Å. The latter value of $2r$ corresponds to a breakdown strength of 1 kV/mm. If acids are being formed, the upper limit of 500 Å will shift towards larger values, and correspondingly the breakdown strength may drop below 1 kV/mm.

§ 1. *Introduction.* It is a well-known fact that contaminants may considerably lower the electrical breakdown strength of liquid insulators. In the first stage of a breakdown the impurities, which are assumed to be electrically polarizable particles of high dielectric constant, gather in a place of maximum stress by the action of transverse gradient forces and form a bridge along the lines of force, just as happens with induced magnetic dipoles (iron filings) in a magnetic field.

If the radii r of the particles are equal and if their dielectric constant is assumed to be infinite, then the polarizability may be assumed to be r^3. If the locally concentrated stress is thrice the average field strength, such as occurs on top of a hemispherical hump on one of the electrodes, then the breakdown strength E_0 after a long time may be shown to depend only on r and the absolute temperature T [1]):

$$r^3E_0^2 = \tfrac{1}{4}\,kT. \qquad (1)$$

With $T = 300°\mathrm{K}$ this formula gives for $E_0 = 20\ \mathrm{kV/mm} : r = 30\ \mathrm{Å}$; $E_0 = 100\ \mathrm{kV/mm} : r = 9.5\ \mathrm{Å}$. The order of magnitude of the particle diameter $2r$ in extremely pure oil may be as small as the length of the oil molecules, perhaps slightly larger. In these cases the breakdown may be caused by slightly oxidized oil molecules. It follows for instance from Watson and Higham's [2]) and Crowe, Sharbaugh and Bragg's [3]) measurements on very pure hydrocarbon oils that: $E_0 = 150\ \mathrm{kV/mm}$, $2r = 15\ \mathrm{Å}$, which latter value is slightly larger than the length of a *n*-hexane molecule. This correspondence is rather close.

It may be asked whether the experiments on the formation of a bridge in colloid suspensions are a true model of the electric breakdowns of liquid dielectrics.

§ 2. *Formation of a bridge by colloid particles.* The phenomenon of the formation of bridges by particles in colloid suspension was discovered by Cotton and Mouton [4]) who used a well-defined suspension. Since this first observation a number of measurements on this phenomenon have been carried out either on specially prepared suspensions or on several commercial substances varying from insulating oil to lacquers and diluted milk.

Hirobe and co-workers [5]) investigated the breakdown of insulating oil. They observed the breakdown to take place after a bridge between the electrodes had been formed. They assumed the bridge to consist of moist cellulose fibres. Muth [6]) confirmed the formation of a bridge consisting of fat particles in diluted milk. Kruyt and Vogel [7]) observed the same phenomenon in suspensions of gold particles. Further measurements have been carried out by Gindin and co-workers [8]) (suspensions of aluminium powder in gasoline), Brintzinger and co-workers [9]) (pigments in lacquers), Stauff [10]) (suspensions of paraffin oil in water) and the authors [1]) (aluminium particles, graphite powder and fuller's earth in insulating oil).

§ 3. *Particles of high dielectric constant.* Colloid particles are often surrounded by an atmosphere consisting of ions, but which may also contain dipoles and electrons (for a review see Brintzinger's articles [9])). This atmosphere will not exist with particles of molecular dimensions.

The electrical behaviour of colloid particles depends mainly on the presence of their ion atmosphere and is to a considerable extent independent of the kind of substance of the particles (see § 4).

Owing to the presence of the ion atmospheres the particles may acquire an induced electric dipole moment in an electric field by the motions of the positive and negative charges inside this atmosphere (see Kruyt and Kunst [11])). By this process their dielectric constant may become r^3 as a maximum if the frequency of the field is not too high. In fields of low frequency the electric charges may be assumed to move in phase with the field, but in h.f. fields the ions may be unable to follow the field in phase. The polarizability will then sink considerably below the value r^3 and the breakdown by formation of a bridge may become impossible or will be shifted towards higher field strengths.

It will be clear that by absorption of traces of water the dielectric constant of cellulose fibres may increase considerably. Dry cellulose fibres in pentachlor diphenyl (clophen, aroclor) have the same dielectric constant as the fluid, show no polarizability and are not subjected to transverse gradient forces by which they might flow towards a place of maximum stress. They will not align in a bridge, but remain dispersed. Moist cellulose fibres, on the contrary, will have a high dielectric constant and thus they are strongly polarized, hence they will partake in the formation of a bridge and may become the cause of a breakdown.

§ 4. *Ion atmospheres.* Colloid particles may be electrically charged by an adsorption of ions. Further they may be surrounded by an atmosphere consisting of ions of the opposite sign (counter ions, Gegenionen).

Coehn [12]) has empirically found for two phases in contact that the one with a higher dielectric constant tends to be positively charged, the other negatively charged. This rule holds, strictly speaking, for non-conductors, but it is of such wide applicability that, since the dielectric constant of water is exceptionally high, namely 80, almost all colloid particles, bubbles and suspensions in water are negatively charged.

Together the adsorbed ions and the surrounding counter ions may form a double sheath. In fig. 1 such a so-called von Helmholtz double sheath at the surface of a fibre has been represented. In some cases the situation is more complex by the presence of dipoles in the atmosphere of the particle (see fig. 2, which has been copied from Kruyt and Klompé 13)). In this case it is possible to distinguish the following layers when passing from the particle into the neutral liquid: a sheath consisting of adsorbed negative ions, a layer of positive counter ions, which may be interchanged (together they form a double sheath), further a layer consisting of permanent dipoles, a diffuse double sheath and finally the neutral liquid.

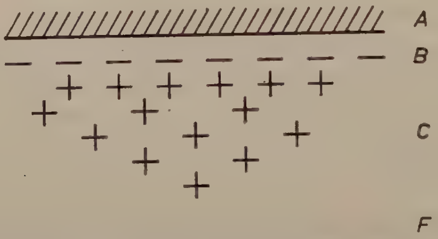

Fig. 1. Von Helmholtz double sheath at a particle-liquid interface A which is charged by negative ions B. C is a diffuse sheath of positive counter ions (Gegenionen), F is the neutral liquid. The strongest electric fields are at the border line of B and C.

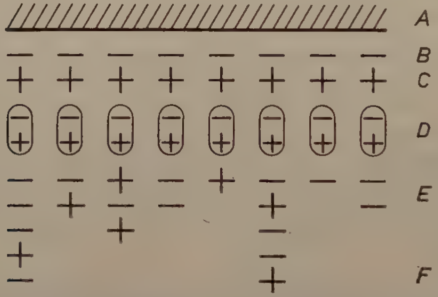

Fig. 2. Double sheaths according to Kruyt and Klompé. Owing to the precence of a dipole sheath D the double sheath B + C is more sharply defined. Outside D a diffuse double sheath E occurs which gradually merges into the neutral liquid F.

§ 5. *Flocculation.* Small particles tend to unite by the attractive London- van der Waals forces. Between the atmospheres of the particles repulsive forces exist. Whether the resultant force is repulsive or attractive depends on several factors, i.e. the particle radii and the thickness, the composition and the density of the ion atmospheres. In the first case (repulsion) the suspension may be called more or less stable, in the second case (attraction) the particles may stick together at every collision and form larger complexes at which the ion atmospheres unite to form a single atmosphere around the enlarged particle (flocculation).

With Overbeek [14]) we assume having a suspension consisting of foreign particles of say 10 Å diameter in insulating oil. This diameter is approximately the length of the elementary cell of a cellulose molecule. Proper repulsive ion atmospheres will not exist and thus the particles may adhere together at every collision by artractive London-van der Waals forces (rapid flocculation). Particles of a diameter larger than say 50 Å may gradually have collected an ion atmosphere, thus the repulsive forces between those atmospheres come into existence. The energy of repulsion may be expressed by an energy barrier, which may be higher than kT and increases proportional to r, even to values of $10kT$ or $20\,kT$. In that case collisions of two particles with a relative velocity of an energy kT will in general not result in a formation of larger complexes, the suspension hence being stable.

However, by the presence of a trace of electrolyte or dipoles, the repulsive action of the ion atmosphere may be more or less neutralized, so that the energy barrier may sink below the value kT. After a collision the two particles will adhere, whereas their atmospheres unite to form a single atmosphere enveloping the enlarged particle This phenomenon is called slow flocculation.

§ 6. *Size maximum of flocculation.* It is a necessary condition for flocculation that the attractive London- van der Waals forces acting between the particles proper should be more powerful than the repulsive forces acting between the ion atmospheres.

The particle diameters will slowly grow but attain a certain upper limit of say 500 Å. The slow flocculation is a self-retarding process for particles of that size, as the London-van der Waals forces fall rapidly off for particles larger than 500 Å, this according to Overbeek, who also pointed to the applicability of Casimir and Polder's [15]) calculations showing that an extra fall-off takes place by relativistic retardation effects not included in London's non-relativistic theory. Thus the upper size limit of 500 Å may, in the absence of electrolytes, be rather sharp. Particles with a diameter of 500 Å give a breakdown strength of 0.9 kV/mm.

If the repulsive action of the ion atmosphere is neutralized by a trace of acids, then the particles may grow further and the breakdown strength drops below 0.9 kV/mm.

It is interesting from a scientific point of view that this upper limit of the diameter of 500 Å for colloid particles, derived from considerations of colloid chemistry, has turned up in speculations on the breakdown strength of liquid insulators. To the fact of the rapid fall-off of the London-van der Waals forces at diameters exceeding 500 Å may be ascribed the possibility of using mineral oil as an insulator.

§ 7. *E_0 vs r for colloid particles in suspension.* From the foregoing paragraphs it is evident that (1) may be verified by determining E_0 and r for particles in colloid suspension or by the values of r calculated from E_0 for pure insulating oil which may be compared with the known diameters of hydrocarbon molecules. The latter method has been described in § 1.

Watson and Higham's [2]) and Crowe, Sharbaugh and Bragg's [3]) measurements of E_0 for very pure insulating oil led to values of $2r$ which are slightly larger than the length of n-hexane molecules. In the measurements on colloid particles carried out thus far the radii of the particles are generally not determined with sufficient accuracy. Moreover, the direct determination of the *average* particle size is not conclusive for the comparison with particle sizes calculated with (1). The gradient forces are propor-tional to r^3, thus a bridge is preferentially formed by the *largest* particles of the suspension. The *average* size of the particles is not important.

Determinations of r have been carried out by visual observation of the particles through a microscope, by the Debye-Scherrer X-ray method or by calculation from the observed velocity of sedimentation of the particles. These values may be compared with the values of r obtained by measurements of the breakdown strength E_0 and (1). However, in general most of the previous data needed for our verification must be called fragmentary and incomplete. The most complete comparison could be obtained by using measurements carried out by Stauff [10]), Vogel [6]) and Gindin [8]).

Stauff [10]) observed the formation of bridges consisting of paraffin oil drops in water. The radii of the paraffin oil drops were determined by microscopic measurements and ranged in several series of measurements from 1.3 μ to 0.33 μ, corresponding to measured breakdown strengths of 1.25 V/mm and 15.6 V/mm. With our formula (1) these breakdown strengths may be found to correspond to particle radii of 1.8 μ and 0.34 μ respectively, which values agree well with 1.3 μ and 0.33 μ as determined by a microscope. It is pointed out here that the correspondence between the values of the radii of smaller particles is closer than with larger particles. The larger particles may have had a relatively extensive ion atmosphere which cannot be observed by visual means, but which may become important for the verification of our formula. With much smaller particles the ion atmospheres may be less extensive or even absent.

Kruyt and Vogel [7]) measured the formation of bridges consisting of gold particles having initially diameters of 100 Å to 200 Å, which increased by flocculation to sizes of 2500–5000 Å. The voltages they used were 3 to 10 V, the electrode gaps 0.5 to 2 mm. The field strengths were not given exactly for every measurement. If it is assumed that the value of the breakdown strength was of the order of magnitude of 20 V/mm, then our formula gives a particle diameter of 6000 Å or 0.6 μ, which is of the same order of magnitude as 5000 Å, the largest average particle diameter after the flocculation had taken place. Thus the correspondence may be considered to be satisfactory.

Gindin and collaborators [8]) observed the formation of bridges of aluminium particles in gasoline. The value of $r = 2.5\ \mu$ they report do not correspond to the observed breakdown strength of 400 V/mm, as our formula (1) gives a value of $r = 0.02\ \mu$ with $E_0 =$ $= 400$ V/mm. Gindin states that a five-fold decrease of the particle diameter results in an increase of E_0 by a factor 3.25. According to our formula this proportion should be 11. In this case the correspondence is rather poor, which may be due to the petrol and the aluminium having very different specific gravities. As the bridge tends to be destroyed by the proper weight of its particles, the breakdown strength shifts towards higher voltages.

§ 8. *Deterioration of the oil.* The insulating oil may deteriorate if it contains very small particles

1. by rapid or slow flocculation which may take place even if no field is being applied. This phenomenon may be promoted by acids present in the oil, but will not be fatal except in oils in contact with the open air.

2. by slow flocculation if a strong field higher than 1 kV/mm is applied and acids are being formed. In this case the formation of particle complexes with a diameter larger than 500 Å and a breakdown strength below 1 kV/mm may follow. In every bridge which is being formed by gradient forces and destroyed by the Joule heat, discharges in a gas occur which may give rise to a local carbonization of the oil and the formation of acids. The carbon particles may flocculate, in the presence of an acid, to complexes larger than 500 Å.

In general it may be stated that, with fields stronger than 1 kV/mm, we are working on a downhill slope for the insulating value of the oil. This effect may be aggravated by a deterioration of the oil by corona discharges, causing acids to be formed by which the particle diameter may increase to values larger than 500 Å. The determination of acidity and formation of sludges may be considered a measure of the deterioration of the oil, as has been pointed out by Childs and Stannett 16).

In another article the deterioration of the insulating oil by corona discharges will be treated.

Reseived 12 April 1958.

REFERENCES

1) Kok, J. A., and M. M. G. Corbey, Appl. Sci Res. **B4** (1955) 474.; **B6** (1957) 197, 449.

2) Watson, P. K. and J. B. Higham, Symposium on insulating materials, Proc. Instn. Electr. Engrs **100** II A, nr. 3 (1953) 168.

3) Crowe, R. W., A. H. Sharbaugh and J. K. Bragg, J. Appl. Phys. **25** (1954) 1480, 392.

4) Cotton, A. and H. Mouton, J. Chim. Phys. **4** (1906) 365.

5) Hirobe, F., W. Ogawa and S. Kubo, Electrician **78** (1917) 656.

6) Muth, E., Kolloidzschr. **41** (1927) 97.

7) Kruyt, H. R. and J. G. Vogel, Kolloidzschr. **95** (1941) 2. Also J. G. Vogel, Thesis Utrecht 1938.

8) Gindin, L. G., c.s., Dokl. Akad. Nauk S.S.S.R. **72** (1950) 671; Chem. Abstr. **44** III, 10405, 1950; J. Techn. Phys., U.S.S.R. **20** (1950) 937; Chem. Abstr. **44**, II, 6237, 1950.

9) Brintzinger, H., R. Haug and G. Sachs, Farbe und Lack, **58** (1952) 5, 143,522; **59** (1953) 407; **60** (1954) 15, 59, 95. Contains a number of useful references.

10) Stauff, J., Kolloidzschr. **143** (1955) 162.

11) Kruyt, H. R. and H. Kunst, Kolloidzschr. **91** (1940) 1.

12) Coehn, A., Ergebnisse Exakt. Naturwiss. **1** (1922) 175.

13) Kruyt, H. R. and M. A. M. Klompé, Koll. Beihefte **54** (1943) 484.

14) Overbeek, J. Th. G., Symposium 1946 on Boundary Effects (Grenslaagverschijnselen), p. 130–152. Verh. Kon. Acad. Wetensch. België. H. R. Kruyt, Colloid Science I, Elsevier 1952, 58–89, 264–266.

15) Casimir, H. B. G. and D. Polder, Phys. Rev. **73** (1948) 360.; Nature **158** (1946) 787.

16) Childs, D. G. and A. W. Stannett, see ref.2), p. 61.

Appl. sci. Res. Section B, Vol. 7

A CRITICAL COMPARISON OF PROJECTION MICRORADIOGRAPHY AND THE 2X METHOD

by ONG SING POEN and J. B. LE POOLE

Technical Physics Laboratory, Technological University, Delft, Netherlands.

Summary

It is shown that Cosslett's [1]) criticism on the 2X method [2]) is based partly on a misconception of the resolving power of the photographic film and partly on a fundamentally wrong comparison between projection and 2X method. A generally valid comparison is given for the cases where the resolving power is not limited by Fresnel diffraction. Finally it is shown that Fresnel fringes are smaller in the 2X method than in a comparable projection system.

§ 1. *Grain size and resolving power of photographic emulsions.* In our previous publication [2]) the expression "resolution of the film" is used and in connection herewith no mention was made of the grain size. Admittedly the resolving power depends very much on the contrast in the image and consequently it is not the most suitable characteristic of the emulsion, but it is decidedly more so than the grain size. It is more or less generally accepted that the resolution of the best films is between $\frac{1}{2}$ and 1 μ. Bohatirchuk [3]) shows the grains of Lippmann film, the size of which amounts to some 500 Å. Ehrenberg and White [4]) quote a grain size of less than 500 Å for Kodak Maximum Resolution.

Obviously grain size and resolution are closely related.

§ 2. *Intensity distribution.* It will be shown that under reasonable conditions the intensity distributions in the projection- and the 2X method are exactly the same, be it on a different scale.

Consider an X-ray source with an arbitrary intensity distribution $F(p, q)$. A specimen at a distance a has a density distribution $\psi(u, v)$. If the dimensions of the source are small compared to $a + b$ (i.e. $p \ll a + b$ and $q \ll a + b$), the intensity distribution $\varphi(x, y)$ on the film may be written as

$$\varphi(x, y) = c \int_{-\infty}^{+\infty} \int_{-\infty}^{+\infty} \psi(u, v)\, F(p, q)\, \mathrm{d}p\, \mathrm{d}q. \tag{1}$$

From fig. 1 it follows that

$$u = a \frac{x - p}{a + b} + p = \frac{ax}{a + b} + \frac{bp}{a + b}, \tag{2}$$

$$v = a \frac{y - q}{a + b} + q = \frac{ay}{a + b} + \frac{bq}{a + b}. \tag{3}$$

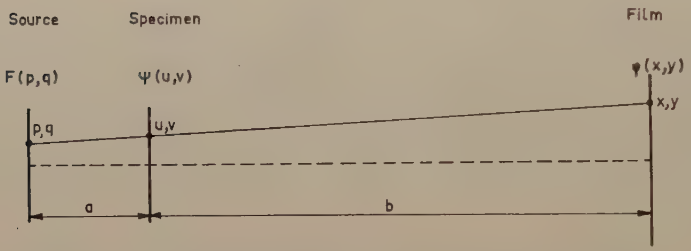

Fig. 1. Coordinate system for source, specimen and film.

The new coordinates x_1, y_1 and p_1, q_1 will now be introduced according to

$$x_1 = \frac{a}{a + b} x = \eta x, \qquad y_1 = \frac{a}{a + b} y = \eta y, \tag{4}$$

$$p_1 = \frac{b}{a + b} p = (1 - \eta) p, \quad q_1 = \frac{b}{a + b} q = (1 - \eta) q. \tag{5}$$

Here

$$\frac{1}{\eta} = \frac{a + b}{a} = M, \tag{6}$$

where M denotes the magnification. Equation (1) then becomes

$$\varphi(Mx_1, My_1) = c \int_{p_1}\int_{q_1} \psi(p_1 + x_1, q_1 + y_1)\, F\left(\frac{p_1}{1 - \eta}, \frac{q_1}{1 - \eta}\right) \frac{\mathrm{d}p_1\, \mathrm{d}q_1}{(1 - \eta)^2}. \tag{7}$$

The projection method with $\eta \ll 1$ yields the intensity distribution

$$\varphi_p(Mx_1, My_1) = c \int_{p_1} \int_{q_1} \psi(p_1 + x_1, q_1 + y_1)\, F_p(p_1, q_1)\, \mathrm{d}p_1\, \mathrm{d}q_1. \tag{8}$$

In the same way the 2X method with $\eta = \frac{1}{2}$ yields

$$\varphi_{2X}(Mx_1, My_1) = c \int_{p_1} \int_{q_1} \psi(p_1 + x_1, q_1 + y_1)\, F_{2X}(2p_1, 2q_1) 4 \mathrm{d}p_1 \,\mathrm{d}q_1 \quad (9)$$

Clearly $\varphi_p(Mx_1, My_1) = \varphi_{2X}(Mx_1, My_1)$ for all values of x_1 and y_1 if

$$F_p(p_1, q_1) = F_{2X}(2p_1, 2q_1) \quad (10)$$

i.e. if the intensity distribution of the source in the 2X method is that in the projection method scaled up by a factor 2.

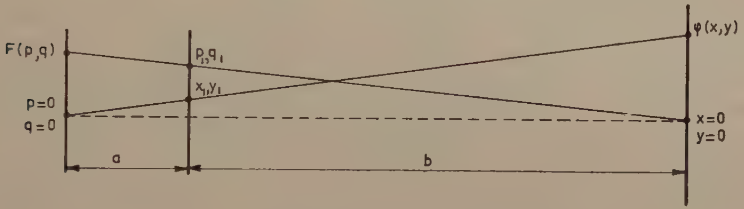

Fig. 2. New variables, introduced for the comparison of the projection method and the 2X method.

Note: The introduction of new variables according to (4) and (5) has a simple physical meaning. Equation (4) means that the X-ray image is projected back into the object plane with $p = 0$ and $q = 0$, the centre of the source, as a projection centre. Equation (5) means that the intensity distribution of the source is projected on the object plane with $x = 0$ and $y = 0$, the centre of the film as a projection centre. The demagnifications are $\eta = a/(a + b)$ and $1 - \eta = b/(a + b)$ respectively (see fig. 2).

From these considerations there follows the general law, valid for contact-, 2X- and projection method: The projection of the image on the object, as seen from the source, does not change if the projection of the source on the object, as seen from the film, remains unchanged.

§ 3. *Intensity considerations.* A reasonable comparison of both X-ray microscopy methods can only be made if both images contain an equal amount of information. This means that the same area of the specimen should be covered in the images, and that the resolution should be equal, i.e. the conditions of the previous paragraph should be fulfilled.

To irradiate the same area, the specimen must be at the same distance from the source because the angular field of an X-ray microscope is limited, either by the pole pieces or by the angular intensity distribution.

Consequently a film with n times better resolution should be at $1/n$ of the distance from the source. Such a film could register n^2 more information per unit area, but requires roughly n^2 times more exposure. With the same source the exposure time would accordingly be the same.

This means that the advantage of the 2X method is a consequence of the larger source exclusively. The gain was established to be a factor 6.3 in our previous publication [2]).

Cosslett's allegation that the shorter times of exposure were due to a smaller source to film distance (in preliminary experiments 5 mm) has no ground. The corresponding distance in the projection method would be 20 × 5 = 100 mm, which even for the projection method is a large value.

§ 4. *Fresnel diffraction.* Hitherto the diffraction effects have not been taken into account. Cosslett correctly quoted for the width of the first fringe

$$f^2 = \frac{\lambda ab}{a+b} \tag{11}$$

and then, incorrectly, assumes $a + b$ to be equal in projection and 2X method. As shown above a should remain unchanged. We therefore have to compare

$$f_p{}^2 = \lambda a_p \text{ (assuming } a_p \ll b\text{, projection method)}, \tag{12}$$

$$f_c{}^2 = \lambda b_c \text{ (assuming } a \gg b_c\text{, contact method)} \tag{13}$$

and

$$f^2{}_{2X} = \tfrac{1}{2}\lambda a_{2X} = \tfrac{1}{2}\lambda b_{2X} \text{ (assuming } a_{2X} = b_{2X}\text{, 2X method)}. \tag{14}$$

The width of the first fringe is there $\sqrt{2}$ times smaller in the 2X method, if $a_p = a_{2X}$.

Up till now the diffraction fringes have not been a limitation in X-ray microscopy. Should they become so, the image might be reconstructed following Gabor's method. To avoid the diffraction effects, however, the object to source distance has to be kept below a certain value.

Putting

$$f^2{}_{2X} = f_p{}^2 \tag{15}$$

we find

$$a_{2X} = 2a_p. \tag{16}$$

Consequently the 2X method yields a field twice as large in diameter, thus containing 4 times more information, in a shorter exposure time.

The authors think that some misunderstanding about the 2X method may have arisen because it was not made sufficiently clear that it is not meant to be an improvement on the projection method as regards resolution. Its advantage lies in the intensity gain, which might eventually be utilized for producing softer radiation. This is also facilitated by the small source to film distance, resulting in low absorption by the air. Clearly the 2X method gives better resolution than the contact method.

The authors wish to express their gratitude to Dr. J. Bouman for the discussions which contributed especially to § 2.

Received 14th April, 1958.

REFERENCES

1) Cosslett, V. E., A. Engström and H. H. Pattee jr., X-ray Microscopy and Microradiography, Academic Press Inc., New York, 1957, p. 321.
2) Le Poole, J. B. and Ong Sing Poen, Appl. Sci. Res. **B5** (1956) 454.
3) Cosslett, V. E., A. Engström and H. H. Pattee jr., X-ray Microscopy and Microradiography, Academic Press Inc. New York, 1957, p. 263, fig. 4.
4) Idem, p. 217.

THE INFLUENCE OF MODULATION ON THE RECORDING OF RESONANCE PHENOMENA

by F. BRUIN *) and D. VAN LADESTEYN **)

Zeeman Laboratory, University of Amsterdam, Netherlands

In nearly all sensitive instruments by which spectral lines are recorded a modulation technique is used. As a result the recorded curves have shapes which are approximately proportional to the first or second derivative of the original line shape. The exact derivative would be obtained only if the modulation amplitude were infinitely small, but it is clear that in this case the resulting signal and therefore the sensitivity of the spectroscope would be zero as well. It is important to know for which modulation amplitude the output signal will be maximum and what is the distortion of the line shape.

Similar points of interest arise in other fields of research where a modulation technique is applied. In the case of frequency stabilization on a microwave cavity resonator for instance it may be important to know for which amplitude of modulation the slope of the 'reactance curve' is maximum. Because of the general application of data of this kind we have calculated a set of curves based on the Lorentzian lineshape, being the resonance curve of a simple harmonic oscillator. The reason that curves of this kind seem not to have been published before is probably that considerable labour is involved to obtain them.

Our calculations are based on the standard resonance curve $y = 1/(1 + x^2)$, having a maximum height of 1 for $x = 0$, a total half-value width of 2 and a total area under the curve of π (see fig. 1).

If the ordinate varies as $x = X_0 + A \sin \omega t$, the abscissa $y(\omega t)$

---

*) Now at American University of Beirut.

**) Now at I.B.M., Amsterdam.

as a function of ωt will be a periodic curve, which will have a shape depending on the values of X_0 and A. In our procedure first 64 functions $y(\omega t)$ were constructed. Then of each one a Fourier analysis at least as far as the third harmonic was made. In the simple cases that X_0 was chosen equal to zero the curves $y(\omega t)$ were symmetrical so that they contained only the even harmonics with periodicity $2\omega t$, $4\omega t$, $6\omega t$ etc. The amplitudes C_h of some of these harmonics as a function of the modulation amplitude A are plotted in fig. 2. The curve C_0, $(h = 0)$, which represents the mean value of the signal $< y(\omega t) >_t - Y_0$, as a function of A, reaches a maximum for $A \sim 2$. The same is true for the second harmonic C_2.

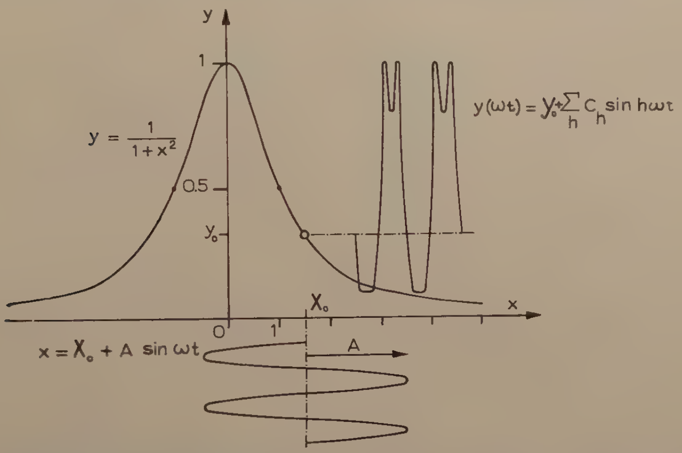
y
1
$y = \frac{1}{1+x^2}$
0.5
Y_0
$y(\omega t) = Y_0 + \sum_h C_h \sin h\omega t$
X_0
x
O
1
$x = X_0 + A \sin \omega t$
A

Fig. 1. Transformation of the wave $x = X_0 + A \sin \omega t$ by means of the function $y = 1/(1 + x^2)$ into a wave $y(\omega t) = Y_0 + \sum_h C_h \sin h\, \omega t$.

Although the first harmonic C_1 of the signal has zero amplitude for $X_0 = 0$, it is of interest to know the change in C_1 as a function of A. When due to a small shift of the resonance curve δx the modulation $x = A \sin \omega t$ is changed into $x = \delta x + A \sin \omega t$, the amplitude of the first harmonic is no longer zero but will reach a value δC_1. It is important to know the slope $S_1 = (\delta C_1/\delta x)_{x=0}$, because e.g. the sensitivity of a frequency stabilizer is proportional to S_1. From fig. 3, in which S_1 and $S_3 = (\delta C_3/\delta x)_{x=0}$ are plotted as a function of A, one may see that the largest sensitivity is obtained for a modulation amplitude of about 1.

Two sets of curves which are of special interest in microwave

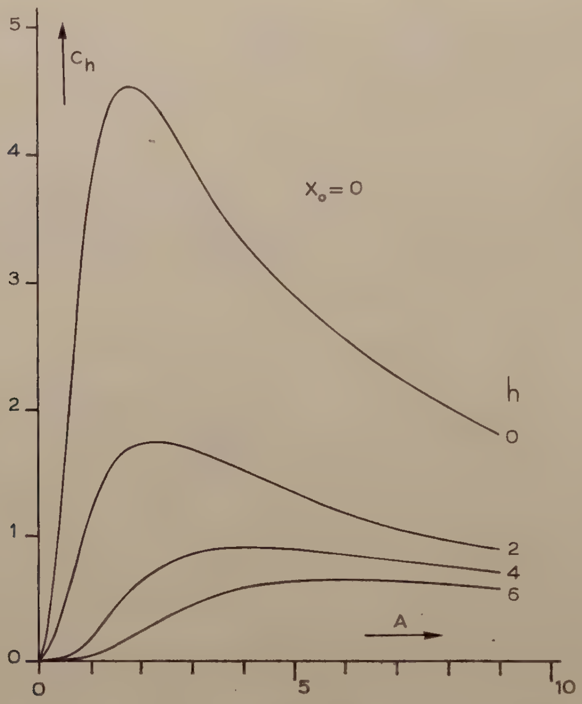

Fig. 2. Amplitudes C_h of the harmonics $h = 0, 2, 4, 6$ of a signal $y(\omega t)$, when $x = A \sin \omega t$ in the function $y = 1/(1 + x^2)$. C_2 and C_6 are negative.

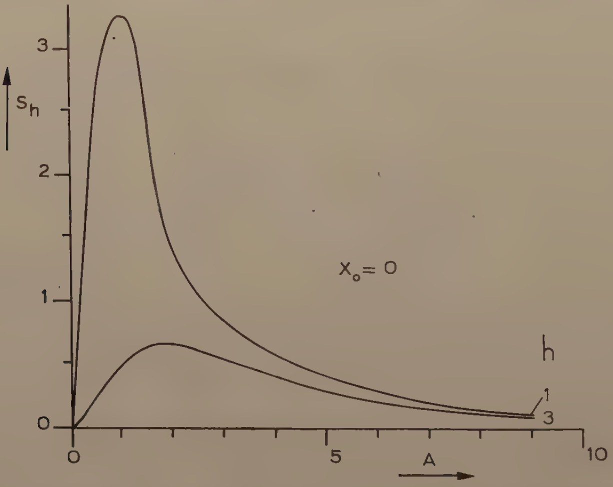

Fig. 3. The slope $S_h = \delta C_h/\delta x$ for $x = 0$ and $h = 1, 3$ as a function of the modulation amplitude A.

spectroscopy are given in the figs. 4 and 5. In fig. 4 the amplitude of the first harmonic C_1 is given as a function of the position of modulation X_0 for different values of A. From these curves one may

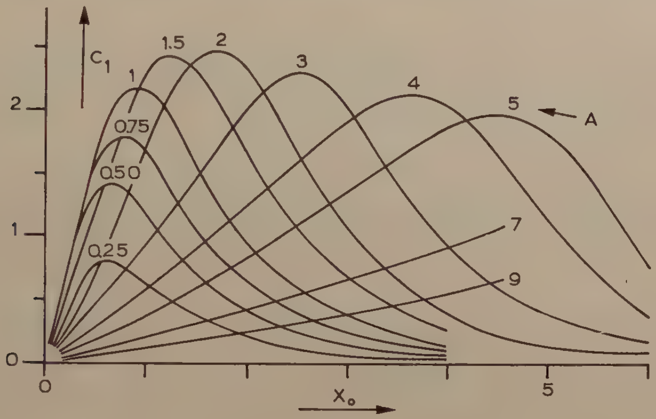

Fig. 4. Amplitude of the first harmonic C_1 as a function of the position of modulation X_0 for different values of the modulation amplitude A.

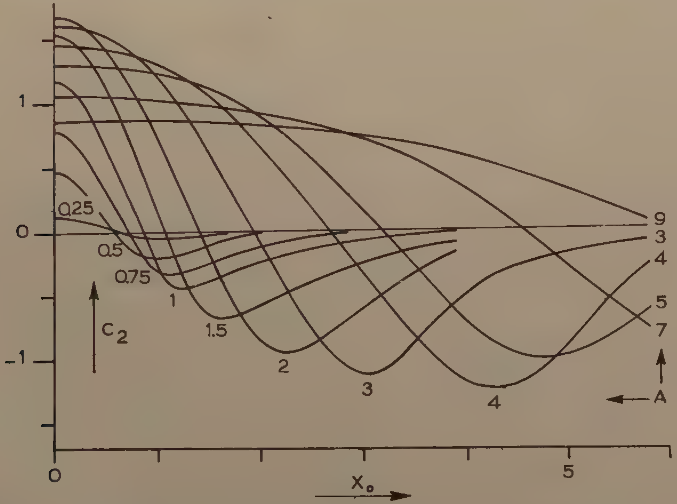

Fig. 5. Amplitude of the second harmonic C_2 as a function of X_0.

learn how much the signal C_1 will deviate from the pure derivative of the resonance curve $dy/dx = -2x/(1+x^2)^2$ when the modulation amplitude A is increased. It also follows that the range of stabilization, i.e. the region of positive slope of the presented curves, increases with A, so that the stability and the flexibility of a frequency stabilizer may be controlled by the adjustment of A.

In many spectrographs of high sensitivity double modulation is applied. If this is the case, the curves of fig. 5 are of interest. A recorded spectral line shows maximum intensity (maximum difference between maximum and minimum value of C_2) if A is about 4. The line is then considerably broadened.

In this short note we have only indicated some major facts which may be deduced from the curves of the figs. 2–5. It is hoped that these and further details may be useful for the construction of spectrographs and for the analysis of recorded spectra.

Received 12th June, 1958.

Appl. sci. Res. Section B, Vol. 7

ON THE POSSIBLE INFLUENCE OF ELECTRON INTERACTION ON THE REFLECTIVITY OF METALS

by C. W. BENTHEM

Laboratorium voor Technische Fysica der Technische Hogeschool, Delft, Nederland

Summary

The influence of the electron viscosity, introduced in an earlier paper [1], on the absorption factor of metals in the infra-red is further investigated. The superposition of the description used there and the anomalous skin effect leads to a paradoxical result, so that we have replaced the electron viscosity model by a relaxation time model. This new description leads to an integro-differential equation of the Wiener-Hopf type, which is solved, the previous difficulties disappearing.

§ 1. *Electron viscosity.* In an earlier paper by Kronig and the present author [1]) attention was drawn to the discrepancy between experimental and theoretical values of the absorption factor (1 — the reflection factor) of metals for infrared radiation. This discrepancy exists even if one considers, with Reuter and Sondheimer [2]) and Dingle [3]), the anomalous skin effect: i.e. the effect of the mean free path of the conduction electrons for collisions with the lattice becoming comparable with the skin depth; this effect is most pronounced at very low temperatures.

It was suggested that better agreement might perhaps be obtained by taking into account the interaction of the conduction electrons with each other by means of a viscosity coefficient η. The introduction of such a coefficient was originally suggested by Kronig and Korringa [4]). Its magnitude was estimated indirectly by Kronig [5]) at

$$\eta = 3Nh/16\pi, \tag{1-1}$$

where N is the number density of the conduction electrons and h Planck's constant.

In the paper referred to [1]) we ignored the anomalous skin effect in the first instance, assuming that the contribution of the electron interaction to the absorption factor would be independent of it. A differential equation was obtained for the average displacement s of the electrons as a function of the depth below the surface of the metal. The boundary condition supposed to hold at the surface was that this displacement, and hence the current density, should be zero; this was meant to represent the conclusion arrived at by Dingle [3]), viz. that the reflection of the electrons at the surface is diffuse. This, however, only means that the electrons reflected from the surface do not contribute to the current density; the electrons arriving there can contribute, so that the supposition that the current density should be zero at the surface is most probably not true.

For the case of normal incidence on the surface of a semi-infinite metal it was found under these suppositions that the contribution A_e, arising from this effect, to the absorption factor A is

$$A_e \approx \frac{2a\omega}{c} \frac{1}{\sqrt{\omega\tau'}}, \tag{1-2}$$

where $a = (m/\mu_0 Ne^2)^{\frac{1}{2}}$ is the high-frequency skin depth ($m =$ = effective mass and $-e =$ charge of the conduction electrons and $\mu_0 =$ the permeability of vacuum, to which that of the metal is put equal), ω is the angular frequency of the radiation, c is the velocity of light in vacuo and $\tau' = m^2/2\mu_0 e^2 \eta$ is a relaxation time related to the internal friction. This contribution to A would be about 2×10^{-3} at 2μm and 1×10^{-3} at $10\,\mu$m for silver, which is of the right order of magnitude to bridge the discrepancy.

§ 2. *Superposition of electron viscosity and anomalous skin effect.* To investigate the superposition of the anomalous skin effect and the effect of electron viscosity, we may incorporate the internal friction force into Reuter and Sondheimer's integro-differential equation, as follows.

The original equation reads, when the distance is made dimensionless by taking a as the unit of length and when the reflection of the electrons at the surface is supposed to be diffuse,

$$\frac{\mathrm{d}^2 E}{\mathrm{d}z^2} = \tfrac{3}{4} i \alpha_c \gamma_c \int_0^\infty E(t) k_c(t-z)\, \mathrm{d}t \quad (z \geq 0), \tag{2-1}$$

with

$$k_c(t-z) = \int_1^\infty \left(\frac{1}{\varepsilon} - \frac{1}{\varepsilon^3}\right) \exp\left[-(1+i\alpha_c)\gamma_c\,|t-z|\,\varepsilon\right] \mathrm{d}\varepsilon, \qquad (2\text{-}2)$$

where E is the electric field strength parallel to the surface, $\alpha_c = \omega\tau_c$, τ_c is the relaxation time for the interaction of electrons with the lattice, $\gamma_c = a/l_c$, $l_c = \bar{v}\tau_c$ is the mean free path of the electrons corresponding to the relaxation time τ_c and $\bar{v}$ is the Fermi velocity of the electrons.

In (2-1) the left-hand side is proportional to the current density, according to Maxwell's laws, whereas the right-hand side gives a kinetic expression for this quantity, where E plays the part of a driving force per unit charge; i.e. $-NeE$ is the force per unit volume.

Now we add to this force a frictional force

$$\eta\, \partial^2 \dot{s}/\partial z^2 = Ne \frac{ia^4}{2\omega\tau'} \frac{\mathrm{d}^4 E}{\mathrm{d}z^4}, \qquad (2\text{-}3)$$

where the distance is not dimensionless; or with the distance in dimensionless form: $iNeE^{(4)}/2\beta$, where $\beta = \omega\tau'$ and $E^{(4)}$ is the fourth derivative of E. Equation (2-1) then becomes

$$E^{(2)}(z) = \tfrac{3}{4} i\alpha_c\gamma_c \int_0^\infty [E(t) - iE^{(4)}(t)/2\beta]\, k_c(t-z)\, \mathrm{d}t \quad (z \geq 0). \qquad (2\text{-}4)$$

The important quantity for deriving the absorption factor is the surface impedance $Z = E(0)/H(0)$, where $E(0)$ and $H(0)$ are, respectively, the electric and magnetic field strengths at the surface. By Maxwell's laws, $Z = -i\omega\mu_0 E(0)/E^{(1)}(0)$. This quantity is connected with the absorption factor by

$$A = 4 \operatorname{Re} Z/\mu_0 c = (4\omega a/c) \operatorname{Im}[E(0)/E^{(1)}(0)], \qquad (2\text{-}5)$$

as long as the value of this expression is small.

In a paper by Sparenberg, Braakman and the present author [6]) the following solution, expanded in a series for small values of $r = 1/(2\beta)$, was found for $E(0)/E^{(1)}(0)$:

$$\frac{E(0)}{E^{(1)}(0)} = -\frac{\pi}{E_1}\left\{1 - ir\left[\frac{E_5}{E_1} + \right.\right.$$
$$\left.\left. + \frac{E_1}{2\pi^2}\left(E_3 - iq\pi \ln \frac{q\pi r}{\mathrm{e}}\right) - \frac{E_1{}^4}{30\pi^4}\right] + \ldots\right\}, \qquad (2\text{-}6)$$

where $q = \frac{3}{4}\alpha_c\gamma_c$, e is the base of the natural logarithms and E_1, E_3, and E_5 are certain complicated expressions depending on α_c and γ_c, whose definition is not important here and will come in more naturally at a later stage (see (6-23)).

§ 3. *Criticism of superposition result.* Now the expression (2-6) is physically very unsatisfactory for the reason here to be explained. On expanding for values of l_c small compared with a, i.e. $\alpha_c \to 0$, $\gamma_c \to \infty$, $\alpha_c\gamma_c = \text{const.}$, (2-4) assumes the form of a differential equation:

$$E^{(2)}(z) = \frac{i\alpha_c}{1 + i\alpha_c}\,[E(z) - iE^{(4)}(z)/2\beta], \tag{3-1}$$

which is of the same form as the differential equation mentioned in § 1. The connection between (2-4) and (3-1) is, in fact, entirely analogous to that between (2-1) and the differential equation

$$E^{(2)}(z) = \frac{i\alpha_c}{1 + i\alpha_c}\,E(z), \tag{3-2}$$

which represents Ohm's law with a relaxation factor $(1 + i\alpha_c)$, i.e. the classical skin effect.

It might now be expected that the solution (2-6) of (2-4) would go over into a solution of (3-1) on passing to the limit $l_c \to 0$. Some boundary condition, whether or not that used in [1]), would have to be applied to (3-1). No boundary condition, however, will produce the logarithm in (2-6), whose coefficient $\frac{1}{2}qr$ does not vanish for $l_c \to 0$.

We think that this unsatisfactory state of affairs is due to the physical assumptions made in deriving (2-4): the collisions between the electrons and the lattice have been introduced kinetically, whereas the collisions of the electrons among themselves have been described by a phenomenological constant η.

§ 4. *Description by means of a relaxation time.* A description which is free from the unequal treatment of the two kinds of collisions and proves not to give rise to the above discrepancy has been found by supposing the collisions between electrons to be governed by a relaxation time τ_e. This gives for Boltzmann's equation

$$\frac{\partial f}{\partial t} - \frac{e}{m}\,E\,\frac{\partial f}{\partial v_x} + v_z\,\frac{\partial f}{\partial z} = -\frac{f - f_0(\boldsymbol{v})}{\tau_c} - \frac{f - f_0(\boldsymbol{v} - \boldsymbol{u})}{\tau_e}, \tag{4-1}$$

where f is the actual distribution function of the conduction electrons, f_0 is the equilibrium distribution function (Fermi function), $\boldsymbol{v}$ is the velocity of an electron, $\boldsymbol{u}$ is the drift velocity of the electrons (a function of position and time). The electric field is in the x-direction. The right-hand side of this equation describes the conflicting tendencies of the electrons to come to rest with respect to the lattice and to assume a uniform velocity $\boldsymbol{u}$, with relaxation times τ_c and τ_e respectively. By expanding $f_0(\boldsymbol{v} - \boldsymbol{u})$ in a power series with respect to $\boldsymbol{u}$ and stopping after the first-order term we get

$$\frac{\partial f}{\partial t} - \frac{e}{m} E \frac{\partial f}{\partial v_x} + v_z \frac{\partial f}{\partial z} = -\frac{f - f_0(\boldsymbol{v})}{\tau} - \frac{u}{\tau_e} \frac{\partial f_0(\boldsymbol{v})}{\partial v_x}, \qquad (4\text{-}2)$$

where

$$\frac{1}{\tau} = \frac{1}{\tau_c} + \frac{1}{\tau_e}. \qquad (4\text{-}3)$$

We introduce the current density $J = -Neu$, write $f(\boldsymbol{v})$ as $f_0(\boldsymbol{v}) + f_1(\boldsymbol{v})$ and suppose the time dependences of f_1, E, J and $\boldsymbol{u}$ to be of the form $\mathrm{e}^{i\omega t}$, which factor we will omit. By Maxwell's laws $J = E^{(2)}(z)/i\omega\mu_0$. Equation (4-2) now assumes the form

$$\frac{f_1}{\tau v_z}(1 + i\omega\tau) + \frac{\partial f_1}{\partial v_z} = \frac{1}{v_z}\left(\frac{eE}{m} + \frac{E^{(2)}}{i\omega\mu_0 N e\tau_e}\right)\frac{\partial f_0}{\partial v_x}. \qquad (4\text{-}4)$$

This equation differs from equation (5) in Reuter and Sondheimer's paper [2]) only by the term containing $E^{(2)}$. Again assuming diffuse reflection of the electrons at the surface, Reuter and Sondheimer's treatment now yields, instead of (2-1), the integro-differential equation

$$E^{(2)}(z) = \tfrac{3}{4} i\alpha\gamma \int_0^\infty [E(t) - iE^{(2)}(t)/\beta_e] k(t - z)\, \mathrm{d}t \qquad (z \geq 0), \qquad (4\text{-}5)$$

where

$$k(t - z) = \int_1^\infty \left(\frac{1}{\varepsilon} - \frac{1}{\varepsilon^3}\right) \exp\left[-(1 + i\alpha)\gamma\, |t - z|\, \varepsilon\right] \mathrm{d}\varepsilon. \qquad (4\text{-}6)$$

Equation (4-6) differs from (2-2) only by the absence of the subscript c. We define α, γ, l by analogy to α_c, γ_c, l_c, using τ instead of τ_c. Evidently $\alpha\gamma = \alpha_c\gamma_c = \frac{4}{3}q = \omega a/\bar{v}$. In (4-5) and (4-6) the lengths have again been made dimensionless.

We write r_e for $1/\beta_e$ and s for $(1 + i\alpha)\gamma$. (4-5) now becomes

$$E^{(2)}(z) = iq\int_0^\infty [E(t) - ir_e E^{(2)}(t)]k(t-z)\,dt \quad (z \geq 0). \tag{4-7}$$

§ 5. *Solution of the integro-differential equation* (4-7). We proceed to solve (4-7) in the same way in which (2-4) was solved in [6]). We assume $E(z)$ to belong to $L(0, \infty)$ and $E^{(2)}(z)$ to $L(-\infty, \infty)$. For $z \to -\infty$, $E^{(2)}(z)$ is of the order e^{sz}.

The following Fourier transformations are defined:

$$\sqrt{2\pi}\,F_+(\lambda) = \int_0^\infty E(z)\,e^{i\lambda z}\,dz \tag{5-1}$$

(regular in S_+, defined by $\operatorname{Im}\lambda > 0$),

$$\sqrt{2\pi}F''_-(\lambda) = \int_{-\infty}^0 E^{(2)}(z)\,e^{i\lambda z}\,dz \tag{5-2}$$

(regular in S_-, defined by $\operatorname{Im}\lambda < \operatorname{Re} s$),

$$\sqrt{2\pi}K(\lambda) = \int_{-\infty}^\infty k(z)\,e^{i\lambda z}\,dz. \tag{5-3}$$

By integrating (4-7) with respect to z from $-\infty$ to $+\infty$ after multiplying by $e^{i\lambda z}$, we find

$$\begin{aligned}&\sqrt{2\pi}F''_-(\lambda) - E^{(1)}(0) + i\lambda E(0) - \sqrt{2\pi}\,\lambda^2 F_+(\lambda) = \\ &= iq\sqrt{2\pi}\,K(\lambda)\{\sqrt{2\pi}\,F_+(\lambda) - ir_e\,[-E^{(1)}(0) + i\lambda E(0) - \\ &\qquad\qquad - \sqrt{2\pi}\lambda^2 F_+(\lambda)]\}.\end{aligned} \tag{5-4}$$

We rearrange this equation so as to have only one of the three symbols $F_+(\lambda)$, $F''_-(\lambda)$ and $K(\lambda)$ in each factor:

$$\begin{aligned}&\sqrt{2\pi}\,F''_-(\lambda)(1 + ir_e\lambda^2) - E^{(1)}(0) + i\lambda E(0) = \\ &= [\lambda^2 + iq\sqrt{2\pi}\,K(\lambda)(1 + ir_e\lambda^2)]\,[\sqrt{2\pi}\,F_+(\lambda)(1 + ir_e\lambda^2) + \\ &\qquad + ir_e\,(E^{(1)}(0) - i\lambda E(0))].\end{aligned} \tag{5-5}$$

We note that

$$\sqrt{2\pi}\,K(\lambda) = -\frac{2s}{\lambda^2} + i\left(\frac{1}{\lambda} + \frac{s^2}{\lambda^3}\right)\ln\frac{\lambda + is}{-\lambda + is}, \tag{5-6}$$

where the logarithm is normalized by

$$\lim_{\operatorname{Re}\lambda\to+\infty} \ln\frac{\lambda + is}{-\lambda + is} = -\pi i. \tag{5-7}$$

The asymptotical behaviour of $K(\lambda)$ for $\mathrm{Re}\,\lambda \to +\infty$ and $|\mathrm{Im}\,\lambda| < \mathrm{Re}\,s$ is

$$\sqrt{2\pi}\,K(\lambda) = \pi\lambda^{-1} - 4s\lambda^{-2} + \pi s^2\lambda^{-3} - \tfrac{4}{3}s^3\lambda^{-4} + \dots \tag{5-8}$$

We now write

$$\lambda^2 + iq\sqrt{2\pi}K(\lambda)(1 + ir_e\lambda^2) = (\lambda^2 + p^2)\Phi_-(\lambda)/\Phi_+(\lambda), \tag{5-9}$$

where the subscripts $-$ and $+$ indicate regularity in S_- and S_+ respectively, as before, and p is an arbitrary positive number. By the Wiener-Hopf technique [7]) we find

$$\Phi_\pm(\lambda) = \exp\left[-\frac{1}{2\pi i}\int_{-\infty}^{\infty}\frac{\ln\dfrac{\theta^2 + iq\sqrt{2\pi}K(\theta)(1 + ir_e\theta^2)}{\theta^2 + p^2}}{\theta - \lambda}\,\mathrm{d}\theta\right](\lambda \subset S_\pm), \tag{5-10}$$

where we have taken as common strip of regularity of $\Phi_+(\lambda)$, $\Phi_-(\lambda)$ and their quotient a sufficiently narrow strip just above the real axis in the λ-plane, containing no zeros or singularities of $\Phi_-(\lambda)/\Phi_+(\lambda)$.

Equations (5-5) and (5-9) now give

$$\frac{\sqrt{2\pi}F''_-(\lambda)(1 + ir_e\lambda^2) - E^{(1)}(0) + i\lambda E(0)}{(\lambda - ip)\Phi_-(\lambda)} =$$

$$= \frac{(\lambda + ip)\,\{\sqrt{2\pi}F_+(\lambda)(1 + ir_e\lambda^2) + ir_e[E^{(1)}(0) - i\lambda E(0)]\}}{\Phi_+(\lambda)} = P(\lambda), \tag{5-11}$$

where $P(\lambda)$ is an arbitrary polynomial; or

$$\sqrt{2\pi}F_+(\lambda) = \left\{\frac{P(\lambda)\Phi_+(\lambda)}{\lambda + ip} - ir_e[E^{(1)}(0) - i\lambda E(0)]\right\}\Big/ (1 + ir_e\lambda^2), \tag{5-12}$$

$$\sqrt{2\pi}F''_-(\lambda) = [P(\lambda)\Phi_-(\lambda)(\lambda - ip) + E^{(1)}(0) - i\lambda E(0)]/(1 + ir_e\lambda^2). \tag{5-13}$$

In order that $F''_-(\lambda)$ and $F_+(\lambda)$ shall be Fourier transforms, it is necessary that $P(\lambda)$ is of degree zero. We may choose $P(\lambda) \equiv 1$, since the problem is homogeneous.

The regions of regularity of $F_+(\lambda)$ and $F''_-(\lambda)$ contain poles, as a result of the factor $(1 + ir_e\lambda^2)^{-1}$. These must be compensated for by choosing values for $E^{(1)}(0)$ and $E(0)$. The poles are

$$\lambda_1 = \mu = r_e^{-\frac{1}{2}}\,\mathrm{e}^{\pi i/4},\ \lambda_2 = -\mu. \tag{5-14}$$

For $r_e \to 0$ the pole λ_1 lies in S_+ and λ_2 in S_-. Therefore the pole

λ_1 must be compensated for in $F_+(\lambda)$ and λ_2 in $F''_-(\lambda)$:

$$E^{(1)}(0) - i\mu E(0) = -\mu^2\Phi_+(\mu)/(\mu + ip) = R_1, \tag{5-15}$$

$$E^{(1)}(0) + i\mu E(0) = \Phi_-(-\mu)(\mu + ip) = R_2. \tag{5-16}$$

Hence we find

$$\frac{E(0)}{E^{(1)}(0)} = \frac{i}{\mu}\,\frac{R_1 - R_2}{R_1 + R_2}. \tag{5-17}$$

We shall need to investigate the behaviour of R_1 and R_2 for large values of $r_e^{-\frac{1}{2}}$. For this we require the asymptotical behaviour of $\Phi_\pm(\lambda)$, or of

$$H(\lambda) = \int\limits_{-\infty}^{\infty} \frac{\ln\{[\theta^2 + iq\sqrt{2\pi}K(\theta)(1 + ir_e\theta^2)]\theta^{-2}\}}{\theta - \lambda}\,\mathrm{d}\theta, \tag{5-18}$$

where we have taken $p = 0$; this choice must also be made in (5-15) and (5-16). We shall avoid putting for λ the special values $\pm\,\mu$ as long as possible.

§ 6. *Asymptotic expansions.* For (5-18) we write

$$H(\lambda) = 2\lambda\int\limits_0^\infty \frac{\ln\{[\theta^2 + iq\sqrt{2\pi}K(\theta)(1 + ir_e\theta^2)]\theta^{-2}\}}{\theta^2 - \lambda^2}\,\mathrm{d}\theta. \tag{6-1}$$

Now we introduce

$$\left.\begin{aligned} r_e &= u^{-2}, \text{ i.e. } \mu = u\,\mathrm{e}^{\pi i/4},\\ \lambda &= v\,\mathrm{e}^{i\varphi}, \end{aligned}\right\} \tag{6-2}$$

so that

$$H(v\,\mathrm{e}^{i\varphi}) = 2v\,\mathrm{e}^{i\varphi}\int\limits_0^\infty \frac{\ln\,[1 + iq\sqrt{2\pi}K(\theta)(\theta^{-2} + iu^{-2})]}{\theta^2 - v^2\,\mathrm{e}^{2i\varphi}}\,\mathrm{d}\theta. \tag{6-3}$$

We divide the integration interval into two parts:

$$\int\limits_0^{v^y} \ldots\,\mathrm{d}\theta + \int\limits_{v^y}^{\infty} \ldots\,\mathrm{d}\theta = I + II,$$

where $y = \frac{1}{2} + \delta$, δ being an arbitrary, but small real quantity. We shall treat I and II separately.

In I the range of integration allows us to expand the denominator.

We may also expand the numerator:

$$I = -2 \sum_{n=0}^{\infty} (v\, \mathrm{e}^{i\phi})^{-2n-1}.$$

$$\cdot \int_{0}^{v^y} \theta^{2n} \left\{ \ln\,[1+iq\sqrt{2\pi}K(\theta)\theta^{-2}] - \sum_{m=1}^{\infty} \frac{1}{m} \left[\frac{qu^{-2}\sqrt{2\pi}K(\theta)}{1+iq\sqrt{2\pi}K(\theta)\theta^{-2}} \right]^m \right\} \mathrm{d}\theta. \tag{6-4}$$

We introduce the expansions

$$\ln\,[1 + iq\sqrt{2\pi}K(\theta)\theta^{-2}] = \sum_{l=3}^{\infty} b_l\, \theta^{-l}, \tag{6-5}$$

$$\left[\frac{\sqrt{2\pi}K(\theta)}{1 + iq\sqrt{2\pi}K(\theta)\theta^{-2}} \right]^m = \sum_{l=m}^{\infty} c_{ml}\, \theta^{-l}\ (m \geq 1) \tag{6-6}$$

and define the integrals

$$B_n = \int_{0}^{\infty} \left\{ \theta^{2n} \ln\,[1 + iq\sqrt{2\pi}K(\theta)\theta^{-2}] - \sum_{l=3}^{2n} b_l\, \theta^{2n-l} - \frac{b_{2n+1}}{\theta + 1} \right\} \mathrm{d}\theta, \tag{6-7}$$

$$C_{mn} = \int_{0}^{\infty} \left\{ \theta^{2n} \left[\frac{\sqrt{2\pi}K(\theta)}{1+iq\sqrt{2\pi}K(\theta)\theta^{-2}} \right]^m - \sum_{l=m}^{2n} c_{ml} \theta^{2n-l} - \frac{c_{m,2n+1}}{\theta + 1} \right\} \mathrm{d}\theta, \tag{6-8}$$

where the b and c terms serve to make the integrals converge at $\theta = \infty$. We further define

$$D_n = B_n - \sum_{m=1}^{\infty} \frac{q^m u^{-2m}}{m} C_{mn}. \tag{6-9}$$

It is allowed to omit from the result of the integration all powers and logarithms of v^y, since the final result for $H(\lambda)$ must evidently be independent of y. These terms must therefore cancel out against terms in II. Working out (6-4) with all this in mind, we have

$$I = -2 \sum_{n=0}^{\infty} (v\, \mathrm{e}^{i\phi})^{-2n-1} D_n. \tag{6-10}$$

For II we write

$$II = 2v\, \mathrm{e}^{i\phi} \sum_{l=1}^{\infty} d_l \int_{v^y}^{\infty} \frac{\mathrm{d}\theta}{\theta^l (\theta^2 - v^2\, \mathrm{e}^{2i\phi})}, \tag{6-11}$$

where

$$d_l = b_l - \sum_{m=1}^{l} \frac{q^m u^{-2m}}{m} c_{ml} \quad (l \geq 1). \tag{6-12}$$

For the purpose of (6-12) we define

$$b_1 = b_2 = 0, \quad c_{ml} = 0 \; (l < m). \tag{6-13}$$

Now in general

$$\int_{\theta}^{\infty} \frac{\mathrm{d}\theta}{\theta^l(\theta^2 - a^2)} =$$

$$= \sum_{n=0}^{\frac{1}{2}(l-3)} \frac{1}{(2n-l+1)a^{2n+2}\theta^{l-2n-1}} + \frac{1}{2a^{l+1}} \ln \frac{\theta^2}{\theta^2 - a^2} \; (l > 0, \text{ odd}), \tag{6-14}$$

$$= \sum_{n=0}^{\frac{1}{2}(l-2)} \frac{1}{(2n-l+1)a^{2n+2}\theta^{l-2n-1}} + \frac{1}{2a^{l+1}} \ln \frac{\theta + a}{\theta - a} \; (l \geq 0, \text{ even}). \tag{6-15}$$

Here the logarithms are to be normalized by putting their limits for $\mathrm{Re}\,\theta \to +\infty$ equal to zero.

Hence (6-11) gives, on dropping powers and logarithms of v^y,

$$II = -\sum_{n=0}^{\infty} (v\,\mathrm{e}^{i\varphi})^{-2n-1} d_{2n+1} \ln (v^{2y} - v^2\,\mathrm{e}^{2i\varphi}) + \\ + \sum_{n=1}^{\infty} (v\,\mathrm{e}^{i\varphi})^{-2n} d_{2n} \ln \frac{v^y + v\,\mathrm{e}^{i\varphi}}{v^y - v\,\mathrm{e}^{i\varphi}}. \tag{6-16}$$

The logarithms may be expanded:

$$\left.\begin{aligned} &\ln (v^{2y} - v^2\,\mathrm{e}^{2i\varphi}) = \mp \pi i + \ln v^2 + 2i\varphi + \text{powers of } v^{y-1}, \\ &\ln \frac{v^y + v\,\mathrm{e}^{i\varphi}}{v^y - v\,\mathrm{e}^{i\varphi}} = \pm \pi i + \text{powers of } v^{y-1}, \\ &\qquad \text{for} \begin{Bmatrix} 0 < \varphi < \pi \\ 0 > \varphi > -\pi \end{Bmatrix}, \end{aligned}\right\} \tag{6-17}$$

so that

$$H(\lambda) = I + II = \sum_{n=0}^{\infty} (v\mathrm{e}^{i\varphi})^{-2n-1} [-2D_n + d_{2n+1}(\pm \pi i - \ln v^2 - 2i\varphi)] \pm \\ \pm \pi i \sum_{n=1}^{\infty} (v\,\mathrm{e}^{i\varphi})^{-2n} d_{2n}. \tag{6-18}$$

To calculate $\Phi_+(\mu)$ and $\Phi_-(-\mu)$ we first put $v = u$. This requires a rearrangement of terms, to obtain a series expansion in u. We decompose D_n and d_n by (6-9) and (6-12) and obtain after some relabelling of summation indices

$$H\,(u\,\mathrm{e}^{i\varphi}) = \sum_{n=0}^{\infty} (u\,\mathrm{e}^{i\varphi})^{-2n-1} \Bigg\{ -2\,B_n + \sum_{m=1}^{n} \frac{q^m}{m} \mathrm{e}^{2mi\varphi} \,.\, 2C_{m,n-m} + \\ + \left[b_{2n+1} - \sum_{m=1}^{[\frac{1}{3}(2n+1)]} \frac{q^m}{m} \mathrm{e}^{2mi\varphi}\, c_{m,2n+1-2m} \right] (\pm\pi i - \ln u^2 - 2i\varphi) \Bigg\} + \\ + \sum_{n=1}^{\infty} (u\,\mathrm{e}^{i\varphi})^{-2n} \left[b_{2n} - \sum_{m=1}^{[2n/3]} \frac{q^m}{m} \mathrm{e}^{2mi\varphi}\, c_{m,2n-2m} \right] (\pm\pi i), \qquad (6\text{-}19)$$

where $[\frac{1}{3}(2n+1)]$ means the greatest integer contained in $\frac{1}{3}(2n+1)$.

We then put $\varphi = \mathrm{e}^{\pi i/4}$ or $\mathrm{e}^{-3\pi i/4}$, so that $\mathrm{e}^{2i\varphi} = i$. It can now be proved that

$$b_n - \sum_{m=1}^{[n/3]} \frac{(iq)^m}{m} c_{m,n-2m} = 0. \qquad (6\text{-}20)$$

For:

$$\ln\,[1 + iq\sqrt{2\pi}K(\theta)\theta^{-2}] + \ln \left[1 - \frac{iq\sqrt{2\pi}K(\theta)\theta^{-2}}{1 + iq\sqrt{2\pi}K(\theta)\theta^{-2}} \right] = 0. \qquad (6\text{-}21)$$

This gives, with (6-5) and (6-6),

$$\sum_{l=3}^{\infty} b_l \theta^{-l} - \sum_{m=1}^{\infty} \frac{(iq)^m}{m} \theta^{-2m} \sum_{l=m}^{\infty} c_{ml}\, \theta^{-l} = 0,$$

$$\sum_{n=3}^{\infty} \left[b_n - \sum_{m=1}^{[n/3]} \frac{(iq)^m}{m} c_{m,n-2m} \right] \theta^{-n} = 0.$$

This proves (6-20). Hence (6-19) becomes

$$H(u\,\mathrm{e}^{i\varphi}) = 2 \sum_{n=0}^{\infty} (u\,\mathrm{e}^{i\varphi})^{-2n-1} \left[-B_n + \sum_{m=1}^{n} \frac{(iq)^m}{m} C_{m,n-m} \right]. \qquad (6\text{-}22)$$

We note that in substituting (6-7) and (6-8) into (6-22) the b and c terms cancel out, since for this too the condition is (6-20). Therefore

$$E_{2n+1} \equiv B_n - \sum_{m=1}^{n} \frac{(iq)^m}{m} C_{m,n-m} = \\ = \int_0^{\infty} \theta^{2n} \Bigg\{ \ln\,[1 + iq\sqrt{2\pi}K(\theta)\theta^{-2}] - \\ - \sum_{m=1}^{n} \frac{1}{m} \left[\frac{iq\sqrt{2\pi}K(\theta)\theta^{-2}}{1 + iq\sqrt{2\pi}K(\theta)\theta^{-2}} \right]^m \Bigg\}\, \mathrm{d}\theta. \qquad (6\text{-}23)$$

This leaves

$$H(\pm\,\mu) = \pm\, 2\, \mathrm{e}^{3\pi i/4} \sum_{n=0}^{\infty} (-\,i)^n\, u^{-(2n+1)}\, E_{2n+1}. \tag{6-24}$$

Now by (5-10) and (5-18),

$$\Phi_{\pm}(\pm\mu) = \exp\left[-\frac{1}{2\pi i}\, H(\pm\,\mu)\right]. \tag{6-25}$$

By (6-24) this gives, on expanding the exponential,

$$\Phi_{\pm}(\pm\,\mu) =$$

$$= 1 \pm u^{-1}\, \mathrm{e}^{-3\pi i/4} \frac{E_1}{\pi} + u^{-2}\, i \frac{{E_1}^2}{2\pi^2} \pm u^{-3}\, \mathrm{e}^{-\pi i/4} \left(\frac{{E_1}^3}{6\pi^3} - \frac{E_3}{\pi}\right) - \ldots \tag{6-26}$$

By (5-15), (5-16) and (5-17)

$$\frac{E(0)}{E^{(1)}(0)} = \frac{i}{\mu}\, \frac{\Phi_+(\mu) + \Phi_-(-\,\mu)}{\Phi_+(\mu) - \Phi_-(-\,\mu)} \tag{6-27}$$

$$= -\,\frac{\pi}{E_1}\left[1 + i r_e \left(\frac{{E_1}^2}{3\pi^2} + \frac{E_3}{E_1}\right) + \ldots\right]. \tag{6-28}$$

We see that for $r_e = 0$ the solution, like (2-6) for $r = 0$, goes over into Reuter and Sondheimer's solution. In contrast to (2-6), however, there is no $r_e \ln r_e$ term. Evidently $\ln r_e$ does not occur in any order of the expansion, whereas in (2-6) $\ln r$ recurs in every order.

§ 7. *Calculation of integrals.* We now calculate the integrals E_1 and E_3. This may be done in the manner indicated by Gordon and Sondheimer [8]). We will derive the expansions for small values of $|\xi|$, where $\xi = iq/s^3$; i.e. for infrared light, not for microwaves.

We have

$$E_1 = \int_0^{\infty} \ln\,[1 + iq\sqrt{2\pi} K(\theta)\theta^{-2}]\, \mathrm{d}\theta, \tag{7-1}$$

$$E_3 = \int_0^{\infty} \theta^2 \left\{ \ln\,[1 + iq\sqrt{2\pi} K(\theta)\theta^{-2}] - \frac{iq\sqrt{2\pi} K(\theta)\theta^{-2}}{1 + iq\sqrt{2\pi} K(\theta)\theta^{-2}} \right\} \mathrm{d}\theta. \tag{7-2}$$

Transformation by $\theta = s/u$ yields

$$E_1 = s \int_0^{\infty} \ln\,\{1 + \xi G(u)\}\, \mathrm{d}u/u^2, \tag{7-3}$$

$$E_3 = s^3 \int_0^\infty \left\{ \frac{\ln\,[1 + \xi G(u)]}{u^4} - \frac{\xi G(u)}{u^4[1 + \xi G(u)]} \right\} du, \tag{7-4}$$

where

$$G(u) = su^2\sqrt{2\pi}K(s/u) = u^3\left[- 2u + i(1 + u^2) \ln \frac{u - i}{u + i}\right] \tag{7-5}$$

$$= u^3\left[\pm\pi - 4u \pm \pi u^2 - \frac{4}{1.3} u^3 + \frac{4}{3.5} u^5 \ldots \right], \ |u| \text{ small, Re } u \gtrless 0, \tag{7-6}$$

$$= u^2\left[\frac{4}{1.3} - \frac{4}{3.5u^2} + \frac{4}{5.7u^4} - \ldots \right], \ |u| \text{ large.} \tag{7-7}$$

Integrating by parts, we have e.g. for E_1:

$$E_1 = s \int_0^\infty \frac{\xi G^{(1)}(u)}{u[1 + \xi G(u)]}\, du. \tag{7-8}$$

This integral may be calculated by complex integration. Integrating along the negative real axis, round the point $+ i$, along the positive real axis and along a very large semicircle in the upper half plane, we have

$$s\xi \int_{-\infty}^{0} \frac{G^{(1)}(u)}{1 + \xi G(u)} \frac{du}{u} + s\xi \int_0^\infty \ldots + s\xi \int_0^i \ldots \ (\text{Re } u < 0) +$$
$$+ s\xi \int_i^0 \ldots \ (\text{Re } u > 0) = 2\pi i s\xi R, \tag{7-9}$$

where R is the residue of the integrand at its pole in the upper half plane. The large semicircle and a small circle round i do not contribute to the integral.

We note in passing that we might have taken $\theta = su$ instead of $\theta = s/u$. The latter gives, according to Gordon and Sondheimer, a somewhat simpler expression, but there does not seem to be much to choose between the two procedures. In taking $\theta = su$, the contour must go round i from $i\,\infty$ instead of from the origin.

Since $G(u)$ is an even function, (7-9) becomes

$$E_1 = \pi i s\xi R - \frac{s\xi}{2} \left[\int^{i} \ldots \ (\text{Re } u < 0) + \int_i^0 \ldots \ (\text{Re } u > 0) \right]. \tag{7-10}$$

Now R is the residue of $G^{(1)}(u)/u[1 + \xi G(u)]$ at the zero u_0 of $1 + \xi G(u)$. This residue is $1/\xi u_0$; hence the first term of E_1 (7-10) is $\pi i s/u_0$.

Using the expansion of u in descending powers of $w = \frac{3}{4}G(u)$ given in [8]), equations (7) and (8), and substituting $w = -3/(4\xi)$ to find u_0, we have for this first term

$$\frac{\pi i s}{u_0} = 2\pi s \sqrt{\frac{\xi}{3}} \left(1 + \frac{2}{15}\xi + \frac{18}{175}\xi^2 + \frac{1604}{14175}\xi^3 + \frac{113\,798}{779\,625}\xi^4 + \dots\right), \qquad (7\text{-}11)$$

where $\sqrt{\xi}$ means that square root of ξ whose real part is positive.

For the second term of E_1 (7-10) we write

$$\frac{s\xi}{2}\left\{ \int\limits_{\substack{0 \\ \mathrm{Im}\, v>0}}^{1} \frac{G^{(1)}(iv)\,.\,i\,\mathrm{d}v}{iv[1 + \xi G(iv)]} + \int\limits_{\substack{1 \\ \mathrm{Im}\, v<0}}^{0} \dots \right\}. \qquad (7\text{-}12)$$

Now

$$G(iv) = -2v^4 + v^3(1 - v^2)\left(\mp \pi i + \ln \frac{1-v}{1+v}\right) \quad (\mathrm{Im}\, v \gtrless 0), \qquad (7\text{-}13)$$

$$\frac{G^{(1)}(iv)}{iv} = 10v^2 + (-3v + 5v^3)\left(\mp \pi i + \ln \frac{1-v}{1+v}\right). \qquad (7\text{-}14)$$

Substituting (7-13) and (7-14) into (7-12) and expanding in ascending powers of ξ, we get

$$s\xi \int_0^1 [g + \xi(gh - fj) + \xi^2(gh^2 - gj^2 - 2fjh) + \dots]\,\mathrm{d}v, \qquad (7\text{-}15)$$

where

$$\left.\begin{aligned} f &= 10v^2 + (-3v + 5v^3) \ln (1 - v)/(1 + v), \\ g &= \pi(-3v + 5v^3), \\ h &= 2v^4 - v^3(1 - v^2) \ln (1 - v)/(1 + v), \\ j &= \pi v^3(1 - v^2). \end{aligned}\right\} \qquad (7\text{-}16)$$

We use the integral

$$\int_0^1 v^n \ln \frac{1-v}{1+v}\,\mathrm{d}v = -\frac{2}{n+1}\left(\ln 2 + \tfrac{1}{2} + \tfrac{1}{4} + \dots + \frac{1}{n}\right) \quad (n \geq 0,\ \text{even}). \qquad (7\text{-}17)$$

For the coefficients of successive powers of ξ we need similar integrals containing higher powers of $\ln (1 - v)/(1 + v)$. These, like (7-17), may be calculated by partial integration. The calculation rapidly grows more complicated with increasing powers of the logarithm; we find for instance

$$\int_0^1 v^n \ln^2 \frac{1-v}{1+v}\,\mathrm{d}v = \frac{8}{n+1}\left[\frac{1}{n}\left(\ln 2 + \tfrac{1}{2} + \tfrac{1}{4} + \ldots + \frac{1}{n-1}\right) + \right.$$

$$\left. + \frac{1}{n-2}\left(\ln 2 + \tfrac{1}{2} + \ldots + \frac{1}{n-3}\right) + \ldots + \tfrac{1}{3}(\ln 2 + \tfrac{1}{2}) + \ln 2\right] \qquad (n \geq 1, \text{odd}). \qquad (7\text{-}18)$$

It turns out that we do not need to know the integral (7-17) for odd and (7-18) for even n.

From (7-11) and (7-15) to (7-18) we find

$$E_1 = 2\pi s\sqrt{\frac{\xi}{3}}\left(1 + \frac{2}{15}\xi + \frac{18}{175}\xi^2 + \frac{1604}{14175}\xi^3 + \frac{113\,798}{779\,625}\xi^4 + \ldots\right) -$$

$$-\tfrac{1}{4}\pi s\xi - \pi s\xi^2\,\frac{86+48\ln 2}{945} - \pi s\xi^3\left(\frac{9776+9168\ln 2}{121\,275} - \frac{\pi^2}{840}\right) - \ldots \qquad (7\text{-}19)$$

E_3 (7-4) can be found in the same way:

$$E_3 = s^3\left\{-\left.\frac{\ln[1+\xi G(u)]}{3u^3}\right|_0^\infty + \frac{\xi}{3}\int_0^\infty \frac{G^{(1)}(u)\mathrm{d}u}{u^3[1+\xi G(u)]} - \xi\int_0^\infty \frac{G(u)\,\mathrm{d}u}{u^4[1+\xi G(u)]}\right\} =$$

$$= s^3\xi\left\{\frac{\pi}{3} + \frac{1}{3}\int_0^\infty \frac{1}{1+\xi G(u)}\,\mathrm{d}\left[\frac{G(u)}{u^3}\right]\right\} =$$

$$= \tfrac{1}{3}s^3\xi\int_0^\infty \frac{G(u)\xi G^{(1)}(u)}{u^3[1+\xi G(u)]^2}\,\mathrm{d}u =$$

$$= \tfrac{1}{6}s^3\xi^2\left\{\int_0^\infty \frac{G(u)G^{(1)}(u)}{u^3[1+\xi G(u)]^2}\,\mathrm{d}u + \int_{-\infty}^0 \ldots\right\} =$$

$$= \tfrac{1}{6}s^3\xi^2\left\{2\pi i\,\bar{R} - \int_0^i \ldots\,(\mathrm{Re}\,u < 0) - \int_i^0 \ldots\,(\mathrm{Re}\,u > 0)\right\}. \qquad (7\text{-}20)$$

The residue $\bar{R}$ of $G(u)G^{(1)}(u)/u^3[1+\xi G(u)]^2$ in the same zero of the denominator is

$$\frac{1}{\xi^2}\left[\frac{1}{u_0{}^3}-\frac{3}{u_0{}^4}\,\frac{G(u_0)}{G^{(1)}(u_0)}\right]=\frac{1}{\xi^2 G^{(1)}(u_0)}\,\frac{\mathrm{d}}{\mathrm{d}u_0}\left[\frac{G(u_0)}{u_0{}^3}\right]=$$

$$=\frac{1}{\xi^2}\,\frac{\mathrm{d}}{\mathrm{d}G(u_0)}\left[\frac{G(u_0)}{u_0{}^3}\right]=\frac{1}{\xi^2}\left[\frac{\mathrm{d}(w/u^3)}{\mathrm{d}w}\right]_{w=-3/(4\xi)}. \qquad (7\text{-}21)$$

We find for the first term of E_3 (7-20)

$$\frac{4\pi s^3\xi^{3/2}}{3^{5/2}}\left(1+\frac{6}{5}\xi+\frac{38}{21}\xi^2+\frac{668}{225}\xi^3+\frac{3\,086\,938}{606\,375}\xi^4+\ldots\right). \qquad (7\text{-}22)$$

The integral from 0 to i and back gives

$$\frac{s^3\xi^2}{3}\int_0^1 v^2\,\mathrm{d}v\,[\bar{g}+2\xi(\bar{g}h-\bar{f}j)+\xi^2(-6\bar{f}hj+3\bar{g}h^2-\bar{g}j^2)+\ldots], \qquad (7\text{-}23)$$

where

$$\left.\begin{aligned}\bar{f}&=-3\pi^2+(20+8\pi^2)v^2-5\pi^2v^4+(-16v+20v^3)\ln(1-v)/(1+v)+\\&\qquad\qquad+(3-8v^2+5v^4)\ln^2(1-v)/(1+v),\\ \bar{g}&=\pi(-16v+20v^3)+2\pi(3-8v^2+5v^4)\ln(1-v)/(1+v).\end{aligned}\right\}(7\text{-}24)$$

In all we have

$$E_3=\frac{4\pi s^3\xi^{3/2}}{3^{5/2}}\left(1+\frac{6}{5}\xi+\frac{38}{21}\xi^2+\frac{668}{225}\xi^3+\frac{3\,086\,938}{606\,375}\xi^4+\ldots\right)-$$

$$-\pi s^3\xi^2\,\frac{17+16\ln 2}{105}-2\pi s^3\xi^3\left(\frac{1598}{14175}+\frac{688}{4725}\ln 2-\frac{\pi^2}{360}\right)-\ldots \qquad (7\text{-}25)$$

§ 8. *Conclusions concerning the absorption factor.* Inserting (7-19) and (7-25) into (6-28), we find

$$\frac{E(0)}{E^{(1)}(0)}=-\frac{1}{s}\left\{\frac{\sqrt{3}}{2}\xi^{-\frac{1}{2}}+\frac{3}{16}-\frac{83\sqrt{3}}{1920}\xi^{\frac{1}{2}}+\left(\frac{4\ln 2}{105}+\frac{8723}{322\,560}\right)\xi+\ldots\right.$$

$$+ir_e s^2\left[\frac{1}{\sqrt{3}}\xi^{\frac{1}{2}}-\frac{17+16\ln 2}{140}\xi+\sqrt{3}\left(\frac{797}{6720}-\frac{\ln 2}{35}\right)\xi^{3/2}-\right.$$

$$\left.\left.-\left(\frac{288\,023}{3\,628\,800}+\frac{77}{360}\ln 2-\frac{\pi^2}{240}\right)\xi^2+\ldots\right]+O\,(r_e{}^2)\right\}. \qquad (8\text{-}1)$$

We see that for $l \to 0$, i.e. Re $s \to \infty$ and $\xi \to 0$, the principal term is the first: $-\sqrt{3}/2s\sqrt{\xi}$. The principal r_e term, which is $-ir_e s\sqrt{\xi/3}$, vanishes. In the classical limit we therefore come to the same result as Reuter and Sondheimer, our internal friction effect being a higher order small quantity. This was to be expected, since for $l \to 0$ the integro-differential equation (4-7) goes over into the differential equation (3-2) for the classical skin effect. The paradox mentioned in § 3 therefore does not arise here.

In order to establish clearly the dependence of the various terms on the frequency ν and the specific resistance ρ, we introduce two dimensionless quantities (see Dingle [3]), pp. 314–315; Dingle uses non-rationalized Gaussian units, we use rationalized Giorgi units):

$$\boldsymbol{\nu} = \nu \frac{2}{3}\frac{1}{\bar{v}}\sqrt{\frac{12\pi^2 m}{Ne^2\mu_0}}, \tag{8-2}$$

$$\boldsymbol{\rho} = \rho \frac{1}{\bar{v}}\sqrt{\frac{4}{3}\frac{Ne^2}{m\mu_0}}. \tag{8-3}$$

We distinguish between ρ_c and ρ_e, by analogy to τ_c and τ_e (4-3):

$$\rho_c = m/Ne^2\tau_c, \;\; \rho_e = m/Ne^2\tau_e, \;\; \rho = \rho_c + \rho_e; \tag{8-4}$$

the same distinction applies to $\boldsymbol{\rho}_c$ and $\boldsymbol{\rho}_e$. Expressed in these quantities, those occurring in (8-1) become

$$q = (\tfrac{1}{2}\sqrt{3})^3\,\boldsymbol{\nu}, \tag{8-5}$$

$$r_e = \boldsymbol{\rho}_e/\boldsymbol{\nu}, \tag{8-6}$$

$$s = \tfrac{1}{2}\sqrt{3}(i\boldsymbol{\nu} + \boldsymbol{\rho}), \tag{8-7}$$

$$\xi = i\boldsymbol{\nu}/(i\boldsymbol{\nu} + \boldsymbol{\rho})^3. \tag{8-8}$$

Introducing these quantities also in (2-5), we finally have for the absorption factor, for the case $\boldsymbol{\nu} \gg \boldsymbol{\rho}$ (i.e. $\omega\tau \gg 1$, which is the case in the infrared, as opposed to the microwave region):

$$\begin{aligned} A = \frac{\bar{v}}{c}\{&1.732\,\boldsymbol{\rho}_c + (0.217\,\boldsymbol{\rho}_c + 0.866\,\boldsymbol{\rho}_e)\boldsymbol{\rho}^2\boldsymbol{\nu}^{-2} + \ldots \\ &+ 0.75 + (-0.75\,\boldsymbol{\rho}_c + 0.454\,\boldsymbol{\rho}_e)\boldsymbol{\rho}\boldsymbol{\nu}^{-2} + \ldots \\ &- (0.749\,\boldsymbol{\rho}_c + 0.235\,\boldsymbol{\rho}_e)\boldsymbol{\nu}^{-2} + \ldots - 0.214\,\boldsymbol{\nu}^{-2} + \ldots\}. \end{aligned} \tag{8-9}$$

Now $\bar{v}/c$ is about 5×10^{-3} for all metals mentioned by Dingle [3]) (pp. 351-362). It remains a problem, what value to use for the electron-electron relaxation time τ_e, since there are no very satisfactory indications in this respect.

We may suppose, first, that τ_e is equal to the quantity τ' previously used (1-2). In this case τ_e is temperature-independent; ρ_e will be small and about the same for all metals mentioned by Dingle ($\approx 2 \times 10^{-3}$).

Whatever ρ_c may be, as long as it is not so large that the expansion (8-9) is meaningless, the influence of ρ_e can thus only produce an extra contribution of something like 10^{-5} to the absorption factor, since $\boldsymbol{\nu} > 1$. The largest term is always the term 0.75 (the principal anomalous skin effect term), giving a contribution of 4×10^{-3}.

If, on the other hand, following Ginzburg and Silin [9]), we take τ_e to be the mean free path for electron-electron collisions, divided by $\bar{v}$, τ_e will depend on the temperature, because of the exclusion principle: electrons can only collide if they are within a certain energy range of the order of kT. For temperatures below 300°K, τ_e is now still larger than τ', which is about 5×10^{-12} s, so that ρ_e, and its contribution to A, will be still smaller than according to our previous supposition.

It seems, therefore, that the effect of electron-electron collisions on the optical properties of metals in the infrared will be too small to measure.

The author is indebted to Prof. Dr. R. Kronig for suggesting this problem and for many stimulating discussions.

Received 19th July, 1958.

REFERENCES

1) Benthem, C. W. and R. Kronig, Physica **20** (1954) 293.
2) Reuter, G. E. H. and E. H. Sondheimer, Proc. Roy. Soc. A **195** (1948) 336.
3) Dingle, R. B., Physica **19** (1953) 311, 348.
4) Kronig, R. and J. Korringa, Physica **10** (1943) 406, 800.
5) Kronig, R., Physica **15** (1949) 667.
6) Sparenberg, J. A., T. C. Braakman and C. W. Benthem, Appl. Sci. Res. **B6** (1957) 312.
7) Titchmarsh, E. C., Introduction to the theory of Fourier integrals, Oxford, Clarendon Press, 1937.
8) Gordon, A. N. and E. H. Sondheimer, Appl. Sci. Res. **B 3** (1953) 297.
9) Ginzburg, V. L. and V. P. Silin, J. Exp. Theor. Phys., U.S.S.R. **29** (1955) 64 = Sov. Phys. **2** (1956) 46.

Appl. sci. Res. Section B, Vol. 7

FAR FIELD SCATTERING FROM BODIES OF REVOLUTION *)

by K. M. SIEGEL

The University of Michigan Ann Arbor, Michigan, U.S.A.

Summary

By use of approximations based on physical reasoning radar cross-section results for bodies of revolution are found. In the Rayleigh region (wavelength large with respect to object dimensions) approximate solutions are found. Examples given include a finite cone, a lens, an elliptic ogive, a spindle and a finite cylinder. In the physical optics region (wavelength very small with respect to all radii of curvature) Kirchhoff theory and also geometric optics can be used. When the body dimensions are only moderately large with respect to the wavelength, Fock or Franz theory can be applied, and examples of the circular and elliptic cylinder are presented. In the region where some dimensions of the body are large with respect to the wavelength and other dimensions are small with respect to the wavelength, special techniques are used. One example, the finite cone, is solved by appropriate use of the wedge-like fields locally at the base. Another example is the use of traveling wave theory for obtaining approximate solutions for the prolate spheroid and the ogive. Other results are obtained for cones the base perimeter of which is of the order of a wavelength by using known results for rings of the same perimeter.

§ 1. *Introduction.* It is the intent in this paper to use different mathematical techniques to obtain approximate results for the far zone scattering of plane electromagnetic waves by perfectly conducting bodies of revolution for all ratios of body dimension to wavelength. In many places speculation based on physical reasoning has replaced mathematical rigour. We shall first discuss the Rayleigh region, then the physical optics region and then the resonance region.

§ 2. *Rayleigh cross-section of bodies of revolution.* Rayleigh scattering [1]) describes the scattering of electromagnetic radiation by a body whose dimensions are much smaller than the wavelength of the radiation. Thus the Rayleigh limit describes the scattered field, due to an incident plane wave, approximated at a large distance from the body by the field of radiating electric and magnetic dipoles located at the scatterer (the magnetic dipole contribution is comparable to that of the electric dipole only for a perfect conductor). To evaluate the electric (magnetic) dipole moment, the static electric (magnetic) field induced on the body by an applied constant field must be known. In other words, the electrodynamic boundary-value problem has been reduced to a corresponding static problem.

---

*) This paper with minor revision is as the author presented it at the URSI XIIth General Assembly in Boulder, Colorado August 22–September 5, 1957.

Although the solution of the Laplace equation is in principle simpler than the solution of the Maxwell equations, there are very few geometrical cases for which even the former is manageable. The question, therefore, arises whether any approximate information can be obtained as to the Rayleigh cross-section when a solution of the Laplace equation is not available. That this should be possible is heuristically plausible. When the wavelength is much longer than the dimensions of a body, one cannot discern details of the structure of the body: the observed effect depends more on the size of the body than on its shape. Thus, knowledge of the size of the body. modified by a rough indication of shape, should suffice for a description of the body in finding the Rayleigh cross-section. It is the purpose of the present discussion to explore this possibility.

As background, it might be helpful to bear in mind a couple of features of the Rayleigh approximation itself. The solution to an electromagnetic scattering problem can be expressed as a multipole expansion. The relative importance of terms in the expansion depends upon the distance of the observer from the scatterer (as well as on the dimensions of the body relative to the wavelength), so that a small error in describing the field in one region can result in completely misrepresenting the corresponding field elsewhere. For a scatterer much smaller than the wavelength, retaining only the dipole terms gives a good approximation to the far zone, though the field in the near zone may be entirely wrong. Specifying the dipole moments of the body does not determine the body uniquely (i.e. different bodies may have the same dipole moments). Thus the Rayleigh cross-section alone cannot identify the body fully. On the other hand, the finer details of the structure of the body, which would be exhibited by the higher moments (and seriously affect the cross-section at small wavelengths), do not affect the Rayleigh cross-section.

For simplicity, consider the scatterer to be a body of revolution, make it a perfect conductor (this is a rather trivial limitation) and examine back-scattering of a plane wave incident along the axis of symmetry (there is then no polarization dependence). Thus, the direction of incidence will be denoted by z, the incident electric vector direction by x, the incident magnetic vector direction by y and the length of the body along the symmetry axis by l. The electric dipole moment $\boldsymbol{p}$ is given by

$$\boldsymbol{p} = \int_S \omega \boldsymbol{r}\, \mathrm{d}S \tag{2-1}$$

where ω is the charge density, $\boldsymbol{r}$ the position vector and S the surface of the body. The boundary condition yields.

$$\omega = \varepsilon \boldsymbol{E} \cdot \boldsymbol{n} = \varepsilon E, \tag{2-2}$$

where $\varepsilon =$ dielectric constant, $\boldsymbol{n} =$ unit outward normal to the surface and $\boldsymbol{E}=$electric field strength. Using cylindrical coordinates,

$$\mathrm{d}S = \rho\sqrt{1 + (\mathrm{d}\rho/\mathrm{d}z)^2}\, \mathrm{d}\phi\, \mathrm{d}z, \tag{2.3}$$

where ρ is a function of z but not of ϕ, so that

$$\boldsymbol{p} = \varepsilon \int_0^l \mathrm{d}z\, \rho \sqrt{1 + \left(\frac{\mathrm{d}\rho}{\mathrm{d}z}\right)^2} \int_0^{2\pi} \mathrm{d}\phi\, E\boldsymbol{r}. \tag{2-4}$$

From uniqueness and symmetry considerations we can write

$$E = \sum_{n=0}^{\infty} a_n(z) \cos n\phi. \tag{2-5}$$

Then $p_y = 0$, $p_z = 0$ and

$$\begin{aligned} p_x &= \varepsilon \int_0^l \mathrm{d}z\, \rho^2 \sqrt{1 + \left(\frac{\mathrm{d}\rho}{\mathrm{d}z}\right)^2} \int_0^{2\pi} \mathrm{d}\phi \cos\phi\, \left[\sum_{n=0}^{\infty} a_n(z) \cos n\phi\right] \\ &= \varepsilon \int_0^l \pi\, \mathrm{d}z\, \rho^2\, a_1(z) \sqrt{1 + \left(\frac{\mathrm{d}\rho}{\mathrm{d}z}\right)^2} = \varepsilon \int_0^l \pi\, \mathrm{d}z\, \rho^2\, a_1'(z). \end{aligned} \tag{2-6}$$

Apart from the factor $a_1'(z)$, the integral is just the volume V of the body. In fact, the whole determination of the electric dipole moment resolves itself into the determination of the factor $a_1(z)$ in

$$E = a_1(z) \cos \phi \tag{2-7}$$

since the other terms in the series do not contribute. If the body is elongated along the axis of symmetry (i.e., if $l \gg \rho$), $a_1'(z)$ will be a slowly varying function of z and can be removed from the integral and replaced by a mean value (or actually by an estimate of its value). To estimate $a(z)$, we resort to an analogy with reflection from a plane. In the latter case the amplitude of the total field is twice that of the incident field. Thus we choose $a = 2E_0$ (phase differences in the incident field at various points on the body can be neglected) to obtain

$$\boldsymbol{p} = \hat{x} 2\varepsilon E_0 V. \tag{2-8}$$

The far-zone electric field at a point on the z-axis due to the electric dipole is 2)

$$\boldsymbol{E} = -\frac{k^2}{4\pi\varepsilon}\, \hat{z} x(\hat{z} \times \boldsymbol{p})\, \frac{e^{i(kr-\omega t)}}{R}. \tag{2-9}$$

The form of the magnetic dipole far-zone field is the same as that for the electric dipole if the electric and magnetic fields are interchanged 2). The symmetry of the problem insures that the magnetic dipole is along the y-axis, just as the electric dipole is along the x-axis. Consequently, the far-zone fields due to the two dipoles have the same orientation and phase. If we again resort to a cylinder-like model for approximation (with the amplitude of the total field at the surface twice that of the incident field), it is obvious from the complete symmetry of occurrence of the electric and magnetic interactions that the two contributions are equal.

Altogether we have in the far zone on the z-axis

$$\boldsymbol{E} = \hat{x} \frac{k^2}{\pi} E_0 V \frac{e^{i(kR-\omega t)}}{R}. \tag{2-10}$$

The back-scattering cross-section is given by

$$\sigma = 4\pi R^2 \left| \frac{\boldsymbol{E}}{\boldsymbol{E}_0} \right|^2 = \frac{4}{\pi} k^4 V^2. \tag{2-11}$$

This, then, is the value of the cross-section to be expected for an elongated body of revolution*). As the flatness of the scatterer increases, the approximation is expected to get worse; in fact an infinitely flat body (i.e. a disc) has zero volume, but a non-zero cross-section. To anticipate the discussion below, for prolate spheroids the error incurred in the cross.-section varies from zero for extreme elongation to 13% for the sphere.

Let us now compare this pseudo-derivation in detail with the exact answer for the special case we do know, the spheroid 1). Let us define for convenience the quantity

$$F = \frac{\pi R\,|\boldsymbol{E}|}{k^2 E_0 V}. \tag{2-12}$$

$F = 1$ yields the magnitude of $\boldsymbol{E}$ given by (2-10). Modifying Rayleigh's notation slightly,

$$F = \frac{1}{2}\left(\frac{1}{L} + \frac{1}{2-L}\right) = \frac{1}{L(2-L)}, \tag{2-13}$$

where for a prolate spheroid 1)

$$L = \frac{1}{e^2} - \frac{1-e^2}{2e^3} \ln \frac{1+e}{1-e} \tag{2-14}$$

with $e =$ eccentricity; i.e. the semi-axes are a, a, $a/\sqrt{1-e^2}$. For an elongated spheroid ($e \to 1$), $L \to 1$ and $F \to 1$, checking the approximation.

Next, let us inquire into the shape correction by first examining its form for the spheroid. We already know the result for the prolate case; for the oblate spheroid 1)

$$L = \left(\frac{\sqrt{1-e^2}}{e^3} \sin^{-1} e - \frac{1-e^2}{e^2}\right), \tag{2-15}$$

where the semi-axes are now a, a, $a\sqrt{1-e^2}$. As these expressions are quite complicated, it is profitable to examine their limiting

---

*) It should be noted that for the acoustic case the treatment would be equivalent except that instead of the two components (electric and magnetic) there would be only one, and thus the cross-section would be

$$\sigma = \frac{1}{\pi} k^4 V^2.$$

values. Consider a sphere ($e = 0$): From (2-14)

$$\ln \left(\frac{1+e}{1-e} \right) = 2 \left(e + \tfrac{1}{3} e^3 + \ldots \right), \qquad (2\text{-}16)$$

$$L = \frac{1}{e^2} \left[1 - (1-e^2) \left(1 + \tfrac{1}{3} e^2 + \ldots . \right) \right] =$$

$$= \frac{1}{e^2} \left[1 - 1 + e^2 - \tfrac{1}{3} e^2 + \ldots\ldots \right] \to \tfrac{2}{3}, \qquad (2\text{-}17)$$

$$F = \left[\tfrac{2}{3} \left(2 - \tfrac{2}{3}\right) \right]^{-1} = \left[\tfrac{2}{3} \cdot \tfrac{4}{3} \right]^{-1} = \tfrac{9}{8}. \qquad (2\text{-}18)$$

It is easily demonstrated that F is monotonically decreasing as we progress from a sphere to an elongated prolate spheroid. Hence, it ranges from $\frac{9}{8}$ to 1, being very nearly constant, of the form 1 + + decaying term.

Examine the disc limit ($e \to 1$ for the oblate spheroid). Let

$$e = \sin x. \qquad (2\text{-}19)$$

Then

$$L = \cos x \csc^2 x \, (x \csc x - \cos x). \qquad (2\text{-}20)$$

Let

$$y = \tfrac{1}{2}\pi - x. \qquad (2\text{-}21)$$

Then

$$L = \sin y \sec^2 y \left[\left(\tfrac{1}{2}\pi - y\right) \sec y - \sin y \right]. \qquad (2\text{-}22)$$

Expand near $y = 0$ (equivalent to $e \to 1$):

$$L \approx y \left[\left(\frac{\pi}{2} - y \right) - y \right] = \frac{\pi y}{2} - 2y^2 = \frac{\pi}{2} y \left(1 - \frac{4}{\pi} y \right), \qquad (2\text{-}23)$$

$$F = \frac{1}{L(2-L)} \approx \frac{1}{(\pi/2)\, y (1 - (4/\pi)\, y)(2 - (\pi/2)\, y)} \approx$$

$$\approx \frac{1}{\pi y} \left(1 + \frac{4}{\pi} y + \frac{\pi}{4} y \right). \qquad (2\text{-}24)$$

For small y, $y \approx \sqrt{1-e^2}$; if we call the semi-axes a, a, b, then $y \approx b/a$.

Combine the information about F. In the oblate case, F is again monotonically increasing toward the disc limit. The discussion for the prolate spheroid indicates that we should split off from F a term unity, and that the remaining term should decay as $b/a \to \infty$. Thus, we write

$$F \approx 1+\frac{1}{\pi y}\left[1+\left(\frac{4}{\pi}+\frac{\pi}{4}-\pi\right)y\right] \approx 1+\frac{1}{\pi y}(1-y) \approx 1+\frac{1}{\pi y}\mathrm{e}^{-y}. \quad (2\text{-}25)$$

We now postulate that for all spheroids (with semi-axes a, a, b) the shape correction factor is approximately

$$F = 1+\frac{1}{\pi y}\mathrm{e}^{-y}, \qquad (2\text{-}25)$$

where $y = b/a$. *Numerical comparison indicates that the approximation is valid to within one percent.* The Rayleigh cross-section of a spheroid for back-scattering along the axis of symmetry is

$$\sigma = \frac{4}{\pi}k^4V^2\left[1+\frac{1}{\pi y}\mathrm{e}^{-y}\right]^2. \qquad (2\text{-}26)$$

The cross-section of the spheroid depends on its volume and on a correction factor involving $y = b/a$. Except for very flat oblate spheroids the shape correction factor can be neglected. Where it is not neglected, the shape correction factor is a simple function of y, which is a measure of the elongation.

The natural extension of the discussion is to postulate that for all bodies of revolution the Rayleigh cross-section for back-scattering along the axis of symmetry can be expressed as

$$\sigma = \frac{4}{\pi}k^4V^2\left[1+\frac{1}{\pi y}\mathrm{e}^{-y}\right]^2, \qquad (2\text{-}26)$$

where y is a measure of the elongation (characteristic dimension along the axis of symmetry)/(characteristic dimension in the perpendicular direction). For elongated bodies the term in y drops out and there is no ambiguity. For flattened bodies the answer is sensitive to the choice of charcteristic dimensions, but a good approximation should still be attainable. The ambiguity can be eliminated in a number of cases by imposing a restriction on the choice of characteristic dimensions: in the limit of extreme flattening the cross-section must tend to the value for the appropriate disc.

Illustration I: Finite cone. Consider a right circular cone of altitude h and radius of base r. As $h \to 0$, the cross-section of the cone must go into the cross-section of a disc of radius r; i.e., we must have

$$VF = \tfrac{1}{3}\pi r^2 h\left(1 + \frac{1}{\pi y}\,\mathrm{e}^{-y}\right) \to \frac{r^2 h}{3y} = \tfrac{4}{3}\,r^3. \tag{2-27}$$

Thus the appropriate ratio of characteristic dimensions to be used in (2-26) is

$$y = h/4r. \tag{2-28}$$

Hence, the cone has the same cross-section as a spheroid of equal volume whose semi-axes are $(r, r, h/4)$.

Illustration II: Lens. Consider a symmetrical convex lens of radius of curvature R (the body of revolution obtained by rotating the shaded area in fig. 2.1 about the η-axis). In the disc limit (d constant, $c \to 0$)

$$VF \to V/\pi y = \tfrac{4}{3}\,d^3. \tag{2-29}$$

Hence we take for the lens

$$y = \frac{3V}{4\pi d^3} = \frac{3V}{4\pi R^3 \sin^3\theta}. \tag{2-30}$$

The volume of the lens is

$$V = \tfrac{2}{3}\pi\, R^3(1 - \cos\theta)(1 - \cos\theta + \sin^2\theta). \tag{2-31}$$

As $\theta \to \pi/2$ (limit of sphere), we reproduce the previous result for the spheroid, as expected.

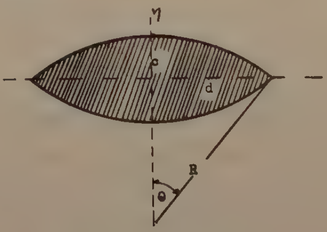

Fig. 2.1 The lens.

Illustration III: Elliptic ogive. Inasmuch as the circular ogive is more elongated than a sphere, the argument from the disc limit cannot be applied to it directly. Instead, we consider the elliptic ogive obtained by rotating the shaded area of fig. 2.2 (a portion of an ellipse) about the η-axis (which is taken parallel to the minor axis). For this body, in the disc limit (d constant, $c \to 0$)

$$VF \to V/\pi y = \tfrac{4}{3}d^3. \tag{2-32}$$

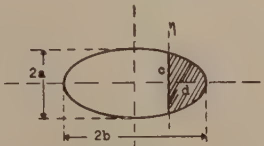

Fig. 2..2 The elliptic ogive.

The equation for the ellipse is

$$c^2/a^2 + (b - d)^2/b^2 = 1, \tag{2-33}$$

which suggests use of the parameter θ:

$$\sin\theta = c/a. \tag{2-34}$$

Then

$$y = \frac{3V}{4\pi d^3} = \frac{3V}{4\pi b^3(1 - \cos\theta)^3}. \tag{2-35}$$

The volume of the elliptic ogive is

$$V = 2\pi ab^2 (\sin\theta - \theta\cos\theta - \tfrac{1}{3}\sin^3\theta). \tag{2-36}$$

As $\theta \to \tfrac{1}{2}\pi$, we reproduce the previous result for the spheroid, as expected.

Special case: Circular ogive. To obtain the cross-section of the circular ogive, we now merely take the special case of the elliptic ogive with $a = b$. From geometry θ can then be identified with the ogive half-angle. Now

$$y = \tfrac{3}{2}\frac{\sin\theta - \theta\cos\theta - \tfrac{1}{3}\sin^3\theta}{(1 - \cos\theta)^3}. \tag{2-37}$$

Illustration IV: Spindle. Consider the body of revolution obtained by rotating the shaded area of fig. 2.3 (bounded by a parabola and a straight line perpendicular to the axis of the parabola) about the η-axis. Using the disc limit just as before, we have

$$y = \frac{3V}{4\pi d^3}, \tag{2-38}$$

where the volume is

$$V = \tfrac{16}{15}\pi c d^2, \tag{2-39}$$

so that

$$y = \tfrac{4}{5}\frac{c}{d}. \tag{2-40}$$

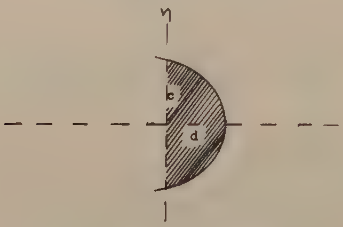

Fig. 2.3. The spindle.

Illustration V: Finite cylinder. Consider a cylinder of radius r and heigth h. From the disc limit

$$y = \frac{3V}{4\pi r^3} = \frac{3h}{4r}. \tag{2-41}$$

We can go on to obtain by further exploitation of this approach the Rayleigh cross-section of a body of revolution for arbitrary separation between transmitter and receiver and for all aspects and all polarizations. The most direct extension is to replace the body by an equivalent spheroid and take over the spheroid results. The equivalent spheroid is a spheroid with the same volume and the same elongation factor as the body. The simplified expression found for back-scattering along the symmetry axis provides a reasonable way to arrive at an elongation factor for many bodies. The logical ultimate extension in the spirit of this approach is to formulate the Rayleigh scattering of a body of revolution at all aspect combinations and polarizations in terms of the following parameters only: the volume, the elongation factor, and the aspect and polarization angles.

§ 3. *The optics region.* By the optics region we mean, generally, that region in wavelength, wherein the techniques of geometric and physical optics yield good approximations to the radar cross-section of a body. The extent of the optics region thus depends on the particular body being studied. By the geometric optics cross-section we mean $\pi R_1 R_2$, R_1 and R_2 being the principal radii of curvature of the body at the point where a ray is reflected toward the receiver. We use physical optics (Kirchhoff) theory to denote the scattered far field, and the cross-section thus defined, given by the expression

$$\boldsymbol{H}_s = \frac{1}{4\pi} \int\limits_{\substack{\textit{illuminated} \\ \textit{area}}} (\boldsymbol{n} \times \boldsymbol{H}) \times \nabla \frac{\mathrm{e}^{ikR}}{R} \, \mathrm{d}s,$$

where $\boldsymbol{H}$ = twice the tangential component of the incident magnetic field, R = the distance from the integration point to the field point, $\boldsymbol{n}$ = the unit outward normal to the surface at the integration point and in which the far field approximations for $\nabla(\mathrm{e}^{ikR}/R)$ are used. That is, with the receiver at a very great distance from the body and if the body is finite, we have

$$\nabla\left(\frac{\mathrm{e}^{ikR}}{R}\right) \approx \frac{ik}{R'} (\mathrm{e}^{ikR}) \boldsymbol{n}_0,$$

where $R = R' + \boldsymbol{n}_0 \cdot \boldsymbol{r}$, R' = the distance from the origin to the field point (receiver), r = the distance from the origin to the integration point on the scatterer ($\boldsymbol{r}$ = the corresponding vector) and $\boldsymbol{n}_0$ = the unit vector directed from the receiver to the origin.

When the wavelength is small with respect to all of the dimensions of the scatterer, the geometric optics cross-section is an excellent approximation to the exact result. When a body is infinite in extent, then geometric optics can be the exact solution. Examples of such exact solutions are the paraboloid of revolution, when we are considering plane wave illumination along the axis of symmetry, and the wedge for particular wedge angles and for particular angles of incidence and polarization.

Let us now consider a body which has one radius of curvature which is small with respect to the wavelength. In three dimensions we can consider the infinite cone and in two dimensions we can consider the wedge. By purely dimensional analysis we find that the tip far field behaves like $1/k$ and the edge in two dimensions behaves like $(1/k)^{\frac{1}{2}}$. We find that physical optics not only predicts these types of k-dependence, but also (for large and small cone angles) that it predicts the leading term of a rapidly convergent expansion in the angle parameter as long as the transmitter or receiver is on the axis of symmetry.

Kirchhoff theory will predict poor results for problems in which the major contribution to the cross-section comes from an edge. For example, consider the case in which the transmitter and receiver are located at a point along the face of a wedge, but far from the edge, with Poynting's vector $\boldsymbol{P}$ parallel to the face of the wedge and normal to the edge (see fig. 3.1). For the $\boldsymbol{E}$-vector perpendicular to the surface the exact result is

$$\sigma_{\perp} = 2\pi \, |f(\phi)|^2 = \frac{\pi\lambda}{2\phi_0{}^2} \tan^2 \frac{\pi^2}{2\phi_0},$$

where the cross-section, in two dimensions, is given by

$$\sigma = \lim_{r=\infty} 2\pi r \left| \frac{E_s}{E_i} \right|^2,$$

while the Kirchhoff answer is zero.

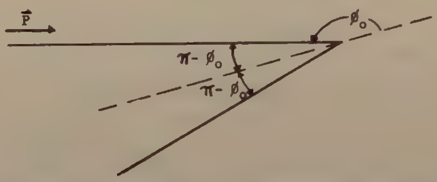

Fig. 3.1. The wedge for incidence along one face of the wedge and normal to the edge.

This leads one to the realization of why Kirchhoff theory would give poor results for a finite thin cone. The major contribution to the cross-section in the non-specular directions for small wavelengths comes from the rear circular edge. The field, locally, would be like that for a wedge. Thus, we need to use an improvement to Kirchhoff theory to obtain good answers for the cone. We will show this improvement and also how we obtain approximate results for thin cones in the resonance region. Thus we will show how to obtain, approximately, a complete cone cross-section curve.

Kirchhoff theory gives excellent first order approximations for bodies with dimensions large with respect to the wavelength, and these results are too well-known to warrant their discussion here. In the region to which we must give the vague characterization as lying somewhere between the resonance region and the optics region there has been a rapid and fruitful development of new ideas during the past ten years.

We begin with the remarkable paper of V. A. Fock [3]) in which he presented a method which we will describe as a local order analysis of the field near the shadow boundary. He succeeds in giving the fields on the diffracting surface near the shadow boundary in terms of one or the other of two "universal" functions according as the incident polarization direction lies parallel or perpendicular to the shadow curve. Strictly, these are solutions of the two-dimensional (scalar) problems and depend on the radius of curvature at the shadow boundary and the wavelength of the radiation. These functions are of the form

$$\begin{aligned} g(\zeta) &= \frac{1}{\sqrt{\pi}} \int_{\Gamma} \frac{e^{i\zeta t}}{w'(t)}\, dt, \\ f(\zeta) &= \frac{1}{\sqrt{\pi}} \int_{\Gamma} \frac{e^{i\zeta t}}{w(t)}\, dt, \end{aligned} \tag{3-2}$$

where

$$w(t) = \frac{1}{\sqrt{\pi}} \int_{\Gamma'} e^{zt - \frac{1}{3}z^3}\, dz \tag{3-3}$$

with the contours shown in fig. 3.2. The arguments used are certain

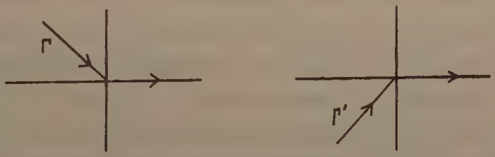

Fig. 3.2. Contours.

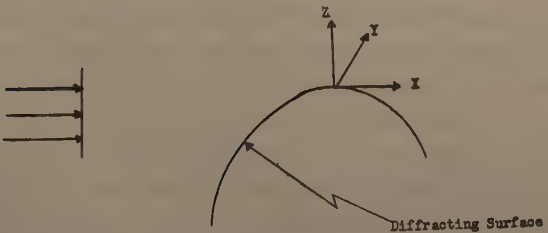

Fig. 3.3. Geometry.

reduced distances measured from the geometrical shadow boundary; i.e., near the origin as indicated in fig. 3.3 we have

$$\zeta = \left(\frac{kR}{2}\right)^{\frac{1}{3}} \frac{X}{R}, \tag{3-4}$$

where R is the radius of curvature and $k = 2\pi/\lambda$.

These same functions appear in the approximate solutions of specific problems. There are two which we particularly wish to note. The fields induced on a parabolic cylinder 4) and on a circular cylinder 5) are given, in a sense, by these same functions. These are not remarkably similar surfaces.

In these examples for the solution continued into the shadow we need to modify the arguments of the universal functions as follows. The motivation for this stems from the "generalized ray optics" of Keller 6). In place of (3-4) we write

$$\zeta = \int_0^S \left[\frac{kR(s)}{2}\right]^{\frac{1}{3}} \frac{ds}{R(s)}, \tag{3-5}$$

where S is the path length measured along the surface of the obstacle from the shadow boundary into the shadow, ds is the element of path length and $R(s)$ is the radius of curvature at the position s.

Franz and Deppermann 7), however, have given the connection between the two in the concept of "creeping waves". We can meaningfully speak of the continuation of the penumbra solution into the shadow of the parabolic cylinder, but in the case of the circular cylinder we find that we are wrapping our solution around the cylinder if we allow the argument of the universal functions to continue increasing. This latter concept is made meaningful if we understand the field in the shadow as arising from waves "launched" at the shadow boundary and "creeping" around the rear and eventually back to the front, etc. The physical interpretation has been justified by Friedlander 8) while the underlying mathematical structure has been illuminated by Wu 9) with his concept of a universal covering space.

In the following is given an account of the general procedure. Let a convex closed surface S, $f(x, y, z) = 0$ be illuminated by a plane wave incident in the direction of the x-axis. The geometrical shadow is then given by the two equations $f(x, y, z) = 0$, $\partial f/\partial x = 0$. Let the origin be located at a point on the shadow boundary with the z-axis the outward normal to S and the y-axis chosen to form a right-handed system. Using the geometric assumption that the surface can be approximated by a paraboloid at any point, i.e.,

$$z + \tfrac{1}{2}(ax^2 + 2bxy + cy^2) = 0, \tag{3-6}$$

so that $\partial f/\partial x = ax + by$, and the physical assumption that the variation of this field in the z direction is much larger than that in either the x- or y- direction for sufficiently small λ, Fock obtains an approximation to Maxwell's equations which lead to the solutions

$$H_y = H_y{}^0 G(\zeta), \quad H_x = (2a/k)^{\frac{1}{3}}\, iH_z{}^0\, \mathrm{e}^{ikx}\, F(\zeta), \quad H_z = 0 \tag{3-7}$$

on the surface. The incident field is given by

$$\boldsymbol{H}_0 = (0, H_y{}^0, H_z{}^0), \tag{3-8}$$

while the functions G and F have the asymptotic bahaviour

$$\lim_{\zeta\to\mp\infty} G(\zeta) = \begin{cases} 2, \\ 0, \end{cases} \qquad \lim_{\zeta\to\mp\infty} F(\zeta) = \begin{cases} 2\zeta, \\ 0, \end{cases} \tag{3-9}$$

where ζ is a reduced distance from the shadow boundary given by

$$\zeta = \left(\frac{k}{2a}\right)^{\frac{1}{3}}(ax + by). \tag{3-10}$$

In fig. 3.4 we compare the result using the Fock-Franz method with the sum of the harmonic series for a circular cylinder (e.g., Bailin's work in 10)) with $ka = 12$. In fig. 3.5 we compare the method with the experimental measurements of Wetzel and Brick 11) on an elliptic cylinder of $ka = 12$ and $kb = 7.5$.

In the case of the three-dimensional problem of scattering by finite obstacles we have an additional complication which appears in both the scalar and vector problems. Since there is a caustic at the rear of the obstacle, we must take account of the fact that the energy converges on the caustic and, in fact, the "creeping waves" lose their identity in this region.

This behaviour is apparent from the work of Fock 12), Franz 5) and, more recently, Belkina and Weinstein 13) and N. Logan 14) who have given a thorough treatment of this approach for the sphere. However, Fock theory can be used to determine a partial creeping wave type field, and if we can find another way to handle the partial field due to the small radii of curvature, we can again obtain good far-field approximations for moderate values of ka. The value of Fock theory is twofold: (1) When the wavelength is very small in respect to the characteristic dimensions of the body, it yields an approximation to the true field in the shadow region where the Kirchhoff result would predict a zero field, and (2) it is a procedure which is easily applied to sphere and cylinder problems for moderate values of ka ($ka > 5$). One finds upon applying this process to spheroids that the values of ka required in order to obtain good results may be very large.

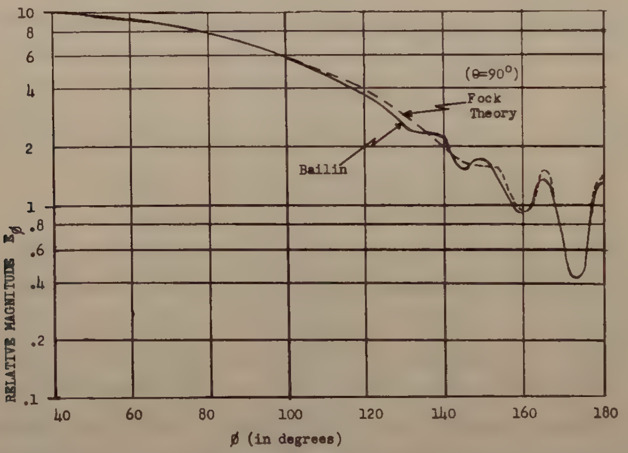

Fig. 3.4. Comparison of amplitudes from exact series and Fock's current distribution for a circular cylinder with $ka = 12$.

In the three-dimensional problems we see that the solution for the sphere with the interpretation of creeping waves and behaviour of the caustic serves as a prototype from which we infer the solution for other shapes provided the characteristic parameters are sufficiently large with respect to the wavelength. For example, a symmetrically illuminated spheroid of large enough dimensions should be an easy generalization.

Suppose we consider a prolate spheroid in somewhat more detail. Let the semi-major and semi-minor axes be denoted by a and b respectively. The condition that we require to be met for the application of the Fock-Franz theory is that $kR_{\min}$ be large where

$k = 2\pi/\lambda$ and $R_{\min}$ is the minimum radius of curvature, $R_{\min} = b^2/a$. As an example of this limitation we note that for a prolate spheroid of $a/b = 10$ the requirement $kR_{\min} \sim 5$ would imply $ka > 500$. This was pointed out by Belkina and Weinstein [13]).

If we let $kR_{\min}$ decrease while we keep ka, kb large, we approach a body which is "large" but which has "sharp" ends. We illuminate this object along the symmetry axis and consider a limited application of our "creeping wave" theory. Certainly for $kR_{\min} < 1$ the forward tip will scatter more like an infinite cone than like a sphere of radius b; hence, our theory is not applicable. In the penumbra region all requirements are met and we feel justified in making a creeping wave analysis. Granted this, we have launched a wave which is creeping toward this effective discontinuity, the rear tip. Here we must again have recourse to another description and consider the

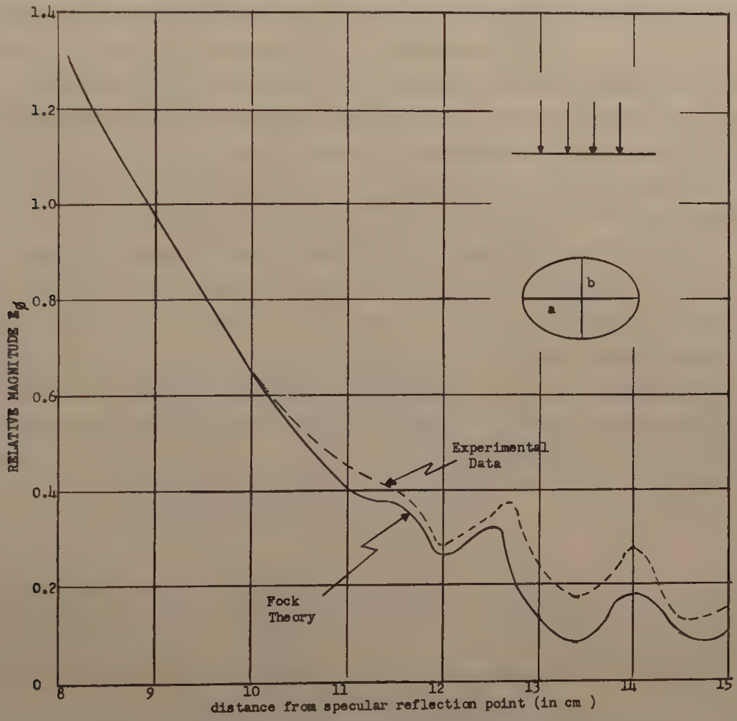

Fig. 3.5. Comparison of amplitudes from experimental data and Fock's current distribution for an elliptic cylinder of eccentricity 0.780 with $ka = 12$ and $kb = 7.5$.

wave to be reflected from the rear tip and again launched along the surface.

An example of this would be the *thin* cone radiation problem when the source is far from the tip ($a =$ distance from tip to source). The Green's function for this case is approximated by that for a cylinder and thus Fock theory should give excellent results. If the infinitesimal slot is along a generatrix of the cone, the Fock answer should be excellent for all ka. If one can obtain an tip answer to add to the Fock result, then one could handle all kinds of slots on cones. We postpone our discussion of the ogive, finite cone and the spheroid approximations (for moderate values of ka) until we reach the discussion of the resonance region in § 4.

In addition to the Fock theory, small wavelength approximations can be improved by making use of known results. Just as Artmann[15]), in his solution for the thick half plane, replaced the cylindrical edge by a polygon, we can obtain an approximation for the thin finite cone by replacing the cone by a regular prism. The base, locally, will be a wedge, and to calculate the field scattered by the cone base we will add up the fields scattered by all the wedge-like segments into which the cone base has been decomposed. We shall consider the cone in some detail; hence, it might be valuable to first present the physical optics approximation.

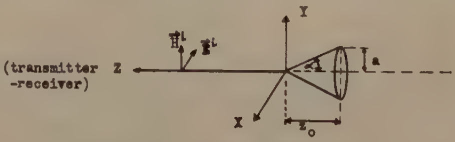

Fig. 3.6. Cone geometry.

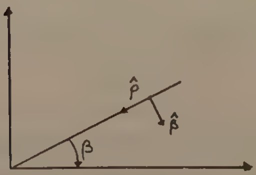

Fig. 3.7. Polar variables.

The problem we shall consider is that of determining the radar cross-section of a thin finite cone when both transmitter and receiver are situated on the axis of symmetry of the cone in the far zone. We will treat the case where the wavelength of the incident radiation is much smaller than the altitude z_0 and the base radius a of the cone. The geometry of the problem is as shown in fig. 3.6. We shall also utilize polar variables in the x-y plane as shown in fig. 3.7.

The following definitions of the radar cross-section (of perfect conductors) will be used:

$$\sigma = \lim_{r\to\infty} 4\pi r^2 \left|\frac{\boldsymbol{E}^s}{\boldsymbol{E}^i}\right|^2 = \lim_{r\to\infty} 4\pi r^2 \left|\frac{\boldsymbol{H}^s}{\boldsymbol{H}^i}\right|^2. \tag{3-11}$$

The Kirchhoff (physical optics) expression for the scattered magnetic field is [16])

$$\boldsymbol{H}^s = \frac{ik}{2\pi}\frac{\mathrm{e}^{-ikr}}{r}[(\boldsymbol{n}_0\cdot\boldsymbol{p})\boldsymbol{f} - (\boldsymbol{n}_0\cdot\boldsymbol{f})\boldsymbol{p}], \tag{3-12}$$

where

$\boldsymbol{f} = \int_S \boldsymbol{n}\,\mathrm{e}^{-ik\boldsymbol{r}\cdot(\boldsymbol{n}_0+\boldsymbol{k})}\,\mathrm{d}s$

S = illuminated area of scatterer

$\boldsymbol{n}$ = unit outward normal to S

$\boldsymbol{r}$ = position vector of point on S

$\boldsymbol{p}$ = direction of incident magnetic field

$\boldsymbol{n}_0$ = receiver to origin direction

$\boldsymbol{k}$ = transmitter to origin direction.

Note. we assume $|H^i| = |E^i| = 1$. In this case, the following relations hold.

$$\boldsymbol{n} = \sin\alpha\hat{\imath}_z + \cos\alpha(\hat{\imath}_x\cos\beta + \hat{\imath}_y\sin\beta),\ \boldsymbol{r} = x\hat{\imath}_x + y\hat{\imath}_y + z\hat{\imath}_z,$$

$$\boldsymbol{p} = \hat{\imath}_y,\quad \boldsymbol{n}_0 = -\hat{\imath}_z,\quad \boldsymbol{k} = -\hat{\imath}_z,\quad \mathrm{d}s = \frac{z\tan\alpha}{\cos\alpha}\,\mathrm{d}z\,\mathrm{d}\beta.$$

Hence

$$\boldsymbol{n}_0\cdot\boldsymbol{p} = -\hat{\imath}_z\cdot\hat{\imath}_y = 0, \tag{3-13}$$

and

$$\boldsymbol{n}_0\cdot\boldsymbol{f} = \int_S \boldsymbol{n}_0\cdot\boldsymbol{n}\,\mathrm{e}^{-ik\boldsymbol{r}\cdot(\boldsymbol{n}_0+\boldsymbol{k})}\,\mathrm{d}s, \tag{3.14}$$

which becomes

$$= -\tan^2\alpha\int_0^{2\pi}\int_0^{-Z_0} z\,\mathrm{e}^{2ikz}\,\mathrm{d}z\,\mathrm{d}\beta. \tag{3-15}$$

The integration with respect to β yields

$$\boldsymbol{n}_0\cdot\boldsymbol{f} = -2\pi\tan^2\alpha\int_0^{-z_0} z\,e^{2ikz}\,dz. \tag{3-16}$$

This integration can also be performed yielding

$$\boldsymbol{n}_0\cdot\boldsymbol{f} = -\,2\pi\tan^2\alpha\left(\frac{-e^{2ikz}}{(2ik)^2}+\frac{z\,e^{2ikz}}{2ik}\right)\Bigg|_0^{-z_0},$$

$$\boldsymbol{n}_0\cdot\boldsymbol{f} = -2\pi\tan^2\alpha\left(\frac{e^{-2ikz_0}}{4k^2}-\frac{z_0\,e^{-ikz_0}}{2ik}-\frac{1}{4k^2}\right). \tag{3-17}$$

Hence

$$\boldsymbol{H}^s = \frac{i\,e^{-ikr}}{r}\tan^2\alpha k\,\hat{\imath}_y\left(\frac{e^{-2ik_0}}{4k^2}-\frac{z_0\,e^{-2ikz_0}}{2ik}-\frac{1}{4k^2}\right), \tag{3-18}$$

which can be written

$$\boldsymbol{H}^s = \frac{i\,e^{-ik(r+2z_0)}}{2kr}\tan^2\alpha\,\hat{\imath}_y\left(\tfrac{1}{2}+ikz_0-\frac{e^{2ikz_0}}{2}\right). \tag{3-19}$$

Since $|kz_0| > 1$ (small wavelength approximation)

$$\boldsymbol{H}^s \approx \frac{i\,e^{-ik(r+2z_0)}}{2kr}\tan^2\alpha\hat{\imath}_y(ikz_0) = -\frac{e^{-ik(r+2z_0)}}{2r}z_0\tan^2\alpha\,\hat{\imath}_y. \tag{3-20}$$

Now using the definition of radar cross-section we have

$$\sigma = \lim_{r\to\infty}4\pi r^2\left|\frac{\boldsymbol{H}^s}{\boldsymbol{H}^i}\right|^2 = \pi z_0^2\tan^4\alpha$$

or

$$\sigma = \pi a^2\tan^2\alpha. \tag{3-21}$$

We will now approximate the cone by a prism and determine the field scattered by the wedge segments that constitute the base.

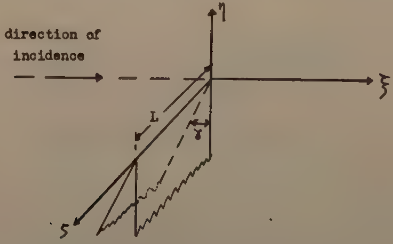

Fig. 3.8. Wedge geometry.

To illustrate the technique we will first use the physical optics approximation for the field scattered by the wedges. We use the Kirchhoff expressions for the scattered field previously presented where in this case (incidence perpendicular to the back face of the wedge, see fig. 3.8) we have

$$\boldsymbol{n} = \sin\gamma\,\hat{\imath}_\eta - \cos\gamma\,\hat{\imath}_\xi,\ \boldsymbol{r} = \xi\hat{\imath}_\xi + \eta\hat{\imath}_\eta + \zeta\hat{\imath}_\xi,$$

$$\boldsymbol{p} = \boldsymbol{p}(\text{no } \xi \text{ component i.e., } \boldsymbol{p}\cdot\hat{\imath}_\xi = 0),\quad \boldsymbol{n}_0 = \hat{\imath}_\xi,\quad \boldsymbol{k} = \hat{\imath}_\xi, \tag{3-22}$$

$$\mathrm{d}s = \frac{\mathrm{d}\xi\,\mathrm{d}\zeta}{\sin\gamma}.$$

Hence $\boldsymbol{n}_0\cdot\boldsymbol{p} = \hat{\imath}\cdot\boldsymbol{p} = 0$, and

$$\boldsymbol{n}_0\cdot\boldsymbol{f} = -\frac{\cos\gamma}{\sin\gamma}\int_0^L\int_0^{-\infty} \mathrm{e}^{-2ik\xi}\,\mathrm{d}\xi\,\mathrm{d}\zeta. \tag{3-23}$$

Integrating with respect to ζ and letting $\xi \to -\xi$, we obtain

$$\boldsymbol{n}_0\cdot\boldsymbol{f} = \frac{L}{\tan\gamma}\int_0^\infty \mathrm{e}^{2ik\xi}\,\mathrm{d}\xi = \frac{L}{\tan\gamma}\,\frac{\mathrm{e}^{2ik\xi}}{2ik}\bigg|_0^\infty. \tag{3-24}$$

Associating the edge contribution with the value at the lower limit (just as in the case of the infinite cone we obtain the "tip" contribution) we find

$$\boldsymbol{n}_0\cdot\boldsymbol{f} = -\frac{L}{2ik\tan\gamma}. \tag{3-25}$$

Hence

$$\boldsymbol{H}^s = \frac{L}{4\pi\tan\gamma}\,\frac{\mathrm{e}^{-ikr}}{r}\,\boldsymbol{p}. \tag{3-26}$$

Now letting $L = a\,\mathrm{d}\beta$, where a = radius of base, and integrating around the base ($\boldsymbol{p}$ = constant vector), we have

$$\boldsymbol{H}^s = \int_0^{2\pi} \frac{\boldsymbol{p}\,\mathrm{e}^{-ikr}}{4\pi r\tan\gamma}\,a\,\mathrm{d}\beta = \frac{a\boldsymbol{p}\mathrm{e}^{-ikr}}{2r\tan\gamma}, \tag{3-27}$$

$$\sigma = 4\pi r^2\left|\frac{\boldsymbol{H}^s}{\boldsymbol{H}^i}\right|^2 = 4\pi r^2\left|\frac{a\,\mathrm{e}^{-ikr}}{2r\tan\gamma}\boldsymbol{p}\right|^2 = \frac{a^2}{\tan^2\gamma}. \tag{3-28}$$

But $\gamma = \frac{1}{2}\pi - \alpha$ (see fig. 3.9), where α is half the cone angle; thus, $\tan \alpha = \tan(\frac{1}{2}\pi - \gamma) \doteq \cot \gamma$ and finally

$$\sigma \doteq \pi a^2 \tan^2 \alpha, \tag{3-29}$$

which is precisely the nose-on result obtained for the cone directly by physical optics.

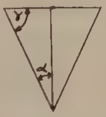

Fig. 3.9. Definitions of γ and α.

Now we are in a position to employ this technique to obtain a new result for the finite cone. We make use [17]) of the following expression for the electric field scattered by an infinite wedge:

$$\boldsymbol{E}^s = \frac{\sqrt{2\pi/kr}}{2(2\pi-\gamma)} \cdot$$

$$\cdot\, e^{ikr+\frac{1}{4}i\pi} \sin\left(\frac{\pi^2}{2\pi-\gamma}\right)\left[\frac{E(a)\hat{\rho} - E(b)\hat{\beta}}{A} - \frac{E(a)\hat{\rho} + E(b)\hat{\beta}}{B}\right], \tag{3-30}$$

where incidence is in a direction perpendicular to the edge of the wedge and

$E(a) = E^i_\perp$ = component of the incident field perpendicular to the edge of the wedge,

$E(b) = E^i_\parallel$ = component of the incident field parallel to the edge of the wedge,

$$A = \cos\left(\frac{2\pi\theta}{2\pi-\gamma}\right) + \cos\left(\frac{\pi^2}{2\pi-\gamma}\right),$$

$$B = 1 - \cos\left(\frac{\pi^2}{2\pi-\gamma}\right),$$

θ = angle of incidence measured from wedge angle bisector and $\hat{\rho}$ and $\hat{\beta}$ are unit vectors perpendicular and parallel, respectively, to the edge of the wedge.

This expression is valid for an infinite wedge. In order to obtain an expression for a wedge of finite edge length, we again look at the current distribution integrals. Noting first that we now have an e^{+ikr} phase term, we know that the integral over the edge length will be in the two-dimensional case

$$\int_{-\infty}^{\infty} e^{ik\sqrt{r^2+\zeta^2}}\, d\zeta \approx \sqrt{r\lambda}\, e^{i(kr+\frac{1}{4}\pi)} \tag{3-31}$$

and in the three-dimensional case

$$\int_{0}^{L} e^{ik\sqrt{r^2+\zeta^2}}\, d\zeta \approx L\, e^{ikr}. \tag{3-32}$$

This is the only difference between the two- and three-dimensional problems so that the three-dimensional fields can be obtained from the two-dimensional fields by multiplying by

$$\frac{L\, e^{-\frac{1}{4}\pi i}}{\sqrt{r\lambda}}.$$

Thus we obtain, for linear polarization, the following expression for the scattered field for a wedge of length L:

$$\boldsymbol{E}^s = \frac{L\, e^{ikr}}{2r(2\pi-\gamma)} \cdot \sin\left(\frac{\pi^2}{2\pi-\gamma}\right)\left[\frac{E(a)\hat{\rho} - E(b)\hat{\beta}}{A} - \frac{E(a)\hat{\rho} + E(b)\hat{\beta}}{B}\right]. \tag{3-33}$$

Again we are really considering the base of a cone and hence

$$\hat{\rho} = -\hat{\imath}_x \cos\beta - \hat{\imath}_y \sin\beta,\quad \hat{\beta} = +\, i_x \sin\beta - \hat{\imath}_y \cos\beta.$$

$\boldsymbol{E}^i$, we recall, is equal to $-\hat{\imath}_x$, but $\hat{\imath}_x = -\,\hat{\rho}\cos\beta + \hat{\beta}\sin\beta$. Hence

$$E_\perp{}^i = \cos\beta, \qquad E_{||}{}^i = -\sin\beta. \tag{3-34}$$

Thus, using these relations for $E_\perp{}^i$, $E_{||}{}^i$, $\hat{\rho}$ and $\hat{\beta}$,

$$E_\perp{}^i\hat{\rho} - E_{||}{}^i\hat{\beta} = \hat{\rho}\cos\beta + \hat{\beta}\sin\beta = -\,\hat{\imath}_x\cos 2\beta - \hat{\imath}_y \sin 2\beta \tag{3-35}$$

in rectangular unit vectors and similarly

$$E_\perp{}^i\hat{\rho} + E_{||}{}^i\hat{\beta} = \hat{\rho}\cos\beta - \hat{\beta}\sin\beta = -\,\hat{\imath}_x. \tag{3-36}$$

Substituting in $\boldsymbol{E}^s$ we obtain

$$\boldsymbol{E}^s = \frac{L\, e^{ikr}}{2r(2\pi-\gamma)} \sin\left(\frac{\pi^2}{2\pi-\gamma}\right) \cdot \left[-\frac{\hat{\imath}_x \cos 2\beta + \hat{\imath}_y \sin 2\beta}{\cos\left(\frac{2\pi\theta}{2\pi-\gamma}\right) + \cos\left(\frac{\pi^2}{2\pi-\gamma}\right)} + \frac{\hat{\imath}_x}{1-\cos\left(\frac{\pi^2}{2\pi-\gamma}\right)}\right]. \tag{3-37}$$

As before, we set $L = a\, d\beta$ and integrate over β from 0 to 2π, obtaining for the scattered field from the cone

$$\boldsymbol{E}^s{}_{cone} = \frac{\pi a\, e^{ikr}}{r(2\pi-\gamma)} \sin\left(\frac{\pi^2}{2\pi-\gamma}\right) \frac{\hat{\imath}_x}{1-\cos\left(\frac{\pi^2}{2\pi-\gamma}\right)}. \tag{3-38}$$

Now, using the definition

$$\sigma = \lim_{r\to\infty} 4\pi r^2 \left|\frac{\boldsymbol{E}^s}{\boldsymbol{E}^i}\right|^2,$$

we obtain

$$\sigma = \frac{4\pi^3 a^2}{(2\pi-\gamma)^2} \frac{\sin^2\left(\frac{\pi^2}{2\pi-\gamma}\right)}{\left[1-\cos\left(\frac{\pi^2}{2\pi-\gamma}\right)\right]^2}. \tag{3-39}$$

Using the familiar half-angle formulae we can simplify σ as follows:

$$\frac{\sin^2\left(\frac{\pi^2}{2\pi-\gamma}\right)}{\left[1-\cos\left(\frac{\pi^2}{2\pi-\gamma}\right)\right]^2} = \cot^2\left[\frac{\pi^2}{2(2\pi-\gamma)}\right]. \tag{3-40}$$

Hence

$$\sigma = \frac{4\pi^3 a^2}{(2\pi-\gamma)^2} \cot^2\left[\frac{\pi^2}{2(2\pi-\gamma)}\right]. \tag{3-41}$$

In terms of the cone angle α we have, since $\gamma = \frac{1}{2}\pi - \alpha$,

$$\sigma = \frac{\pi^3 a^2}{(\frac{3}{4}\pi + \frac{1}{2}\alpha)^2} \cot^2\left(\frac{\pi^2}{3\pi+2\alpha}\right). \tag{3-42}$$

This result is compared with the physical optics result in fig. 3.10. Our method can be applied to any body with a ring singularity.

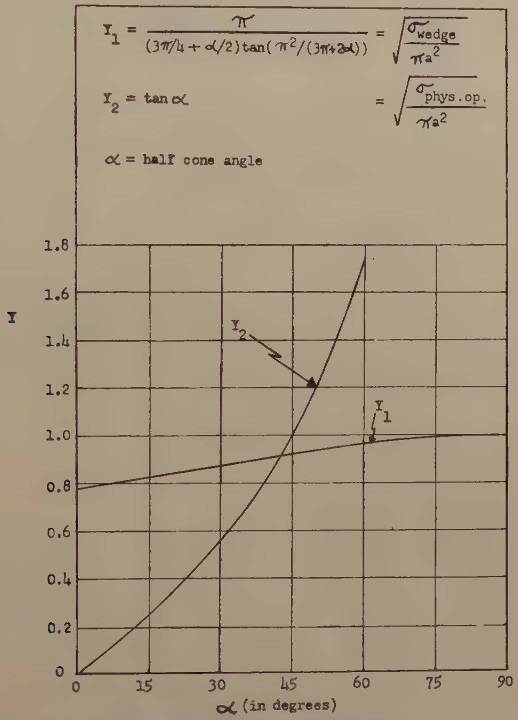

Fig. 3.10. Nose-on finite cross-sections as computed by physical optics and circular wedge approximations.

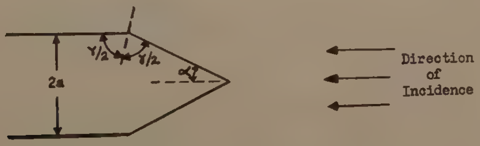

Fig. 3.11. Cone-cylinder combination.

Consider, for example, a cone-cylinder conbination viewed nose-on (see fig. 3.11). The expression derived for the cross-section

$$\frac{\sigma}{\pi a^2} = \frac{\pi^2}{\left(\pi - \dfrac{\gamma}{2}\right)^2} \cot^2\left(\frac{\pi^2}{4\pi - 2\gamma}\right) \tag{3-43}$$

still applies. In terms of the half cone angle α we have, since $\alpha = \pi - \gamma$,

$$\frac{\sigma}{\pi a^2} = \frac{\pi^2}{\left(\frac{\pi}{2} + \frac{\alpha}{2}\right)^2} \cot^2 \left[\frac{\pi^2}{2(\pi + \alpha)} \right]. \tag{3-44}$$

Similarly, for the contribution from any ring singularity (3-43) holds, where γ is the included wedge angle (fig. 3.12). Equations (3-42), (3-43) and (3-44) are plotted in fig. 3.13.

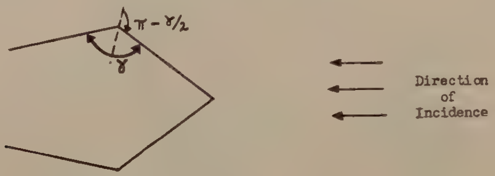

Fig. 3.12. Definition of wedge angle.

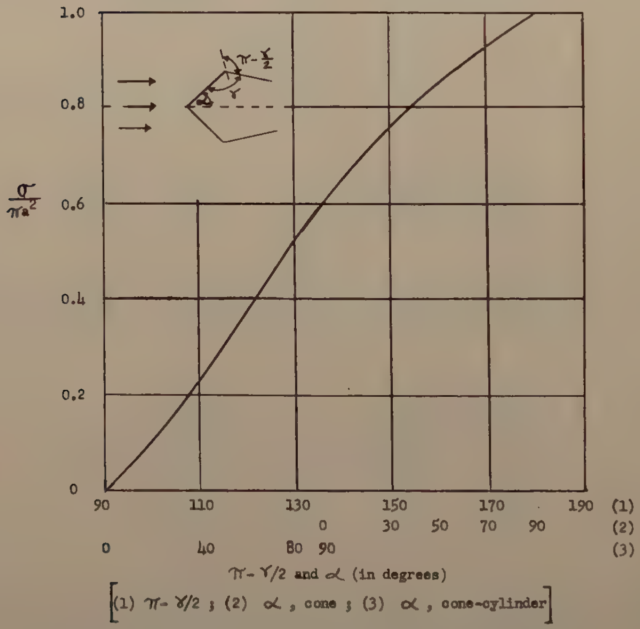

Fig. 3.13. Nose-on cross-section of circular wedge.

A similar technique of decomposition into straight segments was employed by Artmann 15) in his solution of the problem of diffraction by a thick half-plane. He considered a half-plane of thickness $2a$ capped by a half-cylinder of radius a, as in fig. 3.14. For $ka \gg 1$ and incidence as indicated he decomposed the cylindrical portion into a regular N-gon of length $L \gg \lambda$. Then by considering the conditions under which the rays striking near the apex S are diffracted on to the next side of the N-gon he determined the size of the penumbra region and hence the shift in the diffraction pattern as compared with the diffraction pattern of a completely black screen of like form. In order for rays diffracted from one polygonal face to have any effect on the next face, the following inequality must hold:

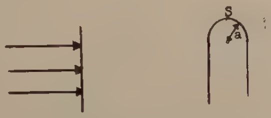

Fig. 3.14. Thick half plane.

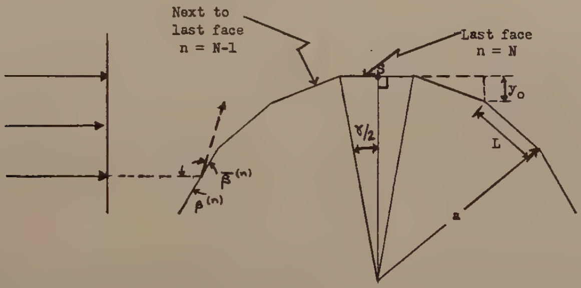

Fig. 3.15. N-gon geometry.

$$kL\,|\cos\beta^{(n)} - \cos\bar{\beta}^{(n)}| \lessapprox 2\pi. \tag{3-45}$$

The quantities involved are shown in figure 3.15. To measure the penumbra width, or in this approximation the number and length of the polygonal sides that have any effect on succeeding sides, Artmann proceeds as follows. First he restricts the sides so that the only ones that affect the next one are the last and next last, where the last side contains the apex and naturally the next to last side immediately precedes it on the lit side (see fig. 3.15). In order that this be true

$$kL\,|\cos\beta^{(N-1)} - \cos\bar{\beta}^{(N-1)}| \approx 2\pi. \tag{3-46}$$

From fig. 3.15 we see that

$$\beta^{(N-1)} = \gamma. \tag{3-47}$$

Since the next to last face ($n = N - 1$) is not affected by rays from the preceding face ($n = N - 2$),

$$\bar{\beta}^{(N-1)} = 0.$$

Substituting these values in (3-46) yields

$$kL\,|\cos\gamma - 1| \approx 2\pi; \tag{3-48}$$

but

$$\cos\gamma \approx 1 - \tfrac{1}{2}\gamma^2, \tag{3-49}$$

hence

$$\tfrac{1}{2}kL\,\gamma^2 \approx 2\pi. \tag{3-50}$$

Again referring to fig. 3.15 we see that

$$\sin\tfrac{1}{2}\gamma = L/2a; \tag{3-51}$$

but

$$\sin\tfrac{1}{2}\gamma \approx \tfrac{1}{2}\gamma, \tag{3-52}$$

hence

$$L \approx \gamma a \tag{3-53}$$

and

$$ka\gamma^3 \approx 4\pi \tag{3-54}$$

or

$$\gamma \approx \left(\frac{4\pi}{ka}\right)^{\frac{1}{3}}. \tag{3-55}$$

Once more referring to fig. 3.15 we see that

$$y_0 = L\sin\gamma, \tag{3-56}$$

or employing the above results

$$y_0 \approx \gamma^2 a \approx \left(\frac{4\pi}{ka}\right)^{\frac{2}{3}} a. \tag{3-57}$$

Hence, according to Artmann, the diffraction pattern of the thick screen is displaced by this distance $(4\pi/ka)^{\frac{2}{3}}\,a$ perpendicular to the direction of incidence as compared with the diffraction pattern of a completely black screen.

The above small wavelength approximations assist us in obtaining approximate far zone cross sections for many bodies of revolution. We must now describe what can be done to obtain results in the resonance region.

§ 4. *The resonance region.* To obtain answers for prolate spheroids when the radius of curvature at the tip (b^2/a) is small with respect to the wavelength and simultaneously when the wavelength is small with respect to the broadside radii of curvature b and a^2/b, we must use another type of approximation. A point in electromagnetics is physically a region where all radii of curvature are small with respect to the wavelength. Thus the thin prolate spheroid looks very much like an ogive.

The approximate theory used by Belkina for thin spheroids, which she compares with her exact answers [18]), and that used by Peters [19]) for thin ogives, as one might expect, are for the problem under consideration almost equivalent. Belkina's approximate theory is a special case of Peters' more general considerations. However, she obtains physical information from exact theory, not obtained by Peters as to when the approximation is valid for spheroids.

For axially symmetric transmission, scattering from infinite cones is extremely small in all directions except the specular direction. Local analysis near the front tip and in the penumbra region for thin prolate spheroids or ogives (since the reradiation is tangent to the path) provides no big scattering effect except in the forward direction. A good portion of energy is guided towards the rear point and again there occurs, primarily, a reflection back. The back flow of energy coming from the rear tip is again primarily in the forward direction (flow towards the front tip), which is in the direction back towards where it originally came from. Thus the back-scattering near nose-on cross-section of an ogive looks as if it is primarily due to the tip in the rear. This has been experimentally checked by Peters [19]).

This suggested to Peters and Belkina that the thin body should act like a travelling wave antenna. Peters derives the results for certain ogives and finds the cross-section for such an antenna (both monostatic and bistatic) for aspects out to 40° off nose-on. The theory would fail exactly nose-on, but provides excellent results for near nose-on aspects.

To illustrate the theory we shall concentrate on a specific example, the thin prolate spheroid with ***E*** polarized field incident. The radar cross-section of a long thin body is given by

$$\sigma = \frac{\gamma^2\lambda^2}{\pi Q^2}\left\{\frac{\sin\theta}{1-p\cos\theta}\sin\left[\frac{kL}{2p}(1-p\cos\theta)\right]\right\}^2 = \frac{\gamma^2\lambda^2}{\pi Q^2}[f(\theta)]^2$$

where Q is given by

$$Q = -(2/p^2) + \frac{\mathrm{Cin}\,[(kL/p)(1+p)] - \mathrm{Cin}\,[(kL/p)(1-p)]}{p^3} +$$

$$+\frac{1}{2p^3}\Big\{(p-1)\cos[(kL/p)(1+p)] + (p+1)\cos[(kL/p)(1-p)] +$$

$$+ (p^2-1)\frac{kL}{p}(\mathrm{Si}\,[(kL/p)(1+p)] - \mathrm{Si}\,[(kL/p)(1-p)])\Big\}$$

with Cin (x) being the modified cosine integral of argument x and Si = the sine integral. We see that there are three parameters besides the wavelength, which serve to describe the body. They are the voltage reflection coefficient γ, the relative phase velocity p and the length L.

Voltage reflection coefficients of thick ogives and thin rods have been experimentally determined by Peters, who found that for a fairly thick ogive the reflection coefficient is about 0.7. For thin rods Peters found that the voltage reflection coefficient is about $\frac{1}{3}$. Physical reasoning indicates that the thin prolate spheroid, near nose-on, should be compared with a thin rod rather than an ogive, and hence for a thin prolate spheroid we use a voltage reflection coefficient of $\frac{1}{3}$. However, as θ increases from zero (the nose-on aspect), the point at which the travelling wave is reflected may be expected to move around the body and in this case will cause it to enter a region of larger radius of curvature. Thus, we would expect the voltage reflection coefficient to increase to 1 as the aspect goes to broadside. The actual values used in the graph (fig. 4.1) are as given in the following table:

θ	0°–40°	40°–60°	60°–75°
γ	0.33	0.7	1.0

The relative phase velocity p is defined as the ratio of the length of the body to that of the current path on the body. For this case it turns out that $p = 0.985$.

As the angle of incidence is increased from zero, a point is ultimately reached at which the travelling wave theory breaks down and the analogy with a thin wire is no longer possible. To deal with such values of θ (i.e., near broadside incidence) an alternative model is required. In this case the body is likened to a thick cylinder; the thick cylinder results are displayed for aspects in the range $\theta = 60°$ to $\theta = 90°$ in fig. 4.1. The thick cylinder results are obtained from [20]). The excellent, but as yet unpublished, experimental results of J. Lotsof of the Cornell Aeronautical Laboratory are included in fig. 4.1 for the purpose of comparison. Indeed, it was the existence of these experimental data which dictated the choice of the dimensions of the spheroid to be used in this illustrative example.

Before terminating this discussion of travelling wave theory, a few words about the $\boldsymbol{H}$ polarization case for the same prolate spheroid are in order. At near nose-on incidence we should expect the same current to be induced, and thus the same cross-section. However, with increasing θ, the spiralling of the current may be expected to lead to an appreciable reduction in the cross-section; this has been confirmed by the above-mentioned experiments.

Now we shall turn out attention to the problem of estimating the nose-on scattering cross-section of thin finite cones for all values of ka *). We need the approximate behaviour in the resonance region as we have already presented small and large wavelength approximations. This is obtained by assuming that the base is still the dominant feature as the resonance region is entered from the small wavelength side. The resonance maximum of the ring singularity would approximate, in both position and amplitude, the last large maximum of the cone. Since in any physically realizable situation the edge of the base of a cone will have a non-zero radius of curvature b ($b \ll \lambda$), the only difference between it and a wire loop (wire radius $\ll \lambda$) relative to incident electromagnetic energy is that currents can exist "inside" the loop, but not "inside" the base of the cone.

When one looks at the axially symmetric cross-section of a ring as a function of wavelength, one finds that there are no minima. This, then, allows one to predict that the contribution of the inner edge is negligible in comparison to the outer edge when the wavelength is equal to the order of the loop radius but greater then the wire radius. (If there were non-negligible contributions from both the outer and inner edges, then at some wavelengths they would add in phase and at some wavelengths they would add out of phase. But there are no noticeable minima in this region!) Thus the cross-section of a loop here looks like a Rayleigh side-type answer, depending only on the loop radius, but not on the wire radius. This,

---

*) The quantity a denotes the radius of the base of the cone as usual $k = 2\pi/\lambda$.

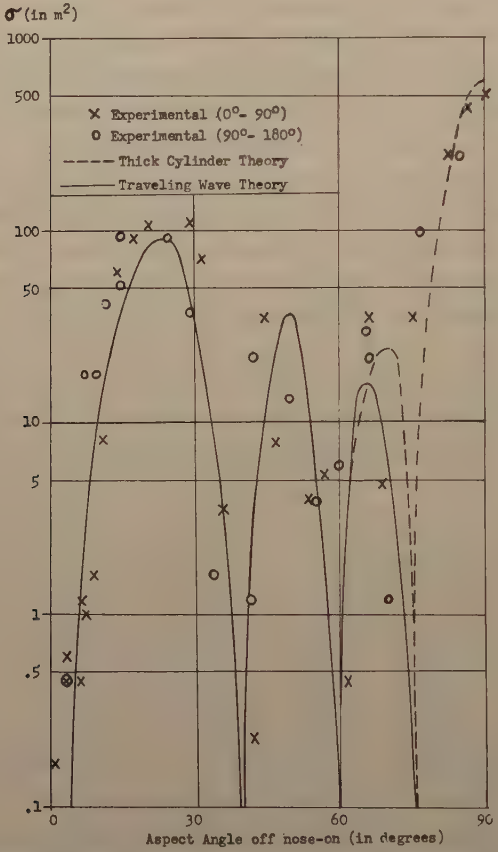

Fig. 4.1. Monostatic radar cross-section of a 10 : 1 prolate spheroid which is 43 cm = 4λ in length.

then, gives added justification for using an analogy between the conical base and the wire loop. Kouyoumjian's variational results [21]) and Weston's exact results [22]) for wire loops in the resonance region can then be utilized. Their results (as a function of wire radius and loop radius) indicate that the resonant peak is fairly insensitive to changes in wire radius, but that as the wavelength decreases the wire radius becomes important. However, when the wavelength decreases, we use the wedge approximation. There may be a region on the small wavelength side of the loop maximum where other maxima, smaller in amplitude, can occur. These lesser extrema are essentially averaged in this approximation.

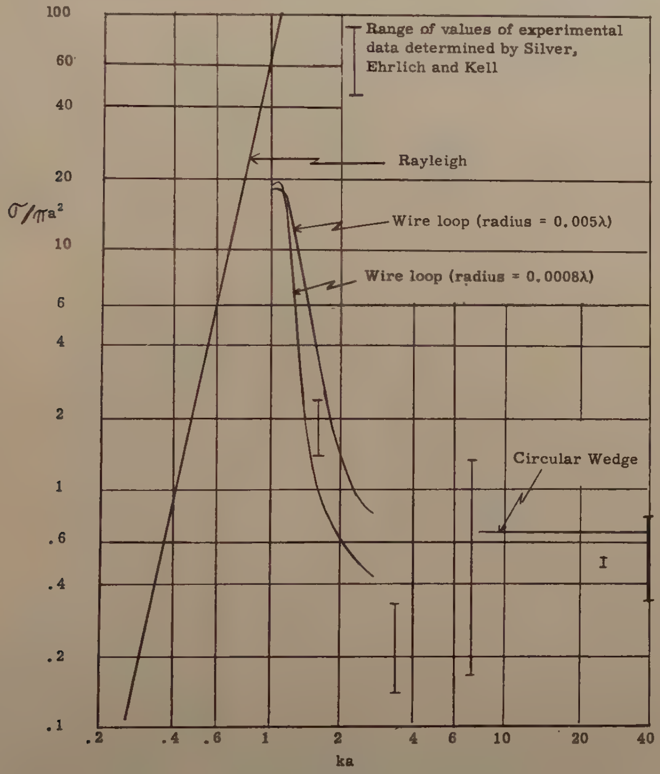

Fig. 4.2. Nose-on cross-section of thin finite cones ($\alpha = 7.5°$).

On the Rayleigh side we find that the Rayleigh line, which is an upper bound on the cross-section, lies so close to the ring maximum (in fact may intersect the ring curve before the maximum) that the existence of any maxima greater than the ring maxima on the Rayleigh side is precluded. This is illustrated in fig. 4.2, where the experimental results of S. Silver of the University of California, R. Kell of the Cornell Aeronautical Laboratory and M. Ehrlich of the Microwave Radiation Company have been included for the purpose of comparison.

In order to obtain off axis finite cone results and to check our assumptions concerning the different reflection coefficients at the two ends, we have compared the off axis results for the cone with the travelling wave antenna result. We have added the Kirchhoff disc contribution to the back-scattering near rear-on answers. These theoretical estimates are compared with the corresponding experimental data obtained by Ehrlich in figs. 4.3 and 4.4. We note that the null near the rear-on aspect is theoretically predicted to be too near to the $\theta = 180°$ aspect. This could have been anticipated since we know from the resonance discussion of the importance of the disc contribution.

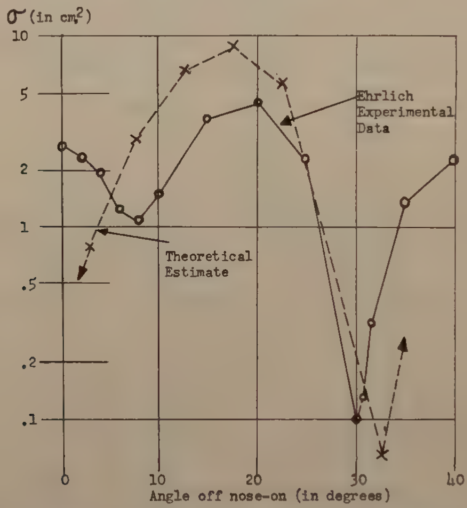

Fig. 4.3. Radar cross-section of a finite cone. A comparison between theory and experiment I.

By using approximations based on a creeping wave type picture we supplement the above theory for nose-on results where $f(\theta) = 0$. For ogives of half angle α, $\alpha \leqslant 20°$, and $ka \geqslant 15$ (a = half maximum minor dimension) we obtain a nose on result of

$$\sigma(0) = \frac{\lambda^2 \tan^4 \alpha}{16\pi} + \tfrac{1}{2}a\lambda.$$

When the creeping wave contribution is neligible, the $\frac{1}{2}a\lambda$ augmentation disappears. This occurs for thick ogives. The above formula holds for all ogive experiments analyzed to date within a factor of two. A feeling for when to drop out the term $\frac{1}{2}a\lambda$ can be obtained from known results for spheres.

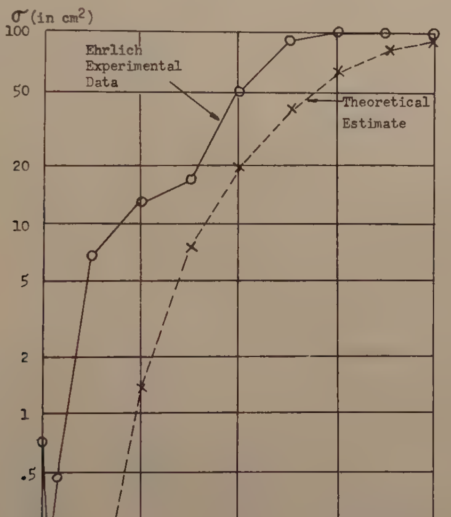

Fig. 4.4. Radar cross-section of a finite cone. A comparison between theory and experiment II.

The reader is now in a position to fill in roughly the complete cross-section curves for ogives and spheroids.

Acknowledgment. I gratefully acknowledge the assistance of H. Brysk, R. F. Goodrich, J. W. Crispin, R. E. Kleinman, D. M. Raybin and C. E. Schensted in the writing up of these remarks. Almost all my efforts associated with slots, directly and by reciprocity, were sponsored by the Hughes Aircraft Company.

I specifically thank M. D. Adcock, R. Bickmore, R. Hansen and M. Chernin for many interesting discussions. I also thank S. Chapman, G. Graham, R. Kell and J. Lotsof of Cornell Aeronautical Laboratory, Inc., for allowing me to use their experimental results and for supporting my effort on the prolate spheroid scattering calculations. Professor Silver of the University of California and Professor Sinclair of the University of Toronto have in many cases helped me to crystallize my ideas and encouraged me through many stimulating discussions.

The speculations in this paper are mine and the above scientists are in no way responsible for my inaccuracies or misguesses.

Received 12th June, 1958.

REFERENCES

1) Strutt, J. W., Baron Rayleigh, Phil. Mag. **44** (1897) 28.
2) Stratton, J. A., *Electromagnetic Theory*, McGraw-Hill, New York, 1941.
3) Fock, V. A., J. Phys. **10** (1946) 399.
4) Rice, S. O., Bell Syst. Tech. J. **33** (1954) 417.
5) Franz, W., Z. Naturforsch. **9a** (1954) 705.
6) Keller, J. B., Trans. Inst. Radio Engrs AP **4** (1956) 312.
7) Franz, W., and K. Deppermann, Ann. Phys. Lpz. **10** (1952) 361.
8) Friedlander, F. G., Comm. Pure Appl. Math., **7** (1954) 705.
9) Wu, T. T., Phys. Rev., **104** (1956) 201.
10) Bailin, L. L., Trans. Instn Radio Engrs AP **3** (1955) 128.
11) Wetzel, L. and D. B. Brick, An Experimental Investigation of High-Frequency Current Distributions on Conducting Cylinders, Air Force Cambridge Research Center, Scientific Report No. 4, Dec. 12, 1955.
12) Fock, V. A., J. Phys. **9** (1945) 255.
13) Belkina, M. G. and L. A. Weinstein, Radiation Characteristics of Spherical Surface Antennas, Appearing in *Diffraction of Electromagnetic Waves on Certain Bodies of Rotation*, Moscow, 1957.
14) Logan, N. A., The Role of Fock Functions in the Theory of Diffraction by Convex Surfaces, Air Force Cambridge Research Center, Paper presented at the URSI meeting held May 22–25, 1957, in Washington, D.C.
15) Artmann, K., Z. Phys. **127** (1950) 468.
16) Siegel, K. M., H. A. Alperin, R. R. Bonkowski, J. W. Crispin, A. L. Maffett, C. E. Schensted and I. V. Schensted. J. Appl. Phys. **26** (1955) 297.
17) Oberhettinger, F., Commun. Pure Appl. Math. **7** (1954) 551.
18) Belkina, M. G., Radiation Characteristics of an Elongated Rotary Ellipsoid, Appearing in *Diffraction of Electromagnetic Waves On Certain Bodies of Revolution*, Moscow, 1957.
19) Peters, L., Trans. Instn Radio Engrs AP **6** (1958).
20) Mentzer, J. R., Scattering and Diffraction of Radio Waves, Pergamon Press, 1955.
21) Kouyoumjian, Appl. Sci. Res. **B6** (1956) 165.
22) Weston, V. H., Solutions of the Toroidal Wave Equation and their Applications, University of Toronto, Thesis 1956.

Appl. sci. Res. Section B, Vol. 7

MEASUREMENTS ON THE MAGNETIC SUSCEPTIBILITIES OF Ag–Mn AND Cu–Mn ALLOYS

by A. VAN ITTERBEEK, R. POLLENTIER and W. PEELAERS

Instituut voor Lage Temperaturen en Technische Fysica, Leuven, Belgium

Summary

Measurements have been carried out on alloys of Ag–Mn and Cu–Mn with different concentrations of manganese between room temperature and liquid hydrogen temperatures. A paramagnetic behaviour has been found. We examined especially the dependence of the susceptibilities on the field strength; no field dependence could be detected except in some of the Ag–Mn alloys, but this effect originated from small ferromagnetic impurities which were determined by means of the method of Honda. The concentration of the maganese has been determined magnetically and compared with determinations based on the electrical resistance.

§ 1. *Introduction.* Preliminary measurements on the same subject have been described at the conference of Wisconsin 1957. Since then, the calibration of the magnetic field has been carried out more exactly. The topography has been measured with Cr- and Ge-samples; and the constant $C_1 = C[H\,\mathrm{d}H/\mathrm{d}x]^{-1}$ (see § 2) has been determined at different field strenghts for the reason that one of our purposes is a check on the field dependence of the susceptibility of the different alloys. These alloys have been placed at our disposal by the Kamerlingh Onnes Laboratory of Leiden.

The determination of the concentration Mn in at. % was done there from resistance measurements (method of Linde):

Ag–Mn: 0.18; 1.10; 4.35 at.%; Cu–Mn: 0.16 at.%.

We have carried out the determination of the concentration by means of susceptibility measurements. Furthermore $\chi^{-1} - T$ diagrams are established from which it is possible to derive the Curie-temperatures.

§ 2. *Experimental method and calibration of the field.*

A. Method. Faraday's method has been used. For a detailed description we refer to a paper of one of us together with Duchateau[1]). A small sample fixed on one arm of a sensitive microgram balance is placed in the field H of an Oerlikon magnet. In an inhomogeneous magnetic field H, with gradient $\mathrm{d}H/\mathrm{d}x$ in the x direction, a sample with susceptibility χ undergoes a force

$$k_x = m\chi H \,\mathrm{d}H/\mathrm{d}x, \tag{1}$$

with m = mass of the sample and χ = mass susceptibility. This force is compensated by the interaction of two coils. One coil is fixed, the second one is movable and attached to the other arm of the balance. Through the fixed coil a variable current I_1 flows, through the moving coil a constant current I_2. Both currents are measured with a potentiometer. For such a system we may write

$$k_x = CI_1I_2. \tag{2}$$

From (1) and (2) it follows that

$$CI_1I_2 = m\chi H \,\mathrm{d}H/\mathrm{d}x. \tag{3}$$

Because equilibrium is realized as well with magnetic field $H = 0$ as with $H \neq 0$ we can write

$$C\Delta(I_1I_2) = m\chi H \,\mathrm{d}H/\mathrm{d}x. \tag{4}$$

$\Delta(I_1I_2)$ is the variation of I_1I_2 between $H = 0$ and the value H. Each measurement has been carried out at room temperatures in vacuum (better than 10^{-4} mm). However at low temperatures the sample is suspended in an atmosphere of carefully purified helium gas at a pressure of 2 mm. The correction for the susceptibility of the gas is negligible, so that (4) still holds.

B. Calibration of the field. We determined at first the position where $C_1 = C[H \,\mathrm{d}H/\mathrm{d}x]^{-1}$ is a minimum, or $H \,\mathrm{d}H/\mathrm{d}x$ a maximum. The minimum values obtained for C_1 at different field strenghts are given in table I.

TABLE I

H Ø	$C_1 = \dfrac{C}{H\mathrm{d}H/\mathrm{d}x}$ c.g.s.u.
6 875.6	1493.9
11 202.5	575.8
13 759.4	431.3

The calibration has been carried out with two samples, one of Cr and another of Ge. The Cr used is spectrographically pure and was furnished by Johnson-Matthey. The characteristics of the Ge-sample which has been used are
1) Specific resistance: 1.5–1.7 Ω cm.
2) Concentration (atoms/cm^3): 10^{15} Sb.
3) Type: *n* type.
4) Origin: Dr. Geballe (Bell Telephone).
5) χ: -0.1050×10^6 at room temperature.
Cr is used for relative calibrations, and the values obtained for C_1 resulted from the calibration with Ge.

§ 3. *Discussion of the results.*

A. Ag–Mn

a. Field dependence. As an example we plotted χ against the field H for the concentration 0.18 at.% (fig. 1). It must be expected

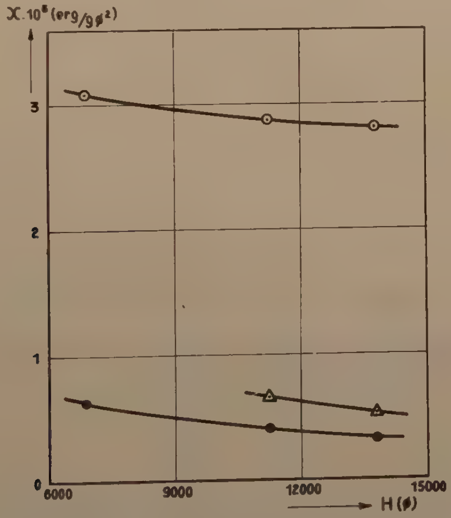

Fig. 1. Susceptibility against field strength, Ag–Mn, 0.18 at %.
● Room temperature
△ Liquid nitrogen temperature
⊙ Liquid hydrogen temperature

that the Ag–Mn alloys at liquid helium temperatures show a certain field dependence because of their antiferromagnetic character in this region.

We find (see fig. 1) that a field dependence already occurs between room temperature and the boiling point of liquid hydrogen. We detected that this field dependence is due to ferromagnetic impurities in the component Ag.

Using the method of Honda (fig. 2), we obtain for this ferromagnetic impurity a concentration of iron: $c = 2.27 \times 10^{17}$ atoms/g. In fig. 2 a determination for the concentration 0.18 at.% is given as an example.

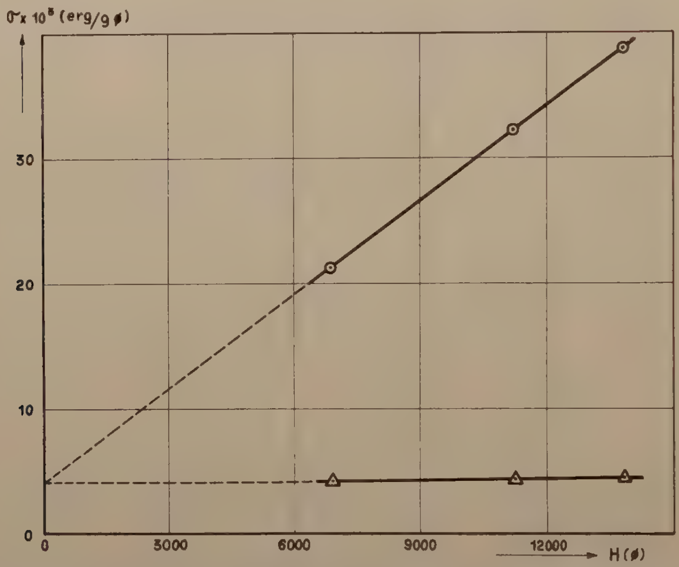

Fig. 2. Determination of ferromagnetic impurity content. Ag–Mn, 0.18 at. %.
⊙ Room temperature
△ Boiling point of liquid hydrogen

b. Calculation of the Curie-temperatures. In fig. 3 $1/\chi$ is plotted against the temperature T for the various Ag–Mn alloys. The Curie-temperatures calculated from this figure by means of the method of least squares are as follows:

$$\begin{array}{lll} \text{Ag–Mn } 0.18 \text{ at } \% & 0 < T_c < & 0.5\,^\circ\text{K}, \\ 1.10 \text{ at } \% & 2 < T_c < & 3\ ^\circ\text{K}, \\ 4.35 \text{ at } \% & 13 < T_c < & 14\ ^\circ\text{K}. \end{array}$$

Thus we obtained for the three samples positive Curie-temperatures, which is in agreement with the results of Owen, Browne, Arp and Kip [2]).

c) Determination of the concentration. The determination of the concentration is based upon the following facts: in the temperature region where the Curie law is followed ($T \gg T_c$) the susceptibility will be proportional to the concentration and $\chi T = C$ where C = Curie constant, which depends on the concentration. Based upon the value $J = 2\frac{1}{2}$ for a Mn atom, we obtain the theoretical value χT/concentration $= 4.06 \times 10^{-4}$. This value should be independent of the temperature. In fig. 4, χT/conc. is plotted against T for the three concentrations. The theoretical value 4.06×10^{-4} is only obtained for the concentration 1.10 at %. The concentrations 0.18 and 4.35 at % are respectively lower and higher than the theoretical value. The concentrations 0.18 and 4.35 at. % are measured with the method of Linde. Now from the susceptibilities these should be changed into 0.14 and 4.73 at. %. A possible explanation is that the differences between the values obtained

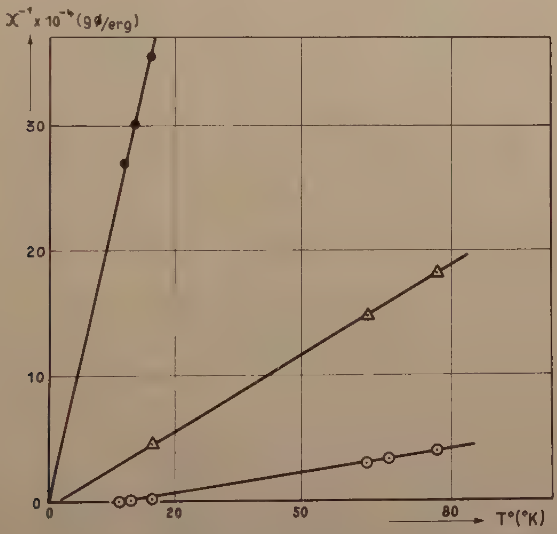

Fig. 3. Ag–Mn alloys. Plot of $1/\chi$ against temperature.
● Ag–Mn 0.18 at.%
△ Ag–Mn 1.10 at.%
⊙ Ag–Mn 4.35 at.%.

at the Leiden laboratory and ours are due to an inhomogeneous distribution of Mn in the alloy.

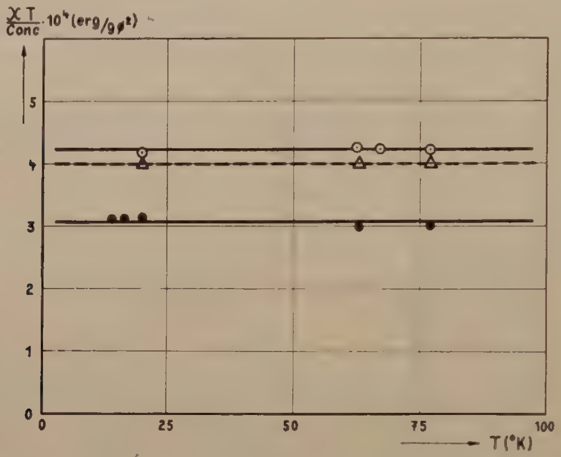

Fig. 4. Ag–Mn alloys. Determination of concentration from the susceptibilities

△ Ag–Mn 1.10 at.%
● Ag–Mn 0.18 at.%
⊙ Ag–Mn 4.35 at.%

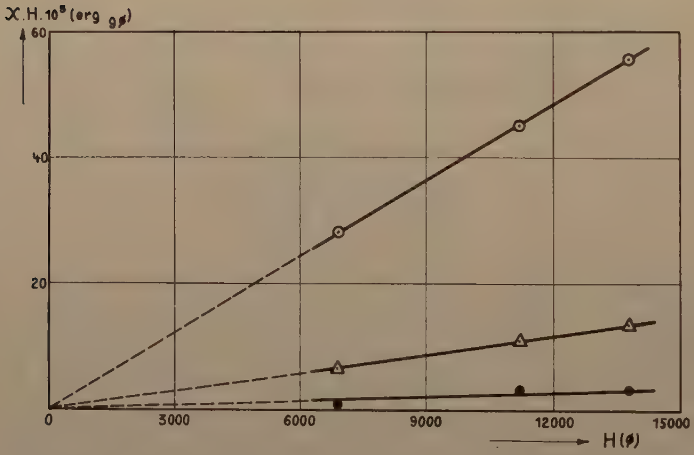

Fig. 5. Cu–Mn alloy, 0.16 at.%. Check on impurities.
● Room temperature
△ Liquid nitrogen
⊙ Liquid hydrogen

B. Cu–Mn: 0.16 at %.

a) Field dependence, detection of ferromagnetic impurities. First of all we checked the degree of impurity of the sample. This is done again with the method of Honda (fig. 5). No ferromagnetic impurities were found. After this we measured the field dependence. In fig. 6 we plotted χ against H for different temperatures. For all these measurements one and the same sample was used.

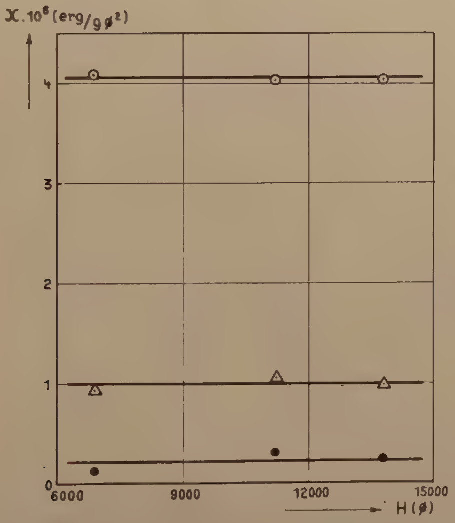

Fig. 6. Cu–Mn alloy, 0.16 at.%. Susceptibility against fieldstrength
● Room temperature
△ Liquid nitrogen
⊙ Liquid hydrogen

b) Curiepoint. The Curie-temperature obtained from fig. 7, (χ^{-1} as a function of T) is situated between 1 and 2°K. This is in agreement with the values obtained by Owen 2).

c) Determination of the concentration (fig. 8). We remark that in the liquid hydrogen temperature region the points measured below 20.35°K deviate from the horizontal line drawn through the points measured in the liquid nitrogen region. The reason for this is that the temperatures below 20.35°K are too close to the Néel temperature T_N of the alloy. The value of the concentration

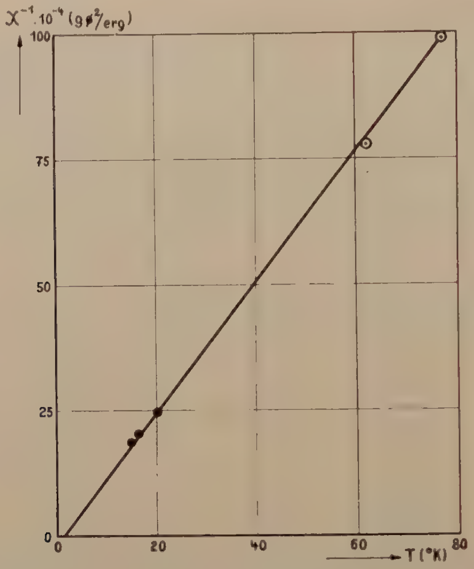

Fig. 7. Cu–Mn alloy, 0.16 at.%. Determination of Curie temperature
⊙ Liquid nitrogen
● Liquid hydrogen

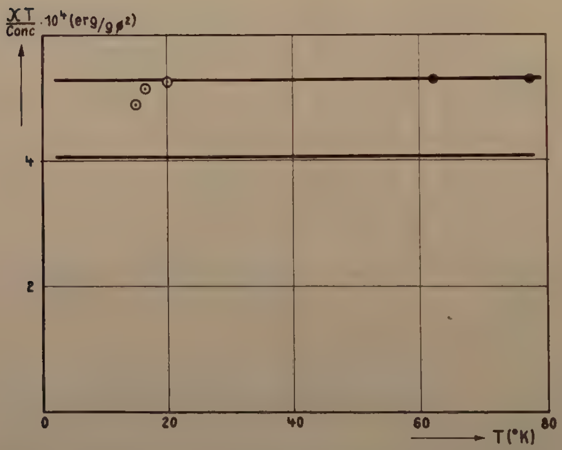

Fig. 8. Cu–Mn alloy, 0.16 at.%. Determination of the concentration.
— Theoretical curve
● Liquid nitrogen
⊙ Liquid hydrogen

obtained is 0.20 at.%. This value differs from that of 0.16 at. %, obtained by resistance measurement.

We take the opportunity to express our warm thanks to the Union Minière du Haut Katanga for financial help during these measurements. We also thank Dr. G. J. van den Berg, conservator at the Kamerlingh Onnes Laboratory. Leiden, who put the samples at our disposal.

Received 21st July, 1958.

REFERENCES

1) Itterbeek, A. van, L. De Greve and W. Duchateau, Appl. Sci. Res. **B 4** (1955) 300.
2) Owen, J., M. Browne, W. D. Knight and C. Kittel, Phys. Rev. **102** (1956) 1501.

THE COMPARATIVE MERITS OF DIFFERENT METHODS OF MICRORADIOGRAPHY

by V. E. COSSLETT

Cavendish Laboratory, University of Cambridge, England

Summary

In comparing the speeds of the various microradiographic methods, it has been usual to take as basis the exposure time needed for recording the X-ray image. It is more realistic to include the time required to make available the information stored in the negative, by producing an image magnified up to the resolution of the eye. From this point of view the projection method is much faster than the times-two method or contact microradiography, for a given field of view, i.e., they stand in reverse order to that of their initial exposure times. In given camera length, on the other hand, the initial exposure is the same for both projection and contact, and is much longer for the times-two method. But the overall time for production of the final image is now much the same for all three methods. As regards resolution, the projection method offers the best ultimate performance.

§ 1. *Introduction.* In reply to a criticism of the "times-two" method (Cosslett[1]), Ong and Le Poole[2]) take, as basis of comparison with the projection method, the provision of equal amounts of information, i.e., equal fields of view in the image. In applying this criterion, however, they have omitted certain important practical factors, especially the difference between stored and available information, the inclusion of which radically alters the conclusions. It is also doubtful if equality of field, implying given object-source distance, is in fact the proper basis for comparing methods of radiography. Given camera length provides a basis more in accord with the limiting conditions of experiment, and, judged from this standpoint, the relative merits of the "times-two" and projection methods appear in a quite different light. It is illuminating to consider also their relation to the contact method.

§ 2. *At constant field of view.* (*a*) Intensity and speed of working. If the same field of view is covered in both the x2 and projection methods, the object-source distance *a* must be the same (fig. 1). As Ong and Le Poole correctly say, the x2 method then gives an intensity of illumination at the object larger by a factor of 6.3 than that in the projection method, because the source width can be twice as large. They are also right in pointing out that the ratio of the exposure times in the two methods is independent of the magnification at which the projection image is recorded, provided that the film resolution is appropriately adjusted to the distance. We agree, therefore, that the x2 method allows an exposure 6.3 times shorter than of the projection method, at given resolution and field. The two negatives obtained will contain the same amount of information, but the authors fail to point out that it is not equally available in the two cases. The x2 method gives a micro-negative, which must be enlarged to make the stored information visible to the eye, but the projection method gives direct enlargement, so that the information is immediately available.

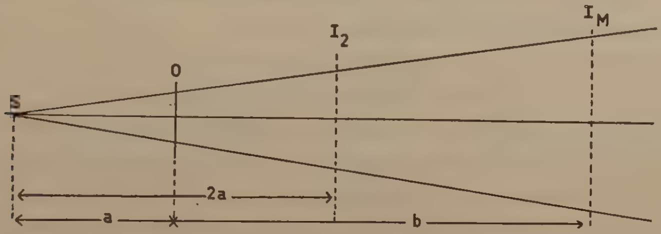

Fig. 1. Geometry for the methods discussed.
S = source, O = object, I_2 and I_m = film.

A full comparison of the two methods must take into account the field of view of the system used to enlarge the x2 negative. Since the detail in a maximum resolution emulsion lies at the resolving limit of the optical microscope, an objective of high aperture and short focal length must be used with a total magnification of the order of 1000 x. The field of view of such a system will be of order 100 μ, which is very much smaller than the original field recorded on the negative. In the preliminary experiments of Le Poole and Ong 3)4) the field was several mm, so that several hundred optical photomicrographs would have to be made in order to reproduce all the stored information. The time required for this will clearly be much more than 6.3 times the original exposure of the micro-negative, which is of order 1 minute. On the basis of the time (and effort) needed to obtain final images of equal size of the same object field, the projection method is at least an order of magnitude faster than the x2 method.

It may be noted further that the contact method is more efficient than either of the others for recording a given field, at given source-object distance. For given object resolution, the width of source that can be used varies in proportion to $M/(M - 1)$ and the available intensity (at the film) with the square of this ratio. On moving from x2 to x1.1 magnification, for example, the X-ray intensity could be increased 20 times, and at x1.01 by 2 400 times. The increase will be still greater so long as spherical aberration is limiting the current in the focal spot.

For the purpose of increasing X-ray intensity, therefore, the x2 method does not go far enough. A magnification as near as possible to unity offers the greatest advantage in exposure time. However, a reduction from 10 min (in projection) to a few seconds does little to offset the time needed for making a large number of optical micrographs, to extract the recorded information from the contact negative. Furthermore, it may not be practicable to obtain the full increase in X-ray intensity because thermal dissipation in the target sets a limit to the beam current. The projection method is thus preferable to either the x2 or the contact method when the total time to produce visible information about the object is reckoned.

(*b*) Resolution. The resolution in the image is limited by the width of penumbra, as determined by geometrical relations, and by Fresnel diffraction, which involves also the wavelength of the illumination λ. As to penumbra formation, the authors [2]) have now completely clarified the situation and it is agreed that the criticism of the x2 method on this account (Cosslett [1])) was founded on a misconception. In regard to the effect of Fresnel diffraction, a more detailed discussion is necessary.

The authors correctly show that, at fixed object-source distance a, the fringe widths (in object space) in projection (f_p) and in x2 conditions (f_2) are given by

$$f_p = (a\lambda)^{\frac{1}{2}},\ f_2 = (a\lambda/2)^{\frac{1}{2}}. \qquad (1)$$

Thus the fringe in projection is relatively broader than in x2 conditions by the factor $\sqrt{2}$. But the authors fail to point out that the *absolute* width of both fringes will be so large in practicable experimental conditions that resolution is seriously limited. For instance, with $a = 2.5$ mm and $\lambda = 8$ Å, as used by the authors, $f_2 = 1\ \mu$. To obtain a resolution of 0.1 μ in the x2 method, the value of a would have to be reduced to 0.25 mm., i.e. a camera length of 0.5 mm, which is hardly practicable. The projection method overcomes the difficulty by reducing a and sacrificing field to resolution. The point made in the earlier criticism, that Fresnel diffraction prevents the use of the x2 method at high resolution, must be regarded as established. One of the main reasons for introducing the x2 method was to give increased intensity at high resolution, but there is little point in gaining intensity by means which inevitably lose resolution.

In this respect also the contact method is preferable to the x2 method. The fringe width is now given by

$$f_c = (b\lambda)^{\frac{1}{2}}, \qquad (2)$$

where b is the object-image distance. At constant a, the fringe width can be reduced to negligible width by bringing the film up to the object. Since the intensity can be increased at the same time by increasing the source size, the best conditions for microradiographic recording of a large area (as distinct from final evaluation of the stored information) are provided by the contact method. The advantages of this method, when operated with a tube of moderately fine focus and a short camera length, have only lately been realised (Nixon and Pattee [5]), Pattee [6])). With the recent development by Pattee [6]) of an ultrafine-grained viewing screen, microfluoroscopy by the contact method has also become practicable.

§ 3. *At constant camera length.* It is desirable to shorten the camera length as much as possible, in the interest of both intensity and resolution. Ultimate performance is therefore limited by the minimum practicable distance between source and film ($a + b$), and not by that between source and object. Field of view, as well as resolution and time of exposure, will now depend on the position of the object.

Compared with constant field conditions, the main difference is that the resolution in projection is now much greater, owing to the reduction of the Fresnel fringe width (eq. (1)) and the exposure time much shorter, since the film is always close to the source. As the object is moved towards the source, the penumbra width in the film plane increases, for given source width, so that a film of poorer resolution and higher speed can be used. Assuming the speed to be inversely proportional to the square of the film resolution, the exposure time T varies with magnification according to

$$T \propto [(M-1)/M^2]^2. \tag{3}$$

Exposure is thus small for both large and small M, the contact and projection methods being symmetrical in this respect. For $M = 2$, however, it is a maximum, since both a small source and a high resolution film are needed. The ratio of the exposure time at x2 to that at x100 (or at x1.01) is approximately $(100/4)^2 = 625$.

The exposure time in projection is thus very much less than in the x2 method, but the field of view is also much smaller. A given field now would have to be covered by making a large number of projection micrographs, requiring about the same effort as making a large number of photomicrographs from the x2 micronegative. The contact method will again be preferred, in most cases, since it has the same high speed as in projection, contains the whole field in a single negative and requires no more photography than the x2 method.

As regards ultimate resolution, both the contact and x2 methods are limited by the film resolution. For very high resolution the projection method alone comes into consideration. Its small field is not a great disadvantage in these conditions, since the best region for high resolution imaging can be selected by searching the specimen under an optical microscope, or by preliminary X-ray microscopy by any of the methods.

§ 4. *Conclusion.* For a field of given size, the x2 method will give a greater visible brightness for focusing and a shorter exposure than the projection method, as stated by Ong and Le Poole. But the overall time, i.e. that needed to present the recorded information on photographs at given final magnification, is much less in the projection method. This is the proper basis for comparing micrographic methods: that information should be made available to the eye, not simply recorded. As regards initial exposure time, contact microradiography is faster than either of the other two methods. It also allows the best conditions for resolution, since the Fresnel effect is smaller in contact than in x2 or projection conditions, at given object-source distance.

At minimum camera length, as required for high resolution, the initial exposure time is the same in both projection and contact methods, and very much shorter than in the x2 method. In projection the field is now very restricted, and the overall time for reproducing visibly the whole of a given field will now be much the same in all three methods. Projection permits the highest ultimate resolution; Fresnel diffraction most affects the x2 method.

In each respect the times-two method is inferior to either the contact or the projection method, or to both. Its main merit is in providing greater brightness and shorter initial exposure when contact of the object with the film is not desirable, – with a reactive specimen, for instance, or when thermal or mechanical treatment is to be carried out. But even so, a magnification closer to unity would give still greater intensity, without bringing the specimen on to the film.

Acknowledgements. The author wishes to express his thanks to Mr. Ong and Dr. Le Poole for kindly supplying him with the text of their recent publication before it went to press.

Received 23rd July, 1958.

REFERENCES

1) Cosslett, V. E., X-ray microscopy and microradiography; ed. V. E. Cosslett, A. Engström and H. H. Pattee, Academic Press, New York, 1957, p. 321.
2) Ong, S. P. and J. B. Le Poole, Appl. Sci. Res. **B 7** (1958).
3) Poole, J. B. Le and Ong Sing Poen, Appl. Sci. Res. **B 5** (1956) 454.
4) Poole, J. B. Le and Ong Sing Poen, X-ray microscopy and microradiography; ed. V. E. Cosslett, A. Engström and H. H. Pattee, Academic Press, New York, 1957, p. 91.
5) Nixon, W. C. and H. H. Pattee jr., X-ray microscopy and microradiography; ed. V. E. Cosslett, A. Engström and H. H. Pattee, Academic Press, New York, 1957, p. 397.
6) Pattee, H. H. jr, Science 1958 (in publication).

COMMENTS ON V. E. COSSLETT: THE COMPARATIVE MERITS OF DIFFERENT METHODS OF MICRORADIOGRAPHY[1])

by ONG SING POEN and J. B. LE POOLE

Laboratorium voor Technische Physica van de Technische Hogeschool, Delft, Nederland

1. Admittedly we did not consider the time it takes, to make the recorded information available. We believe however, that the exposure time is the most important quantity in most cases. Often

the exposure time is so long that only with great difficulty the requirements of stability can be met.

Moreover the exposure time in contact microradiography cannot be compared to that in the projection method, since the latter gives more information in the same field, due to the great depth of focus.

2. The resolving power of the 2x method is some 0.3–0.5 micron 2). Hence we see no point in comparing its intensity with that of the contact method, where resolution is some 0.8–1 micron, or in comparing its resolution with that of the projection method. At the resolution of 0.4 micron, the source to specimen and source to film distance can usually be made sufficiently small, i.e. some 0.5–1 mm to avoid Fresnel fringes.

Cossletts conclusion that at 0.1 micron resolution the 2x method would in practice be impossible because of Fresnel fringes is true but unnecessary because this resolution is not possible with the 2x method.

3. The main reason for introducing the 2x method was not "to increase intensity at high resolution", but to show that the gain of a factor 2 in resolution is a practical reality, which was doubted by Haine and Mulvey 3). The method can only be compared to the projection method if no better resolution than 0.3 μ is required. In that case the gain in intensity is an unquestionable advantage. We seldom use the 2x method ourselves and certainly do not want to advocate its general use.

Acknowledgement. The authors want to express their gratitude to Dr. V. E. Cosslett for kindly supplying them with a copy of his article before it went to press and hope that the discussions have promoted a proper evaluation of the comparative merits of the various methods in microradiography.

Received 29th September, 1958.

REFERENCES

1) Cosslett, V. E., Appl. Sci. Res. **B7** (1959) 338.
2) Le Poole, J. B. and Ong Sing Poen, Appl. Sci. Res. **B5** (1956) 454.
3) Haine, M. E. and T. Mulvey, Nature **170** (1952) 202.

Appl. sci. Res. Section B, Vol. **7**

MAGNETIC ABSORPTION PHENOMENA IN GERMANIUM AT LOW TEMPERATURES

by L. VAN GERVEN *), A. VAN ITTERBEEK and L. DE LAET

Instituut voor Lage Temperaturen en Technische Fysica, Leuven, Belgium

Summary

By means of an experimental set-up and the usual methods for magnetic resonance absorption studies, some magnetic absorption phenomena have been found and investigated in Sb-doped germanium at low temperatures, using relatively low radio frequencies (20 to 100 MHz). Two different absorption lines have been observed. They differ by the sign of their top and by the temperature region, where they occur. One of the lines is single-valued, but the other is multi-valued and shows some kind of hysteresis. Their properties and possible origins are discussed.

§ 1. *Introduction.* Much work has been done these last years on absorption phenomena in germanium, and especially on the effects of magnetic resonance. There is e.g. at this time a considerable interest for diamagnetic or cyclotron resonance, which is, as is well known, an electric absorption phenomenon (i.e. an absorption occurring in an electric h.f. field), showing resonance maxima at certain values of an applied steady magnetic field. A few months ago we started a more detailed research concerning some magnetic absorption effects which we had observed already before in germanium at very low temperatures [1]). The first results of this investigation will be discussed here.

It is worth noticing in the first place that the radiation frequencies used in these experiments are situated in the range from 30 to about 100 MHz and not as usual (e.g. for cyclotron resonance) in the range from 5000 to 25000 MHz. There are some practical advantages in using such relatively low frequencies, as e.g. larger samples, smaller skin-effect, well defined direction of the linear h.f. field, high quality and maniability of the experimental set-up, obtained by simple means (especially at low temperatures), very homogeneous and well known steady field. The main disadvantage, on the other hand, is the lack of resolution. Indeed those frequencies do not lie mainly in the resonance range but in the so-called relaxation range (especially when δ and γ are large). However this is not always a hindrance, and of course not if one just wishes, for some reasons, to study the magnetic absorption at low steady fields. At low fields e.g. one can describe very easily a cycle of alternatively positive and negative fields. A last, but important advantage of this technique lies in the fact that the h.f. field in the sample, which is placed in the h.f. coil, is purely magnetic.

---

*) Research fellow at the Belgian Interuniversitary Institute for Nuclear Sciences.

§ 2. *Experiments.* The experimental set-up is the same as that for magnetic resonance work, as it was used before by us for measurements on electron spin paramagnetic resonance in organic free radicals and coals, and on nuclear paramagnetic resonance in aqueous solutions. The whole set-up is described in detail in a recent paper[2]). The block diagram is shown in fig. 1.

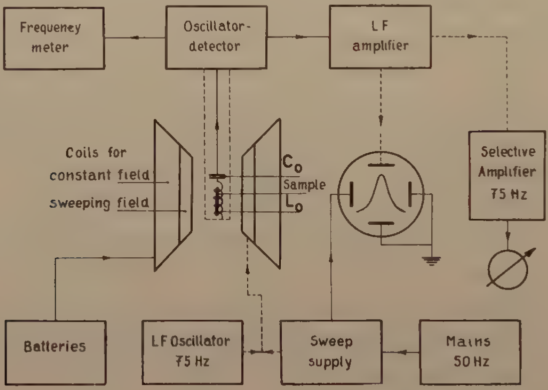

Fig. 1. Block diagram of the experimental set-up.

Only some slight modifications were applied:

1) The oscillator frequency was raised. L_0 is now 0.6 μH, C_0 is a few $\mu\mu$F and is now placed in the coaxial transmission-tube just above L_0, down in the dewar. The oscillator is of the Clapp-type. The oscillations are weak, but well stable. We were able to control the level and in this way the amplitude $2H_1$ of the h.f. magnetic field (and at the same time the sensitivity). Several frequencies (by

changing C_0) have been used: 31, 85, 97 and 114 MHz. The output of the oscillator is proportional to the variation of the resistance of the h.f. coil, and thus also to χ'', the absorption term of the h.f. susceptibility, if present. In this paper we will call the observed absorption χ'', even if it is not sure at first sight that this absorption is a susceptibility effect.

2) A selective amplifier at 75 Hz is incorporated for point-to-point-registrations of the derivative of the absorption curve. When this recording system is used, the steady magnetic field is swept by a 75 Hz alternating field with an amplitude of about 1 Ø.

3) The h.f. apparatus can be introduced either in a pair of Helmholtz coils if one performs measurements at low fields, or in a large iron electromagnet if one takes measurements at high fields. Unfortunately until now we could not use the high fields of the iron magnet during measurements at liquid helium temperatures.

Measurements were performed on three samples of germanium, which were kindly put at our disposal by Dr. Geballe of the Bell Telephone Laboratories U.S.A. All three are monocrystalline and of the *n*-type, Sb-doped. Sample I has a specific resistivity of 45 Ωcm, sample II 1.6 Ωcm, sample III 0.04 Ωcm. The 1,0,0-axis of the crystals was always nearly parallel to the h.f. magnetic field and thus perpendicular to the steady field with the exception of sample III, of which the direction of the 1,0,0-axis was not known.

The measurements were carried out in two temperature ranges, viz. at liquid helium temperatures and at the boiling point of nitrogen. The cryogenic set-up is described in detail in 2).

During the first runs two absorption peaks, or better tops of peaks, were observed on the oscilloscope screen. These tops were found to be near 0 Ø. The striking difference between the two absorption phenomena lies in the sign. The first peak, which we will call the positive one, has the same sign as e.g. the peaks of electron spin magnetic resonance in diphenylpicrylhydrazyl and other similar substances. The other peak has the opposite sign; we call it the negative peak. Whether the former or the latter appears seems to depend on the amplitude $2H_1$ of the h.f. field. Moreover a variation of H_1 sometimes induced a slight shift of the top of the positive peak. Table I gives a survey of the observations on the oscilloscope screen. As one may see, the positive peak in sample I appears only at 77°K (and probably also at some temperatures between 77°K and

TABLE I

Summary of the observations of magnetic absorption in germanium (Sb-doped)

Frequency MHz	Sample	Temperature °K	H_1	Absorption	
				Negative	Positive
85 (and 97)	I (45 Ωcm)	77	W	—	+
			S	—	+
		4.2	W	+	—
			S	—	—
		3.7	W	+ (stronger)	—
			S	—	—
		1.4	W	+ (stronger)	—
			S	—	—
85 (and 31)	II (1.6 Ωcm)	77	0		
		4.2	W	+ (weak)	—
			S	—	+
		1.9	W	+ (stronger)	—
			S	—	+ (weaker)
		1.4	W	+ (stronger)	—
			S	—	+ (weaker)
114	III (0.04 Ωcm)	4.2	0		
		1.4	W	—	—
			S	—	—

W = weak, S = strong, + = yes, — = no.

4.2°K) and not at liquid helium temperatures. The negative peak becomes stronger when the temperature decreases. In sample II both peaks appear at liquid helium temperatures. Here also the negative one becomes stronger while the positive one becomes weaker when the temperature decreases. In sample III no peaks are observable. The conductivities of II at 77°K and of III at 4.2°K are still so high that the oscillator does not oscillate when these samples are in the h.f. coil. In fig. 2 one sees the positive peak, occurring in sample II (1.6 Ωcm) at 4.2°K in a moderate h.f. field. On the screen the absorption χ'' is plotted against the steady magnetic field. This field is zero at the centre, and the total range of the oscillogram is about 220 Ø. In fig. 3 is shown the negative peak, occurring in sample I (45 Ωcm) at 1.4°K in a weak h.f. field. The field is also zero at the centre and the range is about 43 Ø.

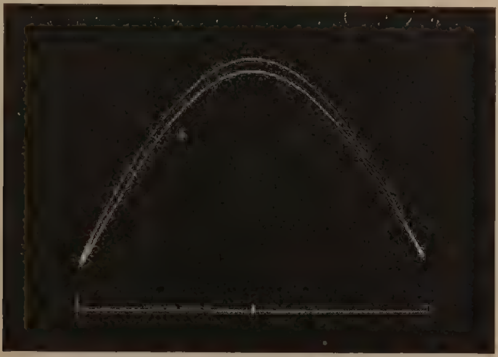

Fig. 2. Sample II. Positive peak at 4.2°K in a moderate h.f. field.

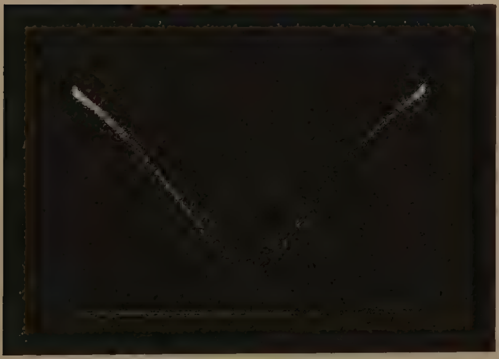

Fig. 3. Sample I. Negative peak at 1.4°K in a weak h.f. field.

In order to obtain more clear and complete absorption curves we desisted from the overall-oscilloscope-registration with large sweep, since it might disturb the shape of the curve. Moreover the sweep was not large enough to describe the whole curve. We proceeded to point-to-point-recording, using a low sweep and a selective amplifier instead of the oscilloscope. The output-meter of the amplifier gives the absolute value of the derivative of the absorption with respect to the steady field $|d\chi''/dH_c|$. The sweep amplitude should be low and was taken always at about 1 Ø, which is low enough in comparison to the line widths. We can give only the absolute value of the derivative; unfortunately we did not dispose of an apparatus determining at the same time the sign of the derivative.

On sample I records were taken of the positive peak at 77°K and of the negative peak at 1.4°K. On sample II records were taken of the positive peak at 4.2°K and 1.4°K (only at low fields) and of the negative peak at 1.9°K and 1.4°K. All the positive absorption curves were very simple, symmetrical and single-valued, but the negative ones became very complicated.

As an example of a record of a negative peak we show the one obtained from sample II (1.6 Ωcm) at 1.4°K (fig. 4). The two other records of negative peaks have practically the same general aspect. The magnetization cycle is given in the small graph (t = time). The corresponding lines in the small and in the big graph are drawn in the same way (dotted, dotted-dashed, full, dashed). Moreover the arrows in the big graph indicate the cycle described. In this way one can follow this cycle easily. The decreasing positive fields are described twice; all the points of these two records are plotted in the graph. The curve is symmetrical with respect to H_c, but multi-valued as one can notice at first sight. There are three cases:

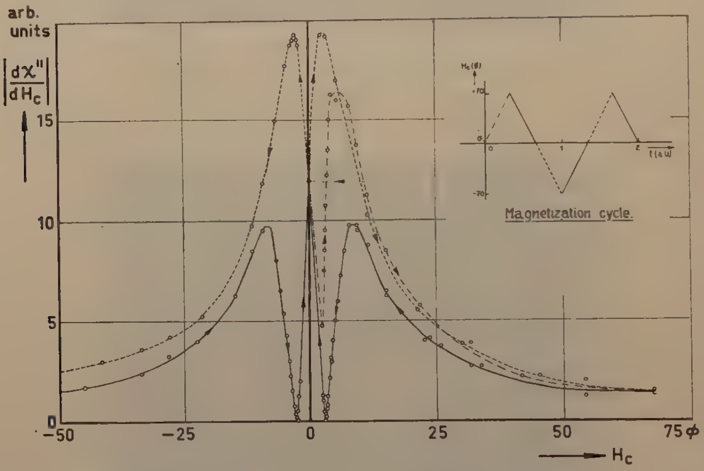

Fig. 4. Sample II. Negative peak at 1.38°K. Frequency 84.0 MHz, sweep amplitude 1.1 Ø.

1) coming from high fields: the full line is always followed;

2) coming from zero field:

a) the dashed line is followed if the magnetization just before was opposite;

b) the dotted-dashed line (some intermediate curve between the two former lines) is followed if the magnetization just before had the same sense.

There are only zero-points of the derivative (corresponding to maximum absorption) on the full lines. They are found at the fields $\pm H_m$: $H_m = 2.8\,\text{Ø}$. For all the recorded negative peaks H_m is near $3\,\text{Ø}$, which may be assumed to be the mean value of H_m. It is possible also to assume $H_m = 0\,\text{Ø}$, referring to the oscilloscope observations and to the other lines (dashed) in the graph of fig. 4. In principle it is possible to obtain the absorption curve from the derivative curve by graphical integration. However, owing to the complicated shape this cannot be done easily and in an exact way, the more so as we do not know the sign of the derivative. Nevertheless we did make the integration, making assumptions about the sign, in order to get some information as regards the experimental half line width $\varDelta$. The values of $\varDelta$ from all the records are displayed between 10 and $16\,\text{Ø}$. As mean value for the $\varDelta$ of all the investigated negative peaks we find $13\,\text{Ø}$. If we assume that the observed absorption is a susceptibility effect and thus a relaxation absorption, we are able to deduce the value of the gyromagnetic ratio γ, using the low field corrections on the ideal line shapes (Lorentzian or Gaussian), which we have computed in general, following an idea given in the so called modified Bloch theories. A paper on these corrections will be published in the near future. Using the values $H_m = 3\,\text{Ø}$, $\varDelta = 13\,\text{Ø}$ and $\omega_0 = 2\pi \times 84$ MHz one obtains (δ is the natural half linewidth, which one measures at frequency ∞):
in the case of a Lorentzian shape: $\gamma = 8.1 \times 10^7\ \text{Hz}/\text{Ø}$, $\delta = 10.4\,\text{Ø}$;
in the case of a Gausian shape: $\gamma = 6.1 \times 10^7\ \text{Hz}/\text{Ø}$, $\delta = 9.0\,\text{Ø}$.
Even if one assumes $H_m = 0\,\text{Ø}$, using still $\varDelta = 13\,\text{Ø}$, one obtains: in the case of a Lorentzian shape: $\gamma \geqslant 7.0 \times 10^7\ \text{Hz}/\text{Ø}$, $8.8\,\text{Ø} \leqslant \delta \leqslant 13\,\text{Ø}$;
in the case of a Gaussian shape: $\gamma \geqslant 4.8 \times 10^7\ \text{Hz}/\text{Ø}$, $7.6\,\text{Ø} \leqslant \delta \leqslant 13\,\text{Ø}$.
In any way γ appears to be greater than $4.8 \times 10^7\ \text{Hz}/\text{Ø}$ and δ appears to lie between $7.6\,\text{Ø}$ and $13\,\text{Ø}$.

As an example of a record of a positive peak we show in fig. 5 that obtained from sample I (45 Ωcm) at the boiling point of nitrogen. This record is taken mainly in the large iron magnet. As one may see at a glance, this positive curve is much broader than the negative ones, and this is also the case for the positive curves at liquid helium temperatures. Consequently the records of these latter curves were incomplete, since they were taken only at the low fields of the Helmholtz coils. The lower part of the curve of fig. 5 (between 0 and 80 Ø) was also recorded in the Helmholtz coils in order to obtain a more detailed graph in the neighbourhood of the zero field. For all the recorded positive peaks the zero point of the derivative and consequently the top of the absorption curve lie exactly at 0 Ø. All the curves are symmetrical and single-valued as may be seen in fig. 5 for the positive peak at 77°K. The experimental points taken at positive fields and at negative fields, at increasing fields and at decreasing fields, all lie on the same curve. Graphical integration gives the absorption curve (fig. 6). The half line width Δ is 1840 Ø. Using the above-mentioned assumptions and theory, we find the γ of this peak to be larger than 49.4×10^4 Hz/Ø in the Lorentzian case or larger than 34.0×10^4 Hz/Ø in the Gaussian case. δ lies between 1250 and 1840 Ø in the Lorentzian case and between 1080 and 1840 Ø in the Gaussian case.

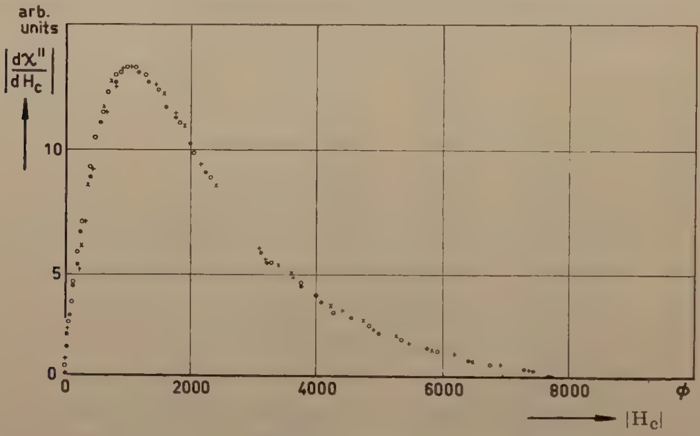

Fig. 5. Sample I. Positive peak at 77°K.
Frequency 84.5 MHz, sweep amplitude < 1.75 Ø.
● increasing positive magnetic field.
○ decreasing positive magnetic field.
+ increasing negative magnetic field.
× decreasing negative magnetic field.

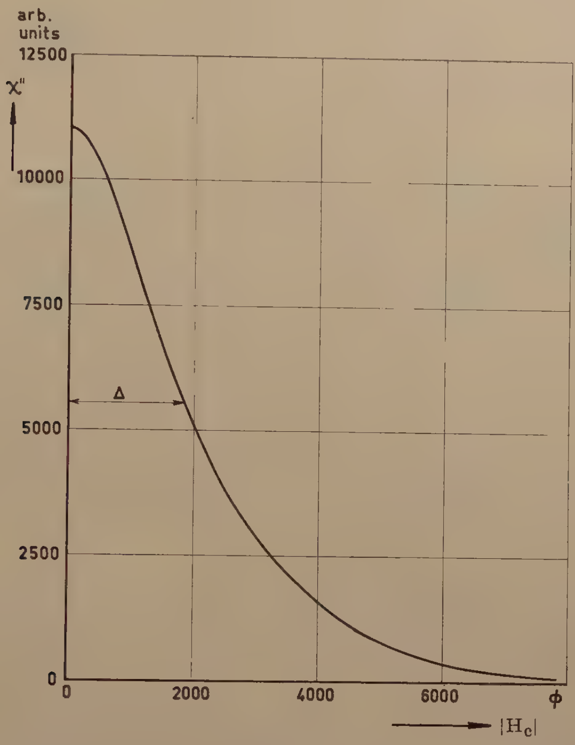

Fig. 6. Sample I. Positive peak at 77°K. Frequency 84.5 MHz.

§ 3. *Discussion.* The first question which arises is: what is the origin of these absorptions? It is possible that magneto-resistance effects are present. In order to check this suggestion *), it is necessary to do further experiments. It is worth while to notice that, indeed, a magnetic resonance spectrometer (of the χ''-mode) is well adapted for measuring such effects, since it can detect very small resistance variations in the sample. However, if one assumes in view of the line shapes, which are similar to magnetic resonance line shapes, that the phenomena are due to magnetic relaxation (considered as a limiting case of magnetic resonance), one may make the following remarks.

Since the value of γ for free electron spins is 1.76×10^7 Hz/Ø and for nuclear spins is usually of the order of 10^4 Hz/Ø, it is quite possible that the positive peak is a magnetic electron spin absorption peak, the more as its appearance seems to depend upon the concentration of the impurity Sb-atoms. If we assume for the peak of fig. 6 the value of γ to be equal to 1.76×10^7 Hz/Ø, we have

---

*) made to us by Dr. G. Feher.

$$\Delta \cong \delta \text{ and } \delta = 1840\ \text{Ø}.$$

The negative peak has too high a γ-value to be an electron spin or orbit absorption peak (nearly 3 times or more too large). The effective mass of the electrons involved (if electrons at all) thus appears to be smaller than the normal electronic mass. This reminds of cyclotron resonance; but we must now remember that the h.f. field used in these experiments is magnetic and not electric. Moreover the puzzling facts remain that the derivative is multi-valued and that the absorption has a negative maximum.

Further investigations with other samples, with higher and lower frequencies, in other temperature ranges and with higher steady fields are desirable.

We take the opportunity to express our sincere thanks to the Union Minière du Haut-Katanga for finantial aid during these measurements.

Received 4th August, 1957.

REFERENCES

1) Wolf, E. de, A. van Itterbeek and L. van Gerven, Bull. Inst. Intern. Froid Annexe 1956-2 (p. 125).

2) Gerven, L. van, A. van Itterbeek and E. de Wolf, Med. Kon. Vl. Acad. Brussel **19** (1957) 6.

Appl. sci. Res. Section B, Vol. 7

ON THE THEORY OF REFLECTION FROM A WIRE GRID PARALLEL TO AN INTERFACE BETWEEN HOMOGENEOUS MEDIA (II)

by JAMES R. WAIT

National Bureau of Standards, Boulder, Colorado, U.S.A.

Summary

A previous analysis is extended to include coupling between the TM and TE modes. This can be important when the incidence and polarization are both arbitrary.

In a previous paper¹) of the above title, a solution was presented for the reflection of a plane wave from a grid which is parallel to a plane interface between homogeneous media. The grid is composed of thin equi-spaced wires of high but finite conductivity. It was concluded that subject to the smallness of the wires the equivalent circuit of the grid is also a shunt element and the respective homogeneous media are semi-infinite transmission lines. It is now apparent that for both arbitrary polarization and oblique incidence this is not generally so. The failure of the single shunt representation results from coupling between TM (transverse magnetic) and TE (transverse electric) modes²). In the previous paper, denoted hereafter as (I), the coupling was neglected. This is rigorously justified for (*a*) oblique incidence, when the electric vector is always parallel to the wires, (*b*) normal incidence for any polarization, (*c*) perfectly reflecting interface for any angle of incidence and polarization. As is shown below, however, there is still a single shunt representation for oblique incidence with the magnetic vector always parallel to the wires. In this case though, there is mode coupling of the evanescent field of the grid by the interface and this modifies slightly the equivalent circuit.

The geometry of the problem was described in detail in (I), but for convenience a brief outline is given here. The grid wires (with spacing d) are of circular cross-section (of radius a) and are located in the plane $x = h$ of a rectangular coordinate system chosen such that the dielectric interface is the plane $x = 0$. The z-axis is chosen to be in the direction of the wires. The homogeneous dielectric medium in front of the interface ($x > 0$) has a propagation constant k and the medium behind the interface ($x < 0$) has a propagation constant k', which in (I) was allowed to be complex. The permeability of the whole space is taken to be a constant μ. The indicent wave is now taken to have arbitrary polarization and incidence. The z components of these electric and magnetic fields are given by

$$E_z{}^p = \alpha \exp\left[ik\left(x \cos\theta \cos\phi + y \cos\theta \sin\phi - z \sin\theta\right)\right] \tag{1}$$

and $H_z{}^p = \alpha^* \exp\left[ik\left(x \cos\theta \cos\phi + y \cos\theta \sin\phi - z \sin\theta\right)\right],$ (2)

where α and α^* are independent of x, y, z.

The total fields are now represented in terms of an electric and magnetic Hertz vectors which have only z components, Π and Π^* respectively. The connecting relations for the tangential fields are

$$E_z = \left(k^2 + \frac{\partial^2}{\partial z^2}\right)\Pi, \tag{3}$$

$$H_z = \left(k^2 + \frac{\partial^2}{\partial z^2}\right)\Pi^*, \tag{4}$$

$$E_y = \frac{\partial^2 \Pi}{\partial y \partial z} + i\mu\omega \frac{\partial \Pi^*}{\partial x}, \tag{5}$$

$$H_y = \frac{\partial^2 \Pi^*}{\partial y \partial z} - i \frac{k^2}{\mu\omega} \frac{\partial \Pi}{\partial x} \tag{6}$$

for the region $x > 0$. Primes are added to all these quantities when they refer to the region $x < 0$. It should be noted that in (I) it was assumed that the fields generated by $H_z{}^p$ did not react with the grid.

Employing the methods of (I), it follows that

$$(k \cos\theta)^2\, \Pi =$$

$$= \cos^2\theta \frac{i\mu\omega I\, e^{-ikz\sin\theta}}{4\pi} \sum_{m=-\infty}^{+\infty} \frac{e^{i2\pi My/d}}{N_1} \left[e^{2\pi|x-h|N_1/d} + R_m e^{-2\pi(x+h)N_1/d}\right]$$

$$+ e^{-ikz\sin\theta}\, e^{iky\cos\theta\sin\phi}\left(\alpha\, e^{ikx\cos\theta\cos\phi} + \beta\, e^{-ikx\cos\theta\cos\phi}\right), \tag{7}$$

$$(k\cos\theta)^2\,\Pi^*$$
$$= \cos^2\theta\,\frac{i\mu\omega I}{4\pi}\,\mathrm{e}^{-ikz\sin\theta}\sum_{m=-\infty}^{+\infty}\frac{\mathrm{e}^{i2\pi My/d}}{N_1}\,A_m\,\mathrm{e}^{-2\pi(x+h)N_1/d}$$
$$+\,\mathrm{e}^{-ikz\sin\theta}\,\mathrm{e}^{iky\cos\theta\sin\phi}\,(\alpha^*\,\mathrm{e}^{ikx\cos\theta\cos\phi}+\beta^*\,\mathrm{e}^{-ikx\cos\theta\cos\phi}), \qquad (8)$$

$$(k'\cos\theta')^2\Pi'$$
$$= \cos^2\theta\,\frac{i\mu\omega I}{4\pi}\,\mathrm{e}^{-ikz\sin\theta}\sum_{m=-\infty}^{+\infty}\frac{\mathrm{e}^{i2\pi My/d}}{N_1}\,T_m\,\mathrm{e}^{2\pi xN_1'/d}\,\mathrm{e}^{-2\pi hN_1/d}\,+$$
$$+\,\mathrm{e}^{-ikz\sin\theta}\,\mathrm{e}^{iky\cos\theta\sin\phi}\,\gamma\,\mathrm{e}^{ikx'\cos\theta'\cos\phi'}, \qquad (9)$$

$$(k'\cos\theta')^2\Pi^{*\prime}$$
$$= \cos^2\theta\,\frac{i\mu\omega I}{4\pi}\,\mathrm{e}^{-ikz\sin\theta}\sum_{m=-\infty}^{+\infty}\frac{\mathrm{e}^{i2\pi My/d}}{N_1}\,A_m^*\,\mathrm{e}^{2\pi xN_1'/d}\,\mathrm{e}^{-2\pi hN_1/d}$$
$$+\,\mathrm{e}^{-ikz\sin\theta}\,\mathrm{e}^{iky\cos\theta\sin\phi}\,\gamma^*\,\mathrm{e}^{ikx'\cos\theta'\cos\phi'}, \qquad (10)$$

where the actual current $I_a = I\,\mathrm{e}^{iky\cos\theta\sin\phi}\,\mathrm{e}^{-ikz\sin\theta}$ and where $M = m + (d\cos\theta\sin\phi/\lambda)$ and $N_1 = [M^2 - (d\cos\theta/\lambda)^2]^{\frac{1}{2}}$.

As indicated above, θ and ϕ are angles which determine the direction of incidence. From the laws of Snellius it follows that $k\sin\theta = k'\sin\theta'$ and $k\cos\theta\sin\phi = k'\cos\theta'\sin\phi'$, which enable θ' and ϕ' to be determined from θ and ϕ and the relative refractive index k'/k. Matching tangential fields at the interface $x = 0$ leads to

$$R_m = \frac{\left[N_1 + N_1'\left(\dfrac{k\cos\theta}{k'\cos\theta'}\right)^2\right]\left[N_1 - N_1'\left(\dfrac{\cos\theta}{\cos\theta'}\right)^2\right] + (M\sin\theta)^2\left[1-\left(\dfrac{k\cos\theta}{k'\cos\theta'}\right)^2\right]^2}{\left[N_1 + N_1'\left(\dfrac{k\cos\theta}{k'\cos\theta'}\right)^2\right]\left[N_1 + N_1'\left(\dfrac{\cos\theta}{\cos\theta'}\right)^2\right] - (M\sin\theta)^2\left[1-\left(\dfrac{k\cos\theta}{k'\cos\theta'}\right)^2\right]^2} \qquad (11)$$

and $A_m = 1 + R_m$. Furthermore

$$\beta = \frac{c_1a_2 - c_2a_1}{b_1a_2 - b_2a_1}, \quad \beta^* = \frac{b_1c_2 - b_2c_1}{b_1a_2 - b_2a_1}, \qquad (12)$$

$$\gamma = 1 + \beta,\ \gamma^* = 1 + \beta^*, \qquad (13)$$

where

$$a_1 = \mu\omega \left[\frac{k_x}{(k \cos \theta)^2} + \frac{k_x'}{(k' \cos \theta')^2} \right],$$

$$b_1 = k_y k \sin \theta \left[\frac{1}{(k \cos \theta)^2} - \frac{1}{(k' \cos \theta')^2} \right],$$

$$c_1 = \alpha^* \mu\omega \left[\frac{k_x}{(k \cos \theta)^2} - \frac{k_x'}{(k' \cos \theta')^2} \right] - \alpha k_y k \sin \theta \left[\frac{1}{(k \cos \theta)^2} - \frac{1}{(k' \cos \theta')^2} \right],$$

and

$$a_2 = b_1,$$

$$b_2 = - \frac{1}{(\mu\omega)} \left[\frac{k_x}{(\cos \theta)^2} + \frac{k_x'}{(\cos \theta')^2} \right],$$

$$c_2 = - \frac{\alpha}{\mu\omega} \left[\frac{k_x}{(\cos \theta)^2} - \frac{k_x'}{(\cos \theta')^2} \right] - \alpha^* k_y k \sin \theta \left[\frac{1}{(k \cos \theta)^2} - \frac{1}{(k' \cos \theta')^2} \right],$$

where $k_x = k \cos \theta \cos \phi$, $k_x' = k' \cos \theta' \cos \phi'$ and $k_y = k \cos \theta \sin \phi$. The current I on the wires is now obtained from

$$- I_a Z_i = k^2 \cos^2 \theta \, [\Pi_z]_{\substack{x = h+a \\ y = z = 0}}$$

where Z_i is the internal series impedance of the wires defined in (I). This is transformed to

$$I = -d(\alpha \, e^{ik_x h} + \beta \, e^{-ik_x h}) \Bigg/ \left\{ \frac{\eta \cos \theta}{2 \cos \phi} \left(1 + \frac{\beta}{\alpha} e^{-2ik_x h} \right) + \right.$$

$$\left. + \frac{i\mu\omega d}{2\pi} \cos^2\theta \left[\ln \frac{d}{2\pi a} - R^0 \ln (1 - e^{-2\pi(2h+a)/d}) + \Delta \right] + dZ_i \right\}, \quad (15)$$

where $\eta = \mu\omega/k$ and $R^0 = [R_m]_{d=0}$ and

$$\Delta = \tfrac{1}{2} \sum_{m=-\infty}^{\infty}{}'' \frac{1 + R_m \exp(-4\pi h N_1/d)}{N_1} - \frac{1 + R^0 \exp(-4\pi h |m|/d)}{|m|}, \quad (16)$$

where the double prime indicates that the term $m = 0$ is to be omitted from the summation.

This is the complete answer to the problem since the coefficients β, β^*, γ, γ^* and the current I are specified in terms of α and α^*. The resulting equation for I is rather interesting. It illustrates that in the general case the equivalent single shunt element representation is not adequate since I depends both on α and α^*. If, however, $\sin^2\theta \ll 1$, the dependence of I on α^* can be neglected. In the special case where the electric vector is always parallel to the wires (i.e. $\theta = 0$) the current I does not depend on α^* and the results are as given by equations (30) to (34) in (I). The other important special case is where the magnetic vector is always perpendicular to the wires (i.e. $\phi = 0$). Attention was focused on this case in (I). Here, while the current I does not depend on α^*, there is coupling in the sense that there is mode conversion of the evanescent field of the grid. Now

$$I = \frac{-\,\mathrm{d}\alpha\,(\mathrm{e}^{ikh\cos\theta} + R_0\,\mathrm{e}^{-ikh\cos\theta})}{\frac{1}{2}\,\eta\cos\theta\,(1 + R_0\,\mathrm{e}^{-2ikh\cos\theta}) + Z_g}, \tag{17}$$

where

$$Z_g = \frac{i\mu\omega d\cos^2\theta}{2\pi}\left[\ln\frac{d}{2\pi a} - R_0\ln\left(1 - \mathrm{e}^{-2\pi(2h+a)/d}\right) + \Delta\right] + \mathrm{d}Z_i, \tag{18}$$

where R^0 is explicitly given by

$$R^0 = \frac{\left[1+\left(\frac{k\cos\theta}{k'\cos\theta'}\right)^2\right]\left[1-\left(\frac{\cos\theta}{\cos\theta'}\right)^2\right] + \sin^2\theta\left[1-\left(\frac{k\cos\theta}{k'\cos\theta'}\right)^2\right]^2}{\left[1+\left(\frac{k\cos\theta}{k'\cos\theta'}\right)^2\right]\left[1+\left(\frac{\cos\theta}{\cos\theta'}\right)^2\right] - \sin^2\theta\left[1-\left(\frac{k\cos\theta}{k'\cos\theta'}\right)^2\right]^2} \tag{19}$$

and

$$\Delta = \sum_{m=1}^{\infty} \frac{1 + R_m\exp\left(-\frac{4\pi h}{d}N_0\right)}{N_0} - \frac{1 + R^0\exp\left(-\frac{4\pi h}{d}m\right)}{m} \tag{20}$$

with

$$R_m = \frac{\left[N_0 + N_0'\left(\frac{k\cos\theta}{k'\cos\theta'}\right)^2\right]\left[N_0 - N_0'\left(\frac{\cos\theta}{\cos\theta'}\right)^2\right] + (m\sin\theta)^2\left[1-\left(\frac{k\cos\theta}{k'\cos\theta'}\right)^2\right]^2}{\left[N_0 + N_0'\left(\frac{k\cos\theta}{k'\cos\theta'}\right)^2\right]\left[N_0 + N_0'\left(\frac{\cos\theta}{\cos\theta'}\right)^2\right] - (m\sin\theta)^2\left[1-\left(\frac{k\cos\theta}{k'\cos\theta'}\right)^2\right]^2} \tag{21}$$

and

$$N_0 = [m^2 - (d \cos \theta/\lambda)^2]^{\frac{1}{2}},\ N_0' = [m^2 - (d' \cos \theta'/\lambda')^2]^{\frac{1}{2}}. \qquad (22)$$

When the incidence is near normal, the terms containing $(\sin \theta)^2$ in the above expression can be neglected and R_0 and Δ reduce to the respective forms given in (I). The equivalent circuit given previously still is valid for this case although Z_g, the shunt impedance as given here, is more accurate*).

In the last section of (I) an analysis is given for the power absorption from a magnetic line source over a lossy half space with a wire grid in the interface (i.e. the case $h = 0$). Strictly speaking, the more accurate form of Z_g should be employed since the integration is over all angles of incidence (including complex angles). It turns out, however, that for the important part of the integrand the angles of incidence are near normal and consequently, none of the final conclusions of this section are modified.

Acknowledgment. I am deeply indebted to H. M. Altschuler who questioned the adequacy of the simple shunt representation of the grid when both incidence and polarization are arbitrary.

Received 24th July, 1958.

REFERENCES

1) Wait, J. R., Appl. Sci. Res. **B 6** (1956) 259.

2) Examples of such coupling are discussed in J. R. Wait, Appl. Sci. Res. **B 6** (1956) 117 and H. M. Altschuler and L. O. Goldstone, Polytech. Inst. Brooklyn-Report No. 485, 1957.

---

*) In the limiting case where the grid is in the interface, equation (18) for the impedance becomes

$$Z_g = \frac{i\mu\omega d \cos^2\theta}{2\pi}\left[(1 + R^0)\ln\frac{d}{2\pi a} + \Delta\right] + \mathrm{d}Z_i$$

with Δ given by (20) with $h = 0$.

Appl. sci. Res. Section B, Vol. 7

EQUIVALENT BASE RESISTANCE OF POINT-CONTACT TRANSISTORS

by FREDERICK J. YOUNG

Carnegie Institute of Technology, Pittsburgh, Pennsylvania, U.S.A.

Summary

A theoretical expression for the equivalent base resistance R_b of point-contact transistors is derived by consideration of a three-dimensional electric field problem. The analysis shows that the equivalent base resistance depends on the location of the emitter, resistivity of the semiconductor and the dimensions of the configuration.

§ 1. *Introduction.* In the design of circuits it is customary and most useful to use equivalent circuits to represent the various components contained therein. The equivalent base resistance of point-contact transistors is a well-known quantity defined as the ratio of emitter voltage to collector current. This definition has been experimentally verified for the case of small signal operation with fixed bias[1]). It is the purpose of this paper to derive a relationship for the equivalent base resistance which is a function of not only electrode spacing and resistivity but is also dependent upon all the physical dimensions of the semiconductor die and the exact location of the emitter.

§ 2. *Physical model.* An exact solution to the problem would be quite difficult because 1) of the effect of widening of the space-charge layer of the collector junction, 2) of the influence of diffusion currents and 3) of conductivity modulation caused by minority carrier injection. Experimental evidence indicates that these effects can be neglected in the low signal, low frequency case[1]). Hence, the physical model used herein is an approximation to the actual physical situation. The model used is shown in fig. 1. In this model it is assumed that the collector barrier is hemispherical in shape and has a radius r_c which is small compared to the thickness of the die, and that the emitter makes contact only at the point $P(x_e, y_e, 0)$, where x_e, y_e and $z = 0$ are the coordinates of the emitter. Maxwell's equations are applied to the model in order to obtain the potential V_e of the emitter. The equivalent base resistance R_b is given by

$$R_b = V_e/I_c, \tag{1}$$

where I_c is the collector current.

§ 3. *Solution.* Under the assumptions made Maxwell's equations may be combined to yield

$$\nabla^2 V = 0. \tag{2}$$

The solution to (2) must fit the following boundary conditions (see fig. 1):

$$\frac{\partial V}{\partial x}(\pm x_0, y, -z_0 < z < 0) = \frac{\partial V}{\partial y}(x, \pm y_0, -z_0 < z < 0), \tag{3}$$

$$\frac{\partial V}{\partial z}(x > x_c, y > y_c, 0) = 0, \tag{4}$$

$$V(x, y, -z_0) = 0, \tag{5}$$

$$V(\sqrt{x^2 + y^2 + z^2} = r_c) = 0, \tag{6}$$

where V_c is the voltage applied to the collector. In this analysis a voltage V_c is assumed to exist on the surface of a small hemisphere of radius r_c which is excavated from the die in the region of the origin. Equations (3) and (4) indicate that no current can enter or leave the semiconductor except through the collector-formed region and the base. Direct solution to (2) is complicated because of the boundary conditions which must be satisfied. However, the physical model may be replaced by a mathematical model consisting of an infinitely extended lattice of current sources. The potentials due to each current source can be superimposed to yield the solution to (2). The potential due to a current source of radius r_c located at the origin is easily found to be

$$V = -\frac{C_1}{\sqrt{x^2 + y^2 + z^2}}. \tag{7}$$

By the boundary condition of (6)

$$C_1 = -V_c r_c. \tag{8}$$

Therefore

$$V = \frac{V_c r_c}{\sqrt{x^2 + y^2 + z^2}}. \tag{9}$$

Let $x^2 + y^2 + z^2 = r^2$. Then $V = (r_c/r)V_c$. Because $J = -\sigma \nabla V$,

$$J_r = \sigma V_c r_c / r^2, \tag{10}$$

where J_r is the current density in the radial direction. Let a total current of $2I_c$ emanate from the sphere. Then

$$V_c = \frac{I_c}{2\pi\sigma\sqrt{x_c^2 + y_c^2 + z_c^2}}. \tag{11}$$

Substitution of (11) into (9) yields

$$V = \frac{I_c}{2\pi\sigma\sqrt{x^2 + y^2 + z^2}}. \tag{12}$$

From (12) it is clear that the potential at a given point in space due to a current source of strength $2I_c$ is inversely proportional to the distance between the point and the current source.

The physical model of fig. 1 can be replaced by the mathematical model of fig. 2. In fig. 2 an infinite number of current sources are distributed in xy planes at the points $P_{ij}(2ix_0, 2jy_0)$. These images satisfy the boundary conditions of (3). In order to satisfy the boundary conditions of (4) and (5) an infinite number of xy planes of the sort described above must be placed one above the other, but the polarity of the current sources must alternate from plane to plane. Therefore, all of space is filled with current images of strength $2(-1)^k I_c$, fixed at the points $P_{ijk}(2ix_0, 2jy_0, 2kz_0)$ where i, j and k are any positive or negative integers. For the sake of clarity fig. 2 shows only a few of the images located in the first octant. The distance d between any point $P(x, y, z)$ and any image is

$$d = \sqrt{(x - 2ix_0)^2 + (y - 2jy_0)^2 + (z - 2kz_0)^2}. \tag{13}$$

The potential at the point $P(x, y, z)$ is the sum of the potentials due to all images. The total potential at $P(x, y, z)$ is given by

$$V(x, y, z) = \\ = \frac{I_c}{2\pi\sigma} \lim_{n\to\infty} \sum_{k=-n}^{n} \sum_{j=-n}^{n} \sum_{i=-n}^{n} \frac{(-1)^k}{\sqrt{(x-2ix_0)^2+(y-2jy_0)^2+(z-2kz_0)^2}}. \tag{14}$$

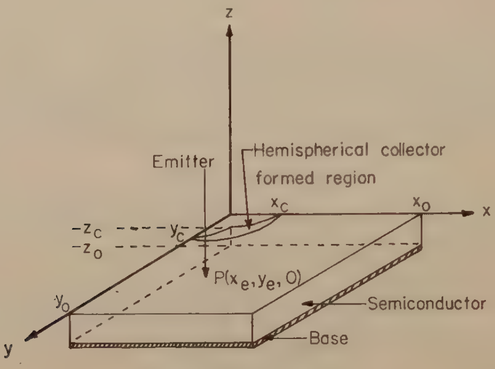

Fig. 1. A point-contact transistor.

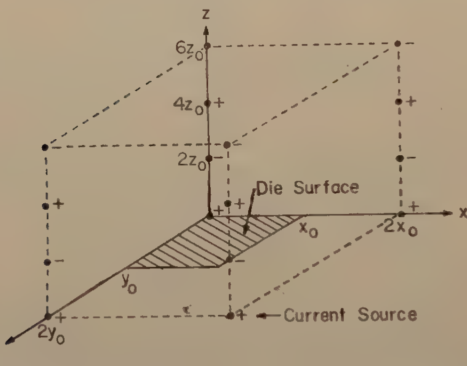

Fig. 2. A mathematical model of a point-contact transistor.

By definition the equivalent base resistance is

$$R_b = \frac{V(x_e, y_e, 0)}{I_c} \tag{15}$$

or

$$(4\pi\sigma R_b z_0) = \lim_{n\to\infty} \sum_{k=0}^{2n} \sum_{j=0}^{2n} \sum_{i=0}^{2n} \frac{(-1)^{(k-n)}}{\sqrt{\left(\frac{x_e}{2z_0} - (i-n)\frac{x_0}{z_0}\right)^2 + \left(\frac{y_e}{2z_0} - (j-n)\frac{y_0}{z_0}\right)^2 + (k-n)^2}} . \tag{16}$$

If x_0 and y_0 are very large, (16) reduces to

$$(4\pi\sigma R_b z_0) = \lim_{n\to\infty} \sum_{k=0}^{2n} \frac{(-1)^{(k-n)}}{\sqrt{\left(\frac{x_e}{2z_0}\right)^2 + \left(\frac{y_e}{2z_0}\right)^2 + (k-n)^2}}. \quad (17)$$

Equation (17) has been reduced to a very simple form in [1]). In the general case (16) is most useful and $(4\pi\sigma R_b z_0)$ can be calculated by a digital computer. The number of terms which must be included to approximate the infinite number of terms indicated by (16) depends upon the dimensions of the transistor under consideration. Because of the amount of numerical work involved only one value of the base resistance is calculated here. That value is computed for a transistor die having the following dimensions: $z_0 = 0.05$ cm, $x_0 = y_0 = 0.15$ cm and $x_e = y_e = 0.005$ cm. The resistance obtained from (16) was 20% higher than that obtained from (17).

§ 4. *Conclusions.* The formula derived here for the equivalent base resistance of point-contact transistors accounts for the geometry and position of the emitter. It is more exact than previous analyses and is limited by the same simplifying assumptions. Equation (16) should be used sparingly, for in many cases the standard formula resulting from (17) is adequate. However, in certain cases (16) is a useful tool for circuit analysis and for understanding the effect of transistor geometry upon base resistance.

Received 6th August, 1958.

REFERENCE

1) Valdes, L. B., Proc. Instn Radio Engrs **40** (1952) 1429.

A NULL-COIL MAGNETOMETER

by P. JONGENBURGER *) and C. W. BERGHOUT

Philips Research Laboratories, N.V. Philips' Gloeilampenfabrieken,
Eindhoven, Netherlands

Summary

A magnetometer has been developed in which the saturation-magnetization of small samples of ferromagnetic materials can be measured. The sample, which is situated at the centre of a small coil, is placed in an inhomogeneous magnetic field. The current through the coil is adjusted to such a value that the forces on coil and sample balance each other. Then under certain conditions the magnetic moment of the sample equals the magnetic moment of the coil; these conditions are discussed. The method is suitable for use in ordinary laboratory magnets and in solenoids, also at low temperatures. With a second version of this magnetometer it is possible to measure para- and even diamagnetism.

§ 1. *Introduction*. The method described was originally used by Domenicali 1) for measurements at room temperature and in rather small magnetic fields (about 5000 oersted.) A similar instrument was also described by Bozorth *et al.* 2). We wanted to extend our measurements to low temperatures and fields up to 25000 oersted, such as were available in our magnet. It appeared to be impossible, however, to obtain the proper field geometry as calculated by Domenicali at both low and high fields, because of the saturation of the pole-pieces. Therefore a more detailed analysis of the instrument was necessary.

The adaptation of the apparatus for use at low temparatures consisted mainly in making it smaller, in order that measurements might be performed inside a Dewar vessel in an air gap not wider than about 4 cm.

§ 2. *Principle*. We consider a magnetic dipole in an inhomogeneous magnetic field; the components of its magnetic moment are m_x, m_y and m_z, while the components of the field-strength H are H_x, H_y and H_z. The x-component of the force exerted on the dipole by the field is given by

---

*) Now at Technological University, Delft.

$$F_x = m_x \frac{\partial H_x}{\partial x} + m_y \frac{\partial H_x}{\partial y} + m_z \frac{\partial H_x}{\partial z}, \tag{1}$$

where $\partial H_x/\partial x$ etc. should be taken at the position of the dipole. We assume, that for the dipole m_y and m_z are zero; (1) then takes the simple form

$$F_x = m_x \frac{\partial H_x}{\partial x}. \tag{2}$$

We now consider a sample, magnetized in the x-direction, placed with its centre on the x-axis; moreover, we assume the field to have cylindrical symmetry around the x-axis. In this case we have

$$F_x = m_x \left(\frac{\partial H_x}{\partial x}\right)_{cs}, \tag{3}$$

where the subscripts c and s mean that the gradient should be taken at the magnetic centre of the sample. As a matter of fact, the position of this centre, or rather its x-coordinate, is defined by (3); in principle, therefore, it depends upon the geometry of the field and is not a fixed point of the sample. It will be shown in the next section, however, that in our practical cases the error arising from taking the gradient in (3) at the centre of mass instead of at the magnetic centre never exceeds 0.1%. So within this accuracy the magnetic centre can be regarded as a fixed point, coinciding with the centre of mass.

We next consider a cylindrical coil; its magnetic moment M, directed along its axis, is given by

$$M = i \sum_{1}^{N} A_n, \tag{4}$$

where i is the current through the coil, A_n the cross-sectional area of the n-th turn and N the number of turns.

This coil is situated in the magnetic field, its axis coinciding with the x-axis. If the coil is given the proper shape, as will be discussed in the next section, the force exerted on it by the field is given by

$$F_x = M\left(\frac{\partial H_x}{\partial x}\right)_{cc}, \tag{5}$$

where the subscripts c and c mean that the gradient should be taken at the geometrical centre of the coil.

We now place the sample inside the coil; the current through the coil is adjusted to such a value that the forces on coil and sample balance each other. Then, disregarding the sign, we have

$$m_x\left(\frac{\partial H_x}{\partial x}\right)_{cs} = M\left(\frac{\partial H_x}{\partial x}\right)_{cc}. \tag{6}$$

In each of the two following cases:

1. $\partial H/\partial x$ has the same value everywhere in the region of space considered,
2. the centres of sample and coil coincide,

we have

$$\left(\frac{\partial H_x}{\partial x}\right)_{cs} = \left(\frac{\partial H_x}{\partial x}\right)_{cc}, \tag{7}$$

and consequently

$$m_x = M. \tag{8}$$

When the magnetic field is produced by means of a water-cooled solenoid, it is fairly easy to make a gradient which is reasonably uniform in a sufficiently large volume by means of separate gradient-coils. When working with a large electromagnet as we did, it is not very difficult, following the method given by Fereday³), to construct polepieces giving a uniform gradient if only the field remains well below the saturation value of iron. If the polepieces become saturated, however, they cannot be regarded as equipotential surfaces, and the calculation breaks down. It is possible, of course, to construct polepieces by trial and error which yield a uniform gradient at high fields; but they will not perform equally well at low fields. So we are left with the fact that in general the gradient will be a function of x. Therefore it is necessary that the centres of sample and coil coincide (case 2). This is not always easy to achieve, however, in particular when the sample has an irregular shape; consequently we have in general the situation of fig. 1*a*. Let us call the balancing magnetic moment of the coil in this case M_a. Now we rotate the magnetic field through 180° around an axis AA which is perpendicular to the X-axis and passes through

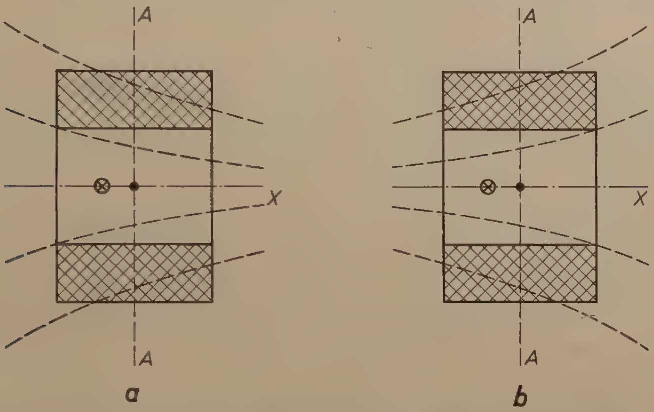

Fig. 1. Coil and sample in an inhomogeneous magnetic field with cylindrical symmetry around the axis of the coil.

a: First position.
b. Second position, generated from the first one by rotating only the field through 180° around AA.
● Centre of Coil.
⊗ Centre of sample.
- - - - Lines of force

it at (or near) the centre of the coil*); we then obtain the situation of fig. 1*b* and the balancing moment M_b. If the distances involved are sufficiently small, the gradient $\partial H_x/\partial x$ can be considered as a linear function of x, and the mean value of M_a and M_b will equal the value M which we should have found with the sample in the correct position; so we have

$$m_x = \tfrac{1}{2}(M_a + M_b). \qquad (8a)$$

Mind, that this derivation only holds when the magnetic centre can be considered as a fixed point.

---

*) AA should go through the centre of the *sample* to be sure that it is exposed to the same fieldstrength in both situations. Obviously this cannot be done; when measuring saturation moments, however, the magnetic moment is nearly independent of the field, so the error can be neglected in these cases. In other cases the centres of coil and sample should be made to coincide as well as possible. When rotating the field, care should also be taken with regard to hysteresis effects.

When working in the air-gap of a magnet, the main advantage of this method of measuring m_x is that little or no trouble can be caused by image forces in the polepieces, because the net magnetic dipole moment of coil and sample together is zero.*)

A disadvantage of the method, when working in the air gap of a magnet, is its low sensitivity at low fields because of the low gradient. (when working in a solenoid with separate gradient coils this difficulty does not exist, of course.) Moreover a correction which is a function of field and temperature has to be applied for the magnetic moment of the coil.

Till now we assumed the sample to be magnetized in the x-direction only. Sometimes, however, this condition is not satisfied and the magnetic moment also has components m_y and m_z, for instance when measuring magnetically anisotropic samples. In this case a more careful analysis, starting from (1), is necessary. This is done in the last part of the next section, where it is shown that the y- and z-components of the magnetic moment only appear in the result with a very small factor, so that virtually only the x-component is measured in this case.

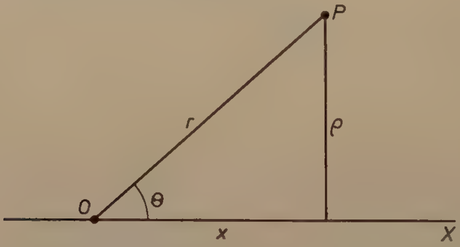

Fig. 2. Coordinate system for cylindrical geometry.

§ 3. *Calculations.* Using the coordinates of fig. 2, the potential of a static magnetic field around an axis of cylindrical symmetry can be written as

$$V = V_0 + A_1 r P_1(\cos\theta) + A_2 r^2 P_2(\cos\theta) + A_3 r^3 P_3(\cos\theta) + + A_4 r^4 P_4(\cos\theta) + \ldots, \quad (9)$$

---

*) Of course the quadrupole or higher moments still can have a small influence which in most circumstances can be neglected, however. When the dipole moment is not compensated, the corrections for the image forces sometimes are very large, in particular when working at high fields in narrow air gaps. In the wellknown ballistic work of Weiss and Forrer ^{4}), for instance, the correction for images even was about 50% in the worst case!

where the P_n (cos θ) are the well-known Legendre polynomials. We assume that terms with r^5, r^6 etc. can be neglected. By introducing x and ρ this formula can be rewritten in the form

$$V = V_0 + A_1x + \tfrac{1}{2}A_2(2x^2 - \rho^2) + \tfrac{1}{2}A_3(2x^3 - 3x\rho^2) + \\ + \tfrac{1}{8}A_4(8x^4 - 24x^2\rho^2 + 3\rho^4). \quad (10)$$

By differentiation with respect to one of the coordinates the component of the fieldstrength in the direction concerned is obtained. Disregarding the sign we find

$$H_x = \frac{\partial V}{\partial x} = A_1 + 2A_2x + 3A_3x^2 - \tfrac{3}{2}A_3\rho^2 + 4A_4x^3 - 6A_4x\rho^2,$$

$$\frac{\partial H_x}{\partial x} = 2A_2(1 + 3\frac{A_3}{A_2}x + 6\frac{A_4}{A_2}x^2 - 3\frac{A_4}{A_2}\rho^2) \quad (11)$$

and

$$H_\rho = -\rho(A_2 + 3A_3x + 6A_4x^2 - \tfrac{3}{2}A_4\rho^2). \quad (12)$$

We now place a coil with its centre at O, its axis coinciding with the x-axis. Its length is $2l$, its inner radius R and its outer radius aR; its number of turns is n, the current i. The x-component of the force exerted on the unit length of wire is given by $H_\rho i$. By integration the total force on the coil is obtained:

$$F_x = ni\frac{\pi R^2(a^3 - 1)}{3(a - 1)}2A_2\left[1 + \frac{A_4}{A_2}(2l^2 - \tfrac{9}{10}\frac{a^5 - 1}{a^3 - 1}R^2)\right]. \quad (13)$$

If the shape of the coil is chosen in such a way that

$$2l^2 - \tfrac{9}{10}\frac{a^5 - 1}{a^3 - 1}R^2 = 0, \quad (14)$$

we find

$$F_x = ni\frac{\pi R^2(a^3 - 1)}{3(a - 1)}2A_2. \quad (15)$$

Keeping in mind that $\pi R^2(a^3 - 1)/3(a - 1)$ is the mean cross-sectional area and $2A_2$ is the gradient $\partial H_x/\partial_x$ in O, we conclude that

$$F_x = M\left(\frac{\partial H_x}{\partial x}\right)_{cc} \quad (15)$$

if condition (14) is satisfied, i.e. if the coil has the proper shape. Some solutions of (14) are given in table I.

TABLE I

a	l/R
1	$\frac{1}{2}\sqrt{3} = 0.866$
$1\frac{1}{2}$	1.12
2	1.41
$2\frac{1}{2}$	1.73
3	2.04

Coil: length $= 2l$
inner radius $= R$
outer radius $= aR$

Now we consider a sample placed on the x-axis, homogeneously magnetized in the x-direction. As stated before, the force on the dipole $\mathrm{d}m_x$ is given by $\mathrm{d}F_x = \mathrm{d}m_x \partial H_x \partial x$, and the total force is found by integration. When the sample is a sphere with its centre at O, all terms with A_3 and A_4 vanish during integration because of certain symmetry properties of the Legendre polymomials, and we find $F_x = m_x . 2A_2$. Comparing this result with (3) and keeping in mind that $2A_2$ is the gradient of the magnetic field at O, we see that in this case the magnetic centre indeed coincides with the geometrical one.

When the sample is a cylinder of length $2l$ and radius R, with its axis along the x-axis, the force exerted on it by the field is found to be

$$F_x = m_x . 2A_2 \left[1 + \frac{A_4}{A_2} (2l^2 - \tfrac{3}{2} R^2) \right]. \qquad (16)$$

When the shape of the cylinder is chosen in such a way that $l/r = \frac{1}{2}\sqrt{3}$, we have $F_x = m_x . 2A_2$ as in the case of the sphere. When the cylinder has another shape or when the sample is very irregularly shaped, the relative error will certainly be smaller than $2A_4\delta^2/A_2$, where δ is half the maximum dimension of the specimen. Now in our case, when the field is 25000 oersted, the gradient is about 500 oersted/cm, $A_3/A_2 \approx 1/30$ cm^{-1} and $A_4/A_2 \approx -1/180$ cm^{-2}. Consequently, if the sample is smaller then 0.6 cm, the error is smaller than 0.1%. Our samples always being much smaller than 0.6 cm, the error can be neglected and we may consider the magnetic centre as a fixed point even in irregularly shaped specimens.

We now suppose that the magnetic moment of the sample also has components other than in the x-direction. This will be the case, for instance, when measuring magnetically anisotropic samples with one or more directions of easy magnetization not coinciding with the x-axis. To investigate this case, we start with (1), still assuming $m_z = 0$, however:

$$F_x = m_x \frac{\partial H_x}{\partial x} + m_y \frac{\partial H_x}{\partial y}. \tag{1a}$$

Using the coordinates of fig. 3, we can rewrite (10) in the form

$$V = V_0 + A_1 x + \tfrac{1}{2}A_2(2x^2 - y^2 - z^2) + \tfrac{1}{2}A_3(2x^3 - 3xy^2 - 3xz^2) + + \tfrac{1}{8}A_4(8x^4 - 24x^2y^2 - 24x^2z^2 + 3y^4 + 6y^2z^2 + 3z^4), \tag{10a}$$

from which we derive

$$\frac{\partial H_x}{\partial x} = 2A_2 + 6A_3 x + 12A_4 x^2 - 6A_4 y^2 - 6A_4 z^2 \tag{17}$$

and

$$\frac{\partial H_x}{\partial y} = -3A_3 y - 12A_4 xy. \tag{18}$$

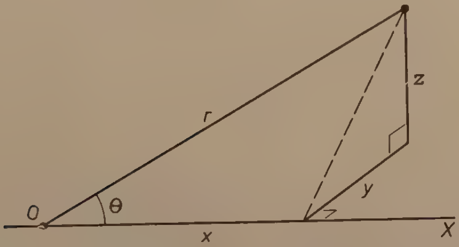

Fig. 3. Coordinate system used for magnetically anisotropic samples.

Introducing this into (1a) we obtain

$$F_x = m_x . 2A_2 \left[1 + 3\frac{A_3}{A_2} x + 6\frac{A_4}{A_2} x^2 - 3\frac{A_4}{A_2}(y^2 + z^2) - - \tfrac{3}{2}\frac{m_y}{m_x} y \left(\frac{A_3}{A_2} + 4\frac{A_4}{A_2} x \right) \right]. \tag{19}$$

We call the ratio of the forces F_x due to equal magnetic moments m_y and m_x the discrimination factor f, which in the ideal case should be zero. In first approximation we have

$$f = \tfrac{3}{2}\frac{A_3}{A_2} y. \tag{20}$$

If m_y is homogeneously distributed in the sample and if the sample is placed symmetricaly with respect to the XZ-plane, the integrated discrimination factor will be zero. Let us allow a maximum displacement y from the symmetry position of 0.2 mm, then with our former value of A_3/A_2 we find $f = 0.01$, which is considered to be sufficiently small for our purpose.

§ 4. *The magnet.* For the production of the magnetic field we use an Oerlikon magnet which enables us to obtain a fieldstrength up to 27 kØ in an air-gap of 4 cm between polepieces with a diameter of about 11 cm. For reasons indicated in the preceding section the shape of the polepieces was determined by trial and error in such a way, that the gradient on the axis of symmetry is an approximately linear function of x with a rather small slope and a very small quadratic term. The dimensions of our polepieces are indicated in fig. 4, but it should be emphasized that they depend strongly on the type of the magnet, the maximum fieldstrengths which can be reached and the range of fieldstrength in which the best accuracy is wanted. Our polepieces are designed to give the best results at high fields, because we are mainly interested in measurements of saturation magnetization.

§ 5. *The magnetometers.* Till now, two magnetometers of this kind have been constructed. The first one (fig. 4) was primarily made for the determination of the saturation magnetization of small ferromagnetic samples at liquid nitrogen and hydrogen temperatures. C is the coil in which the sample is placed; its dimensions are inner diameter 5 mm, outer diameter 10 mm, length 7 mm, corresponding to the model listed in table I under $a = 2$. The maximum magnetic moment which can be measured without heating the coil too much is about 4 c.g.s. units. By a glass rod G.R. the coil is connected to the moving platform B of a parallel spring movement with three phosphor-bronze springs S of dimensions $35 \times 5 \times 0.15$ mm. The net force F exerted on coil and sample by the magnetic field causes a deflection of the platform B, which can be measured by means of a small differential transformer D.T. and the Philips measuring bridge PR 9300. The coils of the differential transformer have the following dimensions: inner diameter 5 mm, outer diameter 15 mm, length 5 mm, primary coil 680, secondary coils 1450 turns each. The deflections are detected with a sensitivity of about 0.05 μ, corresponding to a force of about 1 dyne and a magnetic moment of about 0.002 c.g.s.-units

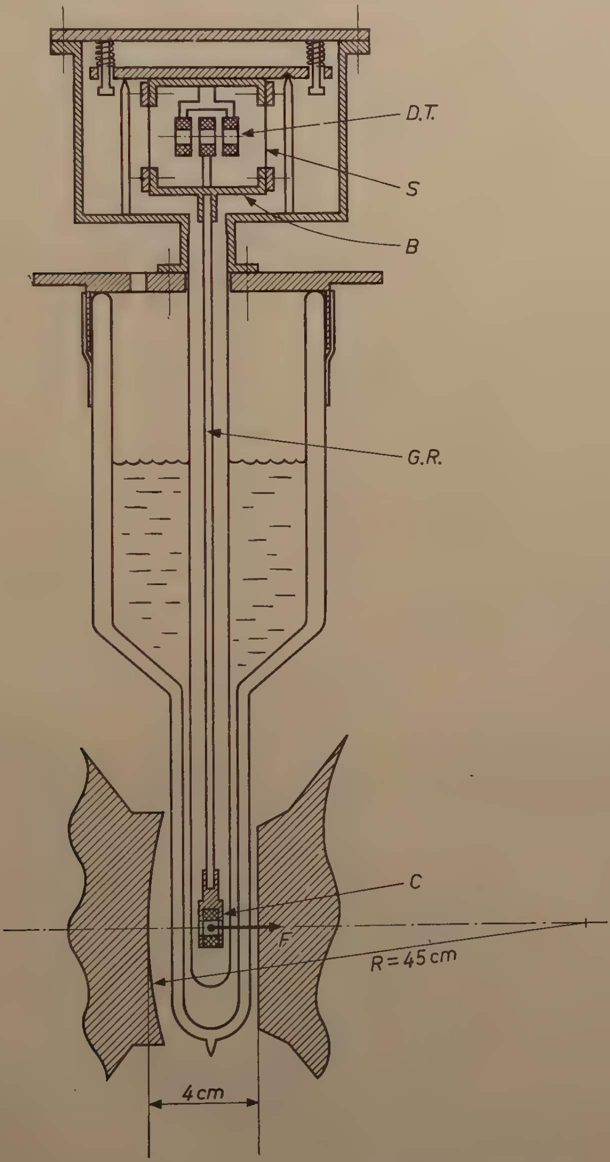

Fig. 4. Magnetometer for ferromagnetic samples.

when the gradient is 500 oersted/cm. When measuring, the force F is made equal to zero; consequently it is not necessary to make the glass rod G.R. very stiff. To prevent the condensation of moisture or, still worse, oxygen on the sample or the sample coil, the space around the measuring system is kept filled with a dry, oxygen-free gas of a pressure somewhat exceeding one atmosphere; of course a. gas should be chosen which does not condense at the measuring temperature. When the magnetic field is on, the aluminium housing of coil C provides sufficient damping; it also contains a carbon resistor thermometer. No special care was taken when making coil C and its housing; as a consequence its magnetic moment is rather high, of the order of 0.1 c.g.s. unit. It is dependent upon the field and the temperature; fortunately, however, it is very well reproducible and can be easily determined by experiments with the empty coil. The whole apparatus is rather sturdy and has performed very well during a couple of years.

A second model with a sensitivity of about 10^{-2} dyne under normal working conditions and even a few times 10^{-3} dyne under very favourable conditions, enabling us to measure diamagnetic susceptibilities with good accuracy, was made by one of us (*B.*); its construction is shown in fig. 5. In so sensitive an apparatus the utmost care should be taken to keep the magnetic moment of the empty sample coil low. This is done by using carefully selected iron-free copper wire and a former of quartz. The temperature measurement is done by means of a platinum resistance thermometer Th inside the sample coil C.

Of course the apparatus should be very insensitive against vibrations of the building (mainly 10–15 Hz). To achieve this, the moving part was made to pivot around its centre of gravity, its resonance frequency was made low (about 2 Hz) and its movement was nearly critically damped. This moving part is a pendulum suspended by means of a cross-spring system S of suitable stiffness and consists of a quartz rod QR, carrying the sample coil at its lower, the differential transformer D.T. and the damping device at its upper end. The latter consists of the small copper damping-rings D.R. connected to the pendulum and moving in the vicinity of the poles of a fixed bar magnet M. Due to the careful construction the zero of the apparatus is sufficiently stable and matches the sensitivity very well; even when measuring as a function of temperature the position of the coil C is reproducible within 10^{-4} cm, corresponding to a force of 10^{-2} dyne. When measuring at constant

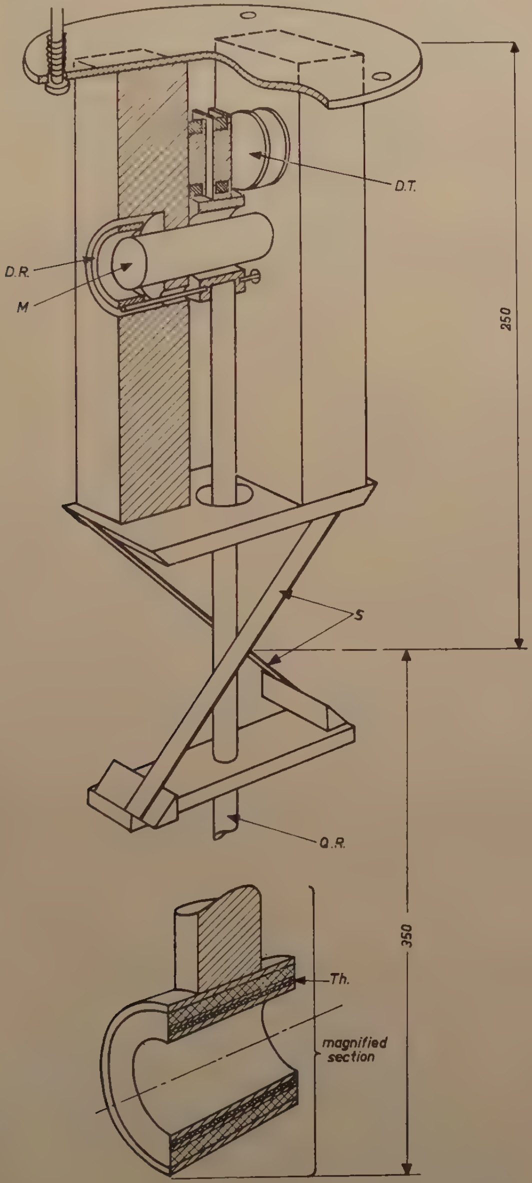

Fig. 5. Magnetometer for susceptibility measurements.

temperature after a sufficiently long waiting time the reproducibility even corresponds to about 3 × 10^{-3} dyne.

As in the preceding apparatus, the measuring system is surrounded by a space which can be filled with a suitable, dry and clean protecting atmosphere.

Received 9th October, 1958.

REFERENCES

1) Domenicali, C. A., Rev. Sci. Instr. **21** (1950) 327.
2) Bozorth, R. M., H. J. Williams and D. E. Walsh, Phys. Rev. **103** (1956) 572.
3) Fereday, R. A., Proc. Phys. Soc. **42** (1930) 251.
4) Weiss, P and R. Forrer, Ann. Phys. Paris **12** (1929) 279.

Appl. sci. Res. Section B, Vol. 7

THE GASDISCHARGE MECHANISM FOR THE ARGON-ALCOHOL PROPORTIONAL COUNTER

by K. v. DUUREN *) and G. J. SIZOO

Natuurkundig Laboratorium der Vrije Universiteit Amsterdam, Netherlands

Summary

Accurate measurements of the gas multiplication factor A were done for a number of proportional counters with various wire diameters ranging from 0.003 to 0.1 cm and for various gas pressures ranging from 67 to 220 mm Hg. From these results the ionization coefficient for the argon-alcohol gasmixture 9 : 1 could be deduced. It appeared that in a few cases the equilibrium between the mean electron energy and the electrical field was slightly disturbed and the conditions for the non-equilibrium situation could be established from the experiments. Rose's and Korff's calculations of the gas multiplication factor in proportional counters were compared with our experimental results, whereby rather large discrepancies were found. Comparison of our experimental values of the ionization coefficient for argon-alcohol with the earlier published values for pure argon and alcohol gives an insight in the mechanism of the electron multiplication process in the argon-alcohol gasmixture 9 : 1.

§ 1. *Introduction.* The mechanism of the proportional discharge in counters filled with a mixture of argon and alcohol is comparatively simple as a consequence of the absence of secondary multiplication effects [1]).

The ionization potential of alcohol is 10.8 eV [2]); this value is lower than the excitation energy 11.5 eV corresponding to the lowest excited level of argon. By collisions with metastable argon atoms the alcohol molecules may be ionized. A small addition of alcohol will therefore have the same effect as the presence of argon in neon-argon mixtures [3]), viz. an increase of the ionization at those values of F/p whereby excitation of argon atoms is a dominant process (F = electrical field strength, p = pressure). However, in this region of F/p a higher concentration of alcohol will cause a decrease of the ionization coefficient α due to the high value of the cross-section for inelastic impact at electron energies below 10 eV [4]).

---

*) At present at the Synchro-cyclotron of the Philips' Research Laboratories, Amsterdam, Netherlands.

The cross-section of alcohol for ionization is not known, but measurements for other polyatomic gases as ethylene [5]) give a strong indication that it will be considerably higher than for argon. This effect makes it possible that at very high values of F/p the ionization coefficient for alcohol-argon mixtures is higher than for pure argon, even at high alcohol concentrations.

With the exception of extremely high values of F/p the mean energy of the electrons moving in a homogeneous field will be in equilibrium with the electrical field [6]). Under this condition a single-valued relation between α/p and F/p will exist. In the highly inhomogeneous fields that occur in the central region of proportional counters no equilibrium may be reached by the electrons. In a convergent electrical field the mean electron energy will always be lower than in a homogeneous field at the same value of F/p. This means that the ionization coefficient will generally be lower in a convergent field. Only at very high values of F/p, where the mean energy of the electrons is higher than the energy corresponding to the maximum of the ionization cross-section curve, the ionization coefficient could be higher for convergent fields than for homogeneous fields. In most of these cases no single-valued relation between α/p and F/p will exist.

The gas multiplication for a cylindrical counter is given by

$$A = \exp\left(-\int_b^a \alpha \, \mathrm{d}r\right) \tag{1}$$

with a = anode radius, b = cathode radius and r = distance from cylinder axis. The electrical field strength is

$$F = V/[r \ln (b/a)].$$

By straightforward transformation of the variable (1) may be written

$$A = \exp\left[ap(F/p)_{max} \int_{(F/p)_{min}}^{(F/p)_{max}} (\alpha/p)(F/p)^{-2} \, \mathrm{d}(F/p)\right] \tag{2}$$

with $(F/p)_{max}$ = value of F/p at the anode and $(F/p)_{min}$ = value of F/p at the cathode. For proportional counters in most cases the lower integration limit can be taken equal to zero.

If a single-valued relation between α/p and F/p exists, the value of α/p can be deduced from the experimental value of A by differentiating the function

$$\Phi[(F/p)_{max}] = \frac{\ln A \ln (b/a)}{V} \tag{3}$$

with respect to $(F/p)_{max}$.

On the other hand it is possible to conclude from the measurements if really a single-valued relation between α/p and F/p exists. A series of curves $\Phi[(F/p)_{max}]$ is plotted for a set of measurements taken for different tube parameters, i.c. a and p. If all these curves coincide, it can be shown by elementary calculation that in the region of F/p under consideration a single-valued relation between α/p and F/p exists.

A straightforward method for evaluation of α/p, which even may be used in the case that no single-valued relation between α/p and F/p exists, consists of differentiation of the function $A(r)$. This function may be deduced from the experimental values of A in the following way: for a set of counters with the same cathode radius and gas filling, but with different values a_k of the anode radii, A is measured as a function of V. For all counters the values of A corresponding to one given value of F/p at the cathode surface are taken from the graphs $A(V)$. In this way A is found as a function of the value of $r = a_k$ in the counter. This procedure may be repeated for various values of $(F/p)_{cath}$. The value of α follows from the differentiation of A:

$$\alpha = -\frac{1}{A} \cdot \frac{\mathrm{d}A}{\mathrm{d}r}. \tag{4}$$

The aim of our research was to determine the ionization coefficient α for the argon-alcohol mixture 9 : 1 by measurements of the gas multiplication factor A and to investigate in how far equilibrium between the mean electron energy and the electrical field exists for the very inhomogeneous fields occurring in the vicinity of the anode wire of proportional counters. An additional aim of this research was to verify experimentally the calculations of the gas multiplication factor as they were given by Rose and

Korff [7]). The experimental results may also be of practical use with regard to the design of a proportional counter because the value of A for every given combination of counter parameters a, b and p can be determined from the graph Φ *versus* $(F/p)_{max}$.

§ 2. *Measurement of the gas multiplication factor A*. For a given counter at the counter voltage V the value A may be determined as the ratio of the total amount of ionization charge or current and the amount of ionization charge or current for a voltage at which no gas multiplication occurs. Therefore no absolute measurements of charge or current are necessary. The method of measuring the current induced by a radioactive source [7]) as well as a method of measuring the charge liberated by individual particles were used [8]) with our experiments.

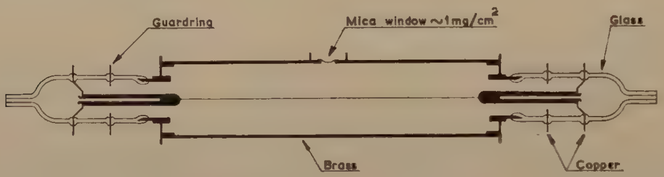

Fig. 1. Schematic drawing, showing the construction of the proportional counters.

The construction of the counters is shown in fig. 1. To minimize the adsorption of the filling gases to the wall a glass-metal construction was chosen. The insulators supporting the counter wire are provided with copper guard rings kept at the same voltage as the anode. By appropriate choice of the ratio of length and diameter of the cathode [12]) [13]) the occurrence of end effects was avoided. Extremely good care was paid to the purification of the alcohol used for the filling of the counter. Water vapour was eliminated by the process of Wislicenius and Kaufmann and oxygen by destillation in vacuo.

The current was measured in a conventional way with the aid of an electrometer compensation circuit. The amount of charge was determined by a measurement of the height of the electrical pulse on the anode of the counter.

The linear amplifier showed a very good gain stability (better than 1‰ during the course of one measurement). As the ion transit time may change by a factor of 15 from low to high values of V, the time constant of the amplifier has to be chosen very carefully. Extensive calculation [9]) indicated that a time constant of about 50 milliseconds would be sufficient to guarantee an accuracy of 1% for the relative measurement of charge.

A precision square pulse generator was built according to the principles of the model 100 pulser of Elmore [10]). The pulse amplitude was variable between 0.5 and 1000 millivolts and was measured with a comparator.

The discriminator was built according to the circuit of Lewis [11]). The threshold was adjustable for pulses between 20 and 120 V.

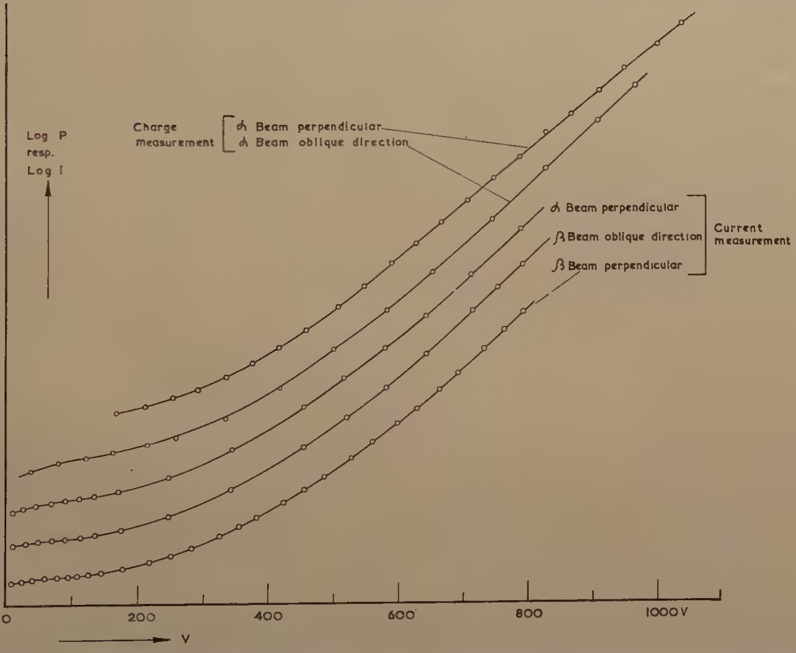

Fig. 2. Set of experimental curves for the various measurements done with one counter; the current I and the pulse height P are plotted in arbitrary units.

The high voltage supply had a stabilization factor of 1/500, while the drift amounted to less than 1‰ per hour. As the gas multiplication factor A changes very rapidly with counter voltage, it is very stringent to keep the fluctuations of this voltage within close limits.

The entire procedure for the measurement of A consisted of the following steps:

1) Measurement of the current for narrow collimated beams of α- and β-particles for counter voltages corresponding up to A equal to about 100;

2) Relative measurements of pulse height for a narrow collimated α-beam perpendicular to the counter axis for values of A from about 5 up to about 1000;

3) A check was carried out to verify that no space effects occurred. In this case the α-beam was in an oblique direction with respect to the counter axis.

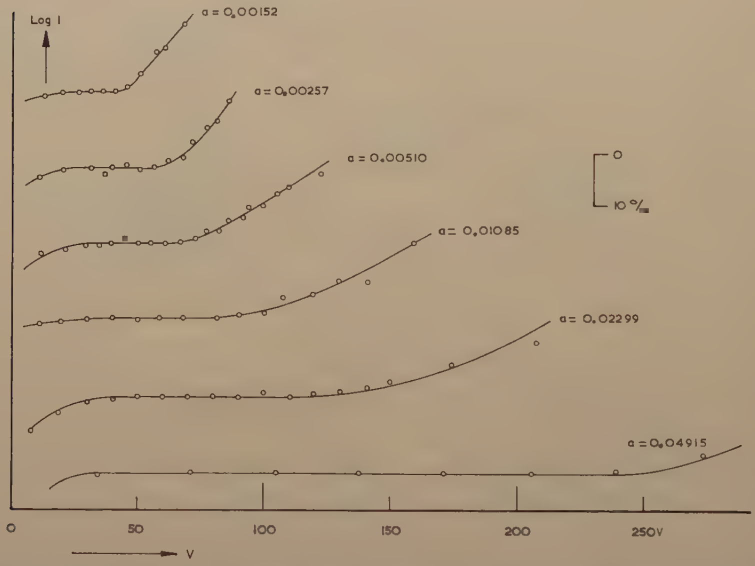

Fig. 3. Survey of the curves obtained from the current measurements in the ionization region for the counters of series B. The current I is expressed in arbitrary units. The wire radii are indicated along the curves in cm.

A set of curves from this series of measurements for one counter is given in fig. 2. For the region of low voltage the current measurements were done at very small intervals and with high accuracy. In all cases an essentially horizontal section of the *I versus V* curve was found, see fig. 3. This showed that in the region under consideration neither recombination and diffusion losses nor gas multiplication occurred. Therefore the absolute value of the gas multiplication factor could simply be determined as a ratio of two currents. The higher values of A were found by fitting the overlapping parts of the curves as obtained in step 2) and 3) with the curves as obtained in step 1).

TABLE I

The gas multiplication factor for argon-alcohol 9 : 1 measured with the various counters of series A

$a = 0.00509$ $p = 67.4$		$a = 0.00509$ $p = 107.9$		$a = 0.00517$ $p = 154.3$		$a = 0.00509$ $p = 219.2$	
V	$^{10}\log A$	V	$^{10}\log A$	V	$^{10}\log A$	V	$^{10}\log A$
100.0	0.047	120.0	0.055	130.0	0.038	138.3	0.043
120.0	0.088	142.7	0.093	164.7	0.082	210.3	0.124
165.0	0.250	190.0	0.227	211.3	0.186	242.7	0.173
223.2	0.457	213.4	0.285	258.4	0.300	277.1	0.231
258.6	0.607	261.5	0.434	282.4	0.364	294.8	0.275
281.5	0.705	307.7	0.602	328.9	0.515	336.7	0.368
331.1	0.955	331.1	0.695	376.5	0.677	379.2	0.482
365.0	1.119	355.1	0.792	400.2	0.774	414.7	0.586
391.1	1.239	377.8	0.895	424.1	0.871	449.9	0.692
417.7	1.410	403.9	1.010	470.5	1.068	484.4	0.811
447.1	1.561	427.5	1.113	492.3	1.156	519.3	0.934
476.5	1.723	451.2	1.227	538.5	1.363	553.3	1.059
502.1	1.884	474.3	1.338	583.9	1.582	588.1	1.190
533.0	2.051	495.8	1.442	607.2	1.694	631.5	1.361
561.0	2.221	518.8	1.558	654.4	1.922	672.9	1.532
587.3	2.389	539.9	1.664	677.9	2.041	689.2	1.610
616.3	2.565	565.8	1.799	726.0	2.280	724.0	1.758
643.0	2.751	588.3	1.915	747.9	2.377	791.8	2.067
670.7	2.908	611.3	2.044	772.7	2.516	839.7	2.275
698.8	3.095	630.4	2.172	816.5	2.790	924.4	2.688
740.3	3.492	735.9	2.778	863.9	3.035	966.5	2.894

The gas multiplication factor was measured for two series of counters all filled with the argon-alcohol mixture 9 : 1.

Series A: Four counters with the same value of wire radius, but with various pressures, varying between 67.4 and 219.2 mm Hg.

Series B: Six counters with the same value of gas pressure, but with various wire radii, varying between 0.00152 and 0.04915 cm.

The values of A are given in the tables I and II and are plotted graphically in fig. 4 and fig. 5.

From the measurements of series B we evaluated the function $A(r)$ from $r = 0.00152$ to $r = 0.04915$ cm for various values of $(F/p)_{min}$. The results are plotted in fig. 6. It may be seen that

TABLE II

The gas multiplication factor for argon-alcohol 9 : 1 measured with the various counters of series B

$p = 107.8$ $a = 0.00152$		$p = 107.6$ $a = 0.00257$		$p = 107.8$ $a = 0.01084$		$p = 108.0$ $a = 0.02298$		$p = 107.5$ $a = 0.0491$	
V	$^{10}\log A$	V	$^{10}\log A$	V	$^{10}\log A$	V	$^{10}\log A$	V	$^{10}\log A$
104.0	0.133	85.0	0.047	208.5	0.137	243.6	0.097	342.4	0.066
130.3	0.213	100.0	0.073	260.3	0.235	278.2	0.125	410.3	0.125
156.3	0.307	110.0	0.095	311.9	0.380	312.3	0.184	445.1	0.176
182.3	0.410	120.0	0.122	363.7	0.533	347.4	0.244	479.2	0.229
207.4	0.520	130.0	0.154	416.3	0.721	416.1	0.414	547.5	0.344
232.5	0.630	138.4	0.174	468.3	0.921	485.8	0.614	581.7	0.416
258.7	0.750	173.5	0.282	519.1	1.125	520.8	0.726	616.1	0.498
285.1	0.874	208.1	0.409	545.1	1.243	590.2	0.965	649.5	0.583
309.9	1.001	242.7	0.546	571.0	1.355	625.1	1.099	682.7	0.673
336.1	1.127	277.1	0.690	596.6	1.472	659.3	1.236	716.3	0.773
363.9	1.265	311.4	0.850	622.7	1.603	693.0	1.377	750.5	0.874
388.1	1.388	346.4	1.016	673.0	1.844	727.5	1.525	783.4	0.983
415.7	1.543	380.7	1.182	699.3	1.979	761.8	1.678	791.9	0.997
441.3	1.687	414.9	1.360	728.1	2.120	796.9	1.840	817.2	1.097
469.2	1.836	449.9	1.542	754.2	2.258	833.2	2.003	827.6	1.125
495.1	1.981	484.0	1.731	777.6	2.390	867.6	2.181	851.4	1.220
519.1	2.100	518.8	1.921	804.1	2.548	904.8	2.369	884.0	1.334
544.9	2.262	554.4	2.115	858.0	2.831	937.5	2.530	918.7	1.470
595.8	2.579	589.3	2.335	908.9	3.125	971.5	2.715	953.8	1.623
652.1	2.914	657.4	2.743	935.2	3.268	1040.5	3.131	987.9	1.756
702.0	3.263	726.1	3.142	960.4	3.423			1020.5	1.887

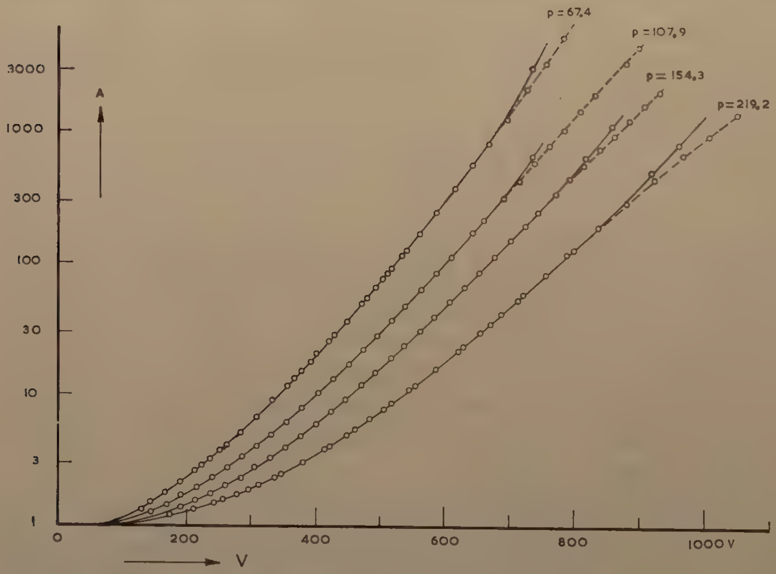

Fig. 4. Set of graphs $A(V)$ for the counters of series A. The dotted curves correspond to cases where space charge effects occur. The pressures are given along the curves in mm Hg.

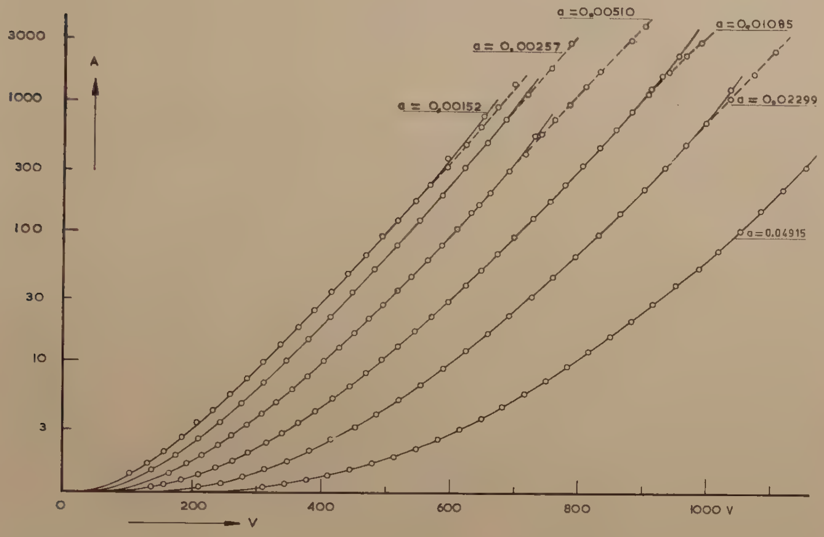

Fig. 5. Set of graphs $A(V)$ for the counters of series B. The dotted curves correspond to cases where space charge effects occur. The wire radii are given along the curves in cm.

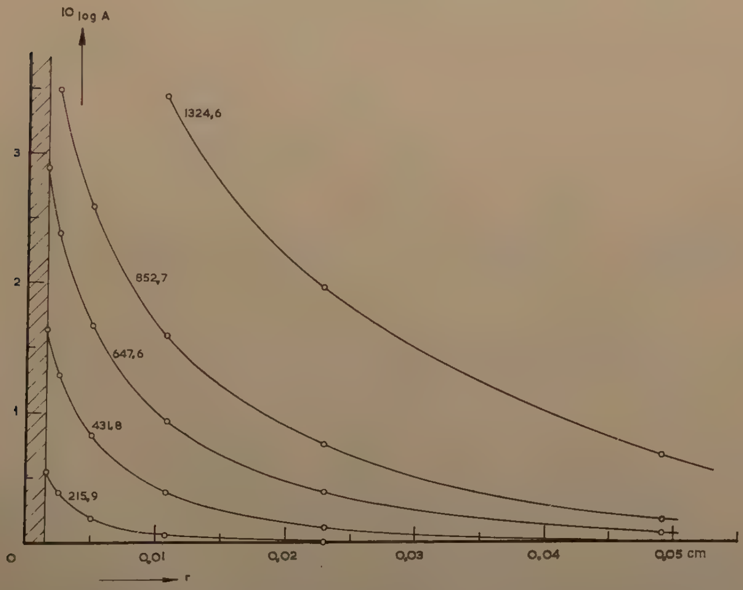

Fig. 6. Graphs giving the relation between A and the radial position r for a counter with anode radius and cathode radius of 0.00152 cm and 1.91 cm respectively. The corresponding counter voltages are indicated along the curves in volt.

gas multiplication by electron impact begins at radial distances as much as 10 to 30 times the wire diameter.

§ 3. *The ionization coefficient.* The ionization coefficient may be deduced from the family of curves $A(r)$ of fig. 6 with the aid of the relation

$$-\frac{\mathrm{d}\ln A}{\mathrm{d}r} = \alpha. \tag{5}$$

Differentiation of the function

$$\Phi = (F/p)^{-1}{}_{max}\,(ap)^{-1}\ln A$$

yields a second method for the evaluation of α/p:

$$\alpha/p = \frac{\mathrm{d}\Phi}{\mathrm{d}(F/p)_{max}}\,(F/p)^2{}_{max}. \tag{6}$$

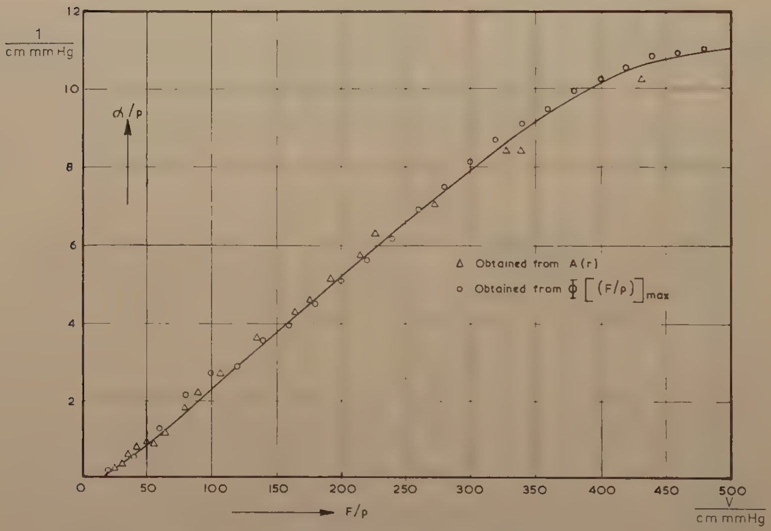

Fig. 7. α/p as a function of F/p for argon-alcohol 9 : 1.

The curve $\Phi(F/p)_{max}$ was found by taking the average of the results found for all counters of series A and B. The results from both methods are given in fig. 7 and table III. As the values of α/p all fitted smoothly on one curve, it may be concluded that within the limits of this experiment a single-valued relation between α/p and F/p exists.

TABLE III

α/p calculated from $A(r)$				α/p calculated from $\Phi\ (F/p)_{max}$			
F/p	α/p	F/p	α/p	F/p	α/p	F/p	α/p
25	0.25	193	5.07	20	0.18	280	7.45
30.5	0.35	218	5.67	40	0.53	300	8.09
37.5	0.55	227	6.23	60	1.25	320	8.65
42.5	0.76	273	7.01	80	2.12	340	9.06
51	0.90	328	8.35	100	2.70	360	9.41
55	0.92	339	8.35	120	2.84	380	9.89
64.5	1.18	432	10.2	140	3.50	400	10.2
80	1.80			160	3.92	420	10.5
90	2.17			180	4.43	440	10.8
107	2.67			200	5.05	460	10.9
138	3.55			220	5.60	480	11.0
164.5	4.24			240	6.13	500	11.0
178	4.54			260	6.85		

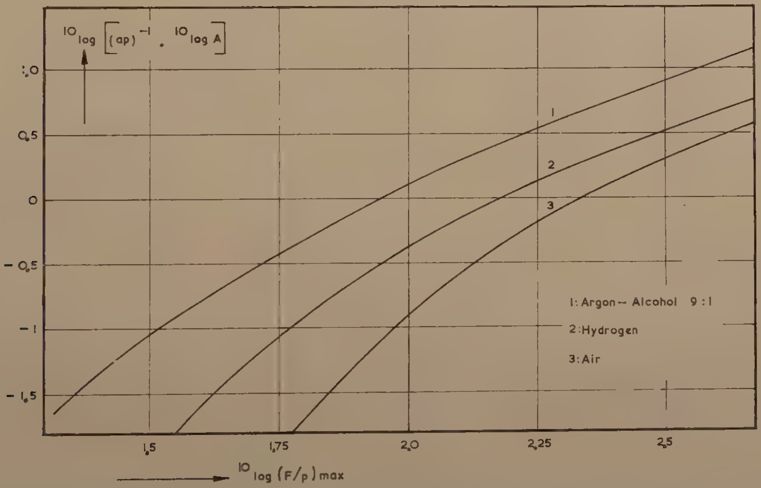

Fig. 8. $^{10}\log (ap)^{-1} . {}^{10}\log A$ as a function of $^{10}\log (F/p)_{max}$ for argon-alcohol, hydrogen and air.

In fig. 8 the values of $f = (ap)^{-1}\,{}^{10}\log A$ for all counters of both series A and B plotted *versus* $(F/p)_{max}$. For comparison the corresponding values for air and hydrogen obtained by Morton and Johnson 16) are plotted in the same graph. This graph is of practical value as it may in turn be used to calculate the gas multiplication factor for a proportional counter filled with argon-alcohol 9 : 1 with given values of a, b, p and V.

§ 4. *Effect of field inhomogeneity.* Although we found a single valued relation between α/p and F/p before, a more careful and accurate analysis of the experimental data showed the existence of small systematic differences. This is demonstrated in fig. 9 where $(1/ap)\ln A$ is plotted on an enlarged scale for the counters no. 10, 3, 7 and 9 with anode radii 0.01085 cm, 0.00510 cm, 0.00257 cm and 0.00152 cm respectively. The curves do not coincide and therefore it must be concluded that no single-valued relation between α/p and F/p exists. The differences are greatest for the counters with the smallest anode radius. For the series of counters with different pressures (series B) similar differences are found, in this case the differences being greatest for the smallest pressure. For both series the curves $f(F/p)_{max}$ are approaching monotonically the same limiting curve for the higher pressures and larger anode radii respectively.

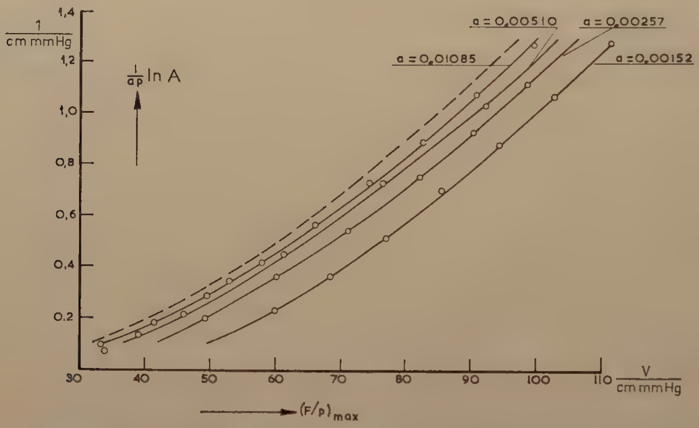

Fig. 9. Enlarged plot of $(ap)^{-1}\ln A$ versus $(F/p)_{max}$ for four counters of series B. The wire radii are given along the curves in cm.

From the fact that the curves of fig. 9 are parallel it may be concluded that the relation between the gas multiplication factor A and the counter parameters a, b, p and V will have the form

$$A = \exp\,[ap\cdot f\{V/[ap\ln(b/a)] - (F/p)_0\}], \qquad (7)$$

where $(F/p)_0$ may be a function of a, b and p but not of V.

On quite general grounds it has been shown by Rossi and Staub [14]) that for every geometry and gas pressure the gas multiplication factor for a proportional counter can be expressed as a function of only two quantities, viz. $V/\ln(b/a)$ and ap. Thus, in view of the foregoing one must conclude that $(F/p)_0$ will only be dependent on the quantity ap. We found the relation

$$(F/p)_o = 2.8/ap \text{ V/cm·mm Hg}.$$

Thus

$$A = \exp\{ap \cdot f[(F/p)_{max} - 2.8/ap]\}. \tag{8}$$

From this the value α/p may be deduced everywhere in the counter. From (6) it follows that the number of electrons $A(r)$ originating from one single primary electron that arrives at the surface of a cylinder with radius r amounts to

$$A(r) = \exp[rp \cdot f(cv/rp - 2.8/rp)] \tag{9}$$

with $c =$ half the value of the capacity of the counter per cm length. As $\alpha = \mathrm{d}\ln A/\mathrm{d}r$ one finds

$$\alpha/p = (F/p)_{red} \cdot \frac{\mathrm{d}f}{\mathrm{d}(F/p)_{red}} - f(F/p)_{red} = \frac{\mathrm{d}\Phi}{\mathrm{d}(F/p)_{red}} (F/p)_{red}{}^2, \tag{10}$$

where

$$(F/p)_{red} = F/p - 2.8/rp \tag{11}$$

and

$$\Phi = \frac{\ln A \ln b/a}{V}. \tag{11a}$$

From (9) it is evident that for small values of rp there is no equilibrium between the mean energy of the electrons of the avalanche and the electrical field. In our case this effect becomes perceptible below $rp = 2$ cm·mm Hg.

The ionization process, however, may completely be described by the introduction of a new quantity $(F/p)_{red}$, whereby α/p is a single valued function of $(F/p)_{red}$. Due to the gradient of the electrical field the electrons are lagging behind the electrical field strength on the spot, and this lag may be described by an apparent reduction of the field strength amounting to $2.8/rp$. The mean energy of the electrons is thus found to be a function of $(F/p)_{red}$:

$$\varepsilon = \varepsilon(F/p)_{red},$$

which may be written as

$$\varepsilon = \varepsilon(F/p) - \frac{\mathrm{d}\varepsilon}{\mathrm{d}(F/p)}\, 2.8(rp)^{-1} = \varepsilon(F/p) + 2.8\,\frac{\mathrm{d}\varepsilon}{\mathrm{d}r}\, F^{-1}. \qquad (12)$$

The first member denotes the energy corresponding to the situation in which equilibrium exists between the mean electron energy and the electrical field, while the second gives the apparent energy deficit due to the field inhomogeneity and is evidently determined by the quotient

$$\frac{\text{increase of mean electron energy per cm path length}}{\text{amount of energy taken from the electrical field per cm path length}}.$$

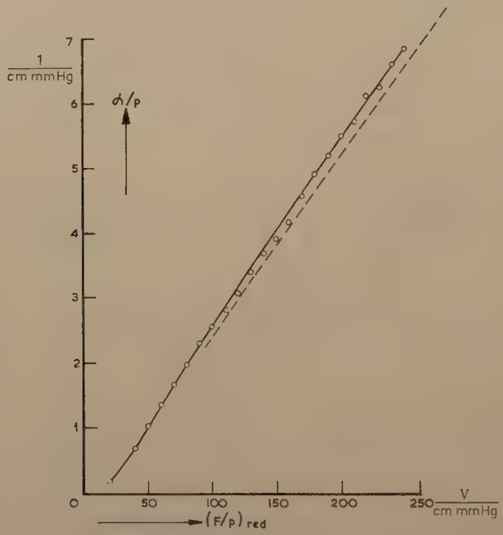

Fig. 10. α/p as a function of $(F/p)_{\mathrm{red}}$. The dotted line represents the actual value of α/p as a function of (F/p) for a counter with the following parameters:
$a = 0.00152$; $b = 1.91$ cm; $p = 107.8$ mm Hg
argon – alcohol 9 : 1; $V = 600$ V.

In fig. 10 and table IV α/p is given as a function of $(F/p)_{red}$. The dotted curve represents the value of α/p as a function of the actual value of F/p for a counter with $a = 0.00152$ cm; $b = 1.91$ cm; $p = 107.8$ mm Hg argon-alcohol 9 : 1; $V = 600$ V. The difference in α/p is relatively small, but as α enters in the exponent, the corresponding values of A may differ as much as 20%.

TABLE IV

α/p as a function of $(F/p)_{red}$

$(F/p)_{red}$	α/p	$(F/p)_{red}$	α/p	$(F/p)_{red}$	α/p	$(F/p)_{red}$	α/p
20	0.17	80	1.96	140	3.67	200	5.49
30	0.39	90	2.29	150	3.89	210	5.71
40	0.67	100	2.54	160	4.16	220	6.09
50	1.01	110	2.81	170	4.54	230	6.24
60	1.35	120	3.06	180	4.89	240	6.51
70	1.66	130	3.39	190	5.17	250	6.83

A discussion of similar effects for cylindrical geometry has been given by Loeb 15) and by Morton 16) and Johnson 16). The first author supposes that the appearance of the phenomena of non-equilibrium depends on the magnitude of F/p, while the latter authors assume that the gradient of F over a free path is the actual quantity determining this effect. At first sight this seems to be contradictory, but actually the two theories pertain two different effects.

A similar effect as cited by Loeb for the homogeneous field geometry occurs even for relatively low values of F/p. An effect of non-equilibrium of mean electron energy and of F/p was indicated by Druyvestein and Penning 17), who found that the electrons liberated from a photocathode have to pass a certain potential drop V_0 before the energy distribution becomes steady. This potential V_0 is constant for low values of F/p and starts to increase at higher F/p values. At very high values, actually when the mean electron energy reaches the value corresponding to the maximum of the $\eta - F/p$ curve, no equilibrium will be reached at any point of the discharge gap. This effect will therefore only be determined by the value of F/p and by the shape of the $\eta - F/p$ curve; however, in itself it has nothing to do with the field inhomogeneity. In the case of the cylindrical geometry an additional effect may very well be caused by the inhomogeneity of the electrical field.

Morton and Johnson assume the deviation of the equilibrium to be determined by the quantity

$$y = l(\varepsilon)\,\frac{\mathrm{d}F}{\mathrm{d}r}$$

with $l(\varepsilon)$ = mean free path for collision and ε = mean energy.

As the first factor will be proportional to $1/p$, one finds

$$y = \text{const.}\, \frac{1}{rp} F,$$

being in contradiction to the a fore-mentioned experimental results, where $(F/p)_o$ was found to be independent of the counter voltage V. However, if we modify the criterion of Morton and Johnson into

$$y = l_i(\varepsilon)\, \frac{\mathrm{d}F}{\mathrm{d}r}$$

with $l_i(\varepsilon)$ = mean free path for ionization and if we assume that in the region of (F/p) under consideration α/p is proportional to (F/p) (compare fig. 10), we find

$$y \sim 1/rp,$$

which is in complete agreement with our experimental results.

Naturally one is inclined to believe that the value of α/p as a function of $(F/p)_{red}$ will be the same as α/p as a function of F/p for homogeneous fields, since for greater values of rp the geometry can be considered as a limiting case of the cylindrical case. Strictly speaking this need not be true. But as even for very small values of rp the differences in α/p are rather small, it is most likely that if any difference exists, its magnitude will be small.

§ 5. *Rose's and Korff's calculation of A*. Rose and Korff [18]) calculated the gas multiplication factor for proportional counters. They started from the fact that the mean free path for ionization is inversely proportional to $(\varepsilon - E_i)$:

$$l_i(\varepsilon) = \beta N_m (\varepsilon - E_i)^{-1} \tag{13}$$

with ε = mean kinetic energy of the electrons in the avalanche, E_i = ionization energy and N_m = number of molecules per unit volume. By using a few simplifying assumptions they find

$$\alpha/p = \tfrac{1}{2}(N_m/p)^{\frac{1}{2}}(F/p)^{\frac{1}{2}}, \tag{14}$$

and for the gas multiplication factor

$$A = \exp \sqrt{2}(\beta N_m c a V)^{\frac{1}{2}}[(V/V_p)^{\frac{1}{2}} - 1], \tag{15}$$

where c = capacity of the counter tube per cm length and V_p = = threshold voltage for proportional multiplication.

From the experimental data of the tables I and II we tried to obtain a verification of (15). For every individual counter values of β and V_p could be found that yielded a reasonable fit of the gas multiplication factor A according to (15), with the experimental curve of A *versus* V. It appeared, however, that the values of β found for the various counters differed very much, viz. from 0.05 to 0.63×10^{-17} cm^2/V, while according to the calculation of Rose and Korff this quantity should be 1.95×10^{-17} cm^2/V.

A second and also more direct test for the theory of Rose and Korff may be done by comparison of the calculated and experimental values of α/p. In table V the calculated values of α/p for argon-alcohol 9 : 1 and our experimental data are given. It appears that very large discrepancies exist, especially for low values of F/p. Most probably this is due to the nature of their simplifying assumptions:

TABLE V

α/p as a function of F/p for argon-alcohol.
Comparison of Korff's theory and experiment.

F/p	20	50	100	200	500
α/p calculated according to Korff's formula	3.7	5.7	8.1	11.4	18.3
experimental values of α/p	0.18	0.88	2.70	5.05	11.0

1) at the moment of their creation all electrons possess a kinetic energy just equal to the ionization energy;

2) the energy loss due to inelastic impacts is negligible in the proportional discharge;

3) the energy spread of the electrons is entirely neglected.

The error due to the incorrectness of these assumptions is to be expected to be most serious for low mean electron energies. This is completely in agreement with the observed differences between the calculated and experimental values of α/p.

§ 6. *The rôle of the polyatomic gas in the proportional discharge.* The function of the polyatomic molecules may most easily be seen from the comparison of the curves of the ionization coefficients of argon, argon-alcohol and alcohol. In fig. 11 the graphs are plotted. For argon-alcohol two curves are given, viz. the value of η obtained by simply taking the average of the experimental values of $(ap)^{-1} \ln A$ for all counters and η as a function of $(F/p)_{red}$. The last one will of course be more readily comparable with the data for argon and for alcohol given by Kruithof and Penning [19]) and by Raether and Costa [20]) respectively which were both measured for homogeneous fields.

The ionization coefficient of argon-alcohol is considerably higher than for pure argon for low values of F/p. This indicates that in this region a considerable fraction of the ions is formed by collision with metastable atoms and by photoionization.

For argon the maximum of η is reached at about 200 V/cm·mm Hg, while for argon-alcohol this maximum lies at higher F/p. This will be due to the higher total cross-section for inelastic impacts of the polyatomic mixture. Also for $F/p = 250$ and higher, α/p is greater for the mixture than for pure argon. As ionization by impact with metastable atoms and photoionization becomes less important for this region, the difference must be due to direct ionization of alcohol by electronic impact. The value of σ_{ion} for alcohol is not known. The maximum value of σ_{ion} for C_2H_2 is found to be 17.5 cm^{-1} per mm Hg at 0°C [21]), this being already considerably higher than the corresponding value for argon, viz. 11.8 cm^{-1} [22]). Due to the more complex constitution of the ethyl-alcohol molecule the σ_{ion} will be greater still than for C_2H_2, and consequently probably more than twice the value of σ_{ion} for argon, and from the observed difference of argon-alcohol mixture 9 : 1 and argon we find an indication that for alcohol σ_{ion} should probably have a magnitude of about 30 cm^{-1}.

From all this we may conclude that in the region under consideration the lowering of the mean energy by inelastic impact with alcohol molecules does not play a dominant rôle. With this concentration the main change caused by the mixture of alcohol and argon is an increase of the total cross-section for ionization. This result is quite in contradiction to the suggestion of Liebson [23]) that the presence of the polyatomic constituent of the gas mixture primarily causes a decrease of electron energy due to the large cross-section for inelastic impacts. More detailed data about the result of the above-mentioned counteracting effects could be obtained from measurements with various alcohol percentages.

The curve representing α/p as a function of F/p for pure alcohol for values of F/p up to 100 V/cm·mm Hg is also plotted in the graph of fig. 11, and we clearly see that although the ionization energy of alcohol is about 5eV lower than for argon and the ionization cross-section is considerably higher, the ionization coefficient for alcohol is very much lower than for argon in this region. No measurements have been done beyond this region, but it is to be expected that for alcohol at very high F/p the value of η should be much greater than for argon; moreover the maximum of the $\eta - F/p$ curve is expected to occur at much higher F/p values, implying that the non-equilibrium effect for plane-geometry will start at a much larger field strength than with argon.

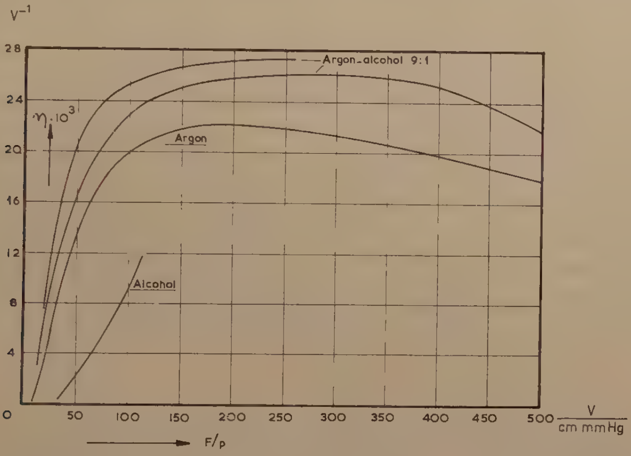

Fig. 11. The ionization coefficient η as a function of (F/p) for argon-alcohol 9 : 1; pure argon and pure alcohol. The upper argon-alcohol curve gives η as a function of $(F/p)_{red}$. The lower curve for argon-alcohol 9 : 1 is obtained by simply averaging Φ for all counters, neglecting the effect of field inhomogeneity.

§ 7. *The occurrence of space charge effects.* In the case that the ionization current was being measured with a narrow beam of β-particles perpendicular or in an oblique direction with respect to the counter axis (see fig. 3), no indication for space charge effects was found. This behaviour was predicted with an elementary approximative calculation which indicated the absence of space change effects as long as the total current per cm counter-length met with the condition

$$i \ll \frac{V^2 K_o\, 10^{-11}}{p a^2 (\ln b/a)^2} \,\mathrm{A \cdot cm} \tag{16}$$

in which K_o = ion mobility constant.

However, space charge effects for individual α-particles were found for most counters (see fig. 3). For the counter with $a = 0.00509$ cm, $b = 1.91$ and $p = 107.9$, a decrease of A from 600 to 540 occurred at a counter voltage of 735 V. The air aequivalent of the gas along the path of the α-particles was 12 mm. The residual range of the α-particles at the point where they strike the cathode amounted to 13 mm. Using the ionization data of Stetter [24]) we find a total charge density of 4×10^7 electrons per cm of the wire. This is about 10% of the static electrical charge of the anode. Thus we see a decrease of A amounting to 10% as soon as the total ionization charge constitutes a fraction of 10% of the static electrical charge.

The authors wish to thank J. G. van Santen and Joh. Blok for their assistance in the construction of the instruments used for the experiments; J. Hoogendorf for the considerable labour required to carry out the measurements and H. C. Hamers for the many helpful discussions during the experiments and the preparation of the manuscript.

Received 17th October, 1958.

REFERENCES

1) Nawijn, A., Het gasontladingsmechanisme van de Geiger-Müller teller, Thesis. Delft 1943; F. Huber, e.a., Helv. Phys. Acta **19** (1946) 207; F. Alder, e.a., Helv. Phys. Acta **20** (1947) 87; S. A. Korff, Nuclear Counters, D. v. Nostrand, New York, 1947; S. A. Korff and R. D. Present, Phys. Rev. **65** (1944) 274; H. den Hartog, Telbuizen met Argon en Alcohol, Thesis Amsterdam, S.U., 1948; M. E. Rose and S. A. Korff, Phys. Rev. **59** (1941) 850.

2) Cummings, C. and W. Bleakney, Phys. Rev. **57** (1940) 1072.

3) Kruithof, A. A. and F. M. Penning, Physica **3** (1936) 515, Physica **4** (1937) 430.

4) Schmieder, F., Z. Elektrochemie **36** (1930) 700.

5) Tate, J. T. and P. T. Smith, Phys. Rev. **39** (1932) 270.

6) Loeb, L. B., Basic Processes of Gaseous Electronics, California, 1955.

7) Rose, M. E. and S. A. Korff, Phys. Rev. **59** (1941) 850.

8) Rose, M. E. and W. E. Ramsay, Phys. Rev. **61** (1942) 198; M. E. Rose and W. E. Ramsay, Phys. Rev. **61** (1942) 504.

9) Duuren, K. van, The proportional discharge in counters, Thesis Amsterdam V.U., 1952.
10) Elmore, W. C. and M. Sands, Electronics, MacGraw Hill, New York, 1949.
11) Lewis, W. B., Electrical Counting, Cambr. Univ. Press, 1948.
12) Curran, S. C., J. Angus and A. L. Cockroft, Phil. Mag. **40** (1949) 36.
13) Diven, B. C. and B. Rossi, M.D.D.C., 282, (L.A.D.C.-148), U.S. Atomic Energy Commission.
14) Rossi, B. and H. Staub, Ionization chambers and counters, Mac Graw Hill, New York, 1949, p. 73.
15) Loeb, L. B., Basic Processes of Gaseous Electronics, Univ. of California Press, Berkeley and Los Angelos, 1955, p. 747.
16) Morton, P. L., Phys. Rev. **70** (1946) 358; G. W. Johnson, Phys. Rev. **73** (1948) 284.
17) Druyvestein, M. J. and F. M. Penning, Mechanism of Electrical Discharges in Gases of Low Pressure, Rev. Mod. Phys. **12** (1940) 98.
18) Rose, M. E. and S. A. Korff, An Investigation of the Properties of Proportional Counters, Phys. Rev. **59** (1941) 850.
19) Kruithof, A. A. and F. M. Penning, Determination of the Townsend ionization coefficient for pure argon, Physica **3** (1936) 515.
20) Raether, H., Z. Phys. **107** (1937) 91.
21) Tate, I. P. and P. T. Smith, Phys. Rev. **39** (1932) 270.
22) Bleakney, W., Phys. Rev. **36** (1930) 1303.
23) Liebson, S. H., Phys. Rev. **72** (1947) 602.

Appl. sci. Res. Section B, Vol. **7**

A DIAGRAM FOR THE DESCRIPTION OF PHOTOCONDUCTIVITY

by H. J. DIRKSEN

Physical Laboratory of the National Defence Research Council T.N.O.
the Hague, Netherlands

Summary

In a diagram, briefly called E–B diagram, a discrete electron level of a photoconductor is represented by a point of which the E-coordinate is a measure for the electron occupation in thermal equilibrium and of which the B-coordinate is a measure for the electron occupation under illumination. From the location of the different points in this E–B diagram the change of the electron distribution caused by illumination can be read for different temperatures. The two parts of the E–B diagram where this change is pronounced are called the inversion regions; a material, such as CdSe, that has its discrete levels in these regions will show a characteristic photoconductivity 1).

List of symbols

c, i, v	indices referring respectively to the conduction band, a discrete electron level and the valence band
E	energy
E_F	Fermi energy
N	(effective) density of electron levels
N_d	concentration of donors
n	concentration of free electrons
n_α	concentration of free electrons when thermal equilibrium prevails
p	concentration of free holes
p_α	concentration of free holes when thermal equilibrium prevails
n_i	concentration of electrons bound in the discrete level of energy E_i
T	absolute temperature
k	Boltzmann's constant
α	thermal excitation coefficient
β	recombination coefficient
a	absorption coefficient of the radiation
d	thickness of the crystal
L	diffusion length of electrons and holes in the material

J_0	excitation rate of free electrons (and holes) per s in a thin surface layer of 1 m^2 area
t	time in seconds
τ_n	time constant of photoelectrons
B_i	$= \ln (\beta_{iv}/\beta_{ci})$
B_J	$= \ln (n/p)$
α_n-region	part of the E–B diagram in which the electron concentration n_i depends on E_i, n and T
α_p-region	part of the E–B diagram in which the electron concentration n_i depends on E_i, p and T
β-region	part of the E–B diagram in which the electron concentration n_i depends on B_i and B_J
L_n	borderline between the α_n- and β-region of the E–B diagram
L_p	borderline between the α_p- and β-region of the E–B diagram

§ 1. *Introduction.* Consider a homogeneous photoconductor that is illuminated with radiation in the fundamental absorption band. The thickness d of the material is chosen such that

$$1/a \ll d \ll L. \tag{1.1}$$

Formula (1.1) means that nearly all the photoelectrons and holes are generated close to the surface and that in the crystal all the electron concentrations are practically independent of position. If therefore J_0 electrons and holes per s are optically generated in a thin surface layer of 1 m^2 area, we may proceed as if J_0/d electrons and holes per m^3 per s are homogeneously generated in the crystal of thickness d. The different transition processes of the electrons in the crystal to and from a discrete electron level are shown in the well-known energy diagram of fig. 1.

The number of transitions per m^3 per s as represented by one of the arrows in fig. 1 is given by the product of the transition coefficient (α or β), the concentration of available electrons and the concentration of available (unoccupied) levels. The difference between the transition rates to and from a given discrete level i equals the increase per s of the concentration n_i, or

$$\mathrm{d}n_i/\mathrm{d}t = (\beta_{ci}n + \alpha_{vi}N_v)(N_i - n_i) - (\beta_{iv}p + \alpha_{ic}N_c)n_i. \tag{1.2}$$

The increase per second of the free electron concentration n equals the quasi-homogeneous excitation rate of J_0/d electrons per m^3 per s added to the total thermal excitation rate of electrons from the different discrete levels i minus the recombination rate of free electrons to the unoccupied discrete levels i (we neglect the direct recombination of electrons and holes), or

$$\mathrm{d}n/\mathrm{d}t = J_0/d + \sum_i \alpha_{ic} n_i N_c - n \sum_i \beta_{ci}(N_i - n_i). \tag{1.3}$$

The analogous equation for the free holes is

$$\mathrm{d}p/\mathrm{d}t = J_0/d + \sum_i \alpha_{vi}(N_i - n_i) N_v - p \sum_i \beta_{iv} n_i. \tag{1.4}$$

If there is no net charge density in the crystal, the different concentrations must satisfy the neutrality equation

$$N_d + p = n + \sum_i n_i \tag{1.5}$$

with N_d = concentration of donors.

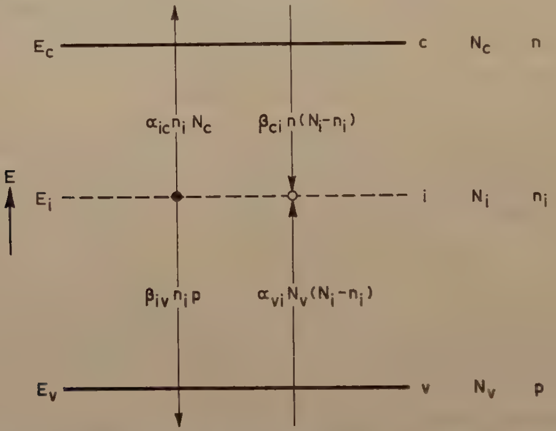

Fig. 1. Energy diagram showing the electron transitions to and from a discrete electron level i. The optical excitation of electrons from the valence band to the conduction band is not indicated.

Even for the stationary state and a small number of electron energy levels the solution of the equations (1.2) to (1.5) becomes complex [2]) [3]). If the different concentrations n_i did not change with time, temperature and light intensity or if these changes could be neglected, the photoconductive behaviour would be simply described by the equation

$$n = \tau_n[1 - \exp(- t/\tau_n)](J_0/d + \sum_i \alpha_{ic} n_i N_c) \tag{1.6}$$

where

$$\tau_n = [\sum_i \beta_{ci}(N_i - n_i)]^{-1},$$

and a similar equation for the free holes p. Complications are due to the fact that the concentrations n_i are functions of time, temperature and illumination. For this reason we tried to deduce in a more direct way, without solving the equations, the general behaviour of a photoconductor from its set of constants E, α and β. This is done in an E–B diagram in which the different discrete electron levels are represented as points. The coordinates of a point indicate respectively the concentration n_i in thermal equilibrium without illumination and under illumination at the absolute zero of temperature. From the location of the points in the E–B diagram the different concentrations n_i can be considered as a function of temperature and light intensity.

§ 2. *E–B diagram.* Under stationary conditions (1.2) reduces to

$$n_i/(N_i - n_i) = (\beta_{ci}n + \alpha_{vi}N_v)/(\beta_{iv}p + \alpha_{ic}N_c). \qquad (2.1)$$

If $\alpha_{vi}N_v/\beta_{ci}n$ and $\alpha_{ic}N_c/\beta_{iv}p \ll 1$ (low temperatures), (2.1) may be written as

$$n_i/(N_i - n_i) \simeq \beta_{ci}n/\beta_{iv}p. \qquad (2.2)$$

If we define two quantities B_i and B_J such that

$$B_i = \ln\,(\beta_{iv}/\beta_{ic}), \qquad (2.3)$$

$$B_J = \ln\,(n/p), \qquad (2.4)$$

we can write equation (2.2) in a form

$$n_i/(N_i - n_i) = \exp[-\,(B_i - B_J)_0], \qquad (2.5)$$

that is similar to the expression for thermal equilibrium in the absence of illumination

$$n_i/(N_i - n_i) = \exp[-\,(E_i - E_F)/kT]. \qquad (2.6)$$

The index 0 in $(B_i - B_J)_0$ of (2.5) refers to $T = 0$°K. In what we call an E–B diagram with the two axes $(E - E_F)/kT$ and $(B - B_J)$, every discrete electron level i is represented by a point of which the $(E_i - E_F)/kT$ ordinate is a measure by (2.6) for the electron occupation in thermal equilibrium and of which the

$(B_i - B_J)$ ordinate is a measure for the stationary electron occupation under illumination.

At higher temperatures (2.5) is no longer correct. Formally there exists a number on the $(B - B_J)$-axis that in (2.5) gives the correct answer. This number is indicated by the symbol $(B_i - B_J)_T$ and can be found from the formal expression

$$n_i/(N_i - n_i) = \exp[-(B_i - B_J)_T] \tag{2.7}$$

and equation (2.1). We find

$$(B_i - B_J)_T = (B_i - B_J)_0 - \ln (1 + \alpha_{vi}N_v/\beta_{ci}n)/(1 + \alpha_{ic}N_c/\beta_{iv}p). \tag{2.8}$$

In our E-B diagram we distinguish with the aid of (2.8) three regions

1) Both $\alpha_{vi}N_v/\beta_{ci}n$ and $\alpha_{ic}N_c/\beta_{iv}p \ll 1$ and therefore

$$(B_i - B_J)_T \simeq (B_i - B_J)_0. \tag{2.9}$$

This region of the E–B diagram we call the *β-region*; only recombination processes occur here. The concentration n_i depends on the quantity B_i and the quotient n/p.

2) $\alpha_{vi}N_v/\beta_{ci}n \ll 1 \ll \alpha_{ic}N_c/\beta_{iv}p$ and therefore

$$(B_i - B_J)_T \simeq (E_i - E_F)/kT - \ln (n/n_\alpha). \tag{2.10}$$

n_α is the concentration of free electrons in thermal equilibrium. This region of the E–B diagram we call the *α_n-region*; the concentration n_i depends on E_i, the temperature T and the concentration of free electrons n.

3) $\alpha_{ic}N_c/\beta_{iv}p \ll 1 \ll \alpha_{vi}N_v/\beta_{ci}n$ and therefore

$$(B_i - B_J)_T \simeq (E_i - E_F)/kT + \ln (p/p_\alpha). \tag{2.11}$$

p_α is the concentration of free holes in thermal equilibrium. This region of the E–B diagram we call the *α_p-region*; the concentration n_i depends on E_i, the temperature T and the concentration of free holes p.

The case $1 \ll \alpha_{vi}N_v/\beta_{ci}n$ and $1 \ll \alpha_{ic}N_c/\beta_{iv}p$ is physically non-existent.

The statistical consideration of Rose [4]) and of Broser-Warminsky [5]) apply only to discrete electron levels that are represented in the α_n- or α_p-region of the E-B diagram; for a level i

in the α_n-region

$$n_i/(N_i - n_i) \simeq \beta_{ci}n/\alpha_{ic}N_c = (n/N_c)\exp[(E_c - E_i)/kT]. \tag{2.12}$$

The three regions in the E–B diagram are separated by two straight lines in the direction + 1. The borderline between the α_n- and β-region is the line L_n. For the points of this line we have $\alpha_{ic}N_c = \beta_{iv}p$,

$$(B - B_J) = (E - E_F)/kT - \ln(n/n_\alpha). \tag{2.13}$$

Similarly the equation for line L_p between the α_p- and β-region is

$$(B - B_J) = (E - E_F)/kT + \ln(p/p_\alpha). \tag{2.14}$$

From (2.10) and (2.13) it follows that every point in the α_n-region with the same $(E_i - E_F)/kT$ value has the same $(B_i - B_J)_T$ value and therefore the same electron occupation as the point on line L_n; the same applies to the α_p-region. From this follows the construction of $(B - B_J)_T$ as indicated in fig. 2.

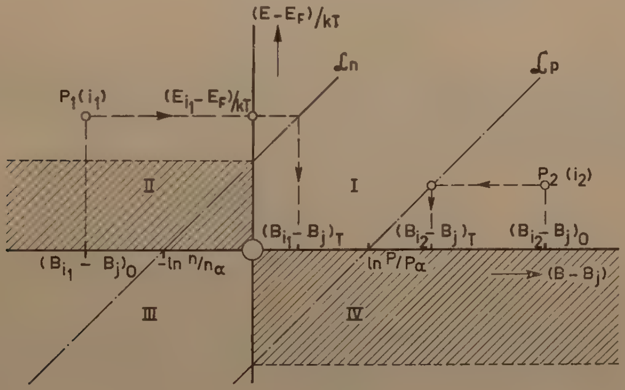

Fig. 2. E–B diagram. To the left of L_n lies the α_n-region, between L_n and L_p the β-region and to the right of L_p the α_p-region. The two shaded parts are the inversion-regions. The constructions of the point $(B_i - B_J)_T$ on the $(B - B_J)$-axis is indicated by arrows.

§ 3. *Illumination- and temperature dependence of* n_i. We assume as a first approximation that E_F does not change with temperature and that p/n is constant for different intensities of illuminations. The values $-\ln(n/n_\alpha)$ and $\ln(p/p_\alpha)$, where L_n and L_p cross the $(B - B_J)$ axis, indicate the extension of the β-region. This region expands with increasing light intensity and contracts for higher temperatures. From (2.12) it follows for points in the α_n-region that

$$(B_i - B_J)_T \simeq -(E_c - E_i)/kT + \ln(N_c/n), \tag{3.1}$$

and similarly for points in the α_p-region that

$$(B_i - B_J)_T \simeq (E_i - E_v)/kT + \ln(p/N_v). \tag{3.2}$$

These two equations give the electron concentration in the corresponding levels as a function of temperature T and illumination-intensity (via n or p). The regions of the E–B diagram where the electron occupation after illumination changes from nearly filled to nearly empty or vice versa we call the inversion regions. At 0°K the whole quadrants II and IV are inversion regions. At increasing temperature these inversion regions become smaller, the ordinates $(E_i - E_F)/kT$ of the points also becoming smaller. A point leaves the inversion region and the electron occupation of the corresponding level changes strongly as soon as

$$(B_i - B_J)_T \simeq 0. \tag{3.3}$$

At still higher temperature this expression changes in sign. This temperature depends on the intensity of illumination (via n or p) and follows with (3.3) from (3.1) and (3.2):

$$(E_c - E_i)/kT \simeq \ln(N_c/n) \tag{3.4}$$

and

$$(E_i - E_v)/kT \simeq \ln(N_v/p). \tag{3.5}$$

§ 4. *Classification of photoconductors.* We believe that the E–B diagram is suitable for the classification of photoconductors and of different types of photoconductive behaviour. As examples we briefly mention three cases:

1) the points lie somewhere along the line through the origin in the direction $+1$;

2) the points lie somewhere along the line through the origin in the direction -1;

3) all the points lie in the β-region and remain there. We dealt already with the first case; the different n_i do not change, no redistribution of electrons occurs, and photoconductivity is described by (1.6). In the second case a strong redistribution occurs. All the

electron processes which are associated with this redistribution are slow. The temperature dependence of this redistribution is given by (3.4) and (3.5). A more than linear increase of n is associated with the fact that the number of points in the β-region is a function of light intensity.

We will show that an increase more strong than linear is not possible in the third case. The stationary equations are now

$$n_i/(N_i - n_i) = \beta_{ci} n/\beta_{iv} p, \tag{4.1}$$

$$n = \frac{J_0/d}{\sum_i \beta_{ci}(N_i - n_i)}, \tag{4.2}$$

$$n = p + N_d - \sum_i n_i, \tag{4.3}$$

respectively derived from (1.2), (1.3) and (1.5) for $\alpha = 0$. Substitution of (4.1) into (4.2) and (3.4) gives the two equations

$$n = \frac{J_0/d}{\sum_i \beta_{ci} N_i/(1 + \beta_{ci} n/\beta_{iv} p)} \tag{4.4}$$

and

$$n = \frac{N_d - \sum_i N_i/(1 + \beta_{iv} p/\beta_{ci} n)}{1 - p/n}. \tag{4.5}$$

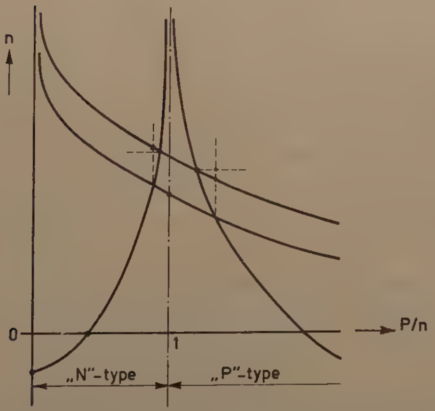

Fig. 3. Diagram of the equations (4.4) and (4.5) for two different values of J_0.

These two expressions for n are represented in fig. 3 as a function of p/n for two different values of J_0. With the help of fig. 3 we see that only the minorities can increase in a more than linear way in contrast to the majority carriers.

Thanks are due to prof. dr. M. J. Druyvesteijn of the Technological University Delft, for many helpful discussions. Acknowledgment is also due to the chairman of the National Defence Research Council T.N.O., for permission to publish this paper.

Received 20th October, 1958.

REFERENCES

1) Dirksen, H. J., Fotogeleiding in Cadmium Selenide, Thesis Delft 1958.
2) Duboc, C. A., Brit. J. Appl. Phys., Suppl. No. 4 (Luminescence), 1955, p. 107
3) Dirksen, H. J. and O. W. Memelink, Appl. Sci. Res. B4 (1954) 205.
4) Rose, A., Phys. Rev. **97** (1955) 322.
5) Broser, I. und R. Warminsky, Ann. Phys. **16** (1955) 361.

Appl. sci. Res. Section B, Vol. 7

MEASUREMENTS ON HALOGEN–QUENCHED COUNTERS

by D. H. LE CROISSETTE *)

Electrical Engineering Department, Drexel Institute of Technology,
Philadelphia, Pa., U.S.A.

Summary

Measurements have been made of the gas amplification factor ot a cylindrical counter filled with neon-bromine and argon-bromine mixtures. Information has been obtained as to the mechanism of gas multiplication when the gas amplification is less than 100. The transit time of electrons across a tube of average dimensions operated in the proportional region was found to be less then 0.2 microseconds. The duration and the mechanism of the discharge build-up was found to change with the amount of bromine present in the counter.

§ 1. *Introduction.* A study of the discharge mechanism of G.M. counters involves a knowledge of the basic gas discharge phenomena which contribute secondary electrons to the initial avalanches. By observations of the pulses upon the passage of ionizing particles Colli and Facchini[1]) have indicated the elementary processes acting in counters filled with very pure argon and argon mixed with a small proportion of carbon dioxide. They were able to deduce the nature of the secondary mechanism acting in the proportional region and have made a great contribution to the understanding of these counters. In halogen-quenched counters the proportional region is only of small extent, but similar measurements of the gas amplification and observations of the discharge build-up time allow deductions of the fundamental discharge process to be made.

§ 2. *Apparatus.* As with previous measurements, observations have been made on the pulse which was produced when ionizing particles were passed through the counter. The apparatus which was used in the production of the initial ionization has been previously described[2]). It produced a pulse of electrons of energy about 40 keV by sweeping a focussed electron beam across a small mica-covered aperture in the end face of a demountable evacuated tube. The system was arranged so that the electron beam was deflected in unison with the spot on the cathode ray tube of an oscillograph. Exact synchronisation between the time-base sweep and the pulse can be achieved and, since the pulse occurred after the time-base had been initiated, both the ionizing pulse and the pulse collected from the anode wire of the counter could be viewed at the same time on the same time-base sweep.

---

*) This work was performed at the Physics Department, Southampton University England.

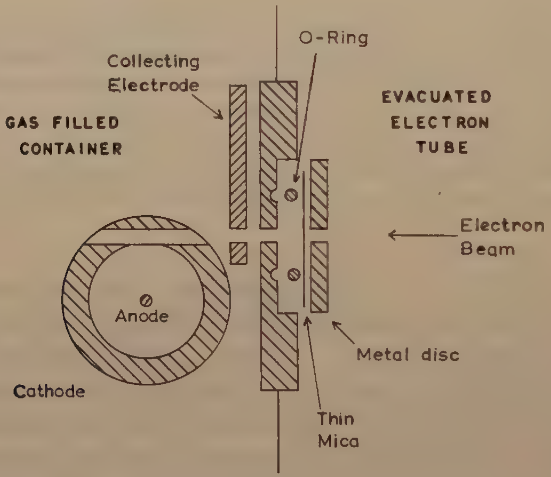

Fig. 1. Exploded view of the seal between the electron tube and the gas-filled container.

Ionization of the gas in the counter took place close to the cathode as shown in fig. 1. In this apparatus the cathode diameter was 1.95 cm and provision was made for varying the diameter of the anode wire. The counter and container were machined from stainless steel and all the insulators inside the container were made of pyrex glass. The counter was filled with mixtures of argon, neon and bromide from a conventional filling system [3]).

The collecting electrode shown in fig. 1 intercepted a small proportion of the electron pulse and produced an indication on the oscillograph screen at the time of the initial ionization. The charge in each pulse was made small to reduce the effects of space charge in the counter. When the counter was operated as an ionization chamber the charge collected by the anode wire was about 10^{-13} coulomb. The charge intercepted by the collecting electrode was of about the same value.

The oscillograph amplification was augmented by a pre-amplifier and the total gain of the system was $10^4 \times$ with a rise time of less than 0.07 microseconds. The input stage of the pre-amplifier was a cathode follower of low input capacitance and the time constants throughout the system were made less than the rise time of the ionizing electron pulse. Thus the profile of the pulse from the collecting electrode as displayed on the oscillograph was a true representation of the ionizing pulse of electrons. Furthermore, the structure of the leading edge of the pulse collected from the anode wire gave an indication of the time of build-up of the discharge and the onset of delayed production of secondary electrons. By switching in additional capacitors in the cathode follower input stage of the pre-amplifier, the time constant of the circuit could be increased to be above the time of observation of one time base sweep (1 to 10 microseconds). The heights of the pulse collected from the anode wire under these conditions was proportional to the total number of ion pairs produced in the counter.

Operation of the counter was confined to the ionization and proportional regions. Bromine is very electronegative and negative ion formation is likely to occur when the field across the counter is small. However, in all the measurements reported here, saturation in the ionization region was achieved and the resulting output pulse from the anode wire was used as a measure of the initial ionization in the gas. The extra ionization occurring in the proportional region caused a proportionate increase in the height of the pulse recorded from the anode wire and the gas amplification factor is equal to the ratio of the heights of the pulses in the proportional and the ionization chamber regions.

§ 3. *Measurements*. The gas amplification factor was measured as a function of the voltage applied to the counter for gas filling mixtures of neon-bromine and argon-bromine. Fig. 2 and 3 show some measured curves for the above mixtures together with the calculated values of M for the rare gases alone. All the measurements were limited to the range where the gas amplification was below 100 so that the processes active in the initial discharge could be studied.

Neon-bromine mixtures. The metastable potentials of neon (16.53 and 16.62 V) are above the ionization potential of bromine and a metastable neon atom has a high probability of ionizing a bromine molecule. Consequently, ionization of the gas by this mechanism is likely to take place at a lower value of the electric field E than that required for direct ionization by collision.

Druyvesteyn and Penning [4]) have given curves of the variation in η (ionization produced by one electron in one cm in unit field) as the reduced electric field E/p is varied. The ionizing power of the electron may be calculated for any point in the counter by finding the value of η for the appropriate field. A curve of ηE (Townsend's first coefficient α) may then be plotted against the radius r.

The gas amplification factor is given by

$$M = \exp \int_b^a \eta E \, \mathrm{d}r,$$

where a and b are the anode and cathode radii respectively and may be found by measuring the area under the curve of the above graph. This calculation assumes that the velocity of an electron is determined by the value of the electric field at that point. Close to the anode wire the electric field is varying so rapidly that the electron velocity does not reach the terminal value appropriate to the value of the field. The calculated value of the gas amplification factor may be as much as 10% high because of this effect.

The gas amplification factor has been calculated for pure neon, plus 0.1% argon and neon plus 6% argon as shown in fig. 2. In the case of the gas mixtures, allowance has been taken of the effect on the value of η of ionizing collisions of the second kind between metastable neon atoms and argon atoms as given by Druyvesteyn and Penning. Fig. 2 shows that neon plus 0.16% bromine is approximately equivalent to neon plus 6% argon.

Argon-bromine mixtures. The values of the gas amplification factor for pure argon have also been calculated from the figures given by Druyvesteyn and Penning [4]). The calculated values are plotted in fig. 3 together with the measured values for argon plus various amounts of bromine. The gas amplification for the mixtures is considerably higher than for pure argon, indicating that the ionization potential of bromine is less than the metastable potentials of argon [5]) and that ionizing collisions of the second kind are contributing electrons to the discharge.

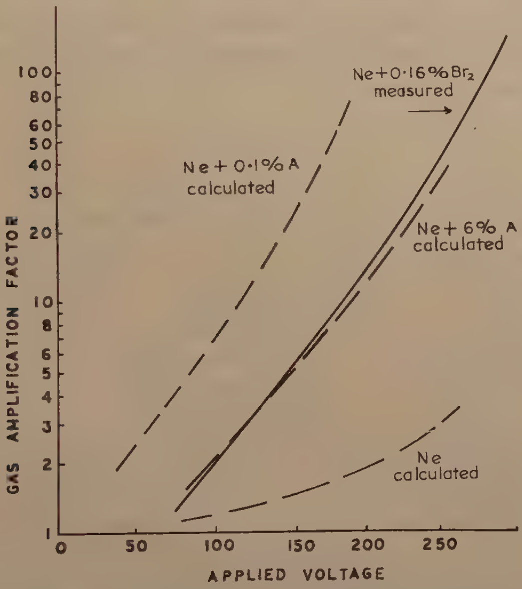

Fig. 2. Measured and calculated curves of gas amplification factor vs applied voltage for neon-bromine mixtures.

For mixtures of argon and bromine, the graph of gas amplification factor departs from a smooth curve at a certain critical value which depends on the amount of bromine present. At this voltage, the time of build-up of the discharge starts to increase. It is believed that resonance radiation in the gas mixture is responsible for the additional production of electrons and this phenomena is discussed later.

Discharge build-up times. Below the critical value of gas amplification factor, where the curve departs from its smooth form, the time taken for the discharge to develop was measured to be less than 0.2 microseconds for both neon-bromine and argon-bromine mixtures containing more than 0.08 mm Hg of bromine.

As the gas amplification factor was increased above this critical value, the discharge build-up time increased to about 0.5 microseconds.

Transit times. Throughout the whole of the measurements, employing a counter of diameter 1.95 cm and an anode wire of 1.0 mm diameter, the time of transit of the electrons across the counter in the proportional region was less than the resolving time of the apparatus (0.2 microseconds). The total pressure of neon-bromine or argon-bromine gas mixtures was either 50 or 100 mm Hg throughout the experiments.

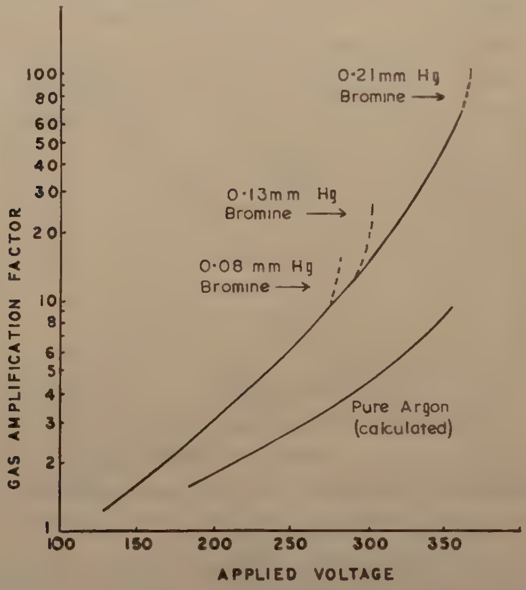

Fig. 3. Measured and calculated curves of gas amplification factor vs applied voltage for argon-bromine mixtures.

§ 4. *Discussion. a)* Gas amplification factor low. The onset of the proportional region in neon-bromine and argon-bromine mixtures is the result of the production of electrons in the gas by collisions of the second kind between metastable rare gas atoms and bromine molecules. Since the time taken for the discharge to develop is less than 0.2 microseconds, the collision cross-section of bromine for this process must be considerably higher than that indicated by a previous measurement [3]). A recalculation of the data given in[3]) has shown that the cross-section of bromine for the destruction of the neon metastable state with ionization of the bromine molecule is at least twenty times that of argon.

b) Gas amplification factor high. When the graph of gas amplification factor against applied voltage departs from the smooth curve at a critical value, another mechanism is creating ion pairs in the gas mixture. It is considered that collisions of the second kind are occurring between argon atoms which have been excited by resonance radiation and molecules of bromine, resulting in the ionization of the latter. Colli and Facchini[1]) have shown that photons of resonance radiation are emitted by argon atoms which have been excited in a discharge. Emitted photons which have an energy of 11.62 or 11.82 eV are capable of exciting other argon atoms in the gas. These newly excited atoms, in turn, will emit photons of the same energy after remaining in an excited state for about 10^{-8} seconds and the process will continue. In very pure argon the radiation will be absorbed and re-emitted many hundred times, giving a time delay of a few microseconds between the initial avalanche and the production of an electron when the photon reaches the cathode surface.

In argon-bromine mixtures, resonance radiation is unlikely to reach the cathode. The cross-section of the bromine molecule for de-excitation of a metastable or excited argon atom is sufficiently great (greater than 10^{-16} cm^2) that only a few atoms take part in the chain of reasonance chain in the gas mixtures used here before a bromine molecule is finally ionized. Thus new avalanches will be formed about 10^{-7} seconds after the initial electrons reach the high field region near the anode.

It is considered that the spreading of the discharge down the counter wire in the proportional region is a result of the above mechanism. Each secondary avalanche will introduce a time delay of about 10^{-7} seconds making the total time for the discharge spread considerably longer than for argon-alcohol counters.

An increase in the proportion of bromine in an argon-bromine counter has three effects:

1. The mean agitation energy of the electrons will be reduced.
2. Metastable and excited atoms of argon will be de-excited more rapidly in the gas mixture.
3. Photons which are produced in the discharge upon the de-

excitation of the rare gas atoms will be absorbed in a shorter distance.

All three factors have the effect of decreasing the number of electrons produced by secondary processes but a full analysis is not possible since the cross-sections for the various processes are not known with sufficient accuracy.

Applications to halogen-quenched counters

1. Transit time of an electron across a tube of normal dimensions operating above the ionization chamber region is less than 0.2 microseconds.

2. The avalanche which is produced when the tube is operated with a gas amplification factor of less than 10 has a build-up time of less than 0.2 microseconds.

3. When the gas amplification is above 10, the additional electrons are produced as a result of resonance radiation. A photon produced in the discharge excites a chain of rare gas atoms untill de-excitation of one of these atoms takes place with consequent ionization of a bromine molecule. This is a process involving time delays of between 0.1 and 1.0 microseconds and is responsible for the long build-up time of the discharge.

Received 7th February, 1959.

REFERENCES

1) Colli, L. and U. Facchini, Phys. Rev. **88** (1952) 987.
2) Le Croissette, D. H., Electronic Engng **28** (1956) 356.
3) Le Croissette, D. H. and J. Yarwood, J. Sci. Instrum. **28** (1951) 225.
4) Druyvesteyn, M. J. and F. M. Penning, Rev. Mod. Phys. **12** (1940) 87.
5) Kuiper, J. and D. van Zoonen, Appl. Sci. Res. **B4** (1954) 235.

Appl. sci. Res. Section B, Vol. 7

SCATTERING OF A PLANE MONOCHROMATIC WAVE BY A SYSTEM OF STRIPS

by K. SÆRMARK

Physics Department, Technical University of Denmark, Copenhagen, Denmark.

Summary

The diffraction of a plane wave by a general system of strips is treated by means of separation of variables. A new addition theorem for Mathieu functions is used to satisfy the boundary conditions on the strips. Numerical calculations are performed for the case of two strips lying in the same plane, the boundary conditions being $\text{grad}_n \psi = 0$, while the angle of incidence of the plane wave is arbitrary. The transmission coefficient for a system of two slits in a plane, perfectly conducting screen is calculated for a range of values of the parameters. An approximate expression relating the transmission coefficient for the system of two slits to the transmission coefficient for a system of a single slit is given. As the distance between the two slits is increased, the transmission coefficient for the system of two slits *very* rapidly becomes nearly identical with the transmission coefficient for a single slit.

§ 1. *Introduction.* The theory of the diffraction of plane, monochromatic waves by obstacles of different kinds has in the later years been the subject of numerous papers, and many elegant mathematical methods have been taken into use [1]). Among these we may mention the differential-integral equations of Bouwkamp[2]), the Wiener-Hopf technique as used for instance by Baldwin and Heins [3]), the Fourier-method used by Hönl [4]) and the variational principles of Schwinger [5]). The more straightforward technique of separation of variables is often discarded as being too tedious and unsuited to the handling of scattering of waves by obstacles of a complicated geometrical shape. However, it seems that also the more refined mathematical methods of attack are well-suited only in the case of simple geometrical shapes of the scattering objects (e.g. the two-dimensional problem of the diffraction of a plane wave by an infinitely long slit in a thin, plane screen or by an infinite, periodic array of such slits). Furthermore, in case the variational principles are used, it may be difficult to estimate the degree of accuracy obtained.

In this paper we will treat the two-dimensional scattering of a plane monochromatic wave by a system of strips using the technique of separation of variables. In the derivation of the equations we will restrict ourselves to the consideration of only two strips, the configuration of which will be almost arbitrary. We assume that their axes are parallel and that the strips do not overlap in a sense to be specified in § 2. The treatment may readily (at least formally) be extended to three or more strips.

§ 2. *Formulation of the problem.* We consider two strips A and B of infinite length with their axes parallel to the z-axis and make the non-essential assumption that they are of equal width $2b$. The one, A, will be placed in the $x-z$ plane extending from $x = -b$ to $x = +b$. The other, B, will be placed with its axis at the point with the polar coordinates (l, u) (see fig. 1) and the angle between the two strips will be called t. We further assume that the strips do not overlap in the sense that a circle with centre at one strip-axis and radius b will not cut the other strip.

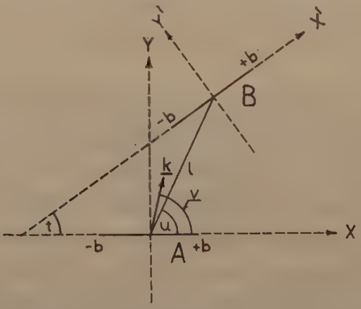

Fig. 1. The geometrical arrangement of the strips A and B. **k** is the wave vector of the incoming plane wave.

Suppressing the time factor $\exp(-i\omega t)$, the incoming plane monochromatic wave will be taken as

$$\psi_i = \exp ik(x \cos v + y \sin v), \quad k = 2\pi/\lambda. \tag{1}$$

Here the wave-vector **k** lies in the $x-y$ plane and makes an arbitrary angle v with the x-axis.

The problem to be discussed can now be formulated in the following way. We look for a solution

$$\psi = \psi_i + \psi_s, \tag{2}$$

consisting of a sum of the incoming plane wave and a scattered wave ψ_s, to the Helmholtz equation

$$\Delta\psi + k^2\psi = 0 \tag{3}$$

and require that it satisfies Sommerfeld's radiation condition

$$\psi_s \sim f(\vartheta, v) \cdot \frac{e^{ikr}}{\sqrt{r}}, \tag{4}$$

together with some boundary conditions on the strips. In the following, the last named conditions will be that the normal gradient of ψ shall vanish on both the strips:

$$\mathrm{grad}_n\, \psi = 0 \text{ on A and B.} \tag{5}$$

We might of course have chosen other boundary conditions on A and B, as for instance $\psi = 0$ on A and B or $\psi = 0$ on A and $\mathrm{grad}_n\, \psi = 0$ on B, but, as the calculations will be almost identical, we will consider only the boundary conditions (5). The equations (1) through (5) define the problem uniquely.

§ 3. *Calculation of the scattered wave.* The problem formulated in § 2 is not directly separable in any coordinate system. However, it is well-known (e.g. Eyges[6]) that a modified separation technique may be brought into use. This will lead to an infinite system of linear equations for the determination of certain expansion coefficients. Convergence provided, this infinite system of equations, and thereby the diffraction problem, may be solved. The procedure will be as follows.

In the case strip A is present *alone*, it is well-known that the diffraction problem is separable in elliptical cylinder coordinates defined by

$$x = b \cosh \mu \cos \alpha, \;\; y = b \sinh \mu \sin \alpha. \tag{6}$$

Using the notation of [7][8] the solution to the wave equation with boundary conditions (4), (5) is in this case given by

$$\psi = \psi_i + \psi', \tag{7a}$$

$$\psi_i = \sqrt{8\pi}\sum_{m=0}^{\infty} Ke_m Se_m(s,\alpha) Je_m(s,\mu) + \sqrt{8\pi}\sum_{m=1}^{\infty} Ko_m So_m(s,\alpha) Jo_m(s,\mu), \tag{7b}$$

$$\psi' = -\sqrt{8\pi}\sum_{m=1}^{\infty} \frac{Ko_m}{1+if_{o,m}} \cdot So_m(s,\alpha) Ho_m(s,\mu), \tag{7c}$$

with

$$Ke_m = i^m \frac{Se_m(s,v)}{M_m{}^e}, \quad Ko_m = i^m \frac{So_m(s,\, v)}{M_m{}^0}. \tag{8}$$

The parameter s is defined by $s = (kb)^2$ and the functions $Se_m(s,\, \alpha)$, $So_m(s,\, \alpha)$ are, respectively, the periodic even and odd Mathieu-functions, while $Je_m(s,\, \mu)$, $Jo_m(s,\mu)$ and $Ho_m(s,\mu)$ are corresponding solutions to the modified Mathieu differential equation. $Ho_m(s,\, \mu)$ behaves asymptotically like $(1/\sqrt{kr}) \exp i[kr - \frac{1}{2}\pi(m+\frac{1}{2})]$ and will thus secure the fulfillment of the radiation condition (4). Further the normalization factors $M_m{}^e$ and $M_m{}^o$ are defined

$$M_m{}^e = \int_0^{2\pi} (Se_m)^2\, \mathrm{d}\alpha$$

and the analogous expression for $M_m{}^o$. Finally $(1 + if_{o,m})$ is the ratio between the derivatives with respect to μ of Ho_m and Jo_m, evaluated for $\mu = 0$. The quantities $f_{o,m}$ are tabulated in [14]).

When both strip A and strip B are present, we introduce a further Cartesian coordinate system x', y', z' with the z'-axis parallel to the z-axis and let the $x' - z'$ plane coincide with the plane of strip B (see fig. 1). In terms of x', y' we may define a new elliptical cylinder coordinate system by the equations:

$$x' = b \cosh \rho \cos \beta, \; y' = b \sinh \rho \sin \beta. \tag{9}$$

We now assume that (2) may be written in the form

$$\psi = \psi_i + \psi_A + \psi_B, \tag{10}$$

where ψ_i is given by (1) and where ψ_A and ψ_B are given by the following expressions:

$$\psi_A = \sqrt{8\pi}\sum_{m=1}^{\infty} A_m So_m(s,\, \alpha) Ho_m(s,\mu), \tag{11a}$$

$$\psi_B = \sqrt{8\pi}\sum_{m=1}^{\infty} B_m So_m(s,\, \beta) Ho_m(s,\, \rho). \tag{11b}$$

In these expressions only the odd Mathieu functions appear. The correctness of this assumption will be shown in the following. Further A_m and B_m are expansion coefficients to be determined by the boundary conditions (5). These now read

$$\mathrm{grad}_n(\psi_i + \psi_A + \psi_B) = 0 \text{ on A and B.} \tag{12}$$

However, by means of an addition theorem for the Mathieu-functions [9]) it is possible to express the function ψ_A on B in terms of the coordinates β, ρ, and the function ψ_B on A in terms of the coordinates α, μ. Denoting the functions produced in this way by $\psi_{A\to B}$ and $\psi_{B\to A}$, respectively, (12) becomes

$$\begin{aligned} &\frac{\partial}{\partial\mu}(\psi_i + \psi_A + \psi_{B\to A}) = 0 \text{ for } \mu = 0, \\ &\frac{\partial}{\partial\rho}(\psi_i + \psi_{A\to B} + \psi_B) = 0 \text{ for } \rho = 0. \end{aligned} \tag{13}$$

Here we have supposed ψ_i to be expanded in the elliptical cylinder coordinate systems (6) and (9), respectively.

As shown in the appendix, the addition theorem to be used states

$$So_m(s,\beta)Ho_m(s,\rho) = \\ = \sum_{q=1}^{\infty} \Gamma_{-m,-q}\, So_q(s,\alpha)Jo_q(s,\mu) + \sum_{q=0}^{\infty} \Gamma_{-m,+q}\, Se_q(s,\alpha)Je_q(s,\mu), \tag{14a}$$

$$So_m(s,\alpha)Ho_m(s,\mu) = \\ = \sum_{q=1}^{\infty} \Gamma'_{-m,-q}\, So_q(s,\beta)Jo_q(s,\rho) + \sum_{q=0}^{\infty} \Gamma'_{-m,+q}\, Se_q(s,\beta)Je_q(s,\rho). \tag{14b}$$

The first of these expressions will be valid inside a circle with radius l and centre at $x = y = 0$, but outside a circle with centre at $x' = y' = 0$ and radius b, while the region of validity of (14*b*) is given by interchanging the two circles. Explicit expressions for the coefficients Γ and Γ' are given in the appendix. They depend on s and the geometrical arrangement of the strips.

The correctness of the expressions (11) now follows from the boundary conditions (13) and the fact that the derivative of the function $Je_m(s,\mu)$ (appearing in (7*b*), (14*a*, *b*) and the analogous expressions for the even Mathieu functions) is zero for $\mu = 0$. In case the boundary conditions had been $\psi = 0$ on A and B, the odd Mathieu functions should have been replaced by the even Mathieu functions. For the mixed boundary conditions, $\psi = 0$ on A and $\text{grad}_n \psi = 0$ on B both types of Mathieu functions will appear in (11).

We now use the expansion of the plane wave (1) in the two elliptical cylinder coordinate systems, viz. (7*b*) and the analogous expansion in the other coordinate system together with (11) and (14). In view of the definition of $(1 + if_{o,m})$ given in connection with (7) we get from (13)

$$\begin{aligned} &\sum_{q=1}^{\infty} [Ko_q + A_q(1 + if_{o,q}) + \sum_{m=1}^{\infty} B_m \Gamma_{-m,-q}] So_q(s, \alpha) Jo_q'(s, o) = 0, \\ &\sum_{q=1}^{\infty} [Ko_q^B + B_q(1 + if_{o,q}) + \sum_{m=1}^{\infty} A_m \Gamma'_{-m,-q}] So_q(s, \beta) Jo_q'(s, o) = 0. \end{aligned} \tag{15}$$

Here Ko_q^B denotes the "odd" expansion coefficients in the expansion of (1) in the coordinate system (9). They are connected with Ko_q by the relation

$$Ko_q^B = Ko_q(s, v - t) \exp[ikl \cos(u - v)]. \tag{16}$$

As (15) is to be satisfied identically in α and β, the following equations result:

$$\begin{aligned} &A_q + \sum_{m=1}^{\infty} B_m \gamma_{-m,-q} = -\frac{Ko_q(s, v)}{1 + if_{o,q}}, \\ &B_q + \sum_{m=1}^{\infty} A_m \gamma'_{-m,-q} = -\frac{Ko_q(s, v - t)}{1 + if_{o,q}} \exp[ikl \cos(u - v)] \quad q = 1, 2, \ldots \end{aligned} \tag{17}$$

where we have put

$$\frac{\Gamma_{-m,-q}}{1 + if_{o,q}} = \gamma_{-m,-q} \tag{18}$$

and analogously for $\gamma'_{-m,-q}$.

If (17) has a unique solution for A_q and B_q, we may, by insertion of this solution into (11), find ψ_A and ψ_B and therefore also ψ_s, and the diffraction problem is formally solved. It is of course difficult to show rigorously that (17) has a unique solution and we shall not attempt to do so. It is, however, immediately clear that in the limit $l \to \infty$ equation (17) will give the usual expressions for the expansion coefficients in the expansion of the wave scattered by two *isolated* strips (see (7*c*)). This follows because $\gamma_{-m,-q}$ and $\gamma'_{-m,-q}$ go to zero for $l \to \infty$.

For the other boundary conditions mentioned earlier in this paper one may derive equations of the same general type as (17). These equations will involve also Ke_q and all of the $\Gamma_{\pm m,\pm q}$, but present no other new features.

§ 4. *A special system of strips.* The equations (17) simplify considerably if the two strips are placed in the same plane. In the following we will therefore consider the geometrical arrangement shown in fig. 2. With this arrangement of the strips it follows from the expressions for Γ and Γ' given in the appendix that the following relation is valid:

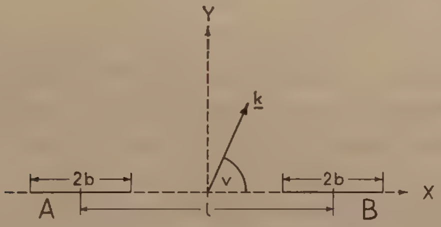

Fig. 2. Arrangement of strips A and B in the same plane.

$$\Gamma_{-m,-q} = (-1)^{m+q}\Gamma'_{-m,-q}, \tag{19}$$

and, furthermore, the angle t is zero. For the incoming wave we will still use the expression (1); but now the origin of the $x - y$ coordinate system will be placed midway between the two strip axes. Equations (17) therefore become

$$\begin{aligned} A_q + \sum_{m=1}^{\infty} B_m\,\gamma_{-m,-q} &= -\frac{Ko_q(s, v)}{1 + if_{o,q}}\,\mathrm{e}^{-\frac{1}{2}ikl\cos v}, \\ B_q + \sum_{m=1}^{\infty} A_m(-1)^{m+q}\gamma_{-m,-q} &= -\frac{Ko_q(s, v)}{1 + if_{o,q}}\,\mathrm{e}^{+\frac{1}{2}ikl\cos v} \qquad q = 1, 2, \ldots \end{aligned} \tag{20}$$

A further simplification results if we consider the special case of normal incidence, i.e. $v = \frac{1}{2}\pi$. In this case, the scattered wave is symmetric about the y-axis. However, this does not imply that $A_m = B_m$, but only

$$A_m = (-1)^{m+1}B_m. \tag{21}$$

This follows from the symmetry properties of the Mathieu functions together with the fact (see (6) and (9)) that both of the coordinate lines $\alpha = 0$ and $\beta = 0$ point in the positive direction of the x-axis. For $v = \frac{1}{2}\pi$ the right hand sides of (20) are identical and different from zero only if q is an odd integer. This implies that (20) for $v = \frac{1}{2}\pi$ is invariant against $A_m \leftrightarrow (-1)^{m+1}B_m$ in accordance with (21). For normal incidence the equations (20) may therefore be written in the form

$$\sum_{m=1}^{\infty} [\delta_{m,q} + (-1)^{m+1}\gamma_{-m,-q}]A_m = -\frac{Ko_q(s, \pi/2)}{1 + if_{o,q}}, \quad q = 1, 2, \ldots \quad (22)$$

$$B_m = (-1)^{m+1}A_m.$$

Here the calculation of ψ_s accordingly simplifies considerably.

As mentioned in § 3, a rigorous verification of the convergence of the whole scheme is very difficult. With the special configuration of the strips considered in this section, however, a possibility for a practical check of the method turns up. In the limit $l \to 2b$, the wave ψ_s calculated by means of (20) and (11) should approach the scattered wave calculated for a *single* strip of width $4b$, and the same will be true for quantities like the total cross-section, etc. However, the fundamental point in the derivation of the equations mentioned above was the existence of the addition theorem given in the appendix, and this theorem is not valid for $l = 2b$, but only for $l > 2b$. It may therefore happen that the convergence will fail for $l = 2b$ and be rather slow for values of l immediately above $2b$. Actually, numerical calculations seem to show that the calculated wave ψ_s does approach the scattered wave calculated for a single strip of width $4b$ as $l \to 2b$. At the same time, an interesting difference between the case of the boundary condition (5), treated here, and the case of the boundary condition $\psi = 0$ on A and B appears. The latter case has been treated by E. B. Hansen[10]). If the boundary conditions are given by (5), the interaction between the strips vanishes much more rapidly with increasing values of l than if the boundary conditions are $\psi = 0$ on A and B. We shall return to this in connection with the numerical calculations.

§ 5. *Approximate solution of* (20). As mentioned in the preceding paragraph the interaction between the two strips will vanish, rapidly with increasing l. Further it is known that for the wave ψ', (7c), scattered by a single strip, it is a good approximation (at least with regard to the calculation of the total scattering cross-section) to neglect values of m greater than 1 when the parameter $s = (kb)^2$ is smaller than 4–5. We may therefore reasonably expect that, for values of s below this limit and for values of l somewhat larger than $2b$, the scattered wave $\psi_s = \psi_A + \psi_B$ may be rather well approximated by retaining only A_1 and B_1 in (11) and (20). For A_1 and B_1 one then gets

$$A_1 = -\frac{1}{1-\gamma^2_{-1,-1}}\left[\mathrm{e}^{-\frac{1}{2}ikl\cos v} - \gamma_{-1,-1}\,\mathrm{e}^{+\frac{1}{2}ikl\cos v}\right]\frac{Ko_1(s,v)}{1+if_{o,1}},$$
$$B_1 = -\frac{1}{1-\gamma^2_{-1,-1}}\left[-\gamma_{-1,-1}\,\mathrm{e}^{-\frac{1}{2}ikl\cos v} + \mathrm{e}^{+\frac{1}{2}ikl\cos v}\right]\frac{Ko_1(s,v)}{1+if_{o,1}}. \tag{23}$$

Here, for sufficiently large values of l, we may further neglect $\gamma^2{}_{-1,-1}$. In this approximation one can get a rather simple expression for $\gamma_{-1,-1}$. As shown in the appendix, $\Gamma_{-1,-1}$ is given by the expression

$$\Gamma_{-1,-1} = \sum_{n,p=\div\infty}^{\infty} i^{(n-p)}\, c^{-1}_{p+1}\, c^{-1}_{n+1}\, H^{(1)}_{p-n}\,(kl) = \sum_{p=0}^{\infty} a_p(s)\, H^{(1)}_{2p}\,(kl). \tag{24}$$

Using the asymptotic expression

$$H^{(1)}_{p-n}\,(kl) \simeq \sqrt{\frac{2}{\pi kl}}\exp i[kl - \tfrac{1}{2}\pi\,(p - n + \tfrac{1}{2})]$$

for the Hankel functions in the first of the expressions (24), together with the fact that both n and p are odd integers and the property $c^{-1}_{j+1} = -\,c^{-1}_{-j+1}$ of the Fourier coefficients of the Mathieu functions (see appendix), one gets $\Gamma_{-1,-1} = 0$. However, using the Stokes type asymptotic expansions of the Hankel functions 11)

$$H^{(1)}_{2p}\,(kl) \simeq \sqrt{\frac{2}{\pi kl}}\,(U - iV)\exp i[kl - \tfrac{1}{2}\pi(2p + \tfrac{1}{2})],$$
$$U = 1 - 0[(kl)^{-2}],$$
$$V = \frac{1 - 4\cdot(2p)^2}{8\,kl} - 0[(kl)^{-3}],$$

one gets from the second expression in (24) the following result for $\Gamma_{-1,-1}$:

$$\Gamma_{-1,-1} = \kappa(1+i)\,\frac{\mathrm{e}^{ikl}}{(kl)^{3/2}} \tag{25}$$

with κ given by

$$\kappa = \kappa(s) = \frac{2}{\sqrt{\pi}} \sum_{p=0}^{\infty} (-1)^p p^2 a_p(s). \tag{26}$$

Finally $\gamma_{-1,-1}$ is by (18)

$$\gamma_{-1,-1} = \frac{\kappa}{1 + i f_{o,1}} (1 + i) \frac{e^{ikl}}{(kl)^{3/2}} . \tag{27}$$

For the special case of normal incidence, $v = \frac{1}{2}\pi$, (23) becomes $(\gamma^2_{-1,-1} \approx 0)$

$$A_1 = B_1 = -\frac{Ko_1(s, v)}{1 + i f_{o,1}} (1 - \gamma_{-1,-1}) \tag{28}$$

with $\gamma_{-1,-1}$ given by (27).

It is interesting to notice that essentially the same approximate solution to (20) may be obtained in another way. This may be seen as follows. In (11) we retain again only A_1 and B_1; but instead of using the addition theorem, we replace the Hankel-like function Ho_1 by its asymptotic expression and evaluate ψ_A together with $\partial\psi_A/\partial y$ at the axis of strip B. In the same way, we evaluate ψ_B together with $\partial\psi_B/\partial y'$ at the axis of strip A. The boundary condition (5) may now be satisfied at the two strip axes only, yielding two equations for the determination of A_1 and B_1. The solutions of these equations are again given by (23) if we here neglect $\gamma^2_{-1,-1}$ and replace $\gamma_{-1,-1}$ by

$$\tilde{\gamma} = \frac{\kappa'}{1 + i f_{o,1}} (1 + i) \frac{e^{ikl}}{(kl)^{3/2}} \tag{29}$$

with

$$\kappa' = -\frac{2}{\sqrt{\pi}} \frac{1}{Do_1(s, 1)}, \tag{30}$$

where $Do_1(s, 1)$ is the first Fourier coefficient of $So_1(s, \alpha)$ as tabulated in [14]). The numerical value of κ' will, of course, differ slightly from that of κ. In deriving these formulae we have used well-known relations between the functions $So_m(s, \alpha)$ and $Jo_m(s, \mu)$ (see for instance [7]), [13])).

In spite of the many approximations made, numerical calculations given in the following paragraphs show a rather good agreement with more exact calculations.

§ 6. *Calculation of transmission coefficients.* By means of the expressions derived in the preceding paragraphs it is now possible to calculate various quantities of interest in connection with the diffraction problem. We again restrict ourselves to a consideration of the simple geometrical arrangement shown in fig. 2.

The incoming plane wave (1) may be regarded either as an acoustical wave or an electromagnetic wave. In the first case ψ is to be interpreted as the velocity potential and the strips are supposed to be absolutely rigid. In the second case ψ is to be interpreted as H_z, while the E-vector is polarized perpendicular to the z-axis and the strips are supposed to be perfectly conducting. However, using Babinet's principle, we may also interpret the diffraction problem as the diffraction of a plane monochromatic electromagnetic wave, polarized along the z-axis, through two infinitely long slits, congruent with the strips used hitherto, in a plane thin perfectly conducting screen occupying the $x - z$ plane. In this case $-\psi_s$ is to be interpreted as $E^s{}_z$ in the region $y \geqslant 0$. In the rest of this paper, we will adopt the latter point of view and calculate the transmission coefficient as a function of the various parameters kb, kl, and v. In a later paper[12]) we will adopt the acoustical interpretation and calculate the forces and torques acting on the system and its separate parts.

The quantity we want to calculate in this paragraph is the transmission coefficient T per unit length in the z-direction, defined by

$$T = \frac{1}{\sigma} \int_0^\pi |f(\vartheta, v)|^2 \, \mathrm{d}\vartheta. \tag{31}$$

Here $\sigma = 4b$ is the total width of the two slits, while $f(\vartheta, v)$ is the amplitude of the scattered wave ψ_s in the far field region:

$$\psi_s(r \to \infty) = f(\vartheta, v) \, \frac{\mathrm{e}^{ikr}}{\sqrt{r}}. \tag{32}$$

r and ϑ are the polar coordinates in a coordinate system with the x-axis as the polar axis and $x = y = 0$ as origin. However, using the connection $T = Q/\sigma$ between the total transmission cross-section and the transmission coefficient on the one hand, and the well-known relation[1])[15]) between the total cross-section and the amplitude of the scattered wave in the forward direction $\vartheta = v$ on the other hand, we get

$$T = -\frac{1}{\sigma}\sqrt{\frac{2\pi}{k}}\,\mathrm{Re}\,[\mathrm{e}^{\frac{1}{4}i\pi} f(v,v)]. \tag{33}$$

Here the minus sign appears on account of the use of Babinet's principle.

The amplitude $f(\vartheta, v)$ of the scattered wave in the far field region may be found from (11) by insertion of the asymptotic expression for $Ho_m(s, \mu)$. This gives the following expression:

$$f(\vartheta, v) =$$

$$= \sqrt{\frac{8\pi}{k}}\,\mathrm{e}^{-\frac{1}{4}i\pi} \sum_{m=1}^{\infty} (-i)^m So_m(s, \vartheta)\,(A_m\,\mathrm{e}^{ika\cos\vartheta} + B_m\,\mathrm{e}^{-ika\cos\vartheta}), \tag{34}$$

where we have put $a = \frac{1}{2}l$. The dependence of $f(\vartheta, v)$ on v enters through the coefficients A_m and B_m. Equation (33) then gives the following transmission coefficient:

$$T = -\frac{\pi}{kb} \sum_{m=1}^{\infty} (-1)^m So_m(s, v)\,\mathrm{Re}\,[i^m(A_m\,\mathrm{e}^{ika\cos v} + B_m\,\mathrm{e}^{-ika\cos v})]. \tag{35}$$

For normal incidence of the plane wave, $v = \frac{1}{2}\pi$, (35) simplifies greatly. Firstly, for $v = \frac{1}{2}\pi$ only odd values of m will contribute to (35) as $So_{2q}(s, \frac{1}{2}\pi) = 0$. Secondly, from (22) and (8) we get

$$A_{2m+1} = B_{2m+1} = -\sum_{q=0}^{\infty} \varepsilon_{2m+1,\,2q+1} \frac{Ko_{2q+1}(s, \frac{1}{2}\pi)}{1 + if_{o,2q+1}}, \tag{36}$$

where the $\varepsilon_{2m+1,2q+1}$ are determined as the elements of the reciprocal of the coefficient matrix in (22). Introducing (36) together with the explicit expression (8) for $Ko_{2q+1}(s, \frac{1}{2}\pi)$ in (35) then gives

$$T\left(v = \frac{\pi}{2}\right) =$$

$$= \frac{2\pi}{kb} \sum_{\substack{m=0\\q=0}}^{\infty} (-1)^{m+q} \frac{So_{2m+1}(s, \frac{1}{2}\pi)\, So_{2q+1}(s, \frac{1}{2}\pi)}{M^0{}_{2q+1}}\,\mathrm{Re}\left[\frac{\varepsilon_{2m+1,2q+1}}{1 + if_{o,2q+1}}\right]. \tag{37}$$

Although the expressions (35) and (37) are quite complicated, they are not unmanageable. As an example we have used (35) and (37) to calculate T as a function of the angle v for fixed values of s and

kl, viz. $s = 1$ and $kl = 2.1$. This corresponds to a distance d between the two innermost strip edges which is very small compared to the wavelength λ, viz. $d < \lambda/60$. In this calculation we have included the values $m \leqq 3$ and $q \leqq 3$ in the equations (20). The results are shown in fig. 3 together with curves of the transmission coefficient for the two limiting cases: 1) a single slit af width $4b$, corresponding to the limit $l = 2b$, and 2) a single slit of width $2b$, corresponding to the limit $l \to \infty$. The last mentioned two curves may be taken for instance from the formulae and curves in [8]).

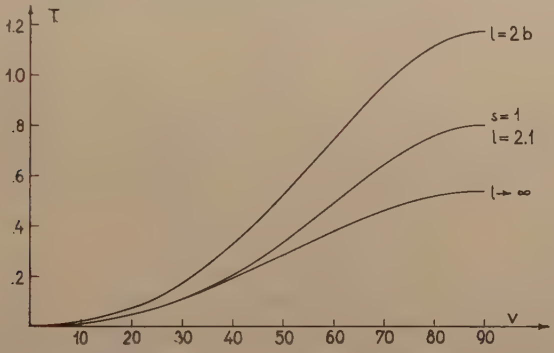

Fig. 3. The transmission coefficient T for a system of two slits in an infinite plane screen plotted as a function of the angle v. The parameters are $s = (kb)^2 = 1$ and $kl = 2.1$. The electric field vector is parallel to the slit axes. The two curves $l = 2b$ and $l \to \infty$ correspond, respectively, to a single slit of width $4b$ and a single slit of width $2b$.

It is rather surprising that, in spite of the fact $d \ll \lambda$, the transmission coefficient for the system of two slits lies much closer to the limit $l \to \infty$ than to the limit $l = 2b$. In fact, for angles $v < 45°$ it is almost identical with the values of T in the limit $l \to \infty$.

The above-mentioned property of the transmission coefficient for the two slits may be illustrated in other ways. In fig. 4*a* we have plotted the angular distribution of the scattered wave calculated for $v = \frac{1}{2}\pi$ and, as above, $s = 1$ and $kl = 2.1$. The quantity plotted is $(2b)^{-\frac{1}{2}}|f(\vartheta, \frac{1}{2}\pi)|$ and the values of m included are $m \leqq 3$. For comparison we again show the curves corresponding to the two limiting values of l. The same tendency as in fig. 3 is visible in fig. 4*a*. For further comparison we have in fig. 4*b* plotted the angular dependence of the scattered wave corresponding to the values $s = 1$ and $kl = 5$.

In a still more striking fashion this behaviour of the transmission coefficient is shown in fig. 5. Here we have, for $v = \frac{1}{2}\pi$ and $s = 1$, plotted T as a function of kl. The curve 1 is calculated by means of (22) and (37), but except for the point at $kl = 2.1$ we have only included the values $m \leq 2$. The two limiting cases $l = 2b$ and $l \to \infty$ are again shown. We have further, somewhat artificially, extended curve 1 below the value $kl = 2$ in the following way. As mentioned above, $kl = 2$ corresponds to the situation that the strips touch each other, while $kl < 2$ corresponds to overlapping of the strips.

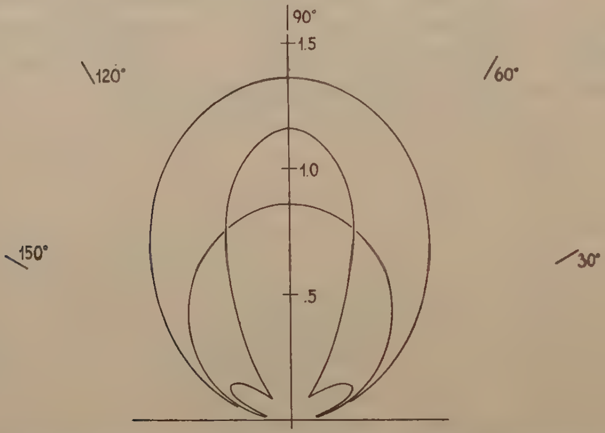

Fig. 4*a*. The angular variation of the amplitude of the scattered wave in the far field region for normal incidence of the plane wave. The curves show the ratio between the numerical value of the amplitude and the square root of half the total slit width. $l = 2b$ and $l \to \infty$ correspond, respectively, to a single slit of width $4b$ and a single slit of width $2b$. $s = 1$ in all cases.

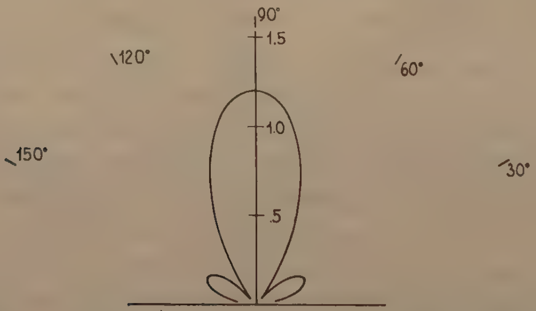

Fig. 4*b*. The angular variation of the scattered wave for $s = 1$ and $kl = 5$.

This case cannot be treated by the methods used in this paper. However, we may regard the overlapping strips as a single strip of total width $2b' = 2b + l$ and plot the transmission coefficient, for the complementary problem, as a function of kl. This has been done as a broken curve in fig. 5.

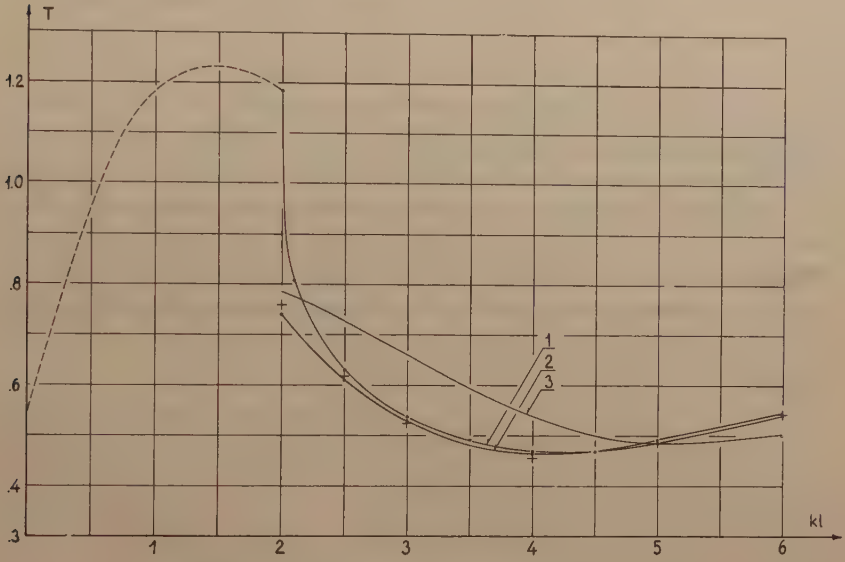

Fig. 5. The transmission coefficient for a system of two slits as a function of kl. The parameters are $v = \frac{1}{2}\pi$ and $s = (kb)^2 = 1$. The electric fieldvector is *parallel* to the slit axes. See the text for further explanation.

The behaviour of the transmission coefficient, as shown by fig. 5, curve 1, is quite distinct from the behaviour of the transmission coefficient found in the case that the incoming plane wave is polarized perpendicular to the slit-axis. E. B. Hansen[10]) has treated the latter case by means of methods analogous to those of Bouwkamp[2]). On the basis of the results in[10]) we have in fig. 6 plotted a curve analogous to curve 1 in fig. 5. However, fig. 6 corresponds to $s = \frac{1}{4}$ while fig. 5 corresponds to $s = 1$. In spite of this difference in the value of s the different behaviour of T in the two cases is of significance. In fact, for $s = \frac{1}{4}$, the different behaviour in the two cases would be even more marked (see fig. 10).

The behaviour of T, shown by the figs. 3–5, makes it plausible that the approximate solution of (20), derived in the preceding

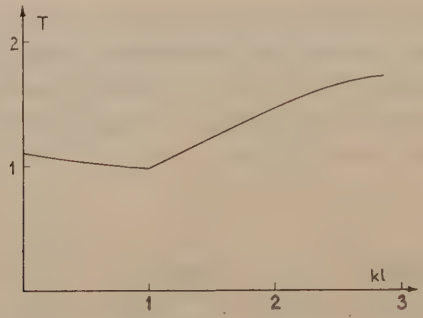

Fig. 6. The transmission coefficient for a system of two slits as function of *kl*. The parameters are $v = \frac{1}{2}\pi$ and $s = \frac{1}{4}$. The electric field vector is *perpendicular* to the slit axes. The curve is based on the results of 10).

paragraph, may be used to find a simple, approximate and yet rather accurate expression for T. Thus, introducing (23), with neglect of $\gamma^2{}_{-1,-1}$, and (27) in (35) with $A_m = B_m = 0$ for $m \geqslant 2$, one gets

$$T = T_1 \left[1 - \cos(kl \cos v) \frac{\kappa_1 \cos kl - \kappa_2 \sin kl}{(kl)^{3/2}} \right], \qquad (38)$$

where

$$T_1 = \frac{2\pi}{kb} \frac{[So_1(s, v)]^2}{M_1{}^o} \frac{1}{1 + f^2{}_{o,1}}$$

is the first approximation to the transmission coefficient for a *single* slit of width $2b$, and

$$\kappa_1 = \kappa \frac{1 + 2f_{o,1} - f^2{}_{o,1}}{1 + f^2{}_{o,1}}, \qquad \kappa_2 = \kappa \frac{1 - 2f_{o,1} - f^2{}_{o,1}}{1 + f^2{}_{o,1}}. \qquad (39)$$

We may, of course, use (29) instead of (27), i.e. replace κ by κ' in (39). Fig. 5, curve 2, shows the result of using the expressions (38) and (39) in the calculation of T, while the crosses show the effect of replacing κ by κ'. It will be seen that this, over most of the range of kl, is a rather good approximation to the more exact calculations. In fig. 7, κ, κ_1, κ_2 and κ' are plotted as functions of s.

Concerning the region of validity of (38) with respect to s, the following may be said. The upper limit of s is determined by the requirement that the transmission coefficient for a *single* slit shall be well approximated by T_1; i.e. $s < 4 - 5$. Regarding the lower limit where $s \ll 1$, (38) will be a good approximation only when kl is large. One might attempt, for $kl \ll 1$, to use the series expansions of the Hankel functions occurring in (24) and, by means of (23), (24) and (33), derive an approximate expression for the transmission coefficient T valid in the region $\sqrt{s} < kl \ll 1$. However, this turns out to be a very impractical procedure and will accordingly be omitted here. In this connection it may be mentioned that for $s \ll 1$ the quantities $a_p(s)$ occurring in (24) may be expanded in powers of s. Combining this with the above-mentioned expansions of the Hankel functions, one may find an expansion of T in terms of s and kl. This expansion will, if at all, be *very* slowly convergent. This result is in accordance with the conclusion reached by E. B. Hansen by other means[10]).

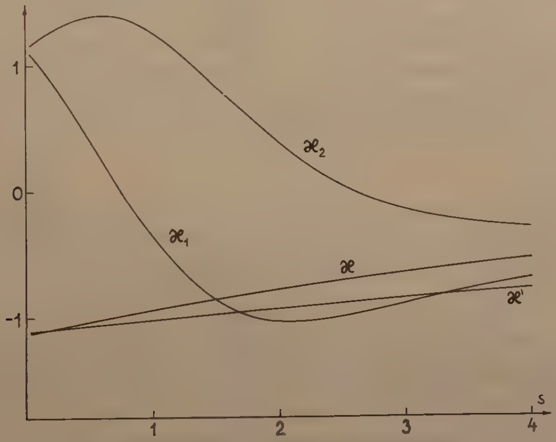

Fig. 7. κ, κ_1, κ_2 and κ', occurring in (38) and (39), as function of s.

In fig. 5 we have further (curve 3) shown the results found by using for ψ_s the "zero order" approximation, viz. $\psi_s{}^0 = \psi_A{}' + \psi_B{}'$, where $\psi_A{}'$ and $\psi_B{}'$ are the waves scattered by two isolated strips (i.e. $\psi_A{}'$ and $\psi_B{}'$ are given by (7*c*) and the analogous expression in the coordinates β, ρ). In this case, however, it is necessary to calculate the transmission coefficient by means of the definition (31). This approximation is not as good as the one given above.

Concerning the accuracy of the calculations leading to curve 1 in fig. 5 we may say the following. For values of l immediately above $2b$ the quantities $\gamma_{-m,-q}$ occurring in (20) converge very slowly. With increasing values of l the convergence rapidly becomes better. In table I we show some calculated values of T, the accuracy being indicated by the number of decimal places used. Also shown are the results of using (38) and (39) with κ given by (27).

TABLE I

The transmission coefficient for a system of two slits calculated by means of (22) and (33). Also shown are the values obtained by using the approximation (38). $s = 1$; $v = \frac{1}{2}\pi$

kl	$m = 1$	$m = 2$	$m = 3$	(38)
2.0				0.739
2.1	0.779	0.801	0.808	0.709
2.5	0.626	0.629		0.610
3.0	0.5380	0.5374		0.527
3.5	0.4913	0.4900		
4.0	0.4697	0.4687		0.464
4.5	0.4684	0.4681		
5.0	0.4838	0.4840		0.491
6.0	0.5401			0.545

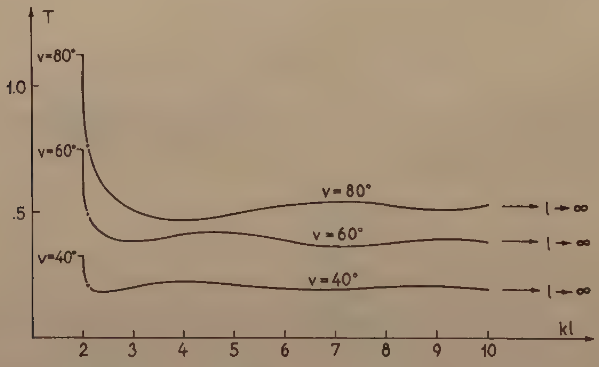

Fig. 8. The transmission coefficient for a system of two slits as a function of kl for $s = 1$ and $v = 40°$, $60°$ and $80°$, respectively. The electric field vector is parallel to the slit axes.

In fig. 8 we have, for various values of the angle v, plotted T as a function of kl for the fixed value $s = 1$. However, in view of the agreement between (38) and the more exact calculations, we have here, except for the point $kl = 2.1$, used the approximate expression

(38) for the calculations. In fig. 9 we have shown the variation of T with kb for the fixed ratio $l/b = 3$ and normal incidence. Also shown are the two limiting cases $l/b = 2$ and $l \to \infty$. The calculations are again based on (38).

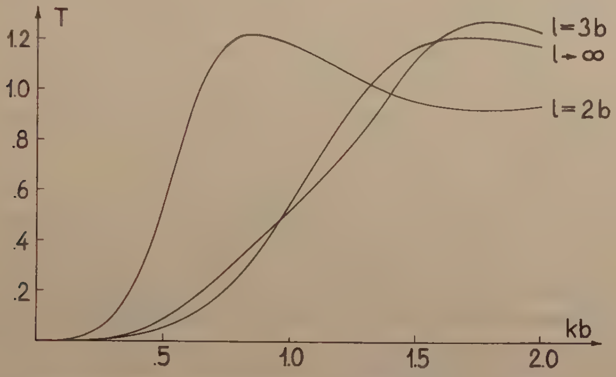

Fig. 9. The transmission coefficient for a system of two slits as a function kb. The parameters are $v = \frac{1}{2}\pi$ and $l/b = 3$. The electric field vector is parallel to the slit axes. The curves $l/b = 2$ and $l \to \infty$ correspond, respectively, to a single slit of width $4b$ and a single slit of width $2b$.

Finally in fig. 10 we have plotted T as a function of kl, again for normal incidence, but different values of s. The calculations leading to the curves shown are based upon the approximation (38) in connection with the known values of T in the two limiting cases $l = 2b$ and $l \to \infty$. Some points, however, have been calculated more accurately by means of (22) and (33). From the curves shown we conclude that in the upper part of the region of validity with respect to s the approximation (38) represents a good approximation to T for all values of kl. Furthermore, for increasing values of s there is a marked increase in the oscillations of the curves. Extrapolating this behaviour to smaller values of s, we conclude that for $s \ll 1$ the transmission coefficient will behave in the following way. From the initial value, assumed for $l = 2b$ and shown in fig. 10 by the dotted curve, there will be a *very* sharp drop followed by a practically constant value of T equal to the value of the transmission coefficient for a *single* slit of width $2b$. This is in full accord with the failure, mentioned above, of a series expansion in terms of s and kl.

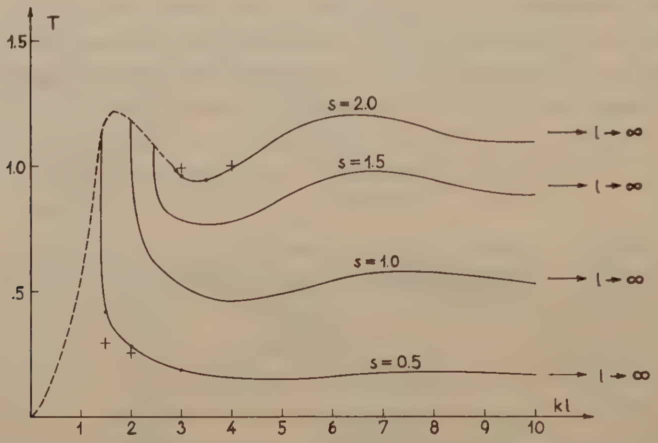

Fig. 10. The transmission coefficient for a system of two slits as a function of kl, for varying values of $s = (kb)^2$ and $v = \frac{1}{2}\pi$. With the exception of the curve $s = 1$ and the points explicitly shown on the other curves, the calculations have been based upon the approximate formula (38). For $s = 0.5$ and $s = 2$ the crosses give the values found by using (38). The broken curve shows the value of T in the limiting case $l = 2b$. The electric field vector is parallel to the slit axes.

§ 7. *Concluding remarks.* In the preceding paragraphs we have formally solved the problem of the diffraction of a plane monochromatic wave by a system of two strips in an almost arbitrary configuration, subject to the boundary condition $\text{grad}_n\ \psi = 0$ on the strips. Further we have, for a range of values of the parameters $s = (kb)^2$, kl and v, given some numerical calculations concerning a system of two slits in a thin plane perfectly conducting screen. As mentioned earlier, the calculations may readily be extended to more general systems of strips or slits. We might mention, for instance, the case of three or more parallel slits in a plane screen as being of interest. No restriction in the form of "equal width of the slits", "equal distances between the slit axes" etc. need be fulfilled, although such restrictions, of course, will simplify the numerical calculations.

The important thing to be noted from the foregoing calculations is the sharp variation of T, occurring at least for smaller values of s, when l increases from the initial value of $2b$. We should like to mention that an analogous situation also may be found in other cases. Interpret for instance, fig. 2 as a single strip, extending from $x = -\frac{1}{2}l - b$ to $x = +\frac{1}{2}l + b$, that is, of total width $l' = l + 2b$, containing a slit of width $d = l - 2b$, and consider the following problem of *hydrodynamical* fluid flow. Let the velocity of the fluid flow at great distances from the strip be directed along the positive y-direction and of magnitude u and calculate, for instance by means of the theory of conformal mapping, the quantity $T' = Q/l'u$. Here Q is the amount of fluid transported through the slit per unit time and unit length of the slit. If we plot T' as a function of $d/4b$, we get a curve showing the same rapid variation for $d \rightarrow 0$. Thus, if we choose the values $l = 2.1$ and $b = 1$, corresponding to the values $kl = 2.1$ and $kb = 1$ considered in fig. 5, we find $d/4b = 0.025$ and $T' = 0.31$, i.e. T' has, already for this small width of the slit, risen to $\sim \frac{1}{3}$ of the final value $T' = 1$, obtained for $d \rightarrow \infty$.

Finally we should like to mention that, although in this paper we have adopted the electromagnetic interpretation of ψ, the quantity T calculated in § 6. may also be interpreted as the total acoustical radiation force on the strips, provided this force is measured in units of $8\rho_0 \overline{u_0{}^2} b$, where ρ_0 is the mean density of the surrounding medium and $\overline{u_0{}^2}$ is the mean square of the particle velocity in the incoming plane acoustical wave.

Acknowledgement. It is a pleasure to thank professor H. Højgaard Jensen and Mr. V. Frank, M.Sc. for many interesting discussions on diffraction problems. Finally Mr. Algreen-Ussing has helped with numerical calculations.

Appendix.

Meixner and Schäfke[13]) have given an addition theorem for Mathieu functions. Referring to fig. 1, this theorem will be valid in a region of the x—y plane *not* including the two strips A and B, and will, accordingly, be of no use with regard to the problem of satisfying the boundary condition (5). However, it may be shown [9]) that, in another region of the x—y plane including the *in casu* interesting part, another addition theorem may be found. In [9]) this was given in the notation of Meixner and Schäfke. However, in order to use the most important table of Mathieu functions[14]), it was felt necessary in this paper to use the notation of[14]). In this appendix we summarize the relevant transcription.

The two-dimensional wave equation separates in the elliptical cylinder coordinates (6), the separated equations being the Mathieu differential equation, the α-equation, and the associated Mathieu differential equation, the μ-equation. The α-equation defines, for all values of the parameter $s = (kb)^2$, a complete set of eigenfunctions which in the notation of[14] are

$$\begin{aligned} &\text{odd functions } So_m(s, \alpha) = \sum_n Do_n(s, m) \sin n\alpha, \\ &\text{even functions } Se_m(s, \alpha) = \sum_n De_n(s, m) \cos n\alpha, \end{aligned} \qquad \text{(A 1)}$$

where the Fourier coefficients are tabulated in[14]. Here n and m are both even or both odd integers. The normalization of the functions are given by $So_m'(s, o) = 1$ and $Se_m(s, o) = 1$, where the differentiation is with respect to α. Further one has

$$M_m{}^o = \int_0^{2\pi} [So_m(s, \alpha)]^2 \, d\alpha; \;\; M_m{}^e = \int_0^{2\pi} [Se_m(s, \alpha)]^2 \, d\alpha. \qquad \text{(A 2)}$$

The functions $Jo_m(s, \mu)$ and $Ho_m(s, \mu)$ are solutions of the μ-equation corresponding to the same eigenvalue as $So_m(s, \alpha)$. They behave asymptotically like $(kr)^{-\frac{1}{2}} \sin (kr - \frac{1}{2}\pi(m + \frac{1}{2}))$ and $(kr)^{-\frac{1}{2}} \exp i[kr - \frac{1}{2}\pi(m + \frac{1}{2})]$ respectively.

The appropriate addition theorem now states that, in the region given by the *inside* of the circle with centre at $x = y = 0$ and radius l, but *outside* the circle with centre at $x' = y' = 0$ (see fig. 1) and radius b, the following relation will hold:

$$M_m^{(j)}(\rho, h) me_m(\beta, h^2) = \sum_{q=-\infty}^{\infty} B_{q,m}^{(j)} M_q^{(1)}(\mu, h)\, me_q(\alpha, h^2)$$

$$j = 1, 2, 3, 4; \;\; m = \text{integer} \gtreqqless 0, \qquad \text{(A 3)}$$

where

$$B_{q,m}^{(j)} = \sum_{n,p=-\infty}^{\infty} i^{(q-p+n-m)} \{c_{p-q}^{q}(h^2)\, c_{n-m}^{m}(h^2)\, Z_{p-n}^{(j)}(kl)\}\, e^{i(n-p)u}\, e^{-int},$$

$$(q - p) \text{ and } (n - m) \text{ both even integers.} \qquad \text{(A 4)}$$

Here the angles u and t are shown in fig. 1, while $h^2 = (\frac{1}{2}kb)^2 = \frac{1}{4}s$, and $Z^{(j)}(kl)$ are the usual cylinderfunctions, $j = 1, 2, 3, 4$ corresponding to, respectively, Bessel-, Neumann- and Hankel-functions of the first and second kind. With respect to the rest of the symbols occurring in (A 3) and (A 4) a comparison of the notation in[13]) with that of[14]) or [7]) gives the following results:

$$\begin{aligned} me_q(\alpha, h^2) &= \sqrt{\frac{2\pi}{M_q{}^e}}\, Se_q(s, \alpha), && q \geqslant 0, \\ me_{-q}(\alpha, h^2) &= -\, i \sqrt{\frac{2\pi}{M_q{}^o}}\, So_q(s, \alpha), && q \geqslant 1, \\ M_q^{(j)}(\mu, h) &= \sqrt{\frac{2}{\pi}}\, Je_q(s, \mu) \text{ for } j = 1, && q \geqslant 0, \\ &= \sqrt{\frac{2}{\pi}}\, He_q(s, \mu), \text{ for } j = 3, && q \geqslant 0, \\ M_{-q}^{(j)}(\mu, h) &= (-1)^q \sqrt{\frac{2}{\pi}}\, Jo_q(s, \mu), \text{ for } j = 1, && q \geqslant 1, \\ &= (-1)^q \sqrt{\frac{2}{\pi}}\, Ho_q(s, \mu), \text{ for } j = 3, && q \geqslant 1. \end{aligned} \qquad \text{(A 5)}$$

With the boundary condition (5) used in the text we may in (A 3) and (A 4) restrict ourselves to the values $m \leqslant -1$, and (A 3) may therefore be written in the form

$$So_m(s, \beta) Ho_m(s, \rho) =$$

$$= \sum_{q=1}^{\infty} \Gamma_{-m,-q} So_q(s, \alpha)\, Jo_q(s, \mu) + \sum_{q=0}^{\infty} \Gamma_{-m,+q} Se_q(s, \alpha)\, Je_q(s, \mu) \qquad \text{(A 6)}$$

which is (14a) of the text. Equation (14*b*) may be found similarly. The general expression for $\Gamma_{-m,\pm q}$ (and analogously $\Gamma_{\pm m,\pm q}$) may be deduced from (A 3), (A 4) and (A 5) together with the definitions of the quantities c^q_{p-q} and c^m_{n-m} occurring in (A 4). We will confine ourselves to the simple geometry of fig. 2. As the functions $So_m(s, \alpha)$ are antisymmetric and the functions $Se_m(s, \alpha)$ are symmetric with respect to reflections about the x-axis, it follows that $\Gamma_{-m,+q}$ in (A 6) is zero. For $\Gamma_{-m,-q}$ we get $(m, q > 0)$

$$\begin{aligned} \Gamma_{-m,-q} &= (-1)^{m+q} \sqrt{\frac{M_m^o}{M_q^o}}\, B^{(3)}_{-q,-m}, \\ B^{(3)}_{-q,-m} &= i^{(q-m)} \sum_{n,p=\div\infty}^{\infty} i^{(n-p)}\, c^{-q}_{p+q}\,(h^2)\, c^{-m}_{n+m}\,(h^2)\, H^{(1)}_{p-n}\,(kl), \end{aligned} \qquad \text{(A 7)}$$

where $H^{(1)}_{p-n}(kl)$ is the Hankel function of the first kind. Analogously the quantities $\Gamma'_{-m,-q}$ occurring in (14*b*) may be found by replacing the angle u in (A 7) and (A 4) by $u + \pi$. As $(q - p)$ and $(n - m)$ are even integers, the following equation will be true:

$$\Gamma'_{-m,-q} = (-1)^{m+q}\Gamma_{-m,-q}. \qquad \text{(A 8)}$$

Finally it follows from[13]) and[14]) that the Fourier coefficients c^{-q}_{p+q} may be found from

$$c^{-q}_{-p+q} = -c^{-q}_{p+q} = \sqrt{\frac{\pi}{2M^o_q}}\, Do_p(s, q), \qquad (p, q > 0). \qquad \text{(A 9)}$$

As an example we give the expression for $\Gamma_{-1,-1}$. After insertion of (A 9) in (A 7) and rearrangement of the terms one finds

$$\Gamma_{-1,-1} = \frac{\pi}{M^o_1} \sum_{n,p>0}^{\infty} i^{(n-p)}\, Do_p(s, 1) Do_n(s, 1)[H^{(1)}_{p-n}(kl) + H^{(1)}_{p+n}(kl)]$$

$$= \sum_{p=0}^{\infty} a_p(s)\, H^{(1)}_{2p}(kl).$$

The last expression, which is the same as (24) in the text, follows because both p and n are odd numbers in this case.

Received 12th February, 1959

REFERENCES

1) Bouwkamp, C. J., Rep. Prog. Phys. **17** (1954) 35.
2) Bouwkamp, C. J., NY Univ. Math. Res. Rep. No EM-50 1953.
3) Baldwin, G. L. and A. E. Heins, Math. Scand. **2** (1954) 103.
4) Hönl, H., Z. Phys. **131** (1952) 290; H. Hönl and E. Grosschwitz, Z. Phys. **131** (1952) 305; H. Hönl and E. Zimmer, Z. Phys. **135** (1953) 196.
5) Levine, H. and J. Schwinger, Phys. Rev. **74** (1948) 958.
6) Eyges, L., Annals of Physics **2** (1957) 101.
7) Morse, P. and H. Feshbach, Methods of Theoretical Physics McGraw-Hill, New York 1953.
8) Højgaard Jensen, H. and K. Særmark. Acoustica **8** (1958) 79.
9) Særmark, K., Submitted to ZAMP.
10) Hansen, E. B., Thesis Technical University of Denmark, Copenhagen 1958, unpublished.
11) Jeffreys, H. and B. S. Jeffreys, Methods of Mathematical Physics, 2.ed Cambr. Univ. Press, 1950.
12) Særmark, K., to be published.
13) Meixner, J., and F. W. Schäfke, Mathieusche Funktionen und Sphäroidfunktionen, Springer Verlag, Berlin 1954.
14) Tables relating to Mathieu functions. Columbia Univ. Press 1951.
15) Keller, J. B., Res. Rep. No. EM-104. New York University 1957.

Appl. sci. Res. Section B, Vol. 7

NEW CALCULATIONS ON THE FARADAY EFFECT IN WAVE GUIDES

A. P. VAN GELDER, A. M. DE GRAAF and R. KRONIG

Laboratorium voor Technische Physica der Technische Hogeschool, Delft, Netherlands

Summary

The propagation of electromagnetic waves is investigated theoretically for a round wave guide, containing a gyroelectric-gyromagnetic medium with gyroaxis parallel to the guide in the form of a cylindrical shell of thickness δ, adjacent to the wall of the guide. An equation is set up, permitting to compute the change in the propagation constant γ due to the presence of the shell, including terms proportional to δ^2. Assuming only the presence of gyromagnetism, the change $\Delta_1\gamma$ of first order in δ for TE-waves is determined and is found to be the same for right- and left-circular polarization. The second order difference $\Delta_2^+\gamma - \Delta_2^-\gamma$ for the two senses of polarization, however, appears to have a non-vanishing value which, just like $\Delta_1\gamma$ can be expressed in terms of the radius of the guide, the frequency, the dielectric constant and the elements of the gyromagnetic permeability tensor which characterize the medium of the shell.

§ 1. *Introduction.* The propagation of electromagnetic waves in wave guides containing non-conducting ferromagnetic materials magnetized in the longitudinal direction has first been discussed by van Trier[1]). He considered both the case that a round wave guide is completely filled with this material and the case that the material is present in the form of a concentric round rod of radius ρ_1, small compared with that of the guide. For the last-mentioned problem the change in the propagation constant due to the introduction of the rod was explicitly computed by him up to terms proportional to ρ_1^2 for TE_{11}-waves, special attention being given to the Faraday rotation which these waves will suffer. The results of van Trier were subsequently rederived by Suhl and Walker[2]) with the aid of a perturbation method.

Van Trier himself carried out measurements with rods of ferroxcube of different composition, using a standing wave technique in a cylindrical cavity with the rod along the axis, rather than travelling waves in an extended guide. He confined his measurements to static magnetizing fields so small as to be far outside the region of ferromagnetic resonance. Some years later Snieder [3]) performed experiments on travelling waves right through resonance with round wave guides containing concentric rods of the same materials as used by van Trier. Near resonance the absorption becomes important and can be taken into account by considering the elements of the gyromagnetic permeability tensor as complex quantities. In the measurements of Snieder the influence of the temperature of the rod on the wave propagation was investigated, the rod being heated or cooled by an air current blown through the wave guide.

The purpose of the present note is to discuss an arrangement, different from that of van Trier and Snieder, which in several respects may offer advantages. We shall assume the ferromagnetic material to be introduced, not in the form of a concentric rod, but in the form of a thin cylindrical shell, adjacent to the cylindrical metallic boundary of the wave guide or cavity. In this arrangement the difficulty of having to support and to center the rod with respect to the guide is avoided. In addition, in experiments where the influence of temperature is to be studied, the heating or cooling of the ferromagnetic material is directly brought about by the thermal contact with the walls of the guide, immersed for instance in a suitable temperature bath. Particularly at a very low temperature such as that of liquid helium this greatly simplifies matters. Also the measurement of the temperature is now much easier and more precise since no thermocouples need be introduced into the interior of the guide where they would have a perturbing influence on the electromagnetic field. Finally we shall see that from those quantities, characterizing the wave propagation which can easily be measured, more can be learned about the magnetic permeability tensor than in the arrangement employing concentric rods.

§ 2. *The equation determining the propagation constant.* Let the internal radius of the wave guide be ρ_0, equal to the external radius of the shell of material. Let the internal radius of the shell be $\rho_1 = \rho_0 - \delta$, so that δ is the thickness of the shell. As dielectric constant and permeability of the air we shall use the vacuum values ε_0 and μ_0, the difference being negligible in experiments of the kind considered. Choosing the z-axis in the direction of the guide, we shall characterize the medium of the shell by a dielectric tensor and a permeability tensor, given respectively by

$$||\varepsilon|| = \left\| \begin{matrix} \varepsilon_1 & -j\varepsilon_2 & 0 \\ j\varepsilon_2 & \varepsilon_1 & 0 \\ 0 & 0 & \varepsilon_3 \end{matrix} \right\|, \qquad ||\mu|| = \left\| \begin{matrix} \mu_1 & -j\mu_2 & 0 \\ j\mu_2 & \mu_1 & 0 \\ 0 & 0 & \mu_3 \end{matrix} \right\|, \tag{1}$$

just as was done by van Trier. Later we can easily specialize for the case of ferrites by putting $\varepsilon_1 = \varepsilon_3 = \varepsilon$, $\varepsilon_2 = 0$.

As shown by van Trier, the transversal components of the electric and magnetic field for a wave in the guide, depending on the time and z through the factor $\exp(j\omega t - \gamma z)$, can be expressed in terms of the longitudinal components E_z and H_z by means of the following relations referred to cylindrical coordinates ρ, ϑ, z (see eq. (2.16) of van Trier's paper, applied to this case):

$$\begin{aligned} E_\rho &= p\frac{\partial E_z}{\partial \rho} + \frac{q}{\rho}\frac{\partial E_z}{\partial \vartheta} + r\frac{\partial H_z}{\partial \rho} + \frac{s}{\rho}\frac{\partial H_z}{\partial \vartheta}, \\ E_\vartheta &= -q\frac{\partial E_z}{\partial \rho} + \frac{p}{\rho}\frac{\partial E_z}{\partial \vartheta} - s\frac{\partial H_z}{\partial \rho} + \frac{r}{\rho}\frac{\partial H_z}{\partial \vartheta}, \\ H_\rho &= t\frac{\partial E_z}{\partial \rho} + \frac{u}{\rho}\frac{\partial E_z}{\partial \vartheta} + p\frac{\partial H_z}{\partial \rho} + \frac{q}{\rho}\frac{\partial H_z}{\partial \vartheta}, \\ H_\vartheta &= -u\frac{\partial E_z}{\partial \rho} + \frac{t}{\rho}\frac{\partial E_z}{\partial \vartheta} - q\frac{\partial H_z}{\partial \rho} + \frac{p}{\rho}\frac{\partial H_z}{\partial \vartheta}. \end{aligned} \tag{2}$$

Here (see v. Tr. eq. (2.11) and (2.10)) the abbreviations p, q, r, s, t, u are defined by

$$\begin{aligned} p &= -\gamma[\gamma^2 + \omega^2(\varepsilon_1\mu_1 + \varepsilon_2\mu_2)]\Delta^{-1}, \\ q &= -j\gamma\omega^2(\varepsilon_1\mu_2 + \varepsilon_2\mu_1)\Delta^{-1}, \\ r &= \omega[\mu_2\gamma^2 - \omega^2(\mu_1^2 - \mu_2^2)\varepsilon_2]\Delta^{-1}, \\ s &= -j\omega[\mu_1\gamma^2 + \omega^2(\mu_1^2 - \mu_2^2)\varepsilon_1]\Delta^{-1}, \\ t &= -\omega[\varepsilon_2\gamma^2 - \omega^2(\varepsilon_1^2 - \varepsilon_2^2)\mu_2]\Delta^{-1}, \\ u &= j\omega[\varepsilon_1\gamma^2 + \omega^2(\varepsilon_1^2 - \varepsilon_2^2)\mu_1]\Delta^{-1}, \\ \Delta &= [\gamma^2 + \omega^2(\varepsilon_1 + \varepsilon_2)(\mu_1 + \mu_2)][\gamma^2 + \omega^2(\varepsilon_1 - \varepsilon_2)(\mu_1 - \mu_2)]. \end{aligned} \tag{3}$$

In the air-filled region we must put $\varepsilon_1 = \varepsilon_3 = \varepsilon_0$, $\varepsilon_2 = 0$, $\mu_1 = \mu_3 = \mu_0$, $\mu_2 = 0$.

The longitudinal components themselves must obey the differential equations (see v. Tr. eq. (2.14))

$$\nabla_t^2 E_z + aE_z + bH_z = 0,\ \nabla_t^2 H_z + cH_z + dE_z = 0, \tag{4}$$

with ∇_t^2 the transversal Laplace operator given by

$$\nabla_t^2 = \frac{\partial^2}{\partial \rho^2} + \frac{1}{\rho}\frac{\partial}{\partial \rho} + \frac{1}{\rho^2}\frac{\partial^2}{\partial \vartheta^2}$$

and the abbreviations (see v. Tr. eq. (2.15))

$$\begin{aligned} a &= -\, j\omega\varepsilon_3 s(q^2 - su)^{-1}, & b &= -\, j\omega\mu_3 q(q^2 - su)^{-1},\\ c &= j\omega\mu_3 u(q^2 - su)^{-1}, & d &= j\omega\varepsilon_3 q(q^2 - su)^{-1}. \end{aligned} \tag{5}$$

Considering first the electromagnetic field in the air-filled core of the wave guide, we have from (4), (5) and (3) by putting $\varepsilon_1 = \varepsilon_3 = \varepsilon_0$, $\varepsilon_2 = 0$, $\mu_1 = \mu_3 = \mu_0$, $\mu_2 = 0$

$$\nabla_t^2 E_z + \sigma^2 E_z = 0,\ \nabla_t^2 H_z + \sigma^2 H_z = 0 \tag{6}$$

with

$$\sigma^2 = \gamma^2 + \omega^2 \varepsilon_0 \mu_0. \tag{7}$$

The solutions of (6), finite for $\rho = 0$ and with the variables separated, are

$$E_z = A_1 J_n(\sigma\rho)\, e^{jn\vartheta},\ H_z = A_2 J_n(\sigma\rho)\, e^{jn\vartheta}, \tag{8}$$

J_n being the Bessel functions of integral order n and A_1 and A_2 arbitrary constants.

In the medium of the shell the longitudinal electromagnetic field can be represented in the form (see v. Tr. eq. (2.19), (2.23), (2.28), (2.21))

$$E_z = \varphi_1 + \varphi_2, \qquad H_z = g_1\varphi_1 + g_2\varphi_2, \tag{9}$$

where φ_1 and φ_2 obey the differential equations

$$\nabla_t^2 \varphi_i + \sigma_i^2 \varphi_i = 0, \qquad i = 1, 2, \tag{10}$$

with

$$\left.\begin{matrix}\sigma_1^2\\ \sigma_2^2\end{matrix}\right\} = \tfrac{1}{2}[\gamma^2(\varepsilon_3/\varepsilon_1 + \mu_3/\mu_1) + \omega^2\varepsilon_3(\mu_1^2 - \mu_2^2)/\mu_1 + \omega^2\mu_3(\varepsilon_1^2 - \varepsilon_2^2)/\varepsilon_1]$$
$$\pm \tfrac{1}{2}\{[\gamma^2(\varepsilon_3/\varepsilon_1 - \mu_3/\mu_1) + \omega^2\varepsilon_3(\mu_1^2 - \mu_2^2)/\mu_1 - \omega^2\mu_3(\varepsilon_1^2 - \varepsilon_2^2)/\varepsilon_1]^2$$
$$- 4\gamma^2\omega^2\varepsilon_3\mu_3(\varepsilon_2/\varepsilon_1 + \mu_2/\mu_1)^2\}^{\frac{1}{2}}, \tag{11}$$

$$g_i = (\sigma_i^2 - a)/b = d/(\sigma_i^2 - c), \qquad i = 1,2. \tag{12}$$

The solutions of (10) take the form

$$\varphi_i = [B_i J_n(\sigma_i \rho) + C_i N_n(\sigma_i \rho)]\, e^{jn\vartheta}, \qquad i = 1,2, \tag{13}$$

with B_i and C_i arbitrary constants, the Neumann functions N_n occurring next to the Bessel functions J_n since $\rho = 0$ does not belong to the region in question.

For a given n we have available in (8) and (13) six arbitrary constants A_1, A_2, B_1, B_2, C_1, C_2. They must be so chosen as to fulfil the boundary conditions at the wave guide and at the interface between the air and the medium of the shell. At the interface, i.e. for $\rho = \rho_1$, the tangential components E_ϑ, E_z, H_ϑ, H_z must be continuous; at the wave guide, i.e. for $\rho = \rho_0$, the two tangential components E_ϑ and E_z must vanish. Making use of (9), (12), (13) and (2), we thus get six homogeneous linear equations for the six arbitrary constants, leading to the requirement that the determinant of their coefficients must vanish. From this determinantial equation the propagation constant γ can be found as a function of the angular frequency ω.

In the determinant there occur the functions $J_n(\sigma\rho_1)$, $J_n(\sigma_i\rho_1)$, $N_n(\sigma_i\rho_1)$, $J_n(\sigma_i\rho_0)$, $N_n(\sigma_i\rho_0)$ with $i = 1, 2$, as well as their first derivatives with respect to the argument. All the functions involving σ_1 or σ_2 appear in the form of factors of the type

$$\begin{gathered}
J_n(\sigma_i\rho_0)\, N_n'(\sigma_i\rho_0) - J_n'(\sigma_i\rho_0)\, N_n(\sigma_i\rho_0), \\
J_n(\sigma_i\rho_1)\, N_n'(\sigma_i\rho_1) - J_n'(\sigma_i\rho_1)\, N_n(\sigma_i\rho_1), \\
J_n(\sigma_i\rho_1)\, N_n(\sigma_i\rho_0) - J_n(\sigma_i\rho_0)\, N_n(\sigma_i\rho_1), \\
J_n(\sigma_i\rho_1)\, N_n'(\sigma_i\rho_0) - J_n'(\sigma_i\rho_0)\, N_n(\sigma_i\rho_1), \\
J_n'(\sigma_i\rho_1)\, N_n(\sigma_i\rho_0) - J_n(\sigma_i\rho_0)\, N_n'(\sigma_i\rho_1), \\
J_n'(\sigma_i\rho_1)\, N_n'(\sigma_i\rho_0) - J_n'(\sigma_i\rho_0)\, N_n'(\sigma_i\rho_1).
\end{gathered}$$

These can be eliminated by developing the functions with arguments $\sigma_i\rho_1$ in powers of δ around the values for $\sigma_i\rho_0$ and by making use of the well-known relation

$$J_n(\sigma_i\rho_0)\, N_n'(\sigma_i\rho_0) - J_n'(\sigma_i\rho_0)\, N_n(\sigma_i\rho_0) = D/\sigma_i\rho_0,$$

with D a constant, together with the relations resulting from it by differentiation. Thus up to terms quadratic in δ we have

$$\begin{aligned}
&J_n(\sigma_i\rho_1)\,N_n(\sigma_i\rho_0) - J_n(\sigma_i\rho_0)\,N_n(\sigma_i\rho_1) = D(\delta/\rho_0 + \tfrac{1}{2}\delta^2/\rho_0^2),\\
&J_n(\sigma_i\rho_1)\,N_n'(\sigma_i\rho_0) - J_n'(\sigma_i\rho_0)\,N_n(\sigma_i\rho_1) =\\
&\qquad = (D/\sigma_i\rho_0)[1 - \tfrac{1}{2}(\sigma_i^2\rho_0^2 - n^2)\,\delta^2/\rho_0^2],\\
&J_n'(\sigma_i\rho_1)\,N_n(\sigma_i\rho_0) - J_n(\sigma_i\rho_0)\,N_n'(\sigma_i\rho_1) =\\
&\qquad = -(D/\sigma_i\rho_0)[1 + \delta/\rho_0 - \tfrac{1}{2}(\sigma_i^2\rho_0^2 - n^2 - 2)\,\delta^2/\rho_0^2],\\
&J_n'(\sigma_i\rho_1)\,N_n'(\sigma_i\rho_0) - J_n'(\sigma_i\rho_0)\,N_n'(\sigma_i\rho_1) =\\
&\qquad = (D/\sigma_i^2\rho_0^2)[(\sigma_i^2\rho_0^2 - n^2)\delta/\rho_0 + \tfrac{1}{2}(\sigma_i^2\rho_0^2 - 3n^2)\,\delta^2/\rho_0^2].
\end{aligned}$$

After dividing out common factors the determinantal equation finally becomes

$$P + Q\delta/\rho_0 + R\delta^2/\rho_0^2 = 0 \tag{14}$$

with

$$P = (q^2 - su)(j\omega\mu_0/\sigma\rho_0)\,J_n(\sigma\rho_1)\,J_n'(\sigma\rho_1), \tag{15}$$

$$\begin{aligned}
Q = &\{(q^2 - su)(qb + sc) - (n^2/\rho_0^2)[(q^2 - su)s +\\
&+ (pq - ru)r - (ps - qr)(p + 2\gamma/\sigma^2) - s\gamma^2/\sigma^4]\}J_n^2(\sigma\rho_1) -\\
&- n(ru - st)(\omega\mu_0/\sigma\rho_0)J_n(\sigma\rho_1)J_n'(\sigma\rho_1) + s(\omega^2\varepsilon_0\mu_0/\sigma^2)J_n'^2(\sigma\rho_1),
\end{aligned} \tag{16}$$

$$\begin{aligned}
R = &\{\tfrac{1}{2}(q^2 - su)(qb + sc) + jn(pq - st + q\gamma/\sigma^2)(qb + sc) -\\
&- \tfrac{3}{2}(n^2/\rho_0^2)[(q^2 - su)s + (pq - ru)r - (ps - qr)(p + 2\gamma/\sigma^2) -\\
&- s\gamma^2/\sigma^4] + (jn^3/\rho_0^2)[(q^2 + rt)r - (pq - st)s -\\
&- (pr + qs)(p + 2\gamma/\sigma^2) - r\gamma^2/\sigma^4]\}\,J_n^2(\sigma\rho_1) - \{[s(qb + sc)\,\rho_0^2 -\\
&- n^2(r^2 + s^2)](j\omega\varepsilon_0/\sigma\rho_0) - [\tfrac{1}{2}u(qb + sc)\rho_0^2 + \tfrac{1}{2}s(qd + ua)\rho_0^2 +\\
&+ \tfrac{1}{2}jn(ru - st) - n^2(rt + su)](j\omega\mu_0/\sigma\rho_0)\}\,J_n(\sigma\rho_1)\,J_n'(\sigma\rho_1) -\\
&- (\tfrac{1}{2}s + jnr)(\omega^2\varepsilon_0\mu_0/\sigma^2)\,J_n'^2(\sigma\rho_1).
\end{aligned} \tag{17}$$

§ 3. *Determination of the propagation constant.* In order to find the propagation constant from (14) we write

$$\gamma = \gamma_0 + \Delta_1\gamma + \Delta_2\gamma,\ \sigma = \sigma_0 + \Delta_1\sigma + \Delta_2\sigma, \tag{18}$$

where $\Delta_1\gamma$ and $\Delta_1\sigma$ are considered to be of the first degree in δ, $\Delta_2\gamma$ and $\Delta_2\sigma$ of the second degree. It must also be remembered that γ according to (3) occurs in some of the quantities p, q, etc. The zeroth approximation is then obtained by putting $\delta = 0$ in (14) and replacing σ by σ_0, ρ_1 by ρ_0 in the expression (15) for P. This leads to the condition

$$J_n(\sigma_0\rho_0)\, J_n'(\sigma_0\rho_0) = 0,$$

which can be fulfilled either by $J_n(\sigma_0\rho_0) = 0$, corresponding to TM-waves, or by $J_n'(\sigma_0\rho_0) = 0$, corresponding to TE-waves, propagated in the empty guide. From the values σ_0 satisfying one of these conditions we obtain by means of (7) the appropriate values of the propagation constant γ_0.

Let us now further consider the case of TE-waves and let us put $\varepsilon_1 = \varepsilon_3 = \varepsilon$, $\varepsilon_2 = 0$ as ferrites show no gyroelectric behaviour. Going to the next approximation we must on account of (18) write the argument of $J_n(\sigma\rho_1)$ and $J_n'(\sigma\rho_1)$ in P as $\sigma\rho_1 = (\sigma_0 + \Delta_1\sigma)(\rho_0 - \delta)$ and develop up to terms linear in δ, while in Q as given by (16) we can everywhere replace γ and σ by γ_0 and σ_0. We then obtain an equation for $\Delta_1\sigma$ in the evaluation of which the following relations resulting from (3) are convenient to remember:

$$\begin{aligned}
&q^2 - su = -\omega^2\varepsilon_1\mu_1\Delta^{-1}, && q^2 + rt = -\omega^2\varepsilon_2\mu_2\Delta^{-1},\\
&pq - st = j\omega^2\varepsilon_1\mu_2\Delta^{-1}, && pq - ru = j\omega^2\varepsilon_2\mu_1\Delta^{-1},\\
&ps - qr = j\gamma\omega\mu_1\Delta^{-1}, && pr + qs = -\gamma\omega\mu_2\Delta^{-1},\\
&rt + su = \omega^2(\varepsilon_1\mu_1 - \varepsilon_2\mu_2)\Delta^{-1}, && ru - st = j\omega^2(\varepsilon_1\mu_2 - \varepsilon_2\mu_1)\Delta^{-1},\\
&r^2 + s^2 = -\omega^2(\mu_1{}^2 - \mu_2{}^2)\Delta^{-1}, && qb + sc = -j\omega\mu_3, \quad qd + ua = j\omega\varepsilon_3.
\end{aligned}$$

Making use of (7) we have $\Delta_1\gamma = (\sigma_0/\gamma_0)\,\Delta_1\sigma$ and get thus finally

$$\begin{aligned}\Delta_1\gamma = \frac{1}{\gamma_0(\sigma_0{}^2\rho_0{}^2 - n^2)}&\left\{\gamma_0{}^2\left[\sigma_0{}^2\rho_0{}^2\left(1 - \frac{\mu_3}{\mu_0}\right) - n^2\left(1 - \frac{\mu_1{}^2 - \mu_2{}^2}{\mu_0\mu_1}\right)\right] + \right.\\
&\left. + \,\omega^2\varepsilon_0\mu_0\left[\sigma_0{}^2\rho_0{}^2\left(1 - \frac{\mu_3}{\mu_0}\right) - n^2\left(1 - \frac{\varepsilon_0}{\varepsilon}\right)\right]\right\}\frac{\delta}{\rho_0}. \qquad (19)\end{aligned}$$

Here $\sigma_0\rho_0$ is a root of the equation $J_n'(\sigma_0\rho_0) = 0$. In particular for TE_{11}-waves it is the first root while $n = 1$.

From (19) it is seen that the first order change in the propagation constant is quadratic in n, signifying that no difference for the values $+n$ and $-n$ and hence no Faraday effect occurs in this approximation. To get a non-vanishing Faraday rotation it hence is necessary to pass on to terms quadratic in δ. We shall confine ourselves to computing the expression $\Delta_2\gamma^+ - \Delta_2\gamma^-$ for right- and left-circular waves of given n. To this difference only terms in (14) that are odd in n contribute. In the term P as given by (15) we must on account of (18) now use as argument $\sigma\rho_1$ of the Bessel functions the expression $(\sigma_0 + \Delta_1\sigma + \Delta_2\sigma)(\rho_0 - \delta)$, developing again around the values for the argument $\sigma_0\rho_0$. For the reason mentioned only the last but one term of the expression (16) for Q contributes, it being sufficient here to use as argument of the Bessel functions the expression $(\sigma_0 + \Delta_1\sigma)(\rho_0 - \delta)$ with $\Delta_1\sigma$ as previously determined. In R as given by (17) the quantities γ and σ may again everywhere be replaced by γ_0 and σ_0. We find thus $\Delta_2\sigma^+ - \Delta_2\sigma^-$, from which by (7) we ultimately get

$$\Delta_2\gamma^+ - \Delta_2\gamma^- =$$

$$= \frac{2n\gamma_0}{\sigma_0^2\rho_0^2 - n^2} \frac{\mu_2}{\mu_1} \left(\sigma_0^2\rho_0^2 \frac{\mu_3}{\mu_0} - n^2 \frac{\mu_1^2 - \mu_2^2}{\mu_0\mu_1} \right) \frac{\delta^2}{\rho_0^2}, \quad n > 0. \qquad (20)$$

The equations (19) and (20) can serve to determine the quantities ε, μ_1, μ_2, μ_3 from experiments. It is noteworthy that μ_3 occurs in these expressions. When using concentric rods this is not the case in the approximation considered by van Trier; only in higher approximations, which, however, give rise to very involved formulae, μ_3 makes its appearance.

Received 11th March, 1959.

REFERENCES

1) Van Trier, A. A. T. M., Thesis Delft, 1953; Appl. Sci. Res. **B3** (1953) 142, 305.
2) Suhl, H. and L. R. Walker, Bell. Syst. Techn. J. **33** (1954) 1133.
3) Snieder, J., Thesis Delft, 1958; Appl. Sci. Res. **B7** (1958) 185.

Appl. sci. Res. Section B, Vol. 7

CALCULATED PATTERNS OF SLOTTED ELLIPTIC-CYLINDER ANTENNAE

by JAMES R. WAIT and WALTER E. MIENTKA

National Bureau of Standards, Boulder, Colorado, U.S.A.

Summary

The model assumed is a perfectly conducting elliptic cylinder of infinite length which has a narrow axial slot of finite length. Patterns are presented for various ratios of the major to minor axis. It is indicated that for reasonably large elliptic cylinders the patterns are dependent mainly on the surface curvature in the neighborhood of the slot.

The slot antenna in various forms is now used extensively in microwave radiating systems. To predict the radiation pattern of such an antenna in a given situation is often very difficult because it is a function of the shape of the metallic object in which the slot is cut. To a crude first approximation, the metal surface is represented as an infinite conducting plane which is tangent to the slot. Thus the radiation diffracted around the edges is neglected. The next approach is to seek a solution of Maxwell's equation which satisfy the appropriate boundary conditions on the surface. For actual shapes this task is usually impossible because of the non-separability of Maxwell's equations except in certain co-ordinate systems. However, if the object can be approximated by spheres, cylinders or spheroids, a solution can be obtained which provides valuable information to the designer. For example, if the surface is an aircraft wing, a reasonable representation is an elliptic cylinder. A missile might be represented by a circular cylinder which is a special case of an elliptic cylinder with zero eccentricity. Other plate-like structures could be approximated by a ribbon or an elliptic cylinder of vanishing minor axis.

It is the purpose of this paper to present radiation patterns of slot antennas on elliptic cylinders of various sizes and eccentricities.

The elliptic cylinder is assumed to be of perfect conductivity and infinite length. For metallic surfaces the first of these assumptions is quite reasonable unless the surface is modified by a dielectric coating or corrugated in some fashion. The second assumption would seem to be rather restrictive. However, if the slot or slots are cut on the cylindrical structure in such a way that the radiation is directed broadside, the end effects would be minimized. An alternative way of looking at this is to consider the nature of the induced currents. For example, in the case of narrow axial slots cut on a circular cylinder, the currents flow mainly in the azimuthal direction so that the truncation of the cylinder will not seriously impair the behaviour of the induced currents. On the other hand, a circumferential slot on a circular cylinder tends to drive currents in an axial direction towards the ends of the cylinder and truncation would profoundly modify the induced current distribution. For the above reasons, only the axial slotted elliptic cylinder is considered here.

In a previous paper [1]) a derivation was given for the electromagnetic field produced by an arbitrary slot cut in the surface of an elliptic cylinder of perfect conductivity and infinite length. The electric field tangential to the slot was assumed to be a prescribed function. When the results were specialized to the far zone region and to axial or transverse slots, agreement was obtained with the earlier results of Wong [2]) who employs a different method. In the present paper calculated radiation patterns are presented for narrow axial slots on thin elliptic cylinders.

The perfectly conducting cylinder is taken to be of infinite length with minor axis $2a$ and major axis $2b$. If the cylinder axis is coincident with the z axis of a rectangular coordinate system (x, y, z), the surface of the cylinder is specified by

$$x^2/b^2 + y^2/a^2 = 1 \tag{1}$$

as indicated in fig. 1. As in the previous paper, it is convenient now to introduce elliptic cylinder coordinates (u, v, z) which are defined by the following transformation:

$$x = d \sinh u \sin v, \;\; y = d \cosh u \cos v, \;\; z = z, \tag{2}$$

where $2d$ is the distance between the foci of the ellipse. The foci are located at the points $(x = \pm d, y = 0)$. The surfaces $u =$ constant represent a family of confocal cylinders of elliptic cross-section. The semi-major and semi-minor axes of the ellipse $u = u_0$ are given by $b = d \cosh u_0$, $a = d \sinh u_0$.

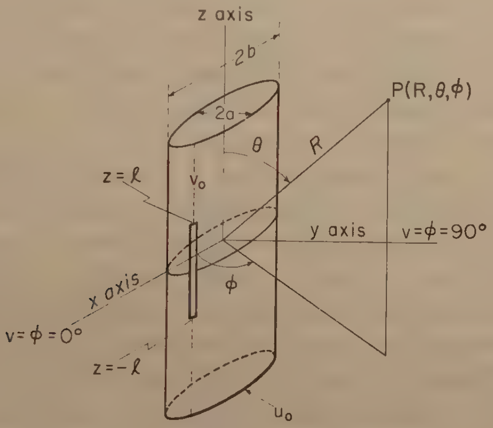

Fig. 1. Narrow axial slot on an elliptic cylinder.

A narrow rectangular slot is located on the cylinder at $v = v_0$, extending from $z = -l$ to $z = +l$ in the axial direction. As a result of the assumed small width of the slot, only the transverse voltage $V(z)$ along the slot contributes to the radiated fields. From previous analysis ¹) it then follows that, in terms of spherical coordinates (R, θ, ϕ), the electric field at large distances from the cylinder has only a significant ϕ component and is given by

$$E_\phi = (2/\pi)^{\frac{1}{2}} \exp(-ikR + i\omega t) R^{-1} S(\theta) P(\theta, \phi), \qquad (3)$$

where

$$S(\theta) = \tfrac{1}{2}k \sin\theta \int_{-l}^{+l} V(z') \exp(ik \cos\theta z')\, \mathrm{d}z' \qquad (4)$$

with $k = 2\pi/\text{wavelength}$ and $S(\theta)$ the pattern of the slot if it were cut in an infinite plane conducting sheet. The factor $P(\theta, \phi)$, which accounts for diffraction by the elliptic cylinder in the far zone (i.e. $kR \gg 1$), is given by the rather cumbersome expression

$$P(\phi, v_0) = \sum_{m=0}^{\infty} \frac{i^m \,\mathrm{Se,\,o}_m(s, v_0)\, \mathrm{Se,\,o}_m(s, \phi)}{N_m^{e,o}(s)[\partial \mathrm{He,\,o}_m^{(2)}(s, u_0)/\partial u_0]} \qquad (5)$$

where $\sqrt{s} = kd \sin\theta$. The functions $\mathrm{Se,\,o}_m$, $\mathrm{He,\,o}_m^{(2)}$, and $\mathrm{N}_m^{e,o}$ are the angular, radial, and normalization constants, respectively, of the Mathieu functions of order m. The double suffix e, o indicates that the summation takes place over both even and odd Mathieu functions.

It should be noted that the function $P(\phi, v_0)$ is independent of the voltage distribution $V(z)$ along the narrow axial slot. This function can be called the "elliptic-cylinder space factor" as it fully describes the effect of the finite width of the conducting surface on which the slot is located.

The function $P(\phi, v_0)$ when plotted as a function of ϕ characterizes the azimuthal radiation pattern for a fixed value of $\sqrt{s} = kd \sin\theta$. Since, as mentioned above, in certain systems slots are cut in surfaces which can be approximated by elliptic cylinders, it is worth while to carry out computation of $P(v_0, \phi)$ for various values of s. In the case of the strip, that is if $a \ll b$, the quantity u_0 in (5) can be replaced by zero. The infinite series solution can now be simplified by making use of the following identities [3]):

$$[\partial \mathrm{He}_m^{(2)}(s, u)/\partial u]_{u=0} = -\,i/\mathrm{Je}_m(s, o), \qquad (6)$$

$$\sum_{m=0}^{\infty} i^m\, \mathrm{Se}_m(s, v_0)\, \mathrm{Se}_m(s, \phi)\, \mathrm{Je}_m(s, 0)/N_m{}^e(s) = \\ = (8\pi)^{-\frac{1}{2}} \exp(is^2 \cos v_0 . \cos\phi). \qquad (7)$$

The space factor for the thin elliptic cylinder is then written in the form

$$P(s, \phi) = i(8\pi)^{-\frac{1}{2}} \exp(is^2 \cos v_0 . \cos\phi) + \\ + \sum_{m=0}^{\infty} \frac{i^m\, \mathrm{So}_m(s, v_0)\, \mathrm{So}_m(s, \phi)}{\mathrm{N}_m{}^o(s)\, \mathrm{Ho}_m^{(2)\prime}(s, 0)}, \qquad (8)$$

where

$$\mathrm{Ho}_m^{(2)\prime}(s, 0) = [\partial\, \mathrm{Ho}_m^{(2)}(s, u)/\partial u]_{u=0}.$$

The amplitude and phase of the function $P(\phi, v_0)$ has been calculated from the series expressions given above. Various values of the ratio a/b and the parameter x $(= kb \sin\theta)$. The results of these rather laborious computations are shown in tables I, II and III. The azimuthal patterns are characterized by plotting $|P(\phi, v_0)|$ as a function of ϕ and these are shown in fig. 2 for a slot at the centre of the broad face and in fig. 3 for a slot at the edge. In these plots, the ratio of major to minor axis is 2 with the addition of one

TABLE Ia

Amplitude for $P(\phi, \frac{1}{2}\pi)$; $a/b = \frac{1}{2}$					
ϕ degrees	$kb = 1.15$	$kb = 2$	$kb = 4$	$kb = 6.11$	$kb = 8$
−90	0.185	0.142	0.104	0.0832	0.0673
−80	0.180	0.132	0.0773	0.0383	0.0178
−70	0.168	0.106	0.0276	0.0608	0.0740
−60	0.150	0.0769	0.0845	0.0964	0.0552
−50	0.133	0.0761	0.130	0.0706	0.0872
−40	0.125	0.110	0.141	0.128	0.114
−30	0.131	0.154	0.140	0.154	0.120
−20	0.153	0.194	0.156	0.177	0.175
−10	0.184	0.230	0.207	0.208	0.217
0	0.218	0.259	0.259	0.257	0.253
10	0.253	0.285	0.303	0.311	0.311
20	0.287	0.309	0.341	0.350	0.356
30	0.318	0.332	0.363	0.372	0.378
40	0.347	0.355	0.381	0.384	0.389
50	0.371	0.376	0.390	0.390	0.390
60	0.390	0.392	0.394	0.394	0.392
70	0.405	0.404	0.390	0.396	0.402
80	0.413	0.410	0.393	0.396	0.400
90	0.416	0.412	0.393	0.396	0.394

TABLE Ib

Phase in degrees for $P(\phi, \frac{1}{2}\pi)$, $a/b = \frac{1}{2}$					
ϕ degrees	$kb = 1.15$	$kb = 2$	$kb = 4$	$kb = 6.11$	$kb = 8$
−90	340.4	271.9	123.7	329.8	190.3
−80	342.1	275.2	131.7	349.0	258.1
−70	347.2	287.1	206.4	128.4	4.43
−60	356.8	316.0	277.0	155.6	64.2
−50	12.1	4.15	299.5	205.9	167.8
−40	33.1	39.0	324.2	232.2	223.2
−30	56.3	58.9	359.6	329.5	295.8
−20	76.3	73.2	41.1	11.2	357.9
−10	91.4	85.5	73.2	56.4	45.4
0	102.8	97.1	98.4	96.5	94.1
10	111.5	108.3	119.6	129.2	137.6
20	118.5	118.8	139.2	157.5	174.5
30	124.2	128.4	155.4	183.5	209.6
40	128.8	136.6	170.3	207.2	241.8
50	132.4	143.2	183.0	227.8	268.9
60	135.1	148.1	193.3	244.7	290.8
70	137.0	151.4	201.3	257.1	306.7
80	138.1	153.3	206.0	264.6	317.3
90	139.5	153.9	207.8	267.2	321.6

TABLE IIa

Amplitude for $P(\phi, 0)$, $a/b = \frac{1}{2}$					
ϕ degrees	$kb = 1.15$	$kb = 2$	$kb = 4$	$kb = 6.11$	$kb = 8$
0	0.279	0.298	0.327	0.354	0.361
10	0.279	0.297	0.327	0.352	0.360
20	0.278	0.292	0.327	0.345	0.356
30	0.277	0.285	0.326	0.337	0.353
40	0.275	0.276	0.318	0.333	0.348
50	0.270	0.268	0.301	0.327	0.336
60	0.263	0.263	0.284	0.309	0.322
70	0.252	0.263	0.279	0.292	0.298
80	0.236	0.263	0.279	0.286	0.287
90	0.218	0.259	0.259	0.257	0.253
100	0.199	0.245	0.224	0.239	0.248
110	0.181	0.219	0.210	0.230	0.208
120	0.168	0.186	0.215	0.186	0.208
130	0.163	0.155	0.200	0.174	0.164
140	0.165	0.140	0.153	0.175	0.154
150	0.171	0.143	0.103	0.127	0.142
160	0.177	0.156	0.104	0.0732	0.0770
170	0.182	0.168	0.134	0.103	0.0795
180	0.184	0.173	0.149	0.127	0.109

TABLE IIb

Phase in degrees for $P(\phi, 0)$, $a/b = \frac{1}{2}$					
ϕ degrees	$kb = 1.15$	$kb = 2$	$kb = 4$	$kb = 6.11$	$kb = 8$
0	166.3	219.0	329.3	90.5	196.2
10	165.4	217.2	325.8	85.2	190.3
20	162.5	212.0	315.5	69.4	170.9
30	158.0	203.1	299.3	43.3	136.7
40	151.9	190.6	277.6	7.8	90.6
50	144.4	174.6	249.6	324.9	33.1
60	135.8	156.0	214.6	275.1	327.1
70	126.0	136.0	175.4	217.1	253.6
80	115.1	116.1	136.8	157.5	176.3
90	102.8	97.1	98.4	96.5	94.0
100	88.8	78.8	55.3	29.4	12.6
110	73.0	60.2	7.6	329.2	290.2
120	55.8	39.6	327.1	269.6	211.0
130	38.6	14.9	296.1	204.0	139.9
140	23.2	346.6	266.8	156.4	60.9
150	10.9	320.9	224.9	118.6	9.1
160	2.3	303.1	171.7	56.2	313.8
170	357.2	293.4	144.3	356.1	224.8
180	355.6	290.3	137.4	343.6	202.8

TABLE III

Amplitude for $P(\phi, \frac{1}{2}\pi)$ $kb = 4$; $v_0 = \frac{1}{2}\pi$, $a/b = \frac{1}{4}$				Amplitude for $P(\phi, 0)$ $kb = 4$, $v_0 = 90°$, $a/b = \frac{1}{4}$			
ϕ degrees		ϕ degrees		ϕ degrees		ϕ degrees	
0	.221			0	.270	100	.212
10	.273	—10	.172	10	.270	110	.221
20	.326	—20	.136	20	.271	120	.219
30	.377	—30	.129	30	.268	130	.196
40	.420	—40	.142	40	.259	140	.166
50	.441	—50	.136	50	.248	150	.149
60	.435	—60	.087	60	.247	160	.152
70	.405	—70	.026	70	.252	170	.163
80	.371	—80	.090	80	.243	180	.169
90	.357	—90	.124	90	.221		

Phase for $P(\phi, \frac{1}{2}\pi)$ $kb = 4$; $v_0 = \frac{1}{2}\pi$, $a/b = \frac{1}{4}$				Phase for $P(\phi, 0)$ $kb = 4$, $v_0 = 0$, $a/b = \frac{1}{4}$			
ϕ degrees		ϕ degrees		ϕ degrees		ϕ degrees	
0	98.0			0	330.5	100	52.6
10	111.1	—10	79.7	10	326.9	110	11.6
20	121.8	—20	51.9	20	316.4	120	337.7
30	130.6	—30	17.2	30	299.6	130	306.2
40	137.5	—40	350.4	40	276.6	140	272.7
50	142.3	—50	333.5	50	246.4	150	237.2
60	144.7	—60	318.0	60	210.9	160	207.3
70	144.9	—70	235.3	70	174.8	170	189.4
80	143.6	—80	164.5	80	138.6	180	183.6
90	142.7	—90	159.0	90	98.0		

pattern in fig. 3 where it is 4. The corresponding patterns are shown in figs. 4 and 5 for a strip (i.e. $a/b \to 0$) where the slot is at the centre. Also for comparison purposes, the patterns for an axial slot on a circular cylinder are shown in fig. 5 (i.e. $a = b$). The numerical data for figs. 4 and 5 were taken from earlier work [4]) [5]).

For the patterns shown in figs. 2 to 5, an effort was made to chose the maximum transverse dimension of the objects to be the same. That is the major axis of the elliptic cylinder, the width of the strip and the diameter of the cylinder all have approximately the same set of values (i.e. $x = 1, 2, 4, 6$ and 8). As might be expected, the patterns are similar in appearance. In all cases, the field diffracted to the rear diminishes with increasing x, but the lobes become more numerous. In a crude sense the elliptic cylinder

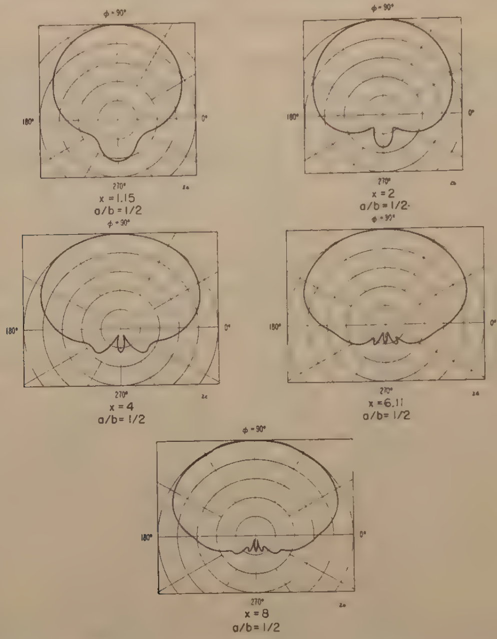

Fig. 2. Radiation patterns of axial slot on elliptic cylinder, $v_0 = 90°$.

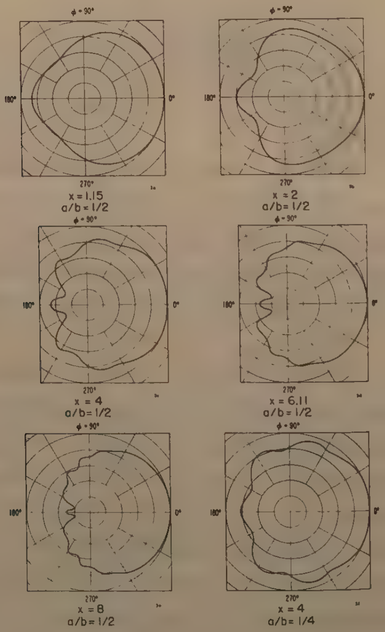

Fig. 3. Radiation patterns of axial slot on elliptic cylinder, $v_0 = 0°$.

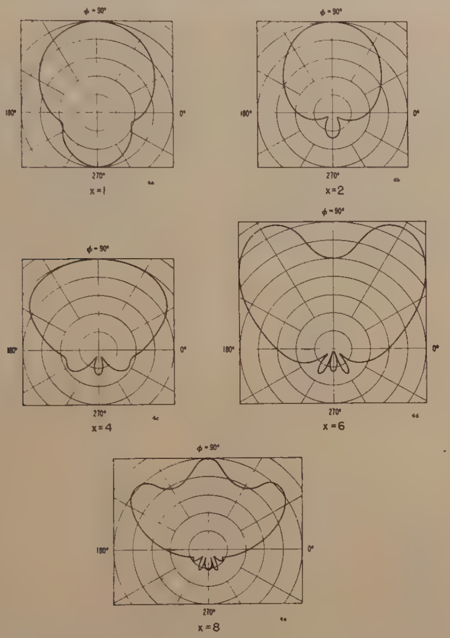

Fig. 4. Radiation patterns of axial slot on strip, $v_0 = 90°$.

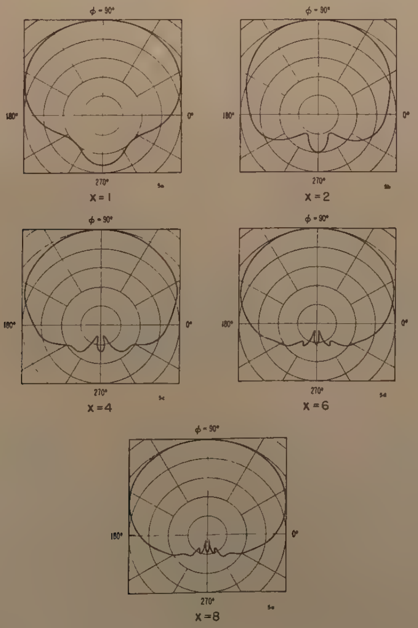

Fig. 5. Radiation patterns of axial slot on circular cylinder, $v_0 = 90°$.

patterns for the case $a/b = 1/2$ in fig. 2 are intermediate to the strip patterns in fig. 4 and the circular cylinder patterns in fig. 5. It would thus seem possible to employ these patterns to provide rough estimates for elliptic cylinders of other eccentricities. Certain features of the strip patterns such as the splitting of the main lobe must be attributed to the fields scattered by the sharp edges which are not present with the elliptic cylinder of finite minor axis.

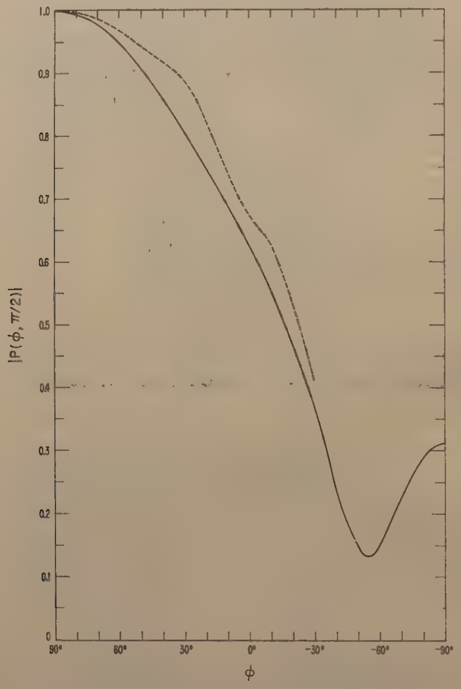

Fig. 6. Comparison of radiation patterns of slotted elliptic cylinder and circular cylinder $|P(\phi, \frac{1}{2}\pi)|$ vs ϕ, matching curvature at $\phi = 90°$.

———— $x = 2$ elliptic cylinder: $a/b = \frac{1}{2}$,

- - - - - - $x = 4$ circular cylinder.

It is of interest to note that the patterns in fig. 3 for a slot at the narrow edge of an elliptic cylinder are less directional than the patterns in fig. 2 for the slot in the broad face. In the limiting case for a slot at the edge of a strip, the pattern would be omni-directional so that patterns in fig. 3 are therefore quite reasonable. The transition to a circular pattern is quite evident on examining the case for $a/b = 1/4$ for $x = 4$ in fig. 3 which is almost omni-directional.

The patterns shown above are generally applicable to any narrow axial slot on the elliptic cylinder. To completely describe the three-dimensional pattern, of course it is also necessary to specify $S(\theta)$ which depends on the functional form of $V(z)$. For convenience it is usually assumed that the voltage along the slot is sinusoidal such that

$$V(z) = V_0 \frac{\sin k(l - |z|)}{\sin kl}, \tag{9}$$

where V_0 is the voltage at the center of the slot, and consequently for $2l = \frac{1}{2}\lambda$

$$S(\theta) = V_0 \frac{\cos\left(\frac{1}{2}\pi \cos\theta\right)}{\sin\theta}. \tag{10}$$

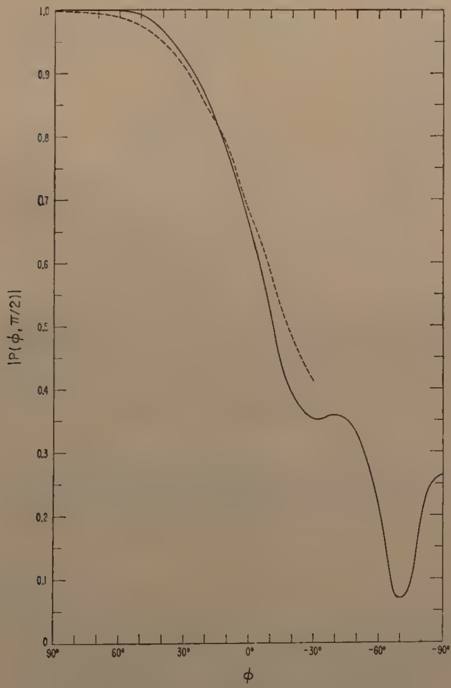

Fig. 7. As fig. 6, $|P(\phi, \frac{1}{2}\pi)|$ vs ϕ.
———— $x = 4$ elliptic cylinder: $a/b = \frac{1}{2}$,
- - - - - - $x = 8$ circular cylinder.

It has been conjectured by Fock [6]) and others that currents excited by a plane wave on a convex surface are only determined by the local radius of curvature. As pointed out in an earlier paper [7]), such an assumption is equivalent to stating that the pattern of a slot is only a function of the local curvature of the surface. As far as the authors are aware, this local field principle has never been well established. An important check on this concept is to compare the pattern of the slot at the centre of the broad face of the elliptic cylinder with the pattern of an axial slot on a circular cylinder. Such a comparison is illustrated in figs. 6, 7, 8 and 9, where $P(\phi, v_0)$ for $v_0 = \frac{1}{2}\pi$ is plotted as a function of ϕ from 90° to — 90° for an elliptic cylinder with $a/b = \frac{1}{2}$ and a circular cylinder whose radius is taken to be $2b$. The radius of the circular cylinder considered is thus twice the semi-major axis of the elliptic cylinder.

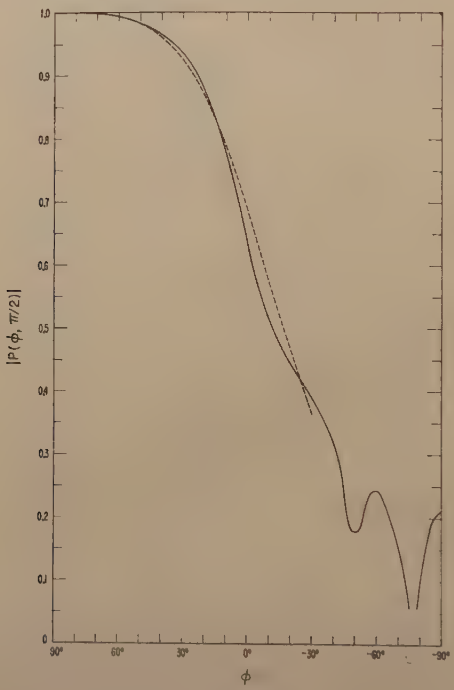

Fig. 8. As fig. 6, $|P(\phi, \frac{1}{2}\pi)|$ vs ϕ.
——— $x = 6.11$ elliptic cylinder: $a/b = \frac{1}{2}$,
- - - - - - $x = 12$ circular cylinder.

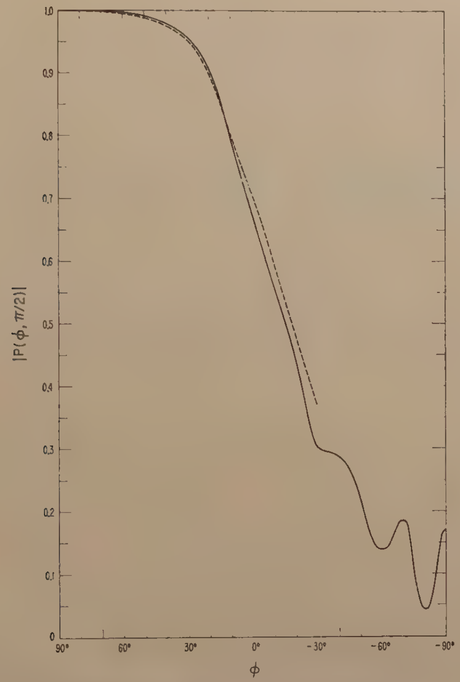

Fig. 9. As fig. 6, $|P(\phi, \frac{1}{2}\pi)|$ vs ϕ.
———— $x = 8$ elliptic cylinder: $a/b = \frac{1}{2}$,
- - - - - - $x = 15$ circular cylinder.

The results indicate that the similarity between the patterns improves as x becomes larger. Consequently, there is some basis to the local field concept when the radius of curvature is large compared to the wavelength and slowly varying.

Acknowledgement. The work reported here was supported by Electronics Research Directorate of the U.S. Air Force Cambridge Research Center.

Received 29th November, 1958.

REFERENCES

1) Wait, J. R., J. Appl. Phys. **26** (1955) 458.
2) Wong, J. Y., Proc. Instn Radio Engrs **4**b (1953) 1172.
3) Morse, P. M. and H. Feshbach, Methods of Theoretical Physics, Part II, McGraw Hill Book Co., New York 1953, p. 1571.
4) Wait, J. R. and S. H. Kahana, Can. J. Tech. **33** (1955) 211.
5) Wait, J. R., Wireless Engr **32** (1955) 316; also Nat. Bur. Stand. J. Res. **59** (1957) 255.
6) Fock, V. A., J. Phys. USSR **10** (1946) 130 and 399.
7) Wait, J. R., Electromagnetic Radiation from Cylindrical Structures Pergamon Press, London, 1959.

Also see the articles by J. Y. Wong, Trans. Instn Radio Engrs AP-**3** (1955) 200 (for patterns of single and multiple axial slots on elliptic cylinders of vanishing minor axis, i.e. strips) and George Sinclair, Proc. Instn Radio Engrs **39** (1951) 660 (shows an *E*-plane pattern for a small axial loop at the end of the major axis for the case $kb = 4$ and $b/a = 1.63$ which is very similar to our fig. 3*c* for $kb = 4$ and $b/a = 2$).

ERRATUM

Appl, sci. Res. **B7** (1959) 361.

EQUIVALENT BASE RESISTANCE OF POINT-CONTACT TRANSISTORS

by FREDERICK J. YOUNG

Eq. (3) should read

$$\frac{\partial v}{\partial x}(\pm x_0, y, -z_0 < z < z_0) = \frac{\partial v}{\partial y}(x, \pm y, -z_0 < z < 0) = 0$$

Appl. sci. Res. Section B, Vol. 7

ON THE PLANE-WAVE EXTINCTION CROSS-SECTION OF AN OBSTACLE

by A. T. DE HOOP

Laboratorium voor Theoretische Elektrotechniek en Elektromagnetische Straling der Technische Hogeschool, Delft, Netherlands

Summary

A time-harmonic plane electromagnetic wave is incident upon an obstacle of finite dimensions. The properties of the obstacle are such that electromagnetic power is both absorbed and scattered. A close relation exists between the extinction cross-section of the obstacle and the amplitude and phase of the scattered wave in the direction of propagation of the incident wave. The exact form of this relation, the "cross-section theorem", is proved by making use of an explicit representation of the scattered field. The result is valid for a plane wave with arbitrary elliptic polarization. Finally, a similar relation for the scattering of sound waves is given.

§ 1. *Introduction.* In the study of the scattering and diffraction of a time-harmonic plane electromagnetic wave by an obstacle of finite dimensions, one of the major problems is the evaluation of the average power absorbed and the average power scattered by the obstacle. It has been argued by Van de Hulst [1]) [2]) that, on physical grounds, the sum of absorbed and scattered power is expected to be closely related to the amplitude and phase of the scattered wave in the direction in which the incident wave propagates. When expressed in terms of the extinction cross-section (for its definition, see § 3), the indicated relation is called the "cross-section theorem".

The special case of perfectly conducting obstacles has been investigated by Levine and Schwinger [3]) (scattering by plane obstacles of vanishing thickness) and by Storer and Sevick [4]) (scattering by obstacles of arbitrary shape). The proof given by these authors is based on the integral equation to be satisfied by the surface-current density at the boundary of the obstacle. The generalization to the case of an obstacle with arbitrary electromagnetic properties is due to Jones [5]) who, in order to prove the theorem, employed the method of stationary phase for two-dimensional integrals. However, in studying Jones' paper, the present author observed that this complicated method can be avoided by using an explicit representation of the far-zone scattered field. The latter method leads to the proof given in § 3, where the general case of an elliptically polarized incident plane wave is considered.

At this point *) it may be remarked that cross-section theorems similar to the ones given in § 3 and § 4 hold in any type of scattering problem [6]). In the field of scattering by atomic systems a relation of this kind has been known at least since 1932 [7]). For details the reader is referred to the literature on the subject [6]) [7]) [8]).

§ 2. *The far-zone scattered field.* A time-harmonic, elliptically polarized, plane electromagnetic wave is incident upon an obstacle of finite dimensions. The boundary of the obstacle is a sufficiently regular closed surface S. The electric and magnetic properties of the obstacle are assumed to be such that electromagnetic power is both absorbed and scattered. The medium in the domain outside S is assumed to be homogeneous, isotropic and non-conducting (which includes the case of free space), with inductive capacities ε_0 and μ_0. In the exterior domain, the electric field vector $\mathbf{E}$ and the magnetic field vector $\mathbf{H}$ are written as the sum of the incident field $\mathbf{E}_i$, $\mathbf{H}_i$ and the scattered field $\mathbf{E}_s$, $\mathbf{H}_s$:

$$\mathbf{E} = \mathbf{E}_i + \mathbf{E}_s, \tag{2.1}$$

$$\mathbf{H} = \mathbf{H}_i + \mathbf{H}_s. \tag{2.2}$$

Both the incident and the scattered field satisfy Maxwell's equations

$$\operatorname{curl} \mathbf{H} = -\, i\omega\varepsilon_0 \mathbf{E}, \tag{2.3}$$

$$\operatorname{curl} \mathbf{E} = i\omega\mu_0 \mathbf{H}, \tag{2.4}$$

where ω is the angular frequency of the exponential time dependence of the form $\exp(-\, i\omega t)$. This factor, which has been omitted throughout, is common to all field components.

---

*) For this remark the author is indebted to Professor R. Kronig, Technische Hogeschool, Delft, Netherlands.

Let $\mathbf{r}$ be the radius vector drawn from a fixed origin located somewhere in the domain occupied by the obstacle. The incident field is then given by

$$\mathbf{E}_i(\mathbf{r}) = \mathbf{A}\exp(-ik\boldsymbol{\alpha}\cdot\mathbf{r}), \tag{2.5}$$

$$\mathbf{H}_i(\mathbf{r}) = (\varepsilon_0/\mu_0)^{\frac{1}{2}}(\mathbf{A}\times\boldsymbol{\alpha})\exp(-ik\boldsymbol{\alpha}\cdot\mathbf{r}), \tag{2.6}$$

where $\mathbf{A}$ specifies the polarization of the incident wave (in general, elliptic) and $\boldsymbol{\alpha}$ is the unit vector pointing *toward* the source at infinity. Further,

$$k = \omega(\varepsilon_0\mu_0)^{\frac{1}{2}} = 2\pi/\lambda, \tag{2.7}$$

λ being the wave length.

The next problem is to obtain an expression for the scattered field. It has been stated already that $\mathbf{E}_s$ and $\mathbf{H}_s$ satisfy Maxwell's equations (2.3) and (2.4). In addition, the field vectors shall satisfy the radiation condition 9) *)

$$\int_{S_R} |\mathbf{E}_s - (\mu_0/\varepsilon_0)^{\frac{1}{2}}(\mathbf{H}_s \times \boldsymbol{i}_R)|^2\, \mathrm{d}S = o(1) \qquad (R \to \infty), \tag{2.8}$$

where S_R is a sphere of radius R around some point of observation and $\boldsymbol{i}_R$ is the unit vector in the direction of the outward normal to S_R. Under these conditions the following representation holds 10)

$$4\pi\mathbf{E}_s(\mathbf{r}) = \operatorname{curl}\int_S [\mathbf{n}\times\mathbf{E}_s(\boldsymbol{\rho})]\frac{\mathrm{e}^{ikR}}{R}\,\mathrm{d}S - \\ -\frac{1}{i\omega\varepsilon_0}\operatorname{curl}\operatorname{curl}\int_S [\mathbf{n}\times\mathbf{H}_s(\boldsymbol{\rho})]\frac{\mathrm{e}^{ikR}}{R}\,\mathrm{d}S, \tag{2.9}$$

$$4\pi\mathbf{H}_s(\mathbf{r}) = \operatorname{curl}\int_S [\mathbf{n}\times\mathbf{H}_s(\boldsymbol{\rho})]\frac{\mathrm{e}^{ikR}}{R}\,\mathrm{d}S + \\ +\frac{1}{i\omega\mu_0}\operatorname{curl}\operatorname{curl}\int_S [\mathbf{n}\times\mathbf{E}_s(\boldsymbol{\rho})]\frac{\mathrm{e}^{ikR}}{R}\,\mathrm{d}S. \tag{2.10}$$

In (2.9) and (2.10) $\mathbf{n}$ is the unit vector in the direction of the outward normal to S and $R = |\mathbf{r} - \boldsymbol{\rho}|$ is the distance from the point of observation $\mathbf{r} = (x, y, z)$ to the point of integration $\boldsymbol{\rho} = (\xi, \eta, \zeta)$. Although S in (2.9) and (2.10) could be any suffi-

---

*) For a vector $\mathbf{A}$ whose components are complex numbers, we have $|\mathbf{A}|^2 = \mathbf{A}\cdot\mathbf{A}^*$, where $\mathbf{A}^*$ denotes the complex conjugate to $\mathbf{A}$.

ciently regular bounded closed surface completely surrounding the obstacle, we take, for the sake of simplicity, S to be the surface of the obstacle.

Let $\boldsymbol{\beta}$ denote the unit vector in the direction of observation; then, $\mathbf{r} = r\boldsymbol{\beta}$. At large distances from the obstacle we have

$$R^{-1} \exp(ikR) = r^{-1} \exp(ikr - ik\boldsymbol{\beta}\cdot\boldsymbol{\rho}) + O(r^{-2}) \quad (r \to \infty). \quad (2.11)$$

Using this type of expansion we obtain from (2.9) and (2.10)

$$\mathbf{E}_s(\mathbf{r}) = \mathbf{F}(\boldsymbol{\beta}) \frac{e^{ikr}}{ikr} + O(r^{-2}) \quad (r \to \infty), \quad (2.12)$$

$$(\mu_0/\varepsilon_0)^{\frac{1}{2}}\mathbf{H}_s(\mathbf{r}) = [\boldsymbol{\beta} \times \mathbf{F}(\boldsymbol{\beta})] \frac{e^{ikr}}{ikr} + O(r^{-2}) \quad (r \to \infty), \quad (2.13)$$

where the (complex) factor $\mathbf{F}(\boldsymbol{\beta})$ is given by

$$4\pi\mathbf{F}(\boldsymbol{\beta}) = - k^2\boldsymbol{\beta} \times \int_S [\mathbf{n} \times \mathbf{E}_s(\boldsymbol{\rho})] \exp(- ik\boldsymbol{\beta}\cdot\boldsymbol{\rho})\, dS +$$
$$+ (\mu_0/\varepsilon_0)^{\frac{1}{2}}k^2\boldsymbol{\beta} \times \{\boldsymbol{\beta} \times \int_S [\mathbf{n} \times \mathbf{H}_s(\boldsymbol{\rho})] \exp(- ik\boldsymbol{\beta}\cdot\boldsymbol{\rho})\, dS\}. \quad (2.14)$$

The first term of the right-hand side of (2.12) and (2.13) is called the "far-zone approximation". The special case of forward scattering is obtained by taking $\boldsymbol{\beta} = -\boldsymbol{\alpha}$.

In obtaining (2.12), (2.13) and (2.14) we have used the fact that each Cartesian component of the integrals on the right-hand side of (2.9) and (2.10) admits a representation of the form

$$u(\mathbf{r}) = \frac{e^{ikr}}{r} \sum_{n=0}^{\infty} \frac{a_n(\boldsymbol{\beta})}{r^n}, \quad (2.15)$$

where $u(\mathbf{r})$ denotes any of these Cartesian components. This expansion converges absolutely and uniformly in the domain $r \geqq r_0 + \delta > r_0$, where $r = r_0$ is the smallest sphere around the origin, completely surrounding the obstacle. The series (2.15) can be differentiated term by term with respect to the coordinates any number of times and the resulting series is absolutely and uniformly convergent in $r \geqq r_0 + \delta > r_0$. Performing the necessary differentiations we then obtain for each Cartesian component of $\mathbf{E}_s(\mathbf{r})$ and $\mathbf{H}_s(\mathbf{r})$ a representation of the form (2.15). In fact, the first term of the right-hand side of (2.12) and (2.13) is the first term of the relevant series expansion. Further, it can be shown that all coefficients of this expansion are determined by $\mathbf{F}(\boldsymbol{\beta})$.

Finally, the result satisfies the radiation condition (2.8). For a proof of these statements we refer to a paper by Wilcox [9]).

§ 3. *Proof of the cross-section theorem.* From the complex form of Poynting's theorem [11]) it follows that the average power *absorbed* by the obstacle is given by

$$P_a = -\tfrac{1}{2}\,\mathrm{Re}\int_S (\mathbf{E} \times \mathbf{H}^*)\cdot\mathbf{n}\,\mathrm{d}S. \tag{3.1}$$

The average *scattered* power is *defined* as

$$P_s = \tfrac{1}{2}\,\mathrm{Re}\int_S (\mathbf{E}_s \times \mathbf{H}_s^*)\cdot\mathbf{n}\,\mathrm{d}S. \tag{3.2}$$

Substituting (2.1) and (2.2) in the right-hand side of (3.1) and taking into account that

$$\tfrac{1}{2}\,\mathrm{Re}\int_S (\mathbf{E}_i \times \mathbf{H}_i^*)\cdot\mathbf{n}\,\mathrm{d}S = 0, \tag{3.3}$$

we get

$$P_a + P_s = -\tfrac{1}{2}\,\mathrm{Re}\int_S (\mathbf{E}_i^* \times \mathbf{H}_s + \mathbf{E}_s \times \mathbf{H}_i^*)\cdot\mathbf{n}\,\mathrm{d}S. \tag{3.4}$$

When (2.5) and (2.6) are used in the integral on the right-hand side of (3.4), the result is closely related to the expression for $\mathbf{F}(-\boldsymbol{\alpha})$ following from (2.14). By inspection we have

$$\int_S (\mathbf{E}_i^* \times \mathbf{H}_s + \mathbf{E}_s \times \mathbf{H}_i^*)\cdot\mathbf{n}\,\mathrm{d}S = 4\pi k^{-2}(\varepsilon_0/\mu_0)^{\frac{1}{2}}\mathbf{A}^*\cdot\mathbf{F}(-\boldsymbol{\alpha}). \tag{3.5}$$

Substitution of (3.5) in (3.4) yields an expression that relates $P_a + P_s$ to the far-zone scattered field in the forward direction.

Finally, the absorption cross-section σ_a and the scattering cross-section σ_s of the obstacle are introduced. These quantities are defined as follows: the absorption (scattering) cross-section is the ratio of the mean power absorbed (scattered) by the obstacle to the mean intensity of power flow in the incident field. The latter quantity is given by

$$P_i^{(1)} = -\tfrac{1}{2}\,\mathrm{Re}\,[(\mathbf{E}_i \times \mathbf{H}_i^*)\cdot\boldsymbol{\alpha}],$$

which reduces to

$$P_i^{(1)} = \tfrac{1}{2}(\varepsilon_0/\mu_0)^{\frac{1}{2}}\,|\mathbf{A}|^2. \tag{3.6}$$

Equations (3.4), (3.5) and (3.6) lead to the result

$$\sigma_a + \sigma_s = -\frac{4\pi}{k^2}\,\frac{\mathrm{Re}\,[\mathbf{A}^*\cdot\mathbf{F}(-\boldsymbol{\alpha})]}{|\mathbf{A}|^2}. \tag{3.7}$$

Equation (3.7) is known as the "cross-section theorem". The sum of the absorption cross-section and the scattering cross-section is often called the extinction cross-section [12]).

§ 4. *The extinction cross-section for scattering of sound waves.* In concluding this paper we want to remark that a similar cross-section theorem holds for the scattering of a plane sound wave by an obstacle of finite dimensions. The corresponding problem can be formulated in terms of a scalar function, viz. the velocity potential. Since the proof of the theorem is analogous to the one outlined in the preceding sections, we confine ourselves to stating the result. Again, the complex time factor $\exp(-i\omega t)$ is omitted.

If $\mathbf{v}$ is the (irrotational) particle velocity, a velocity potential Φ is introduced such that

$$\mathbf{v} = -\operatorname{grad}\Phi. \tag{4.1}$$

The excess pressure p is related to the velocity potential through

$$p = -i\omega\rho_0\Phi, \tag{4.2}$$

where ρ_0 is the density of the medium.

Let $\Phi_i(\mathbf{r})$ and $\Phi_s(\mathbf{r})$ be the velocity potential of the incident and the scattered sound field, respectively; then, $\Phi = \Phi_i + \Phi_s$. Further, let $\Phi_i(\mathbf{r})$ be given by

$$\Phi_i(\mathbf{r}) = A\exp(-ik\boldsymbol{\alpha}\cdot\mathbf{r}), \tag{4.3}$$

in which $k = \omega/c$, c being the velocity of sound. At large distances from the obstacle, $\Phi_s(\mathbf{r})$ is written in the form [13])

$$\Phi_s(\mathbf{r}) = F(\boldsymbol{\beta})\frac{e^{ikr}}{ikr} + O(r^{-2}) \quad (r \to \infty). \tag{4.4}$$

The average power absorbed by the obstacle is given by

$$P_a = -\tfrac{1}{2}\operatorname{Re}\int_S p\,\mathbf{n}\cdot\mathbf{v}^*\,\mathrm{d}S, \tag{4.5}$$

or, expressed in terms of the velocity potential,

$$P_a = -\tfrac{1}{2}\operatorname{Re}\{i\omega\rho_0\int_S \Phi\,(\mathbf{n}\cdot\operatorname{grad}\Phi^*)\,\mathrm{d}S\}, \tag{4.6}$$

where $\mathbf{n}$ is the unit vector in the direction of the outward normal to the boundary S of the obstacle. The average scattered power is defined as

$$P_s = \tfrac{1}{2}\,\mathrm{Re}\,\{i\omega\rho_0 \int_S \Phi_s(\mathbf{n}\cdot\mathrm{grad}\,\Phi_s^*)\,\mathrm{d}S\}. \tag{4.7}$$

The mean intensity of power flow in the incident wave is

$$P_i^{(1)} = \tfrac{1}{2}\omega\rho_0 k\,|A|^2. \tag{4.8}$$

When the expression for $P_a + P_s$ is compared with the representation of $F(\boldsymbol{\beta})$ it follows by inspection that $P_a + P_s$ can be expressed in terms of $F(-\boldsymbol{\alpha})$. Introduction of the absorption cross-section $\sigma_a = P_a/P_i^{(1)}$ and the scattering cross-section $\sigma_s = P_s/P_i^{(1)}$ then yields

$$\sigma_a + \sigma_s = -\frac{4\pi}{k^2}\,\frac{\mathrm{Re}\,[A^*F(-\boldsymbol{\alpha})]}{|A|^2} = -\frac{4\pi}{k^2}\,\mathrm{Re}\left[\frac{F(-\boldsymbol{\alpha})}{A}\right]. \tag{4.9}$$

Equation (4.9) is known as the cross-section theorem for sound waves. The special case of scattering by a plane obstacle of vanishing thickness has been investigated by Levine and Schwinger[14]).

Acknowledgement. The author wishes to thank Professor C. J. Bouwkamp, Philips Research Laboratories, Eindhoven, Netherlands, for his valuable remarks concerning the composition of this paper.

Received 20th November, 1958.

REFERENCES

1) Hulst, H. C. van de, Physica **15** (1949) 740.
2) Hulst, H. C. van de, Light Scattering by Small Particles, John Wiley and Sons, New York, 1957, p. 31.
3) Levine, H. and J. Schwinger, Comm. Pure Appl. Math. **3** (1950) 355.
4) Storer, J. E. and J. Sevick, J. Appl. Phys. **25** (1954) 369.
5) Jones, D. S., Phil. Mag. (7) **46** (1955) 957.
6) Kronig, R., Ned. Tijdschr. Natuurk. **18** (1952) 186.
7) Feenberg, E., Phys. Rev. **40** (1932) 40.
8) Lax, M., Phys. Rev. **78** (1950) 306.
9) Wilcox, C. H., Comm. Pure Appl. Math. **9** (1956) 115.
10) Bouwkamp, C. J., Diffraction Theory, Repts. Progr. Phys. **17** (1954) 35–100, p. 57.
11) Stratton, J. A., Electromagnetic Theory, McGraw-Hill Book Company, New York, 1941, p. 137.
12) Hulst, H. C. van de, ref. 2, p. 13.
13) Wilcox, C. H., Proc. Amer. Math. Soc. **7** (1956) 271.
14) Levine, H. and J. Schwinger, Phys. Rev. **74** (1948) 958.

ANALYTIC SUBJECT INDEX

page

Antenna theory, Induction by an oscillating magnetic dipole over a two layer ground — J. R. Wait 73
–, On the calculations of transverse current loss in buried wire ground systems — J. R. Wait 81
–, On the theory of reflection from a wire grid parallel to an interface between homogeneous media II — J. R. Wait 355
–, Calculated patterns of slotted elliptic-cylinder antennas — J. R. Wait and W. E. Mientka 449

Counters, The gasdischarge mechanism for the argon-alcohol proportional counter — K. van Duuren and G. J. Sizoo 379
–, Measurements on halogen quenched counters — D. H. le Croissette 409

Electrical breakdown, Aspects of electrical breakdown of liquid insulating material I — J. A. Kok and M. M. G. Corbey 257
Electrical networks, Note on the reciprocity theorem for electrical systems — V. Frank and H. Højgaard Jensen 145

page

Electrical recording, The influence of modulation on the recording of resonance phenomena — F. Bruin and D. van Ladensteyn 270
Electromagnetic field, The electromagnetic theory of the spherical Luneberg lens — C. T. Tai. 113
–, see **antenna theory, extinction, scattering**
Electron interaction, see **reflectivity**
Extinction, On the plane wave extinction cross-section of an obstacle — A. T. de Hoop 463

Faraday effect, New calculations on the Faraday effect in wave guides — A. P. van Gelder, A. M. de Graaf and R. Kronig 441
Ferrites, Ferromagnetic resonance in polycrystalline ferrites — J. Snieder 185

Hall effect, Hall coefficient of technically pure metals from 80°K to 800°K — V. Frank. 41

Magnetic resonance absorption, Magnetic absorption phenomena in germanium at low temperatures —

page

L. van Gerven, A. van Itterbeek and L. de Laet 345

Magnetic focusing, Theory of the aberrations in the focusing properties of a magnetic field with one plane of symmetry — A. J. H. Boerboom 52

Magnetic susceptibility, Measurements on the magnetic susceptibilities of Ag-Mn and Cu-Mn alloys — A. van Itterbeek, R. Pollentier and W. Peelaers 329

Magnetometer, A null-coil magnetometer — P. Jongenburger and C. W. Berghout 366

Mathematical methods, Some generalization of the Schwarz-Christoffel mapping formula — L. C. Woods . . . 89

–, Certain two-dimensional solutions to Poisson's equation — G. Power and H. L. W. Jackson 249

Microwaves, Two capacitive windows in a rectangular wave guide — H. Bosma 131

–, Transmission in a rectangular waveguide loaded with an arbitrary number of capacitive screens — F. A. W. van den Burg 153

–, see Faraday effect, ferrites

Neutrons, detection of, New scintillators for the detection of thermal neutrons — Letter to the editor — G. Thielens. 87

Photoconductivity, A diagram for the description of photoconductivity — H. J. Dirksen 400

page

Radioactivity, Increased atmospheric radioactivity in the Netherlands after the Windscale accident — Letter to the editor — Joh. Blok, R. H. Dekker and C. J. H. Lock. 150

Reciprocity theorem, see electrical networks

Reflectivity, On the possible influence of electron interaction on the reflectivity of metals — C. W. Benthem . . 275

Scattering, Far field scattering from bodies of revolution — K. M. Siegel. 293

–, Scattering of a plane monochromatic wave by a system of strips — K. Særmark. . . 417

Schlieren method, A simple method for photographing transparent objects — Addendum — L. J. F. Broer, A. Deeleman and J. A. Rietdijk 184

Scintillators, see neutrons, detection of

Skin effect, The theory of the anomalous skin effect in metals for obliquely incident radiation — J. G. Collins . . 1

Transistors, Equivalent base resistance of point-contact transistors — F. J. Young. 361

–, *Erratum* — Equivalent base resistance of point-contact transistors — F. J. Young. 462

Vacuum technique, On the measurements of speed of a vacuum pump — N. A. Florescu. 63

X-ray diffraction, Particle statistics in X-ray diffractometry. I. General theory — P. M. de Wolff 102

page
X-ray microscopy, A focusing aid for the X-ray projection microscope — Ong Sing Poen and J. B. le Poole. 233
–, A critical comparison of projection microradiography and the 2 X method — Ong Sing Poen and J. B. le Poole . . . 265
–, The comparative merits of different methods of microradiography — V. E. Cosslett. 338
–, Comments on V. E. Cosslett: The comparative merits of different methods of microradiography — Ong Sing Poen and J. B. le Poole 343

PERIODICAL